1984

Summer Undergraduate

Research Fellowships

SURF

Annual Report

California Institute of Technology

Pasadena, California 91125

October 13, 1984

SURF Annual Report
Prepared by
Carolyn Merkel
California Institute of Technology
SURF Office
Room 3 Dabney 101-40
Pasadena, California 91125

Table of Contents

Biology

Chemistry and Chemical Engineering

Engineering and Applied Science

Geological and Planetary Sciences

Humanities and Social Sciences

Physics, Mathematics, and Astronomy

JPL

Off-Campus Projects

Brief Background of SURF

The Summer Undergraduate Research Fellowships program at Caltech began in 1979 to encourage creative research, to promote interaction between undergraduates and faculty, and to improve the undergraduate program. This program was the brainchild of Dr. Fredrick H. Shair, Professor of Chemical Engineering, and Dr. Harold Zirin, Professor of Astrophysics and Director of Big Bear Solar Observatory. The program has grown from 18 students in 1979 to 106 students in 1984.

A student applies for SURF by developing a research proposal in collaboration with a faculty member who has agreed to sponsor him or her. The proposals are reviewed by a committee of faculty members familiar with the fields represented. Awards are made on the basis of perceived merit and on the enthusiasm of the sponsor and the student for the project.

SURF students are expected to work full time for ten weeks during the summer to complete their projects. At the end of the ten weeks each student submits a report of his or her work. In addition to providing an enjoyable learning opportunity, the tutorial relationship between student and sponsor aids in the development of judgment. The program culminates in SURF Seminar Day when each student has the opportunity to present a fifteen-minute oral summary of his or her work to other students, faculty, and visitors.

In 1984 each student was paid $2800. Room, board, and personal expenses are supported by this. In addition, students receiving financial aid from Caltech are required to save a portion of their summer earnings toward their next year's tuition. Expenses of supplies, equipment, computing, travel, etc., are paid by the faculty sponsor. This action on the part of the Caltech faculty is another indication of their commitment to the training and development of young scientists and engineers.

In January, 1984, a SURF Administrative Committee was appointed by President Goldberger. The Committee (1) plans and administers the SURF program; and (2) provides the administration with advice on the long-term planning and development of the SURF program and possible related programs which may evolve.

The SURF Board is a voluntary support organization consisting of individuals who are dedicated to the educational values of undergraduate research at Caltech and who, through their advice, encouragement, and financial support, contribute to the vitality, continuity and effectiveness of the SURF program. The members of the SURF Board, under the leadership of a Chairman and the Chairman of the SURF Administrative Committee, participate in activities of SURF such as the SURF Noon Seminars, SURF Seminar Day, and the annual SURF Recognition Banquet at The Athenaeum. The Board conducts promotional and fund raising activities in cooperation with the Institute's Development Office.

Acknowledgements

We wish to acknowledge with great appreciation the help of the following people:

Kaye Adler for her assistance with the SURF Seminar Series and with SURF Seminar Day.

Ed Baum for his leadership, dedication and successful efforts in helping to develop SURF.

Don Browning and **Dini Shotwell** for their work on all the financial aspects of SURF.

Jean E. Cass for conducting Communications Workshops for the SURF students and for her cheerful and enthusiastic administrative support.

Ruth Gilmore and the Financial Aid Office for their help in processing College Work Study funds for SURF.

Debbie Shair for her assistance in the SURF Office throughout the program.

SURF Board

Mr. Samuel P. Krown, Chairman
Dr. Fredrick H. Shair, Vice Chairman
Mr. Arthur Adams
Dr. Marcella Bonsall
Mrs. Hannah Bradley
Mr. Theodore Coleman
Mr. Hugh Colvin
Mr. Joseph Cullen,
Carnation Research Laboratory
Mr. Joseph Earl
The O.K. Earl Corporation
Dr. Norman Gjostein
Ford Motor Company
Mr. Richard Hayman
Dr. Paul Hu
IBM Corporation
Dr. Laird Johnston
General Motors
Mrs. Joanna Muir
Mr. Douglas Nickerson
Mrs. Elizabeth Nickerson
Mr. Robert Shafer
Mr. Loyd Sigmon

SURF Administrative Committee

Dr. Fredrick H. Shair, Chairman
Dr. Charles D. Babcock
Dr. Chris E. Brennen
Mr. George L. Browning*
Dr. Bruce E. Cain
Dr. Glen R. Cass
Dr. Terry Cole
Dr. Richard A. Dean
Ms. Ruth W. Gilmore
Dr. Robert E. Ireland
Dr. Steven E. Koonin
Ms. Susan C. Pearce*
Dr. Thomas A. Tombrello
Dr. David C. Van Essen
Ms. Chris Wood*
Dr. Yuk L. Yung

Student Representatives

Aaron Roodman
Tad White
Minami Yoda

* - Ex Officio

Corporate Sponsors

AMETEK, Inc.
Carnation Research Laboratory
Ford Motor Company
General Motors Corporation
IBM Corporation
The O.K. Earl Corporation

Individual Sponsors

Mr. Arthur Adams
Mr. Royal Akin
Mrs. Hannah Bradley
Mr. Richard Burke
Mr. Richard Hayman
Mr. George Jagels
Mr. and Mrs. Samuel Krown
Dr. Jack Leonard
Mr. Ross McCollum
Mrs. Joanna Muir
Mr. and Mrs. Douglas Nickerson
Mr. and Mrs. Robert Shafer
Dr. Alan Vetter
Mr. Victor Veysey
Dr. George Webster

SURF Noon Seminar Speakers

Arden L. Albee, Professor of Geology, Chief Scientist, JPL
Sally J. Asmundson, Director, Career Development Center
Roger D.Blandford, Professor of Theoretical Astrophysics
Bruce E. Cain, Associate Professor of Political Science
Paul Carroad, Carnation Research Laboratory
Fred E.C. Culick, Professor of Applied Physics and Jet Propulsion
Peter B. Dervan, Professor of Chemistry
Robert Durbeck, IBM Corporation
Norman A. Gjostein, Ford Motor Company
Norman H. Horowitz, Professor of Biology, Emeritus
Hans W. Liepmann, Theodore von Karman Professor of Aeronautics
Thomas R. McDonough, Lecturer in Engineering
John D. Roberts, Institute Professor of Chemistry
George R. Rossman, Associate Professor of Mineralogy
Gerald D. Skellenger, General Motors Research Laboratories
Shirley Thomas, Technical Writer and Consultant
William M. Whitney, Manager, Information Systems Research Section, JPL
Barbara J. Wold, Assistant Professr of Biology

SURF Roundtable Leaders

Dr. Robert Durbeck, Research Technical Staff Manager, IBM Reseach Division
Mr. Richard Hayman, Chairman and Chief Executive Officer, Haskel, Inc.
Mr. Al Schaff, Vice President, Electronics Development, AMETEK, Inc.
Mr. Robert L. Shafer, Certified Management Consultant
Mr. Victor Veysey, Director Emeritus, Industrial Relations Center
Mr. Robert Zurbach, Vice President (Retired), Reliance Steel

Students and Sponsors

STUDENT	YR	OP	SPONSOR
1. Acevedo, Manuel-Ruiz	Sr	EAS	A. Roshko, Professor of Aeronautics M.Hernan, Member of the Technical Staff, Thermochemical and Biological Systems (JPL)
2. Adams, Mark S.	Sr	Eng	G.R. Cass, Assistant Professor of Environmental Engineering
3. Ashcroft, Peter D. (Ford-SURF)	Jr	APh	A. Johnston,Group Supervisor, Optoelectronics Systems Technical Group (JPL)
4. Asthana, Praveen (IBM-SURF)	Sr	EE	T. Strand, (IBM)
5. Bailey, Gregory C. (IBM-SURF)	So	APh	G.C. Fox, Dean for Educational Computing and Professor of Theoretical Physics
6. Bellare, Mihir	Sr	Eng	F.B. Thompson, Professor of Applied Philosophy and Computer Science
7. Bronikowski, Michael J.	Jr	Ch/Ma	W.P. Schaefer, Senior Research Associate in Chemistry
8. Buchholz, Donald A.	Sr	ChE	M.R. Hoffmann, Associate Professor of Environmental Engineering Science
9. Buffet, Marc	Sr	Ph	D.H. Fender, Professor of Biology and Applied Science/ J. Hestenes, Group Supervisor, Bioinformation Sciences (JPL)
10. Bures, Clea	So	Ph/ME	A. Harris, Group Supervisor, Planetary Geophysics Group (JPL)
11. Burnett, Gregory A.	Sr	Ph	G.E. Danielson, Member of the Professional Staff
12. Butler, William H.	Sr	Ph	B. Tsurutani, Member of the Technical Staff, Inner Planetary Fields Group (JPL)
13. Carter, Margaret C.	Jr	Eng	W.J. North, Professor of Environmental Science
14. Chan, Susanna M.	Sr	Bi	B.J. Wold, Assistant Professor of Biology
15. Chang, Cathy	So	Ch	T.J. Ahrens, Professor of Geophysics
16. Chang, Dara J.	Jr	Eng	R. Stanton, Experiment Manager, ASTROS Star Tracker (JPL)

17. Chang, Wen Teh	Sr	EE	M.J.P. Van Rossum, IBM Research Fellow in Applied Physics
18. Chen, Diane L.	Jr		S.J. Rose III, Research Fellow in Biology
19. Chen, Jim C.	Sr	EE	B.E. Cain, Associate Professor of Political Science
20. Chen, Yi-Hong (Ford-SURF)	Sr	APh	W.L. Johnson, Associate Professor of Materials Science
21. Chew, Phye Keng (Larry) (GM-SURF)	Sr	Eng	F.E.C. Culick, Professor of Applied Physics and Jet Propulsion
22. Cho, Peter L.	So	Ph	I-J. Sackmann, Faculty Associate in Physics
23. Choy, Tammy L.	Jr	EE	D. Psaltis, Assistant Professor of Electrical Engineering
24. Chung, Young Hoon	Sr	EE	A. Yariv, Thomas G. Myers Professor of Electrical Engineering and Professor of Applied Physics
25. Crawford, Glen D.	Sr	Ph	D.J. Stevenson, Associate Professor of Planetary Science
26. Crawford, Michael D.	Jr	Ph	J.R. Mould, Associate Professor of Astronomy
27. Cuellar, Edward Louis	Sr	Ph	R.D. Blandford, Professor of Theoretical Astrophysics
28. Cummings, Lisa A.	Jr	Eng	G.R. Cass, Assistant Professor of Environmental Engineering
29. Doan, Larry R. (GM-SURF)	Jr	EE	W. Read, Group Supervisor, Electronic Packaging Engineering Group (JPL)
30. Douma, D. James (Ford-SURF)	So		M. Morari, Professor of Chemical Engineering
31. Dunn, James	Sr	ChE	C. Colton, MIT
32. Eddy, Sean R.	Jr	Bi	C.M. Rice, Research Fellow in Biology
33. Fatland, Dennis R.	Jr	Ph	P.K. Haff, Senior Research Associate in Physics
34. Fernando, Timothy (GM-SURF)	Sr	Ma	A.S. Kechris, Professor of Mathematics
35. Feuerabendt, Stefan	Sr	Eng	S. Sander, Member of the Technical Staff, Molecular Physics and Chemistry Section (JPL)

36. Garren, Hideki	Jr	Bi	J.M. Allman, Associate Professor of Biology
37. Gee, Allen (IBM-SURF)	So	Ph	G.C. Fox, Dean for Educational Computing and Professor of Theoretical Physics
38. George, Edward	Sr	Bi	E.H. Davidson, Norman Chandler Professor of Cell Biology
39. Ghosh, Anirvan	Sr	Ph	T. Reese, Woods Hole.
40. Ghosh, Supriya (IBM-SURF)	Jr	Eng	C.E. Brennen, Professor of Mechanical Engineering; Master of Student Houses
41. Gibbs, George G.	Jr	Bi	S.I. Chan, Professor of Chemical Physics and Biophysical Chemistry
42. Goldstein, Simon	Jr	ChE	G.R. Gavalas, Professor of Chemical Engineering
43. Gould, Timothy R. (Veysey-SURF)	Sr	Eng	J.J. McGann, Doris and Henry Dreyfuss Professor of the Humanities
44. Greeley, Burnham H. (IBM-SURF)	Sr	Ph	M.H. Shapiro, Visiting Associate in Physics
45. Grossman, Scott A.	Jr	Ph	C.A. Barnes, Professor of Physics
46. Haase, Paul C.	Sr	Ge	K.E. Sieh, Associate Professor of Geology
47. Hernandez, Kevin	Jr	APh	J. Pine, Professor of Physics
48. Houde, John F. (Akin-SURF)	Sr	EE	D.C. Van Essen, Associate Professor of Biology
49. Hua, Nhi G.	So	Ch	W.P. Schaefer, Senior Research Associate in Chemistry
50. Hudson, Scott	Sr	Ph	W. Whaling, Professor of Physics
51. Hughes, Keith	Sr	Eng	F.B. Thompson, Professor of Applied Philosophy and Computer Science
52. Jungman, Gerard J.	So	Ph	J. Slavin, Member of the Technical Staff, Space Physics Section (JPL)
53. Kan, Pui-Tak (IBM-SURF)	Jr	Ma	R.J. McEliece, Professor of Electrical Engineering
54. Kao, Ting-Lin	Jr	Ch	H.B. Gray, Arnold O. Beckman Professor of Chemistry
55. Kawamoto, Eric H.	Sr	Ph	T.A. Tombrello, Professor of Physics

56.	Kegel, Daniel R.	Sr	Eng	H.A. Lester, Professor of Biology
57.	Kinney, Rodney M.	Sr	Ph	S. Solomon, Bantrell Research Fellow in Theoretical Physics
58.	Konopka, Peter F.	Jr	APh	S. Zweben, Senior Research Fellow in Applied Physics
59.	Kovalik, Joseph M.	Jr	Ph	J.L. Kirschvink, Assistant Professor of Geobiology
60.	Krishnan, Santosh N.	Jr	Bi	E. Rothenberg, Assistant Professor of Biology
61.	Kuo, Stanley D.	Sr	Ph	A. Yariv, Thomas G. Myers Professor of Electrical Engineering and Professor of Applied Physics
62.	Lewenberg, Adam H.	Jr	Ma	T.M. Apostol, Professor of Mathematics
63.	Lewicki, Scott A.	So	Ph	S.W. Otto, Research Fellow in Theoretical Physics/ N.P. Warner, Weingart Fellow in Theoretical Physics and Lecturer
64.	Mak, Raymond	Jr	Eng	T.Y.T Wu, Professor of Engineering Science
65.	Marumoto, Alan K.	Jr	Ch	S.I. Chan, Professor of Chemical Physics and Biophysical Chemistry
66.	McGowan, John F.	Sr	Ph	R.W. Oliver, Professor of Economics
67.	Megeath, Samuel Thomas	Jr	Ph	T.A. Prince, Assistant Professor of Physics
68.	Mitha, Salman	Jr	Ph	P.K. Haff, Senior Research Associate in Physics
69.	Morrison, John H.	Sr	Ph	J.M. Lo Secco, Assistant Professor of Physics
70.	Newman, William H.	So	Bi	C.M. Rice, Research Fellow in Biology
71.	Nguyen, Truong Quang (Ford-SURF)	Sr	EE	P.P. Vaidyanathan, Assistant Professor of Electrical Engineering
72.	Nolan, Michael C.	Sr	Ch	J.E. Bercaw, Professor of Chemistry
73.	Pata, Janice D.	Jr	Bi	C.M. Rice, Research Fellow in Biology
74.	Peterson, Karla A.	Sr	APh	J.L. Kirschvink, Assistant Professor of Geobiology
75.	Phoniadakis, Mark	So	ChE	G.N. Stephanopoulos, Associate Professor of Chemical Engineering

76. Pitt, Mark L.	Sr	Ph	C.A. Barnes, Professor of Physics
77. Pitts, Stephen	Sr	Eng	F.B. Thompson, Professor of Applied Philosophy and Computer Science
78. Reel, Charles C.	Sr	Bi	B.J. Wold, Assistant Professor of Biology
79. Rigler, Michael A.	Jr	Ph	B. Thomas, Member of Technical Staff, Space Physics (JPL)
80. Roodman, Aaron J.	Sr	Ph	C.A. Barnes, Professor of Physics
81. Sakai, Janice F.	Jr	Bi	J.L. Campbell, Associate Professor of Chemistry
82. Santoro, Sarah J.	Jr	Eng	D.E. Coles, Professor of Aeronautics
83. Schwartz, Kurt M. (IBM-SURF)	Jr	Eng	P.P. Vaidyanathan, Assistant Professor of Electrical Engineering
84. Sharpe, William D.	Sr	Ch	D.A. Dougherty, Assistant Professor of Chemistry
85. Shin,Se Jung	Jr	Bi	E.G. Strauss, Senior Research Fellow in Biology
86. Solberg, Teresa C.	Sr	Ch	G.R. Rossman, Professor of Mineralogy
87. St. Jacques, Jeannine-M (IBM-SURF)	Sr	Ma	Y.S. Abu-Mostafa, Assistant Professor of Electrical Engineering and Computer Science
88. Tiller, Christine L.	Sr	Eng	M.R. Hoffmann, Associate Professor of Environmental Engineering Science
89. Toy, Anna	Jr	Ch	P.B. Dervan, Professor of Chemistry
90. Tsai, Brian J	Jr	ChE	F.H. Shair, Professor of Chemical Engineering
91. Tyebkhan, Yosufi M.	Jr	Ph	D.J. Stevenson, Associate Professor of Planetary Science
92. Valenti, Jeffrey A.	So	Ay	E. Smith, Group Supervisor/Research Scientist, Space Physics Group (JPL)
93. Wall, John B.	Sr	Bi	M.B. Kennedy, Associate Professor of Biology
94. Watanabe Ryoji (IBM-SURF)	Jr	Ph	G.C. Fox, Dean of Educational Computing and Professor of Theoretical Physics
95. White, Tad P. (Akin-SURF)	Sr	Ma	P.J. Henninger, Research Fellow in Biology
96. Wilson, Kevin E.	Jr	Ph	R.D. McKeown, Assistant Professor of Physics

97. Wilson, Robin K.	Jr	Bi	E.M. Meyerowitz, Assistant Professor of Biology
98. Wolf, Sven A. (Ford-SURF)	Sr	AMa	J. Chen, Member of the Technical Staff, Structures and Dynamics Technology Group (JPL)
99. Workman, Thomas W.	Jr	Ph	P.M. Bellan, Associate Professor of Applied Physics
100. Wu, Mingjim	Sr	Ch	J.H. Richards, Professor of Organic Chemistry
101. Yo, Christopher	Sr	Bi	D.C. Van Essen, Associate Professor of Biology
102. Yoda, Minami	Sr	Eng	H.W. Liepmann, Theodore von Karman Professor of Aeronautics
103. Young, Paul M. (GM-SURF)	Jr	APh	E.E. Zukoski, Professor of Jet Propulsion and Mechanical Engineering
104. Yun, Min Su	Jr	Ph	N.Z. Scoville, Professor of Astronomy
105. Zaritsky, Dennis F.	Jr	Ph	K.Y. Lo, Assistant Professor of Radio Astronomy
106. Zupke, Craig A.	Sr	ChE	F.H. Shair, Professor of Chemical Engineering

SURF Seminar Day Schedule
Saturday, October 13, 1984

12:00 - 1:00	Buffet Luncheon in Dabney Garden
1:25 - 4:30	SURF Student Presentations (See Schedule Below)
4:30 - 5:30	SURF Reception Home of President and Mrs. Goldberger 415 South Hill, Pasadena

Session 1
Room 102 Spalding
Biology
Chairman: Charles M. Rice
Research Fellow in Biology

1:25	Introduction	Dr. Rice
1:30-1:50	Neural Correlates of Preceptual Rivalry (Sponsor: Dr. J. Allman)	Hideki Garren
1:50-2:10	The Kinetics of Ion Channels in Neuronal Membranes (Sponsor: Dr. H. Lester)	Daniel R. Kegel
2:10-2:30	Connections and Functional Organization of the Middle Superior Temporal Visual Area (MST) in the Macaque Monkey (Sponsor: Dr. D. Van Essen)	John F. Houde (Akin-SURF)
2:30-2:50	Task Difficulty Induces Increasing Right Ear Advantage in Normals (Sponsor: Dr. P. Henninger)	Tad P. White (Akin-SURF)
2:50-3:10	A Technique for Elucidating the Time Course of Polyinnervation Elimination in Fast and Slow Twitch Muscle Fibers (Sponsor: Dr. D. Van Essen)	Christopher Yo
3:10-3:30	Construction of a Plasmid Containing the Yellow Fever Virus Genome (Sponsor: Dr. C. Rice)	Sean R. Eddy
3:30-3:50	Sequencing Antigenic Mutations of Sindbis Viris (Sponsor: Dr. C. Rice)	William H. Newman
3:50-4:10	Preliminary Characterization of Yellow Fever Virus Structural and Nonstructural Proteins (Sponsor: Dr. C. Rice)	Janice D. Pata
4:10-4:30	Sequencing of Viral DNA (Sponsor: Dr. E. Strauss)	Se Jung Shin

Session 2

Room 104 Spalding
Biology
Chairman: Samuel J. Rose III
Research Fellow in Biology

1:25	Introduction	Dr. Rose
1:30-1:50	Oncogene Expression (Sponsor: Dr. B. Wold)	Susanna M. Chan
1:50-2:10	Genetic Recombination in Animal Cells (Sponsor: Dr. B. Wold)	Charles C. Reel
2:10-2:30	Cloning of Myosin Heavy Chain Gene from Stronglyocentrotus Purpuratus (Sponsor: Dr. S. Rose)	Diane L. Chen
2:30-2:50	Transcription in Lampbrush Chromosomes in Xenopus Levels (Sponsor: Dr. E. Davidson)	Edward George
2:50-3:10	Expression of IL-2 Receptor on Thymocytes: Evidence for IL-2 Independent Thymic Proliferation (Sponsor: Dr. E. Rothenberg)	Santosh Krishnan
3:10-3:30	Type II Calcium-Calmodulin Dependent Protein Kinase in Drosophila (Sponsor: Dr. M. Kennedy)	John B. Wall
3:30-3:50	The Highly Repetitive DNA of <u>Arabidopsis thaliana</u> (Sponsor: Dr. E. Meyerowitz)	Robin K. Wilson
3:50-4:10	Growth of Sympathetic Neurons in Culture (Sponsor: Dr. J. Pine)	Kevin Hernandez
4:10-4:30	Effect of Transmitter Release on Membrane Morphology of Squid Synaptosomes (Sponsor: Dr. T. Reese, Woods Hole Marine Laboratory)	Anirvan Ghosh

Session 3

Room 106 Spalding Laboratory
Chemistry
Chairman: Peter B. Dervan
Professor of Chemistry

1:25	Introduction	Professor Dervan
1:30–1:50	The Crystal Structure of a Zirconium Ketene Dimer (Sponsor: Dr. W. Schaefer)	Michael J. Bronikowski
1:50–2:10	X-ray Crystallography: The Structure of the W_6I_{14} Dianon (Sponsor: Dr. W. Schaefer)	Nhi G. Hua
2:10–2:30	The Upscaling of the Procedures to Reconstitute Single Cytochrome C Oxidase Dimer Vesicles (Sponsor: Dr. S. Chan)	Alan K. Marumoto
2:30–2:50	Development of Strategy for Solubilizing Water-Insoluble Proteins (Sponsor: Dr. S. Chan)	George G. Gibbs (Carnation-SURF)
2:50–3:10	MPE·Fe (II) of Echinomycin Binding to Native DNA (Sponsor: Dr. P. Dervan)	Anna Toy
3:10–3:30	Synthesis and Study of $(NH_3)_5Ru(His\text{-}113)^{3+}$ myoglobin(Co^{2+}) (Sponsor: Dr. H. Gray)	Ting-Lin Kao
3:30–3:50	Substituent Effects on the Rate of Addition of Para-Substituted Styrenes to Permethylscandocene Methyl Complex (Sponsor: Dr. J. Bercaw)	Michael C. Nolan
3:50–4:10	Elucidation of the Mechanism of Rop Protein Inhibition of ColE1 Plasmid Replication in E Coli (Sponsor: Dr. J. Campbell)	Janice F. Sakai
4:10–4:30	The Date Analysis of the IO Radical Self-Reaction (Sponsor: Dr. S. Sander)	Stefan Feuerabendt

Session 4

Room 113 Spalding Laboratory
Chemistry, Mechanical Engineering, Aeronautics
Chairman: Christopher E. Brennen
Professor of Mechanical Engineering

1:25	Introduction	Professor Brennen
1:30–1:50	Designing the Azurin Gene and Site-Saturation as a Useful Method in the Study of Proteins (Sponsor: Dr. J. Richards)	Mingjim Wu
1:50–2:10	The Development of a System for Measuring Temperatures Remotely in Freely Moving Bodies (Sponsor: Dr. F. Shair)	Brian J. Tsai (Carnation-SURF)
2:10–2:30	Size Distributions of Immune Complexes (Sponsor: Dr. C. Colton, MIT)	James Dunn
2:30–2:50	The Design and Synthesis of Biominetic Chiral Cavities (Sponsor: Dr. D. Dougherty)	William D. Sharpe
2:50–3:10	Efficient Techniques Permitting the Increase of the Flow Rate in a Continuous Fermentor (Sponsor: Dr. G. Stephanopoulos)	Mark Phoniadakis
3:10–3:30	Granular Flow Mechanics: An Experimental Study on the Granular Flow of Sand Particles (Sponsor: Dr. C. Brennen)	Supriya Ghosh (IBM-SURF)
3:30–3:50	Non-Instrusive Measurement of Particle Loading in Flow Through Pipes (Sponsor: Dr. F. Culick)	Phye Keng (Larry) Chew (GM-SURF)
3:50–4:10	Free-Surface Phenomena Under Low and Zero Gravity (Sponsor: Dr. D. Coles)	Sarah J. Santoro
4:10–4:30	Second Sound Shocks at a Superfluid and Gaseous Helium II Interface (Sponsor: Dr. H. Liepmann)	Minami Yoda

Session 5

Room 111 Dabney
ME, Environmental Engineering Science,
Social Science
Chairman: Michael R. Hoffmann
Associate Professor of Environmental Engineering Science

1:25	Introduction	Professor Hoffmann
1:30–1:50	Runaway Solitary Waves Generated by a Submerged Moving Disturbance in Homogeneous and Stratified Fluids (Sponsor: Dr. T. Wu)	Raymond Yu Shun Mak
1:50–2:10	Effects from Nutrient Pulsing and PCB Exposures on Growth by *Macrocystis* Gametophytes (Sponsor: Dr. W. North)	Margaret C. Carter
2:10–2:30	Characterization of Sulfur–Aldehyde Nitrogen Adducts in Hydromedia (Sponsor: Dr. M. Hoffmann)	Christine L. Tiller
2:30–2:50	Dew Chemistry in Pasadena (Sponsor: Dr. M. Hoffmann)	Donald A. Buchholz (Adams–SURF)
2:50–3:10	A Literature Review on the Effects of Air Pollutants on Works of Art (Sponsor: Dr. G. Cass)	Lisa Cummings (Adams–SURF)
3:10–3:30	Control of the Exposure of Works of Art to Photochemical Smog (Sponsor: Dr. G. Cass)	Mark S. Adams (IBM–SURF)
3:30–3:50	Floating Exchange Rates and International Trade (Sponsor: Dr. R. Oliver)	John F. McGowan (Adams–SURF)
3:50–4:10	The Impact of Video Technology on the Film Industry (Sponsor: Dr. J. McGann)	Timothy R. Gould (Veysey–SURF)
4:10–4:30	Chinese and Other Asians in California -- The Political Roles (Sponsor: Dr. B. Cain)	Jim C. Chen

Session 6

Room 115 Dabney Hall
Engineering
Chairman: Demetri Psaltis
Assistant Professor of Electrical Engineering

1:25	Introduction	Professor Psaltis
1:30–2:50	Implementation Techniques of FIR and IIR Filters (Sponsor: Dr. P. Vaidyanathan)	Truong Q. Nguyen (Ford-SURF)
2:10–2:30	Some Models of Neural Memory Network (Sponsor: Dr. R. McEliece)	Pui-Tak Kan (IBM-SURF)
2:30–2:50	An Upper Bound to the Number of Stable States of the Hopfield Model (Sponsor: Dr. Y. Abu-Mostafa)	Jeannine-M. St. Jacques (IBM-SURF)
2:50–3:10	Spatial Characteristics and Sensitivity of the Photorefractive Incoherent-to-Coherent Optical Converter (Sponsor: Dr. D. Psaltis)	Tammy L. Choy
3:10–3:30	Experimental Verification of Nonlinear Coupled Wave Theory for Photorefractive Medium (Sponsor: Dr. A. Yariv)	Young Hoon Chung
3:30–3:50	Photorefractive Crystal Time Response in Nonlinear Optics (Sponsor: Dr. A. Yariv)	Stanley D. Kuo
3:50–4:10	Waveform Time-Scale Stretching by Doppler Shift (Sponsor: Dr. P. Bellan)	Thomas W. Workman
4:10–4:30	Electrical Properties of MoSi$_2$ (Sponsor: Dr. M.Van Rossum)	Wen Teh Chang
1:30–1:50	The Spreading of Plane Salt Water Gravity Currents (Sponsor: Dr. E. Zukoski)	Paul M. Young (GM-SURF)

Session 7

Room 121 Dabney Hall
Geological and Planetary Sciences
Chairman: Yuk L. Yung
Associate Professor of Planetary Science

1:25	Introduction	Professor Yung
1:30–1:50	Biological Magnetometry and Magnetite in Poisonous Newts and Blue Sharks (Sponsor: Dr. J. Kirschvink)	Karla A. Peterson (Adams-SURF)
1:50–2:10	A Search for Gravitational Lenses (Sponsor: Dr. E. Danielson)	Gregory A. Burnett
2:10–2:30	The Shock Pyrometry Experiments of Iron (Sponsor: Dr. T. Ahrens)	Cathy Chang
2:30–2:50	Resurfacing of Europa with Water (Sponsor: Dr. D. Stevenson)	Glen D. Crawford
2:50–3:10	An Experimental Search for Bound GUT Monopoles Using a SQUID Magnetometer (Sponsor: Dr. J. Kirschvink)	Joseph M. Kovalik
3:10–3:30	A Laboratory Study of Ti^{II}–Ti^{III} Intra-Valent Charge Transfer Systems (Sponsor: Dr. G. Rossman)	Teresa C. Solberg
3:30–3:50	Formation of the Earth's Moon through Large Body Impact (Sponsor: Dr. D. Stevenson)	Yosufi M. Tyebkhan
3:50–4:10	Distribution of Late Holocene Tephra of Mono Craters (Sponsor: Dr. K. Smith)	Paul C. Haase

Session 8

Room 125 Baxter Hall
Physics
Chairman: Ward Whaling
Professor of Physics

1:25	Introduction	Professor Whaling
1:30–1:50	A Saltation Simulation (Sponsor: Dr. P. Haff)	Dennis Fatland
1:50–2:10	Model of a Mildly Relativistic Pair Plasma (Sponsor: Dr. R. Blandford)	Edward L. Cuellar
2:10–2:30	Small-angle X-ray Scattering Studies of the Structure of Latent Nuclear Damage Tracks in Dielectric Solids (Sponsor: Dr. T. Tombrello)	Eric H. Kawamoto
2:30–2:50	Splash Function for Discrete Particles (Sponsor: Dr. P. Haff)	Salman Mitha
2:50–3:10	Design of a Target Chamber for use in Isotope Separation (Sponsor: Dr. C. Barnes)	Scott A. Grossman
3:10–3:30	A Pair-Spectrometer Detector for $t(d,\gamma)^5He$ (Sponsor: Dr. C. Barnes)	Mark L. Pitt
3:30–3:50	An Ionization Detector for the Carbon Twelve (alpha, gamma) Oxygen Sixteen Recoil Spectrometer (Sponsor: Dr. C. Barnes)	Aaron J. Roodman
3:50–4:10	Fe (II) Level Populations in the Hollow Cathode Discharge (Sponsor: Dr. W. Whaling)	Raymond S. Hudson
4:10–4:30	QCD, Lattice, Monte Carlo, Instantons (Sponsor: Dr. S. Solomon)	Rodney M. Kinney

Session 9

Room 127 Baxter Hall
Physics, Mathematics, and Astronomy
Chairman: Jeremy R. Mould
Associate Professor of Astronomy

1:25	Introduction	Professor Mould
1:30–1:50	Neutrino Background and Data Trackfit in Proton Decay (Sponsor: Dr. J. LoSecco)	John H. Morrison
1:50–2:10	Experimental Search for Fractional Charges Produced by Relativisitc Heavy-Ion Collisions (Sponsor: Dr. R. McKeown)	Kevin E. Wilson
2:10–2:30	Positive Elementary Induction on Finite Fields and Finite Cyclic Groups (Sponsor: Dr. A. Kechris)	Timothy Fernando (GM-SURF)
2:30–2:50	The Luminosity Function of the Coma Cluster and the Color Gradient (Sponsor: Dr. J. Mould)	Michael D. Crawford
2:50–3:10	Galaxy Simulation with Concurrent Processors (Sponsor: Dr. S. Otto/Dr. N. Warner)	Scott A. Lewicki
3:10–3:30	Study of Extragalactic HI and CO in IRAS Galaxies (Sponsor: Dr. N. Scoville)	Min Su Yun
3:30–3:50	Evidence for Non-Axisymmetric Nuclear Bulges in Spiral Galaxies (Sponsor: Dr. K.Y. Lo)	Dennis F. Zaritsky
3:50–4:10	A Computer Graphics Representation of Stellar Nuclear Burning Processes (Sponsor: Dr. J. Sackmann)	Peter L. Cho
4:10–4:30	Obtaining Pictures of High-Speed Tokamak Fluctuations (Sponsor: Dr. S. Zweben)	Peter F. Konopka

Session 10
Room 128 Baxter Hall
JPL Projects
Chairman: Terry Cole
Senior Research Associate in Chemistry and Chemical Engineering
Chief Technologist, JPL

1:25	Introduction	Dr. Cole
1:30-1:50	A Handheld Emergency Locator Transmitter (Sponsor: Dr. W. Read)	Larry R. Doan (GM-SURF)
1:50-2:10	Survey of MHD Waves in Earth's Distant Magnetotail (Sponsor: Dr. B. Tsurutani)	William H. Butler
2:10-2:30	Guide Star Availability for the ASTROS Star Tracker (Sponsor: Dr. R. Stanton)	Dara J. Chang
2:30-2:50	Asteroid Photometry at Table Mountain Observatory (Sponsor: Dr. A. Harris)	Clementina Bures
2:50-3:10	The Relationship between Full Disk Solar Magnetic Flux and IMF Strength at 1 AU: An Overview (Sponsor: Dr. J. Slavin)	Gerard J. Jungman
3:10-3:30	Modeling Jupiter's Magnetospheric Using Pioneer Data: Polynomial Approximation of Dusk Dawn Current Systems (Sponsor: Dr. B. Thomas)	Michael A. Rigler
3:30-3:50	Solar Wind Characteristics Beyond 1 Astronomical Unit (Sponsor: Dr. E. Smith)	Jeffrey A. Valenti
3:50-4:10	A New Concept for the Passive and Active Control of Turbulent Shear Flows (Sponsor: Dr. A. Roshko/Dr. M. Hernan)	Manuel Acevedo-Ruiz
4:10-4:30	The Use of Piezoelectrics for Stiffness Modulation (Sponsor: Dr. J. Chen)	Sven A. Wolf (Ford-SURF)

Session 11

Room 210 Baxter Hall
Mathematics and Computer Science
Chairman: William L. Johnson
Associate Professor of Materials Science

1:25	Introduction	Professor Johnson
1:30–1:50	Thermodynamic Properties of a Real Gas (Sponsor: Dr. G. Gavalas)	Simon Goldstein
1:50–2:10	Development of Hardware and Software to Permit an Inexpensive Computer to be Used as a Storage Oscilloscope (Sponsor: Dr. F. Shair)	Craig A. Zupke
2:10–2:30	Filter Analysis System (Sponsor: Dr. P. Vaidyanathan)	Kurt M. Schwartz (IBM-SURF)
2:30–2:50	Development of Physics Software Using the Pascal Language (Sponsor: Dr. G. Fox)	Gregory C. Bailey (IBM-SURF)
2:50–3:10	Calculation of Eigenvalues of Symmetric Matrices Using the Caltech Nearest Neighbor Concurrent Processor (Sponsor: Dr. G. Fox)	Allen Gee (IBM-SURF)
3:10–3:30	A Study of Ising Lattice Gas Model for Materials of Long-Range and Short-Range Order via Computer Simulation (Sponsor: Dr. W. Johnson)	Yi-Hong Chen (Ford-SURF)
3:30–3:50	The Reconfigurable Distributed Processor: A Bus Based Approach (Sponsor: Dr. M. Morari)	D. James Douma (Ford-SURF)
3:50–4:10	Visula-1: A Softward Package for Interactive Three-Dimemsional Graphics on the IBM Personal Computer (Sponsor: Dr. G. Fox)	Ryoji Watanabe (IBM-SURF)
4:10–4:30	Specific Problems in Diophantine Analysis (Sponsor: Dr. T. Apostol)	Adam H. Lewenberg

Session 12

Room 218 Baxter Hall
Engineering and Computer Science
Chairman: Thomas A. Prince
Assistant Professor of Physics

1:25	Introduction	Professor Prince
1:30–1:50	Sputtering Simulations with the Caltech Concurrent Processor (Sponsor: Dr. M. Shapiro)	Burnham H. Greeley (IBM-SURF)
1:50–2:10	Computer Simulations of the Stability of a Balloon Suspended Telescope (Sponsor: Dr. T. Prince)	Samuel T. Megeath
2:10–2:30	An Overview of the Field of Optical Computing (Sponsor: Dr. A. Johnston)	Peter D. Ashcroft (Ford-SURF)
2:30–2:50	SQUID'S Tentacles Probe the Mind (Sponsor: Dr. D. Fender/Dr. J. Hestenes)	Marc Buffet
2:50–3:10	Experiments in Real Time Image Processing (Sponsor: Dr. T. Strand)	Praveen Asthana (IBM-SURF)
3:10–3:30	Implementing the Forms Package in ASK (Sponsor: Dr. F. Thompson)	Mihir Bellare (IBM-SURF)
3:30–3:50	Timing Comparisons Between a Pascal (Sponsor: Dr. F. Thompson)	Keith Hughes (IBM-SURF)
3:50–4:10	Assisting Borg Warner Corporation in the use of ASK (Sponsor: Dr. F. Thompson)	Stephen Pitts (Borg Warner-SURF)

Biology

POLYCATION TRANSFECTION OF TK RNA INTO L CELLS

Susanna Chan
Faculty Sponsor: Barbara Wold

ABSTRACT

Two polycations, ornithine and DEAE (diethylaminoethyl) dextran were used to mediate transfection of *in vitro* synthesized thymidine kinase (TK) RNA into fibroblast (L) cells. These transfections yielded a measurable amount of positive TK activity in LTK^- cells. Translation of this RNA *in vitro* yielded large quantities of protein as well. This technique, once optimized, will prove useful in elucidating the consequences of gene function at a cellular level.

INTRODUCTION

Currently with our vast array of biological techniques involving the use of restriction enzymes, simple physical methods for separating and visualizing DNA molecules, molecular cloning and DNA sequencing, we are able to deduce anatomical details of genes and chromosomes. We do not yet, however, have equal facility in deducing the consequences of protein production for a given gene or group of genes. My project has focused on the latter point by devising a technique to "assay" the biological activity of proteins whose corresponding genes have been cloned. One well-documented technique for introducing DNA or RNA back into cells is microinjection. Unfortunately, this approach is limited in that only a few cells can be injected with nucleic acid at a time and subsequent biochemical analyses are difficult to perform. An alternate route is to use polycation transfection where the above disadvantages are not present. My project centered around the use of polycations which augment the penetration of RNA into cells. The idea here is to introduce a specific, *in vitro* synthesized RNA into cells in large quantities and observe whether this message will be translated into protein in the cell. If such an approach of message amplification works with great efficiency, this signifies that one can express a protein encoded by any cloned gene in many cells. Since RNA is only transiently expressed, one can observe a cell where a gene has virtually been turned "on" and see the effects for a short while and then observe the following effects when the cell is expected to revert back to its normal production of message or when the gene has been turned "off". Such generalization of application has great significance.

Specifically, I used the model system of the Herpes Simplex Virus thymidine kinase (TK) gene which makes protein expression easy to assay and I transfected TK RNA into mouse fibroblast (L) cells. There were four steps in my experiment:

I. Cloning and preparation of DNA template.
II. *In vitro* transcription of template.
III. *In vitro* translation of RNA.
IV. Polycation transfection of synthesized RNA.

RESULTS

I. Cloning and preparation of DNA template

In vitro synthesis of RNA was necessary for several reasons. One reason is that an *in vivo* synthesis in cells produces relatively low levels of message.

Additionally, this message will be impure because it is contaminated with approximately 10^5 other mRNAs. Finally, an advantage of an *in vitro* synthesis is that one can alter the sequence content if necessary.

To obtain large quantities of TK RNA, I used a recombinant plasmid containing a 400 base pair promoter fragment from the bacteriophage SP6. SP6 is a Salmonella phage that encodes an RNA polymerase specific for its own promoter. In this *in vitro* transcription, SP6 RNA polymerase initiates transcription exclusively at the SP6 promoter and extends through a cloned DNA sequence to a specified terminator site. The starting point for my plasmid construction is a particular SP6 vector called SP64T, which was kindly supplied to me by Professor Doug Melton of Harvard. The important feature of this particular SP6 vector is that it provides for translation of the inserted protein coding sequence. SP64T was derived from a parental plasmid (SP64xβm) which contains the Xenopus β-globin cDNA and can be transcribed to produce functional β-globin mRNA. The protein coding region from SO64xβm has been removed leaving the 5' flanking region of the mRNA up to, but not including, the start codon of "ATG". The 3' flanking region of the globin mRNA also remains, including the stop codon "TAA" and poly A tail. Consequently, any protein coding sequence containing an "ATG" can be cloned into the restriction endonuclease BglII site of SP64T and transcripts of that DNA should serve as functional mRNAs *in vitro*.

My specific cloning plans called for introducing the protein coding region of the Herpes Simplex Virus thymidine kinase gene into SP64T (Figure 1). I first gel isolated a TK gene fragment from a plasmid, bounded by the restriction enzymes BglII and SmaI. This 1,300 base pair gene fragment contains 55 base pairs of 5' flanking sequence and is short of about 23 base pairs from the 3' end. I also cut the SP64T vector open with BglII and used calf intestinal phosphatase (CIP) to phosphatase the "sticky ends" of the now linearized molecule. The latter procedure prevents these sticky ends from ligating to each other (which could result in the regeneration of many vector molecules, an undesirable outcome). Mixing this linearized vector and the TK gene fragment in a ratio of $7{:}2\frac{1}{2}$, I inserted the TK gene using some T4 ligase and Klenow large fragment DNA polymerase. To check my construction, I did two kinds of analyses. The first was a restriction map where I cut my new plasmid with a variety of enzymes showing that it was the predicted clone. Secondly, I performed a hybridization by the method of Grunstein *et al.* and found that this new clone hybridized as expected to TK DNA. Thus, I now had a TK gene fused downstream to a highly efficient SP6 promoter. *In vitro* transcription of this plasmid with the corresponding SP6 RNA polymerase should yield substantial quantities of a single RNA species that should closely resemble a genuine messenger transcript.

II. RNA transcription

The next step was to transcribe RNA from the newly constructed TK DNA template (Figure 2). The template was first linearized at an EcoRI site after the poly A tail to ensure that there wouldn't be several continuous transcriptional rounds about the circular vector resulting in linear concatemer transcripts. An important point to note is that the *in vitro* synthesized RNA is not thought to be efficiently translated into protein *in vivo* because it lacks the 5' terminal cap structure of a methylated guanosine residue necessary for stabilization of message inside the cell. In the ordinary course of RNA production *in vivo*, the cap structure is added in the cell nucleus. Capping can be accomplished *in vitro* in two steps. Vaccinia virus guanyltransferase will convert the 5' triphosphate

termini of RNA into the 5' structure GpppG. The methyl donor S-adenosylmethionine is also included in the capping reaction so that the capped structure is now ^{7}mGpppG. Because the viral capping enzyme is expensive and somewhat unreliable as a reagent *in vitro*, I decided to accomplish the same objective in a different way. It has been recently observed by others (P. Sharp, personal communication) that the inclusion of diguanosine triphosphate, GpppG, in the transcription reaction results in the incorporation of GpppG at the 5' end of the transcript. These unmethylated, capped RNAs are found to serve as substrates in *in vitro* splicing systems and in fact become methylated. An unexpected bonus from diguanosine triphosphate is that the polymerase initiates more efficiently to increase the amounts of transcripts produced. The optimum conditions for a transcription reaction as set forth by Professor Doug Melton and Mike White (from N. Davidson's lab) were 500 µM rATP, rUTP, rCTP, 100 µM rGTP, and 500 µM GpppG. This five-fold ratio of GpppG compared to rGTP results in the incorporation of GpppG in larger than 95% of the 5' ends.

In my early transcription reactions, the RNA product was found to be degraded with prolonged reaction time. The problem was soon discovered to be one of ribonuclease in the DNA template solution. To rid this nuclease problem, the template solution was preincubated with proteinase K to digest the ribonuclease. The proteinase K was subsequently removed by phenol extraction. Thereafter, from one microgram of DNA template, I averaged two to three micrograms of completely full-length RNA from a two-hour reaction with a double dose of polymerase. I knew my product was all full-length transcripts because I ran some of this RNA labeled with ^{32}P-rGTP on a denaturing formaldehyde gel and observed a discrete band on the consequent autoradiogram (Figure 3). There was little if any degradative activity and the size of the transcript expected to be about 1,400 bases ran at the correct length when compared to some end-labeled DNA markers. Below is a time course of the kinetics of the reaction. I was able to measure the amount of RNA synthesis by a De81 assay measuring the amount of incorporation of ^{32}P-rGTP. SCI denotes my sense TK template and SCII denotes an anti-sense TK template I had also made earlier. Reactions SCIB and SCIIB both had extra polymerase added after 60 minutes, whereas the other reactions did not.

Time (minutes)	SCIA	SCIB	SCIIA	SCIIB
0 (background)	---	595	780	844
30	46,620	46,390	45,209	73,708
60	82,917	54,355	68,065	128,403
90	91,852	153,514	73,844	227,630
120	120,471	197,389	78,823	293,887

III. In vitro translation

To see if this synthesized RNA would translate into the appropriate sized protein, I did an *in vitro* translation using the rabbit reticulocyte system. A SDS gel showed that this lysate system synthesized protein quite efficiently from the synthesized TK RNA (Figure 4). In Figure 4, the different samples are from left to right: 1) endogenous lysate with no RNA; 2) lysate with 0.25 micrograms reticulocyte RNA; 3) lysate with reticulocyte RNA + TK1 RNA; 4) lysate + TK1 RNA; 5) lysate with 60 nanograms TK1 RNA; 6) lysate with 0.25 micrograms TK1 RNA; 7) lysate with reticulocyte RNA + TK2 RNA; 8) lysate with 60 nanograms TK2 RNA; 9) lysate with 0.25 micrograms TK2 RNA. The TK protein band can be seen quite clearly near the lower middle portion of the gel.

IV. Polycation Transfection

Confident that I could make TK RNA in sufficient quantity, I now proceeded to see if I could incorporate TK RNA into cells and see if it would give TK enzyme activity. I tried two polycations, ornithine and DEAE dextran, for the transfection. The actual mechanism of polycation-nucleic acid entry into cells is not well understood. The nucleic acid probably associates with the polycation through charge interactions and the nucleic acid somehow adsorbs to and penetrates the cell. A mouse fibroblast cell line deficient in thymidine kinase activity (LTK^- cell) was used. TK activity if present in cells can be assayed by their uptake of tritiated thymidine from the media. They incorporate this thymidine into the DNA and this label can then be seen by laying a photographic emulsion (Kodak NTB) over the cells and exposing for at least 24 hours. The positive cells are then visualized as those with an accumulation of black silver grains over their nuclei.

Both ornithine and dextran transfection procedures are very similar and were adapted from methods designed to introduce DNA into cells. L cells were grown on 6 cm plates with a density of 4×10^5 cells. They grew in Eagle's medium supplemented with 10% calf serum. Fifteen to twenty-four hours later, the cells were washed and 300 microliters of a polycation-RNA solution was added. The plates were "rocked" every 20-30 minutes for six hours to ensure that the 300 microliters of solution covered the plate evenly. Afterwards, the cells were washed and placed in medium with 10 μCi/ml ^3H-thymidine. After 34-40 hours, I put the plates under emulsion to expose. The idea above is that more cells will take up the RNA when the polycation-RNA mixture is left on top of the cell monolayer for long periods of time. The only difference between the ornithine and dextran procedures is that the ornithine plates are incubated at 37°C during the six hours, whereas the dextran plate are at 31°C.

Several experimental conditions were tried to optimize the yield of LTK^+ cells. For the ornithine plates, I used an ornithine concentration of 10.24 microgram/ml in 300 microliters (four-fold increase made the cells sick). At 0.3 micrograms of TK RNA, I did not observe any positive TK activity, but at a level of 2.5 micrograms, I observed 0.5-1% labeling on one side of the plate (2% even in some areas). The extent of label ranged from the same as or less than that seen in a LTK^+ control cell line. The dextran plates were found to give a bit better results and were more dependable and consistent. DEAE dextran was used at a concentration of 0.67 micrograms/microliter. The TK RNA plates of 2.5 micrograms here turned out to label pretty much the same if not better than my ornithine plates. To see if the RNA was being degraded during the six-hour "rocking" period, I put a 300 microliter sample of ^{32}P-labeled TK RNA on one of the plates. After a DE81 assay, all timepoints appeared to retain the same number of counts meaning that the TK RNA was not being degraded into small nucleotides.

Other experiments were tried to increase transfection efficiency—these included chloroquine, dimethylsulfoxide, and a higher dose of RNA. Unfortunately, the efficiency did not increase to any great extent in all these tries. It also appears interesting that a dose response curve seems not to be linear in this case. Furthermore, to ensure that my TK DNA template had not evoked the positive signals, I transfected this DNA in a similar fashion and found no positive TK enzyme activity.

DISCUSSION

Overall, the results were very pleasing as there were many uncertainties when I began this approach. For example, in using diguanosine triphosphate, my RNA was introduced into cells in an unmethylated form and conceivably may not have been translated. Fortunately, because we do see expression, we can say that this problem was solved *in vivo*, though we do not know whether the RNAs are being methylated, and if they are, where in the cell this is taking place. Other problems may have arisen as to the integrity of the message itself in the construction and nature of the DNA template. From my translation results, it is comforting to know that the RNA does give a protein with the appropriate size, and from the transfections we know that this protein has enzymatic activity.

Another interesting observation in looking at my RNA transfected cells are the cell stages at which the labeled cells are found. In a side by side experiment, DNA plates of TK-transfected DNA contained labeled cells mostly physically apart from one another. But in my RNA plates, I find a biased picture where many more cells than expected or roughly 80% are labeled while they are duplicating. Thus, the RNA plates appear to be labeled with some sort of partial synchrony.

There are also some reasons why directed RNA transfer (allowing expression of protein) would sometimes be favored over the introduction of DNA. DNA must enter the nucleus to be transcribed, whereas the RNA only needs to enter the cytoplasm where translation takes place. When DNA reaches the nucleus, there is also the question of whether it will be transcribed according to the gene regulation pattern in the recipient cell and whether the transcript, if made, will be transported properly out to the cytoplasm. RNA is advantageous in that it is not encumbered by the above problems in the steps of gene expression. Thus, RNA transfer should allow us to "short circuit" several levels of control which we do not currently understand. RNA is also advantageous in its versatility in experiments involving mixtures and arrays of different nucleic acids (as well as different concentrations) needed to be introduced into the cell.

Finally, I would like to mention a system in which the application of the above techniques would prove very useful. I am referring specifically to the "oncogenes", those genes believed to be the molecular basis of cancer. One oncogene, cMyc, resides normally in cells and produces a nuclear protein which may be involved in determining the number of rounds of cellular division. Thus, in dividing cells we find the oncogene being expressed and in non-dividing cells, we find much lower levels of expression. The particular oncogene I am interested in is called "c-myc"—it is known to cause Human Burkitts' lymphoma (B^- cells). This oncogene, through the genetic change of a chromosomal translocation, becomes "activated" and contributes to the transformation of a normal cell into a cancerous state. One possible explanation is that activation induces overexpression. Thus, forcing expression by amplifying the amount of oncogene message inside a normal B^- cell may give us some very interesting results such as unscheduled rounds of cell division, demonstrating its postulated role in the control of the cell cycle.

More experiments will be done to examine the conditions and nature of these transfections. Once a suitable control assay is achieved, this technique will be used on the c-myc gene in B cells.

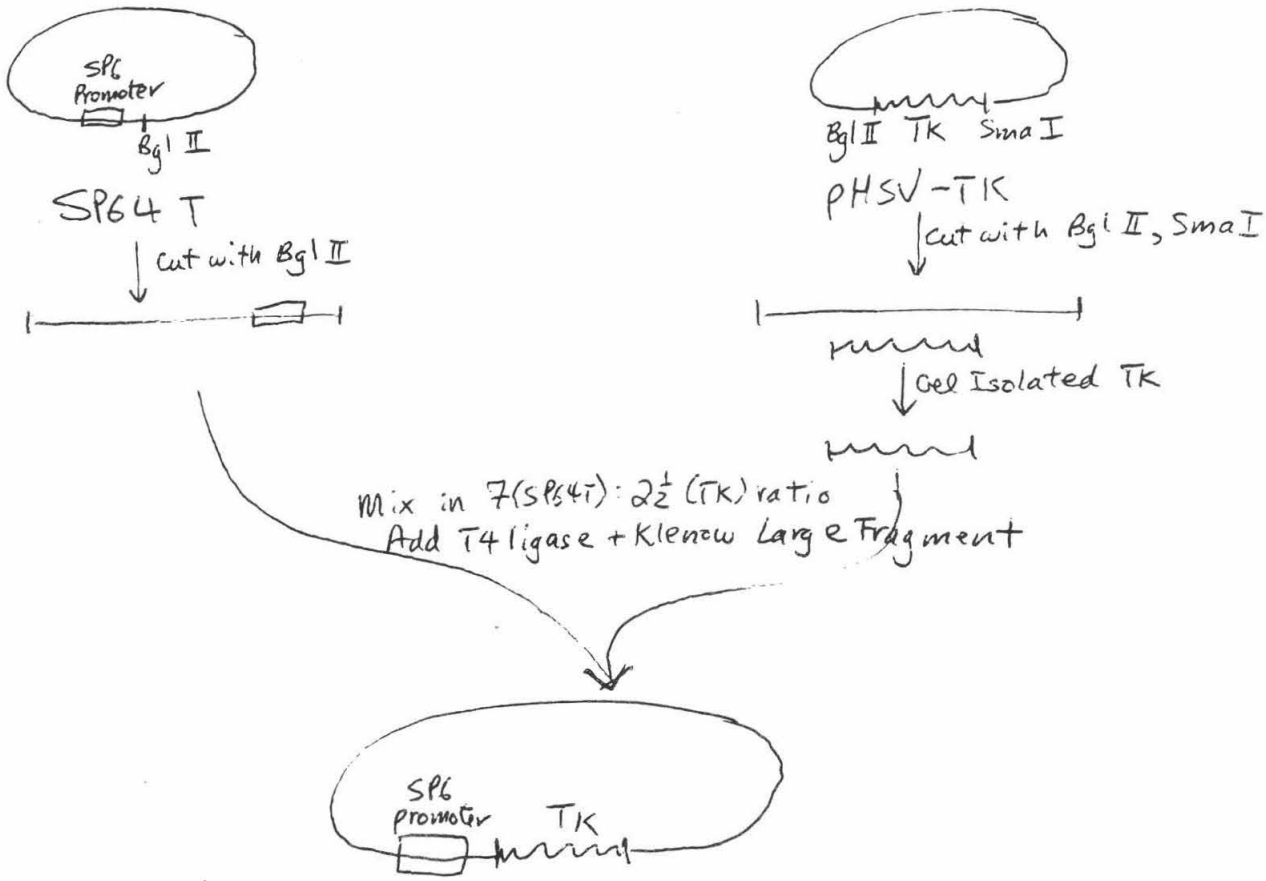

FIGURE 1

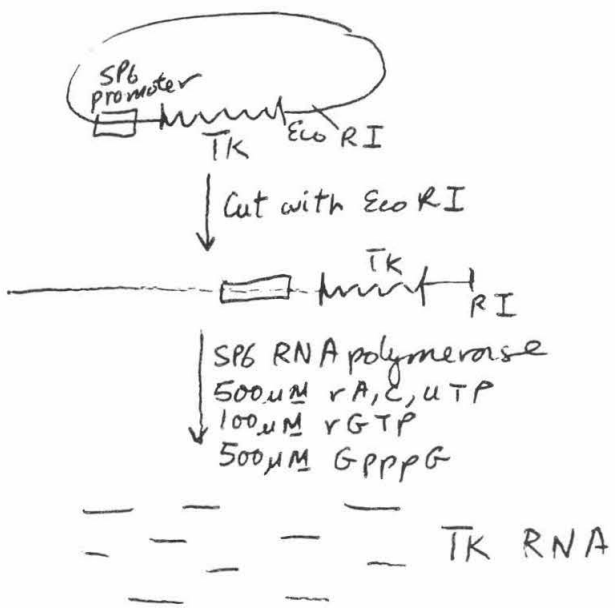

FIGURE 2

Figure 3

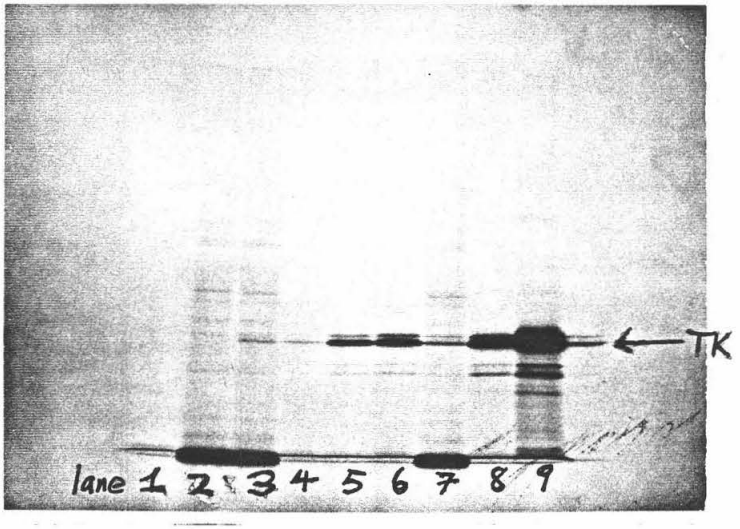

Figure 4

CLONING OF MYOSIN HEAVY CHAIN GENE FROM STRONGYLOCENTROTUS PURPURATUS

Diane L. Chen

Faculty Sponsor: Dr. Samuel J. Rose III

Abstract

Using two probes from the 5' end and the 3' end of the fruitfly Drosophila Melanogaster myosin heavy chain gene, each of molecular weight 5.8 kb and 6.0 kb respectively, we screened the sea urchin Strongylocentrotus Purpuratus genomic library in λ vector to isolate and to clone the myosin heavy chain gene(s) from the sea urchin. We have isolated two λ clones, λ1 and λ3, which hybridized to the probes. The clones are being sequenced. Southern blot analysis of S. Purpuratus genomic DNA digested with Hind III and hybridized to 6.0 kb probe yielded two bands of molecular weight 21.9 kb and 16.6 kb; hybridization to 5.8 kb yielded 1.9 kb and 1.25 kb bands. We concluded that the myosin heavy chain gene(s) in sea urchin can be isolated and cloned, and that the number of the gene could not be greater than three.

Introduction

The goal of this project is the isolation and the cloning of the myosin heavy chain gene from Strongylocentrotus Purpuratus, a Pacific water sea urchin. This gene is interesting to me for several reasons. First, it codes for myosin heavy chain, a muscle protein that interacts extensively with other muscle proteins. In the muscle sacromere, thick filaments and thin filaments slide over each other to produce contractile movement. Actin, tropomyosin and troponin are the components of the thin filament. Myosin forms the thick filament. There are "bridges"(S1 units) that protrude from the thick filament and attach themselves to actin. The hydrolysis of ATP produces the tilting motion of S1 and thus the sliding motion of filaments past each other. Half of each myosin heavy chain molecule composes the rod portion of myosin. The other half of the molecule together with one regulatory light chain and one essential light chain comprises the S1 region of myosin. Thus we see that myosin heavy chain and other muscle proteins are intimately related, and that therefore the genes coding for them must be coexpressed during development. Dr. Eric Davidson and his group at Caltech had previously studied the actin multi-gene family in S. Purpuratus and had followed its expression throughout the various stages of sea urchin development. Thus it is of interest to me to study the myosin heavy chain gene in the same biological system. Further, more is known about the molecular biology in sea urchin embryonic system than any other living organism. Thus the choice of sea urchin as the experimental animal seems appropriate.

With all these reasons for studying myosin heavy chain gene in sea urchin, previous works have indicated that there is a myosin heavy chain protein in S. Purpuratus. To start with, lantern muscle of sea urchin is a striated

muscle. This is a morphological indication that the muscle has thick and thin filaments and thus will likely to have myosin heavy chain in it. A second piece of evidence comes from work done by Jonathan Kabat-Zinn and Robert H. Singer. They found that in vitro translation of mRNA from sea urchin tube feet cells produced a 220,000 dalton protein which comigrated with myosin heavy chain protein from vertebrate muscle myosin on gel electrophoresis. A further evidence comes from Bernard Nadal-Ginard and his group. When they hybridized a myosin heavy chain cDNA probe from rat myotube to sea urchin genomic DNA digested with EcoRI, they found single hybridizing bands, indicating that there are sequence homology between myosin heavy chain of the rat and the sea urchin. They also found that there are single hybridizing bands when the rat cDNA probe was hybridized to the Drosophila Melanogaster's genomic DNA digested with EcoRI.

Results

Armed with these evidences, we screened mRNA, genomic DNA, genomic library and cDNA library from S. Purpuratus, using two probes from the myosin heavy chain coding region from Drosophila. The first probe is the 5.8 kb fragment from the 5' end of the coding region. The second probe is the 6.0 kb fragment from the 3' end of the coding region.

For the 6.0 kb probe, when we hybridized it to the Hind III digest of sea urchin genomic DNA at high criterion(40°C, 50% formamid, 5xSSC, 5xDenhardts, 10% dextrand sulfate), we found distinct hybridizing bands of molecular weight 21.9 kb and 16.6 kb. When we hybridized the 6.0 kb probe to mRNA from sea urchin lantern muscle, we found a band that is 6.0 kb long, long enough to code for a protein like myosin heavy chain. A third experiment using the 6.0 kb probe was to screen a sea urchin genomic DNA library. We have isolated λ clones that hybridized to this probe. Their DNA is now being purified and will be sequenced.

For the 5.8 kb probe, we found two bands of sizes 1.9 kb and 1.25 kb when we hybridized it to a Hind III digest of sea urchin genomic DNA under a much weaker hybridization condition(65°C, 5xSET, 1xDenhardts, no formamid, no dextrand sulfate). However, an attempt to hybridize this probe to the lantern muscle mRNA yielded negative results. This may be due to the possibility that there are few mRNA molecules remaining on the nitrocellulose filter; it may also be due to the fact that the sequence from the 5' end 5.8 kb probe is not as well conserved interspecieswise as the 6.0 kb probe.

However, using this probe, we have isolated from the genomic DNA library ten positive λ clones. Restriction analysis with EcoRI yielded two and only two different digestion patterns. We named these two types of clones λ1 and λ3. Hybridization of λ1 DNA cut with EcoRI back to 5.8 kb probe yielded a single band of molecular weight 6.7 kb. Another preparation of λ1 DNA cut with three other different restriction enzymes Sau3A, TaqI and HpaII had produced low molecular DNA fragments when hybridized to 5.8 kb probe. These hybridizations indicated that λ1 indeed is the clone with the myosin heavy chain gene. The DNA fragments resulted from digestion by the enzymes Sau3A, TaqI and HpaII have been cloned into M13, a vector suitable for sequencing analysis. We are now rescreening these M13 clones to purify them.

A later experiment indicated that the clone λ3 hybridized not only to the 5.8 kb but also to the 6.0 kb probe. It could be a clone which spans the entire length of the myosin heavy chain coding region. Its DNA is being

purified right now.

Both of these probes are cloned in pBR322 vector. When we used them to screen the cDNA library, we have obtained positive clones. But we have found that the cDNA library was contaminated with pBR322. Therefore our positive result is not reliable, and we have abandoned this approach to clone the myosin heavy chain gene.

Conclusions

From these results we drew the following conclusions:

A) Probes from Drosophila myosin heavy chain coding region hybridize to specific DNA fragments and mRNA from sea urchin Strongylocentrotus Purpuratus at high criterion. This result justies our hypothesis that myosin heavy chain gene(s) can be cloned from sea urchin.

B) There are few(2) bands on southern blots of genomic DNA for both probes, indicating that there is likely only one or at most several myosin heavy chain genes in S. Purpuratus. If this indeed is the case, then it will be relatively easy to clone all the myosin heavy chain genes and to follow their expression during the sea urchin development.

C) Both Drosophila probes have hybridized to specific λ genomic clones, and they are now being subcloned and rescreened for sequencing analysis.

BIBLIOGRAPHY

Kabat-Zinn, Jonathan and Singer, Robert H.. Sea urchin tube feet: unique structure that allow a cytological and molecular approach to the study of actin and its gene expression. The Journal of Cell Biology April 1981; 89:109-114.

Nguyen, Hanh Thi; Gubits, Ruth M.; Mydro, Robert M. and Nadal-Ginard, Bernardo. Sacromeric myosin heavy chain is coded by a highly conserved multigene family. Proc. Natl. Acad. Sci. USA September 1982; 79:5230-5234.

Rozek, Charles E. and Davidson, Norman. Drosophila has one myosin heavy-chain gene with three developmentally regulated transcripts. Cell January 1983; 32:23-34.

Construction of a Plasmid Containing the Yellow Fever Virus Genome

Sean Eddy
Dr. Charles Rice

ABSTRACT

This report summarizes the first steps of an attempt to construct a plasmid that contains the entire 10861 nucleotide sequence of the yellow fever virus (YFV) genome, inserted into the vaccinia virus thymidine kinase (TK) gene sequence on the 3' side of the 7.5K vaccinia promoter which has also been inserted in the TK sequence. When complete, this plasmid will be used in a marker rescue experiment with vaccinia virus to obtain vaccinia recombinants that express YFV proteins.

INTRODUCTION

Recent work at the National Institutes of Health has demonstrated vaccinia virus' ability to produce the proteins of another virus. The NIH is currently exploiting the practical advantages of this knowledge and is creating new vaccines. By constructing recombinant vaccinia virus (vaccinia is a quite effective vaccine itself, against smallpox) that expresses only the structural proteins of a different virus that are recognized by the immune system (usually one or two surface glycoproteins), the NIH has produced vaccines that have been shown to induce substantial immunity to hepatitis B and influenza in lab animals.

We are more concerned with the study of how viral proteins are expressed, and therefore are interested in using the vaccinia virus expression system as a tool in our work on yellow fever and related viruses. The system would eliminate the need for culturing live yellow fever virus, which is difficult, expensive, and somewhat hazardous; instead, vaccinia recombinants would be cultured, an inexpensive, probably safer alternative.

Dr. Charles Rice in our lab has already successfully constructed vaccinia recombinants that express the structural proteins of yellow fever virus (YFV). My work expands on his a bit, attempting to produce recombinant vaccinia that expresses the entire genome of YFV. This report details my work on the first part of this project, which is to construct a plasmid that contains the entire YFV sequence, next to the 7.5K vaccinia promoter, with all of this inserted into the thymidine kinase (TK) gene sequence of vaccinia. This plasmid would then be made to undergo homologous recombination with vaccinia (known as 'marker rescue'). The flanking TK sequence would serve as the recognition for where we want the 7.5K promoter and YFV sequence inserted -- right in the middle of vaccinia's TK gene, disabling the gene and allowing me to screen for TK- virus in order to locate successful recombinants.

RESULTS

The largest successful single ligation step we have heard of is a 4-piece ligation -- 4 separate fragments put together in one reaction to form a plasmid. The best I could come up with for a one-step ligation was a 5-piece using our library of YFV clones and VV5.1, a plasmid containing the 7.5K promoter inserted into the vaccinia TK gene. Clearly it had to be tried, just for the sake of the record books. Predictably, it failed, requiring the planning of a sequential, more practical construction strategy.

Dr. Charles Rice had previously constructed the plasmid designated VV51YFS.1. This plasmid contained the TK gene sequences flanking the 7.5K promoter and slightly more than 2.7 kb of the extreme 5' end of the YFV genome (which totals about 10.9 kb), an area which contains the sequence coding for the YFV structural proteins. The original plasmid vector also carries a gene conveying ampicillin resistance, allowing selection of recombinants from wild-type E. coli by growing the cells in the presence of ampicillin.

However, I intended to put this amp gene to another use in the last step of the construction -- to do this, I needed a unique restriction site in the amp gene. Most convenient was a Pvu I site, but unfortunately there was another Pvu I site in the original VV51YFS plasmid. This site was removed from the plasmid. The plasmid was partially digested with PvuI and the resulting linearized fragments were isolated from the mix of completely cut, linear, and uncut plasmid. The 3' overhanging ends of these linearized plasmids were chewed back a little with T4 polymerase, filled in, and then religated, adding a few nucleotides and consequently destroying one of the two PvuI sites. Since destruction of the PvuI site in the amp gene (the one site I needed) would also destroy the amp resistance, growing the transformant cells in the presence of ampicillin left only plasmids with one PvuI site in the amp gene intact, as I wanted it. This slightly modified plasmid was designated VV51YFS.2.

The rest of the construction is easier understood from a diagram, as shown on the next page. The first three constructions are straightforward. The final construction, of VV/YFT, incorporates the PvuI trick to greatly simplify what would otherwise be a difficult three-piece ligation. Only if the PvuI site of VV/YF5 ligates correctly to the PvuI site of VV/YF3 will the amp gene remain functional; all other ways of ligating the PvuI sites together are eliminated by growing the transformant cells in the presence of ampicillin.

CONCLUSION

To date, only the construction of VV/YF5 and VV/YF53 have been completed. I am currently screening recombinants looking for

CONSTRUCTION STRATEGY

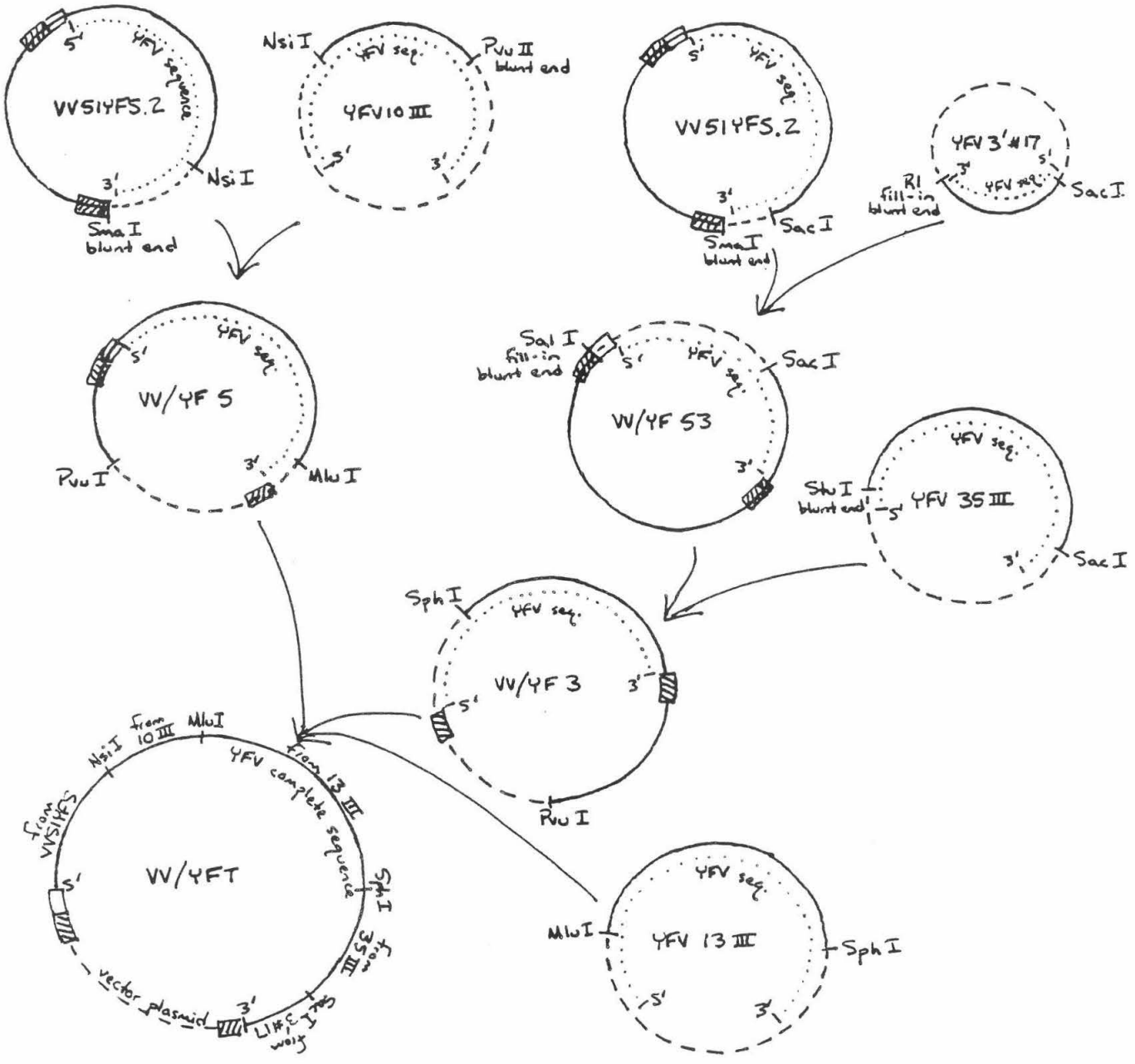

KEY

- discarded plasmid fragment
- plasmid fragment used in ligation
- region of yellow fever sequence
- vaccinia TK gene
- 7.5 K vaccinia promoter

a successful construction of VV/YF3. Delays were caused by the unsuccessful first construction attempt and the tedious though effective nature of the second construction attempt. I am continuing the project and anticipate finishing the construction sometime during October.

FURTHER REFERENCE

Mackett, Michael, Geoffrey L. Smith, and Bernard Moss. "Vaccinia virus: a selectable eukaryotic cloning and expression vector." Proc. Natl. Acad. Sci. USA, 79, 7415-7419, Dec. 1982.

Nakano, Eileen, Dennis Panicali, and Enzo Paoletti. "Molecular genetics of vaccinia virus: Demonstration of marker rescue." Proc. Natl. Acad. Sci. USA, 79, 1593-1596, March 1982.

Smith, Geoffrey L., Michael Mackett, and Bernard Moss. "Infectious vaccinia virus recombinants that express hepatitis B virus surface antigen." Nature, 302, 490-495, 7 April 1983.

Smith, Geoffrey L., Brian R. Murphy, and Bernard Moss. "Construction and characterization of an infectious vaccinia virus recombinant that expresses the influenza hemagglutinin gene and induces resistance to influenza virus infection in hamsters." Proc. Natl. Acad. Sci. USA, 80, 7155-7159, Dec. 1983.

NEURAL CORRELATES OF PERCEPTUAL RIVALRY

Hideki Garren

Faculty Sponsor: John M. Allman

Abstract

The responses of two neurons of the visual cortex were recorded from a monkey that was experiencing binocular rivalry at the time. The results indicated that in one of the cases, the neural activity was independent of the stimulus perceived and in the other case the neural activity depended on the stimulus perceived.

Symbols

The following symbols are used to indicate the orientation of the gratings presented to the left eye, the orientation of the gratings presented to the right eye, and the monkey's response.

	left eye	right eye	response
H	horizontal	none	
$\overline{H}$	none	horizontal	
V	vertical	none	
$\overline{V}$	none	vertical	
H$\overline{H}$	horizontal	horizontal	
VV	vertical	vertical	
HVR	horizontal	vertical	right key
HVL	horizontal	vertical	left key
VHR	vertical	horizontal	right key
VHL	vertical	horizontal	left key

Definitions

orientation selective cells - neurons that respond greatest to a particular orientation of bar-shaped stimuli

ocular dominance - the degree to which neurons respond more toward one eye than the other

Introduction

Many neurophysiological studies have shown that the responses of neurons of the visual cortex varies with changes in the stimulus presented. The purpose of this study was, however, to determine how the responses of single neurons varied with changes in the perception of the stimulus. In order to explore this concept, binocular rivalry was used as a tool for creating changes in the perceived stimulus while not producing any changes in the presented stimulus. Binocular rivalry results when two stimuli, so disparate that no meaningful composite can be created, are presented to each eye separately (Lack, 1978; Uttal, 1981). In such a situation, one or the other of the stimuli is partially or completely suppressed such that there is an alternation back and forth in the perceived image.

Neurophysiological recordings were collected from two neurons of the striate cortex (area V-I) of a monkey that was experiencing binocular rivalry. This particular visual area was chosen because Hubel and Wiesel (1968) have shown that there are cells in this area that are orientation selective, ocular dominant, or both. Finding these specific cells would allow the study of the correlation between neural activity and perceptual rivalry to begin. The results showed that in one of the cases the neural activity was independent of the stimulus perceived, but in the other case the cell's activity was dependent on the stimulus perceived.

Methods

The monkey used for this study was a female Macaca fasicularis. The monkey had been trained with an accuracy of about 95% to discriminate between vertical and horizontal gratings. The monkey reported which of the two stimuli it perceived by pressing one of two keys positioned under each hand. It pressed and held down the left key for the duration of the period in which it perceived the vertical grating and the right key for the horizontal grating.

Since the monkey was totally awake during the experiments, eye movements caused the receptive field of neurons that were being recorded to deviate from the stimulus. Because of this movement, eye position had to be monitored with the use of a search coil surgically implanted in the monkey's right eye and a magnetic field surrounding the entire monkey. By securely fixing the monkey's head at the center of the field, this system allowed us to monitor any horizontal or vertical movements of the eyes. Data were only collected while the monkey was fixating its gaze within a circle of diameter 4.5 degrees, as monitored by the magnetic search coil.

The stimuli were presented on two color television

sets that were masked off such that only a two degree circular opening was visible on each. Each eye was constrained to look at only one of the television sets by use of a mirror system. The stimuli were vertical and horizontal counterphase-flickered green gratings. Orthogonal gratings were used because it has been shown in human subjects that the rivalry rate is highest when gratings are oriented at 90 degrees with respect to each other, rather than at any other orientation (O'Shea, 1983). Also, the stimuli were counterphase-flickered for maximum suppression of the unperceived stimulus.

Responses of single neurons of the visual cortex were recorded by a glass-insulated microelectrode inserted into the surface of the brain. The microelectrode was driven hydraulically into the brain and was mounted on a movable stage. Similar procedures for recording from single neurons have been done regularly and successfully in Dr. John Allman's laboratory for many years now.

When recording from neurons, the stimuli were presented in two different series: an eye dominance series and a binocular rivalry series. During the eye dominance series, ocular dominance, if any, was determined by alternately displaying stimuli to only one of the television sets at one time. During the binocular rivalry series, we could be relatively certain that the monkey was correctly reporting rivalry because of two facts. The first fact was that the monkey had to correctly respond to real trials (i.e., trials in which both stimuli were oriented in the same direction) both before and after rivalrous stimuli were presented in order for the data to have been collected. The second fact was that it has been shown previously that macaques and human subjects report binocular rivalry similarly (Myerson et.al., 1981).

Results

Data collected from the cells are summarized in the tables at the end of this report. The activities of the neurons were recorded as the number of spikes per second fired by the cell.

The first cell, which I will call cell A, was one in which all of the collectable data could not be obtained. The reason for this incompleteness was that the series had to be stopped short for technical reasons. As can be seen from table 1, this cell was definitely orientation specific and slightly left-eye dominant. Table 2 shows that with a presentation of VH, the activity of the cell was nearly the same no matter what the reported percept was. However, it is evident from table 1 that the cell was more responsive to the stimulus V_ than to the stimulus _H by a ratio of about 4:1. Therefore, we would have expected the cell to be more responsive to the phase VHL than to the phase VHR by about the same ratio. Since that

was not the case, the activity of this cell must have been independent of the image perceived. This conclusion could not be confirmed with the other orientation of the stimuli (HV) because of the missing data.

The next cell, cell B, was similar to cell A in that it was orientation specific for vertical gratings. The difference was that it was slightly right-eye dominant. Table 4 shows that with a presentation of VH, the activity of the cell was the same no matter what the reported percept was. This result agreed with the data in table 3 which shows that the cell activity was nearly the same with both of the stimuli V_ and _H. There was an indication, however, from the data for the presentation HV, that the activity of this cell depended on the perceived stimulus. Table 4 shows that the neural activity was greater for the phase HVR than for the phase HVL by a ratio of about 2:1. However, it is evident from table 3 that the cell was more responsive to the stimulus _V than to the stimulus H_ by a ratio of about 7:2. These results indicated that this cell may have been more responsive to the suppressed stimulus rather than toward the perceived stimulus during binocular rivalry. This explanation also agreed with the data from the presentation of VH.

Summary and Discussion

In summary, the results indicated that the activity of one of the cells was independent of the stimulus perceived, but that of the other cell depended on the stimulus perceived. From the data that were available, the neural activity of cell A appeared to not be related to the alternation of perception during binocular rivalry. The activity of cell B was related to the stimulus perceived in the sense that the cell was apparently more responsive toward the suppressed stimulus. However, unless more cells are found that have this same property, this explanation for the activity of cell B should be considered speculative, at best. Instead, what we had expected to find were cells whose activities were directly correlated to the stimulus perceived (i.e., cells that responded when the monkey reported seeing the stimulus, but not when she reported seeing the opposite orientation during binocular rivalry).

The results given here are only preliminary. This work is presently being continued to collect data from many more neurons of the visual cortex.

References

Hubel, D.H., Wiesel, T.N. Receptive fields and functional architecture of monkey striate cortex. Journal of Physiology, 1968, 195, 215-243.

Lack, L.C. Selective Attention and the Control of Binocular Rivalry. The Hague, The Netherlands: Mouton Publishers, 1978.

Myerson, J., Miezin, F., and Allman, J. Binocular rivalry in macaque monkeys and humans: a comparative study in perception. Behaviour Analysis Letters, 1981, 1, 149-159.

O'Shea, R.P. Spatial and temporal determinants of binocular contour rivalry. Ph.D. Dissertation, University of Queensland, 1983.

Uttal, W.R. A Taxonomy of Visual Processes. Hillsdale, New Jersey: Lawrence Erlbaum Associates, 1981.

Tables

Table 1. Eye Dominance Series, Cell A

Phase	Cell Activity (spikes/sec.)
$\underline{H}$	15.2
$H\underline{\ }$	22.0
$H\underline{H}$	16.4
$\underline{V}$	33.0
$V\underline{\ }$	63.0
$V\underline{V}$	61.0

Table 2. Binocular Rivalry Series, Cell A

Phase	Cell Activity (spikes/sec.)
HVR	4.0
HVL	---
VHR	37.0
VHL	33.0
HH	8.7
VV	42.0

Table 3. Eye Dominance Series, Cell B

Phase	Cell Activity (spikes/sec.)
$\underline{H}$	12.8
$H\underline{\ }$	5.2
$H\underline{H}$	8.4
$\underline{V}$	18.8
$V\underline{\ }$	13.2
$V\underline{V}$	20.8

Table 4. Binocular Rivalry Series, Cell B

Phase	Cell Activity (spikes/sec.)
HVR	24.7
HVL	12.0
VHR	8.0
VHL	8.0
HH	9.0
VV	18.0

Connections and Functional Organization of The Middle Superior Temporal Visual Area (MST) in the Macaque Monkey

John F. Houde
Faculty Sponsor: David C. Van Essen

Abstract

The primate brain is composed of many different, functionally distinct areas that are organized hierarchically. In the visual system, there appear to be two sets of areas, one for processing form information and one for movement information. One of the movement processing area is called area MST and its organization and connections are investigated in this project.

Introduction

At one time it was thought to be impossible to assign specific functions to specific neurons of groups of neurons in the brain. Research has shown however that this is not the case - that the brain is actually composed of many functionally distinct areas. The organization of these areas appears to be hierarchical; in a given sensory pathway, vision or hearing for example, there are cortical areas that perform elementary processing of sensory data and other areas that perform more high level processing on inputs from the lower areas. To understand how the brain as a whole works involves understanding what each functional area specializes in and where it fits into the hierarchy.

One of the important sensory pathways of the brain is the visual system and in Dr. David Van Essen's lab a lot has been learned about vision processing cortical areas and their hierarchy. Fig 1. is a diagram of the known visual areas of the cortex, showing their hierarchy and their known interconnections. It appears that the visual system can be divided into two systems: a form analysis system made up of areas V2, V3, V4, and VP, and a motion analysis system made up of areas MT and MST, with both systems getting input from the lowest level visual area V1. Of the motion analysis system quite a bit is known about area MT but not much is known about area MST. In J.H.R. Maunsell's 1983 study of the connections of area MT it was found that MT projects to MST and that MST projects to area 7A, a high level area that appears to be involved with attention. It was also found that MST receives input from area 8, an area which monitors eye postion. It has been postulated that MST may be polysensory -i.e. it may receive inputs from other senses.

In addition to questions about its connections, not much is known about the internal organization of MST. In the visual system actually has two equal pathways in it, one in the left hemisphere and one in the right, each with the same visual areas and each processing the visual data from one half of the field of view of both eyes. Thus in one brain there are actually two area MSTs, one in the left hemisphere and one in the right. In a given hemisphere the visual data reaching the visual areas comes in a topographically organized fashion and although lower areas preserve this organization it is not clear whether higher ones such as MST do. There has also been some speculation that MST is not just one area but is actually two distinct ones.

In this project, I have begun to find some answers to these questions, in particular, with regards to topographic organization and connections. The project was broken into two parts: an electrophysiological study of the cells in MST and an anatomical study of the connections of MST. Both studies produced interesting results and encourage further study of MST.

Experimental Approach

The two studies were both done on one monkey over a three week period. Before the final terminating session the posterior portion of the corpus callosum joining the two hemispheres was cut to allow three independent experiments to be done on this same monkey. After the terminal session,

there was a four week period in which brain sections were examined for tracer labelled cells and for electrode tracts. I was assisted in all of these experiments by Dr. H.S. Orbach, a post-doctoral research fellow in Dr. Van Essen's lab.

The electrophysiology study was aimed at finding out something about the internal organization of MST. As mentioned above, visual field imformation comes to the lower visual areas in a topographically organized pattern. Each cell in a given area is connected to a certain part of the visual field and thus will respond only to light stimulation in this certain part of the visual field. This certain part of the visual field that the cell responds to is called the cell's receptive field. Thus in a given visual area, each cell has a receptive field in a different part of the field of view so that the whole field of view is covered by the area. So the distribution of receptive fields in MST is one part of the description of the area's internal organization. Not only do receptive fields vary in position but also in size, color selectivity, velocity sensitivity, orientation selectivity, and direction selectivity. The size of a cell's receptive field is the size of the area of the visual field that stimulates the cell. Some cells respond best to light of a certain wavelength and are said to be color selective, while others respond equally well to all visible wavelengths of light. Most cells do not respond well to a uniform illumination of their receptive fields but instead prefer a more varied stimulus with edges such as a bar of light. Some cells do not care what the orientation of the bar is while others have an orientation preference. Finally, some cells not only require that the light bar is of a certain orientation, but require that it be moving in a certain direction. This is called direction selectivity. The size, color selectivity, orientation selectivity, and direction selectivity of a cell's receptive field are usually characteristic of the visual area the cell is in. So, for example in areas MT and MST, the motion processing areas, we find cells that are highly direction selective but not very color selective, while in areas V3 and V4 we find fewer cells that are direction selective and more cells that are color and orientation selective. Cells in MST have very large receptive fields that are highly direction selective, so this information was used to decide when we were recording from MST.

During the three week period of the experiment there were five separate recording sessions in which we attempted to record from neurons in MST, four one day sessions and one four day terminating session. Each recording session was spent making microelectrode penetrations into the monkey's brain and attempting to stimulate cell responses by moving bars of light in front of the monkey. Since a lot is known about the size and position of receptive fields of other visual areas, we could use this information to help decide where our microelectrode was in the brain and thus where MST was likly to be. The data collected was in the form of plots of the size and position of the receptive fields of the cells we encountered, along with a sheet describing the depths at which these cells were found and any other attributes of the cells' receptive fields.

The anatomy study was commenced in the terminal session by separate injections of horseradish peroxidase (HRP) and tritiated proline into the region we believed to be MST.

HRP is a substance that is taken up by a neuron at its terminal and

shipped back through the axon to its cell body. There, certain reactions will cause the HRP to become black, allowing the cell body to be seen, and the cell is then said to be labelled. So when we made our injection of HRP, only those cells whose terminals were in the region of injection took up the HRP and subsequently became labelled by reaction. In this way, the HRP injection labelled those cells in the monkey's brain that send input to MST. The total volume of the HRP injection was 200 nanoliters of which half by weight was HRP, the rest, distilled water.

Proline is an amino acid that is taken up by the cell bodies of neurons and sent down their axons to their terminals. The tritiated form of it is radioactive and can be shown up in brain sections by photographic techniques. Thus the cell bodies at the injection site of the tritiated proline took it up and sent it out to their terminals which will show up with special photographic techniques. From these results we can find out where cells in MST send their inputs to. The total volume of the tritiated proline injection was 300 nanoliters which contained 50 microcuries of tritiated proline in distilled water.

Two other processes will also be performed on the brain sections to help show up area boundaries. They are the Wiitanen process, which stains for callosal fiber degeneration, and a method which stains for myelination. The results from these processes will not be available until after the due date of this report, but they are important data in deciding which areas the HRP labelled cells and tritiated proline labelled terminals are in.

Results and Discussion

The results of the electrophysiology study are summarized in fig. 2. The line drawings are of actual brain sections from which the electrode tracts were recovered. The other two drawings are receptive field plots. They show that we managed to record from MST at its dorsal end and its ventral end. The dorsal end penetration (P2) recorded from cells with receptive fields characteristic of V4 (recep. fields A, B, and C), then crossed a white matter gap where there was no significant activity, and finally entered the posterior bank of the Superior Temporal Sulcus (STS) where highly direction selective MT-like cells were recorded from (recep. fields D through G). The last cell with a receptive field encountered on the penetration was cell I and it too had a receptive field that was highly direction selective. However, the large size of it indicated that it was probably a cell in MST. The field is in the upper quadrant of the field of view and is about eight degrees away from where the animal's foveas were looking. The ventral end penetration (P5) proceeded for many millimeters without recording from any cells that were responsive to light stimuli. Finally, at a depth of 8.7 millimeters, cells with receptive fields were found. The cells were direction selective and the size of the receptive fields indicated that they were all in MST. The penetration seemed to stay in MST for several millimeters until it came out into the STS. The receptive fields of the cells in MST were all in the lower quadrant of the field of view.

The two penetrations we made in MST (P2 and P5) indicate something about the topography of MST. P2 was in the dorsal tip of MST when it recorded a receptive field in the upper field of view, while P5 in the ventral end of MST recorded receptive fields in the lower field of view.

Also, there was a general trend towards lower and larger receptive fields in P5. Many more recording sites in MST will be needed to establish the complete topographic organization and extent of the area.

Fig. 3 is a line drawing of a brain section that shows where the tritiated proline and HRP injection sites were. On the basis of the previous electrophysiology recordings, it appears that both of the injections were in MST. The injection syringe for these injections is able to record cell activity and on the HRP injection, MST-like receptive fields were encountered just before the injection was made. On the proline injection, however, the brain was apparently very disturbed by the previous injections that had been made and no receptive fields could be found. Since the posterior end of the corpus callosum was severed, neither proline nor HRP could travel from the right hemisphere, where the injections were made, to the left, and so the search for labelled cells could be confined to the right hemisphere.

The results of the HRP injection are summarized in fig. 4. Fig. 4 shows a two dimensional map of the surface of the monkey's cortex with several area boundaries drawn in. The dots indicate the approximate positions of the HRP labelled cells. Several labelled cells were found in the anterior bank of the STS, which is the probable location of area STP. Four other cells were found on the anterior bank of the Lunate Sulcus. Two of them were in a region that is probably V3a and the other two were in a region that places them in area DPL. No labelled cells were found in the frontal lobe, and so no evidence for the area 8 connection could be found. Neither was there evidence for the area 7a or V4 connections. This, however, may be due to the generally small number of labelled cells found in any of the sections. The exact assignment of area boundaries in the monkeys cortex was not possible at the time of the writing of this report because it depends on the results of the Myelin and Wiitanen staining processes which are still forthcoming. Also, the results from the tritiated proline injection will not be available for another two weeks because of the length of their photographic processing time.

Conclusions

The complete description of a new cortical area is a slow process that can take years to do and many experiments. Some of my own data is still yet to come. However, this summer's experiment did produce some interesting results. Something was learned of the topography of MST as well as its possible connections to areas STP, DPL, and V3a. Although these results are not complete, they offer clues about MST that encourage its further study.

In conclusion, I would also like to thank Dr. Van Essen, Drs. DeYoe and Felleman, and K. Tazumi for their help on this project.

BIBLIOGRAPHY

Area names and figures by personal correspondence with D.C. Van Essen

Also used:

Maunsell, J.H.R. and Van Essen, D.C., The Connections of the Middle Temporal Visual Area (MT) and Their Relationship to a Cortical Hierarchy in the Macaque Monkey. 1983

Fig. 1

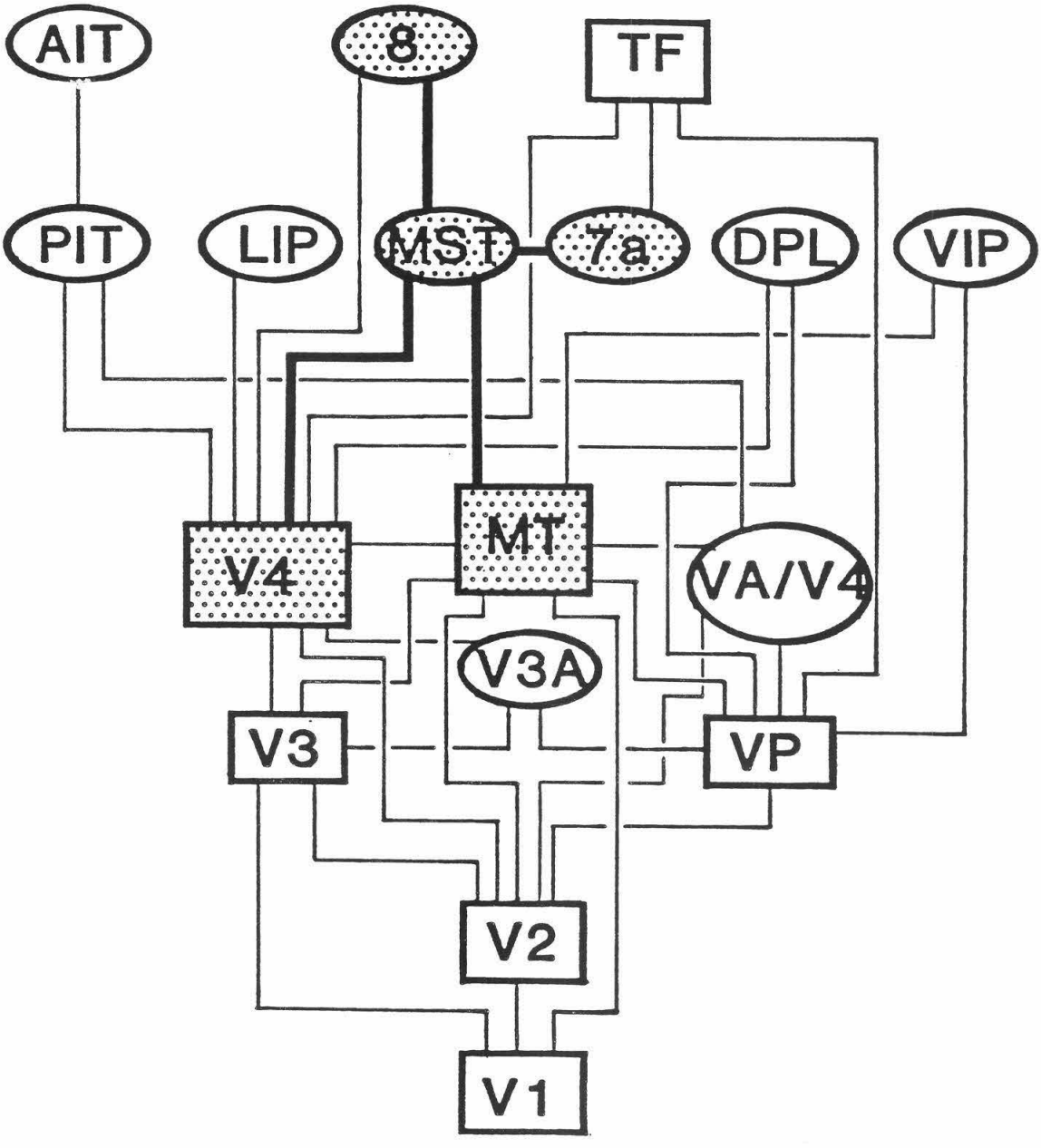

Fig.2

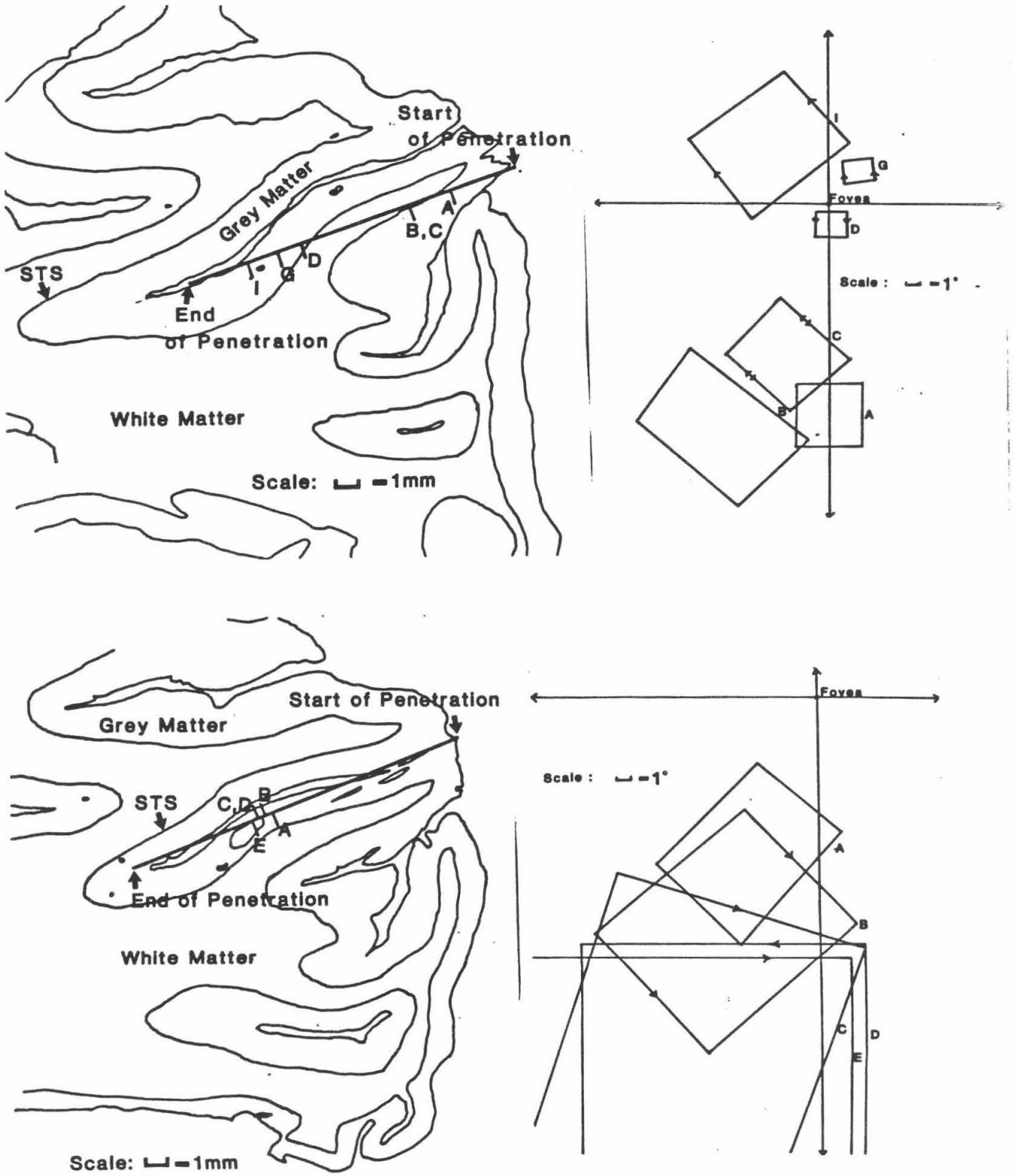
Start of Penetration
Grey Matter
STS
End of Penetration
White Matter
Scale: ⌴ =1mm
B,C
A
I
G
D
Fovea
Scale : ⌴ =1°
C
B
A
Start of Penetration
Grey Matter
STS
C,D
B
A
E
End of Penetration
White Matter
Scale: ⌴ =1mm
Fovea
Scale : ⌴ =1°
A
B
C
D
E

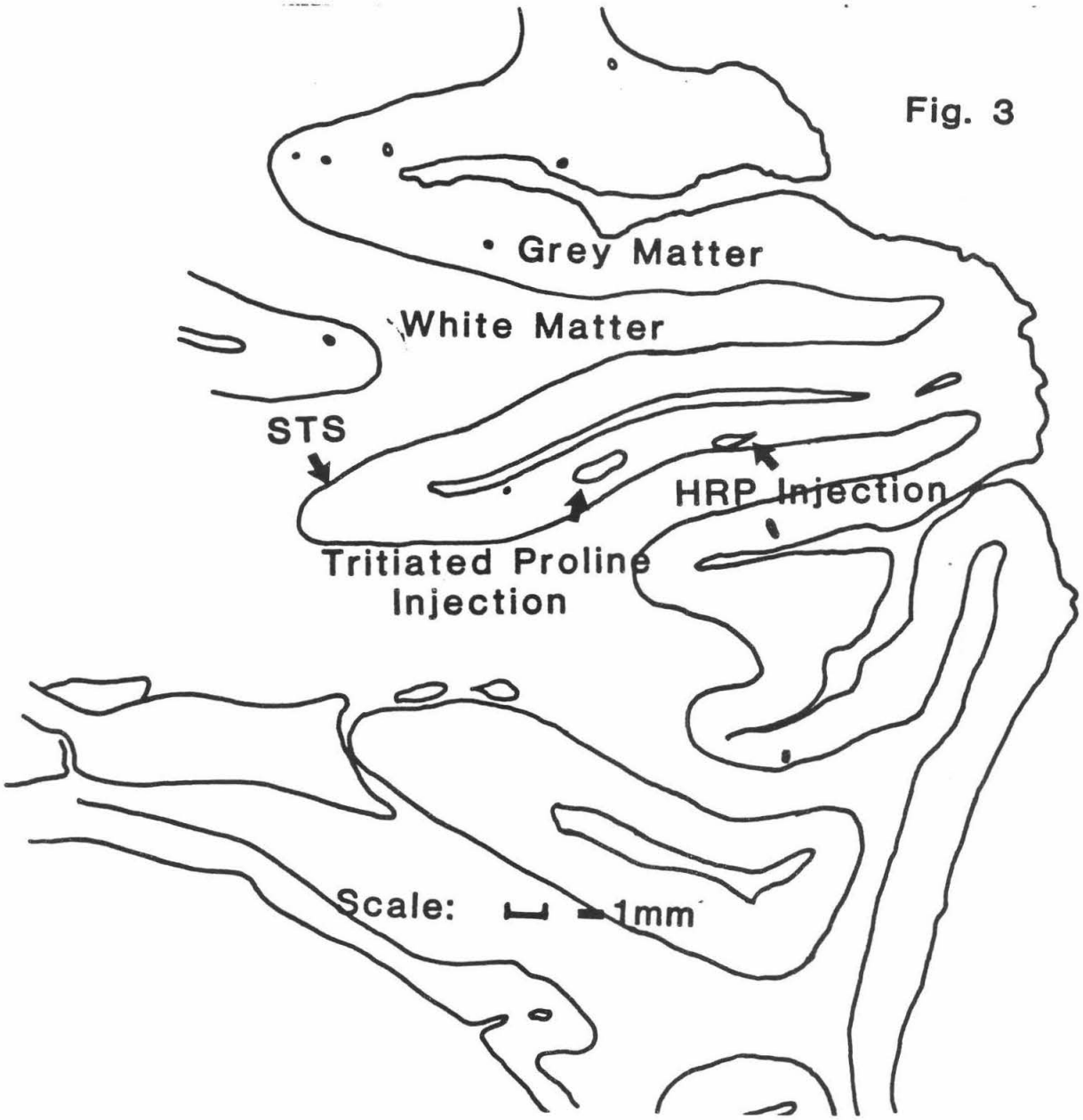
Grey Matter
White Matter
STS
HRP Injection
Tritiated Proline
Injection
Scale:
1mm

Fig. 3

Fig. 4

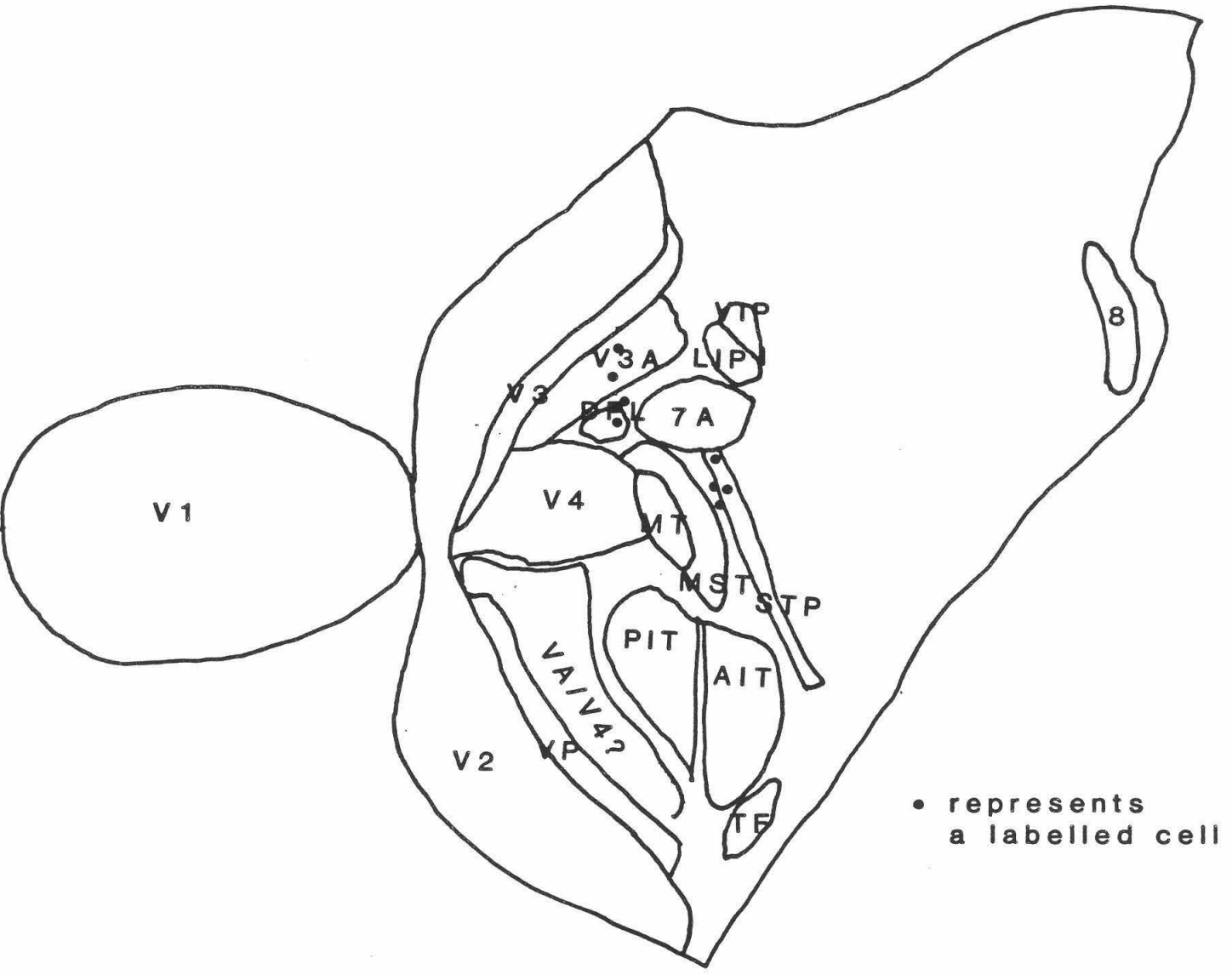
V1
V2
V3
V3A
V4
VP
VTP
LIP
7A
MT
MST
STP
PIT
AIT
TF
8
V4-V4?
• represents
a labelled cell

1984
Summer Undergraduate Research Fellowship
Final Report

Expression of IL-2 Receptor on Thymocytes: Evidence for IL-2 Independent Thymic Proliferation

Santosh N. Krishnan
Sponsor: Dr. Ellen Rothenberg

ABSTRACT

Mature T-lymphocytes recognize foreign antigens with the assistance of self denoting molecules. Upon contact with a particular antigen, T-cells proliferate and amplify. The thymus has been well established as the site of T-lymphocyte differentiation. Several lines of evidence indicate that it is here that T-cells "learn" to discriminate between self and non-self. Only 10-15% of all thymocytes are proliferating. It has been hypothesized that these proliferating cells are reacting against self and are therefore being subjected to reforming influences. If the response to antigens is controlled similarly in mature T-cells and thymocytes, then thymocytes proliferating in response to self antigens must express the receptor for the polypeptide hormone Interleukin-2 (IL-2).

In this study, we show that expression of the IL-2 receptor is limited to a particular subset of proliferating thymocytes. We therefore postulate an IL-2 independent mechanism for most intra-thymic proliferation. Thus the majority of proliferating thymocytes are unlikely to beproliferating in response to self antigens. The minority of proliferating cells expressing IL-2 receptors could be proliferating in response to self antigens. Further experiments are underway to investigate the functional capabilities of these cells and their expression of other molecules that correlate with functional reactivity.

Introduction

Although it is well known that the thymus is the site for the differentiation of T (thymus derived) lymphocytes (Cantor and Weissman, 1976), the molecular aspects of this differentiation are still largely unknown. The population dynamics of the thymus indicate significant waste. About 10% of all thymocytes are proliferating at a rate sufficient to repopulate the thymus every 3-5 days (Metcalf, 1966; Bryant, 1972). These proliferating cells are primarily blasts, and are predominantly located in the outer cortex with a few in the medulla. The remaining 90% of cells, which result from their proliferation, are quiescent. Most of these are destined to die, but about 1% a day are exported to the periphery as viable T-cells. Thus the blast cells are likely to be the precursors of all thymocytes and all mature T-lymphocytes.

We are interested in determining the signals that drive thymocyte proliferation. The polypeptide hormone Interleukin-2 (IL-2) has been shown to be an important stimulant for immunologically active cells (Smith, 1980). Originally identified as a necessary growth factor for the long-term maintainance of continuously proliferating, antigen specific, T-lymphocyte clones (Gillis and Smith, 1977), IL-2 has been purified and shown to be a growth hormone for all normal T-cells but no other known cell type (Smith, 1980; Howard et al., 1982). Previous work in this laboratory has examined the functional competence of thymocyte sub-populations by assessing their ability to produce IL-2 (Caplan and Rothenberg, 1984). In this paper, we examine the expression of the receptor for IL-2 on these thymic sub-classes.

Materials and Methods

Animals. C57BL/6 (B6) mice and two congenic mice lines, C57BL/6-*Tla*^{a} (B6-TL$^+$), and C57BL/6-*Lyt-2.1:3.1* (B6-Lyt-2.1:3.1) were bred and maintained in the animal facility at the California Institute of Technology. Mice between 4 and 6 wk of age were used in all experiments.

Tissue Culture Medium. Tissue culture medium RPMI 1640 (GIBCO, Grand Island, N.Y.) containing 2 mM L-glutamine, 50 μM 2-mercaptoethanol, and 10% heat inactivated fetal bovine serum (FCS; Hy-Clone, Sterile Systems Inc., Logan, UT.) was used in all experiments. Medium was also supplemented with 10^5IU/liter penicillin G potassium, and 0.1 g/liter streptomycin sulfate. MTL2.8.2 cells (Bleackley et al., 1982) were cultured at 4×10^4cells/ml for 3 days in the presence of 30U/ml IL-2.

Antisera. IL-2 receptor was detected with a monoclonal antibody specific for the murine IL-2-IL-2 receptor complex. This antibody, a rat IgM, is produced by the hybridoma 7D4 (Malek et al., 1984) was generously provided as a culture supernatant by Thomas R. Malek (National Institute of Health, Bethesda, Md.). Fluorescein-isothiocyanate-conjugated goat anti-rat IgG was obtained through the Research Resources program of the Division of Cancer Cause and Prevention, Biological Carcinogenesis Branch of the National Cancer Institute, Bethesda, Md., courtesy of Dr. John Cole.

Cell Fractionation by Centrifugal Elutriation. Elutriation was performed as previously described (Rothenberg, 1982; Caplan and Rothenberg, 1984). Briefly, single cell suspensions of thymocytes were prepared by mincing thymus fragments and passing them through a 200 mesh stainless steel screen into tissue culture medium. The cells were then washed once with Ca^{2+}- and Mg^{2+}- free Dulbecco's phosphate-buffered saline (PBS^-) and resuspended at up to 2×10^8 cells/ml in tissue culture medium. A sample of 10 ml (up to 2×10^9 cells) was loaded into a spinning JE-6 elutriator rotor (Beckman Instruments, Inc., Spinco Div., Palo Alto Calif.) at 4°C and elutriated with a continuous flow of Ca^{2+}- and Mg^{2+}- free Hanks' balanced salt solution supplemented with 2.5 mg/ml bovine serum albumin (BSA) and 5 mM Na azide (CBSS/BSA). The flow rate was controlled by a Cole-Parmer Masterflex pump equipped with a ten-turn Helipot potentiometer (Beckman Instruments, Inc.) The first 150-200 ml was collected and subsequently, small, medium, and large cell fractions of the same volume were harvested by sequential increases in the pump speed. In these experiments, the rotor speed for the JE-6 rotor was set at 2,860 rpm. Flowthrough cells were collected

at 12 ml/min, small cells at 16.5 ml/min, medium cells at 24 ml/min, and large cells at 30 ml/min (Rothenberg, 1982). The elutriated cells were collected in centrifuge bottles containing 5 ml FCS and kept on ice therafter. After fractionation, cells were recovered by centrifugation at 1,500 rpm for 10 min at 4°C. Cells were washed once in medium or in isotonic buffered saline without azide before further use. Generally, recovery was > 70%. Usually, cells in the medium fraction included 30-50% small cells; cells in the large fraction included no more than 10% and usually <5% small cells.

Fractionation based on Peanut Agglutinin (PNA) Binding. Cell fractionation was performed by a modification of the "panning" technique of Wysocki and Sato (Wysocki and Sato, 1978) as previously described (Rothenberg, 1982, Coplan and Rothenberg, 1984). Briefly, non tissue-culture treated Petri dishes (no. 1005, Falcon Labware, Becton, Dickinson, and Co., Oxnard, Calif.) were coated at room temperature with 4 ml of a 20μg/ml solution of PNA (Vector Laboratories, Inc., Burlingame, Calif.) in 0.15 M NaCl, 0.05 M Tris-HCl, pH 9.5. After 2 h, excess PNA was removed and plates were washed twice with chilled Dulbecco's phosphate-buffered saline (PBS^+) and once with chilled PBS^+ supplemented with 1% FCS and 1 mM Na azide ($PBS^+/1\%$). 4×10^7 cells in 4 ml of PBS^+ supplemented with 5% FCS and 1 mM Na azide were gently applied to the plates and incubated at 4°C for 90 min. Unbound PNA^- cells were then gently poured off the plate and were also collected after one wash with $PBS^+/1\%$. The adherent PNA^+ cells were eluted by incubating the plates for 5-10 min at room temperature with 4-5 ml of 0.2 M D-galactose in $PBS^+/1\%$; they were harvested by vigorously flushing the plates with the galactose solution through a Pasteur pipette. The plates were then washed once more with 4-5 ml of 0.2 M D-galactose in $PBS^+/1\%$ to complete the elution. Overall recovery was usually > 65%.

Fluorescence Staining of Surface IL-2 Receptor. Fluorescence staining was performed as previously described (Rothenberg, 1982). Briefly, 2×10^6 cells were pelleted in 3-ml glass conical tubes and were resuspended in 50 μl of either CBSS/BSA or a 1:10 dilution dilution of monoclonal 7D4 antibody in CBSS/BSA. They were incubated on ice for 30 min, diluted with 1 ml CBSS/BSA, and centrifuged through a 0.4 ml cushion of FCS. The pellets were then resuspended in 50 μl (165 μg) of fluorescein-conjugated goat anti-rat IgG. After 30 min on ice, the cells were diluted and centrifuged as before and resuspended in PBS^- supplemented with 1% (vol/vol) formaldehyde. Before analysis on the cell sorter, the suspensions were filtered through nylon mesh (Nytex; TETKO, Inc., Elmsford, N.Y.). For flow microfluorometry, an Ortho Cytofluorgraph cell sorter was used, with an excitation wavelength of 488 nm. The cell distribution histogram was displayed on a 1000 × 1000-channel dual-parameter matrix plotting the logarithm of fluorescence intensity vs. forward light scatter (linear scale). Fractions of IL-2 receptor positive cells, (log fluorescence channels 60-990) were calculated for populations gated according to light scatter to exclude dead cells (in scatter channels 1-115). The cloned IL-2 receptor positive cytotoxic T-cell line MTL2.8.2 and spleen cells cultured in the presence of 3 μg/ml Concanavalin A (Con A, Vector Laboratories, Inc., Burlingame, Calif.) were used as positive controls. IL-2 receptor negative R1.1 cells stained similarly to the thymocytes exposed to second stage reagent alone.

Determination of DNA content. Cells were fixed in 50% ethanol and 2×10^6 cells were stained in one ml with 100 μg/ml mithramycin A (Sigma Chemical Co., St. Louis, MO.) using methods previously described (Crissman and Tobey, 1974; Hyman and Stallings, 1978; Rothenberg, 1982). For flow microfluorometry, an excitation wavelength of 457.9 nm was used. Data were recorded as linear fluorescence intensity histograms from a 1024 channel pulse-height analyzer. The fraction of cells in G_0/G_1 was calculated from the number of cells in the left half of the 2C DNA content peak, divided by the total number of cells in the distribution (objects with ≥6C DNA content were excluded).

Results

PNA^- cells and lymphoblasts are both minor populations in the thymus. We have employed two techniques for isolating the thymic lymphoblasts. The actively proliferating thymocytes can be separated into large and medium size classes, and can so be isolated from the majority of small resting cells by centrifugal elutriation

(Rothenberg, 1982; Caplan and Rothenberg, 1984). To quantitate cells in different cell-cycle stages in the various size fractions, we have used the DNA-binding fluorescent stain mithramycin. Preliminary results indicate that unfractionated and small thymocytes were predominantly in G_0/G_1 as judged by their 2C (diploid) DNA content, while the "large" and "medium" size fractions were significantly enriched for proliferating (S, G_2, and M phase) cells.

Cells in different micro-environments within the thymus tend to display different cell-surface carbohydrates. This difference is exploited by PNA to differentiate between cortical and medullary cells. PNA binds better to cortical than to medullary cells (Reisner et al., 1976) but does not differentiate between proliferating or non-proliferating cells. Thus, elutriation followed by PNA panning results in six thymic sub-populations, with proliferating cells separated from postmitotic cells and both classes separated into those with "cortical" or "medullary" phenotype. Furthermore, distinct differences can be seen between these populations in terms of biosynthetic activity and functional reactivity (Rothenberg, 1982; Rothenberg and Triglia, 1983; Caplan and Rothenberg, 1984; Rothenberg et al., 1984) Thus our cell-fractionation techniques result in cell fractions where significantly different differentiation states predominate.

We have used fluorescence activated cell sorting to measure the level of IL-2 receptors in a highly sensitive, quantitative fashion. From Table 1, it can be seen that cells expressing IL-2 receptors are found primarily in the large and medium PNA^- cell fractions. Even in these fractions, however, the receptor positive cells are in the minority. Small PNA^- and PNA^+ thymocytes were depleted of IL-2 receptor positive cells. The $\sim$ 5% receptor positive cells seen in the medium and large PNA^+ fractions most likely represent contaminating PNA^- cells. It is unlikely that the receptor positive cells in our thymocyte fractions represent lymph node contaminants, since B-lymphocytes present in lymph nodes would stain with second-stage antibody alone, which has not been the case. We thus believe that a distinct minority of thymocytes do indeed express the IL-2 receptor.

IL-2 Receptor Expression on Thymocyte Subpopulations

Fraction	% Positive with α-IL-2 Receptor Ab	% Positive with Second-Stage Ab	Net Positive
Lg PNA^-	22.6	3.1	19.5
Lg PNA^+	7.3	3.1	4.2
Med PNA^-	23.1	5.8	17.3
Med PNA^+	9.2	4.3	4.9
Sm PNA^-	6.6	7.0	-
Sm PNA^+	3.2	5.9	-

Discussion

The hallmark of the immune system is the clonal amplification of lymphocytes upon contact with a particular antigen. For mature T-cells, this proliferation is mediated by the polypeptide hormone Interleukin-2 (IL-2). The ability both to produce and to respond to IL-2 is tightly regulated. IL-2 is produced only by the "helper" class of T-cells and only when a helper cell is activated by the contact with its particular antigen on the surface of an antigen-presenting cell (Gillis et al., 1980; Glasebrook and Fitch, 1980; Kappler et al., 1981). To utilize the IL-2 thus produced,however, a T-cell must express the receptor for IL-2, which is expressed

only upon stimulation with antigen. Antigen binding alone is not mitogenic for mature T-cells. Therefore, if thymocytes are proliferating in response to self-antigens, they must be using the IL-2 receptor.

We have demonstrated that there are cells endogenous to the thymus that express the IL-2 receptor, although we make no claims as to its use. These cells are enriched in the proliferating subset of thymocytes. Moreover, the IL-2 receptor-expressing cells are confined to one class, that of PNA^- cells. It must be noted, however, that even in the overlap between PNA^- cells and lymphoblasts, which includes only 1-3% of all thymocytes, only a fraction express the receptor. A recent study (Cantrell and Smith, 1983; 1984) concludes that unless an extremely large amount of IL-2 is present, expression of a low level of IL-2 receptors is not sufficient to deliver a mitogenic signal. Since we find a very low level of IL-2 receptor expression on most cells, we believe that it is necessary to postulate an IL-2 independent mechanism for most intra-thymic proliferation.

This does not preclude IL-2 driven proliferation for the subset of cells that do express the receptor. Furthermore, the majority of blasts, which do not express the IL-2 receptor, are unlikely to be responding to self antigens. We speculate that this proliferation may reflect either a "suicide" mechanism or an immature "stem-cell like" proliferation. The cells that we find to be IL-2 receptor positive could be mature thymic T-cells. If so, they may be ready for export or may be a long-term resident population. If the response to antigen is governed identically in the thymus as it is in the periphery, then only these cells can be responding to self antigens. Further analysis of this fraction of thymocytes is being conducted using markers which correlate with functional reactivity (Dialynas et al., 1983; Swain et al., 1984). The functional capabilities of these cells also remain to be investigated. We believe that future studies focusing on the thymic lymphoblasts will be highly fruitful in elucidating the role of the thymus in T-lymphocyte differentiation.

REFERENCES

1. Bleackley, R.C., C. Havele, and V. Paetkau. 1982. Cellular and molecular properties of an antigen-specific T-lymphocyte line. *J. Immunol.* **129:***758.*
2. Bryant, B.J. 1972. Renewal and fate in the mammalian thymus. Mechanisms and inferences of thymocytokinetics. *Eur. J. Immunol.* **2:***38.*
3. Cantor, H., and I. Weissman. 1976 Development and function of subpopulations of thymocytes and T-lymphocytes. *Prog. Allergy* **20:***1.*
4. Cantrell, D.A., and K.A. Smith. 1983. Transient expression of interleukin 2 receptors. *J. Exp. Med.* **158:***1895.*
5. Cantrell, D.A., and K.A. Smith. 1984. The interleukin 2 T-cell system: a new cell growth model. *Science.* **224:***1312.*
6. Caplan, B. and E. Rothenberg. 1984. High level of secretion of interleukin 2 by a subset of thymic lymphoblasts. *J. Immunol.* In press.
7. Crissman, H.A., and R.A Tobey. 1974. Cell cycle analysis in 20 minutes. *Science* (Wash. D.C.) **184:**1297.
8. Dialynas, D.P., Z.S. Quan, K.A. Wall, A. Pierres, J. Quintans, M.R. Loken, M. Pierres, and F.W. Fitch. 1983. Characterization of the murine T cell surface molecule, designated L3T4, identified by monoclonal antibody GK1.5: similarity of L3T4 to the human Leu-3/T4 molecule. *J. Immunol.* **131:***2445.*
9. Gillis, S., and K.A. Smith. 1977 Long-term culture of tumor-specific cytotoxic T cells. *Nature* **268:***154.*
10. Gillis, S., M. Scheid, and J. Watson. 1980. Biochemical and biologic characterization of lymphocyte regulatory molecules. III. The isolation and phenotypic characterization of interleukin 2 producing T-cell lymphomas. *J. Immunol.* **125:***2570.*
11. Glasebrook, A.W., and F.W. Fitch. 1980. Alloreactive cloned T-cell lines. I. interactions between cloned amplifier and cytolytic T-cell lines. *J. Exp. Med.* **151:***876.*
12. Howard, M., J. Farrar, M. Hilfiker, B. Johnson, K. Takatsu, T. Hamaoka, and W.E. Paul. 1982. Identification of a T-cell derived B-cell growth factor distinct from interleukin 2. *J. Exp. Med.* **155:***914.*
13. Hyman, R., and V. Stallings. 1978. Evidence for a gene extinguishing cell-surface expression of the Thy-1 antigen. *Immunogenetics.* **6:***447.*
14. Kappler, J.W., B. Skidmore, J. White, and P. Marrack. 1981. Antigen-inducible, H-2-restricted, interleukin 2 producing T-cell hybridomas. Lack of independent antigen and H-2 recognition. *J. Exp. Med.* **153:***1198.*
15. Malek, T.R., R.J. Robb, and E.M. Shevach. 1983.Identification and initial characterization of a rat monoclonal antibody reactive with the murine interleukin 2 receptor-ligand complex. *Proc. Natl. Acad. Sci. USA.* **80:***5694.*
16. Metcalf, D. The structure of the thymus. 1966. In *The Thymus, Recent Results in Cancer Research*, vol. 5, D. Metcalf (ed.) Springer-Verlag, Berlin, p. 1.
17. Reisner, Y., M. Linker-Israeli, and N. Sharon. 1976. Separation of mouse thymocytes into two subpopulations by the use of peanut agglutinin. *Cell. Immunol.* **25:***129.*
18. Rothenberg, E. 1982. A specific biosynthetic marker for immature thymic lymphoblasts: active synthesis of thymus-leukemia antigen restricted to proliferating cells. *J. Exp. Med.* **155:***140.*
19. Rothenberg, E., and D. Triglia. 1983. Clonal proliferation unlinked to terminal deoxynucleotidyl transferase synthesis in thymocytes of young mice. *J. Immunol.* **130:***1627.*
20. Rothenberg, E., B. Caplan, and R.D. Sailor. Toward a molecular basis for

growth control in T-lymphocyte development. In *Proceedings of the Cetus/UCLA Symposium on the Molecular Biology of Development.* In press.
21. Scollay, R., and K. Shortman. Cell traffic in the adult thymus: cell entry and exit, cell birth and death. In *Recognition and Regulation in Cell Mediated Immunity.* J. Watson and J. Marbrook, eds. Marcel Dekker, New York. In press.
22. Smith, K.A. 1980. T-cell growth factor. *Immunol. Rev.* **51**:*337.*
23. Swain, S.L., D.P. Dialynas, F.W. Fitch, and M. English. 1984. Monoclonal antibody to L3T4 blocks the function of T-cells specific for class 2 major histocompatibility complex antigens. *J. Immunol.* **132**:*1118.*

Sequencing Antigenic Mutants of Sindbis Virus

William Newman and Dr. Charles Rice

ABSTRACT: We are sequencing by a variant of the Sanger method RNA from mutants of Sindbis virus resistant to certain neutralizing antibodies.

Sindbis is the type virus of the genus Alphaviridae. It is a simple RNA virus capable of infecting mammal, bird, and insect cells. Dr. Alan Schmaljohn at the University of Maryland School of Medicine has raised several monoclonal antibodies which neutralize the AR339 strain of Sindbis by binding to the coat protein E2. and has used these to select for resistant mutants. I have worked with Dr. Charles Rice to sequence the E2 gene region in AR339 and in Schmaljohn's mutants using dideoxynucleotide-terminated reverse transcription.[1]

Using the known sequence of the HR strain of Sindbis we arranged the synthesis of oligodeoxynucleotide primers complementary to 5 sites spaced throughout the 1200 nucleotide E2 gene. Before the oligonucleotides were complete I worked to isolate RNA from Sindbis virions and then tried to clone cDNA made from these samples into E. coli for possible Maxam-Gilbert sequencing or other future experiments. I failed at cloning; it appears that I used too little RNA.

Once the first 2 primers were synthesized they were purified, with others not related to my work, by Dr. Ellen Strauss, while I isolated larger quantities of RNA directly from infected cells. Shortly thereafter I began prototype sequencing reactions.

I found that I had a problem with noise, though not so much that all seemed lost. I ran many reactions varying the original protocol and improved my results somewhat by increasing the concentration of dideoxynucleotides and primer, adding RNasin, and omitting melting from the primer/template annealing reaction.

When primer #3 was completed it was purified by Young

Shin Hahn. I tested it in one of my reactions and found beautiful results. Running reactions in parallel showed that primer #3 produced good data under the same conditions that #1 and #2 produced blurry incoherency.

Using Young's protocol I rushed to purify new aliquots of #1 and #2, and to purify #4 and #5. Unfortunately, my new sequencing reactions were no better than those with the old #1 and #2. Comparisons of unpurified primer #3 with other unpurified primers support the conclusion that #3 is inherently superior.

The effectiveness of the primers correlates with their A-T content. This is a common finding, but we have been surprised at the apparent overwhelming importance of this factor.

Today my improved sequencing protocol gives readable data with all primers except #2. I am about to begin sequencing all my RNA with these primers and arrange the synthesis of an A-T rich primer to replace the G-C rich #2; a suitable binding site lies adjacent to the old priming site. If this fails, I may still clone the gene and sequence by the Maxam-Gilbert method from the Sal1 site within the primer #2 region.

REFERENCES

1. Jing-Hsiung Ou, Ellen G. Strauss, James H. Strauss (1983) The 5'-Terminal Sequences of the Genomic RNAs of Several Alphaviruses, J. Mol. Biol, 168, 1-15.

2. Ellen G. Strauss, Charles M. Rice, James H. Strauss (1984) Complete Nucleotide Sequence of the Genomic RNA of Sindbis Virus, Virology, 92-110.

PRELIMINARY CHARACTERIZATION OF YELLOW FEVER VIRUS STRUCTURAL AND NONSTRUCTURAL PROTEINS

Author: Janice Pata

Sponsor: Dr. Charles M. Rice

Yellow fever virus was grown in SW13 host cells and intact virions released into the culture media were purified on a 10-30% glycerol gradient. Purified intact virus particles were digested with 1 mg/ml Trypsin to remove protein exposed on the outside of the virus membrane, producing lighter particles which were isolated on a buoyant density gradient of Potassium-Tartrate. A mouse hyper-immune antisera specific for yellow fever virus proteins effectively immunoprecipitated virus proteins from a Triton X100 solublized, yellow fever infected, host cell lysate and was used to isolate 100K and 76K nonstructural proteins for amino-terminal sequencing.

1. Introduction

Flaviviruses, such as yellow fever virus, are grouped together with the alphaviruses to form the family of Togaviruses. Flavivirus particles consist of a nucleocapsid, containing the single-stranded genomic RNA, surrounded by a lipoprotein envelope. The Flaviviruses have three structural proteins which are apparently translated from a single initiation codon and produced by subsequent proteolytic cleavage. These structural proteins are: a large glycoprotein and a smaller non-glycosylated protein (the M protein), which are both associated with the envelope, and a capsid protein which is complexed with the genomic RNA to form the nucleocapsid.[4,6,7] In the case of yellow fever virus, the complementary DNA sequence of the genome has been determined, and the capsid protein, the M protein, and the amino-terminal end of the glycoprotein have been sequenced[3]. By comparing the direct protein sequences with the amino acid sequence specified by the cDNA, the three structural proteins have been located at the 5' end of the yellow fever virus genome in the order 5'-capsid protein, M protein, glycoprotein, followed by a large region of nonstructural proteins continuing to within 700 nucleotides of the 3' end[3]. The carboxy-terminal end of the glycoprotein has not been determined, and none of the nonstructural proteins have been studied.

In this project we developed methods to purify yellow fever virus (the 17D vaccine strain) and to produce a virus infected host cell lysate containing yellow fever virus proteins. The purified virus particles were digested with the protease Trypsin which cleaved off about 60% of the glycoprotein leaving a small portion (the root) that was protected by the envelope. We will isolate the root for sequencing from the digested virions (called spikeless particles)[2]. This will tell us where the membrane associated portions of the glycoprotein are located in the genome.

We also used a mouse hyperimmune antiserum specific for yellow fever virus proteins to immunoprecipitate virus proteins from the host cell lysate and to then isolate two large nonstructural proteins for sequencing. Knowing the amino-terminal sequence of these nonstructural proteins will place them in the yellow fever virus genome. Also, if all the nonstructural proteins are found and placed in the genome, then a limit to the length of the glycoprotein will be defined.

2. Presentation and Discussion of Results

The overall strategy of this project was first to find appropriate conditions in which to grow yellow fever virus (YFV). That is, to produce larger quantities of the virion and also to produce a YFV infected host cell lysate containing relatively large amounts of the yellow fever virus proteins. From this point the experiments can be divided into two categories: those using the lysate and those using the intact virus particles. The lysate was immunoprecipitated using mouse hyperimmune ascites fluid specific to YFV proteins which helped to identify the virus specific proteins, find their molecular weights, and to isolate the two large nonstructural proteins for amino-terminal sequencing. The intact virions released into the culture fluid were used to develop an alternative procedure for purifying the virus, which was then treated with protease to produce spikeless particles. These experiments are discussed in the following sections.

a. Virus Growth and Labeling

Yellow fever virus (the 17D vaccine strain) was grown at 37°C in confluent monolayers of SW13 cells at a multiplicity of infection of 10-20 plaque-forming-units/cell. The proteins were radiolabeled with either [^{35}S]methionine or [^{3}H]leucine. Intact virus particles were harvested by collecting the labeling media, and a lysate was produced by treating the SW13 cells with a lysis buffer containing either 1% Triton X100 or 0.5% SDS. The virus and lysate used in most of the

following experiments was labeled with [^{35}S]methionine from 22 to 48 hours post-infection.

By adding [^{35}S]methionine to cells which were at various times post-infection, we determined that around 24-30 hours post-infection the virus specified proteins are at their highest concentration in the host cells.

b. Immunoprecipitation and Molecular Weight Determination

Yellow fever virus proteins were immunoprecipitated using a mouse HI (hyperimmune) antiserum specific for yellow fever virus proteins. Virus infected host cell lysate and mouse HI antisera were combined (usually in the ratio of 1 volume lysate : 1/400 volume antisera)and incubated for one hour at room temperature. This allows the antibodies in the mouse HI antisera to recognize and bind to the YFV proteins. Next, a solution of 10% Staph A was added and incubated for 30 minutes at room temperature. Protein A on the surface of Staph A binds to the protein-antibody complexes. Then, the mixture was layered over a 10% sucrose cushion and spun to pellet the Staph A (and anything bound to it). The pellet was resuspended in Laemmli sample buffer containing 1% SDS and heated 15 minutes at 60°C. This dissociates the yellow fever virus proteins from the Staph A, and the proteins can then be separated and analyzed.

Proteins were separated by SDS-polyacrylamide gel electrophoresis using the Laemmli discontinuous buffer system[8]. Immunoprecipitated lysates from YFV infected SW13 cells were run on a 15% acrylamide gel in parallel with a low molecular weight protein standard, a "mock"lysate from SW13 cells not infected with yellow fever virus (to identify the YFV specified proteins), and non-immunoprecipitated YFV infected lysate (to determine how much of the YFV proteins are immunoprecipitated).

We have identified protein bands, which appear to be yellow fever virus specified, with molecular weights (in daltons) of: 100K, 84K, 76K, 57K, 53K, 50K, and 31K. There also appear to be several yellow fever virus specific proteins below 30K, but in this region of the gel, proteins are not being resolved very well, and we do not have proper protein standards to determine such low molecular weights. The bands at 100K and 76K are large nonstructural proteins. The band at 57K is the glycoprotein, and the band at 53K may be a nonglycosylated form of the glycoprotein. This agrees fairly well with other published yellow fever virus protein molecular weights[4,5,6].

The mouse HI antisera effectively immunoprecipitates the YFV specific proteins, especially the two nonstructural proteins. The antisera seems to precipitate more proteins from the Triton X100 solublized lysate than from the SDS

solublized lysate. This may be because the proteins retain a more natural configuration in the presence of TX-100 (a non-ionic detergent) than in the presence of SDS (an ionic detergent). (The ionic detergent would be expected to disrupt more of the interactions which determine the conformation of a protein.)

c. Isolation of Nonstructural Proteins for Sequencing

Triton X100 solublized lysate from yellow fever virus infected cells was immunoprecipitated with mouse HI antisera as described in the preceeding section. The proteins were separated on a small 7.5% acrylamide gel. We tried to isolate the 100K and 76K nonstructural proteins by two methods: electroblotting and electroelution.

Electroblotting is a new technique being developed to isolate proteins for sequencing. In this method, the gel is placed between sheets of filter paper, immersed in a buffer solution, and an electric current is applied to cause the proteins to move out of the gel onto the filter paper. Then, the filter paper and gel are stained to visualize the proteins. We found that there was not a significant amount of the 100K protein transfered to the filter paper, and that less than half of the protein in the 76K band transfered. [9]

Both the 100K and 76K proteins were effectively eluted from the gel by the method of Hunkapiller, et al [1].

We do not yet have any sequence data, but once we have the sequence of the amino terminal ends of the large nonstructural proteins we can determine where they are located in the yellow fever virus genome which would define a limit to the carboxy-terminal end of the glycoprotein (assuming the genes do not overlap). Of course this limit would be more exact if there are not any other nonstructural proteins between the glycoprotein and the first large nonstructural protein.

d. Virus Purification

Yellow fever virus was PEG precipitated by combining three volumes of harvested media with one volume of a 40% PEG solution. This was incubated 1-2 hours on ice, then spun at 9K rpm for 50 minutes at 4°C. The pelleted virus was then resuspended in a small amount of MEM. The PEG precipitation serves to concentrate the yellow fever virus particles. Next, the PEG precipitated virus was layered over a 10-30% glycerol gradient which was then spun at 36K for 90 minutes at 4°C. 0.3 ml fractions were collected from the gradient and counted on a liquid scintillation counter. The fractions containing the mature virus peak were pooled.

We found that the virus peak was located two-thirds of the way down the glycerol gradient (in about 24% glycerol). The PEG precipitated virus was fairly stable when stored at -70°C, but the virus in the pooled fractions from the glycerol gradient appeared to be either agregated or dissociated after being stored at -70°C. This was determined by resedimenting the pooled virus peak fractions which had been stored at -70°C on another 10-30% glycerol gradient. The shape of this virus peak was not as discreet as the original virus peak, and only 26% of the label resedimented in the virus peak. Hence, only virus that had just been freshly purified on a glycerol gradient was used in the spikeless particle experiment. The virus was stable during purification even when the glycerol gradient had a high salt concentration (0.5M NaCl).

e. Spikeless Particle Preparation

Spikeless particles were prepared by treating [^{35}S]methionine labeled purified yellow fever virus particles with fresh protease (either Trypsin or α-chymotrypsin) [2]. The protease digestion was stopped by adding phenylmethylsulfonyl fluoride. The digested particles were layered over a Potassium-Tartrate gradient and spun at 36K rpm overnight (until the particles reached their buoyant density). 0.3 ml fractions were collected and counted on a liquid scintillation counter. To isolate spikeless particles, we were looking for a discreet peak of lower density than an intact virus particle peak, since the proteins are more dense than the average density of the entire virus particle. The fractions containing a spikeless particle peak were pooled, diluted, layered over a 30% glycerol cushion, and spun at 36K rpm for 6 hours. Then the pellet was resuspended in Laemmli sample buffer and was run on SDS-polyacrylamide gels.

Purified intact virus particles which were digested with 1 mg/ml Trypsin and incubated 45 minutes at 37°C were found to produce a discrete spikeless particle peak on the Potassium-Tartrate gradient. If the envelope is impermeable to protease, then we would expect that the capsid protein would be intact and only the portions of the glycoprotein and M protein exposed on the outside of the envelope would be digested.

Intact virus particles and spikeless particles (both derived from the same amount of purified virus) were run in parallel on polyacrylamide gels. There were three bands from the intact virus which corresponded to (in order of decreasing molecular weight) the glycoprotein, the capsid protein, and the M protein. From the spikeless particles (in comparison to the intact particles) all of the glycoprotein and M protein was gone, 90% of the capsid protein was gone, and several additional bands appeared. This may indicate

that the virions are not uniformly digested, and that only about 10% of the digested particles are actually spikeless particles (corresponding to the remaining capsid protein). The most intense of the spikeless particle protein bands migrated at a slightly larger molecular weight than intact M protein, and so was most likely not derived from the M protein. Also, although this band migrated at a lower molecular weight than the intact capsid protein band, it was more intense than if all of the capsid protein had been digested to form this band. Therefore, at least some of the protein in this band was probably derived from the glycoprotein and is the glycoprotein root. The intensity of the band may mean that although a majority of the glycoprotein was cleaved off, a majority of the [^{35}S]methionine label was retained in the root and is therefore a methionine rich hydrophobic region. This would correlate with a methionine-rich segment which is encoded for in the yellow fever virus genome, and (based on the molecular weight of the glycoprotein) maps close to the carboxy-terminal end of the glycoprotein. The protein bands on the gels were assayed by [^{35}S]methionine label. There could be other protein fragment bands which do not appear because they do not contain methionine.

To distinguish between the capsid and M proteins and determine their band order on gels as given above, we treated purified intact virus particles with 0.25% Triton X100. This should have allowed the nucleocapsid to remain intact, but dissociated the M protein and the glycoprotein from the virus. The TX-100 solublized virus was layered over a 30% glycerol cushion and spun at 25K for 12 hours to pellet the nucleocapsids. The pellet was resuspended in Laemmli sample buffer and run in parallel with purified intact virus particles. We found that a single band (the capsid protein) remained and migrated with the middle band from the intact virions. So, we identified the intact virus particle protein bands in the order previously given.

3. Conclusions

To summarize the results of this project, yellow fever virus particles grown in SW13 host cells and released into the growth media can be purified and concentrated on a 10-30% glycerol gradient. When these purified virions are digested with 1 mg/ml Trypsin for 45 minutes at 37°C, a lighter (spikeless particle) peak appears on a Potassium-Tartrate buoyant density gradient, but the virus particles present in this peak are not uniformly digested and perhaps only 10% are actually spikeless particles with the exterior proteins cleaved off and the virion envelope intact. A mouse hyperimmune antisera specific for yellow fever virus proteins effectively immunoprecipitates virus proteins from infected host cell lysate, particularly the large nonstructural

proteins which were isolated for amino-terminal sequencing.

Based on the work reported here, we plan to find better conditions to produce spikeless particles. These will then be studied by isolating and sequencing the membrane associated portion(s) of the glycoprotein and possibly also the M protein. We want to get sequence data for the amino-terminal ends of the large nonstructural proteins and place them in the yellow fever virus genome. Also, we would like to study the other nonstructural proteins proteins which are present in the yellow fever virus infected SW13 cell lysate.

Bibliography

1. M. W. Hunkapiller, et al, Methods in Enzymology, 91, 227-236 (1983)
2. C. M. Rice, et al, J. Mol. Biology, 154, 355-378 (1982)
3. C. M. Rice, S. R. Eddy, S. J. Shin, unpublished data
4. P. K. Russel, et al, The Togaviruses, Chapter 18, 503-529
5. J. J. Schlesinger, et al, Virology, 125, 8-17 (1983)
6. E. G. Westaway, The Togaviruses, Chapter 19, 531-581
7. E. G. Westaway, Intervirology, 14, 114-117 (1980)
8. V. K. Laemmli, Nature, 227, 680-685 (1970)
9. Steve Kent, et al, unpublished data

TYPE II CALCIUM-CALMODULIN DEPENDENT PROTEIN KINASE IN DROSOPHILA

John B. Wall

Advisor: Dr. M. Kennedy

Abstract:

The type II calcium/calmodulin-dependent protein kinase has been observed in Drosophila. The kinase has a higher specific activity in head fractions (2109 pmol/min/mg protein) than in body fractions (313 pmol/min/mg protein). The monoclonal antibody to the rat kinase (4A11) maximally inhibits the Drosophila kinase at 0.16 micrograms 4A11 per microgram 2KSH protein.

Introduction:

Calcium is a major second messenger known to be involved in the response of neurons to regulatory agents (Greengard, 1978). It is believed that one method of calcium action is the activation of specific protein kinases (Kennedy, 1983). The Type II calcium/calmodulin dependent protein kinase, which is a major calcium target in brain, has been characterized in the Kennedy lab (Bennett et al., 1983). It was assayed during purification by its ability to phosphorylate Synapsin I, a brain-specific, synaptic-vesicle-associated protein (Ueda et al., 1973; De Camilli et al., 1983).

The molecular structure of the kinase found in rats has been determined. It is composed of three peptide subunits of molecular weights 50,000, 58,000, and 60,000 daltons, called α, β', β respectively. The molecular weight of the holoenzyme is 650,000 daltons, and it appears to be composed of 9 α-subunits and $3\beta/\beta'$ subunits. All three subunits bind calmodulin in the presence of calcium and are autophosphorylated under conditions in which the kinase is active (Bennett et al., 1983). Initial estimates show the kinase to compose as much as 0.3% of the total brain protein in rat. It phosphorylates a number of brain proteins in a highly specific manner. Thus, it may play a number of distinct regulatory roles in brain.

In order to study these regulatory roles, it is helpful to know if the kinase activity is present throughout the animal kingdom, and if so, if its structure is conserved. A number of invertebrate nervous systems are simpler than the mammalian nervous system and are thus more amenable to physiological and genetic studies. Synapsin I kinase activity has been found in rat brain, the electroplaques of Torpedo californica, and the brain of Manduca sexta (the

tobacco horn worm) (M.B. Kennedy, unpublished observations). An homologous kinase has also been described in the nervous system of the marine mollusk Aplysia californica (Novak-Hofer and Levitan, 1983).

The monoclonal antibody, 4A11, is a potent inhibitor of the rat calcium/calmodulin-dependent Synapsin I kinase against which it was made. The highly specific binding of antibody to antigen makes 4A11 inhibition of an unknown kinase a good measure of the homology between rat and the unknown kinase.

Drosophila, the laboratory fruit fly , is one of the best understood organisms for genetic studies. Its ease of handling and the large body of information about it, make Drosophila an ideal animal in which to carry out molecular genetic and neurogenetic studies on the kinase system.

The purpose of this project was to establish the presence of Type II calcium/calmodulin-dependent protein kinase in Drosophila, and to examine the inhibition of this activity by 4A11.

Materials and Methods:

Preparation of homogenate fractions- Canton Special (wild type) D. melanogaster were grown in the S. Benzer lab at Caltech. Several grams of flies were collected and frozen at -80C. Bodies, heads, and extraneous parts were separated by freezing a bottle containing flies, in liquid nitrogen, banging the bottle sharply to shatter the flies into sections, and using sieves to separate the different parts. One-half gram of heads or bodies was immediately homogenized by 30 up-and-down strokes with a Teflon/glass homogenizer at 900rpm in 5ml volume of Fly H-Buffer (20mM Tris (pH 7.5), 1mM imidazole, 1mM magnesium chloride, 0.02% (w/v) sodium azide, 2mM DTE, 1mM EGTA, 1mM EDTA, 17.4 micrograms/ml PMSF, 5 micrograms/ml aprotinin, 0.5 micrograms /ml antipain, 0.5 micrograms/ml leupeptin, and 0.1 micrograms/ml pepstatin). The homogenization volume was brought to 10ml with Fly H-Buffer. Head and body homogenates were centrifuged at 2000g for 10min. The supernatants from head and body were called 2KSH and 2KSB respectively. The pellets were resuspended in 10ml of Fly H-Buffer and were called 2KPH and 2KPB for heads and bodies respectively. The fractions were aliquoted and frozen at -80C.

Assays for endogenous substrate phosphorylation- Endogenous substrate phosphorylation was assayed by the "gel method" Assays were conducted at 30C. in a reaction mixture (final volume 100microliters) containing 50mM Tris (pH 8.0), 10mM magnesium chloride, 5mM 2-mercaptoethanol, 2micrograms calmodulin, 0.1mM DTE, 10microM [gamma-P32]ATP (0.5-2.5x10E4 cpm/pmol), either 0.4mM EGTA (minus calcium) or 0.4mM

EGTA/0.7mM calcium chloride (plus calcium), and varying amounts of soluble or particulate enzyme. After preincubation for 1min., the reaction was initiated by addition of [gamma-P32]ATP and terminated after 30sec. by addition of 50microliters of "stop solution" (9% SDS, 15% (w/v) glycerol, 6% (v/v) 2-mercaptoethanol, 0.186M Tris HCl (pH 6.7), and approximately 0.05% Bromophenol Blue). The reaction mixture was boiled for 1.5min. Seventy microliters of the solution were subjected to SDS/polyacrylamide gel electrophoresis. The stacking gel was 3.5% acrylamide/bis and the separating gel was 10% acrylamide/bis. Labeled substrates were visualized by autoradiography.

Assays for calcium/calmodulin-dependent Synapsin I kinase activity- Calcium/calmodulin-dependent Synapsin I kinase was assayed under the conditions those used to measure endogenous substrate phosphorylation except that 10micrograms of Synapsin I were included and the [gamma P32]ATP was used at a higher concentration (50micromolar) and lower specific activity (3000 cpm/pmol). Labeled Synapsin I was localized by autoradiography, cut out of the dried gel, placed in liquid scintillation fluid, and quantitated by liquid scintillation spectrometry. Phosphorylation by the calcium-dependent Synapsin I kinase was measured as the difference between [gamma-P32] incorporation into Synapsin I in the presence and absence of calcium.

4A11 inhibition of 2KSH endogenous substrate phosphorylation- Phosphorylation of 2KSH endogenous substrates in the presence of 2.5-4 micrograms of 4A11 was assayed under conditions similar to those previously described. Two bands which were qualitatively inhibited as visualized by autoradiography were removed from the gel and quantitated by liquid scintillation spectometry.

4A11 inhibition of calcium/calmodulin-dependent Synapsin I kinase activity- Inhibition of Synapsin I kinase activity was measured under conditions similar to those used to measure Synapsin I kinase activity except that varying amounts of 4A11 were used. The result was quantitated as described previously.

Results and Discussion:

Synapsin I and endogenous substrate phosphorylation

Assays for calcium-dependently phosphorylated substrates were carried out. Visualization by autoradiography showed the the majority of protein substrates phosphorylated in a calcium dependent way are in the head, not in the body (fig.1). This supports the idea that the Type II calcium-dependent kinase is particularly concentrated in the nervous system in Drosophila, as is also true in the rat.

All phosphorylated substrates observed in the supernatant fractions were also observed in the pellet fractions. However, most of the substrates were phosphorylated more heavily in the soluble fraction than in the particulate fraction.

The 2KSH and 2KSB fractions were assayed for Synapsin I activity. The [gamma-P32] incorporation rate for the head was much greater than for the body: 2109 pmol/min/mg protein and 313 pmol/min/mg protein respectively. From homogenization weights and volumes, it was possible to measure the total[gamma P32] incorporation rate into head and body homogenates: 2.22 pmol/min/head and 3.04 pmol/min/body. It was assumed that a fly head had 16micrograms of protein and a body had 117micrograms of protein. Although there is more synapsin I activity in the body than in the head, this is only because there is a much larger amount of total protein there. The head has a much higher specific activity than the body indicating a larger concentration of the kinase activity.

Specific Activities of Synapsin I Kinase
(pmoles/min/mg protein)

	D.melanogaster	R.norvegicus
head	2109	10,000 (brain) [1]
body	313	542 (spleen) [2] 254 (heart)

[1] Bennett et al (1983)
[2] Kennedy and Greengard (1981)

4A11 inhibition of Synapsin I and endogenous substrate phosphorylation-

The presence of 4A11 in the reaction mixture of Synapsin I phosphorylation assays inhibited [gamma-P32] incorporation into Synapsin I. At 0.08micrograms or greater of 4A11/1microgram 2KSH protein, inhibition was already nearly maximal. At antibody concentrations of 0.16micrograms or greater of 4A11/1microgram of 2KSH protein, 4A11 had its maximum inhibition of Synapsin I activity (fig.2). This means that the Drosophila calcium dependent Synapsin I kinase is similar enough to the rat kinase, that 4A11 will inhibit it.

4A11 also inhibits phosphorylation of several endogenous substrates. When a "gel assay" of endogenous substrate phosphorylation was conducted in the presence of 4A11, six of the phosphorylated substrates were inhibited (fig.3). Quantitation of this result, by counting [gamma-P32] incorporation into two of the substrates, indicated that maximal inhibition occured at concentrations of atleast 0.16micrograms 4A11/1microgram 2KSH protein (fig4). This is in good agreement with the number obtained for Synapsin I. This is good evidence that the same kinase phosphorylates

both Synapsin I and the endogenous substrates, and is inhibited by 4A11.

Conclusions:

1. Type II calcium/calmodulin-dependent protein kinase is present in wild type Drosophila. It is concentrated in the head indicating a probable role in the nervous system.

2. The Drosophila kinase is similar enough to the rat kinase that it is inhibited by the monoclonal antobody 4A11.

3. The kinase has a specific activity of 2109 pmol/min/mg head protein and 313 pmol/min/mg body protein in Drosophila.

Bibliography:

Bennett, M.K., Erondu, N.E., and Kennedy, M.B. (1983) J. Biol. Chem., 258, 12735-12744

DeCamilli, P., Harris, S.M., Huttner, W.B., and Greengard, P. (1983) J. Cell Biol., 96, 1355-1373

Greengard, P. (1978) Science, 199, 146-52

Kennedy, M.B. and Greengard, P. (1981) Proc. Natl. Acad. Sci. U.S.A., 78, 1293-1297

Kennedy, M.B., McGuinness, T., and Greengard, P. (1983) J. Neurosci., 3, 818-831

Novak-Hofer, I. and Levitan, I.B. (1983) J. Neurosci, 3, 473-481

Ueda, T., Maeno, H., Greengard, P. (1973) J. Biol. Chem., 248, 8295-8305

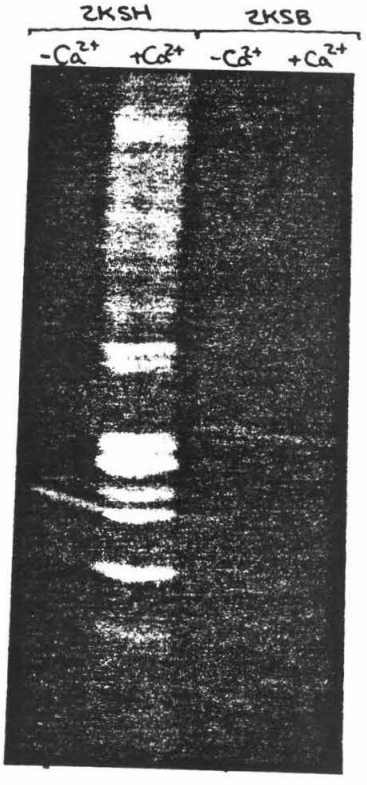

fig. 1 Calcium-dependently phosphorylated substrates. The results show that the majority of the phosphorylated protein is concentrated in the head.

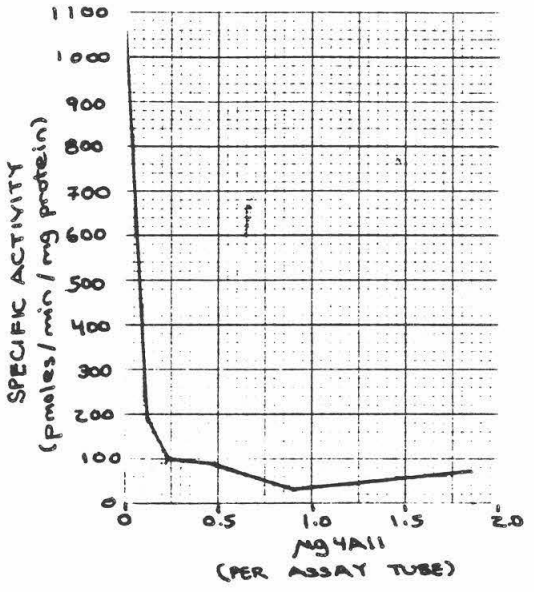

fig. 2 Inhibition of Synapsin I phosphorylation by 4A11. Each assay tube contained 25.3 μg protein.

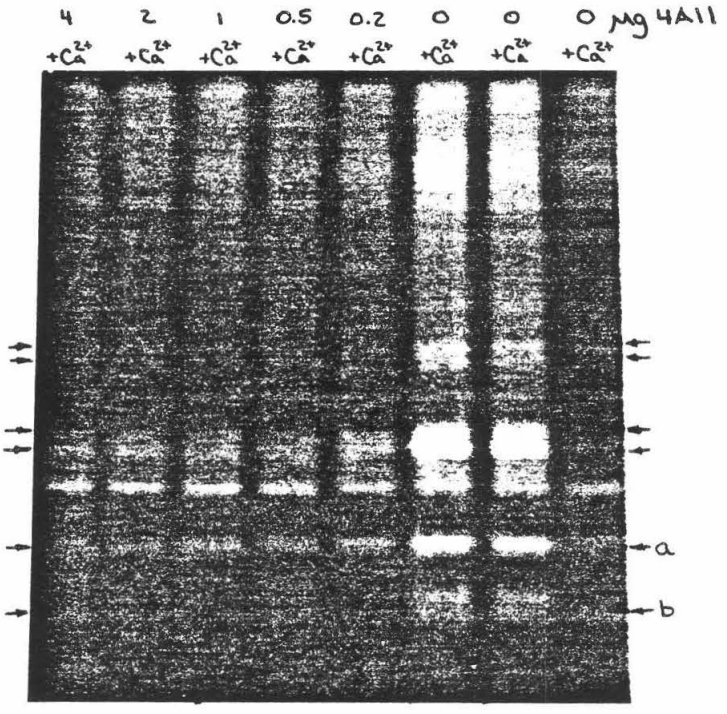

fig. 3 Inhibition of endogenous phosphorylation by 4A11. Each assay tube contained 25.3µg protein.

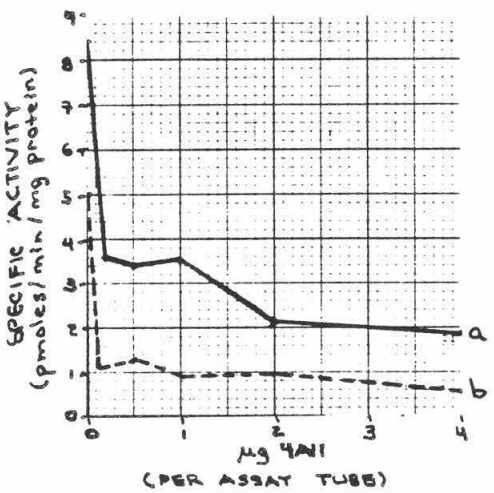

fig. 4 Inhibition of endogenous substrate phosphorylation by 4A11. Bands (a) and (b) are those indicated in fig. 3

Task Difficulty Induces Increasing Right Ear Advantage in Normal Subjects

Tad White

Sponsor: Polly Henninger

ABSTRACT

The purpose of the experiments was to compare the performance of normal subjects with that of hemispherectomy and callosal section patients on an ascending dichotic digits test in which increasing numbers of digits are presented simultaneously to each ear and subjects report all that they hear. The normal subjects were given additional tasks to perform using the digits in order to increase the cognitive load or amount of processing required. The normal subjects showed a significantly greater increase in right ear advantage on these tests than on control tests without the additional tasks ($p < 0.05$). This indicates that in normal subjects, as in the previously investigated clinical cases, cognitive factors increase the relative performance of the right ear compared to the left ear, indicating an increase in left hemisphere performance.

INTRODUCTION

Previous investigations have shown that in normal subjects the left hemisphere is specialized for processing verbally presented material. This has been shown with normal subjects and clinical populations (Kimura, 1967). Kimura used a dichotic testing technique, described by Broadbent (1956), in which two strings of three digits each were presented to both ears simultaneously, and the subjects were asked to report orally the digits they heard. It has been shown that patients with surgical disconnection of the cerebral hemispheres cannot report verbal input to the left ear under these conditions (Milner, Taylor, Sperry, 1968). Henninger (1984) has shown that a left ear response can be elicited from these split-brain subjects if the length of the string of digits is small (one or two to each ear) and if the volume of the left ear input is higher than that of the right ear input. The splits shift to right ear response for longer strings of digits (three or four). This indicates that both cognitive (increased load) and perceptual (intensity) factors influence the right ear advantage observed in dichotic testing.

It is useful to study the split-brain subjects because stimuli can be selectively directed to either hemisphere, as the input from the ear opposite a hemisphere (contralateral) has been observed to suppress the input from the ear nearest the same hemisphere (ipsilateral). This enables one to examine the specialization of the hemispheres for a given task. In the normal brain, however, the hemispheres can communicate, so the processing may be done differently than in the split brain. Thus care must be taken when generalizing results obtained by observing splits to normals. The purpose of this study is to determine whether a shift in ear advantage, such as that which was observed in the splits, can be induced in normal subjects.

METHOD

Twenty-four male right-handed high school students, who were attending summer science courses at Caltech, were given the dichotic digits test under the same volume conditions that the splits had been given: equal volume (55 dB/SPL) in both ears, 55 and 50 dB/SPL in the left and right ears respectively, and 50 and 55 dB/SPL in the left and right ears respectivley.The dichotic tape consisted of ten trials in which the digits were presented binaurally as a control measure, followed by 12 trials of one dichotic pair of digits, and eight trials each of two, three and four dichotic pairs. The subjects were instructed to write down all the digits they heard, in whatever order they chose, on a prepared answer sheet. Scores for each ear were determined on the basis of the total number of digits correctly reported.

These subjects showed a right ear advantage on the tests with equal volume and raised right ear volume, and no ear advantage when the volume was raised in the left ear. Although a few individual subjects showed the predicted shift to a right ear advantage, no such trend was observed for the group. Performance was in general too high to reveal a shift had there been one, with subjects beginning with 100% performance in the left ear and 98% in the right ear at the ones level, and reporting 81% and 80% at the fours. The task was apparently not sufficiently difficult to cause the normal subjects to differentially engage left hemisphere resources.

Two tasks believed to be more demanding of left hemisphere resources were devised using the same stimulus tape to test the hypothesis that normal subjects will show the same shift that the split-brain subjects did. In the first task, subjects were instructed to mentally add all the digits they heard, write down the sum, and then write down the digits summed. It was predicted that this would increase the right ear advantage, as addition is a left hemisphere task (Caramazza, McCloskey, Basili, 1984) which should induce

suppression of the ear ipsilateral to the dominant hemisphere. In the second task they wrote down all the digits, but in sequence from smallest to largest.

The addition test was given to a sample of Caltech students, seven undergraduates and one graduate. The test was given twice, once with the volume up in each ear. Each subject was also given the control test (simply write the digits) under all three volume conditions. In the addition test with the volume raised in the right ear, subjects showed a right ear advantage throughout (i.e. at all four levels of difficulty. With the volume raised in the left ear, the left and right ear scores were roughly the same throughout. However, the subjects showed a left ear advantage throughout the control test under the same volume condition. Thus the addition task brought the right ear performance up to the level of the left ear, even though the volume was raised in the left ear. Furthermore, the increase in the right ear advantage (defined here to be the percentage of right ear digits correctly reported minus the percentage of left ear digits correctly reported) on the addition test between the threes and fours was significantly greater than the increase at the corresponding level of task difficulty on the control test under the same volume conditions (paired comparison $t = 2.44$, $p < .05$).

The sequencing test was given to a sample of nine members of a local Pasadena church. In order to induce an initial left ear response, the volume was lowered 10 dB in the right ear. A control test was also given to each subject with instructions to simply report all digits heard in any order. The control test was given with equal volumes in the two ears. On the sequencing test, the subjects showed a left ear advantage throughout. However, it was a declining advantage. The increase in right ear advantage between the threes and fours was significantly greater than the increase in the same place on the control test under the same volume conditions ($t = 2.541$, $p < .05$).

CONCLUSIONS

The significant increase in right ear advantage observed with increases in task difficulty indicates that it is possible in a normal subject to overcome a perceptual advantage for the left ear, induced by increased volume, by assigning a task that places a high demand on left hemisphere resources. Thus the shift to a right ear advantage observed in split-brain patients can also be seen in normal subjects if the task is sufficiently difficult. This suggests that, although total performance for the normal subjects is higher than for the splits, the mechanism which causes suppression of report of the input to the ear ipsilateral to the dominant hemisphere is present in both populations, and thus does not

directly depend on the presence of the corpus callosum to connect the hemispheres.

REFERENCES

Broadbent, D. (1956). Quart. J. Exp. Psychology, 8, 145.

Caramazza, McCloskey, Basili (1984). Disassociation of calculation processes. Presented at INS.

Henninger, P. (1984). Increasing right ear performance with increasing task difficulty on a dichotic digits test in split-brain subjects. Paper presented at Canad. Psychol. Assoc. Convention.

Kimura, D. (1967). Functional asymmetry of the brain in dichotic listening. Cortex, 3, 163-178.

Milner, Taylor, Sperry (1968). Lateralized Suppression of Dichotically Presented Digits after Commissural Section in Man. Science, 161, 184-186.

The Highly Repetitive DNA of *Arabidopsis thaliana*

Robin Wilson

Sponsored by Elliot M. Meyerowitz

Abstract

The genome of *Arabidopsis thaliana* has little highly repetitive DNA in contrast to other higher plants. With these experiments, I attempted to subclone and characterize some of that repetitive DNA.

Introduction

Last summer, a member of this laboratory constructed an *Arabidopsis* DNA library; 12-18 Kb segments of *Arabidopsis* DNA were put into a λ-phage vector (Leutwiler 1983, unpublished). In one experiment, these clones were cut with a restriction enzyme, run through an agarose gel, and transferred onto nitrocellulose filter paper. These filters were probed with radioactively labeled whole plant DNA. Autoradiography revealed the clones containing sequences which were repeated many times in the genome (Pruitt 1984, unpublished). Since *Arabidopsis* contains very little highly repetitive DNA relative to the higher organisms, the portions which are there are probably important; we would like to discover what these sequences encode.

One clone, designated *026,* was mapped thoroughly with restriction enzymes, then cut with various combinations and screened by the process described above. The repetitive section was thus located exactly. Since only a small part of the total *Arabidopsis* segment contained in this λ-phage vector is repetitive, it would be best to cut out the repetitive section and move it to another vector. We chose a bacterial plasmid.

Presentation & Discussion of Results

Restriction enzymes work by recognizing a specific sequence of nucleotides and cutting the DNA at this point. Some cut in a crooked fashion leaving short single strand overhangs called sticky ends. When enzymes which facilitate ligation are introduced, these sticky ends find matching partners with which to rejoin. In some cases, two enzymes which recognize different original patterns leave the same sticky end. These ends can join, but create a sequence which can't be cut by either enzyme.

Fig 1. a) Nucleotide sequence recognized by restriction enzyme Bam HI. b) Sticky end leftover after Bam HI cuts.

The plasmid DOA 1.8 was chosen for the subcloning. DOA 1.8, when introduced into E. coli, confers resistance to the antibiotic kanamycin. If one starts with cells that are unable to metabolize lactose, this plasmid imparts the ability. In the midst of the region which controls lactose metabolism, there is a sequence of single restriction enzyme sites which are used for subcloning. When a new piece of DNA is ligated into this portion of the plasmid, the plasmid loses the power to restore lactose activity.

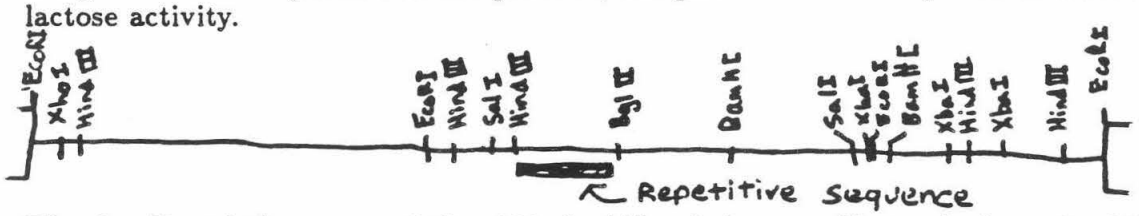

Fig 2. Restriction map of the *026 Arabidopsis* insert. Vector is λ sep6 with right and left arms extending from EcoRI sites flanking the insert (R.E. Pruitt, unpublished).

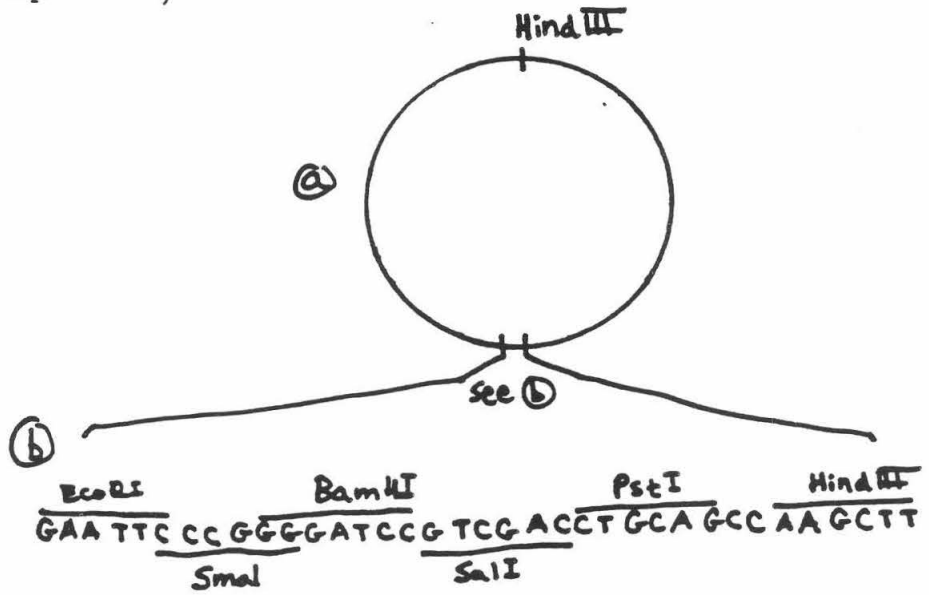

Fig 3. a) Plasmid DOA 1.8, size = 3.0 Kb. b) Stretch of sites within lac Z gene used for subcloning.

For the subcloning, both the phage *026* and the plasmid are cut with the same restriction enzymes, then ligase is added to the mixture. Meanwhile, E. coli cells are treated with CaCl to render them receptive to the plasmids. After ligation, the DOA 1.8 plasmids are introduced into Bozo 2.7 E. coli cells which are then plated on MacKonkey/Kanamycin petri dishes. Bozo 2.7 cells are normally sensitive to Kanamycin and unable to use lactose as a food source. If a Bozo 2.7 cell is simply plated on MacKonkey/Kanamycin plates, it will not survive; If it has been transformed by a DOA 1.8 plasmid it will survive, reproduce, utilize lactose, and produce a red colony. If, however, it has accepted a plasmid which picked up another piece of DNA during the ligation, the cell will survive, reproduce, but will not have gained the ability to use lactose; these colonies appear white. The repetitive region of *026* is flanked by a Hind III site and a Bgl II site. Hind III is not useful for the subcloning since DOA 1.8 has two Hind III sites; the plasmid must be kept intact, opened just enough to add a bit of phage DNA. Though there is no Bgl II site in the plasmid, Bam HI leaves the same sticky end, so we can cut the phage with Bgl II and anneal to the plasmid Bam HI site. I first tried subcloning with Bgl II, Bam HI, and Sal I. Thus, only pieces of phage that had a Bgl II or Bam HI site on one end and a Sal I on the other could be cloned into the opening on the plasmid. I expected white colonies with any one of five inserts, and red colonies from uncut plasmids.

After three attempts, each which took several days, I was still producing only red colonies. I thought that the restriction enzymes might still be cutting in the refrigerator during ligation so I tried a phenol extraction of the enzymes before ligation. Still no white colonies. At this point I took a week to work on other projects while I grew up more phage for *026* DNA.

Next, I started using more reliable enzymes, Bam HI and Eco RI. I tried to subclone a much bigger piece of phage DNA; the plasmid is less likely to accept a piece this large. I performed ligations with varying DNA concentrations. At last I found some white colonies, but when their plasmid DNA was extracted and analyzed, it revealed that I had not subcloned the correct fragment.

In order to assure that the desired piece would be picked up in the next ligation, I isolated that piece of phage DNA from an agarose gel. I added this piece to the plasmid-ligation mixture. Unfortunately, I had not isolated enough DNA, so the procedure did not work. My next attempts were fraught with contaminating foreign bacteria. I located the source of contamination when my SURF time ran out.

My main project did not succeed, but I learned many new techniques and now better understand the theory behind these techniques.

I also worked on two side projects throughout the summer. I grew and harvested seeds from two varieties of *Arabidopsis* and I gathered young plants and ground them to extract whole plant DNA. I cut the DNA from the two related types with various restriction enzymes, and ran each pair side by side on an agarose gel. I then transferred the DNA to nitrocellulose filters. These filters will be used to look for restriction fragment length polymorphisms between the two varieties of *Arabidopsis*.

My final goal was to create a restriction enzyme map of another clone containing repetitive *Arabidopsis* DNA. This was my first mapping job, and *006* is complicated, but I've made some progress.

Conclusions

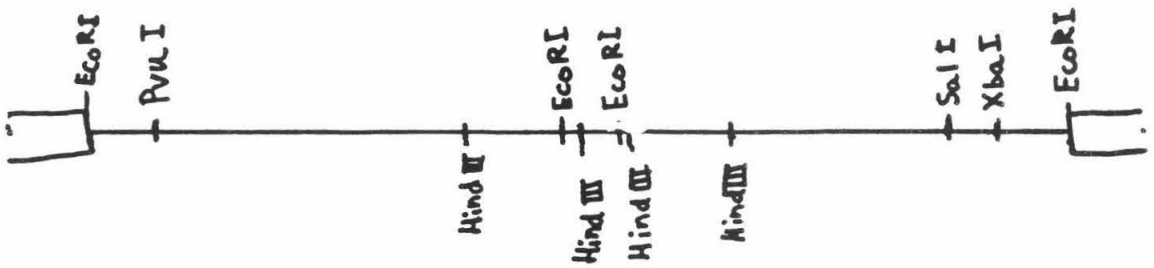

Fig 4. Restriction map of *Arabidopsis* insert *006*. Some sites for Xho I, Bgl II, and Bam HI are also known.

References

Leutwiler, Leslie S., Barbara R. Hough-Evans, and Elliot M. Meyerowitz. 1984. The DNA of *Arabidopsis thaliana. Mol. Gen. Genet.* 194: 15-23.

Maniatis, T., E.F. Fritsch, and J. Sambrook. 1982. *Mol ecular Cloning, A Laboratory Manual.* Cold Springs Harbor Laboratory, Cold Springs Harbor, New York.

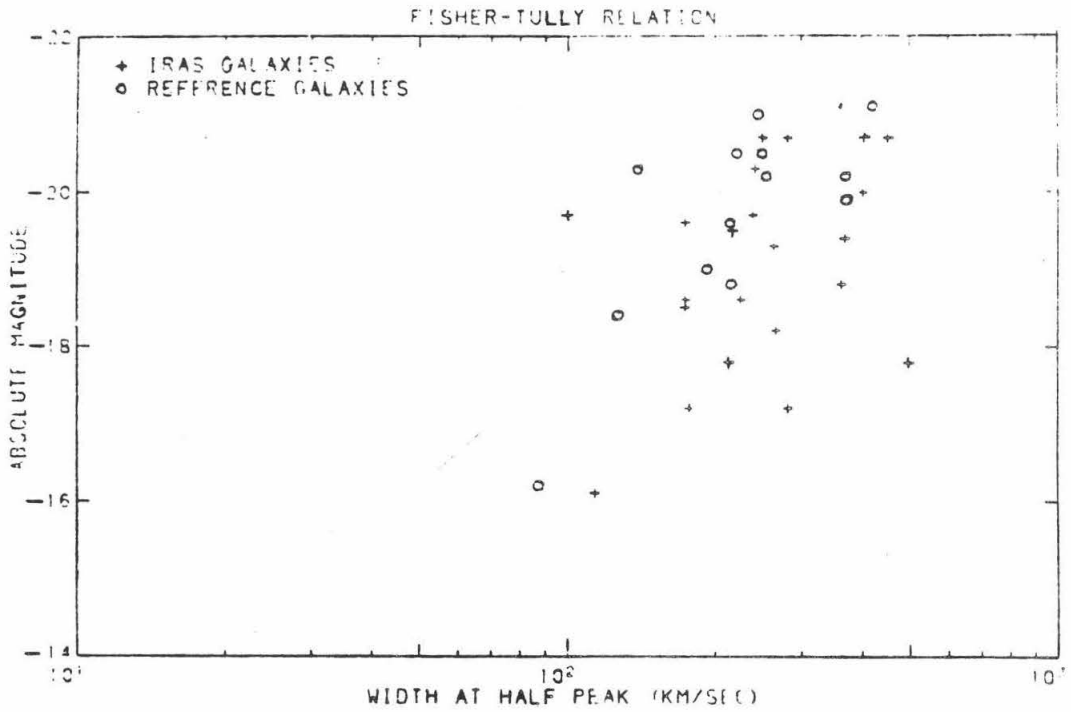

FIGURE 1. Absolute magnitudes of both IRAS and reference galaxies are plotted against the width of the HI profile at half peak in km/sec. The correlation is more apparent in the case of reference galaxies. IRAS galaxies also appear to have lower absolute magnitude for the same half peak width.

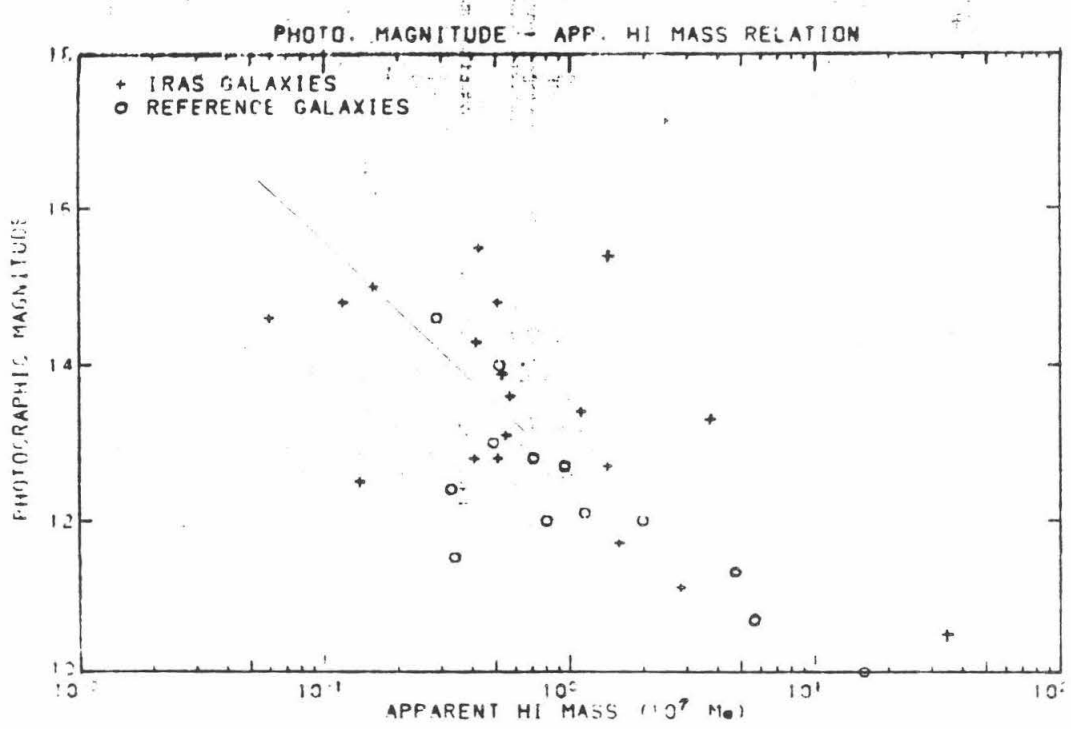

FIGURE 2. Photographic magnitudes of both IRAS and reference galaxies are plotted against the apparent HI mass in the unit of 10^7 Mo. A linear correlation seems to exist here although there is some scattering of points.

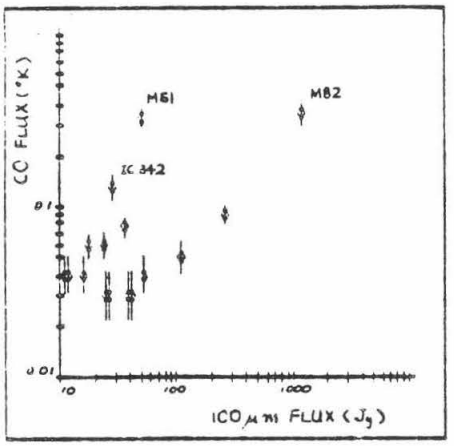

FIGURE 3. CO flux measured in °K is plotted against 100 μm flux in Jy. IC342, M51 and M82 are added to expand the distribution.

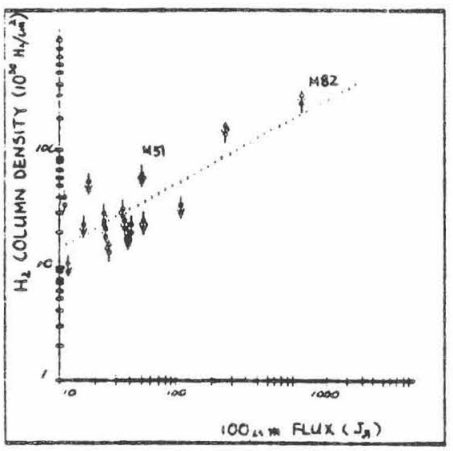

FIGURE 4. Molecular hydrogen column density in the unit of 10^{20} H_2/cm^2 is plotted against 100μm flux in Jy. A good linear relationship is observed.

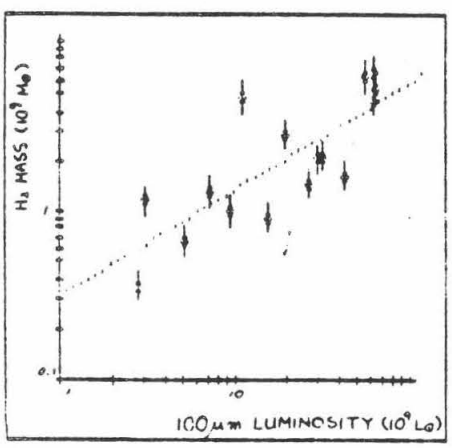

FIGURE 5. Molecular hydrogen mass in the unit of 10^9 $M_\odot$ is plotted against 100μm luminosity in the unit of $10^9 L_\odot$. A linear relation seems to exist.

****

A Technique for Elucidating the Time Course of Polyinnervation Elimination In Fast & Slow Twitch Muscle Fibers

SURFer : Christopher Yo Faculty Sponsor : David C. Van Essen

****

I. ABSTRACT

I have linked together three techniques --- synaptic potential recording, fluorescent dye injection and ATPase histochemistry, to find out the twitch types of singly and polyinnervated muscle fibers. So far the twitch types of 6 polyinnervated fibers have been determined. I also tested my ability to distinguish singly from polyinnervated fibers by doing the polyinnervation elimination time course experiment. There was no obvious discrepency between my data and published results.

II. INTRODUCTION

Initial synaptic connection overproduction and subsequent excess synapse disappearence are notorious events in the mammalian central and peripheral nervous systems. The development of the rabbit soleus muscle is of no exception --- the neonatal (age 1-4 days) muscle fiber receives about 3 nerve inputs while after 2 weeks there is only a one-to-one mapping of axon to muscle fiber <Bixby,1>. The dramatic reduction of synapses during this period is depicted in figure 1. This muscle was chosen in my experiments to investigate synapse elimination for three reasons: (1) the number of muscle fibers and their efferent motor neurons remained constant after birth < Bixby, 1 >. (2) The existence of fast and slow twitch muscle fibers in both neonatal and matured soleus muscle allowed me to study the behavior of synapse elimination (e.g. rate) in two populations of cells within the system. (3) It has been shown for the cat gastrocnemius muscle, fast motorneurons only innervate fast twitch muscle fibers while slow motorneurons only innervate slow twitch muscle fibers < Burke, 2 >. During the period of polyinnervation, Gordon <3> showed that there was a preferential innervation of particular motorneuron type to particular fiber twitch type. One mechanism by which this could be achieved was suggested by Kelly and Rubinstein <5> --- slow motor axons arrive first and innervate the primary myotubes in the soleus muscle, the fast motor axons arrive later and innervate the secondary myotubes. Therefore it would be interesting to find out if there exists two waves of polyinnervationn disappearence. If slow fibers really loose extra synapses sooner than fast fibers, then the above hypothesis would be supported.

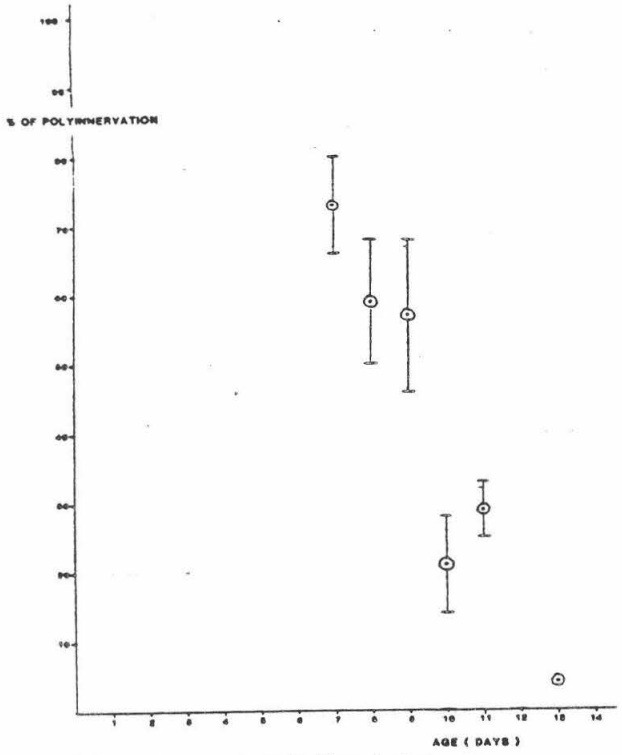

Figure 1: synapse reduction during first and second weeks after birth. Error bars indicate the range of uncertainty.

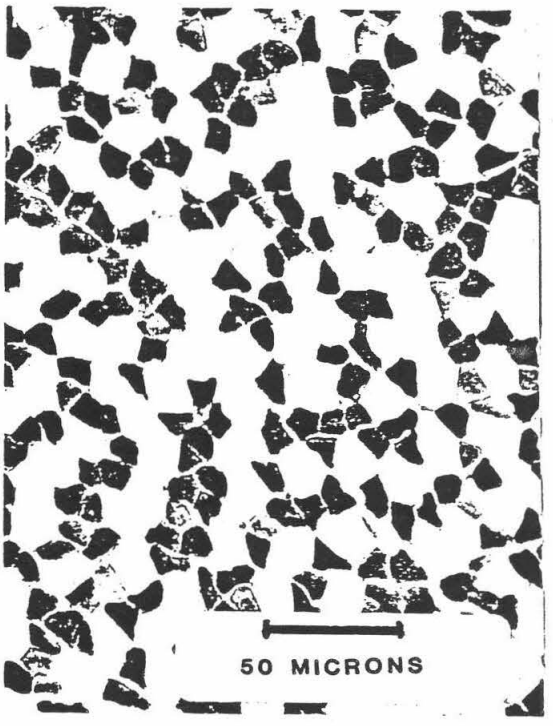

Figure 2: ATPase stained section. Dark fibers are fast twitch. Light fibers are slow twitch.

My goal was to develop a technique capable of finding out the time course of polyinnervation disappearence in both fast and slow twitch muscle fibers. Synaptic potentials from singly innervated fibers showed only one distinctive level of response upon gradual increase in motor nerve stimulation while more than one distinctive level of response could be elicited from polyinnervated fibers. (due to motor axons with different thresholds being recruited at different levels of stimulation.) It was by this criterion that I distinguished the polyinnervated fibers from the singly innervated ones. Then the favorite fibers were labelled by pressure injecting (15-20 psi) a fluorescent dye called Lucifer Yellow into them. Fast and slow twitch muscle fibers could be differentiated histochemically due to the difference in the stability of their actomyosin ATPase <Guth,4>. The ATPase in fast twitch muscle fibers were alkali stable; upon incubation with ATP, Ca^{2+}, Co^{2+}, gave a black precipitate of CoS. The ATPase in slow fibers were alkali labile; there was no reaction at alkaline pH and hence no precipitate. Therefore fast fibers looked dark while slow fibers looked white after this treatment. (Figure 2) With this technique , I found out the twitch type of injected fibers by sectioning the muscle with a cryostat, marking down the positions of the labelled fibers under a fluorescent microscope, performing the ATPase reaction at alkaline pH, and finally matching the ATPase histochemistry profiles with the positions of the labelled fibers.

III. METHOD

The soleus muscle and its nerve were dissected out from heavily etherized New Zealand white rabbits in 4°C Ringer's solution. (150mM NaCl, 5mM KCl, 1mM $MgCl_2$, 5mM $CaCl_2$, 16.5 mM D-glucose, 4.3 mM Hepes buffer (pH 7.4)) The muscle was then pinned out in a recording chamber perfused alternately with oxygenated Ringer's and curare (2mg D-Tubocurarine / liter) Ringer's solution at 23° C. The nerve was then stimulated supramaximally via a suction electrode to verify the success of the dissection. Micro-electrodes were filled with 10% Lucifer Yellow CH dissolved in 1 M LiCl. Typical resistances ranged from 120-200 M ohmes and produced peak-to-peak noise level of about 0.4 mV. Blocked and unblocked electrodes could be differentiated by the observation that when 15-20 psi of compressed air was applied to an unblocked electrode, the resistance would decrease by 50 M ohmes while no such change occured in blocked ones. During the course of the recording session, the nerve-muscle preparation was stimulated with a supramaximal pulse (15 V, 1.5 msec duration) every second which served to stabilize synaptic responses. When synaptic potentials were observed, a second stimulus of varying strength was applied 25 msec before the supramaximal pulse to distinguish singly from polyinnervated fibers. Favorite fibers were then injected with Lucifer Yellow via pressure (15-20 psi) for at least one minute and these fibers were not penetrated through by the electrode to record underlying fibers. The muscle was fixed in 0.5% formaldehyde for 30 sec, washed twice in 30% sucrose solution for 10 sec and then frozen. 10 micron thick cross-sections of the muscle were cut at -20°C, and inspected without coverslipping under the fluorescent microscope. Sections with labelled fiber(s) were photographed with visible light onto Polaroid 4X5 Type 55 Film. The positions of labelled fibers were marked onto the positive and the negative was kept for enlargement. The twitch types of the marked fibers were assessed by ATPase histochemistry according to the method of Guth <4>. Nondehydrated and noncoverslipped ATP stained sections were then compared with the original photos which contained the labelled fibers. When fibers could not be matched with absolute certainty, the ATPase profiles were photographed and enlarged to compare with equally enlarged original photos.

IV. RESULTS

I tested my ability to judge singly and polyinnervated fibers by doing the polyinnervation elimination time course experiment on 7 - 13 days old rabbits. Results were tabulated in Table 1. In comparison with my sponsor's data <1>, the degrees of polyinnervation I obtained at day 11 and 13 were too high; but there was no discrepency in the overall trend of polyinnervation elimination.

Age	7	8	9	10	11	13
Singly & Poly	15	16	28	28	28	23
Ambiguous	2	3	6	4	2	0
Poly	10	8	13	4	7	1

Table 1 : Data for Figure 1

So far , the twitch types of 6 polyinnervated fibers have been identified: in a 7 days old muscle --- one fast, in an 8 days old muscle --- three slow and one fast, in a 9 days old muscle --- one slow. The proposed method of calculation to complete this experiment is included in the appendix (Section VI).

V. DISCUSSION

Lucifer Yellow was commonly dissolved in 0.1 M LiCl for iontophoresis. However, electrodes filled with such low salt concentration have high resistances (250-300 M ohmes) due to the scarcity of charge carriers. The noise level these electrodes produced was 0.7 mV and would seriously hinder the differentiation of singly from polyinnervated muscle fibers since synaptic potential magnitudes ranged from 0.4to 6 mV in partially curarized nerve-muscle preparations. I have tried dissolving Lucifer Yellow in higher concentrations of LiCl but apparently when the smaller charge carriers became abundant, less L.Y. was injected. Therefore I explored the possibility of injecting L.Y. by pressure; and due to the following three reasons, this method was employed. (1) With 15-20 psi of pressure, sufficient dye was injected in one minute. (2) L.Y. could be dissolved in 1 M LiCl and still be injected. Hence the resistance of the electrodes decreased to 120-200 M ohmes and the peak-to-peak noise level became 0.4 mV. (One might be tempted to dissolve L.Y. in even higher concentrations of LiCl in order to lower the noise level even more, but unfortunately, with higher LiCl concentrations less L.Y. could be dissolved!) (3) Synaptic potentials could be monitored during the course of pressure injection. This was a distinct advantage because the zero potential level often drifted by as large as 40 mV , hence the resting potential was not a good indicator for whether the electrode was in a fiber or not. The existence of the same synaptic potential, however, unequivocally proves that the electrode was still in the favorite fiber. This could not be seen during iontophoresis because of the passage of step D.C. pulses through the electrode. I also used the magnitude of the synaptic potential as an indicator for the general health of the penetrated fiber; injection was terminated when it fell below 0.4 mV.

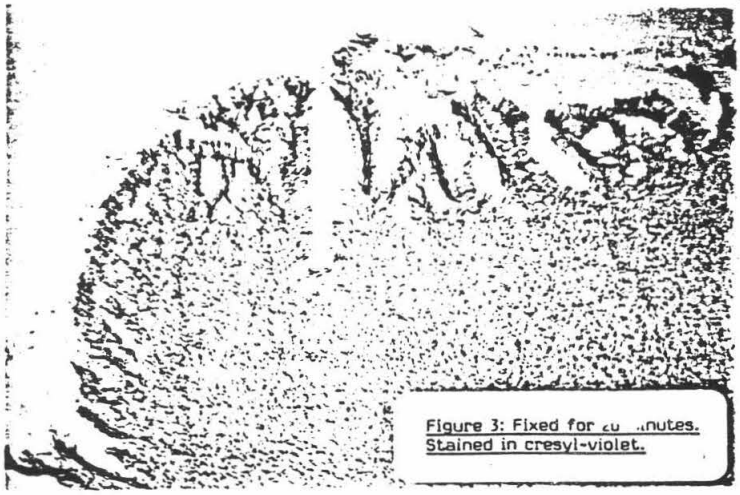

Figure 3: Fixed for 20 minutes. Stained in cresyl-violet.

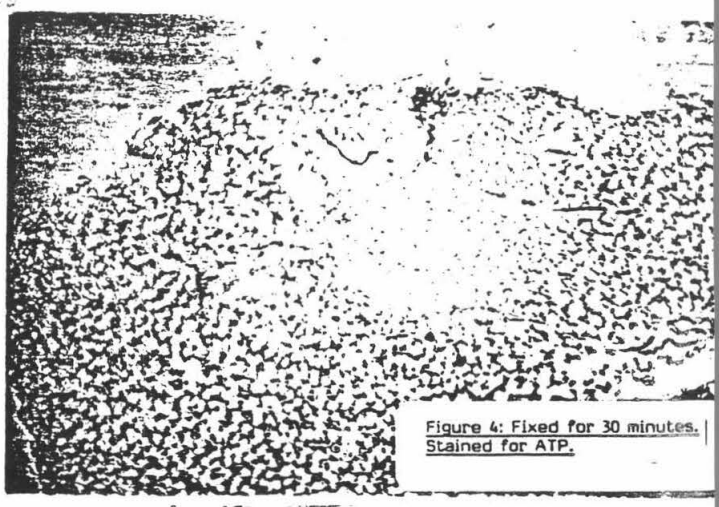

Figure 4: Fixed for 30 minutes. Stained for ATP.

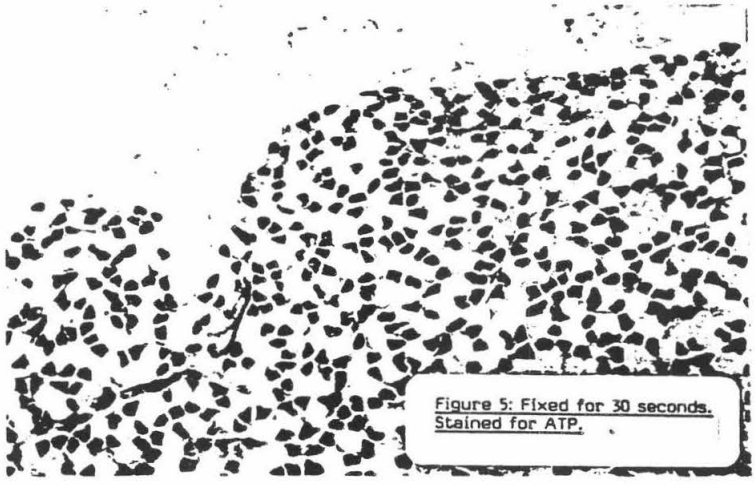

Figure 5: Fixed for 30 seconds. Stained for ATP.

When unfixed muscles that contained the labels were sectioned, nicely labelled fibers could not be seen. I only saw fluorescent dots that appeared in broken-away segments of the peripheral fibers and diffused labels. Fixation before sectioning eliminated all these problems, preserved nicely labelled fibers, and created new problems! The first fixative I used was Guth's<4> ATPase fix, it caused massive shrinkage in the muscle. (Figure 3) The second fixative contained Na Cacodylate, 0.1 % formaldehyde, Na Periodate and Lysine monoHCl. Although the morphology of the fibers was preserved, it eliminated the ATPase activity. (Figure 4) My final decision was to briefly fix the muscle in 0.5 % formaldehyde for 30-60 seconds so that labels would be fixed into position and peripheral fibers would be bound more tightly. The muscle was then washed in 30 % sucrose solution to remove excess formaldehyde and to prevent ice crystal formation in the peripheral fibers. Figure 5 shows the success of this treatment.

The last problem I had to solve was to match the labelled fibers to their contractile type. One method was to cut two sets of sections that are serial to each other. One set would contain the labels and the other set would be used for ATPase histochemistry. I found that even serial sections looked different, especially at the periphery of the muscle, and because the labelled fibers were peripherally located, this method was abandoned. The other method was to photograph uncoverslipped sections, mark the positions of labelled fibers onto the photos and later compare these photos with the ATPase histochemistry profiles. I found this method to be more reliable and fruitful, though not all of the labelled fibers could be matched.

VI. APPENDIX

Age (days)	f=(a+b)/(c+d) -poly/singly	scored poly-innervated dark fiber	scored poly-innervated light fiber	scored singly-innervated dark fiber	scored singly-innervated light fiber
5 - 6	f1	a1	b1	c1	d1
7 - 8	f2	a2	b2	c2	d2
10 - 11	f3	a3	b3	c3	d3

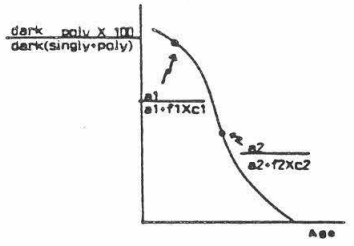

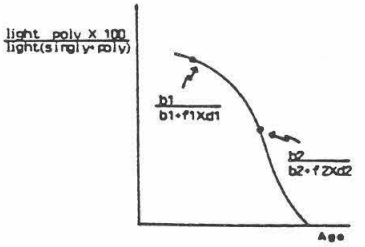

VII. ACKNOWLEDGEMENT

This project was supported by the Caltech Undergraduate Research Fellowship and my sponsor. I am indebted to Professor Van Essen and his graduate student Jim Soha for their invaluable advice, ingenious ideas and constant encouragements. Without the sophisticated instruments in Prof. Van Essen's lab, this project could not have been initiated. Without Jim's suggestion of fixing the muscle before sectioning, five weeks of work would have been in vain. I also thank Prof. Konishi for letting us use the micro-pipette puller in his lab.

VIII. BIBLIOGRAPHY

1) Bixby, J.L. & Van Essen, D.C. Regional Differences in the Timing of synapse elimination in skeletal muscles of the Neonatal Rabbit. Brain Research, 169 (1979) pp 275-286

2) Burke, R.E.; Levine, D.N.; Tsairis, P. & Zajac, F.E. Physiological Types and Histochemical Profiles in Motor Units of the Cat Gastrocnemius. J. Physiol. 234 (1973) pp 723-748

3) Gordon, H. (1983) PhD Thesis

4) Guth, L. & Samaha, F.J. Procedure for the Histochemical Demonstration of Actomyosin ATPase. Exp. Neurol. 28 (1970) pp 365-367

5) Kelly, A.M. & Rubinstein, N.A. Myogenic and Neurogenic Contributions to the Development of Fast and Slow Twitch Muscles in Rat. Nature 288 (1980) pp 266-268

6) Stewart, W.W. Functional Connections between Cells as Revealed by Dye-coupling with a Highly Fluorescent Naphthalimide Tracer. Cell Vol. 14 (July 1978) pp 741-759

Chemistry and Chemical Engineering

The Crystal Structure of a Zirconium Ketene Dimer

by
Michael J. Bronikowski

Faculty Sponsor
William P. Schaefer

Abstract

The crystal structure of the zirconium ketene complex $(Cp_2Zr(C,O\text{-}\eta^2\text{-}OCCHCH_2C(CH_3)_3)_2(\mu\text{-}Al(C_2H_5)_2)(\mu\text{-}H)$ (hereafter "Zr_2") has been determined. The hydrogen atom bridging the two zirconium atoms was found to be placed symmetrically between them, with a H-Zr bonding distance of 2.01(4)Å and a Zr-H-Zr bonding angle of 163.0(2.2)°.

Introduction

Metal ketene complexes are possible intermediates to catalytic reduction of carbon monoxide. These compounds also serve as models for bound states of carbon monoxide. Hence, knowledge and understanding of the structures of these complexes is essential to an understanding of the chemistry of CO. Of special interest are transition metal ketene dimers in which the two metal atoms are "bridged," or connected, by another atom or group of atoms. The reactions of the bridging ligands in these compounds can give much information and insight into the nature and mechanism of CO reactions.

Much work has already been done on bridged zirconium ketene complexes, and several species have been structurally characterized. These include the methylene[1] and chlorine[2] bridged dimers: $(Cp_2Zr(C,O\text{-}\eta^2\text{-}OCCHCH_2C(CH_3)_3)_2(\mu\text{-}Al(CH_3)_2)(\mu\text{-}X)$, where X = CH_3 or Cl. My research was concerned with structural characterization of a related hydrogen bridged dimer. This molecule is similar to the one given above (with X = H), except that the alkyl groups bonded to the aluminum atom are $-C_2H_5$ rather than $-CH_3$.

Experimental Techniques, Discussion, and Results

A crystal of Zr_2 measuring .35 x .30 x .25 mm was used in all our experiments. Preliminary space group and unit cell information was obtained from oscillation and Weissenberg

photographs. The crystal was then mounted on a CAD-4 X-ray diffractometer and centered. Unit cell dimensions of the crystal were calculated, and these are given in Table 1. X-ray diffraction intensity data were collected for 9443 reflections. During the intensity data collection, three check reflections were scanned every 10000 seconds of X-ray time to check for decay of the crystal in the X-ray beam. These three reflections showed no decrease in intensity throughout the data collection. After corrections for Lorentz and polarization factors, equivalent reflections were averaged to give a total of 2845 independent reflections which were used in structural analysis and refinement.

The position of the Zr atom was determined from a Patterson map, and all other heavy (non-hydrogen) atoms were located from Fourier electron density maps. The positions of the hydrogen atoms were determined by a variety of techniques including calculation based on geometry and examination of Fourier maps. The positions and thermal vibration parameters of the heavy atoms and the bridging hydrogen atom were refined by repeated cycles of least squares analysis to give the best fit to the observed data. The parameters of the other hydrogens were not refined, but their positions were adjusted once in the course of the refinement. After several cycles of least squares, convergence was reached. When structural determination and refinement had been completed, interatomic distances and angles were calculated. Important distances and angles are given in Table 2, while a diagram of the molecule is given in Figure 1.

Conclusion

The structure of the zirconium ketene dimer Zr_2 has been determined, with structure as described above. We see that the bridging hydrogen atom is placed symmetrically between the two zirconium atoms. This is somewhat surprising since, in the methyl and chlorine bridged species, the bridging ligand was placed assymmetrically between the two metal atoms; it was closer to one metal atom than the other.

Table 1
Crystal Data

Formula wt. 753.27	ρ, calc. 1.21 g/cm^3
Space group C2/c	z = 4
a = 18.219(2) Å	F(000) = electrons per unit cell
b = 10.364(1) Å	= 1568
c = 20.273(2) Å	λ(MoKα) 0.71069 Å
β = 94.565(8)°	μ = 5.44 cm^{-1}
V, Å^3 = 3816(1)	

Table 2a

Interatomic Distances

Atom	Atom	Distance (Å)
Zr_1	H_{Zr}	2.010(40)
Zr_1	Zr_2	3.976(1)
Zr_1	O_1	2.195(2)
Zr_1	C_1	2.188(3)
O_1	C_1	1.392(4)
O_1	Al	1.812(3)
O_1	O_2	2.658(3)
C_1	C_2	1.315(5)

Table 2b

Bond Angles

Atom	Atom	Atom	Angle
Zr_1	H_{Zr}	Zr_2	163.0(2.2)
Zr_1	O_1	Al	139.89(13)
Zr_1	O_1	C_1	71.18(7)
Zr_1	C_1	O_1	71.77(17)
Zr_1	C_1	C_2	162.51(31)
H_{Zr}	Zr_1	O_1	77.2(1.1)
H_{Zr}	Zr_1	C_1	113.9(1.1)
O_1	C_1	C_2	125.48(34)
O_1	Al	O_2	94.41(12)
O_1	Zr_1	C_1	37.04(11)
C_1	O_1	Al	132.82(22)

Figure 1. Diagram of Zr_2 Molecule

(Hydrogen atoms have been omitted for clarity.)

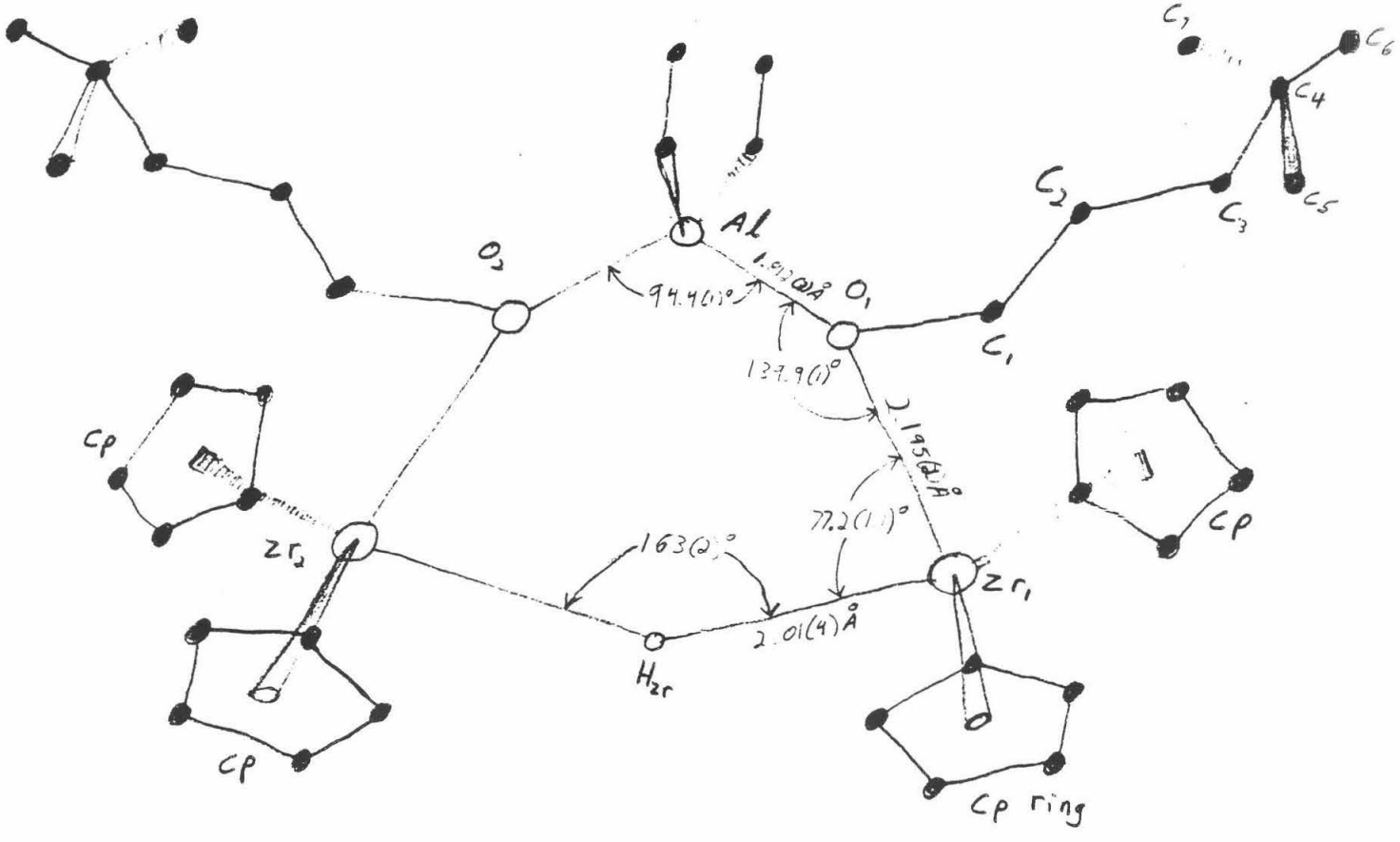

List of Works Cited

[1]Waymouth, Santarsiero, Grubbs., J. Am. Chem Soc., 106, 4050-4051 (1984)

[2]Waymouth, Santarsiero, Grubbs, to be published

The Reconfigurable Distributed Processor: A Bus Based Approach

A Summer Undergraduate Research Fellowship

D. James Douma

Advisor: Dr. Manfred Morari

September 14, 1984

THE RECONFIGURABLE DISTRIBUTED PROCESSOR: A BUS BASED APPROACH

by D. James Douma

Abstract

The distributed processor offers a current, cost effect method for developing high speed computers. A reconfigurable distributed processor is far more versatile than the rigid network based systems in use today and can be easily and economically implemented using the techniques which are this paper's topic.

Introduction

In 1936 Emil Post and Alan Turing independently devised a structure for a general purpose computer, since known as the "Turing" machine. This structure consisted of a finite state machine capable of executing a small set of simple instructions. The importance of this concept is that any operation that can be described can be translated into this set of simple instructions and performed by this finite state machine given enough time and storage space. This is the basic structure of the modern computer.

Since that time, many thousands of computers have been designed and built, virtually all of which use the most simple and obvious manifestation of the Turing machine — the serial processor. Simply put, a serial processor is one Turing machine. It is capable of manipulating one piece of data at a time subject to one instruction at a time. This configuration is also known as the SISD or "single instruction single data stream". The serial processor has many advantages: it is the simplest computer structure to construct and the easiest to program and can be implemented on a great number of scales simply by changing the complexity of the instruction set and the size of the basic data packet. There exist, however, three other basic configurations on which little work has been done, two of which have potential for producing machines with capabilities far beyond those of a comparable serial machine.

The first of these configurations is the SIMD (single instruction multiple data stream), also known as the pipeline and the vector processor. This structure is something like an assembly line for data where multiple Turing equivalent machines are arranged in a series, each one taking its input from the previous processor, doing an operation on this data, and passing it to the next processor in line. For a given operation, each processor need perform only one instruction repeatedly and thus need not fetch a new instruction for each operation. This increases the rate at which a given piece of data is processed and thus the overall speed of the machine.

The third effective configuration is the MIMD which is capable of executing multiple instructions on multiple data streams concurrently. These "concurrent" processors offer the greatest versatility and the greatest power of any of the possible basic structures. They also offer the greatest variety of headaches owing to the complexity of both the hardware and the software necessary to implement this architecture. The study of this class of architectures and their associated strengths and weaknesses, and solutions to the related problems was the object of this project and is the subject of this paper.

Theory

In considering possible architectures for an MIMD class machine, many variables must be considered. For instance, the size and power of the smallest Turing equivalent element in the machine is a major variable. Another is the interconnection method used to tie the various elements together, of which thousands of possible techniques are possible. Then there is the algorithm dependence of the architecture which must be considered: while a given architecture may be ideal for one class of problems, it can be woefully inadequate for another. Along with each of these variables ride hundreds of smaller variations on the basic theme,

and the possibilities quickly become endless. The specific goal of this project was to derive a proposal for the architecture of a general purpose MIMD class machine which could take maximum advantage of the independence of the elements as well as allowing them to operate together closely on a single problem. Also, it is desirable to do all of this with "off the shelf" components to keep development costs and time down.

If the data size of the individual elements is very small, say one bit, the machine architecture is called parallel; that is, it does all of its bit operations simultaneously, hence the name. Due to the fact that no hardware suitable to building a machine of this variety exists commercially, a great deal of VLSI design is necessary to construct a machine of this sort today, as the designers of the MPP, DAP, ILLIAC IV, and CLIP4 machines found [Uhr] As well, the design of algorithms which run efficiently on these machines is radically different from the techniques used commonly today, and thus much research will be needed before machines such as these can be used effectively. So to effect the goals of this project a much larger element size is needed. This can be found in the form of commercial microprocessors in use today whose basic data unit is eight, sixteen, or thirty-two bits. These components are inexpensive, well understood and documented, and most of them have large amounts of software already in existance. This type of machine is known as a distributed processor.

The hardware used to interconnect the individual nodes in a distributed processor is perhaps the most algorithm specific variable dealt with in designing one. Hundreds of networking schemes have been investigated [Uhr] and almost all of them find themselves lent most usefully to only a small class of problems. Trees and hex trees work well in hierarchically structured problems, but their performance is poor when all nodes must work together on an equal basis as in matrix manipulations or array operations. The networks which work well on arrays, such as square and cubical networks, work poorly on the other class of problems. The binary n-cube (a net where the elements are connected similarly to the vertices of an n^{th} dimensional cube) works well on problems in both of these classes, provided the problem is highly symmetric. Also, few of these interconnection methods can be implemented with an arbitrary number of non-identical nodes, i.e. the n-cube for example can only be put together from 2^n identical nodes, so expanding the machine means doubling its size if the network symmetry is to be maintained. Ideally a network which can be reconfigured into a number of possible formats would be used, though the hardware to do such switching is complex and expensive if the actual lines are switched electronically. So again, the solution is still not clear.

The least problems encountered in attacking the problem of creating and using an MIMD processor are not necessarily those of hardware. Software too has its nightmares. In order to circumvent as many of these as possible it is desirable to use standard languages or variations thereof which have already been debugged and may have a large database of software already available. Unfortunately few such languages exist which operate in parallel to any fashion, and those which do tend to be optimized for only a given type of networks. For example, one of these languages is OCCAM, a language developed by Inmos Corporation for use with their transputer (a microprocessor device designed to integrate easily into arrays). Though studying the methods that OCCAM uses to deal with parallel algorithms was quite valuable to this project, the language itself is tightly linked with the channel oriented architecture of the transputers, and does not lend itself easily to use in reconfigurable architectures of the type needed in a general purpose machine.

Proposal

The system design suggestions resulting from this project solve most of the above problems. The system can be put together in an arbitrary size due to its modular style. Also, it is software reconfigurable into any conceivable network up to and including a fully interconnected network. The parts used to construct it can be purchased off the shelf and are common enough that the total machine cost is very economical in terms of power and versatility per dollar. And since the system is fully reconfigurable, quite a variety of node types can be used with perfect integration into the network.

The versatility of this system is owed to the interconnection scheme used to tie the nodes together. A number of buses, each having at least one port into each node are installed as the basis of the inter-node

communication setup. Any bus can be used to transmit a packet of arbitrary size from any port to any other under the control of the transmitting node. Studies of bussing control performed using a software simulator of this machine indicate that, for the majority of operations, a number of high speed buses equal to less than one fourth of the number of nodes is quite adequate. Since the number of buses is quite low, each bus can be of a very high speed variety without increasing the cost of the machine drastically. For instance, to get the most out of this type of bus it could be implemented as follows: Put a DMAC (direct memory access controller) on each bus and set up the ports so that each port reaches directly into nodal memory. Effecting a transfer is done as so: The transmitting node assembles the data to be sent into a packet located in a block of memory near a bussing port. Included in this packet is a header which contains the size of the packet, a packet serial number (for reference by system software), the source and destination nodes. The node then makes a transfer request. At this point the node is done. This protocol requires very little of the node's time, freeing it for computation. After the transfer request has been made, the bus master hardware activates any free DMAC with the header data and the transfer is made directly into the receiving port's memory where it can be used by that node. Using sixteen bit parallel buses and 100ns memory (common components), a burst rate of 20 Mbytes/sec is possible. Total transmission time for an average 40 byte packet would then be less than $3x10^{-6}$ seconds. Due to the extremely high rate of transmission, wait times for transmissions are very small and downloading jobs to nodes uses a minimum of bus time. This networking method has much higher efficiency in terms of total fraction of bus time used constructively than hard-wired buses which normally require many more buses than can be used at any given time.

As to the construction of the node, almost all of the variables in its design can be optimized for a given job, or set up for a general purpose operation since a variety of nodes can be used. However, a good guideline is to invest in a powerful microprocessor, since this represents most of the power of a given node while being less than 5% of its total cost. The other factors such as storage space, number of bus ports, peripherals attached directly to the node and so on can be done according to the specific task of the node.

Most of the software which will be run on this machine is already available in some form. To be precise, the algorithms which run on the individual nodes are of the variety commonly used today in millions of applications. Where the parallelism of the machine comes in is at the multi-nodal interaction level. Several nodes working on a problem together form a distributed operation. In order to implement this, a program which operates as a front end to a compiler is useful. A file consisting of the software to be run on the individual nodes and some logical system of describing the interactions and communication between processes is created by the user. The pre-processor digests this into fractions which can be assigned to the various nodes and outputs those fractions in files which can be reduced to machine code by compilers. The object code files produced by the compiler are treated as a single job and run as such by the operating system. This system is very user friendly (at least as much as the current UNIX variety operating systems can be) and is modular. The modularity of the system is a great asset since only the front end pre-processor need actually be created; it can use common compilers and assemblers to do the rest. Also, this allows the software to be portable to the extent that job files created on any distributed system can be run on any other using the same operating system. For an operating system, some version of UNIX could be modified to handle the additional load of multiple file jobs, but would be essentially the same in other respects.

Tests and Tools

Fairly extensive amounts of the project time were put into simulating this proposed machine and evaluating its usefulness, and the results to date have been promising. Though the machine's architecture does not imitate the structure of any algorithms directly, it performs quite well on almost all of the common varieties of parallel algorithms (trees, arrays, *etc.*) and will operate on some algorithms that no other general architecture is suited for in the least.

In order to keep track of the enormous number of variables and make the hundreds of calculations necessary to predict the performance of this network on given problems a software simulator and a performance evaluator were constructed and run on a Data General MV4000. The simulator accepts a file containing instructions

for each of the nodes and creates the logical equivalent of each of the nodes in memory. It then figures the state of each node as the job progresses watching their interactions and following the protocols that have been defined for the machine's operation. The simulator, SIMON, and the program evaluator which reduced SIMON's output to something readable were invaluable tools in estimating the performance of the distributed processor.

Results

In simulations performed on the operation of the machine in brute force number crunching applications, performance was equal to what would be expected from a dedicated array type of network as long as the inter-node communication was kept down to reasonable amounts. If the type of work being performed between transmissions was on the order of several floating point operations no bogging down of the communications equipment was encountered. Loading the actual job down to each of the nodes actually required more time from the buses than the communications which occurred while the job was in progress. The job simulated was that of performing a relaxation on a matrix of a given size. The tests were run for arrays of 10^3, 10^4, and 10^6 elements. Also, the number of nodes used on the job was varied from two to sixteen. The runs were evaluated to produce figures on bus and node efficiency, total execution time, and several other internal factors relating to the operation of the machine as a whole. The results as a whole indicate that, for a properly designed algorithm, the execution time proceeds as an $N^{-1} + S^{-1}[8A/N + \alpha]$ function where N is the number of nodes, A is the array size, S is the bus speed, and α is the bussing overhead — a figure which describes how much of the time in a transfer is used for purposes other than actually transferring data.

The last problem evaluated for the machine before time terminated the project was one ideally structured for the machine, and one which could not have efficiently run on any other network structure. This problem was the optimization of a function of n variables on m constraints using a method which breaks the function over time into N discrete pieces and optimizes them independently on different nodes. In order to coordinate the optimization of the function as a whole, a supervisor node checked the results of the other nodes and injected two parameters, ρ_i and ρ_{i+1}, to adjust the boundaries between discrete fractions of the problem in order to assure that the final solution was continuous. The procedure is described in some detail in [Singh]. In order to run this algorithm on a distributed processor, a network where one processor (supervisor) is connected to every other in the machine is needed, and none of the standard network types fit this bill, though this reconfigurable net could. The actual calculations done to determine the performance of the machine on this algorithm have so far merely shown that the algorithm does work, at some time in the future it is hoped that results for the same problem on a serial machine will be obtained for comparison.

Conclusions

The reconfigurable distributed processor is capable of operating efficiently on a number of distributed algorithms that cannot be effectively implemented on other, hard-wired networks, and is general enough that it can operate on any distributed algorithm since the network effectively ties every processor to every other. Though this machine will not be capable of out performing a machine whose network is designed optimally for the algorithm it is executing, its versatility and economy, relative to the other possibilities thus far explored, make it quite attractive for more general purpose work. The eventual goal of this project was to produce a hardware/software environment alternative to the rigid networks in use in distributed systems today, and the system proposed here has the potential to replace most of the dedicated machines in use now with a more versatile, economical, and expandable option.

References

Gass, Saul I. ; Linear Programming Methods and Applications; McGraw Hill Publishing, New York (1958).

Uhr, Leonard; Algorithm Structured Computer Arrays and Networks; Academic Press, Orlando (1984).

Singh, M. G. and Titli, A. ;Systems, Decomposition, Optimization, and Control; 86–95 and 150–155; Pergamon Press, New York (1978).

Tou, Julius K. ; Optimum Design of Digital Control Systems; Academic Press, New York (1963).

Evans, David J. (ed); Parallel Processing Systems; Cambridge University Press, Cambridge (1982).

Salukvadze, M. E. ; Vector Valued Problems in Control Theory; Academic Press, New York (1979).

Foster, Caxton L. ; Content Addressable Parallel Processors; Van Nostrand Reinhold Company, San Francisco (1976).

Macki, Jack and Strauss, Aaron; Introduction to Optimal Control Theory; Springer–Verlag, New York (1982).

Siegel, Howard Jay; "Interconnection Networks for Parallel and Distributed Processing: An Overview"; *IEEE Transactions on Computers, vol C-30, NO.4, April 1981*; 245–246.

Horowitz, Ellis and Zorat, Alessandro; "The Binary Tree as an Interconnection Network: Applications to Multiprocessor Systems and VLSI"; *IEEE Transactions on Computers, vol C-30, NO.4, April 1981*; 247–253.

Wu, Shyue B. and Liu, Ming T. ; "A Cluster Structure as an Interconnection Network for Large Multimicrocomputer Systems"; *IEEE Transactions on Computers, vol C-30, NO.4, April 1981*; 254–264.

Wittié, Larry D. ; "Communication Structures for Large Networks of Microcomputers"; *IEEE Transactions on Computers, vol C-30, NO.4, April 1981*; 264–273.

DEVELOPMENT OF STRATEGY FOR WATER-SOLUBILIZING INSOLUBLE PROTEINS

Summer Undergraduate Research Fellowship

George Garing Gibbs

Advisor: Dr. S. I. Chan

September 14, 1984

DEVELOPMENT OF STRATEGY FOR WATER-SOLUBILIZING INSOLUBLE PROTEINS

By G. Gary Gibbs (G^3)

ABSTRACT

N-Acetyl-(L)-Cysteine (NAC), when coupled with the catalyst complex copper ortho-phenanthroline (Cu(o-phen)$_2$, phen = 1, 10 - phenanthroline), has been demonstrated to be effective in water-solubilizing water-insoluble proteins of a fresh rabbit lens. Optimum reaction conditions were found to occur in 20mM Tris buffer, pH = 7.40, at 25° C. In contrast, cytochrome oxidase did not display any increase in solubility under the same reaction conditions. A reaction mechanism for the proposed catalytic oxidation of sulfhydryl groups was developed, and extensive kinetic and mechanistic studies were pursued in hopes of explaining this phenomenon.

INTRODUCTION

Many membrane-bound proteins, such as transmembrane proteins, are found to be highly insoluble in aqueous environments. (Alberts *et al* 1983) A good example is the highly concentrated protein system of the mammalian lens. It has been shown that during human cataractogenesis high molecular weight disulfide-linked chains are formed due to the oxidation of thiol-containing lenticular proteins. These polypeptides aggregate by formation of hydrogen bonds between chains; the bond formation reduces the number of hydrophilic groups in the membrane and thus induces insolubility. (Harding *et al* 1976) Thus both chemical and conformational changes in lenticular proteins may result in cataract formation. (Harding *et al* 1972) To explore the mechanisms of disulfide formation in membrane-bound proteins as well as conformational changes it is necessary to find a simple but efficient method of water-solubilizing insoluble proteins. Complications can arise in that insoluble proteins often precipitate as a mixture of different species in an aqueous medium, making analysis and characterization by electrophoresis and other biochemical techniques literally impossible.

In general, transmembrane proteins can be solubilized only by agents that disrupt hydrophobic associations and destroy the membrane bilayer. (Cantor *et al* 1980) The most useful among these are detergents, small amphipathic molecules that tend to form micelles in water. When mixed with membranes, the hydrophobic ends of detergents bind to the hydrophobic regions on the exterior of membrane proteins, thereby displacing the lipid molecules. Since the other end of the detergent molecule is polar, this binding tends to bring the membrane proteins into solution as detergent-protein complexes. Strong detergents often unfold proteins by complexing to the interior "hydrophobic core" of the native structure; such solubilized proteins are of no use for functional studies because of their loss of their three-dimensional structure.

In a lipid-containing medium, as is found in lenticular systems, micelles are formed with hydrophilic interior and hydrophobic exterior properties. (Cantor *et al* 1980) Consequently, peripheral –SH functionalities group together in the interior of aggregated proteins. Keeping in mind the importance of disulfide formation in inducing insolubility, I have considered the possibility of attaching charged molecules to the sulfhydryl centers of the protein; this in effect would polarize the –SH functionality and cause an unraveling of the protein, inducing solubility through disulfide formation rather than insolubility, and without the use of detergents. A likely candidate for fulfilling this proposition was NAC in the presence of the catalyst complex Cu(o-phen)$_2$, since NAC does indeed have a charged center at the carboxyl functionality.

PRESENTATION OF DATA AND RESULTS

In investigating how NAC may increase solubility of proteins through disulfide formation, the method of Ellman was utilized. (Ellman *et al* 1959) It has been determined by Dr. Kyoichi Kobashi that catalytic amounts of *o*-phenanthroline enhances the rate of air oxidation of all sulfhydryl groups tested in the presence

of copper ions at neutral pH. (Kobashi 1968) A reaction scheme and mechanism was designed, and attempts to test it experimentally were made. The suggested mechanism is as follows:

$$(1)\ 2\ RSH \longrightarrow 1\ RSSR + 2\ H^+ + 2\ e^-$$
$$(2)\ 2\ Cu^{II}(o\text{-phen})_2 + 2\ e^- \longrightarrow 2\ Cu^{I}(o\text{-phen})_2^{\bullet}$$
$$(3)\ 2\ H^+ + 2\ Cu^{I}(o\text{-phen})_2^{\bullet} + 1\ O_2 \longrightarrow 2\ Cu^{II}(o\text{-phen})_2 + 1\ H_2O_2$$

The kinetics of the proposed mechanism were investigated at varying pH strengths (pH = 5.0, 7.0, 9.0) with the thiol-containing molecules cysteine and NAC. The sulfhydryl content of the reaction mixture was determined optically over time with 5,5'-Dithiobis-(2-Nitrobenzoic acid) (DTNB) in 20 mM Tris, pH = 8.20, and 10 mM EDTA. Mercaptan groups present in this assay solution caused the assay to turn a bright yellow as compared to disulfide functionalities which had no effect on the assay mixture. Unless otherwise noted, all reactions took place at room temperature. Content was measured at the wavelength 420 nm.. Reactions typically included 813 μM of cysteine or NAC (in tris or acetic acid buffer as determined by pH of reacting mixture) with a catalytic amount of Cu^{2+}, o-phenanthroline, or both added as a complex to the reaction mixture. It was found that the assay mixture typically "froze" the reaction at the time point the aliquot was taken. Aliquots were taken every two minutes for a period of 20 minutes, and the mM sulfhydryl content was calculated for each aliquot via the Beer-Lambert law. A least squares fit of each study's time points indicated a definite first order reaction had taken place for all three studies. Error was estimated to be about 5% at the most. (See Figure 1)

The catalytic oxidation rate was calculated by obtaining the slope of the above plots in terms of mM Sulfhydryl content used per minute. Cysteine, with the catalyst, was found to be oxidized at a rate decreasing with increasing pH values. With Cu^{2+} only, though, the oxidation rate tended to increase dramatically with increased pH. NAC with Cu^{2+}, in contrast, showed no comparable increase in rate as a function of pH. NAC with catalyst, in fact, demonstrated a marked increase in oxidation rate only at physiological pH values. (pH = 7.00 - 7.60) These results suggest the involvement of the cysteine amino group in the oxidation of these compounds. Point to be made is that the catalyst did increase the oxidation rate in all cases.

Experiments to test the proposed mechanism were conducted, but no effective conclusions could be made on the exactness of the reaction scheme. In the aforementioned mechanism H_2O_2 is formed as an end product in the free-radical reaction; peroxide found in the product solution would support the hypothesis.

Three different techniques were used to assay for hydrogen peroxide in the final reaction mixture: $KMnO_4$ titration (Fritz *et al* 1979), catalase degradation (Sigma Chemical Company, Feb. 1983 Price List, pg. 203), and horseradish peroxidase (HRP) degradation (Private communication: Mr. Steve Witt) studies were used.

$KMnO_4$ titration and catalase degradation did not give conclusive results. When $KMnO_4$ acts as an oxidizing agent in an acidic solution, the manganese is reduced from a valence of +7 to +2, corresponding to a loss of 5 charges in polarity. My reducing substance, H_2O_2, in an acidic solution was supposed to reduce the permanganate to $Mn^{2}+$ as indicated by the following redox half- reaction:

$$(1)\ MnO_4^- + 8\ H^+ + 5\ e^- \longrightarrow Mn^{2+} + 4\ H_2O$$

But eventually it was found that another end product, cystine or N-Acetyl-(L)-Cystine, actively oxidized MnO_4^{2-}. Thus peroxide could not be singled out. Catalase studies, on the same note, were inconclusive because I could not get a reproducible system operational.

Reserved success came through use of the HRP technique which is very sensitive to minute amounts of peroxide in solution. Control studies involving only 10 nmoles of peroxide mixed with an equimolar amount of HRP clearly indicated minute quantities of peroxide could be detected if present at all in solution. In contrast, the reaction was expected to produce 12 nmoles of peroxide per aliquot, but none was detected. All reaction conditions were identical to the initial kinetic studies (pH = 7.40), and all reactions were assured

of being at completion through use of the DTNB assay. Additional steps to the aforementioned oxidation mechanism were postulated as follows:

$$(4)\ \text{HRP} + 1\ H_2O_2 \longrightarrow \text{Compound I} + 1\ H_2O$$
$$(5)\ 2\ \text{RSH} \longrightarrow 1\ \text{RSSR} + 2\ e^- + 2\ H^+$$
$$(6)\ \text{Compound I} + 2\ e^- \longrightarrow \text{Native HRP}$$

Monitoring the reaction optically at 403 nm., I expected to see the formation of compound I and the reformation of native HRP, or at least the formation of the former only, if peroxide was in my reaction mixture. Positive results would have been evidenced by a marked decrease in absorbance at 403 nm.. Only negative results were obtained.

The question arose as to whether a model system could be developed to explain the solubilization phenomenon of lenticular proteins. Cytochrome oxidase, with its 12 sulfhydryl centers, was chosen in hopes of monitoring its solubilization under some of the same reaction conditions. It has been shown that cytochrome oxidase catalyzes the reaction:

$$4\ \text{Ferrocytochrome } c + 4\ H^+ + 1\ O_2 \longrightarrow 4\ \text{Ferricytochrome } c + 2\ H_2O$$

which involves the reduction of oxygen by cytochrome *c*. (Blair *et al* 1983) A polarographic cytochrome *c* oxidase assay was utilized that measured the temperature-dependent rate of decay of active cytochrome oxidase by a change in the rate of O_2 reduction. The reproducible, irreversible, decay pattern followed a probable double exponential curve. Decay was rather abrupt in the first five minutes while gradual in the remaining time period. Unfortunately, under conditions similar to the kinetics experiments, addition of NAC and/or catalyst did not change the decay pattern. If catalyst had changed the pattern, then there would have been the possibility of some form of intra-crosslinking within the protein. As it stands, it appears NAC acts neither as a stabilizing nor as a destabilizing reagent in maintaining the enzyme in a catalytically active form.

Again, using reaction conditions that paralleled my sulfhydryl kinetics experiments, I also monitored the alpha and Sorret bands optically for changes in peak height, shape, and wavelength - only negative results were obtained. Cytochrome oxidase, it was found, in no way mimicked the lenticular system results obtained with introduction of NAC.

It was decided to persue the lenticular system more closely. The mammalian lens contains both water-soluble proteins (α, β, γ) and water-insoluble proteins (albumoid). (Alcala *et al* 1975) Both types of proteins are chemically similar. Specifically, rabbit lenses were studied. Fractionation of the soluble proteins of rabbit lenses by gel chromatography on Sepharose 6B has revealed six components: HM -, α, β_1-, β_2-, β_3-, and γ crystallin. (Liem *et al* 1974a) In my studies I did not fractionate the proteins but rather clearly separated water-soluble and water-insoluble fractions. Fresh rabbit lenses were dissected from the eye cavity, decapsulated, and then suspended in 20 mM phosphate buffer. Stirring slowly in a beaker for 10 minutes on ice, the easily removed cortical portion of the lens was suspended in the liquid phase and decanted off. The heavy, tough nucleus was then homogenized in phosphate buffer. Both cortical and nuclear fractions were then separated into soluble and insoluble fractions. Separation of the two fractions was obtained through differential centrifugation and optical analysis. In a sense, all soluble proteins were "washed" from the insoluble fraction. The water-insoluble protein was spun down at 10K at 4° C for 15 minutes in a Sorvall centrifuge with a SS34 rotor, and then resuspended and recentrifuged 10 times, or until the supernatant showed no u.v. absorption at 280 nm.. Fractions were then dialyzed against 20 mM Tris, pH = 7.40, since it was found that the copper catalyst could coordinate with the phosphate buffer, making the catalyst ineffective, since a copper precipitate would form instead of the functional copper catalyst complex.

A keynote experiment involved monitoring the affect of the NAC/catalyst combination on a nuclear water-insoluble protein suspension in 20 mM tris buffer, pH = 7.40, over time at two different temperature levels:

25° C and 37° C. NAC concentration in the reaction mixture was 50 mM; catalyst concentration was .3 mM. At appropriate time points aliquots were taken from the suspension, ultracentrifuged, and frozen. As a control one aliquot of the insoluble suspension free of NAC and catalyst was also incubated over the time period. Sodium dodecyl sulfate gel electrophoresis in the presence of dithiothreotol (DTT) was used to monitor the resulting water-soluble proteins in each of the reaction mixtures. (Liem *et al* 1974b) Positive results would be indicated by banding in the 20K - 30K region of the gel. (Published results indicate most rabbit lens proteins appear in this region. (Liem *et al* 1974a)) It was found that over a period of 4 hours, the amount of water-soluble proteins present increased dramatically at both temperatures. The control fraction displayed no apparent soluble proteins, as expected.

One last experiment pointed out that the catalyst apparently did not enhance the rate of the system.

CONCLUSIONS

Water-insoluble lenticular proteins are effectively solubilized by the addition of NAC in tris buffer, pH = 7.40. Time course of the reaction appears to reach completion within a six-hour period. Solubilization is apparently achieved by disulfide formation between the sulfhydryl center of NAC and the sulfhydryl centers of the proteins. Preliminary evidence suggests that the catalyst is not necessary for the reaction to reach completion.

Cytochrome oxidase does not become water-soluble under the same reaction conditions. Utilized methods explained in this paper did not bring fruitful results. It appears that NAC acts neither as a stabilizing nor as a destabilizing reagent in maintaining the enzyme in a catalytically-active form.

Further, the oxidation kinetics behind the dimerization of both NAC and cysteine have been worked out as a function of pH and applied to the solubilization reactions. A reaction mechanism has been proposed but not proven. A conclusion at this point is that Cu^{I} may be produced as an intermediate and then oxidized by molecular oxygen to Cu^{II}; H_2O_2 may go to $H_2O + O_2$ and not be seen clearly as an intermediate. Kobashi (Kobashi 1968) dictates this possibility:

$$\text{(1) } 2\ \text{RSH} + 2\ \text{Cu}^{II}(\text{o-phen})_2 \longrightarrow 1\ \text{RSSR} + 2\ \text{Cu}^{II} + 2\ \text{H}^{+}$$
$$\text{(2) } 4\ (\text{o-phen}) + 2\ \text{Cu}^{II} + 1/2\ \text{O}_2 + 2\ \text{H}^{+} \longrightarrow 2\ \text{Cu}^{II}(\text{o-phen})_2 + 1\ \text{H}_2\text{O}$$

$$2\ \text{RSH} + 1/2\ \text{O}_2 \longrightarrow 1\ \text{RSSR} + 1\ \text{H}_2\text{O}$$

Studies in the future should be conducted at mid pH-values, as dictated by my NAC oxidation studies.

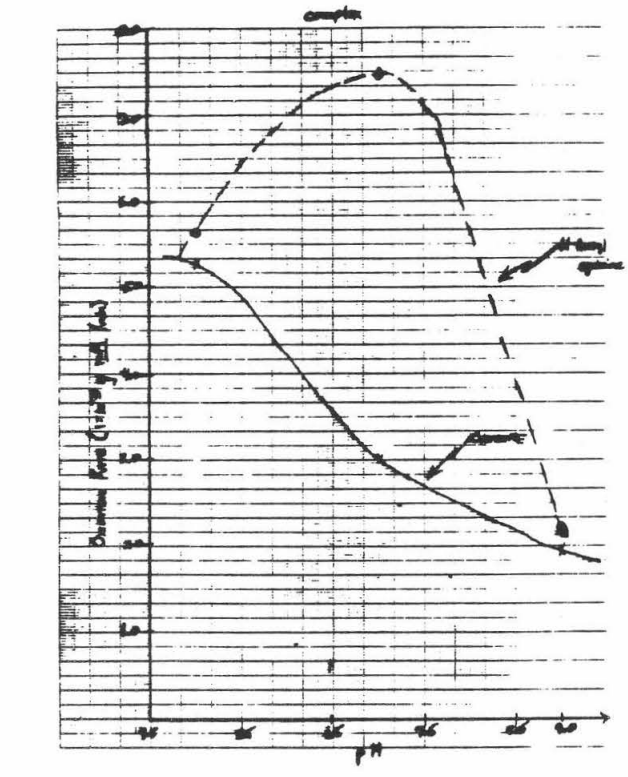

Figure 1: Oxidation rate in terms of mM sulfhydryl content of reaction mixture used per minute as a function of pH. Figure 1A demonstrates oxidation rate when the catalyst complex is added (with the sulfhydryl-containing molecule NAC or cysteine); 1B is demonstrative of just o-phenanthroline added; 1C, finally, investigates the rate when Cu^{2+} is added. Note in 1A that NAC shows a marked increase in oxidation rate only at mid-pH values. 1A further demonstrates that cysteine is oxidized at a rate decreasing with increasing pH values. In 1B, we see that o-phenanthroline has little effect in comparison with Cu^{2+} and the catalyst complex. Finally, it is seen that cysteine is markedly affected by Cu^{2+} alone in 1C, suggesting that the copper ion coordinates with the amino functionality.

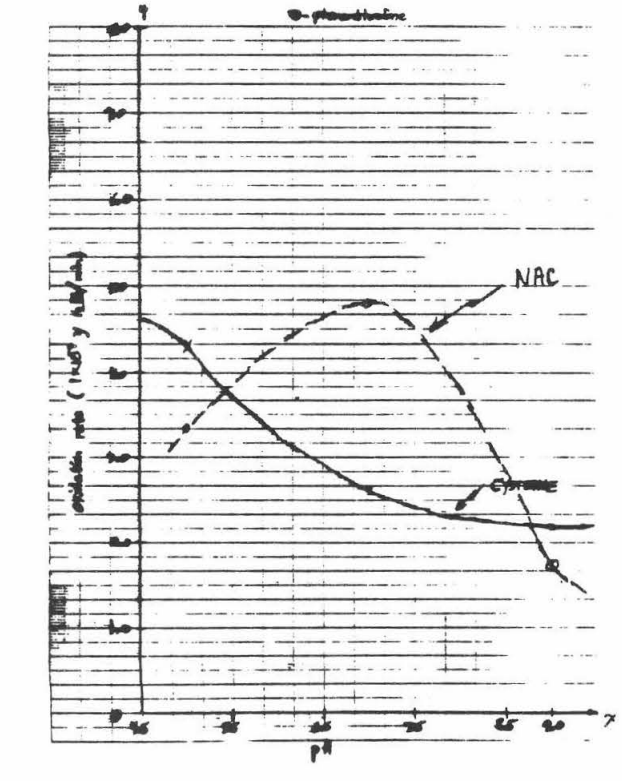

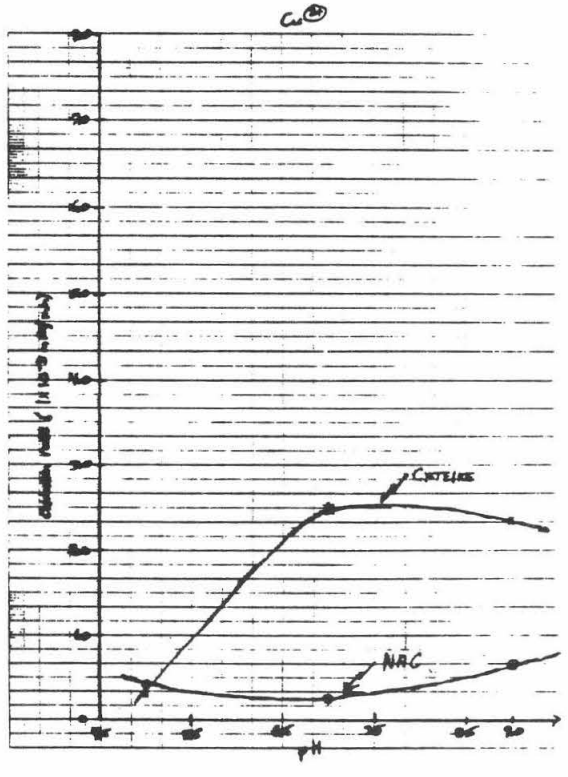

REFERENCES

Alberts, B.; D. Bray, J. Lewis, M. Raff, K. Roberts, J.D. Watson, "The Plasma Membrane" found in *Microbiology of the Cell*, 172-176. New York: Garland Publishing, 1983.

Alcala, J.; N. Lieska, H. Maisel, 1975. Protein Composition of Bovine Lens Cortical Fiber Cell Membranes. *Experimental Eye Research*. 21: 581-595.

Blair, D.F.; C.T. Martin, J. Gelles, H. Wang, G.W. Brudvig, T. H. Stevens, S.I. Chan, 1983. The Metal Centers of Cytochrome c Oxidase: Structures and Interactions. *Chemica Scripta*. 21: 43-53.

Cantor, C.R.; P.R. Schimmel. "Other Biological Polymers" found in *Biophysical Chemistry. Part I: The Conformation of Biological Macromolecules*, 230 - 235. San Francisco: W.H. Freeman and Company, 1980.

Ellman, G.L., 1959. Tissue Sulfhydryl Groups. *Archives of Biochemistry and Biophysics* 82: 70-77.

Fritz, J.S.; G.H. Schenk. "Theory of Oxidation-Reduction Reactions and Titrations" found in *Quantitative Analytical Chemistry*, fourth edition, 254, 267, 272. Boston: Allyn and Bacon, Inc., 1979.

Harding, J.J., 1972. Conformational Changes in Human Lens Proteins in Cateract, *Biochemical Journal* 129: 97-100.

Harding, J.J.; K.J. Dilley, 1976. Structural Proteins of the Mammalian Lens: A Review with Emphasis on Changes in Development, Aging, and Cateract. *Experimental Eye Research* 22: 1-73.

Kobashi, K., 1968. Catalytic Oxidation of Sulfhydryl Groups by o-phenanthroline Copper Complex. *Biochimica et Biophysica Acta* 122: 239-245.

Liem-The, K.N.; H.J. Hoenders, 1974. Characterization of the Soluble Proteins From Rabbit Eye Lens. *Experimental Eye Reasearch* 18: 143-152.

Liem-The, K.N.; H.J. Hoenders, 1974. HM Crystallin as an Intermediate in the Conversion of Water-Soluble into Water-Insoluble Rabbit Lens Proteins. *Experimental Eye Research* 19: 549-557.

Thermodynamic Properties of a Real Gas

by Simon Goldstein
Sponsor: Dr. G. Gavalas

Abstract

A Fortran program was required to calculate the thermodynamic properties of a real gas using an empirically derived equation of state. This was achieved in a format suitable for use on a small personal computer.

Introduction

At Caltech, the first course in the Division of Chemical Engineering that is required of undergraduates in the chemical engineering option is ChE 63, Undergraduate Thermodynamics. This course is, in general, offered to sophomore students and touches all of the major subjects in thermodynamics. This knowledge is then applied in future courses within the division. In short, thermodynamics is a major area of study, and a thorough understanding of the subject is necessary in all parts of chemical engineering.

The primary goal of ChE 63 is to emphasize certain important concepts in thermodynamics, not concentrating on specific cases very much. Consequently, the study of gases is initially limited to a simple set of cases, where the gas is under "ideal" conditions of high temperature and low pressure. This enables the student to use the Ideal Gas Equation:

$$P = \rho R T$$

P = pressure exerted by the gas (or on the gas)
ρ = the density of the gas
R = the Ideal Gas constant
T = the absolute temperature of the gas

From this equation and the standard thermodynamic identities, all of the thermodynamic properties of the gas under those conditions can be found. This allows many first-order applications to be made with this simple, "ideal" approach, such as combustion engines and the accepted gas laws of Charles, Boyle, Gay-Lussac, and Dalton.

Unfortunately, as the course progresses it is necessary to examine real gases, which occur in all non-ideal cases. This makes the simple treatment not quite correct and the Ideal Gas Equation inadequate as an equation of state. Thus it is necessary to find other equations to describe the behaviour of real gases. There have been many attempts to reconcile the differences between the

Ideal Gas Equation and the real gas properties, so most of the attempts have the following form:

$$P = \rho RT + \sum \text{correction terms}$$

In ChE 63, a variety of these equations is used, often with significant differences between the approximations. Another method is to use a graphical or tabular approach, where the thermodynamic properties are plotted or listed against each other. This way suffers from the problem of resolution, that is, results differ according to who reads the graph or table.

This type of inconsistency prompts a need for a satndardization of sorts. The easiest way to do this is to provide a computer solution to the real gas problem. The resulting program would provide identical answers for the same conditions, regardless of the user. This This would make the area of real gases and their thermodynamic properties easily accessible to the undergraduate student. Also, using Fortran and a format suitable for the IBM personal computer would make the access to these properties possible in the classroom.

Theory and Results

The thermodynamic properties necessary for examining a gas are its temperature, pressure, internal energy, enthalpy, entropy, and density or the reciprocal specific volume. Given any two of these properties and a suitable equation of state, the remainder of the properties may be calculated using non-linear approximation methods.

Using Maxwell's relations, standard thermodynamic identities, and specific integration and differentiation, expressions for the properties may be rewritten as:

$$U = \int_{T_o}^{T} C_v^{\circ}(T)\, dT + \int_{0}^{\rho} \frac{1}{\rho^2}\left[\rho RT - T\left(\frac{dP}{dT}\right)\right] d\rho + u_o$$

U = the internal energy of the gas under the set conditions
T_o = a constant reference temperature
T = the temperature of the gas
C_v° = the heat capacity of the gas as a function of the temperature
ρ = the density of the gas
R = the Ideal Gas constant
P = the pressure exerted by the gas

u_o =the internal energy of the gas at the reference temperature

$$S = \int_{T_o}^{T} \frac{c_v^o(T)}{T} dT - R\ln(\rho) + \int_0^{\rho} \frac{1}{\rho^2}\left[\rho R - \frac{\partial \rho}{\partial T}\right] d\rho + s_o$$

S =the entropy of the gas under the set conditions
$\ln(\rho)$ =the natural logarithm of the density
s_o =the entropy at the reference temperature

So using these equations and their required constants, it is possible to calculate from the temperature and the density the rest of the thermodynamic properties.

W. C. Reynolds of Stanford University has devleoped a set of equations of state (pressure as a function of temperature and density) of the form shown above, the Ideal Gas Equation with correction terms of the form of polynomial and exponential functions of the density and temperature. A similar set of equations has been formed for heat capacities. All of these equations, however, have been empirically derived by fitting the functions to curves plotted from experimental results. This means that by using Reynolds' equations, calculations can be made for real gases without the discrepancies normally associated with real gas equations of state. The results from these equations can then be used in the above relations to calculate the required values for the thermodynamic properties from the temperature and density of the real gas.

Using the Newton-Raphson method and associated algorithms for solutions to non-linear equations, all of the thermodynamic properties of the gas can be found given only two of them, enthalpy and entropy for example. By an iterative process, the entropy and enthalpy are evaluated at a guessed temperature and pressure, which are then changed in small increments in the desired direction such that the calculated values match the given values, and hence all of the properties are found from these conditions.

Several factors make a computer solution of these equations preferable. The equations of state are long (up to forty correction terms with exponentials) and contain many constants with many significant digits. They must be explicitly integrated, giving rise to exponential sums and gamma functions. For the iteration to solve the non-linear problems, there is then a repetition of the integrations for each step of the solution. This type of numerical evaluation is ideally suited to the computer and its looping capabilities.

The resulting program was written in Fortran and restricted in size, enabling it to interact with existing software on an IBM Personal Computer. In a typical run of the program the user is asked to supply values for two thermodynamic properties and then guess values for the temperature and the density of the gas (if they are not already known). The computer then returns values for the temperature, pressure, density, internal energy, enthalpy, and entropy of the gas. In all cases studied so far, the values returned are consistent with the experimentatal values tabulated by Reynolds. Run-time errors such as non-convergence of the non-linear solution and data that contradicts itself are caught and displayed by an error-writing routine. The source program is 15,000 bytes long, with the executable version under 48,000 bytes long, and the maximum run-time is under one minute.

Conclusion

The resulting Fortran program uses an accurate empirically derived equation of state and its associated constants to calculate the thermodynamic properties of a real gas given only two of them. The program is quick, accurate, and most importantly, of size suitable for use on a small personal computer, making the program usable in a classroom situation.

Several useful subroutines were developed for use in the main program. An algorithm for solution of non-linear equations was developed. A numerical explicit integration routine was written. And finally, a routine for the explicit integration and evaluation of gamma fuctions was developed.

X RAY CRYSTALLOGRAPHY

The Structure of the W_6I_{14} Dianion

by William P. Schaefer and Nhi Hua

Introduction

A crystal structure has two aspects: a motif, and a mechanism of repetition of the motif. A motif is a cluster of atoms and it is repeated by a mechanism of repetition in three dimension, the entire resulting pattern being the crystal structure. Such a three-dimensional pattern acts as a diffration grating to light having wavelengths in the magnitude as the distance of repeating period in the pattern. This period is around 1 angstrom; and x-ray is light having wavelength of this order.

X-ray crystallography is the technique used to determine unambiguously the structure of tne crystal. A crystal-structure investigation involves two parts. The first part deals with determination of the geometry of the repeating pattern of the crystal: the crystal type, the space group, and the unit cell of the crystal. The second part of the investigation is to find a model for the shape of the motif. Thus, upon completing the investigation of the crystal, one will know how the atoms are arranged in the crystal and the bond lengths and angles of various atoms.

Abstract

The compound $[N(C_4H_9)]_2W_6I_{14}$ crystallizes in space group $P2_1/n$. The unit cell dimensions are a = 11.553(7), b = 11.468(3), and c = 24.553(13) Å; β = 96.77(4)° and z = 2.

Experimental

A crystal with dimensions 0.33 x 0.24 x 0.29 mm was mounted on a glass fiber. Oscillation photographs of the crystal showed only one axis of symmetry which characterizes monoclinic cells. The crystal was then centered on a Nicolet $P2_1$ diffractometer equipped with graphite-monochromated MoKα radiation for intensity data collection. Unit cell dimensions were obtained from the setting angles of 15 reflections with $25° < 2\theta < 28°$. Space group $P2_1/n$, a special setting of #14, was chosen based on the systematic absences h01, h+1 = 2n+1, and 0k0, k = 2n+1 in the intensity data. This space group has four equivalent positions $\pm$(x,y,z; 1/2-x, 1/2+y, 1/2-z). Two sets of data were collected with a total of 9860 reflections in the quadrants h,k,+1, and h,-k,+1. Crystal data are collected in Table 1.

At every 97 reflections, 3 check reflections were monitored to check crystal decay; they showed no variations greater than those expected statistically. The data were corrected for absorption by Gaussian integration over an 8x8x8 grid; transmission factors varied from 0.107 to 0.212. After correcting for background, the two data sets were merged to give 4269 independent reflections, which were all used in the structure solution and refinement. Variances were assigned to the individual reflections based on counting statistics plus an additional term, $(0.014I)^2$, to account for intensity-dependent errors. Final variances were assigned by standard propagation of error plus an additional term, $(0.014\bar{I})^2$.

The centrosymmetric anions are located at a center of symmetry in the unit cell. Intepretation of Patterson maps gave the positions of the three tungsten atoms. From structure factor-Fourier calculation the seven iodine atoms and the non-hydrogen atoms in the cation were located. The position of the hydrogen atoms were calculated from known geometry and assumed staggered conformations. The tungsten and iodine atoms were given anisotropic thermal parameters while the atoms in the cation were given isotropic thermal parameters. Several cycles of least square refinement led to convergence with R of 0.090 for 3463 data with $F_o^2 > 3\sigma F_o^2$. The goodness of fit $(=[\Sigma W(F_o^2-F_c^2)^2/(n-p)]^{1/2})$ is 2.23 for n = 4260 reflections and p = 167 parameters (9 strong, low angle reflections were given zero weight in the refinement). Final parameters are given in Table 2 and bond lengths are listed in Table 3.

Discussion

The tungsten atoms form a nearly regular octahedron with a W-W(cis) average distance of 2.671(5) angstroms and maximum deviation of 0.005 Å from this average. The trans W-W distances average 3.777(8)Å with maximum deviation from this average of 0.009Å. The bonding angles in the octahedron have average deviations of 0.13° from 60° and 0.17° from 90°. The deviations from octahedral symmetry seem random.

It is of special interest to compare the structure of this anion $W_6I_{14}^=$ to that of the similar anion $W_6Br_{14}^=$. The average cis W-W distance in $W_6Br_{14}^=$ is 2.634(7)Å and the average trans distance is 3.716(14)Å. These averages are smaller than those in $W_6I_{14}^=$ (Table 3). In comparing the facial distances of W-I with W-Br, the experimental results agree with the expected distances. The facial distance of W-Br is 2.628(10)Å and that of W-I is 2.792(8)Å, a difference of 0.16Å. This difference is expected since the tetrahedral radius of a bromine atom is 0.17Å smaller than that of an iodine atom.[1] However, the W-I axial distance turns out to be different from the expected distance. The axial

[1]Pauling, Linus. The Nature of the Chemical Bond.

distance of W-Br is 2.588(4)Å and since a bromine atom has a single bond radius of 0.19Å less than that of an iodine atom, one would expect to find the W-I axial distance to be around 2.78Å. However, the experimental W-I axial distance is 2.839(12)Å.

The $[N(C_4H_9)]_2$ cation in this structure shows, within their large standard deviations, normal bond distances and angles. The 14 C-C bonds average 1.521(120)Å, while the 4 N-C bonds have an average of 1.577(32)A. The isotropic thermal parameters of the carbon atoms range from 6.5Å^2 to 12.2Å^2. Since there are no significant interactions between the cation and the anion, the carbon atoms in the cation are not constrained and we find some of them disordered. In our model, the third carbon from the nitrogen in one n-butyl group occupies two positions which leads to two positions for the fourth carbon atoms. Because of this disorder, the esd's of the C-C atoms in this arm are larger than those in the C-C bonds elsewhere in the cation. Correspondingly, the average angle X-C-C (where X is N or C) is 111.6°, very nearly tetrahedral; the maximum deviation from this average is found in the disordered arm.

Acknowledgement: We would like to thank Dr. R. Marsh for many of his helpful discussions.

TABLE 1. Crystal Data for $(TBA)_2W_6I_{14}$

a = 11.553(7) Å	f. wt. 3364.71
b = 11.486(3) Å	Space Group $P2_1/n$ (#14)
c = 24.554(13) Å	T = 21°C
β = 96.77(4)°	λ MoK = 0.71073 Å
V = 3235(3) $Å^3$	d_x = 3.45 g cm^{-3}
μ = 179.96 cm^{-1}	F(000) = 2518 e

TABLE 2. Final Parameters for $N(C_4H_9)_2W_6I_{14}$

x, y , z, and U_{eq} have been multiplied by 10^4

Atom	x	y	z	U_{eq} or B
W1	4454(1)	4328(1)	5624(1)	597(4)
W2	6475(1)	4300(1)	5191(1)	602(4)
W3	4497(1)	3673(1)	4587(1)	622(4)
I1	3634(2)	3344(2)	6568(1)	967(8)
I2	8693(2)	3233(2)	5464(1)	1011(8)
I3	3794(3)	1692(2)	3950(1)	1135(9)
I4	3502(2)	5039(2)	3714(1)	778(6)
I5	5443(2)	2188(2)	5424(1)	800(6)
I6	6586(2)	3584(2)	4112(1)	839(7)
I7	2361(2)	3661(2)	5022(1)	747(6)
N	5154(25)	4758(23)	1675(9)	6.3(6)
C11	3815(37)	4479(32)	1600(14)	8.1(10)
C12	3201(36)	4665(31)	2148(13)	7.5(9)
C13	2080(47)	4058(44)	2126(16)	10.3(12)
C14	2036(50)	2911(46)	2176(18)	12.0(14)
C21	5577(35)	4546(29)	1094(13)	7.0(8)
C22	6822(41)	4875(37)	1079(15)	9.2(10)
C231	6979(**)	4604(87)	485(44)	9.7(27)
C232	7792(**)	4515(**)	649(42)	12.2(33)
C241	7872(86)	5164(79)	299(33)	7.4(20)
C242	6749(72)	4457(66)	643(29)	7.4(20)
C31	5813(33)	3962(31)	2160(12)	6.7(8)
C32	5584(33)	2690(29)	2092(12)	6.5(8)
C33	6087(37)	2208(32)	2613(14)	7.9(9)
C34	5890(46)	840(40)	2587(16)	10.9(12)
C41	5438(30)	6015(26)	1866(11)	5.6(7)
C42	4985(37)	6940(34)	1453(14)	8.2(10)
C43	5474(38)	8178(34)	1654(14)	8.1(9)
C44	5139(40)	9105(35)	1261(15)	9.1(11)

$$U_{eq} = 1/3[\ U_{ij}(a^*_i a^*_j)(\vec{a}_i \vec{a}_j)]$$

$$\sigma(U_{eq}) = \frac{1}{\sqrt{6}} \left\langle \frac{\sigma(U_{ii})}{U_{ii}} \right\rangle U_{eq}$$

**=>100

TABLE 3 Bond Lengths in the Anion

Atom	Atom	Dist(Å)	Atom	Atom	Dist(Å)
W1	W2	2.676(2)	I4	W1	2.800(2)
	W3	2.661(2)		W2	2.790(2)
	W2'	2.671(2)		W3	2.792(2)
	W3'	2.674(2)	I5	W1	2.778(3)
				W2	2.792(3)
W2	W3	2.673(2)		W3	2.792(3)
	W3'	2.668(2)	I6	W1	2.792(3)
				W2	2.792(3)
W1	W1'	3.777(2)		W3	2.803(3)
W2	W2'	3.785(2)	I7	W1	2.788(2)
W3	W3'	3.768(2)		W2	2.785(2)
				W3	2.802(2)
W1	I1	2.842(3)			
W2	I2	2.849(3)			
W3	I3	2.826(3)			

$W_6I_{14}^{=}$	
W-W (cis) avg	2.671(5)
W-W (trans)avg	3.777(8)
W-I (axial)avg	2.839(12)
W-I (facial)avg	2.792(8)

$W_6Br_{14}^{=}$	
W-W (cis) avg	2.634(7)
W-W (trans)avg	3.716(14)
W-Br(axial)avg	2.588(4)
W-Br(facial)avg	2.628(10)

Synthesis and Study of $(NH_3)_5Ru(His\text{-}113)^{3+}$-myoglobin($Co^{2+}$)

Ting-Lin Kao

Sponsor: Dr. Harry B. Gray

Abstract: The reaction of Co^{2+}-protoporphyrinIX with singly modified $(NH_3)_5Ru(His\text{-}113)^{3+}$-apomyoglobin yields $(NH_3)_5Ru(His\text{-}113)^{3+}$-myoglobin($Co^{2+}$). UV-Vis measurements give peaks at 572, 538, and 426nm. The reduction potentials (vs. SSCE) are: $Co^{3+/2+}$, +212mV; $(NH_3)_5Ru(His\text{-}113)^{3+/2+}$, -112mV. Ascorbic acid-catalyzed electron transfer between the cobalt site and the ruthenium site is sought after but not observed.

Introduction:

The main topic of study for Dr. Gray's bioinorganic group is the electron transfer reaction of metalloproteins. Nature proteins modified with ruthenium complex are used as model systems. One of the most extensively studied reaction is the electron transfer between iron and ruthenium in ruthenium-modified myoglobin. The researchers in Gray's group have successfully modified native myoglobin with $Ru(NH_3)_5H_2O^{2+}$. $(NH_3)_5Ru(His\text{-}113)^{3+}$-myoglobin is one of the separated products. In order to understand the effect of different redox potentials on the rate of electron transfer, an exactly the same system with iron replaced by some other metal is to be made. For example, the iron atom on heme site of the myoglobin can be replaced with cobalt protoporphyrin to give a different redox potential in this particular system, with all other conditions unchanged. Although researchers have not tried the substitution of other metalloporphyrins for iron porphyrin in modified myoglobin, Chien and Yonetani have successfully substituted cobalt prophyrins for the heme site of native myoglobin, have proven that the reconstituted myoglobin has the ability to bind reversibly to oxygen, and have published the UV-Vis spectra of several kinds of cobalt myoglobins. However, since the main purpose of all the previous studies is the oxygen-binding behavior, no measurement of the redox potential has been made.

My project is to combine the two projects described above to make cobalt-substituted, ruthenium-modified myoglobin -- $(NH_3)_5Ru(His\text{-}113)^{3+}$-myoglobin($Co^{2+}$), and to test its redox potentials. Since electron transfer in native myoglobin modified by ruthenium complexes can be catalyzed by addition of ascorbic acid, the same thing will be tried on the new-made Co-Mb-Ru to see if electron transfer takes place.

Presentation and Discussion of Results:

(1) Preparation of $(NH_3)_5Ru(His\text{-}113)^{3+}$-myoglobin($Co^{2+}$)

Cobalt protoporphyrinIX was prepared by the method of Dickenson, with a slight modification that after cobalt protoporphyrinIX was dissolved in methanol, it was further cooled, recrystallized by water, centrifuged, and then vacumn-dried. $(NH_3)_5Ru(His\text{-}113)^{3+}$-myoglobin was prepared according to the method of Ruth Margalit, who supplied me with a sample. An apomyoglobin solution (approximately 0.05mM) was prepared from $(NH_3)_5Ru(His\text{-}113)^{3+}$-myoglobin in Tris buffer, pH 7.2, by the acid-butanone method. A 1.2 eq amount of Co^{3+}-protoporphyrin was dissolved in 1 ml pyridine and reduced to Co^{2+}-protoporphyrin by addition of sodium dithionite for half an hour. The resulting solution was added to the apomyoglobin in sodium phosphate buffer (pH 7, 100mM) at 0-5°C with gentle stirring. Immediately after the mixing, the mixture was passed through a Sephadex G-25 column equilibrated with 10mM sodium phosphate buffer, pH 6.0, (column bed 25×3cm^2). The first, darker band was eluted with the same buffer, collected, concentrated, and passed through a 3×1cm^2 CM-52 column equilibrated with pH 7.0, 100mM sodium phosphate buffer to remove the denatured protein. The collected main fraction was stored at 0-5°C.

(2) UV-Vis spectra

According to the Yonetani paper, Co^{2+}-myoglobin absorbs at 577, 539, and 426nm when oxygenated. The UV-Vis spectrum of the oxygenated $(NH_3)_5Ru(His\text{-}113)^{3+}$-myoglobin($Co^{2+}$) was taken on Cary 17. The bands were present at 572, 538, and 426nm. When deoxygenated, the Soret band of Co^{2+}-myoglobin shifts

from 426nm to 406nm. The UV-Vis spectrum of Co^{3+}-myoglobin has a look very much alike that of Co^{2+}-myoglobin. However, Co^{3+}-myoglobin is not capable of binding to oxygen, so it does not deoxygenate. Since sodium dithionite reacts very rapidly with oxygen, taking spectrum of cobalt myoglobin immediately after addition of sodium dithionite and observing the Soret shift can tell if Co^{3+}-myoglobin is present: If immediate shift of Soret band occurs, it indicates that Co^{2+}-myoglobin is present, and if spectra changes occur over 5 min to an hour it means Co^{3+}-myoglobin, which can only be slowly reduced by sodium dithionite, is present. After addition of sodium dithionite to the sample $(NH_3)_5Ru(His\text{-}113)^{3+}$-myoglobin($Co^{2+}$), the Soret band immediately shifted to 406nm, with a smaller shoulder retained at 426nm. This showed that the major product was $(NH_3)_5Ru(His\text{-}113)^{3+}$-myoglobin($Co^{2+}$), but a significant amount of $(NH_3)_5Ru(His\text{-}113)^{3+}$-myoglobin($Co^{3+}$) was present. After the sample was oxidized with potassium ferricyanide, the oxidizing reagent for native Co^{2+}-myoglobin, the spectrum was again taken. The peaks were very similar to those of the oxygenated $(NH_3)_5Ru(His\text{-}113)^{3+}$-myoglobin($Co^{2+}$). As expected, immediate shift of Soret band did not take place upon addition of sodium dithionite.

(3) Redox potentials

The redox potentials for both the cobalt and the ruthenium sites were determined by differential pulse voltammetry. A sample of $(NH_3)_5Ru(His\text{-}113)^{3+}$-myoglobin($Co^{3+}$) was tested. Three peaks were shown. The $(NH_3)_5Ru(His\text{-}113)^{3+/2+}$ peak showed at -112mV vs. SSCE, and the $Co^{3+/2+}$ peak showed at +212mV. The 300mV difference in redox potential indicated that electron transfer between the ruthenium and copper sites could be possible. It is desirable to compare the $Co^{3+/2+}$ potentials of native and modified cobalt myoglobin. Since no literature value of the redox potential of native Co^{3+}-myoglobin was known, a sample of Co^{3+}-myoglobin was prepared and its redox potential was determined. The peak was at +236mV, very near to that of the modified myoglobin (as it should). The third peak of the sample

of $(NH_3)_5Ru(His\text{-}113)^{3+}$-myoglobin($Co^{3+}$) showed at -380mV. Its origin was unknown. Perhaps it was the $Co^{2+/+}$ peak. The differential pulse voltammetry was performed by Ron McHatton of Anson group.

(4) Test for electron transfer

The test was carried out on Cary 219. A sample (approximately 5×10^{-6}M) of $(NH_3)_5Ru(His\text{-}113)^{3+}$-myoglobin($Co^{3+}$) in pH7, 100mM sodium phosphate buffer was degassed with argon, and then mounted on Cary. The position of the Soret band was monitered. Theoretically, addition of ascorbic acid can catalyze the electron transfer between the ruthenium and cobalt sites. Since ascorbic acid is bulky, it cannot directly reduce the cobalt site in myoglobin. Therefore, it will reduce Ru^{3+} to Ru^{2+}, which can in turn transfer an electron to Co^{3+} and thus reduce it to Co^{2+}. Therefore, we expected that upon addition of ascorbic acid, $(NH_3)_5Ru(His\text{-}113)^{3+}$-myoglobin($Co^{3+}$) will be reduced to deoxygenated $(NH_3)_5Ru(His\text{-}113)^{3+}$-myoglobin($Co^{2+}$) and a shift of the Soret band will be observed. However, the observation result indicated that no electron transfer had taken place. A possible reason is that the reduction from $(NH_3)_5Ru(His\text{-}113)^{3+}$-myoglobin($Co^{3+}$) to $(NH_3)_5Ru(His\text{-}113)^{3+}$-myoglobin($Co^{2+}$) takes place very slowly so it cannot be observed over a relatively short period of time (e.g. 3 hours). The test was repeated using oxygenated $(NH_3)_5Ru(His\text{-}113)^{3+}$-myoglobin($Co^{2+}$) since $(NH_3)_5Ru(His\text{-}113)^{3+}$-myoglobin($Co^{2+}$)-$O_2$ could be treated as $(NH_3)_5Ru(His\text{-}113)^{3+}$-myoglobin($Co^{3+}$)-$O_2^-$ and the change from oxygenated Co^{2+}-Mb-Ru to deoxygenated Co^{2+}-Mb-Ru was immediate. But still, no shift of Soret band (deoxygenation) could be observed in this case. The reason for the absence of electron transfer is not known. One possible explanation is that the oxygenated Co^{2+}-Mb-Ru sample is unstable so that it is converted to Co^{3+}-Mb-Ru in a very short period of time and consequently becomes very difficult to reduce. One evidence supports this explanation: after the Co-Mb-Ru sample failed to show electron transfer, another spectrum of the sample was taken upon addition of

of sodium dithionite, and the expected shift of Soret band did not happen. This means all Co^{2+}-Mb-Ru has been somehow converted to Co^{3+}-Mb-Ru. Another possible explanation is that even though the sample is degassed, a very small amount of oxygen still remains, and since Co^{2+}-Mb-Ru can reversibly bind to oxygen, the deoxygenated Co^{2+}-Mb-Ru can quickly pick up an oxygen molecule and become oxygenated again.

Conclusion:

(1) Reconstitution with Co^{2+}-protoporphyrinIX in $(NH_3)_5Ru(His\text{-}113)^{3+}$-myoglobin is possible. The products are a mixture of Co^{2+}-Mb-Ru (major) and Co^{3+}-Mb-Ru, and there are slight differences between the spectra of native and modified cobalt myoglobins. However, no drastic difference has been found so far. Both native and modified cobalt can bind reversibly to oxygen; both share similar spectra and demonstrate same spectral changes upon deoxygenation; both have nearly the same reduction potential at the cobalt site.

(2) The reduction potentials of the cobalt and the ruthenium sites show that it is possible to get electron transfer between them. Electron transfer cannot occur in Co^{3+}-Mb-Ru, possibly because it is difficult to reduce Co^{3+}-Mb-Ru to Co^{2+}-Mb-Ru.

(3) The reason why electron transfer does not occur in oxygenated Co^{2+}-Mb-Ru is unclear. No further work is to be carried out until this problem gets resolved. Perhaps the synthsis should be carried out at a much greater scale so that a better separated sample can be obtained and a more careful analysis be done. With a concentration of 5×10^{-6}M, any small amount of impurity can greatly disturb the result of the experiment. The stability of oxygenated Co^{2+}-Mb-Ru can easily be monitered in time with Cary 219.

BIBLIOGRAPHY

Chien. J.C.W., et. al. "Electron Paramagnetic Resonance of Single Crystal Oxycobaltmyoglobin and Deoxycobaltmyoglobin", Proc. Nat. Acad. Sci. USA, Vol. 69, No. 10, pp. 2783-2787, October.

Dickinson, L.C. "Metal Replaced Hemoproteins", J. of Chemical Education, Vol. 53, No.6, pp. 381-385, 1976.

Margalit, R., et.al. "Oxidation-Reduction Catalytic Activity of a Pentaammineruthenium(III) Derivative of Sperm Whale Myoglobin", JACS, 105, pp. 301-302, 1983.

Smith, K.M. ed. Porphyrins and Metalloprophyrins. Elsevier Scientific Publishing Company, Amsterdam, 1975.

Walker, F.A. et. al. "Electronic Effects in Transition Metal Porphyrins", JACS, 98, pp. 3484-3489, 1976.

Yonetani, T. et. al. "Studies on Cobalt Myoglobins and Hemoglobins", J. of Biol. Chem., Vol. 249, No. 3, pp. 682-690, 1974.

Title: The Upscaling of the Procedures to Reconstitute Single Cytochrome C Oxidase Dimer Vesicles.

Author: Alan K Marumoto

Faculty Adviser: Sunney I. Chan

Abstract

Recently, Pieter R. Cullis of the University of British Columbia has developed a method of reconstituting well sealed, single cytochrome c oxidase dimer vesicles. The two keys to the production of the desire vesicle is the specific ratio of 4:1 of dioleoylphosphatidylethanolamine (DOPE) to dioleoylphosphatidylcholine (DOPC), and then a high ratio (150:1 by weight) of the lipids to protein. The first produces uniformly small well sealed vesicles, and the latter allows for a statistical favoring of a single cytochrome c oxidase dimer per vesicle. (1) Since the method is small scale (.1 mgs oxidase/sample) and also statistical, it is not surprising that the yield of the desired vesicles is small. Therefore, in my SURF I attempt to upscale the procedures by many fold. Once a reproducable upscaled procedure has been found, measurements such as the H^+/e^- transfer rates will be calculated.

Introduction

The cytochrome c oxidase is one of the most studied enzymes in science. This enzyme is a Y-shaped transmembrane protein located on the inner mitochondrial membrame of eucaryotes. The protein is three dimensional and has a net length of 120Å, and a net width of 100Å. The protein extends a single arm (C arm), which contains the cytochrome c binding site, 55Å into the cytosol side of the membrane. On the matrix side of the membrane, two arms (the M arms) extend no greater than 20Å past the membrane; these two arms contain the O_2 binding site. (2) Studies have indicated that the enzyme has two major functions: one to transfer electrons from the cytosol side to the matrix side of the membrane, and the other to pump protons the other direction. The electrons are transferred via the oxidizing of cytochrome c and then the reducing of O_2. The reaction runs with delta G = −55 Kcal/mole, and can be stated chemically as:

$$O_2 + 4\text{ferrocytochrome c} + 4H^+ \longrightarrow 2H_2O + 4\text{ferricytochrome c} \quad (3)$$

The transferring the across the membrane creates an electrical potential of 160 millivolts. The pumping of protons the other directions creates an additional 60 millivolt potential created by the pH gradient of 1 pH unit. (4) Thus for the typical cell, there is a net proton motive force of 220 millivolts produced across its inner

mitochondrial membrane.

Thus well sealed vesicles are necessary, otherwise the gradient will be dissipated immediately. And as it was determined by Efriam Racker, the ratio of 4:1 of DOPE:DOPC produces the best sealed and also the smallest vesicles. (5) Then couple that idea with that of Vik and Capaldi that a high lipid to protein will produce a majority of the desired single dimer vesicles, (6) and thus we can produce the well sealed single cytochrome c oxidase dimer vesicles.

There are two orientations which the dimer may take when being inserted into the vesicle. Fortunately, since the oxidase is topologically different on its two surfaces, the properly oriented vesicles can be separated from the improperly oriented via affinity chromatography using a diethylaminoethyl-cellulose (DEAE) gel column. In addition, the column also can separate the multicytochrome c oxidase dimer vesicles from the single oxidase dimer vesicles.

The major structural features which allow the cytochrome c oxidase to pass the electrons are the four metal centers. These metal centers have acquired the names cytochrome a, cytochrome a_3, copper A and copper B. Each metal can accept one electron when being converted from the fully oxidized stated to the fully reduced state. Each of the metal centers have many ligands. On the cytochrome a and the copper A, these ligands shield the metal centers from binding with other ligands such as O_2, HCN and NO. (7) 0_2, HCN and NO do however bind quite readily at the cytochrome a_3 and the copper B sites. Thus it can be determined that the cytochrome a_3 and the copper B sites must be on the M arm, and therefore located on the matrix side of the membrane. And the cytochrome a and the copper A are located on the cytosol side of the membrane.

The path which the electrons follow when being transferred through the oxidase are as follows: The cytochrome c binds to the oxidase on the cytosol side at the cytochrome a metal center. This electron is then passed along to the copper a site, which has the same reduction potential as the cytochrome a site, and nearly that of the cytochrome c. The electron is then drawn to the cytochrome a_3 and the copper B site due to a drop in the reduction potential. Then the electron is transferred to the O_2 which is bound to the latter two metal centers. The O_2 is then converted into water from this reduction.

The cytochrome a and copper a sites have been found to mediate the passing of the electrons from the cytochrome c to the O_2. (7) Some however believe that the copper a site has another function, that being the location of the proton pump. (8) In addition, Some believe that this copper a site can be bypassed by impairing the sulfur containing ligands with a mercury reagent. Thus it may be possible to pass electrons without the passing of protons in the opposite direction.

Once a reproducable upscaled procedure has been found for the single oxidase dimer vesicles, such calculations as the H^+/e^- ratio of the primary route can be determined. Then by the reconstitution of vesicles containing the modified enzymes, the efficiency of the secondary route can be determined. In each of these cases, the key calculations will be made by titrating the H^+ and comparing that with the known amount of e^- the vesicle were exposed to.

Materials and Methods

The cytochrome c oxidase was prepared by the members of the Sunney I Chan group at the California Institute of Technology. The concentration of the batch being used (batch #17) is determined by means of the Lowry test. (9) The lipids DOPE and DOPC were ordered from Avanti Polar Lipids. The cytochrome c was a product of Sigma. The affinity gel used was DEAE Sephacel bought from sigma made by sepha. The buffers were all prepared from mono basic potassium phosphate in distilled water, titrated with potassium hydroxide. Each potassium chemical were Baker's analyzed. The carbonyl cyanide (triflouro)methoxyphenylhydrazone (FCCP) and the valinomycin were bought from Alderich. The sodium cholate was prepared by Hsin Wang, a member of the Chan Group.

The column used was a 1.6 X 30 cm Pharmacia type c affinity column. The sonicator was a W-225 Heat Systems Ultrasonics Inc., sonicator. The pH meter was a PHM 82 standard pH meter by Radiometers America. The ultrafiltration apparatus is made by Amicon. The Ultrafilter was an XM-50 also by Amicon.

For the non-upscaled reconstitution of the vesicles, .48 mL of 25mg/mL solution of DOPE and .30 mL of a 10mg/mL solution of DOPC were Hamilton syringed into a small test tube. The chloroform solvent was remove via evaporation under a nitrogen flow. To the dried lipids was added 44.2μL of the 17% by weight solution of sodium cholate. Then followed 1 mL of 50 mM potassium phoshate buffer at pH 8.3. The solution was vortexed prior to 5 minutes on the sonicator fitted with a microtip running at 70% maximum power. The sonication was carried out under nitrogen flow and on an ice bath. The .05 mgs of batch 17 cytochrome c oxidase was analytically syringed in. The solution was vortexed prior to being pasteur pipetted into a freshly rinsed dialysis tubing. The solution was allowed to dialyze against 300 mL of the same type buffer for 5 hours. Then after that, the solution was dialyzed against 500 mL of a fresh batch of the same buffer.

One upscaled procedure increased everything by four except the dialysis volumes and times. They were only increased to 500 mL for 8–16 hours and 1000 mL for 15–24 hours. Another upscaled procedure increased the concentration by four, then increased the sonication time by two, and then used the extended dialysis times and volumes of the prior mentioned upscale.

In each case, the solutions were added directly onto a prelayed and pre-equilibrated DEAE sephacel column. The column was packed with DEAE Sephacel gel, which was equilibrated in 10 mM potassium phoshate buffer at pH 8.3, at a flow rate of 10 mL/hr. The column was run at a flow rate of 5 mL/hour while being monitored at 420 nm on the UV photospectrometer via a continuous cell. The fractions caught were 35 drops each, which correlates to about 1 mL per fraction.

The analysis of the four different peaks which were produced from the column chromatography of the vesicles was made on a O_2 polarimeter. The assays were taken in three different solutions. One solution consisted of 3 mL of 50 mM potassium phosphate buffer at pH 7.4 with .6 mgs of cytochrome c and 70μL of sodium ascorbate. The second condition had again 3 mL of the same buffer, .6 mgs cytochrome c, and

70μL of sodium ascorbate, but this sample had .05 % of the detergent Tween-80. The last condition was the same as the first except there was the addition of two uncouplers, 1μM FCCP, and .6μM valinomycin. Each of these solutions were run twice to determine the baseline. Then the largest possible quantity of the sample was added to the respective solutions. These quantities were usually a mL to a mL and a half. (10)

Results and Discussion

The protein concentration of batch 17 was determined via the Lowry test to be 12.6 mgs/mL. The activity assays of the non-inserted enzyme produced an average respiration of 50.48 nmol O_2 consumes per minute per microliter of solution.

During a practice trial, the flow rates were measured at various heights. And after many measurements, it was determined that just shy of 12 cm from top of the eluent reservoir to the bottom tip of the draining tube produced the desired 5 mL/hour.

The first batch of vesicles were not upscaled at all. This batch produced 3.8% peak 1, 32% peak 2, 53.8% peak 3 and 10.2% peak 4. These peak ratios though not exceptional, did produce a significant fraction of the desired peak number 2. The assays however showed rather insignificant activity. The highest activity registered by this batch was the peak 4 when run in the Tween-80 containing solution. Yet even then, the activity (7.7) was such a small fraction higher than the baseline (9.9 and 18.8)that the numbers are not reliable.

The upscaled volume (4X) produced peak ratio of 8.1% peak 1, 5.6 % peak 2, 42.8% peak 3 and 42.8%peak 4. Peak numbers 3 and 4 however were not discrete as they had overlapping tails. Although the decrease in peak 2 fraction of the vesicles, I had to be satisfied with the reasonably high coupling ratios produced by certain peaks. Peak number 4 recorded the highest coupling ratio, that being 6.6. The lower end of the spectrum of activity assays, however, were still too close to the baseline to be considered reliable.

When the concentration was increased (4X), the running of the column produced only three peaks, the third and four coming off as a single peak. The percentages of each peak is as follows, peak 1, $\approx$80%; peak 2, $\approx$1%; and peak 3–4, $\approx$20 %. This time the percentage of peak 2 was horrible. And in retrospect, I can see that it is due to the increase in the volume of material being sonicated. While the amount of energy being put into the solution remained nearly constant, the amount received by the individual vesicles was considerably less. In addition, the activity assays were equally bad as the highest activity was only 11.6 above the baseline. (The baseline itself is nearly 20 units.)

A new added twist which may prove to the key is the Amicon ultrafiltration apparatus which allows for the concentrating of solutions with no harm done to the vesicles, and also without increasing the concentration of the buffer. Although I have yet to have a successful run using the device, none of the failures was due to the ineffectiveness of the ultrafiltration device. Each time, the failure was due to the column.

In addition to the increasing the size of the batches run, I have been working on methods of regenerating the column so that it may be used over many times without having to repack a new one each run. These attempts so far have been futile as many batches of the vesicles have be lost on the so called regenerated columns.

One other minor success has been the area of modifications to the gradient of the buffer used. Initially, a step gradient was used. However, it was realized that by using a continuous gradient the buffer could be increase much more safely and quickly—without causing peak overlap. Thus the column would be much more efficient since with less volume flowing through would cause a smaller amount of dispersion in the peaks.

Conclusion

Upscaling the procedures of Pieter R. Cullis have become more of a challenge than I had expected. Each trial takes nearly a week, and therefore does not allow me the luxury of running many tests in a hit and miss fashion.

Nevertheless, after completing many weeks of work I have come to the conclusion that the procedures I have reached will work. It is just a matter of fine tuning them. The procedures will have the vesicles sonicated in small batches just as Pieter R Cullis did. However, prior to the additon onto the column, many small batches will be concentration with the Amicon ultrafiltration apparatus. The column will be run using a linear continuous gradient which will allow for the column to be run with less eluent and thus with the added concentration of the vesicles the peaks will have a lower dispersion and will less likely to overlap. The peaks which then appear will each be concentrated down, again on the Amicon ultrafiltration apparatus and then the assays will be run in the usual fashion.

References

(1) Madden, T., Hope,M.J., and Cullis, P.R., Influence of Vesicle Size on Respiratory Control in Reconstituted Cytochrome Oxidase Vesicles. Biochemistry (1984) 23, 1413–1418.

(2) Dearthridge, J.F., Henderson, R., Capaldi, R.A., Three Dimensional Structures of Cytochrome C Oxidase: Vesicle Crystals on a Negative Stain. Journal of Molecular Biology, (1982) 158, 487–499.

(3) Lehninger, A.L., Biochemistry, Worth Publishers, New York (1975)

(4) Alberts,B., Bray,D., Lewis,J., Raff,M., Roberts,K., Watson, J., Molecular Biology of the Cell, Garland Publishers Inc., New York (1983).

(5) Racker, Efriam. Reconstitution of Cytochrome c Oxidase and Conferral of Sen-

sitivity to Energy Transfer Inhibitors. Journal of Membrane Biology, (1972) 10 221–235.

(6) Vik,S., and Capaldi,R.A., Biochemistry (1977) 16, 5755.

(7) Blair,D.F., Gelles,J., Wang,H. Brudvig,G.W., Stevens,T.H., and Chan,S.I., The Metal Centers of the Cytochrome C Oxidase Complex: Structures and Interactions. Chemica Scripta (1983) 21, 43–53.

(8) Chan, S.I., Bocian,D.F., Brudvig,G.W., Morse,R.H., and Stevens, T.H., in Cytochrome C Oxidase. (Edited by T.E.King, Y. Orii, B.Chance, and K.Okunuki) pp 177–188. Elevier,Amsterdam (1979).

(9) Lowry Protein Assay. Produces taken from Jeff Gelles XIII p 29.

(10) Polarographic O_2 Assay. Procedures taken from Jeff Gelles IV pp 10–11.

Substituent Effects on the Rate of Addition of Para-Substituted Styrenes to Permethylscandocene Methyl Complex

Michael C. Nolan

Faculty Sponsor - John E. Bercaw

Abstract - In order to test an hypothesized transition state for the insertion of permethylscandocene alkyl complexes into the vinylic protons of olefins, the kinetic parameters for the insertion into para-substituted styrenes were compared. Little effect was found, but this was rationalized as being due to the very large entropies of activation: $\Delta S^{\ddagger} \sim -35$ cal./mole K.

Introduction

The reaction of permethylscandocene alkyl derivatives (e.g. 1) with olefins has been found to give unusual results. If 1 is allowed to react with propene, it gives the expected product 2, which is rationalized as coordination of the double bond, followed by insertion of the methyl group onto the double bond. If however, the olefin is more bulky than propene (or if 2 is allowed to react further with propene), the product seems to be a vinyl adduct 3 (with release of methane)[1]. This is quite unexpected as the vinylic C-H bond is much stronger than the allylic C-H bond of propene (108 kcal/mole vs. 89 kcal./mole). The steric requirements of 1 must disfavor standard insertion enough that another mechanism obtains.

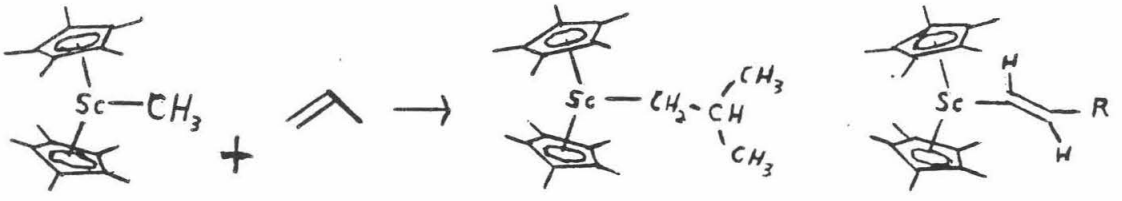

1 2 3

1. M.E. Thompson, J.E. Bercaw, Pure and Appl. Chem. 56, 1 (1984)

Our hypothesized mechanism involves a zwitterionic-like transition state with some positive charge on the β carbon of the (terminal) olefin. (Scheme):

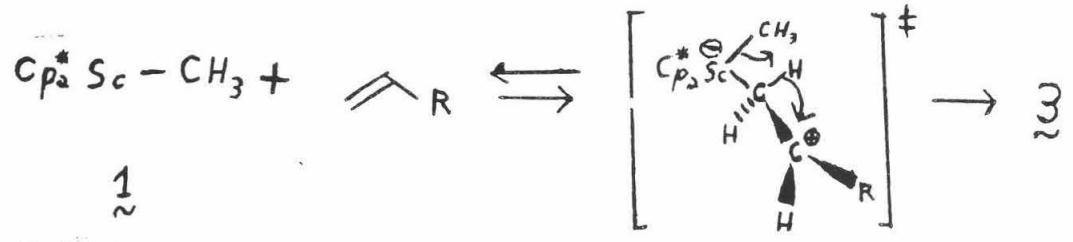

Scheme

In order to test the validity of the proposed mechanism, it would be desirable to compare the electronic effects of olefin substituents on the rate of insertion. To this end it was decided to use para-substituted styrenes as the olefins. Varying the para substituent should change the stability of the charge on the β carbon, allowing comparison of electronic effects without any significant difference in steric bulk.

Results and Discussion

The kinetics of the reaction of 1 with para-trifluoromethyl-styrene were measured through the use of ^{19}F NMR, by watching the dissapearance of the peak due to free styrene and the appearance of the peak due to the adduct 3 (R= p-C_6H_4-CF_3). The rates were measured at seven different temperatures over a 54°C range, yielding $\Delta H^{\ddagger}$=12.6±0.1 kcal/mole, $\Delta S^{\ddagger}$=-34.7±0.1 cal/mole K. The kinetics of the reaction of 1 with para-methoxy-styrene had previously been measured, yielding $\Delta H^{\ddagger}$=11.3kcal/mole and $\Delta S^{\ddagger}$=-36.4±5.3 cal/mole K. It was expected that $\Delta H^{\ddagger}$ would be noticably lower in the para-methoxy-styrene system, as it is significantly more electron releasing than the para-trifluoromethyl-styrene system (to the olefin β carbon). The differance is however not very large. A Hammett plot of the rates vs. substituents gives $|\rho| < 0.1$.

A completely diffent system was then tried to make sure that there is an effect to be measured. The reaction of 1 with methylenecyclohexane was measured at 61°C, and gave a rate thirty times slower than either styrene system. Although this difference is at least partially due to increased steric bulk in the methylenecyclohexane system, it does also seem to indicate some electronic difference due to the poorer electron donating ability of the aliphatic carbon atoms in this system relative to the conjugated aromatic carbon atoms in the styrene systems.

Small kinetic effects of polar transition states with very high transition state entropies have been seen in at

least one other case. Addition of olefins to 1,3-dipoles is believed to be a concerted reaction on a polar substrate. Since it is a concerted reaction, it should have a very high entropy of activation. Huissen has attempted to measure the electronic effects on this reaction by using para-substituted styrenes as his olefins. He tried several 1,3-dipolar substrates. One of them gave a Hammett $\rho = +0.83$ (still quite small), and the rest gave very little dependance on the para substituent[2].

The very large entropies of activation $\Delta S^{\ddagger}$ of these reactions could indicate that the top of the energy profiles could come too early for the electronic properties of the R substituent to significantly affect the hight of the top of the barrier. Thus the electronic aspects of the transition state may be invisable because they come later than the top of the barrier. In this case the kinetic data niether denies nor confirms the hypothesis for the transition state.

It has not been possible yet to isolate either of the Cp^*_2Sc-styrene adducts, possibly due to some oligomerized styrene in the reaction vessel. The para-methyl styrene adduct has however been isolated, although confirmation from elemental analysis was not yet ready at the time of this report.

Conclusions

The substituent electronic effect on the rates of the reactions of the para-substituted styrenes

X=OMe, CF_3 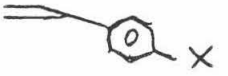

with Cp^*_2ScMe (1) is, for all practical purposes, zero. This does not seem to agree with a proposed zwitterionic-like transition state, unless entropy effects put the top of the reaction energy surface earlier than the substituents can affect; in which case the result is inconclusive. The large transition state entropies ($\Delta S^{\ddagger} \sim -35$ cal/mole K) make this seem plausable. At least one more styrene system should be tested to verify the zero result. The reaction with methylenecyclohexane indicates that there is probably some electronic effect on reaction rate.

2. R. Huissen, Angew. Chem. Int. Ed. Engl. 2, 639 (1963)

Oligonucleotide-Directed Site Specific Mutagenesis of Yeast Iso-1 Cytochrome C

Author: Janice Sakai

Faculty Sponsor: Judith L. Campbell

Oligonucleotide-Directed Site Specific Mutagenesis of Yeast Iso-1 Cytochrome C

Abstract

Studies of the electron transfer mechanism of yeast iso-1 cytochrome c have been hampered by the intermolecular dimerizationof two cysteine residues. To circumvent this problem, oligon ucleotide-directed site-specific mutagenesis was used to change the codon of cysteine 102 to that of a serine. Though the primer used for this mutation encoded a threonine, we were only able to isolate mutants with the serine codon.

Previous work has indicated that studies of electron transfer rates using the yeast iso-1 cytochrome c system has been hindered by the cysteine 102 residue. The ability of this residue to form intermolecular cystine dimers hampers the ability to recover useful electron transfer data. It would be desirable to either inhibit or replace the reactive sulfhydryl group yet still maintain a stable, conformationally intact protein. One approach to producing a stable protein is oligonucleotide-directed site-specific mutagenesis. Developed by Michael Smith in 1977, it is a general method used to specifically change designated bases in a DNA molecule. This technique would enable us to change the codon for the cys 102 residue to a codon of our choice--producing any amino acid desired in the 102 position. The only prerequisite is that the DNA sequence flanking both sides of the target site be known. Then, an oligonucleotide can be synthesized complementary to 12-25 base pairs of the gene, but also including the codon for the new amino acid. This "primer" is then annealed to the gene, which has been inserted into a convenient vector. The most convenient type of vector is one that has a single stranded DNA phase as well as a double-stranded phase during its reproductive cycle, such as the phage M13. The ss-DNA can be purified so that the annealing can take place directly. Then by adding the Klenow fragment of E.coli DNA polymerase, we can extend the 3'end of the primer around the vector to the base before the 5' end of the primer. Using T4 DNA ligase, we can now join the two ends. This double-stranded DNA plasmid is used to transform bacteria. The double-stranded form is also the replicative form of the phage M13, so once transformed, the bacteria are infected with the phage, and will produce phage particles. The bacteria can then be plated with soft agar and plaques containing phage can be picked, some of which will contain the mutated gene.

The screening method is convenient in that it does not require that the mutated protein be expressed, rather, the screening is done entirely at the DNA level. The phage plaques are picked into new media and fresh cells are added and allowed to grow for several hours. Then a small amount

of purified phage from each plaque is spotted onto a piece of nitrocellulose paper. The paper is then allowed to sit for several hours in a solution of radioactive ^{32}P end labeled primer--the same oligonucleotide fragment used earlier to do the mutagenesis. The screening procedure is dependent on the different melting temperatures of oligonucleotides bound to a DNA segment with and without a mismatch. The primer, since it was built complementary to the ss-DNA vector will bind to the gene at the complementary sequence at room temperature, and will melt apart from it at a certain elevated temperature (T_m), dependent on base composition of the primer (+2°C for A-T base pairs and +4°C for G-C base pairs). An audioradiogram of the room temperature hybridization is taken, and then the nitrocellulose paper is "washed" with buffer at a higher temperature, an appropriate number of degrees below the T_m of the oligonucleotide. If the genome does not contain the changed sequence, the hybrid oligonucleotide-gene duplex will melt and the radioactive probe will wash off of the paper. However, if a phage spot contains DNA which incorporated the mutation, then the duplex will not melt, and a subsequent audioradiogram will reveal those as dark spots similar to those on the room temperature autoradiogram. Though this is by no means a conclusive screening procedure, it eliminates those clones which are useless to pursue. The conclusive evidence is a DNA sequence of the putative mutants.

For our system, threonine was chosen to replace cysteine at the 102 position because extensive amino acid sequence information showed its presence there in other cytochrome c's. From the known DNA sequence of yeast iso-1 cytochrome c, this requires a change in codon from "TGT" to "ACT" ,that is, two base changes. We used a 17-mer as our primer, chosen in size and position to minimize the homology with any other sequence on the M13\CYC1 genome.

Since the "dot blot" screening technique is not conclusive, we were fortunate that a simple convincing test for one of the base changes was available. By changing the codon from "TGT"to "NCT" (N being any base) we would create a DdeI restriction site. This site would lie in the middle of a 800 base pairDdeI-PvuI fragment, and would split it into 500 and 300 base pair fragments. This could easily be detected on an agarose gel by the disappearance of the 800 base pair band, and the appearance of the 500 base pair band.

An extension to the basic procedure involved the utilization of a second primer. Since we were trying to incorporate a double mismatch, the probability of its recognition by cellular DNA repair machinery was increased. The 3' end of the primer is protected because extension occurs there immediately, but the mismatch is still close to the free 5' end. Though we can get extension completely

around the genome to meet with the 5'end of the mutagenic primer, we wished to increase the chances of the extendion meeting the 5' end. By annealing a second primer, a 15 base pair exact oligonucleotide complementary copy of the genome, 50 base pairs downstream of the 5' end, we can get immediate extension at the 3' end of this primer also, and can be more assured that it will "meet" the end of the mutagenic primer.

Results

We obtained an efficiency of mutageniesis of approximately 1%. One purified "positive" did not exhibit the restriction site that we should have created. It seemed unlikely that the 3'--TGA--5'
5'--TGT--3' hybrid yielded a 3'--TCA--5' or 5'--AGT--3' since this would require that only one base was repaired when two adjacent bases were wrong. However, dideoxy sequencing showed that this was indeed the case. This change to the "AGT" codon shows that we have instead changed the cysteine 102 to serine 102. However, since serine and threonine are similar in composition, and at least one other known cytochrome c contains serine at the 102 position, we are now going to subclone the gene and express the protein in yeast for future studies in protein chemistry.

We also intend to use the singly mutated cytochrome c genes as a new template for further attempts to isolate the threonine mutation. Other modifications which will increase the efficiency of our technique are the use of a repair deficient bacteria strain and the use of a ss-DNA binding protein which has been professed to increase efficiency by facilitating extension of the primer around the vector.

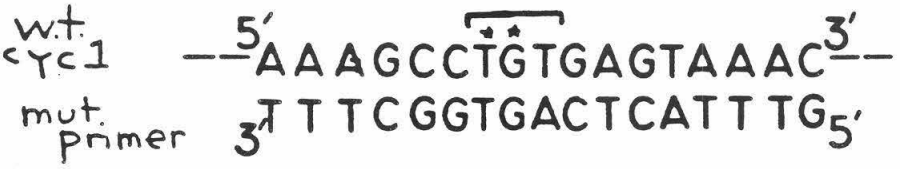
w.t.
cyc1
5'
AAAGCCTGTGAGTAAAC
3'
mut.
primer
3'
TTTCGGTGACTCATTTG
5'

FIG. 1

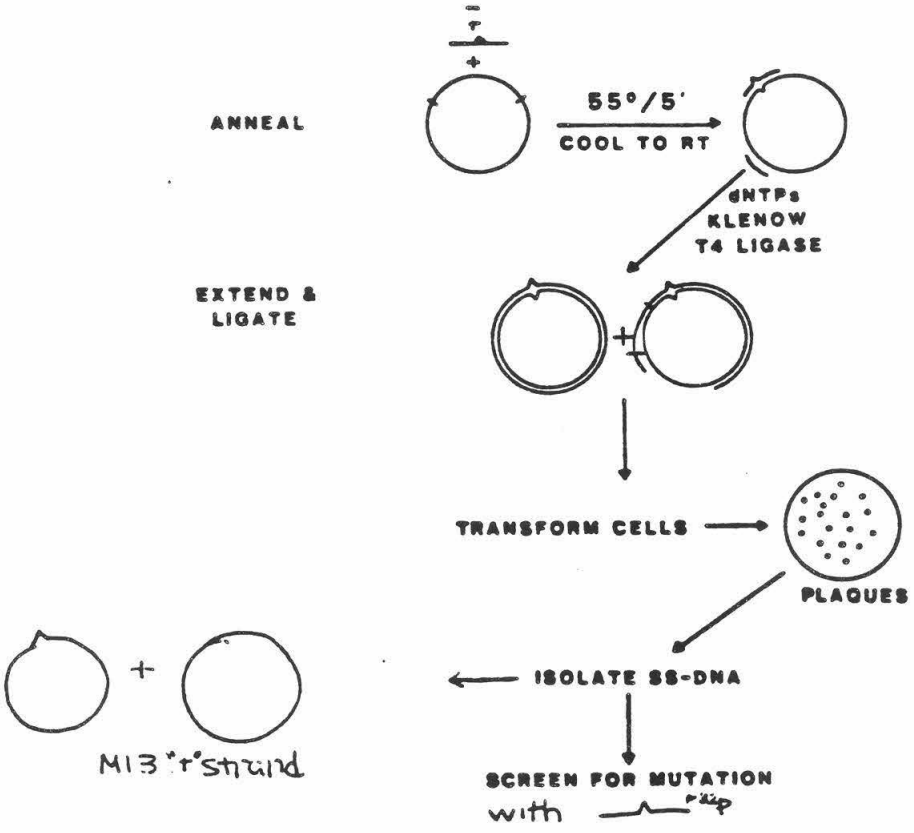
ANNEAL
55°/5'
COOL TO RT
dNTPs
KLENOW
T4 LIGASE
EXTEND &
LIGATE
TRANSFORM CELLS
PLAQUES
ISOLATE SS-DNA
SCREEN FOR MUTATION
with
M13 "r" strand

FIG. 2

Bibliography

1. Messing, J. "New M13 Vectors for Cloning", Methods in Enzymology, Vol. 101, 1983, 21-89.

2. Montgomery, D. L., Hall, B.D., Gillam, S. and Smith, M. Identification and Isolation of the Yeast Cytochrome c Gene, Cell 14, July 1978, 673-680.

3. Smith, M., Leung, D.W., Gillam, S. and Astell, C.R. Sequence of the Gene for Iso-1-cytochrome c in Saccharomyces cerevisiae, Cell 16, April 1979, 753-761

4. Zoller, M. and Smith, M. "Oligonucleotide-Directed Mutagenesis of DNA fragments Cloned into M13 Vectors", Methods in Enzymology, Vol. 100, 1983, 468-500.

THE DESIGN AND SYNTHESIS OF BIOMIMETIC CHIRAL CAVITIES

FACULTY SPONSOR:
DENNIS A. DOUGHERTY
ASST. PROFESSOR OF CHEMISTRY
CALIFORNIA INSTITUTE OF TECHNOLOGY

SUBMITTED BY:
WILLIAM D. SHARPE
CALIFORNIA INSTITUTE OF TECHNOLOGY
SEPTEMBER 14,1984

ABSTRACT: The synthesis of the 1,5-dioxo analogue of (5) (see Scheme I) was attempted. The synthesis was stymied by the extreme unreactivity of the starting material, 1,5-dihydroxyanthraquinone. A number of different synthetic approaches were tried, however, all were unsuccessful.

This project concerned the synthesis of a water soluble organic molecule with a well defined hydrophobic cavity (host) that would efficiently bind a small, organic molecule (guest). The host structure would effect the transport of a lipophilic molecule from the aqueous phase to the host molecule's binding site. Such a host would be biomimetic in that it would allow a guest to be moved across a barrier that would normally be inaccessible to the guest. A naturally occurring example of this would be the action of certain kinds of antibiotics that promote ion transport across membranes. Our project would have been a complement to this in that our host would have complexed nonpolar molecules whereas in the example cited above complexation of charged atoms occurs. It was also thought that our host molecule could serve as a highly selective catalyst, by binding a guest, mediating a chemical transformation on the guest, and then releasing the modified guest. Such behavior would mimic the way enzymes operate. Several other similar projects are under way in these laboratories, with the one most closely related to this project being the synthesis of(5) shown in Scheme I. With these thoughts in mind a synthesis of the 1,5-dihydroxy analogue of the 2,6-dihydroxy derivative (5) was proposed and then attempted.

Initially, it was thought that the synthesis of the 1,5-dihydroxy "pocket" could be achieved in the same manner as the synthesis of (5), a similar compound. The reduction of 2,6-dihydroxyanthraquinone to 2,6-dihydroxyanthracene is a two-step process involving first, conversion to the anthrone, and then taking the anthrone to the anthracene. When 1,5-dihydroxyanthraquinone was treated with a concentrated hydrochloric acid/stannous chloride solution, the anthrone was formed in 81% yield. A reduction with an aluminum/mercury amalgam in an ammonium hydroxide solution was attempted on 1,5-dihydroxyanthrone with disappointing results. Anthracene formation was thought to be occurring as evidenced by blue fluorescence under short-wave UV radiation, however, this was a specious observation as the anthracene was not apparent in a proton NMR spectrum or in a UV spectrum. This amalgam reduction was attempted several times with the same negative results.

At this point a search of the literature revealed that 1,5-dihydroxyanthraquinone is extremly resistant to reduction. Apparently, intramolecular hydrogen bonding renders this system inert toward reduction. It was also discovered that it is possible to produce 1,5-alkoxyanthracenes from 1,5-dialkoxyanthraquinones. Since large quantities of 1,5-dihydroxyanthraquinone and the corresponding anthrone were available, it was decided to try and alkylate or silylate these compounds rather than synthesize the 1,5-dialkoxy/siloxyanthraquinone or 1,5-dialkoxy/siloxyanthrone from other sources. Silylation would have been a preferable alternative as it was thought that removal of a silyl group would have been an easier process than that of an alkyl group. Several methods of alkylation/silylation were attempted, all without success. The methods of alkylation attempted included alkylation with alkyl iodide and potassium carbonate, alkyl iodide and silver (I) oxide, and deprotonation with sodium hydride followed

by addition of alkyl iodide. Methods of silylation tried were similar, usually involving deprotonation of the hydroxyl proton with a nitrogen base followed by attempted silylation with a silyl chloride or iodide. Scheme II shows all the reactions that have been attempted to date. A reaction which is not shown is the attempted methylation of 1,5-dihydroxyanthraquinone with dimethylsulfate; the results of this reaction are not in as of the writing of this report. Deprotonation of the 1,5-dihydroxyanthraquinone or anthrone is apparently not a problem; it would appear that the anion or dianion formed is very non-nucleophilic. This is not unreasonable considering the extremely delocalized nature of the anion or dianion formed upon deprotonation. Further experiments are under way in an attempt to find a suitable reagent for alkylation of these compounds.

When alkylation/silylation proved difficult it was decide to attempt to synthisize 1,5-dialkoxyanthrquinone from 1,5-dichloroanthraquinone and the corresponding alkoxide. Presumably this reaction proceeds by nucleophilic attack on the aromatic system at the chlorinated carbon followed by the elimination of a chloride anion. When this reaction was attempted with sodium methoxide in refluxing methanol no reaction was observed even after 12 hours at reflux; recovery of starting material was in excess of 95%. It was thought that the sodium methoxide might be culpable. However, when methanolic sodium methoxide was freshly prepared by reacting sodium metal with methanol and then carrying out the reaction the result was the same. It was hoped that sodium ethoxide, being a stronger base, would facilitate formation of 1,5-diethoxyanthraquinone. When this reaction was tried with freshly prepared ethanolic sodium ethoxide the result was a brown gelatinous mass that ran at the same rate as 1,5-dichloroanthraquinone by TLC and did not show the characteristic ethyl pattern by proton NMR. These results were puzzling given the fact that the experimental protocol was taken straight from a chemical journal. Experiments are under way in an attempt to perfect reaction conditions so that the 1,5-dialkoxyanthraquinones are formed.

In terms of what we set out to accomplish, this summer's project was highly unproductive. However, there are several things that have been learned as a result of this work. Of primary importance is the fact that 1,5-dihydroxyanthraquinone is virtually impossible to reduce. This was a dissappointing result in light of the ease with which 2,6-dihydroxyanthraquinone is reduced to the anthracene. Also gained was the knowledge that the oxygen atoms in 1,5-dihydroxyanthraquinone are very non-nucleophilic. Perhaps the most important facet of this summer's work was the experience that it afforded me (WDS) in working in a laboratory setting.

BIBLIOGRAPHY

1. Petti,M.A.; unpublished results from these laboratories

2. Cook,J.W., Pauson,P.L.; J. Chem. Soc.;1946;2726

3. Shyamasundar,H., Caluwe,P.; J. Org. Chem.;46;1981;1552

DEFINITIONS

t-BDMSiCl	=tert-Butyldimethylsilyl chloride
TMSiCl	=Trimethylsilyl chloride
TMSiI	=Trimethylsilyl iodide
DBU	=1,8-Diazabicyclo[5.4.0]undec-7-ene

SCHEME I

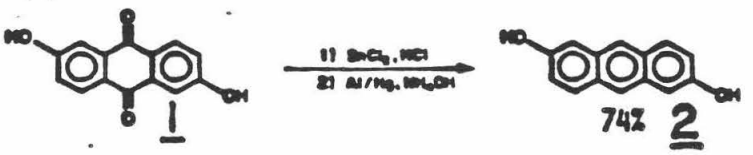

74% 2

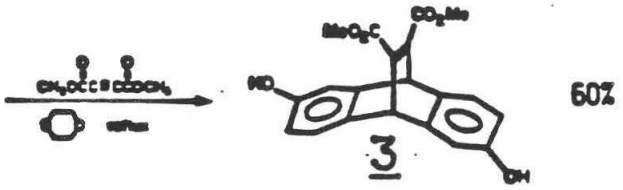

60%

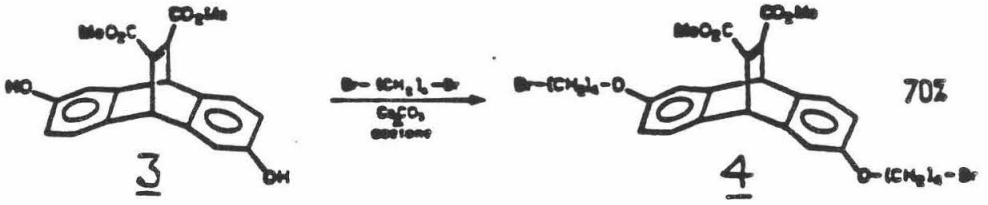

70%

45%

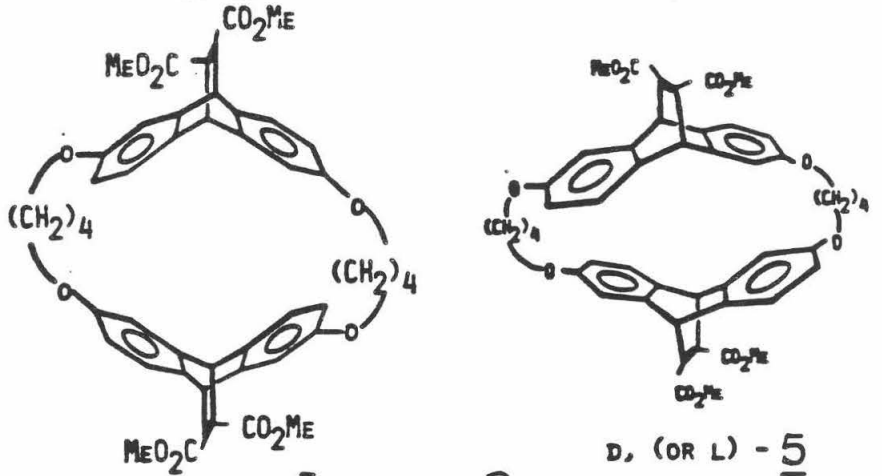

Meso-5 Tetraacids = 6

D, (or L) - 5

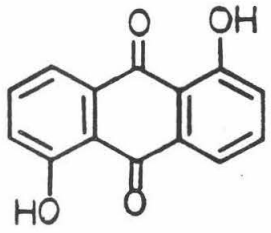

Al/Hg, NH_4OH → No Reaction

t-BDMSiCl / Imidazole → "

" / DBU → "

TMSiCl / Imidazole → "

1) NaH / 2) TMSiCl → "

Ag_2O, TMSiI → "

Ag_2O, EtI → "

K_2CO_3, EtI → "

" , MeI → "

HCl/$SnCl_2$ →

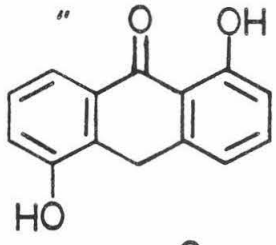

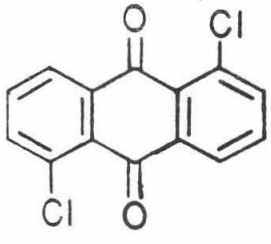

NaOMe / MeOH → No Reaction

NaOEt / EtOH → "

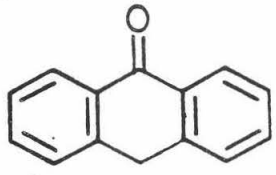

Al/Hg / NH_4OH → No Reaction

Ag_2O / TMSiCl → "

Imidazole / t-BDMSiCl → "

DBU / " → "

K_2CO_3 / EtI → "

Scheme II

MPE*Fe(II) of Echinomycin Binding to Native DNA

by Anna Toy

Faculty Sponsor: Dr. Peter B. Dervan

Abstract. Antibiotics have been found to bind to specific sequences on the DNA molecule. Resolving the locations of the binding sites of these drugs on native DNA can be accomplished by footprinting methods using the synthetic DNA cleaving agent, methidium-propyl-EDTA*Fe(II) (MPE*Fe(II)).

Theory. Antibiotics such as echinomycin, actinomycin, and distamycin have been observed to bind with DNA preventing further reading along the DNA. This changes the protein production in the cell which may be a useful property to prevent or regulate various diseases and possibly cancer.

By locating where the antibiotics bind onto the DNA molecule, a correlation between the binding sites and DNA sequences may be found. If a sequence is favorable then structural observations of the drug:DNA complex may provide information on why the drug has a certain specificity.

Experimental. The antibiotic echinomycin was dissolved in THF before any of the cleavage reactions with the drug:DNA complex took place. In solutions of calf thymus DNA, p32 3'-end labelled DNA restriction fragments (167 and 517 base pair in length) were added to the various concentrations of echinomycin. Allowing time for the drug to bind to the labelled DNA cleavage was initiated by the addition of MPE*Fe(II). Cleavage was stopped by placing the solutions in an ice-water bath before preparing the 8% acrylamide gel for electrophoresis.

Comparing the additional binding sites in the lanes of increasing concentrations display the limits of the antibiotic's ability to recognize specific sequences. Control lanes are needed for the uncleaved DNA, the DNA with MPE*Fe(II) added, and the G lanes. The control lanes for uncleaved DNA determine the amount of separation that occurs naturally. The G lanes serve as markers to determine where on the fragment the sites are, since all the sequences are already known.

Discussion. Due to several difficulties, there were no conclusive results. Because the redioactivity of the gels were too low, the developed plates could not be used for analysis. Had the radioactivity

been higher, densitometry would have been used to measure the intensity of the lane markings to determine what and where the binding sites were.

Acknowledgements. All thanks to the Summer Undergraduate Fellowship and to Professor Peter Dervan and his research group who have helped me in so many ways.

Bibliography.

1) Van Dyke, M.W., Hertzberg, R.P. and Dervan, P.B. (1982) proc. Natl. Acad. Sci. USA 79, 5470-5474.
2) Van Dyke, M.W. and Dervan, P.B. (1983) Cold Spring Harbor Symp. Quant. Biol. 47, 347.
3) Van Dyke, M.W. and Dervan, P.B. (1983) Biochemistry 22, 2373.
4) Van Dyke, M.W. and Dervan, P.B. (1983) Nucleic Acids Res. 11, 5555-5567.

THE DEVELOPMENT OF A SYSTEM FOR MEASURING TEMPERATURES REMOTELY IN FREELY MOVING OBJECTS

by

Brian James Tsai

ABSTRACT:

A Hartley oscillator, modified to exploit the temperature sensitivity of the circuit, was designed, calibrated, and used to study transient heat transfer in freely moving objects. A data aquisition and analysis system based on a micro computer was set up. This temperature measurement system may have application in thermal food processing and sterilization.

INTRODUCTION:

Heating and cooling are frequently used in food processing. Although much experimental and theoretical work has been conducted in the general area of heat transfer, (Carslaw & Jaeger; 1959, Bird, Stewart & Lightfoot; 1960) almost none has been done with objects which are allowed to float or move freely with respect to the surrounding fluid. Such systems of free bodies are quite common and important to the processing of certain types of food. These systems often involve heat transfer through a solid wall into a liquid, within which solid pieces of food are suspended. FDA regulations regarding acceptable scientific methods of establishing heat sterilization processes include process calculations based on product heat penetration data (ref. 3). It is therefore important to accurately determine the temperature-time relationship of the center of the suspended food. Traditionally, the values of important parameter in heat transfer have been correlated by means of dimensionless groups; such correlations are based upon experimental evidence. Few, if any, experimental techniques have been developed which adequately address the problem of transient heat transfer to objects which are free to move within the surrounding fluid. Systems involving either thermocouples or thermistors have connecting wires which tend to interfere with the object's movement relative to the suspending fluid. The

purpose of this work is to first develop, design and construct a temperature measurement system which would not interfere with the movement of such objects. The system would also have to be as small as possible so as to avoid affecting heat conduction within the sphere itself. Secondly, a series of classical experiments need to be conducted to test the accuracy of the system. Thirdly, another set of experiments that test the system in a free-moving environment need to be run.

EXPERIMENTAL:

Several years ago, Dr. Lou Howard (then at MIT) (ref. 4) mentioned the possibility of using a germanium transistor in a Hartley oscillator circuit which emitted a pulse whose period varied with temperature. This oscillator was constructed and after much miniaturization a working model was ready. Due to electrical effects on the circuit by water, calibration was conducted in oil. The resulting calibration curve and temperature vs. pulse function are shown in Figure 1. It was found that picking up the signal by radio and amplifying it sharpened and cleaned the signal greatly. This signal was in turn sent to an HP electronic counter to measure the pulse period and then relayed to a GPID IEEE488 interface card installed in an IBM-PC XT. Once in the computer, the period was converted to a real-time temperature using the temperature function obtained by calibration.

The first set of experiments conducted were with a fixed sphere in a well-stirred constant temperature water bath with the Hartley oscillator embedded in the center of the sphere. This was chosen because this was essentially a classical problem whose solution was well known. Three different materials were used for the spheres. The first was modeling

clay, chosen for its immediate availability and moldability. The next material was castable polyurethane which was chosen for its almost neutral buoyancy and workability. The third run in this set was with polyurethane impregnated with 11% weight aluminum powder, in an attempt to increase thermal conductivity.

The second experiment involved rotating the sphere in an unstirred constant temperature bath at approximately one rps to affect the boundary layer. The sphere used in this and the next experiments was the aluminum impregnated polyurethane sphere.

The third experiment conducted had the sphere freely floating in an unstirred bath with a heat source on the bottom. About 10% salt was added and but stirred. The purpose of this experiment was twofold. The first was to demonstrate the use of the system in a simulated complex process with temperature and density gradients. The second was to compare the effects of this process on the temperature history of the center of the sphere with that of a fixed sphere.

RESULTS:

The results of the fixed sphere experiments were in very close agreement with theoretical calculations, as can be seen in Figure 2, a graph of the dimensionless breakdown of each experiment. The slight deviation of some of the points is most likely due to the imprecision of the thermal diffusivity used in each dimensionless calculation. To calculate the thermal diffusivity (alpha), a series of theoretical curves were generated in the the expected range and then fitted to the experimental curve to obtain the closest and most correct result. Daniel Hillel in Soil Fundamentals and Physics gives the alpha range of clay to be from 0.0045 to 0.0052 CM^2/SEC.

The back-calculated alpha from all clay experiments was 0.0048 CM^2/SEC. Unfortunatley the alpha of the polyurethane was not available to compare with the calculated value.

The results of the rotated sphere experiment can be seen in Figure 3, a comparison with the results of the first set of experiments. The extreme similarity between the two can be attributed to the small difference between the bath temperature and sphere surface temperature. Fourier's law gives us

$$h A (T_f - T_s) = k A \left(\frac{dT}{dr}\right)_{r=R}$$

From this we get

$$\frac{T_f - T_s}{T_f - T_{in}} \leq \frac{k}{Rh}$$

Putting the proper values of k,R,h, and the largest ($T_f - T_{in}$) possible with the oscillator, the temperature difference between the bath and sphere surface is only three degrees. This is too small to cause any significant effects on the temperature history.

The results of the final experiment are shown in Figure 4, a comparison with the fixed sphere experiments. As can be seen, assumption of constant surface temperature is invalid. The sphere initially was at rest very close to the bottom of the bath, but as the bottom heated up more salt dissolved. The resulting increase in the water's density at that level cause the sphere to rise slightly. This continued until the sphere came to a rest just under to bath's surface level. The final temperature gradient between the top of the sphere and the bottom of the sphere was measured at 8 degrees Celsius. A strong density gradient was also very visible,

in fact, the bottom quarter of the bath had a level of extreme salinity that was clearly separated from the rest of the bath. The temperature in that level was 98 degrees Celsius, whereas the water near the surface was at 58 degrees. These complexities, such as the effect of the conduction cells on the dissolving of the salt which in turn affected the density patterns, are very difficult to predict by theory. Yet with the Hartley oscillator system the results of such a process can be obtained experimentally.

CONCLUSIONS:

1. A modified Hartley oscillator device was constructed and calibrated to permit the study of heat transfer in systems involving freely moving objects.

2. A microcomputer (IBM-PC XT) was integrated into the data aquisition and analysis system as controller.

3. Experimental results involving transient heat transfer where the object's surface temperature was well-known (Case 1) were in close agreement with theoretical calculations, indicating the accuracy of the system.

4. An experiment with a sphere freely floating in gradients of temperature and density gave very different results from Case 1, thus demonstrating the use of this system in obtaining data on complex processes.

ACKNOWLEDGEMENTS:

Infinite thanks first go to my advisor, Dr. Fred Shair. Were it not for his patience and constant encouragement, I would not have accomplished as much as I did. Much gratitude also goes to Dr. Hardy Martel, for giving me so much advice on a subject I know so little about, and to the Carnation Research Lab for their continued support and advice. Finally, I wish to

express my appreciation to Craig Zupke for his omniscient common sense, which helped me to see so many of my oversights.

REFERENCES:

1. Carslaw, H.S. & Jaeger, J.C. (1959): "Conduction of Heat in Solids" Oxford Press
2. Bird, R.B., Stewart, W.E. & Lightfoot, E.N. (1960): "Transport Phenomena," Wiley & Sons
3. "Code of Federal Regulations," Title 21, Part 113: "Thermally Processed Low-Acid Foods Packaged in Hermetically Sealed Containers," Rev. April 1, 1983, Publication Office of the Federal Register
4. Howard, Dr. Lou (1977), Personal Communication

HARTLEY OSCILLATOR CIRCUIT AND CALIBRATION CURVE

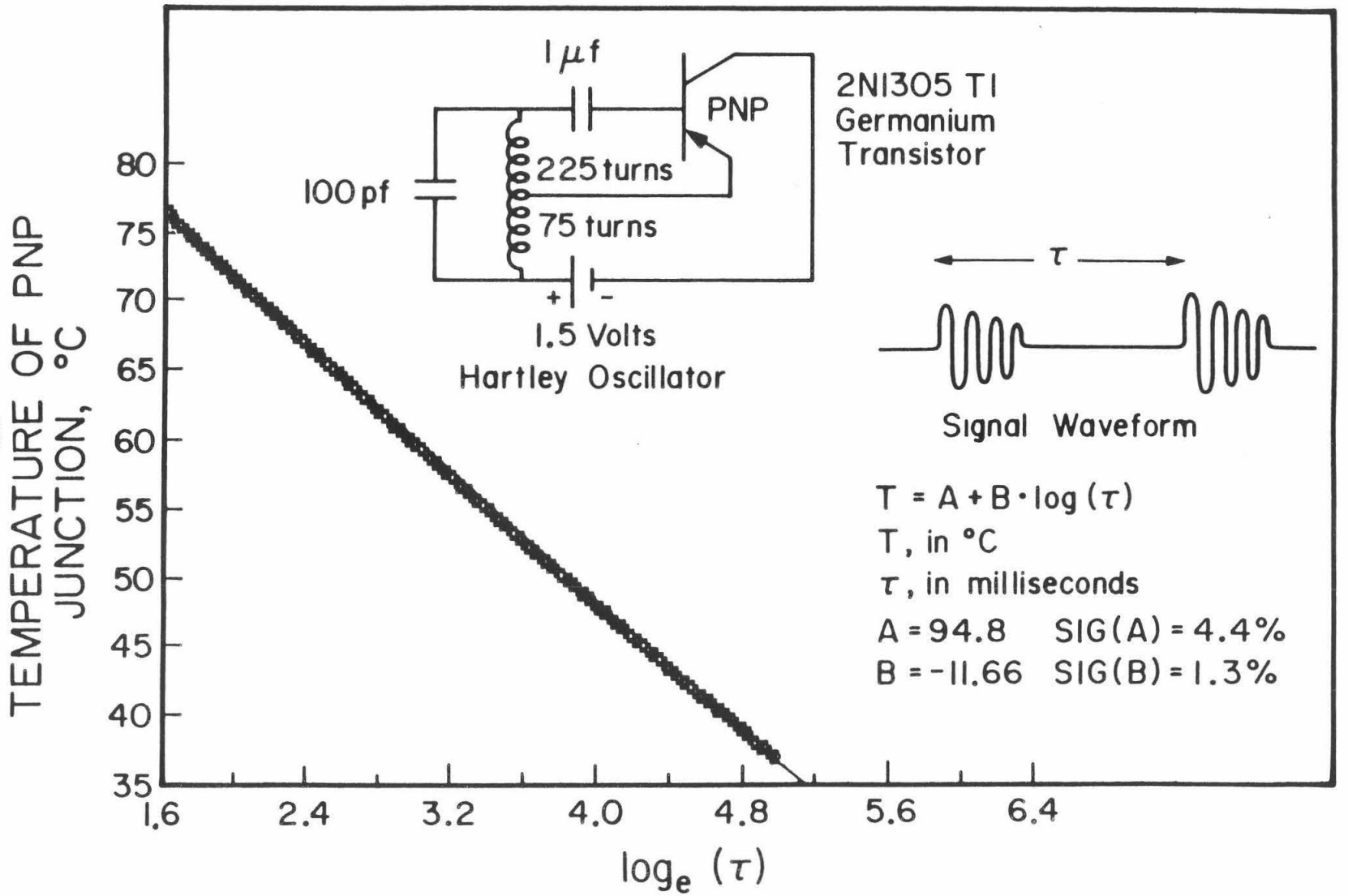

FIGURE 1

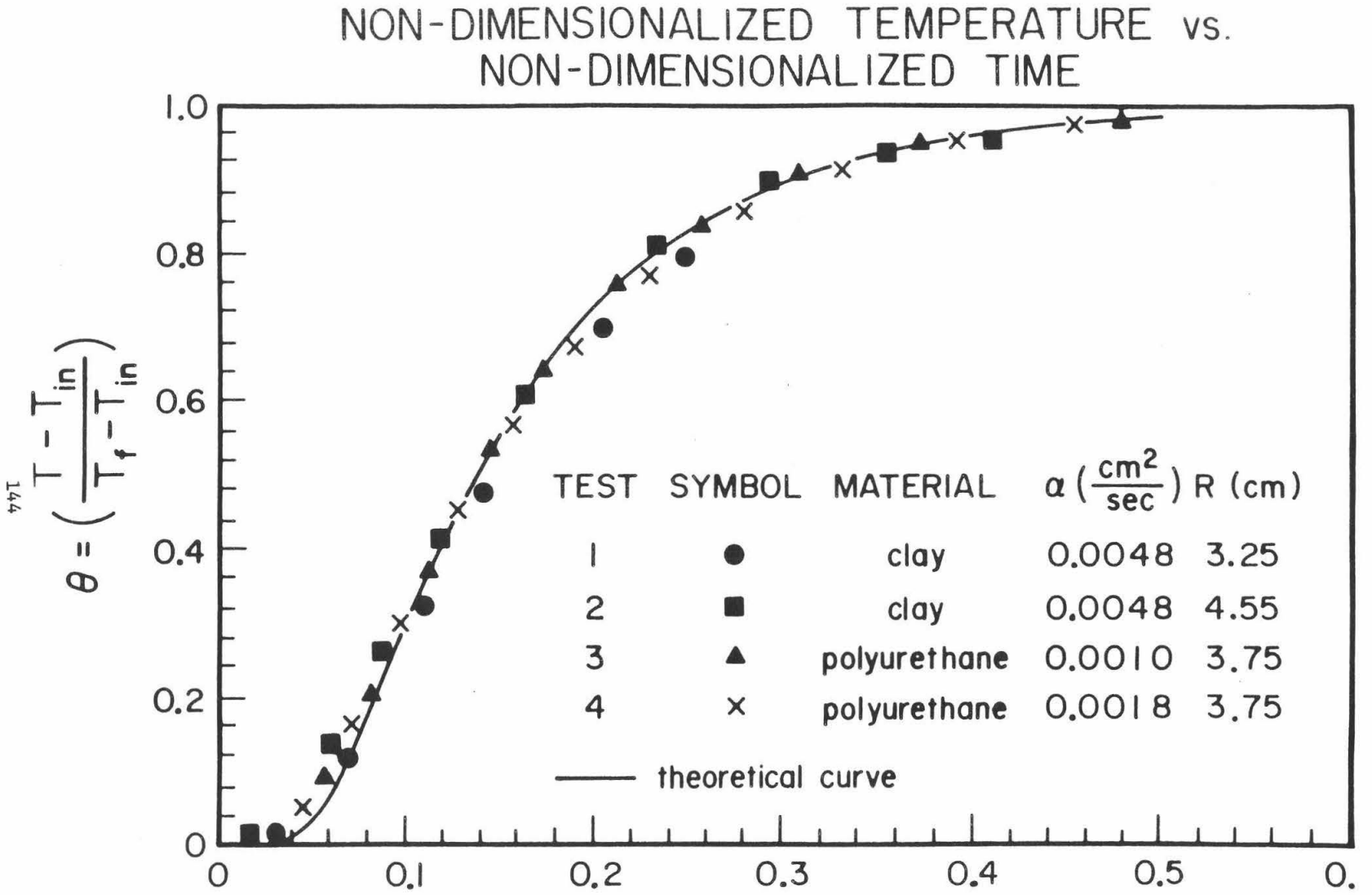
NON-DIMENSIONALIZED TEMPERATURE vs.
NON-DIMENSIONALIZED TIME
$\theta = \left(\frac{T - T_{in}}{T_f - T_{in}}\right)$
1.0
0.8
0.6
0.4
0.2
0
0
0.1
0.2
0.3
0.4
0.5
0.
TEST SYMBOL MATERIAL $\alpha\ (\frac{cm^2}{sec})$ R (cm)
1 ● clay 0.0048 3.25
2 ■ clay 0.0048 4.55
3 ▲ polyurethane 0.0010 3.75
4 × polyurethane 0.0018 3.75
theoretical curve
t = time (sec)
$\tau = \left(\frac{\alpha t}{R^2}\right)$ R = radius (cm)
α = thermal diffusivity $(\frac{cm^2}{sec})$

FIGURE 2

TRANSIENT HEAT TRANSFER DATA FOR FIXED SPHERE AND FOR ROTATING SPHERE

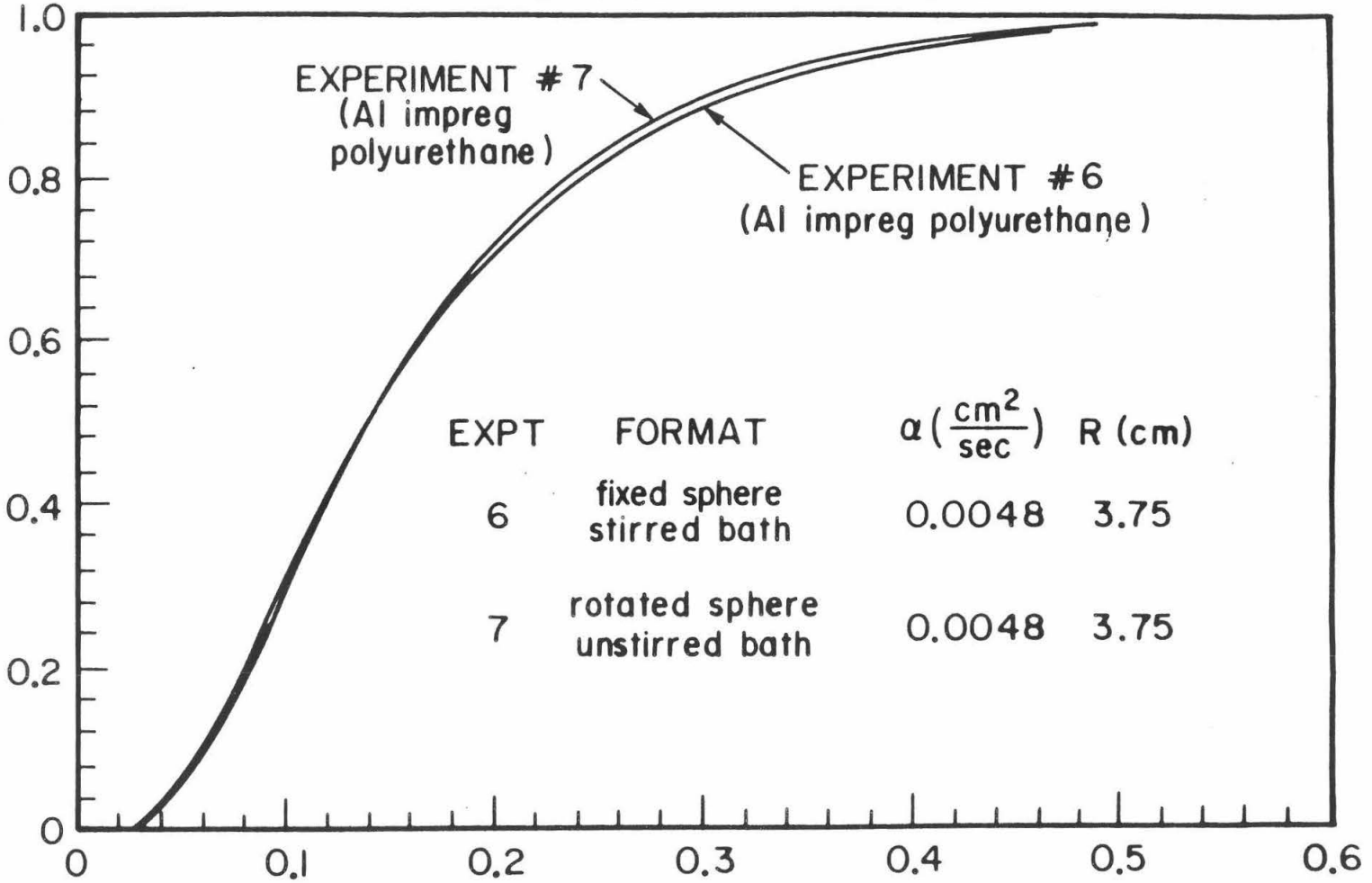

t = time (sec)

$\tau=\left(\frac{\alpha t}{R^2}\right)$ R = radius (cm)

α = thermal diffusivity $\left(\frac{cm^2}{sec}\right)$

FIGURE 3

TRANSIENT HEAT TRANSFER DATA FOR FIXED SPHERE AND FOR FREELY MOVING SPHERE

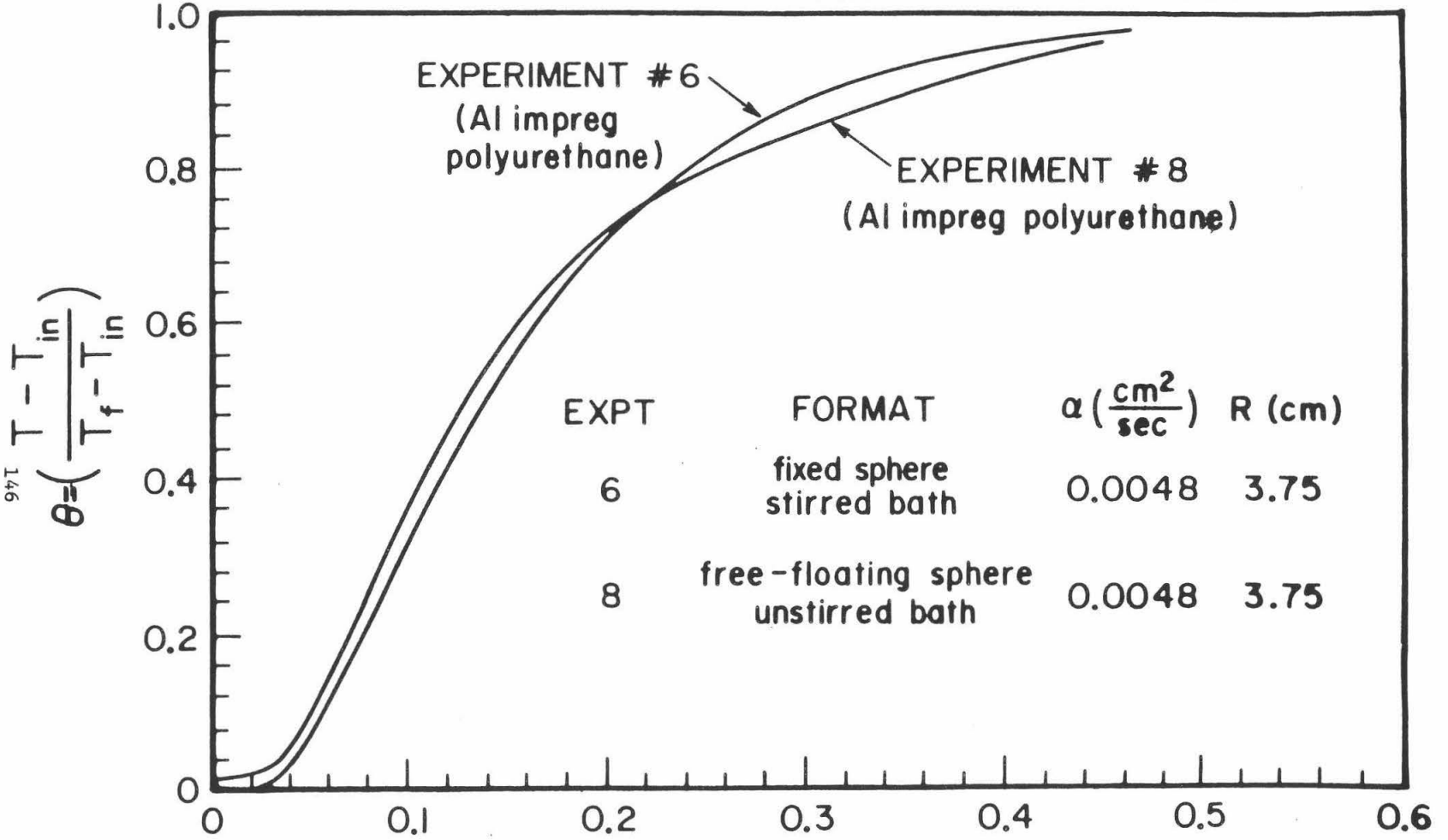

t = time (sec)

$\tau = \left(\frac{\alpha t}{R^2}\right)$ R = radius (cm)

α = thermal diffusivity $\left(\frac{cm^2}{sec}\right)$

FIGURE 4

Designing the Azurin Gene
and
Site-Saturation as a Useful Method
in the Study of Proteins

Mingjim Wu

September 14, 1984

Faculty Sponsor: John H. Richards

California Institute of Technology

Introduction/Abstract

I describe the designing of the gene for the blue-copper protein Azurin. With the use of a Hewlett-Packard data-processor, many desired features such as internal restriction sites for further changes and preferred codons to facilitate translation of the protein are included in the design of the gene. The synthesis of the gene is to be completed in five incorporation "steps" into a plasmid vector. In each "step", oligonucleotides will be synthesized on a machine. These oligonucleotides will be annealed together and inserted into an appropriate vector. The five "steps" are necessary in order to have a satisfactory yield of oligonucleotides from the synthesizing machine.

I also describe a technique by which the codon for the active-site Threonine-71 of pBR322 β-lactamase is replaced by a random selection of codons that code for all the amino acids. By oligonucleotide-directed mutagenesis[1], two specific changes are made in the wild type pBR322. These mutations make it possible to cut out a small segment of the β-lactamase gene that includes the active site. This segment is replaced by synthetic double-stranded oligonucleotides. The synthetic oligonucleotides replace the Thr-71 codon with 32 possible codons that code for all 20 amino acids. Then by sequencing the colonies that grow on ampicillin plates, it can be determined which amino acids in the 71-site produce active β-lactamase.

Designing the Azurin Gene

Azurin is a protein that participates in electron-transfer activity. It is found in the bacteria Pseudomonas aeruginosa. Its three-dimensional structure and functional properties have been determined.[2,3] Its relatively small size and important functions make it an ideal subject for studies of structure:function relationships.

The first step toward learning about these relationships is to design a gene for azurin that can be modified later so that the effects of structural change can be studied. Azurin is composed of 129 amino acids which requires 387 bases to code for it.

The general strategy for making the azurin gene is to insert synthetic strands of DNA into a vector, pBR322. The DNA can then be amplified by cloning the modified vector in a host, E. coli. The inserted sequence will be include internal restriction sites for further manipulations or additions of other synthetic strands. Due to the limited yield of the oligonucleotide-synthesizing machine, it is not possible to synthesize the entire sequence of 387 bases all at one time. Therefore, the sequence is divided into five synthesis "steps". These five "steps" are expected to have fairly successful yields.

The sequence and the five "steps" are designed to facilitate the planned synthesis and the expression of the azurin gene. Whenever possible, the preferred codons of E. coli is used for each amino acid. Some changes, however, are required in order to introduce restriction sites and to reduce the occurrence of homologous sequences. The restriction sites are necessary

in order to add additional strands of DNA. As mentioned above, the gene will be synthesized in five "steps". Each "step" requires the insertion of a segment of the gene into the vector. This segment will comprise of the two ends of the gene. Restriction sites are incorporated into the segment. These sites can be opened to allow another segment of the gene to be inserted. The restriction sites to be used are unique to the vector pBR322 and to the gene itself. This is to insure that no random insertions will occur. Therefore, by building the gene from the two ends and adding more strands toward the middle, the gene should be synthesized in five "steps". These five "steps" are shown in more detail in the Appendix.

Site-Saturation of β-Lactamase

The β-lactamase protein of pBR322 is an enzyme that inactivates many antibiotics such as penicillins by opening the β-lactam rings of the antibiotics. Its amino acid and DNA sequence have been determined.[4,5] Studies are currently under way to determine the structure of the enzyme. It has been found that Serine-70 and Threonine-71 among others comprise the active site of β-lactamase. By changing these amino acids, the effect on the enzymes's activity can be measured and studied. Various mutations of the 70- and 71-active sites have been done.[6] Up to this date, by using oligonucleotide-directed mutagenesis, all the mutations have either reduced activity or no activity.

In this work, the procedure of site-saturation is described. It is designed to be more efficient and less time-consuming that single oligonucleotide-directed mutagenesis. In site-saturation, a small segment of the β-lactamase gene is cut out and removed. In its place, a synthetic segment of double-stranded DNA is inserted. This segment can be synthesized with any changes desired in the sequence.

The Thr-71 site is modified to demonstrate this technique. By using oligonucleotide-directed mutagenesis, two restriction sites, Ava I and Sca I, are made on either side of the active site. The segment between these two sites, 37 bases long, is cut out and removed. A synthetic segment is then inserted in its place. This segment replaces the Thr-71 codon (ACT) with 32 possible codons that code for all 20 amino acids. When synthesized, the bases Adenine and Cytosine of the Threonine codon are randomly replaced by all the bases: Adenine, Cytosine, Guanine, and Thymine. The base Thymine in the Threonine codon is randomly replaced by the bases Guanine or Cytosine. Therefore, in place of Threonine at the 71-site, any of the 20 amino acids will be in the 71-site with specific frequencies depending on their codon degeneracies. (See Appendix).

The synthetic strands are purified by acrylamide electrophoresis. The strands are then run through a NACS Prepac DNA purification convertible following the packaged instructions. The two purified strands are cold-kinased and annealed together.

The vector pBR322 also has to be prepared and purified. The two new restriction sites made by oligonucleotide-directed mutagenesis are not unique to pBR322. The wild type Ava I and Sca I sites have to be destroyed. The wild type Sca I site is destroyed by oligonucleotide-directed mutagenesis. In this method, a small synthetic oligonucleotide probe with a single base mismatch is used to initiate DNA replication. After replication, two homoduplexes will be present. One duplex will have the wild type DNA sequence.

The other duplex will have the wild type DNA sequence with a single base mismatch. Screening colonies with the ^{32}P-labeled synthetic probe allows detection of the desired mutant. The base mismatch is located in the Sca I recognition sequence; therefore, the Sca I site is destroyed.

The wild type Ava I site, however, is to be destroyed by cutting with Ava I and then filling in the sticky ends with DNA Polymerase I. The blunt ends would then be ligated together with T4 Ligase. By filling in the sticky ends of the Ava I digest, the Ava I site will be destroyed. The blunt-end ligation, however, did not succeed. Therefore, in order to remove the Ava I site, the vector without the wild type Sca I site is digested with Sca I. The linear double-strand is purified by 1.2% agarose gel electrophoresis. It is then partially digested with Ava I. The linear piece that is closest in length to linear wild type pBR322 is purified by agarose gel electrophoresis. This piece is desired because it is the vector pBR322 minus the 37 bases between the new Ava I and new Sca I sites. (See Appendix).

The purified double-stranded segment is inserted into the prepared vector with T4 Ligase. The modified pBR322 is transformed into LS1 cells and grown on both ampicillin and tetracycline plates using the non-freezing method of transformation as described in Hanahan's article.[7] The colonies that grow on the ampicillin plates are amplified and will be sequenced to determine which amino acids in the active site-71 produce active β-lactamase.

Discussion

A description of the design of the blue-copper protein Azurin gene has been presented. Many features that are helpful in later studies can be incorporated into the sequence of the gene. Restriction sites for further manipulations, preferred codons of the host, non-homologous sequences, and variable synthesis "step" procedures are just a few of these features. With the development of better techniques and more advanced methods of chemically-cynthesizing oligonucleotided, larger proteins and their genes are now possible to be made more efficiently.

A procedure has also been described by which the active site Thr-71 of pBR322 β-lactamse has been mutated. In place of the Threonine at the 71-site, it is possible to saturate the site with any of the 20 amino acids. The mutated pBR322 is then transformed and grown on ampicillin plates to determine β-lactamase activity. The colonies that are present in the ampicillin plate vary in size depending on the activity of β-lactamase resulting from the amino acid at the 71-site.

The method of site-saturation can be used at almost any site. Using restriction enzymes, small segments of DNA can be removed at specific sites. These segments are then replaced by chemically synthesized sequences. The advantage to this technique is that a large group of amino acids can be tested and studied at a single site or at more that one sites all at once instead of making single muatations for each amino acid at each iste. This technique is advantageous for making general studies about a protein and its activity.

Appendix

Azurin Gene

```
GAA TTC ATG GCA GAA TGC TCT GTA GAC ATC CAG GGT AAT GAT CAG ATG CAG TTC AAC
CTT AAG TAC CGT CTT ACG AGA CAT CTG TAG GTC CCA TTA CTA GTC TAC GTC AAG TTG

ACT AAC GCA ATC ACT GTC GAC AAA TCT TGT AAA CAG TTC ACT GTT AAC CTG TCC CAC
TGA TTG CGT TAG TGA CAG CTG TTT AGA ACA TTT GTC AAG TGA CAA TTG GAC AGG GTG

CCA GGT AAC CTG CCG AAA AAC GTT ATG GGT CAC AAC TGG GTT CTG TCT ACC GCG GCA
GGT CCA TTG GAC GGC TTT TTG CAA TAC CCA GTG TTG ACC CAA GAC AGA TGG CGC CGT

GAC ATG CAG GGT GTT GTT ACT GAC GGT ATG GCC AGT GGT CTA GAC AAA GAC TAC CTG
CTG TAC GTC CCA CAA CAA TGA CTG CCA TAC CGG TCA CCA GAT CTG TTT CTG ATG GAC

AAA CCG GAC GAC TCA CGC GTT ATC GCA CAC ACT AAA CTG ATC GGA TCC GGT GAA AAA
TTT GGC CTG CTG AGT GCG CAA TAG CGT GTG TGA TTT GAC TAG CCT AGG CCA CTT TTT

GAC TCT GTT ACT TTC GAC GTT TCT AAG CTT AAA GAA GGT GAA CAG TAC ATG TTC TTC
CTG AGA CAA TGA AAG CTG CAA AGA TTC GAA TTT CTT CCA CTT GTG ATG TAC AAG AAG

TGC ACT TTC CCA GGT CAC AGC GCG CTG ATG AAA GGT ACC CTG ACC CTG AAA TAA CTC
ACG TGA AAG GGT CCA GTG TCG CGC GAC TAC TTT CCA TGG GAC TGG GAC TTT ATT GAG

GAG
CTC
```

P. aeruginosa Azurin

Ala Glu Cys Ser Val Asp Ile Gln Gly Asn Asp Gln Met Gln Phe Asn Thr Asn Ala

Ile Thr Val Asp Lys Ser Cys Lys Gln Phe Thr Val Asn Leu Ser His Pro Gly Asn

Leu Pro Lys Asn Val Met Gly His Asn Trp Val Leu Ser Thr Ala Ala Asp Met Gln

Gly Val Val Thr Asp Gly Met Ala Ser Gly Leu Asp Lys Asp Tyr Leu Lys Pro Asp

Asp Ser Arg Val Ile Ala His Thr Lys Leu Ile Gly Ser Gly Glu Lys Asp Ser Val

Thr Phe Asp Val Ser Lys Leu Lys Glu Gly Glu Gln Tyr Met Phe Phe Cys Thr Phe

Pro Gly His Ser Ala Leu Met Lys Gly Thr Leu Thr Leu Lys

Synthesis Steps for the Azurin Gene

I.

```
GAA TTC ATG GCA GAA TGC TCT GTA GAC ATC CAG GGT AAT GAT CAG
      G TAC CGT CTT ACG AGA CAT CTG TAG GTC CCA TTA CTA GTC
EcoRI  Init.                                        Bcl I

   AGC GCG CTG ATG AAA GGT ACC CTG ACC CTG AAA TAA C
   TCG CGC GAC TAC TTT CCA TGG GAC TGG GAC TTT ATT GAG CTC
    BssH II             Kpn I                 Term.  Ava I
```

II.

```
GAT CAG ATG CAG TTC AAC ACT AAC GCA ATC ACT GTC GAC
     TC TAC GTC AAG TTG TGA TTG CGT TAG TGA CAG CTG
  Bcl I                                     Sal I

   AAG CTT AAA GAA GGT GAA CAG TAC ATG TTC TTC TGC ACT TTC CCA GGT CAC AG
   TTC GAA TTT CTT CCA CTT GTC ATG TAC AAG AAG ACG TGA AAG GGT CCA GTG TCG CGC
   Hind III                                                          BssH II
```

III.

```
TC GAC AAA TCT TGT AAA CAG TTC ACT GTT AAC CTG TCC CAC CCA GGT AAC C
     G TTT AGA ACA TTT GTC AAG TGA CAA TTG GAC AGG GTG GGT CCA TTG G
Sal I                                                   BstE II

   GGA TCC GGT GAA AAA GAC TCT GTT ACT TTC GAC GTT TCT A
   CCT AGG CCA CTT TTT CTG AGA CAA TGA AAG CTG CAA AGA TTC GA
   BamH I                                              Hind III
```

IV.

```
GT AAC CTG CCG AAA AAC GTT ATG GGT CAC AAC TGG GTT CTG TCT ACC GCG G
     G GAC GGC TTT TTG CAA TAC CCA GTG TTG ACC CAA GAC AGA TGG CGC C
BstE II                                                    Sac II

   A CGC GTT ATC GCA CAC ACT AAA CTG ATC G
   T GCG CAA TAG CGT GTG TGA TTT GAC TAG CCT AG
   Mlu I                               BamH I
```

V.

```
     G GCA GAC ATG CAG GGT GTT GTT ACT GAC GGT ATG GCC AGT GGT CTA GAC
   CGC CGT CTG TAC GTC CCA CAA CAA TGA CTG CCA TAC CGG TCA CCA GAT CTG
   Sac II                                                    Xba I

   AAA GAC TAC CTG AAA CCG GAC GAC TCA
   TTT CTG ATG GAC TTT GGC CTG CTG AGT GCG C
                                     Mlu I
```

Codons with G or C end:

Codon	A.A.	Codon	A.A.	Codon	A.A.	Codon	A.A.
TTC	Phe	TCC	Ser	TAC	Tyr	TGC	Cys
TTG	Leu	TCG	Ser	TAG	Term.	TGG	Trp
CTC	Leu	CCC	Pro	CAC	His	CGC	Arg
CTG	Leu	CCG	Pro	CAG	Gln	CGG	Arg
ATC	Ile	ACC	Thr	AAC	Asn	AGC	Ser
ATG	Met	ACG	Thr	AAG	Lys	AGG	Arg
GTC	Val	GCC	Ala	GAC	Asp	GGC	Gly
GTG	Val	GCG	Ala	GAG	Glu	GGG	Gly

Amino Acid	Codon	Rel. Freq.
Term - 1	TAG	3.125%
Ala - 2	GCC, GCG	6.25%
Arg - 3	CGC, CGG, AGG	9.375%
Asn - 1	AAC	3.125%
Asp - 1	GAC	3.125%
Cys - 1	TGC	3.125%
Gln - 1	CAG	3.125%
Glu - 1	GAG	3.125%
Gly - 2	GGC, GGG	6.25%
His - 1	CAC	3.125%
Ile - 1	ATC	3.125%
Leu - 3	TTG, CTC, CTG	9.375%
Lys - 1	AAG	3.125%
Met - 1	ATG	3.125%
Phe - 1	TTC	3.125%
Pro - 2	CCC, CCG	6.25%
Ser - 3	TCC, TCG, AGC	9.375%
Thr - 2	ACC, ACG	6.25%
Trp - 1	TGG	3.125%
Tyr - 1	TAC	3.125%
Val - 2	GTC, GTG	6.25%

Oligonucleotide-directed mutagenesis of Sca I site (Ref. 1)

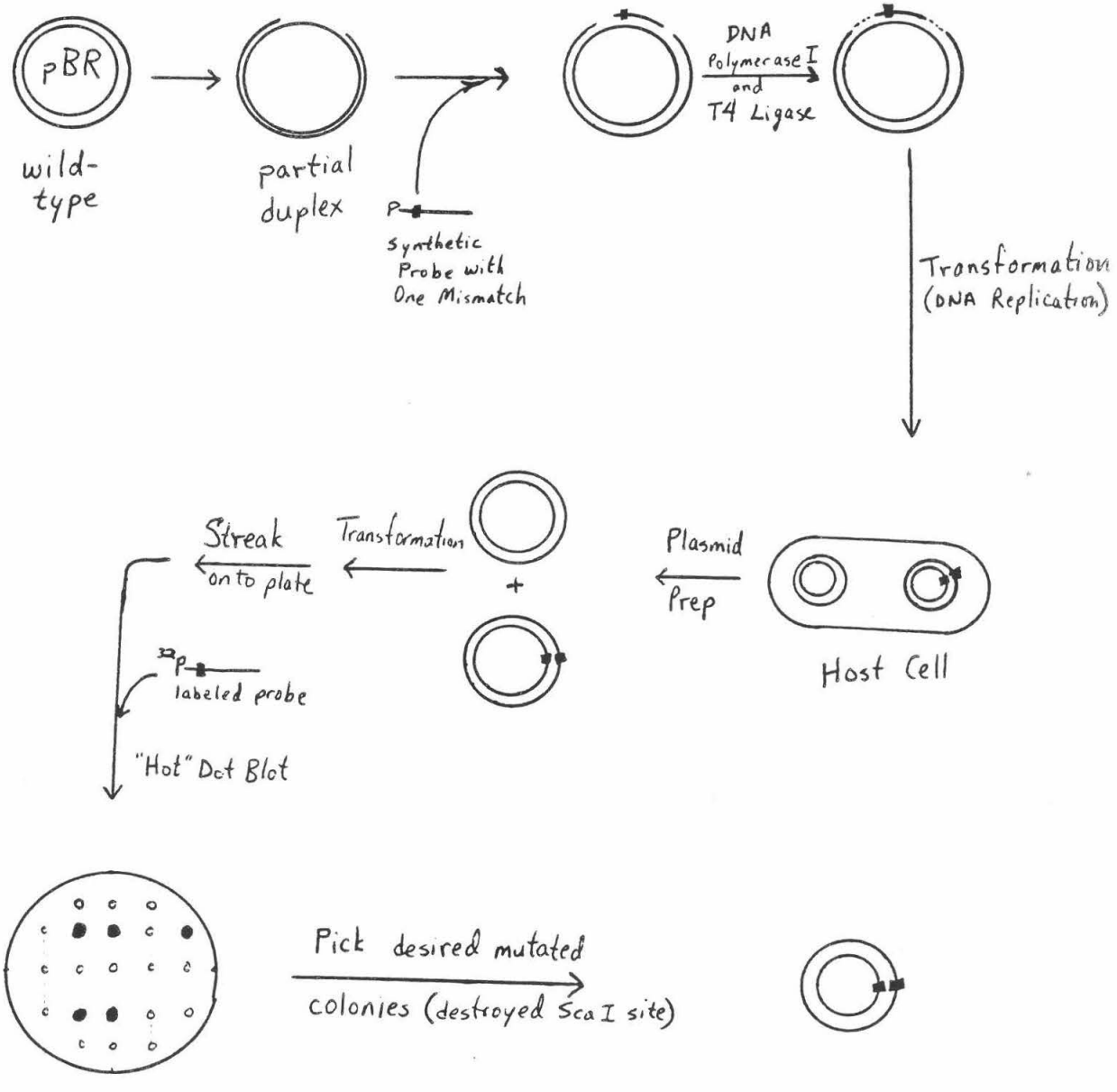

Preparing pBR322 Vector

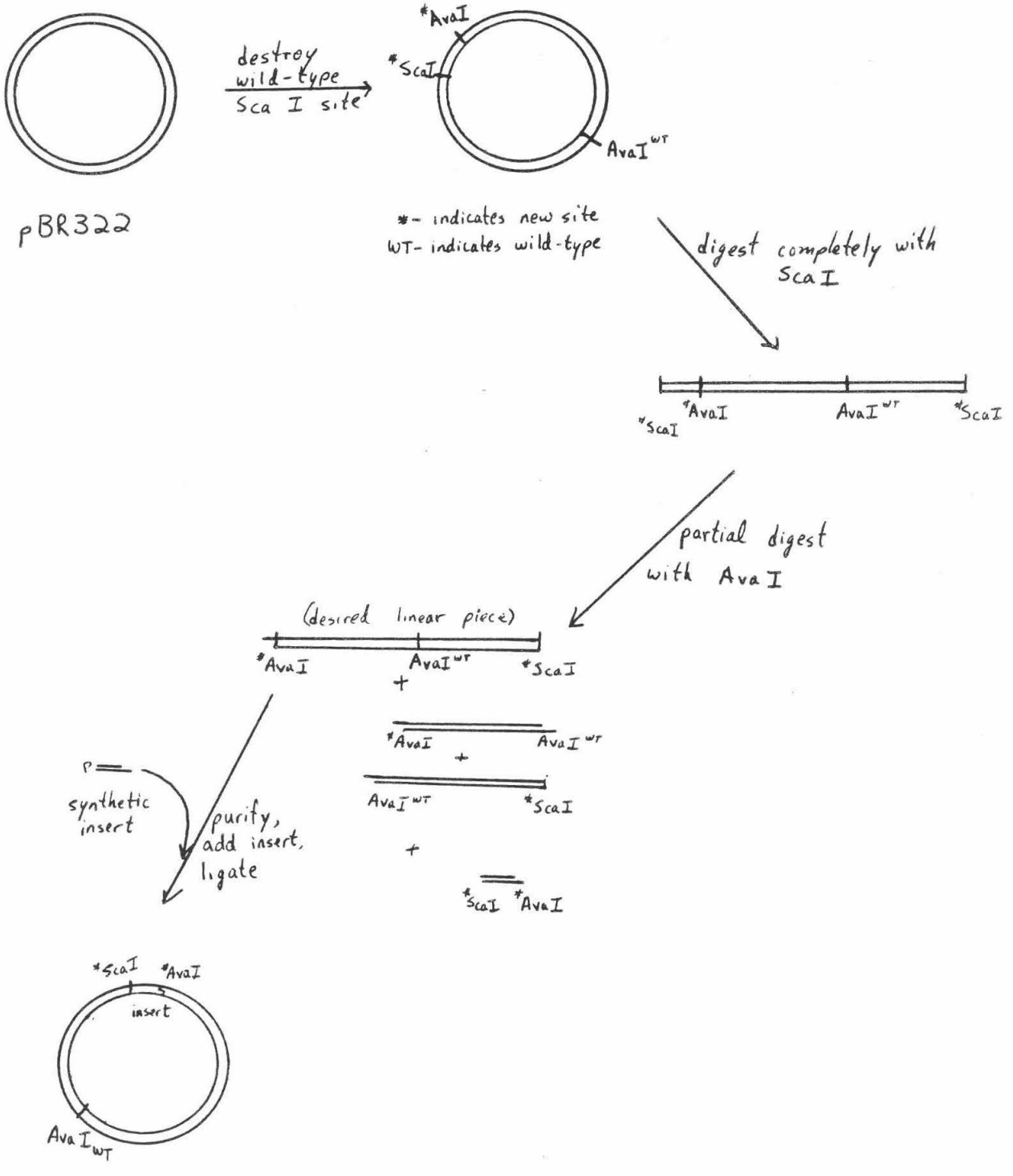

References

1) Dalbadie-McFarland, G., Cohen, L.W., Riggs, A.D., Morin, C., Itakura, K., and Richards, J.H. Oligonucleotide-directed mutagenesis as a general and powerful method for studies of protein function. Proc. Natl. Acad. Sci. USA 79 pp. 6409-6413, 1982.

2) Colman, P.M., Freeman, H.C., Guss, J.M., Murata, M., Norris, V.W., Ramshaw, J.A.M., and Venkatappa, M.P. X-ray crystal structure analysis of plastocyanin at 2.7 A resolution. Nature 272 pp. 319-324, 1978.

3) Clothia, C. and Lesk, A.M. Evolution of proteins formed by -sheets I. Plastocyanin and azurin. J. Mol. Biol. 160 pp. 309-323, 1982.

4) Sutcliffe, J. Gregor. Nucleotide sequence of the ampicillin resistance gene of Escherichia coli plasmid pBR322. Proc. Natl. Acad. Sci. USA 75 pp. 3737-3741, 1978.

5) Ambler, R.P. The structure of β-lactamases. Phil. Tran. R. Soc. Lond. B289 pp. 321-331, 1980.

6) Sigal, Irving S., Harwood, Betty G., and Arentzen, Rene. Thio-β-lactamase: Replacement of the active-site serine of RTEM β-lactamase by a cysteine residue. Proc. Natl. Acad. Sci. USA 79 pp. 7157-7160, 1982.

7) Hanahan, Douglas. Studies on Transformation of Escherichia coli with Plasmids. J. Mol. Biol. 166 pp. 557-580, 1983.

Development of Hardware and Software to Permit an Inexpensive Computer to be Used as a Storage Oscilloscope

by

Craig Zupke
(Sponsor: Dr. Fred Shair)

ABSTRACT

An inexpensive computer-oscilloscope converter was designed, constructed, and tested to permit the Commodore-64 computer to be used as a storage oscilloscope. Software was developed for data acquisition, manipulation, and presentation. Preliminary experiments were conducted to demonstrate the usefulness and flexibility of the system.

INTRODUCTION

As high school administrators became sensitized to budget constraints, the first casualities were generally the science laboratories. A survey by Schlessinger (1973) indicated that the amount of money spent for supplies and equipment is usually between $1 to $3 per student year. Some classes have only demonstration experiments conducted by the teacher. Inquires into this situation are often countered by the statement that "the theory can still be taught".

The future impact of such a response may not be favorable in view of the fact that many of our leading scientists and engineers decided to pursue their fields after becoming acquainted with the mystery and beauty of nature through their own "hands on" experimentation. That is, science is basically experimental, and experimentation plays an important role in the development of science and engineering, as well as in the development of scientists and engineers. As the flow of money to high schools has increased during the last few years, computers and associated equipment have been purchased; however, the laboratories of science often continue to decline. There has been a great deal of concern regarding "computer literacy"; but, "schools seem to have decided that the best use of computers is to teach students about computers" (Hassett, 1984).

Another approach, which may be much more fruitful in the long run, is to use the computer in order to better focus upon experimental science. Much may be gained by developing the computer into a useful tool to help explore nature.

The purpose of this work was to develop the hardware and the software need to use an inexpenive home computer as a storage oscilloscope.

THE STORAGE OSCILLOSCOPE

The storage oscilloscope is an extremely common and useful instrument in laboratories. However, most such instruments cost several thousands of dollars. For example, the TEKTRONIX 468 oscilloscope is a digital oscilloscope with a four-trace, dc-to-100 MHz, vertical deflection system; measurement values are indicated on a four-digit, seven-segment LED display (Tektronix, 1984); this unit costs in excess of $7000. However, many experiments do not require the high speed which makes commercial units so expensive.

HARDWARE

The hardware needed to convert a computer into a storage oscilloscope is mainly an analog-to-digital converter (ADC). The ADC takes an analog voltage from some external source and converts it to a binary number which can be directly read by a digital computer.

For increased flexibility, the ADC should permit multiple inputs selectable by the computer. Also a wide range of input voltages should be permissible. This requires a variable gain amplifier to amplify small signals to an appropriate level. The lowest full scale voltage should be around 10 millivolts; then, a variety of common sensors, such as thermocouples, pressure transducers, and photoelectric diodes can be used. The actual ADC should be a readily available integrated circuit, fast enough not to be the limiting step in the collection of data. The entire unit should interface through an 8-bit parallel port with two handshake lines. This type of input/output is a simple and common feature of many computers. Finally of prime importance is the desire to make the entire system relatively inexpensive. To make a significant impact upon education, the cost of such a unit must be low enough to fit high school and home budgets. Currently, there are about 300,000 computers in schools, and about 6,000,000 in homes (Murray, 1984).

THE COMPUTER-OSCILLOSCOPE CONVERTER

As shown in Figure (1), the oscilloscope interface consists of the ADC, the variable gain amplifier, and the computer controlled analog switch. The National Semi Conductor ADC802 chip has a 100 microsecond conversion time. The variable gain amplifier consists of an Texas Instruments LM324 op-amp. An RCA CD4051 mutiplexer was used to switch between 8 analog inputs. The cost of the components, including the power supply and the case, is less than $100.

THE COMPUTER SYSTEM

The Commodore-64 was found to be well suited for this project. This computer is widely available and sells for about $200. Peripheralls for this computer are also inexpensive. Video display can be through an ordinary TV or a higher quality monitor. The disk drive, for storage of programs and data, costs about $250. A suitable printer can also be obtained for about $250. Therefore, the computer system can be purchased for about $700.

The Commodore-64 supports multi-colored texts and high resolution graphics. Thus, information can be displayed with sufficient detail to be useful, and with enough variety to be interesting. The Commodore-64 has an 8-bit parallel port with the required handshaking lines. Finally, the Commodore-64 comes with 64K of RAM which is enough for most applications. Also, it should be noted that the Commodore-64 is currently the most popular inexpensive home computer.

SOFTWARE

Two types of computer programs were developed for use with the ADC.

The first type of programs were general driver routines which switch input channels, read the ADC, plot bar graphs, and plot graphs of voltage vs. tiime. These programs were written in assembly language to increase their speed of execution.

The second type was a program which can be used in transient experiments involving the measurement of "characteristic times". This was written in BASIC for flexibility and ease of programming.

THE COMMODORE-64 STORAGE OSCILLOSCOPE SYSTEM

The hardware and software, developed during this project, permit the Commodore-64 to be used as a digital storage oscilloscope with 8 traces capable of following millivolt signals at frequencies up to 100 Hz. The total cost of the system components is less than $800.

PRELIMINARY RESULTS

The measurement of the response time of a thermocouple was chosen as the first experiment. From the governing differential equations, the characteristic time of a particular thermocouple was estimated to be approximately 1 second. This estimate was in good agreement with the measured value of 0.8 seconds.

CONCLUSIONS

(1) A computer-oscilloscope converter was designed, constructed, and tested; the components of this unit cost less than $100.

(2) Software was developed for data acquisition, manipulation, and presentation.

(3) Preliminary experiments were conducted to demonstrate the usefulness and flexibility of the computer-oscilloscope system.

RECOMMENDATIONS

A variety of experiments should be developed which demonstrate basic concepts of science. Some experiments might involve using the computer as a stopwatch, as a voltmeter, etc. Sensors, suitable for this system, should be tested in order to expand the types of experiments which can be developed. Local science teachers should be encouraged to use this system and to provide recommendations.

ACKNOWLEDGEMENTS

I would like to thank Said Jackson, James Mitchell, Dr. Hardy Martel, Dr. Bruce Murray, and Dr. Fred Shair for their invaluable help with various aspects of this project.

REFERENCES

(1) Schlessinger, F.R., Howe, R.W., White, A.L., Chin, L.F., Baker , J.H., and Buckeridge, E.C. "A Survey of Science Teaching in Public Schools of the United States--Columbus Ohio: The Ohio State University, (1973).

(2) Hassett, James "Computers in the Classroom", Psychology Today, p.22-28, September, (1984).

(3) Tektronix 468 Digital Storage Oscilloscope Instruction Manual; Tektronix, Inc. P.O. Box 500. Beaverton, Oregon 97077, (1984).

(4) Murray, Bruce; personal communication, Pasadena, California (August, 1984).

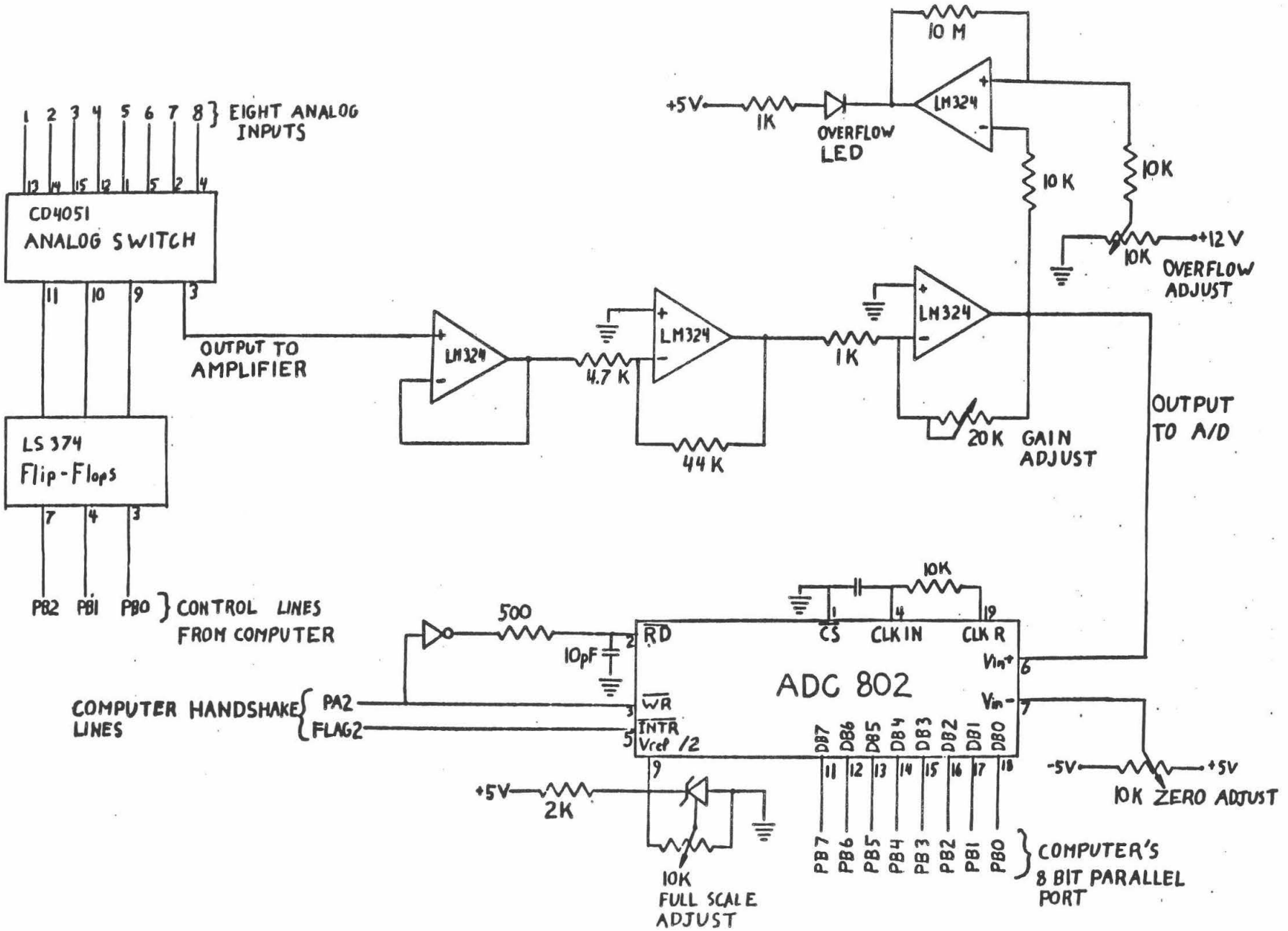
1 2 3 4 5 6 7 8 } EIGHT ANALOG INPUTS
CD4051
ANALOG SWITCH
LS 374
Flip-Flops
PB2 PB1 PB0 } CONTROL LINES FROM COMPUTER
OUTPUT TO AMPLIFIER
LM324
4.7 K
44 K
1K
10 M
+5V
1K
OVERFLOW LED
10K
10 K
+12 V
OVERFLOW ADJUST
20K GAIN ADJUST
OUTPUT TO A/D
500
10pF
RD
WR
INTR
Vref /2
CS
CLK IN
CLK R
Vin+
Vin-
ADC 802
DB7 DB6 DB5 DB4 DB3 DB2 DB1 DB0
COMPUTER HANDSHAKE LINES
PA2
FLAG2
+5V
2K
10K FULL SCALE ADJUST
-5V
+5V
10K ZERO ADJUST
PB7 PB6 PB5 PB4 PB3 PB2 PB1 PB0 } COMPUTER'S 8 BIT PARALLEL PORT

fig. 1

Engineering and Applied Science

A NEW CONCEPT FOR THE PASSIVE AND ACTIVE CONTROL OF TURBULENT SHEAR FLOWS

By

Manuel Acevedo-Ruiz

September, 1984

California Institute of Technology
Pasadena, California 91125

ACKNOWLEDGEMENTS

This report presents the result of one phase of research carried out under the sponsorship of a Caltech-Surf award.

I wish to express my gratitude to the members of the Experimental Fluid Dynamics group at the Jet Propulsion Laboratory, California Institute of Technology, for their invaluable technical support, especially to Dr. M. Gharib and Dr. M. A. Hernan for their help and guidance throughout the whole project. I also thank Prof. Roshko for his advice and understanding.

ABSTRACT

An experimental set-up to produce a turbulent shear layer has been designed and built. A relevant feature of this facility is that it is very adequated for flow visualization studies. Laser induced fluorescence techniques have been used in order to visualize and photograph different flow field patterns. Furthermore, the facility has been used to explore a new concept in controlling entrainment and mixing of fluids. The concept is based on the use of an impinging plate located downstream on the fully developed turbulence region. Both kinds of control have been analyzed: passive, based on the feedback introduced by the vortical structures impinging the plate, and active, based on forcing oscillations upon that plate. Remarkable results, showing the ability of this technique in preventing or enhancing the mixing, are presented.

INTRODUCTION

The original purpose of this project was to examine and characterize the vortical structures of a turbulent shear layer and to find some correlation between secondary and the well-known primary structures. We found that to get a clear shear layer was no trivial matter. Most of the ten weeks were spent on the construction of our shear-layer generating facility and in the selection of a flow visualization technique. By the end, we had a sharp, well-defined mixing layer that was easy to see. Then we tried to control mixing by forcing oscillations downstream, and we observed remarkable results (see Fig. 1). Thus, this summer project has accomplished obtaining a good shear-layer facility, and to open the way for further study in several areas.

EXPERIMENTAL DESCRIPTIONS

Work was done at JPL with Section 345, and we used a water channel facility recently built by Dr. Gharib during his doctoral studies, on control of cavity flows. This channel produces unusually laminar flow, and the test dimensions were ideal for our purposes. We used Rockwell (1982) as reference in the construction of the shear-layer facility. The basic structure is composed of two plexiglass walls which hold between them a stainless steel splitter plate. Across this plate there is a plexiglass impinging plate that slides in and out of a groove carved into the walls, creating a variable-length gap between these two plates. Underneath this combination, there is another plexiglass plate that acts as a floor for the whole arrangement. Figure 2 shows dimensions from two views. This set-up was easily brought in and out the water channel. All the designing and machining were done by myself in the shop area of the lab.

Underneath the channel, we had a laser arrangement. We used a 3-watt Argon-Ion laser, with a surface mirror and a cylindrical mirror to spread out the beam into a sheet of light. To visualize the flow, we injected a fluorescent dye which is excited by the particular frequency of the green laser beam emitted. This optical setup was designed to be able to visualize stream as well as span-wise views (see Fig. 3). For the pictures, we used a Nikon F1 camera with a 55mm macro lens, and high-speed film (Kodak 1000 ASA) with high sensitivity to the green region of the spectrum. The vortex pictures were taken with an aperture of 2.8 and film speed of 1/250. The flow velocity pictures had film speed of 1/8 and 1/15.

DYE-INJECTION

The hardest problem we tackled was the dye-injection. We finally obtained a laminar output of dye, whether at one point or across the whole width.

We tried the following dye-injection arrangements before getting the final one:

(a) a 1/8" diameter steel tube across the upstream edge of the splitter plate, with small holes about 1/8" apart from each other and facing the top surface of the plate. Dye came from plastic tubes connected to the metal tube outside of the plastic walls.

(b) a 1/8" diameter plastic tube at the same location as in (a) but having a slit cut out with an exacto knife.

(c) a Pitot-looking tube we would place either on top of the splitter plate at different locations or outside upstream of the shear-layer facility; dye came from a plastic bottle connected to plastic tubing.

(d) a flap placed at the upstream end of the splitter place and the tube in (b) glued at the edge, so that the dye would come out the tube and mix in the space between the flap and plate before finally appearing on the surface of the plate. This system went through a few variations.

(e) an airfoil-shape device, which consisted on two aluminum shims glued to a tube with holes in it such that they would leave a thin slit between them and more glue around the other end to complete the airfoil shape. This was held outside the shear-layer facility which now had a sheet of foam at its entrance to straighten the dye passing through.

(a), (c), and (d) formed jet-like patterns of dye which had their own wakes and irregularities. (b) and (e) put out irregular amounts of dye with turbulent configurations.

Our final dye-injection technique is actually very simple. It consists of a polystyrene bottle with plastic tubing connecting to a thin metal tube, similar to (c).

Dye comes out the metal tube at the locations where the flap ends on the surface of the splitter plate. Since there is a small step at these points, the flow there goes through a tiny separation. Most of the dye injected remains circulating and only a thin streak comes out laminarly and perfectly attached to the splitter plate. We can lay dye and then watch it create the vortical images for about a minute. These are the laminar streaks of dye which allows us to visualize the shear layer so well. The separation at the edge of the flap was the trick we needed.

PROCEDURE AND OPERATION

Water from the channel divides itself into two sides when passing through the shear-layer facility, the top side being the high velocity one. Straws are packed tight between the floor and the splitter plate, producing a decrease in velocity as well as straightening the flow on the bottom side. The ratio of velocity from top to bottom can be controlled by the height of the water in the channel or by placing additional flow resistances on the bottom side. We took our pictures at a flow speed of 18.8 cm/sec on the top side and an approximate ratio $V_1/V_2 = 2.5$.

Initially, we found some separation at the upstream edge of the splitter plate, and solved that by placing flaps at an angle to the spliter plate, and by finding different ways to get rid of the innumerable bubbles formed inside the straws. Once separation was solved, we had flow attached to the plate and a clear, sharp mixing layer. Dye is injected, and a typical high-speed side mixing layer can be observed. The impinging plate was moved to change the gap length. The control effects from this impinging plate are carried upstream. The number and wavelength of vortical structures change with gap length. Impingement was also shown to control the pairing of vortices. We also observed secondary structures when looking at the flow spanwise. The most

interesting effect we found was the forcing on the impinging plate. We saw that we could enhance or prevent mixing depending on the frequency of oscillation. Dye would get sucked into the core of the vortices and by varying the amplitude and frequency of the oscillations we controlled the mixing to see smaller or larger dye configurations. At around 6" pairing starts forming regardless of the impinging edge - at that length the feedback effects start becoming very weak. However, we can also control pairing formation when oscillating the impinging plate. We can observe these effects in the series of pictures depicting the shear layer at dfferent gap lengths, with and without forced oscillation.

SUMMARY AND CONCLUSIONS

Using a flap to adjust the angle of inclination of the incoming edge, we eliminated the problem of separation at the entrance. The small separation existing between the flap and the surface of the splitter plate enabled us to obtain uniform and laminar streaks of dye to visualize the flow. Laser Induced Fluorescence (LIF) techniques were used in this visualization process. The result is a clear, sharp shear layer with extremely well defined vortical structures. The impinging edge creates feedback effects upstream organizing the mixing in coherent manner, controlling the phase of vortical structures. We observed three-dimensionality in the flow when we saw secondary structures across it. We also found that we were able to control the mixing quite effectivly by oscillating the impinging plate, whether it is enhancing or preventing the mixing process.

Further studies seem appropriate after completing this short project. Characterizing the secondary structure and correlating it with the well known primary one is a clear area for extended research. The control of mixing and entrainment by forced oscillations downstream on the impinging plate appears as a very attractive area for further studies with numerous practical applications.

BIBLIOGRAPHY

GHARIB, M. 1983 , Thesis, California Institute of Technology.

HERNAN, M.A. & JIMENEZ, J. 1982, "Computer analysis of a high-speed film of the plane turbulent mixing layer", J.Fluid Mechanics 119, pp.323-345.

HERNAN, M.A. & JIMENEZ, J. 1979, "Digital image analysis in optical flow measurements", Proc. Second Symposium on Turbulent Shear Flows.

ZIADA,S. & ROCKWELL,D. 1982, "Oscillations of an unstable mixing layer impinging upon an edge", J. Fluid Mechanics 124, pp.307-334.

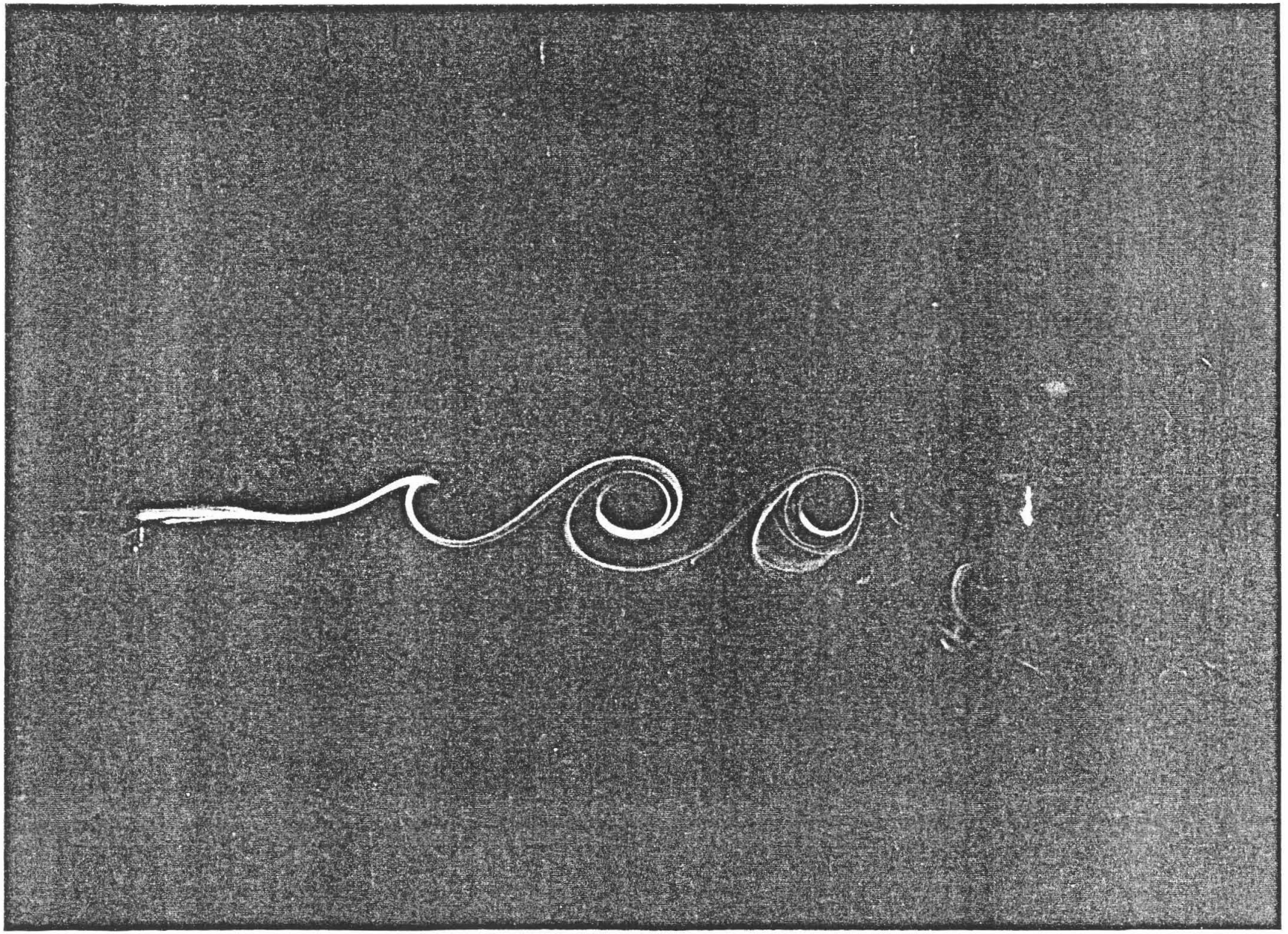

FIG 1a

FIG 16

FIGURE 2

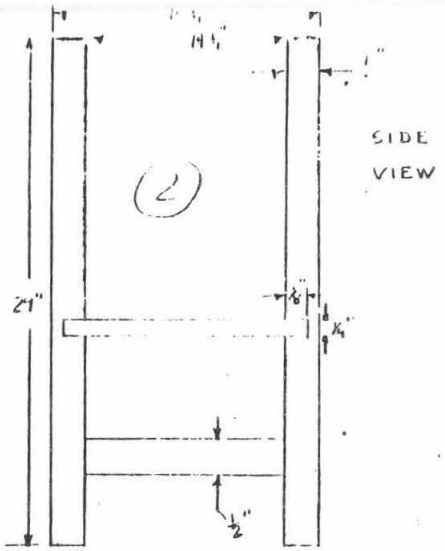

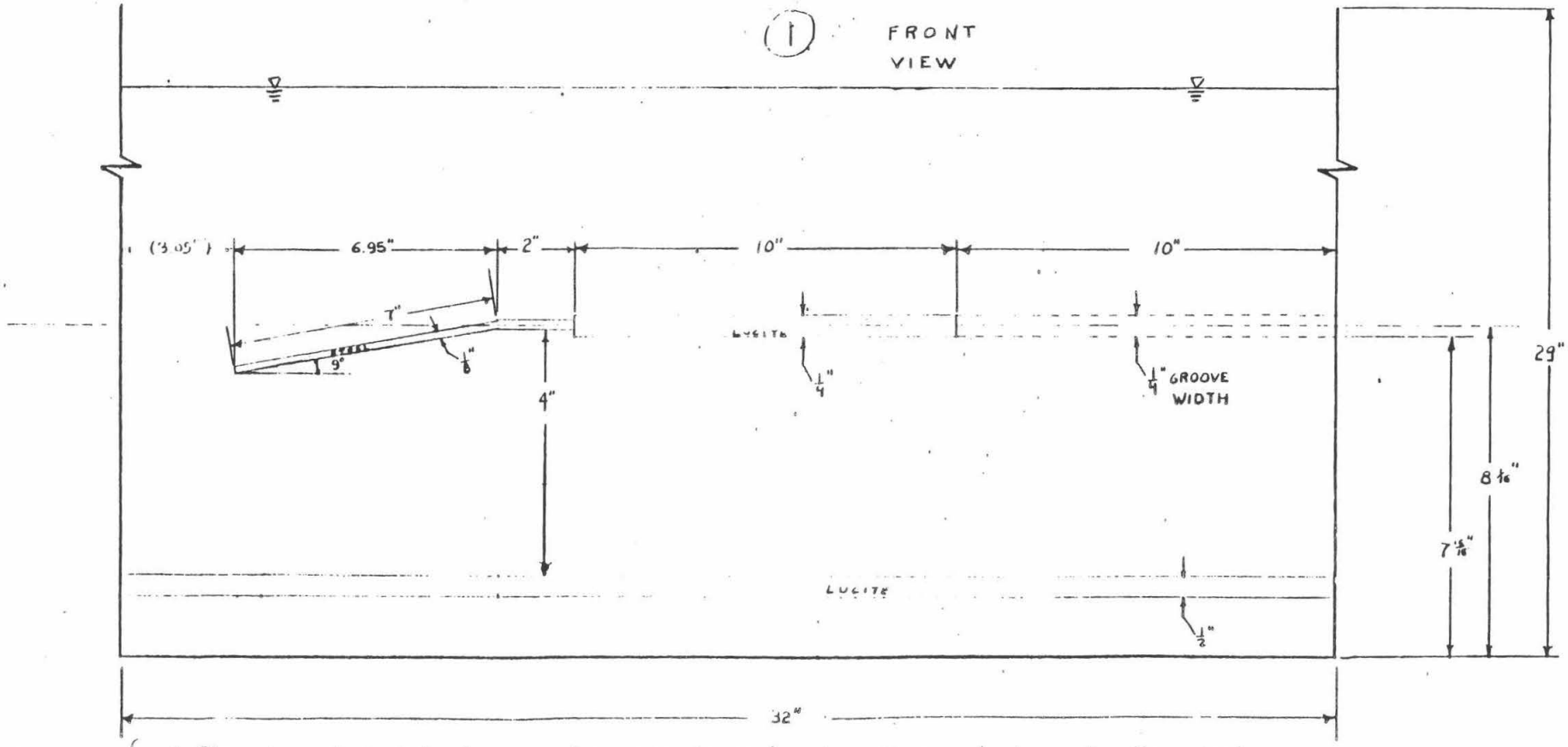

DRAWING 1

1. The outer contours of the box were drawn with heavier lines (numbers are placed inside for clarity
2. Scale is 1:2 unless [illegible]

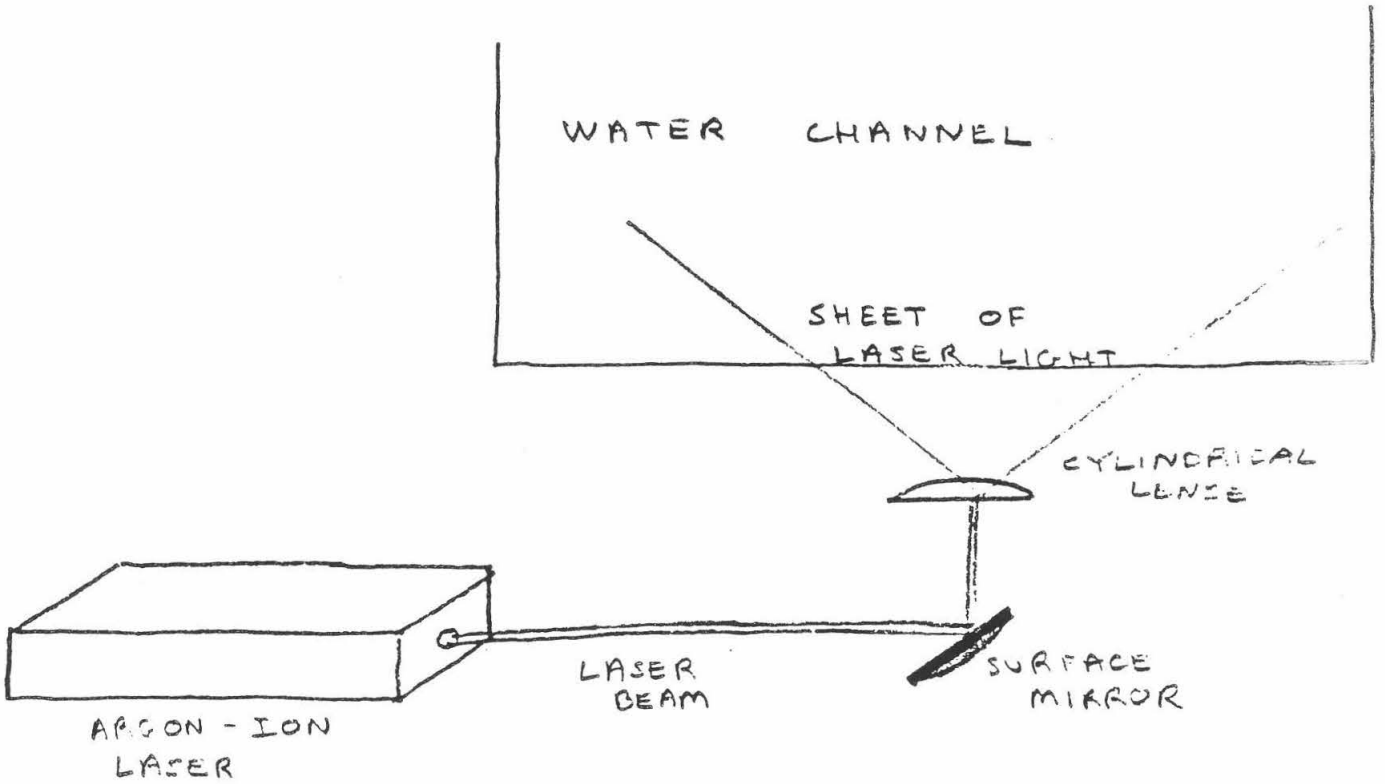

FIGURE 3 OPTICAL SET UP

Pictures of the shear layer at different gap lengths.

On top, the impinging plate oscillates freely.
On bottom, the impinging plate has forced oscillations.

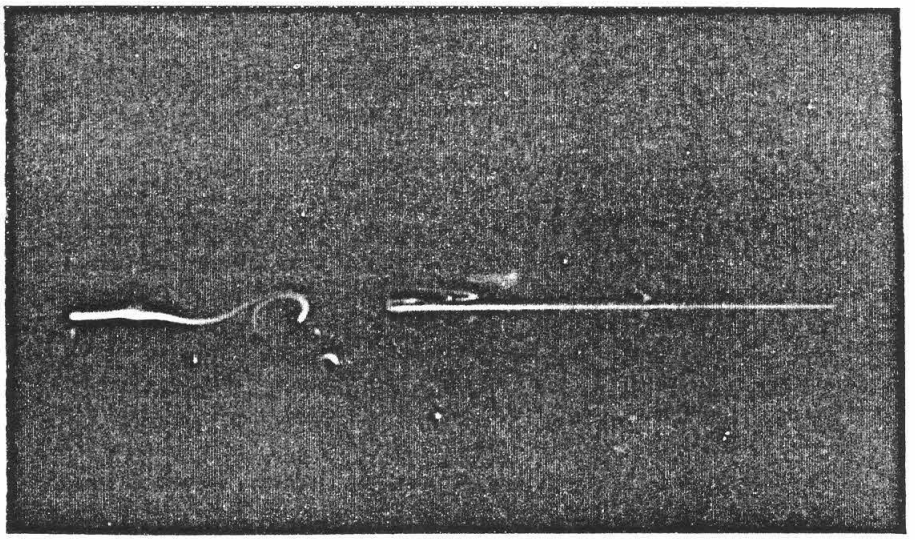

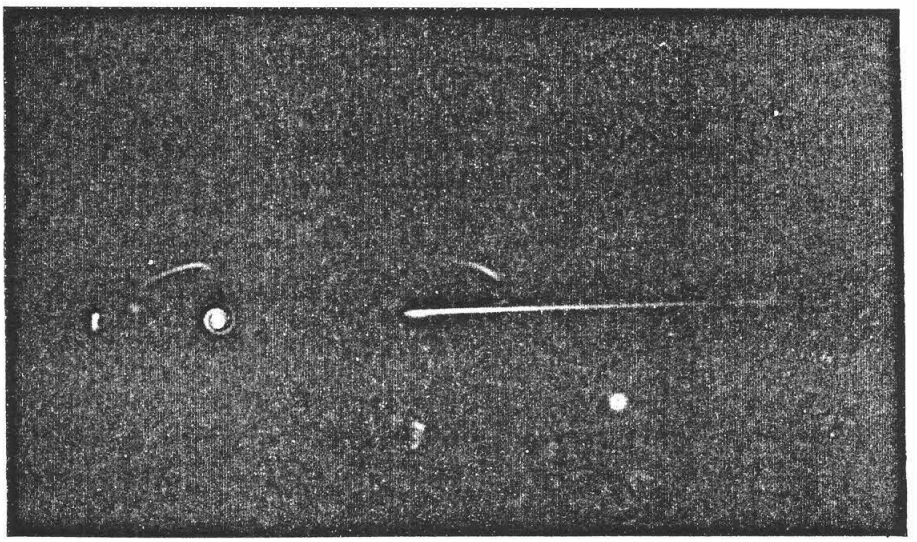

Gap length 1"

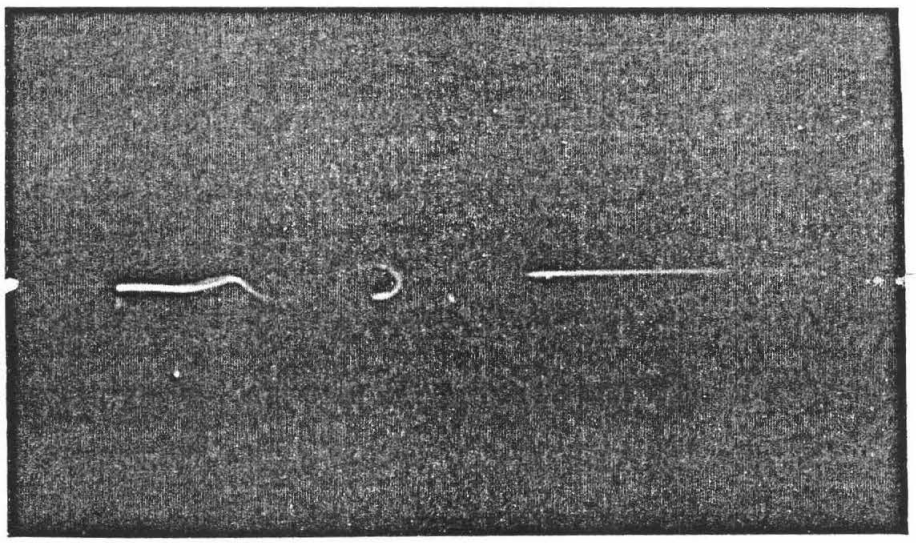

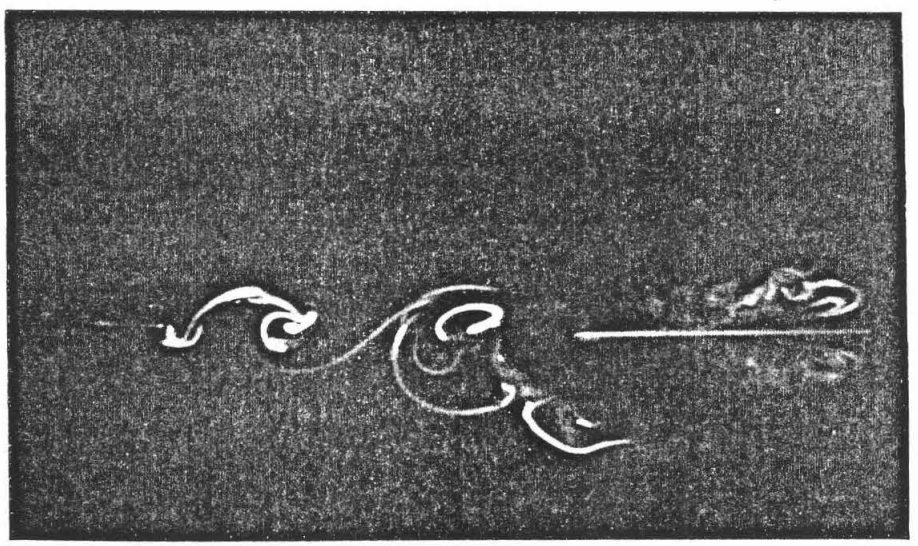

Gap length $2\frac{1}{4}$"

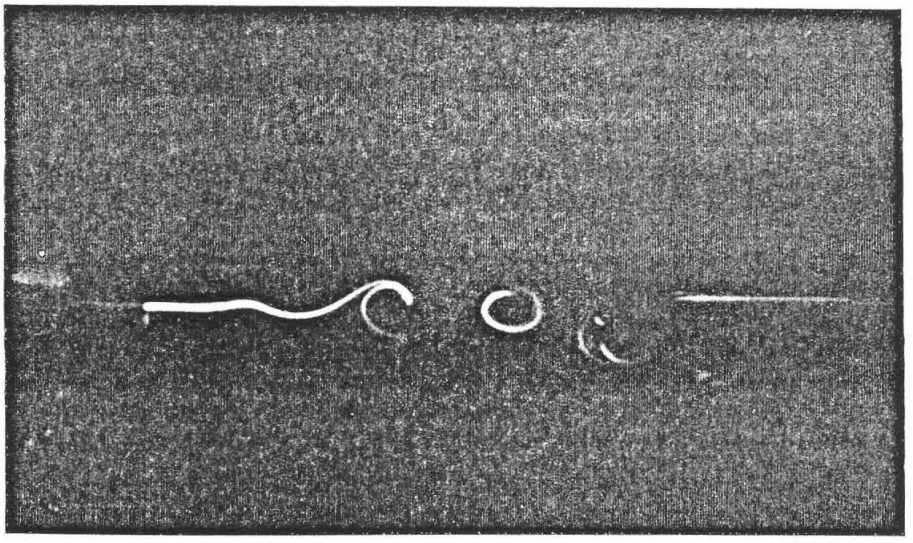

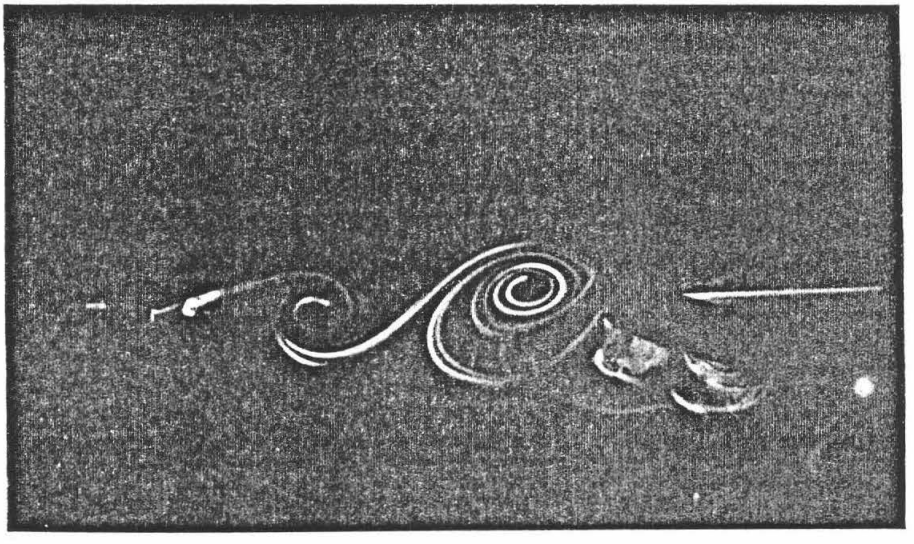

Gap length 4"

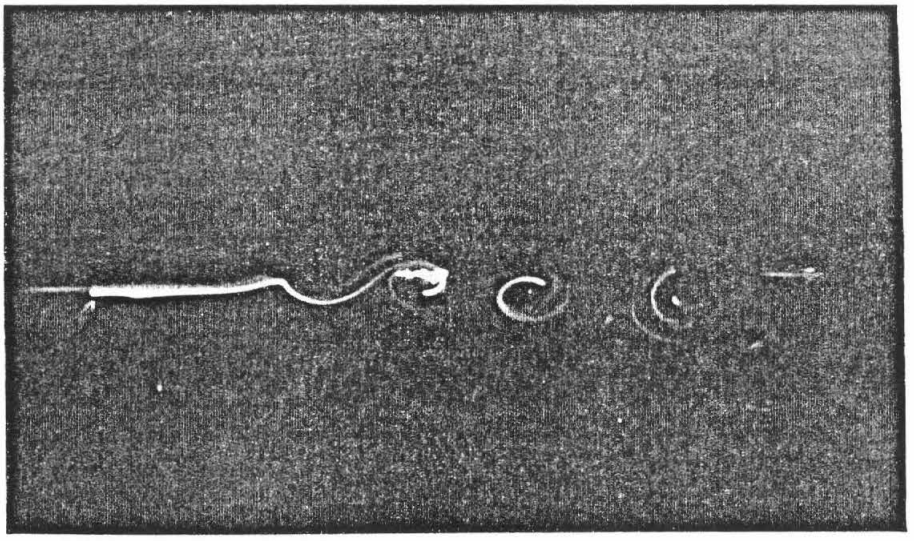

Gap length 5"

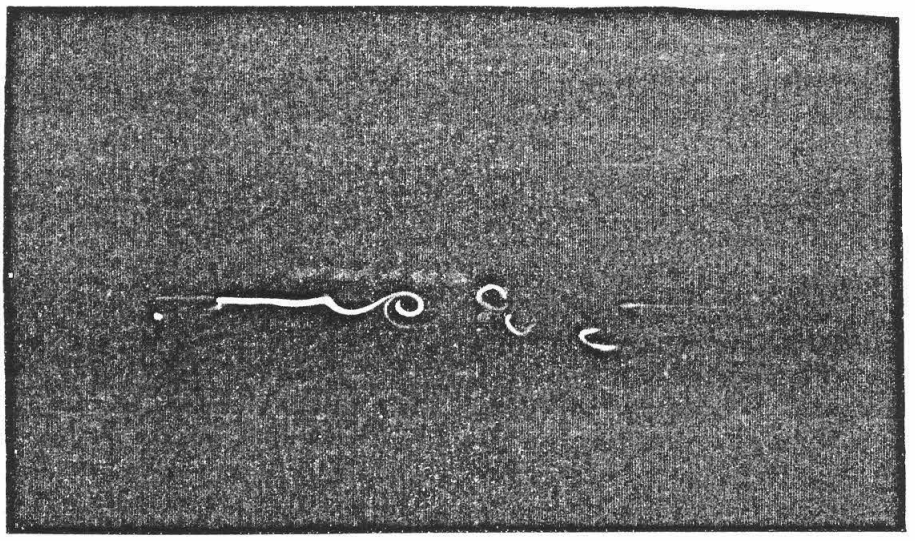

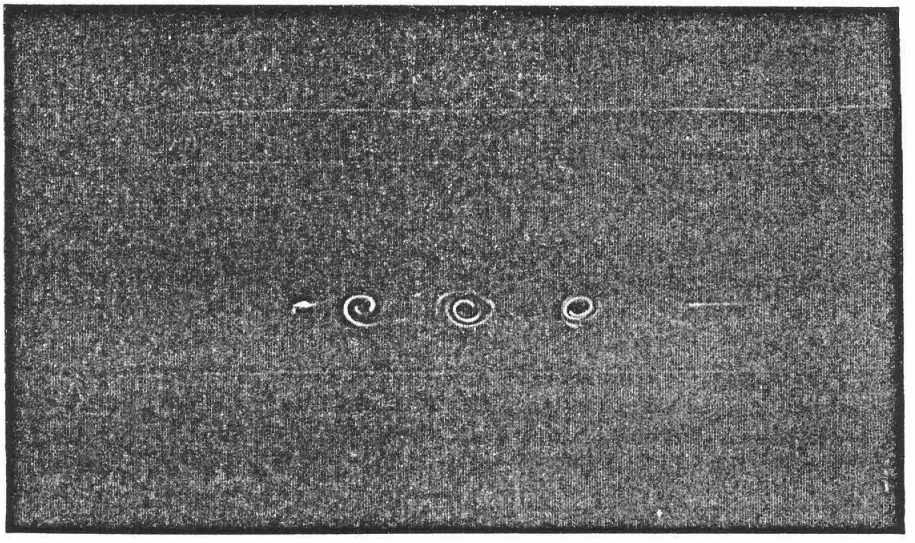

Gap length 6"

Observe the disappearance of pairing as result of forcing

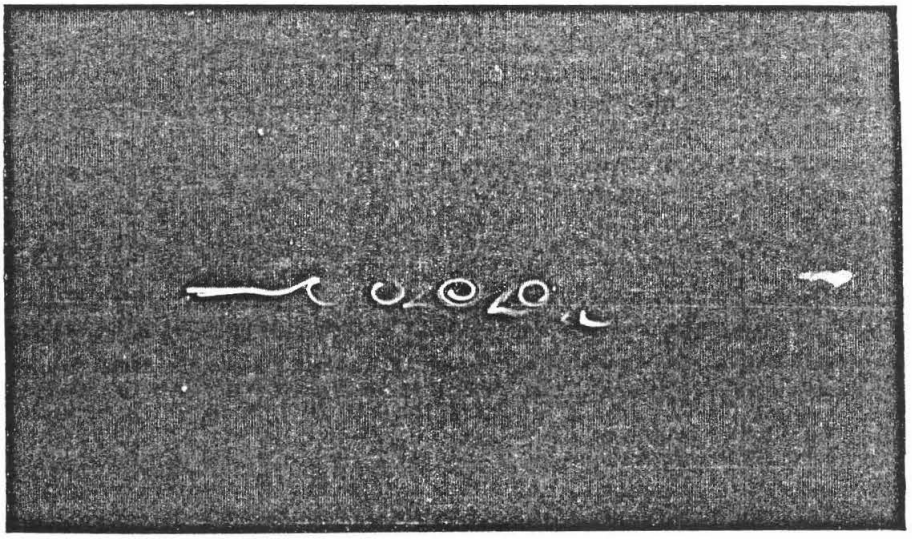

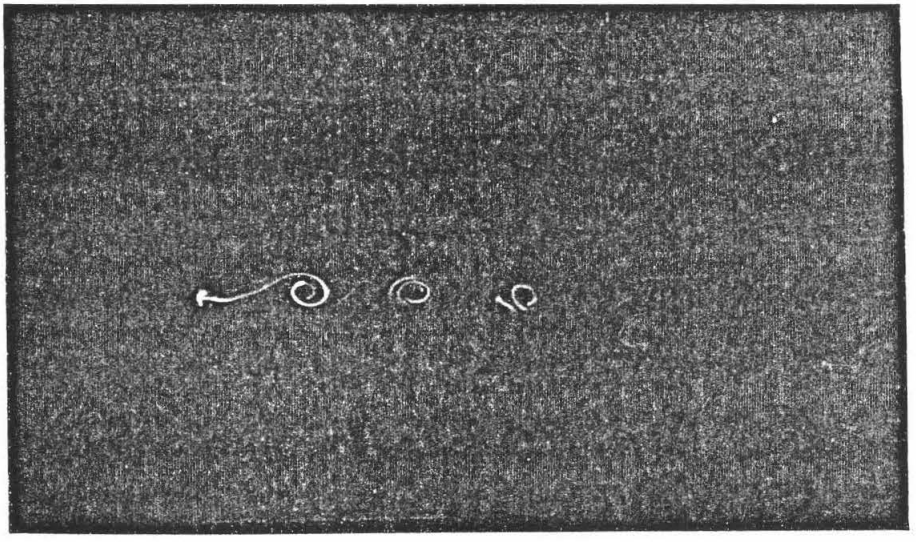

Gap length $6\frac{5}{8}$ "

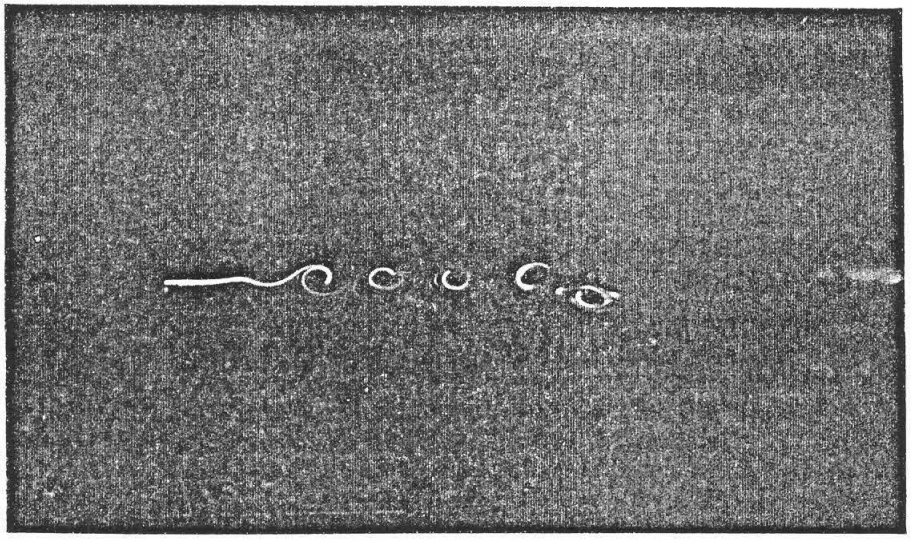

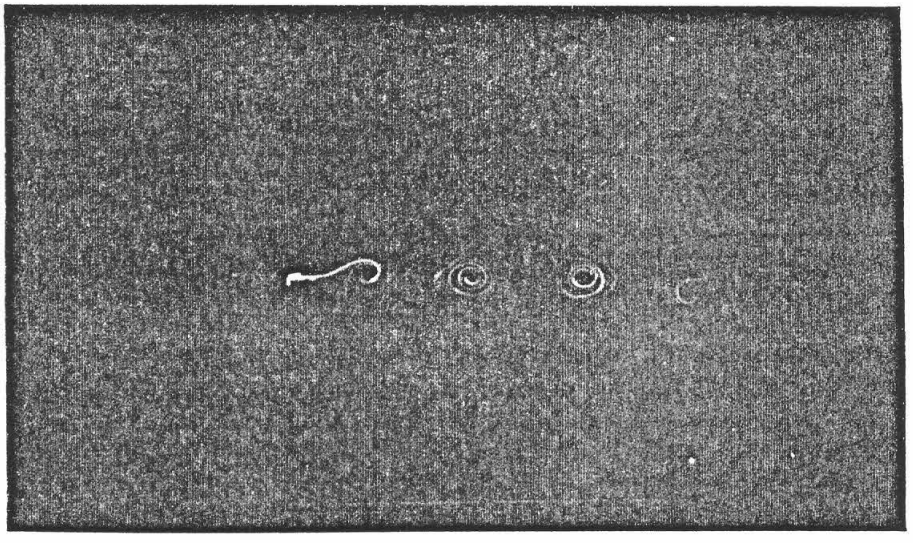

Gap length 7"

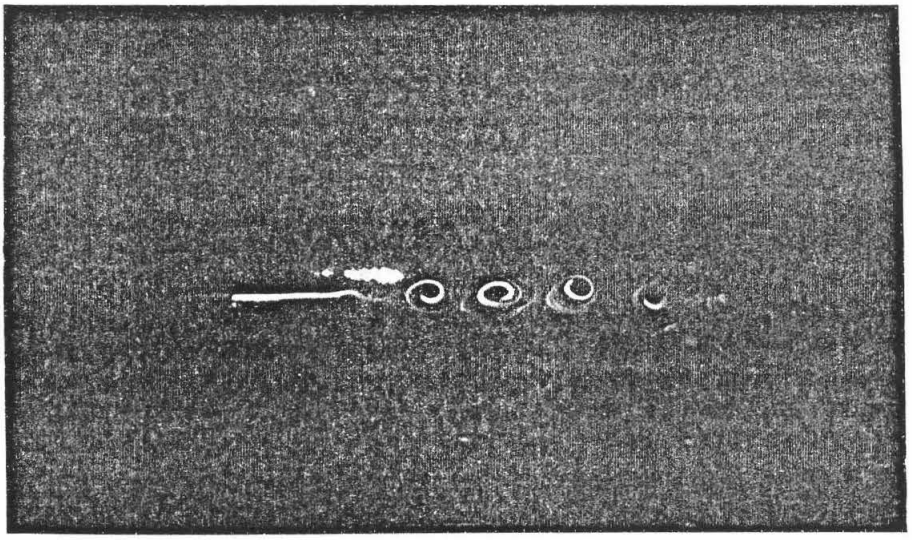

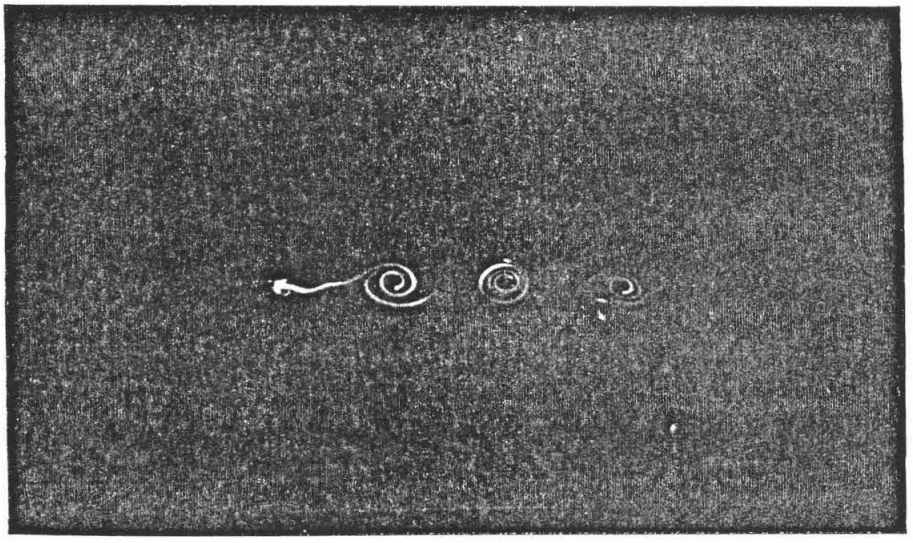

Gap length 8¼"

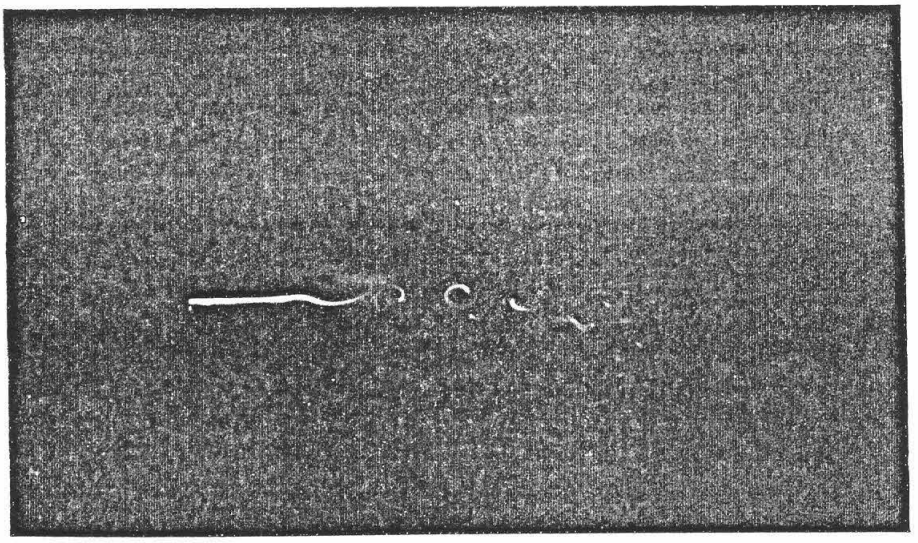

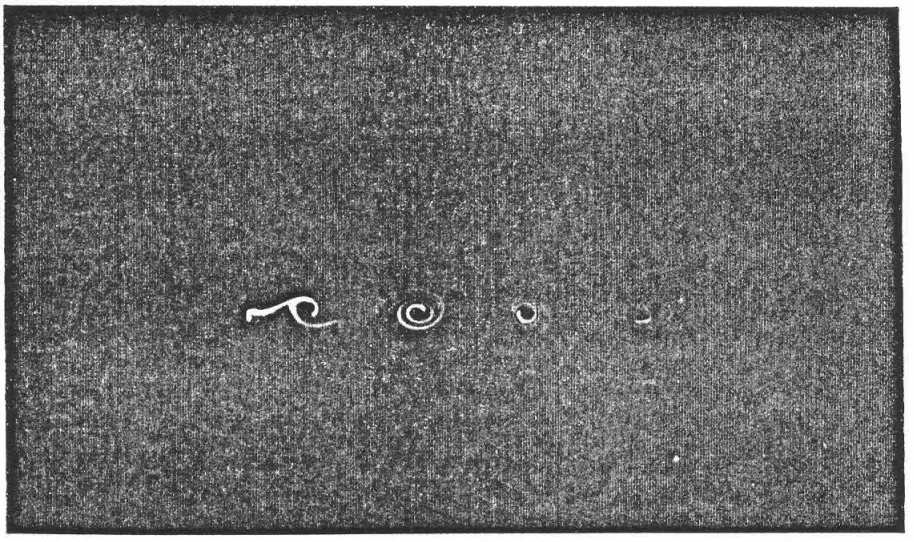

Gap length 9"

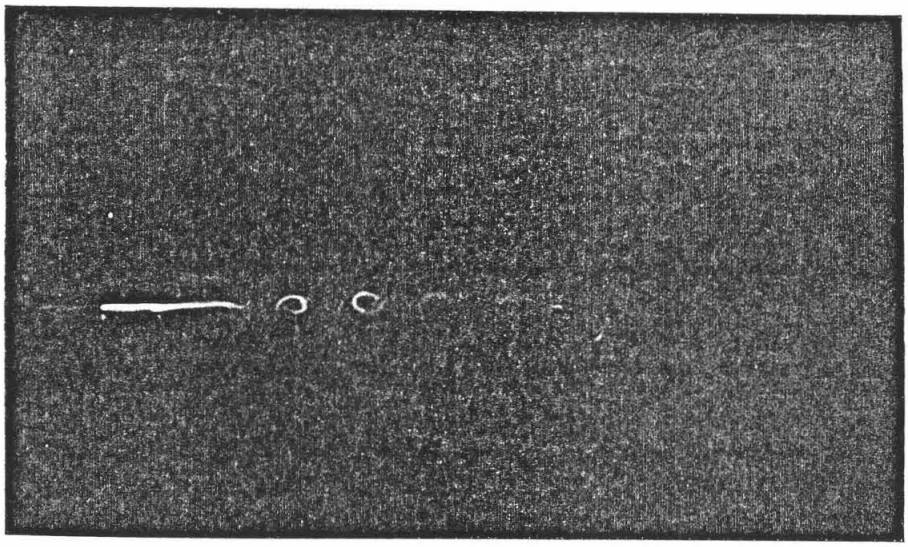

Free shear layer

Control of the Exposure of Works of Art to Photochemical Smog

Mark S. Adams
Dr. Glen R. Cass, Sponsor

ABSTRACT

Studies have shown that a number of artists' pigments will fade rapidly in the presence of ozone, a common component of photochemical smog. In an effort to assess the potential for this process to damage works of art, indoor ozone concentrations and building parameters were measured at a number of Southern California museums. Indoor ozone concentrations as high as 0.146 ppm were found in one museum that lacks a chemically protected air conditioning system. For purposes of comparison, the recommended ozone level in places where historical documents are stored is only 0.001 ppm. A mathematical model was tested that relates indoor air quality to ozone levels in the outdoor air. It was found that the indoor levels observed are consistent with the levels of ozone in outdoor air in Southern California that is supplied to museum air conditioning systems.

INTRODUCTION

The fading of artists' pigments by photochemical smog is a problem which threatens works of art being stored and displayed in the metropolitan museums around the world. In particular, a number of alizarin-lake pigment samples have been found to fade in the absence of light when exposed to atmospheric ozone. In order, however, to adequately assess the effect of the atmospheric ozone on works of art outside the laboratory, it is first necessary to determine the extent to which outdoor ozone is transferred to the inside of the museums and art galleries, for it is this indoor concentration of ozone to which important works of art are actually subjected.

EXPERIMENTAL PROGRAM

The first step in this project was a field study. Air quality measurements were made at a number of museums and art galleries. The following Southern California facilities were used as locations in the field study:

Dates (all 1984)	Site, Location
7/3 to 7/5	Pasadena Historical Museum, Pasadena
7/11 to 7/12	Southwest Museum, Los Angeles
7/13 to 7/15	Southwest Museum Library, Los Angeles
7/25 to 7/26	Virginia Scott Steele Gallery at the Huntington Library, San Marino
7/27 to 7/29	Huntington Art Gallery, San Marino
7/30 to 7/31	Montgomery Gallery, Claremont
8/1 to 8/2	Lang Gallery, Claremont
8/7 to 8/8	Villa Montezuma, San Diego
8/9 to 8/10	Serra Museum, San Diego
8/14 to 8/19	Los Angeles County Museum of Art, Los Angeles
8/20 to 9/4	J. Paul Getty Museum, Pacific Palisades

Simultaneous indoor and outdoor ozone concentrations were measured at each site using a matched pair of DASIBI UV photometric ozone monitors. The blueprints of each facility were examined to determine the volume, surface area, and materials of construction used in each building. Each building's ventilation system was documented. A hot wire anemometer was used to measure air flow into and out of ventilation ducts, doors, and windows at each site. From this information, the air exchange rates and retention times for ozone destruction by reaction with building surfaces could be determined.

RESULTS

Each of these sites fell into one of three distinct groups: not air conditioned (Pasadena Historical, Southwest, Lang, Villa Montezuma, and Serra); air conditioned but without an activated carbon air filtration system (Steele and Montgomery); and air conditioned with activated carbon filters (Southwest Library, Huntington, Los Angeles County Museum, and Getty). The sites with activated carbon filters on their air conditioning systems experienced no appreciable indoor atmospheric ozone, provided that the filters were well maintained and not significantly degraded. The highest indoor ozone levels experienced under such conditions approached, and occasionally surpassed, 0.01 ppm while simultaneous outdoor readings approached 0.20 ppm and higher. This indicates very good ozone removal performance considering the fact that doors are frequently left open for long periods of time during the day to allow for the passage of museum patrons. The Los Angeles County Museum, for example, never attained an hourly average ozone concentration of greater than 0.001 ppm at a site located well within the facility, far from any door opened to outside air.

A summary of peak ozone concentrations observed inside museums with air conditioning but without activated carbon filtration follows:

Site	Date	Indoor Max. O_3 ppm	Outdoor Max. O_3 ppm	Percentage of Outdoor O_3
Steele	7/25/84	0.043 ppm	0.179 ppm	24%
Steele	7/26/84	0.065 ppm	0.221 ppm	29%
Montgomery	7/30/84	0.060 ppm	0.150 ppm	40%
Montgomery	7/31/84	0.067 ppm	0.171 ppm	39%

One possible reason why Montgomery Gallery experiences interior ozone levels that more closely approach those outside is that less of the air at this facility is recirculated more than once through the air conditioning system than at the Steele Museum. This is supported by the shorter lag-time between the occurrence of outdoor and indoor O_3 peaks. Montgomery had an average lag-time of less than 20 minutes, while Steele's lag-time was close to 40 minutes.

Based on the above data, we can expect that a museum with a typical air conditioning system will experience ozone levels inside

the building that are 30 to 40% of that observed outside, with the peak concentration indoors lagging that outdoors by about one half hour.

The greatest variation in indoor ozone levels occurred among the final group of museums studied--those sites with no air conditioning. These buildings rely upon open doors and windows for ventilation and cooling. A description of the ventilation systems observed at these sites follows:

1) Pasadena Historical Museum--A few open windows, mostly on the second floor, provide poor ventilation. An exception occurs when the site is used for luncheons or meetings, when the large front door is left open for the duration of the meeting. On normal days, the building is reasonably well sealed, and outdoor air enters the building at a very slow rate.

2) Southwest Museum--A high-power fan in an open window forces about 5000 cubic feet of air per minute out of the building and initiates convection throughout the main portion of the building. Two exhibit rooms are largely unaffected by this continuous flow. Many open windows and doors allow large amounts of circulatory air to pass through the building.

3) Lang Gallery--One open window and one door open during public hours provide the ventilation at this site. The door is shut when the staff leaves for lunch or in the evening. Very little outside air is permitted to enter the facility. One or two fans circulate the air within the facility, but these fans do not force exchange with air outdoors.

4) Villa Montezuma--A dozen or so open windows and a door provide ventilation, while numerous fans circulate the air within the facility. A large up-draft can be felt on the stairwells of this largely vertical building as the warm interior air rises to be replaced at the ground level. Consequently, many of the first floor doors and windows serve as air inlets.

5) Serra Museum--Open doors and windows, generally large in size and few in number, provide for ventilation at this facility. No general circulation pattern can be noted, except for the one open door facing the ocean, which is subjected to a steadier breeze than the other open ports.

A summary of the ozone data collected at these sites is shown below. Again, all ozone levels are maximum hourly average values.

Site	Date	Indoor Max. O_3 (ppm)	Outdoor Max. O_3 (ppm)	Indoor O_3 as Percentage of Outdoor O_3	Comment
Pasadena Historical Museum	7/03/84	0.098	0.166	59%	1
Pasadena Historical Museum	7/04/84	0.023	0.168	14%	2
Pasadena Historical Museum	7/05/84	0.019	0.148	13%	3
Southwest	7/11/84	0.091	0.132	69%	3
Southwest	7/12/84	0.146	0.173	84%	3
Lang	8/01/84	0.030	0.140	20%	4
Lang	8/02/84	0.012	0.168	7%	5
V. Montezuma	8/07/84	0.014	0.042	33%	3
V. Montezuma	8/08/84	0.022	0.045	49%	6
Serra	8/09/84	0.034	0.049	69%	3
Serra	8/10/84	0.022	0.028	79%	3

Comment code:
1) Worst case. Luncheon held with front door open during peak ozone hours.
2) Building sealed for holiday.
3) Normal operations.
4) Front door open in morning and late afternoon; closed otherwise.
5) Building closed. This is the best case and is observed only when the building is sealed.
6) More windows open than on previous day.

Several trends are apparent from the above table. The most obvious feature is that the better-ventilated locations (Southwest, Serra) experience indoor ozone levels that are at least two-thirds as high as outdoor ozone levels, while the poorly ventilated and sealed-off locations (Lang, Pasadena Historical Museum) experience indoor O_3 levels less than one-fourth of outdoor ozone levels. Consequently, moderately well ventilated facilities (Villa Montezuma; Pasadena Historical Museum, day one) experience moderate indoor ozone levels. Lag-times between outdoor and indoor peaks also tend to be related to ventilation rate, with better-ventilated facilities experiencing very small lag-times and with poorly ventilated facilities generally experiencing longer lag-times.

Having assessed the indoor ozone levels and ventilation systems in a variety of buildings, it becomes possible to calculate how the indoor ozone levels depend on outdoor ozone levels and on various building parameters such as building volume, inside surface area, air conditioning specifications, and the ozone decomposition rates of the various materials found inside the building. The indoor/outdoor ozone air quality model developed by Shair and Heitner (1974) was found to be particularly useful. This model takes into account all of the factors mentioned earlier which would contribute to indoor ozone air quality. The system of modeling equations was reduced to a computer code. Then the data acquired were supplied to the model to check to see if measured indoor O_3 levels were consistent with O_3 levels found in the outside air that supplies the building. The best comparisons between theory and observation were obtained for those buildings with rapid

air exchange but no air conditioning or pollutant removal systems. Results for the Southwest Museum are shown in Figure 1. Generally good agreement between model calculations and indoor measurements was obtained at the other sites, with indoor O_3 levels observed generally falling somewhat below model predictions, particularly during morning hours.

CONCLUSIONS

The distribution of ozone concentrations within museums in Southern California has been documented. Buildings with high rates of air exchange with the outdoor atmosphere but with no pollutant removal system show peak indoor O_3 levels greater than two-thirds as high as those outdoors. Buildings with conventional air conditioning systems show peak O_3 levels inside about 30 to 40% of those outside. Museums with well-maintained activated carbon air filtration systems show low indoor O_3 levels, always below 0.10 ppm O_3, often as low as 0.001 ppm O_3.

Indoor ozone levels generally can be predicted if ozone levels outside the facility are known. Using building parameters obtained from building superintendents and blueprints, the ozone level in many types of buildings can be computed with a reasonable degree of accuracy. The Shair-Heitner model provides an accurately shaped curve, with only a small error in the magnitude of the curve. The model is found to predict indoor O_3 levels in most cases that are slightly higher than those actually experienced. This approach can be used to make estimates of the exposure of works of art to O_3 concentrations on a year-round basis given the outdoor O_3 data routinely collected by government pollution control agencies.

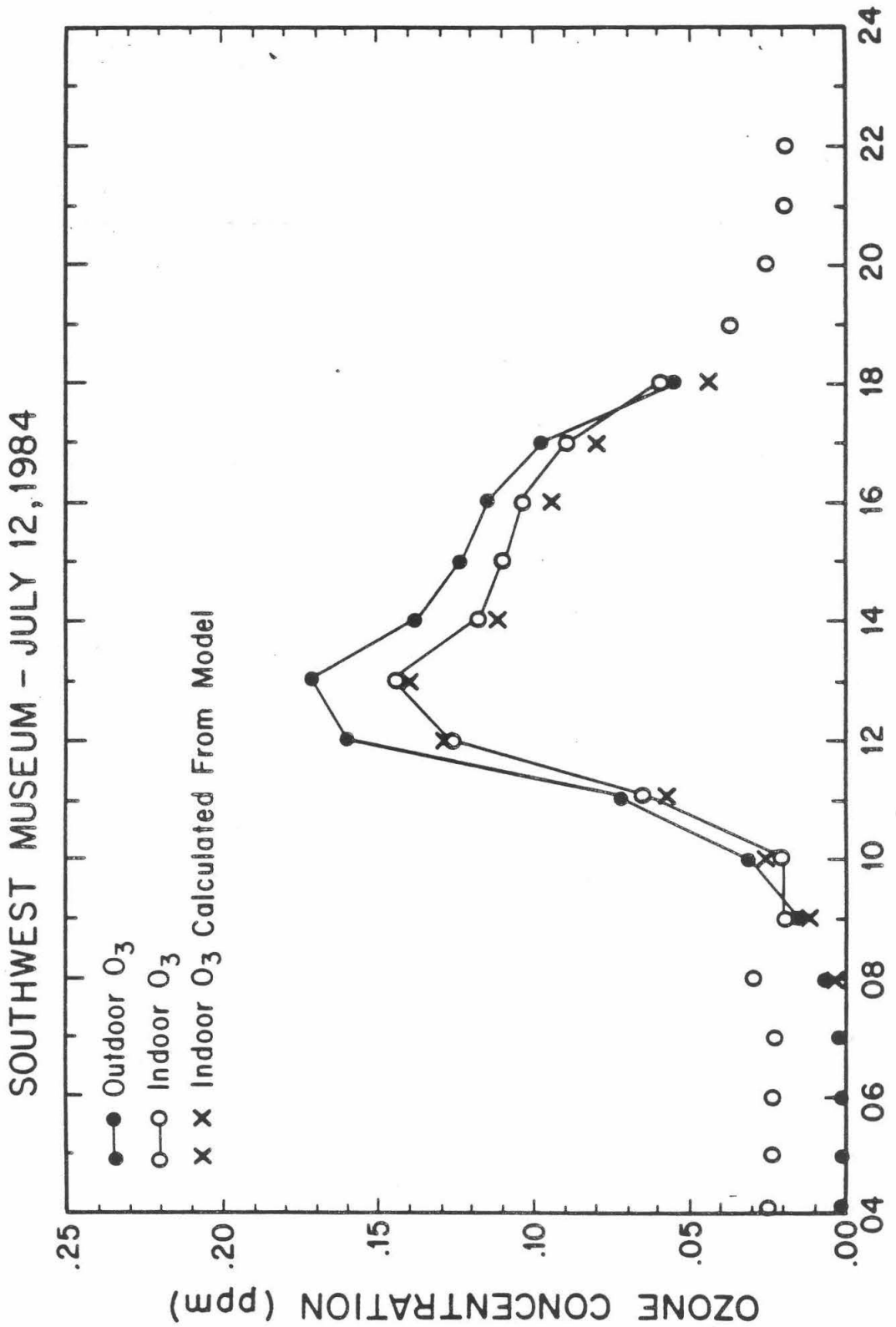
SOUTHWEST MUSEUM - JULY 12, 1984
Outdoor O_3
Indoor O_3
Indoor O_3 Calculated From Model
OZONE CONCENTRATION (ppm)
.25
.20
.15
.10
.05
.00
04
06
08
10
12
14
16
18
20
22
24
HOURS (PDT)

FIGURE 1

BIBLIOGRAPHY

1) T. D. Davies, B. Ramer, G. Kaspyzok, A. C. Delany (1984) "Indoor/Outdoor Ozone Concentrations at a Contemporary Art Gallery," J. Air Pollut. Control Assoc., 31, 135-137.

2) K. Drisko, G. R. Cass, J. R. Druzik (1983) "Fading of Artists' Pigments Due to Atmospheric Ozone," submitted to J. Am. Inst. for Conservation.

3) P. J. Drivas, P. G. Simmonds, F. H. Shair (1972) "Experimental Characterization of Ventilation Systems in Buildings," Environ. Sci. Technol., 6, 609.

4) B. H. Jennings, S. R. Lewis (1965) Air Conditioning and Refrigeration, Scranton, Penn.: International Textbook Co.

5) R. H. Sabersky, D. A. Sinema, F. H. Shair (1973) "Concentrations, Decay Rates, and Removal of Ozone and Their Relation to Establishing Clean Indoor Air," Environ. Sci. Technol., 7, 347-353.

6) J. H. Seinfeld (1975) Air Pollution: Physical and Chemical Fundamentals, New York: McGraw-Hill.

7) F. H. Shair, K. L. Heitner (1974) "Theoretical Model for Relating Indoor Pollution Concentrations to Those Outside," Environ. Sci. Technol., 8, 444-451.

8) C. L. Shaver, G. R. Cass, J. R. Druzik (1983) "Ozone and the Deterioration of Works of Art," Environ. Sci. Technol., 17, 748-752.

DEW CHEMISTRY IN PASADENA

by

Don Buchholz

Student Undergraduate Research Fellowship

Summer 1984

ABSTRACT

Seven dew events were monitored in Pasadena. The mean pH of dew was found to be 5.11. Ion deposition fluxes were calculated for the events and 6 additional daytime periods. Deposition of acidic anions such as sulfate and nitrate was balanced by comparable fluxes of alkalinity. On several occasions, the deposition of measured ions appeared to be enhanced by dew formation.

I. Introduction

In contrast to intermittent rain, the Los Angeles area is subjected to a constant downfall of dry material every day. Dew is a common event in subtropical climates and frequently observed in the coastal and semi-arid regions in Southern California. The interaction of dry deposited matter with dew has been predicted to result in pH values as low as 2.0 (Wysinewski, 1982). As well as dissolving previously deposited material, dew might be expected to modify further flux rates by surface wetting, hence reducing particle rebound as well as providing a sink for soluble gases.

II. Presentation and Discussion of Results

A. Methods

Data was collected from seven dew events plus four periods of dry deposition including two aerosol sampling intervals. A first generation of dew collectors (series "D") were constructed with black polyethylene sheets (10 mil) stretched over a 36" x 36" frame made from two pre-fabricated aluminum-framed window screens (Figure 1). These collectors were generally set out about one hour before dew formation was observed. The sample was picked-up before any noticeable evaporation occurred - usually about one-half hour after sunrise. It was removed from the collector by partially folding the collector making a v-shaped channel to guide the dew into a funnel and using a disposable weigh boat as a squeegee to scrape the thin layer of droplets from the plastic. Sample size was determined by weighing sample bottles before and after collection.

To improve sample liquid recovery, petri dishes were subsequently used to collect on a smaller surface. The "A-series" were Pyrex; both "B" and "C-series" were of the variety; petri dishes were the 150 x 15 mm size. The bottom halves were exposed in the inverted (i.e., flat-side-up position).

Dew amounts were determined by weighing dry and wetted samplers. The extraction/dilution procedure was done by putting 10 ml. of distilled-deionized water (DD-H_2O) into a clean inverted cover; the exposed bottom half was placed downward into it, and manually aggitated for one-half to one minute. The diluted mixture was then pipetted into a sample bottle. Petri dishes were used to sample both wet (i.e., dew) and dry intervals.

The first sampling site (samples coded 0628, 0629 and 0706) was at ground level approximately 30 ft. east of the south undergraduate houses - in the only uncovered area on campus without nightly automatic sprinklers. This site was plagued with foot traffic, however. Subsequently, sampling was relocated to the southeast corner of the Keck Laboratory roof was used.

The collectors (except for unopened packages of sterile petri dishes) were first washed in Alconox and water and rinsed with copious quantities of DD-H_2O. The sample contaminant bottles were well-rinsed Nalgene bottles (30 and 60 ml sizes). The samples were handled carefully to avoid contamination. Prior to exposure and second extractions generally gave satisfactory blanks, indicating complete solute recovery.

When pH measurements were taken, it was immediately after collection using a Radiometer PHM-80 meter with a combination electrode and buffer solutions of pH = 7.0 and 4.0 for calibration purposes. Most samples were analyzed for aqueous ion concentrations. Sodium, potassium, calcium, and magnesium were determined using a Varian atomic absorption spectrophotometer with an air-acetylene flame. Ammonium ion concentrations were determined colorimetrically using an indol-phenol reaction. Concentrations of chloride, nitrate, and sulfate anions were measured using a Dionex 2020i ion chromatograph. Ambient aerosol were collected on Teflon filters (47 mm at 10 lpm), followed by nylon filters for gaseous nitric acid measurements. The filters were extracted in 10 ml DD-H_2O for one hour.

B. Results

The seven dew events were sampled; these differed greatly in the amount of dew deposited to the collectors. The dewfall data is given in Table 1. The dew deposition rates were calculated by dividing individual sample weights by collector area (A, B and C series area = 154 cm^2; D series area = 8360 cm^2) and then averaging for replicate collectors of the same type. The plastic petri dishes (B and C series) showed consistently more dew than other collector types. This is illustrated graphically in Figure 2.

A total of 29 dew samples were collected. All were analyzed for chloride, nitrate, and sulfate anion concentrations. Those collected on, or before, August 3 were also analyzed for the following major cations: Na^+, K^+, CA^{2+}, Mg^{2+}, NH_4^+. A complete summary is listed in Appendix A. The following ranges (in ueq L^{-1}) were observed in dew found on pre-cleaned collectors set out over one night only (< 12 hrs.): Na^+ - 67-484; K^+ - 4-84; Ca^{2+} - 78-1180; Mg^{2+} - 30-460; NH_4^+ - 87-560; Cl^- - 29-875; NO_3^- - 67-980; SO_4^{2-} - 88-712. The pH values ranged from 4.40 to 5.89 on the eight samples that were measured (Table 2) with a mean pH of 5.11.

In addition to the dew, four periods of dry deposition were also sampled (0706, 0810, 0816, 0822). Ion deposition fluxes for these, all dew events, and the daytime hours of August 1 and August 2 have been calculated and are tabulated in Appendix B. Deposition fluxes for most species were found to be higher during a dew event than during daytime hours (Table 3).

Average aerosol concentrations of 0.168 and 0.156 ueq m^{-3} for sulfate and nitrate (= particulate + gaseous) were observed from 10:25 p.m. August 22 to 6:30 a.m. August 23. Dividing these by the average flux measured for this period yielded a sulfate deposition velocity of 0.4 cm s^{-1} and a nitrate deposition velocity of 0.5 cm s^{-1}.

C. Discussion

The difference in dewfall between collector types may be attributed to two different sets of factors. The first are the different thermal characteristics of each material which will affect dew formation, namely heat capacity and emissivity coefficient (Monteith, 1957). The second set is error in sample size measurement. The edges of D-series collectors never had dew on them, whereas dew was found on the petri dish edges during the heavier dews. The edge area of the D-series collector was also less than 10% of the reported collection area, while the edge area of a petri dish is 66 cm^2 or 43% the size of the collection surface area (154 cm^2). In the heavy dews dew drops were occasionally observed to roll off the edge of the petri dish collector. Overall, paired petri dish samples gave good agreement.

The pH values imply that dew in Pasadena is slightly more acid than that reported by Anderson (1979) in the D.C. area. Anderson's value of 5.60 is much closer to the value of 5.7 which he cites to be the pH of clean water in equilibrium with atmospheric CO_2. The pH measurements were taken only from series D collectors, however, as these were the only samples large enough to allow it.

The depositional flux of acidic anions, nitrate and sulfate, were relatively high during both day and nighttime intervals, giving high concentrations in the dew liquid. The moderate pH's were due to similarly high fluxes of alkalinity, mainly in the form calcium and ammonia. The deposition velocities (v_d) for nitrate and sulfate were near the median values given in the current literature. However, nitrate v_d is usually reported to be greater than sulfate v_d, owing to its association with larger aerosol (Hidy et al., 1980). It would be useful in the future to make accompanying measurements of aerosol composition as a function of size. In this way, the contributions of coarse versus fine aerosol deposition could be evaluated.

III. CONCLUSIONS

Larger (1 m^2) polyethylene collection surfaces were good for obtaining large amounts of dew water for chemical analysis. However, owing to unsure recovery, these were not reliable for either dewfall or ion flux measurements. Petri dishes gave more reproducable results for the latter two determination.

Significant nitrate and sulfate were measured in dew liquid samples. The dew pH's measured were between 4.4 and 5.9; sufficient alkalinity was deposited to neutralize the deposited acidic anions. In several cases, dew formation appeared to enhance solute deposition.

Table 1.

DATE CODE	DEWFALL PER NIGHT (mm)		
	Series A[1]	B,C[2]	D[3]
0628	----[4]	----	0.02
0629	----	----	0.01
0801	0.09	0.11	----
0802	0.04	0.05	----
0803	0.16	0.20	0.08
0822	0.09	0.11	0.06
0823	0.20	0.28	0.13

1. Glass petri dish.
2. Plastic petri dish.
3. Black polyethylene sheet.
4. Not measured.

Table 2

Ion Species	FLUX ($\mu eq\ m^{-2}\ hr^{-1}$) Daytime Avg. (8/1 & 8/2)	Nighttime Avg. (8/1-2 & 8/2-3)	TOTAL DEPOSITION (μeq) Measured	Calculated	Difference	% Difference
Na^{+}	.80	1.56	54.64	59.71	5.07	9
K^{+}	.13	.13	6.88	12.60	5.72	83
Ca^{++}	2.95	2.06	136.32	148.37	12.05	9
Mg^{++}	.55	.69	30.15	33.26	3.11	10
NH_4^{+}	.55	2.31	46.25	71.19	24.94	54
Cl^{-}	.72	2.39	47.05	77.56	30.51	65
NO_3^{-}	2.62	2.14	128.80	133.92	5.12	4
SO_4^{-}	1.21	2.66	93.72	100.71	7.0	7

TABLE 3:

Sample		pH
0628	DØ	5.89
	D1	5.70
0629	DØ	4.89
0803	DØ	4.40
0822	DØ	4.95
	D1	5.25
0823	DØ	4.72
	D1	5.04

AVG. pH: 5.11
STD. DEV: .49

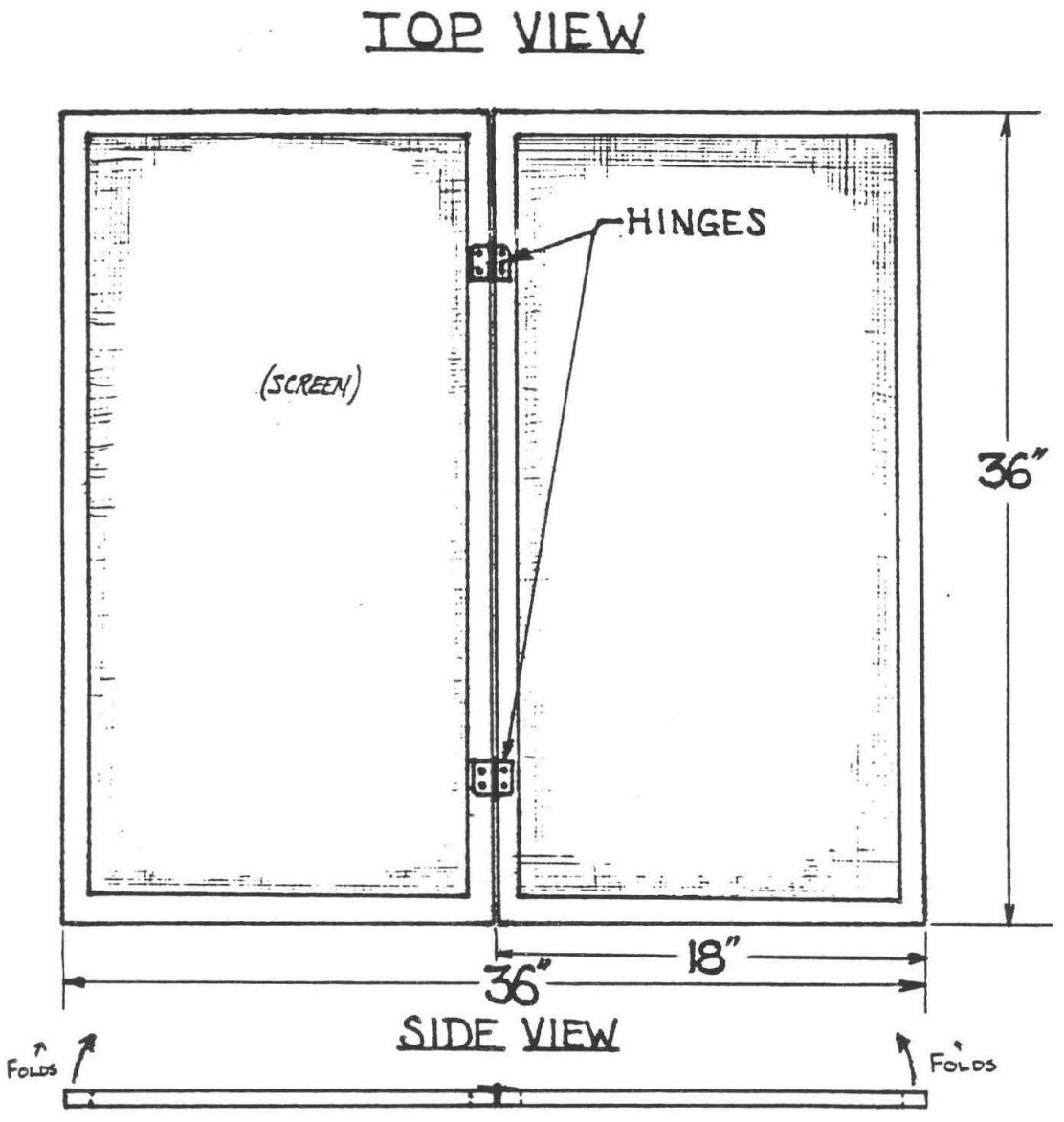

FIG 1. D-COLLECTOR FRAME. The plastic was warmed in direct sunlight and cemented to the top and edge surfaces with Elmer's-brand contact cement. After allowing the cement to set, removing the plastic from the sun let it shrink and become taut and wrinkle-free.

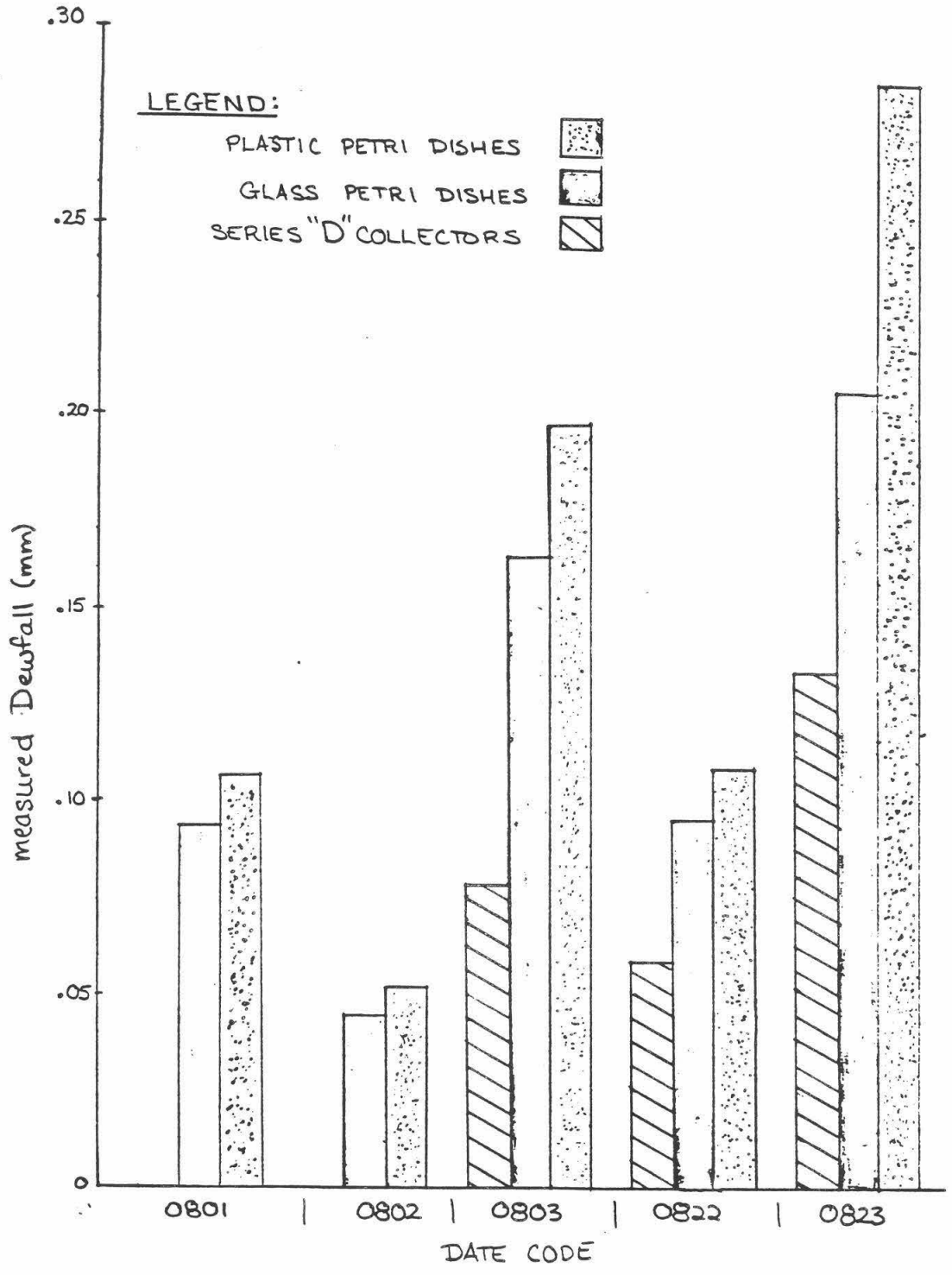

FIG. 2: Comparision of dew formation on different collector surfaces.

APPENDIX A:

ION CONCENTRATIONS IN DEW

Sample ID	Volume (ml)	pH	microequivalents/liter								
			H+	Na+	K+	Ca++	Mg++	NH4+	Cl-	NO3-	SO4-	-/+
0801A2	1.44			88.9		179.6	44.1	154.5	57.0	162.9	141.2	0.776
0801B2	1.68			71.9	11.3	184.1	41.4	162.4	133.8	127.2	181.6	0.941
0801C2	1.59			76.0	11.8	165.1	38.3	136.0	234.6	102.1	188.1	1.230
0802A2	0.75			508.7	82.4	1162.1	265.4	439.2	423.3	1139.5	678.2	0.912
0802B2	0.85			416.4	40.3	1035.4	242.8	337.5	469.9	930.5	689.8	1.009
0802C2	0.84			433.8	54.9	1193.8	254.5	620.0	480.1	1065.9	878.0	0.948
0802A3	0.61			484.4	59.7	564.1	198.4	404.2	473.3	440.1	530.1	0.845
0802B3	0.83			150.2	8.6	225.8	72.0	282.4	215.3	263.6	339.7	1.110
0802C3	0.65			223.8	10.5	521.8	127.9	429.9	187.6	417.8	468.4	0.818
0803A1	2.32			315.4	40.3	774.0	173.1	224.4	332.3	787.0	522.2	1.075
0803B1	3.18			281.8	33.3	704.4	156.8	224.1	198.5	649.1	471.2	0.942
0803C1	3.14			285.3	37.4	719.6	156.6	287.4	245.5	655.3	515.1	0.953
0803A2	2.56			158.7	19.6	378.8	84.9	177.9	206.2	399.9	205.0	0.990
0803B2	3.08			151.9	18.8	406.2	85.0	173.1	174.2	366.9	247.5	0.945
0803C2	3.10			133.4	13.3	337.4	78.7	144.8	230.9	284.0	231.1	1.055
0803A3	2.58			85.1	5.9	77.6	30.2	110.0	116.7	101.4	101.9	1.038
0803B3	2.72			67.3	6.6	80.7	30.4	147.2	174.1	102.9	146.9	1.278
0803C3	2.95			68.2	3.6	87.0	30.8	98.6	149.1	103.6	147.7	1.391
0803D0	65.50	4.40	39.811	107.0	21.6	171.0		87.0	181.0	128.4	123.4	1.016
0822A2	1.45											
0822B2	1.64								44.1	67.4	122.2	
0822C2	1.70											
0822D0	49.05	4.95	11.220						146.0	85.8	267.0	
0822D1	48.71	5.25	5.623						187.0	75.6	160.0	
0823A3	3.15								60.8	126.1	87.6	
0823C2	4.37								28.9	93.7	89.0	
0823D0	104.20	4.72	19.055						226.0	130.0	582.0	
0823D1	116.90	5.04	9.120						595.0	174.0	264.0	
0628D0	14.30	5.89	1.30	361.0		719.	367.	278.	509.	377.	362.	0.620
0628D1	19.0	5.70	2.00	231.	83.9	512.	123.	245.	262.	316.	203.	0.653
0629D0	5.20	4.89	12.88	—	—	1184.	457.	564.	875.	980.	712.	—

Appendix B:

Ion Deposition Fluxes

Sample	Time out		Time in		DT(hrs.)	microequivalents/(sq. meter * hr) H+	Na+	K+	Ca++	Mg++	NH4+	Cl-	NO3-	SO4-	(mm) Dewfall
0801A2	31-JUL	18.00	1-AUG	5.75	11.8		0.707		1.429	0.351	1.230	0.454	1.296	1.123	0.094
0801B2	31-JUL	18.00	1-AUG	5.75	11.8		0.668	0.105	1.709	0.385	1.507	1.242	1.181	1.686	0.109
0801C2	31-JUL	18.00	1-AUG	5.75	11.8		0.668	0.104	1.451	0.337	1.195	2.061	0.897	1.653	0.103
0802A2	1-AUG	6.00	2-AUG	6.00	24.0		1.032	0.167	2.358	0.538	0.891	0.859	2.312	1.376	0.049
0802B2	1-AUG	6.00	2-AUG	6.17	24.2		0.951	0.092	2.365	0.554	0.771	1.073	2.125	1.575	0.055
0802C2	1-AUG	6.00	2-AUG	6.33	24.3		0.972	0.123	2.676	0.570	1.390	1.076	2.389	1.968	0.055
0802A3	1-AUG	22.17	2-AUG	6.00	7.8		2.449	0.302	2.852	1.003	2.044	2.391	2.225	2.681	0.040
0802B3	1-AUG	22.17	2-AUG	6.17	8.0		1.012	0.058	1.521	0.485	1.903	1.450	1.776	2.288	0.054
0802C3	1-AUG	22.17	2-AUG	6.33	8.2		1.157	0.054	2.697	0.661	2.222	0.969	2.159	2.421	0.042
0803A1	31-JUL	18.00	3-AUG	6.67	60.7		0.783	0.100	1.922	0.430	0.557	0.825	1.954	1.297	0.151
0803B1	31-JUL	18.00	3-AUG	7.17	61.2		0.951	0.113	2.378	0.529	0.757	0.670	2.191	1.591	0.206
0803C1	31-JUL	18.00	3-AUG	7.67	61.7		0.943	0.124	2.379	0.518	0.950	0.812	2.167	1.703	0.204
0803A2	2-AUG	6.17	3-AUG	6.67	24.5		1.077	0.133	2.570	0.576	1.207	1.399	2.713	1.391	0.166
0803B2	2-AUG	6.33	3-AUG	7.17	24.8		1.223	0.152	3.271	0.685	1.394	1.403	2.955	1.993	0.200
0803C2	2-AUG	6.50	3-AUG	7.67	25.2		1.067	0.106	2.699	0.629	1.158	1.847	2.271	1.848	0.201
0803A3	2-AUG	23.00	3-AUG	6.83	7.8		1.821	0.125	1.660	0.646	2.353	2.496	2.169	2.178	0.168
0803B3	2-AUG	23.00	3-AUG	7.25	8.3		1.440	0.141	1.728	0.651	3.150	3.727	2.203	3.145	0.177
0803C3	2-AUG	23.00	3-AUG	7.67	8.7		1.507	0.080	1.922	0.681	2.180	3.295	2.290	3.265	0.192
0803D0	2-AUG	23.25	3-AUG	6.00	6.8	0.462	1.242	0.251	1.985		1.010	2.101	1.490	1.432	0.078
0810A2	10-AUG	12.00	10-AUG	16.17	4.2		0.787	0.089				1.646	1.901	0.969	0.0
0810C2	10-AUG	12.00	10-AUG	16.17	4.2		1.317	0.260				1.505	2.649	2.201	0.0
0810A3	10-AUG	12.00	10-AUG	16.17	4.2		0.974	0.260				0.524	1.262	0.938	0.0
0810C3	10-AUG	12.00	10-AUG	16.17	4.2		1.644	0.447				0.726	3.055	2.621	0.0
0816B1	16-AUG	10.33	16-AUG	16.33	6.0							1.165	2.045	0.716	0.0
0816C1	16-AUG	10.33	16-AUG	16.33	6.0							0.245	2.110	0.543	0.0
0822A2	21-AUG	23.33	22-AUG	7.67	8.3										0.094
0822B2	21-AUG	23.33	22-AUG	7.67	8.3							0.564	0.862	1.561	0.106
0822C2	21-AUG	23.33	22-AUG	7.67	8.3										0.110
0822D0	21-AUG	23.33	22-AUG	6.00	6.7	0.099						1.285	0.755	2.350	0.059
0822D1	21-AUG	23.33	22-AUG	6.00	6.7	0.049						1.634	0.661	1.398	0.058
0822C2	22-AUG	10.25	22-AUG	16.00	5.8							0.142	1.965	1.019	0.0
0823A3	22-AUG	22.42	23-AUG	6.92	8.5							1.464	3.034	2.108	0.205
0823C2	22-AUG	22.42	23-AUG	6.92	8.5							0.965	3.129	2.971	0.284
0823D0	22-AUG	22.42	23-AUG	6.75	8.3	0.285						3.380	1.944	8.705	0.125
0823D1	22-AUG	22.42	23-AUG	6.75	8.3	0.153						9.984	2.920	4.430	0.140

Appendix D.

ION DEPOSITION FLUXES (CONT.)

ID CODE	TIMES OUT	TIMES IN	DT (hrs.)	Flux (in $\mu eq \cdot m^{-2} \cdot hr^{-1}$) H^+	Na^+	K^+	Ca^{++}	Mg^{++}	NH_4^+	Cl^-	NO_3^-	SO_4^{--}	Dewfall (mm)
0628 DØ	27-JUN 2200	28-JUN 0530	7.5	.003	.823		1.640	.837	.634	1.161	.860	.826	.017
0628 D1	27-JUN 2200	28-JUN 0530	7.5	.006	.663	.241	1.470	.353	.703	.752	.907	.583	.022
0629 DØ	28-JUN 2030	29-JUN 0500	8.5	.009			.866	.334	.413	.640	.717	.521	.006
0706 A	5-JUL 2200	6-JUL 0500	7.0				1,772	.631		1.085	2.004	.696	0.0
0706 B	5-JUL 2200	6-JUL 0500	7.0				1.716	.482		.538	1.735	.631	0.0
0706 C	5-JUL 2200	6-JUL 0500	7.0				1.772	.408		.798	1.558	.464	0.0
— *	1-AUG 0600	1-AUG 2210	16.17		.711	.122	2.520	.474	.503	.706	2.385	1.242	—
— *	2-AUG 0620	2-AUG 2300	16.58		.891	.137	3.383	.616	.602	.742	2.857	1.187	—

* Calculated from Aug. 1 to Aug. 3 data. Example: Na^+ flux for daytime Aug 1.

(avg. flux)(time period) = (total deposited sodium)

$\frac{1}{3}(1.032 + 0.951 + 0.972)(24.17) = 23.81$ → Na^+ deposited 8/1 0600 to 8/2 0610

$-\ \frac{1}{3}(2.449 + 1.012 + 1.157)(8.0) = 12.31$ → " " 8/1 2210 to 8/2 0610

11.49 → Na^+ deposited 8/1 0600 to 8/1 2210

deposition ÷ time = flux

$11.49 \div 16.17 = 0.711$

EFFECTS FROM NUTRIENT PULSING AND PCB EXPOSURES ON GROWTH BY *MACROCYSTIS* GAMETOPHYTES

Margaret C. Carter

Dr. Wheeler J. North, Faculty Sponsor

ABSTRACT

Laboratory culturing of *Macrocystis pyrifera* gametophytes often encounters difficulty due to competition from marine diatoms occurring as contaminants. The culturing technique of nutrient pulsing was investigated as a possible means to eliminate this competition. Pulsing was found to be unsatisfactory for controlling diatom contamination while having a negative effect on gametophyte growth. Toxicity levels of 4,4'-dichlorobiphenyl(PCB) were also tested for the gametophytes. Concentrations of about 1,5 and 10 μg/l PCB did not have a significant effect on gametophyte growth.

INTRODUCTION

A major problem when culturing gametophytes of Macrocystis pyrifera(Giant Kelp) in the laboratory is contamination by marine diatoms. Studies by Gerard(1982) indicate that M. pyrifera sporophytes store nitrogen in their tissues as internal reserves that can be utilized later in a low nitrogen environment. Phosphorus occurs in marine organisms in about a 1:16 ratio to nitrogen(Sverdrup, et.al., 1946) and can be stored by Macrocystis(North, personal communication). Taking this a step further, we hypothesized that M. pyrifera gametophytes might also store nutrients. Using this hypothesis, we investigated feasibility of the culturing technique of nutrient pulsing. Gametophytes were grown alternately in nutrient rich media for one day and in nutrient poor media for 1-4 days as a way to control diatom contamination. By pulsing nutrients in this manner, we hoped to starve the diatoms during the nutrient poor phases, but, during the same time, leave the gametophytes unaffected if indeed they were able to store and utilize internal nutrient reserves.

A further experiment involved examining toxicity thresholds of 4,4'-dichlorobiphenyl(PCB) among M. pyrifera gametophytes. Concentrations of PCBs as low as 1.0 to 10.0μg/l have been found to be detrimental to photosynthesis and cell division of marine phytoplankton(Harding and Phillips,1978). Thus we exposed gametophytes to concentrations of approximately 1.0, 5.0 and 10.0μg/l of PCBs to observe any effects on growth. Open ocean PCB concentrations are on the order of 0.1μg/l(Harding and Phillips,1978). However PCB concentration in the effluent of the Orange County sewage discharge was 1.55 mg/l in 1981(Schafer,1982). Even though this discharge is immediately diluted by a factor of about 150(Bascom,1983), this still produces a PCB concentration of about 10μg/l near the outfall area.

MATERIALS AND METHODS

Five cultures of gametophytes were grown (A-E). M. pyrifera sporophylls were collected from San Mateo Point, CA on 20 June 1984(A) and from off the pier at Kerckhoff Marine Laboratory, Corona del Mar, CA on 3 July(B), 12 July(C), 27 July(D) and 20 August 1984(E). The collected sporophylls were wiped free from visible epiphytes and put into chilled offshore seawater to release spores. The spores were allowed to settle onto ten slides. Gametophyte growth was monitored by daily measurement of the longest dimension of 20 randomly selected gametophytes per slide using an eyepiece micrometer (1.00 units=602μm). Means were calculated for each slide and plotted against day of growth. The cultures were kept in a refrigerated room at 10.5±1.0°C. All light was provided by cool fluorescent tubes.

Culture A was to characterize the normal growth pattern for gametophytes. It was grown in a plastic shoebox containing 2 liters of nutrient-poor offshore seawater enriched with 100 μM$NaNO_3$ and 6 μMKH_2PO_4. Water and nutrients were changed daily. The culture was maintained under a continuous irradiance of about 8.30 μE/m^2/sec.

The purpose of Culture B was to determine the irradiance level for light saturated growth. This culture was started in a shoebox

but after 2 days was transferred to 5 petri dishes with 2 slides per dish. Offshore seawater enriched same as for A was renewed daily in each of the dishes. Full irradiance was about 11.0 $\mu E/m^2/sec$ at a distance of 33cm from the light source as measured by a YSI-Kettering Model 65 Radiometer. Measurements were taken in $ergs/cm^2/sec$ and converted to the more popular $\mu E/m^2/sec$ after Lüning(1981). Dish 1 was placed close to the light source to achieve more intense light. Dish 2 received 11.0 $\mu E/m^2/sec$. Dishes 3,4 and 5 received 1/2,1/3 and 1/10 respectively of illumination for Dish 2 by use of neutral density filters. However, after 6 days there was no statistically significant difference in the growth curves of gametophytes from the different dishes so we reduced Dish 1 to 1/100 full irradiance and Dish 2 to 1/1000 full irradiance to see if growths would become slower.

Culture C was also started in a shoebox. After 4 days the slides were transferred to 5 petri dishes each containing 80 ml of offshore seawater. Nutrients were added at same concentrations as A. The nutrient schedule was as follows: Dish 1--nutrients renewed every day; Dish 2--renewal every 2 days; Dish 3--every 3 days; Dish 4--every 4 days; and Dish 5--every 5 days. Between feeding times nutrients were allowed to be depleted by the growing gametophytes. Irradiance for C was 8.30 $\mu E/m^2/sec$ (i.e. above the light-saturation irradiance determined by Culture B).

Culture D was started and maintained similar to C except 150 ml of seawater per dish was used to ensure a large reservoir of nutrients. Nutrients were not allowed to be depleted in the dishes as in C. The schedule of nutrient feedings was as in C but water was changed every day in all dishes so that the gametophytes were pulsed in nutrient rich media for about 1 day, then starved in nutrient poor media for either 1,2,3 or 4 days depending on the dish.

Culture E investigated toxicity levels of PCBs. Again we started E in a shoebox and grew it under conditions similar to A for 6 days. Then the gametophytes were transferred to 5 petri dishes containing 100 ml of differing test media: plain filtered seawater(Dish 1), 0.2 ml acetone/l seawater(2), 1.156 $\mu g/l$ PCB(3), 5.780 $\mu g/l$ PCB(4), and 11.56 $\mu g/l$ PCB(5). Solutions were made by dissolving 5.78 mg of 4,4'-dichlorobiphenyl in 100 ml of acetone. 0.2 ml of this solution was added to 1 liter of filtered seawater (0.45 μm Millipore filter) to render a 11.56 $\mu g/l$ PCB concentration. Appropriate dilutions were made to give solutions of 5.780 and 1.156 $\mu g/l$ each also containing 0.2 ml acetone/l seawater. 0.2 ml of plain acetone was mixed with another liter of water to give an acetone control (Dish 2). Dish 1 received plain seawater and acted as the primary control. All seawater was filtered. Solutions and nutrients were renewed daily in all dishes. Each solution was shaken for one full minute before being added to the culture to ensure homogeneous distribution of the acetone and PCBs. Nutrient concentrations were same as for A.

RESULTS

The control curves for Cultures B,C and D were plotted(longest dimension vs. day, Figure 1) using the method of the geometric mean

estimate of the funcional regression of Y on X(GM regression) after Ricker(1973). Control D showed two distinct linear regions which are represented as D and D'. The slopes of the control lines differed significantly at the 95% confidence level. Thus we concluded that rates of growth of gametophytes could only be compared to controls within a culture and not between cultures. In other words, it was necessary to have a control for each culture. On this basis, we discarded the concept of a "normal" growth curve which we had presumed would result from Culture A.

The possibility of significant variation in growth rates between slides located in the same container was also considered. However, after comparing means and 95% confidence limits of the growth on slides raised in the same container under similar conditions, no significant differences were found. Culture A, petri dishes 3,4 and 5 of Culture B, and Culture E(first 6 days only) were used for this observation. In every case, means calculated from slides which were maintained in the same container overlapped at the 95% confidence level.

The gametophytes of Culture B exposed to 1/2,1/3 and 1/10 full irradiance were all found not to differ significantly at the 95% confidence level. This indicated that light saturated growth occurs at irradiances as low as 1.10μE/m^2/sec. This level agrees within our experimental error with Lüning and Neushul(1978) who found gametophyte growth light saturated at about 2μE/m^2/sec. Cultures C,D and E, all grown under an irradiance of 8.30μE/m^2/sec,were thus fully light saturated.

Due to a misunderstanding Culture C was not a pulsing experiment as it was intended to be. However, even though the nutrients were allowed to remain in the dishes between feedings, the gametophytes undergoing the 4 and 5 day nutrient addition regimes did poorly. The shortage of one or more trace elements usually found in seawater necessary for gametophyte growth was considered as a possible cause (Kuwabara,1980). Dishes that had their water changed more frequently would not experience these trace element shortages. We also examined another possible cause for poor growth, namely an insufficient supply of nitrate. A very rough estimate of the amount of nitrate needed for normal growth was made based on the nitrogen demands of the adult M. pyrifera sporophytes and assuming that gametophytes had similar requirements. We concluded that an inadequate supply of nitrate was probably responsible for the poor growth and subsequently increased the nitrate available for gametophyte uptake in Culture D to alleviate this problem.

The growth curves for Culture D and plotted in Figure 2 using the GM regression. Bacterial contamination was a problem with this culture, particularly for the control gametophytes. The two linear regions, plotted in Figure 1 as D and D', are plotted here as 1 and 1'. Due to the large 95% confidence interval of 1' and apparent inconsistency of the graph (possibly resulting form serious bacterial contamination), the control curve was discarded. However, differences in slope of the plots of Dish 2, Dishes 3 and 4, and Dish 5 were significant at the 95% confidence level. Dish 2 had the steepest slope. Dishes 3 and 4 had comparable values for the middle slope while Dish 5 had the smallest slope. Starving the gametophytes definitely had a detrimental effect on their rate of growth. In addition, diatoms were present in all dishes and seemingly survived starvation periods

better than the gametophytes.

The slope of all regression lines from Culture E, except that for Dish 4(5 μg/l), were not significantly different at the 95% confidence level (Figure 3). However, the confidence interval for Dish 4 lay within 0.002 points of those for Dishes 1,2 and 3 and overlapped that of Dish 5 so significance of the difference was questionable. Possibly an unknown adverse factor became manifest in Dish 4.

CONCLUSIONS

The use of nutrient pulsing in laboratory cultures of Macrocystis pyrifera gametophytes as a means to control contamination by marine diatoms proved unsatisfactory. The gametophytes do not possess the ability to develop and/or utilize internal nutrient reserves to the extent needed to kill diatoms by starvation. Concentrations of PCBs up to about 10 μg/l did not seem to have a significant effect on gametophyte growth, except for unexplained poor performance by gametophytes in Dish 4 at an intermediate PCB concentration. The uncertainty resulting from Dish 4 necessitates that this experiment should be repeated to verify lack of toxicity by 4,4'-dichlorobiphenyl concentrations of 10 μg/l or less. Light saturated growth occurred at about 1.10 μE/m^2/sec. Growth rates of gametophytes could only be compared within a particular culture as natural variability between cultures proved significant.

ACKNOWLEDGEMENTS

I would like to extend my thanks and appreciation to Dr. North whose help, understanding and patience made this project a real worthwhile experience for me. I would also like to thank Steve Manley whose suggestions and labcoat were invaluable.

REFERENCES

Bascom, W.: Unrealistic Toxicity Tests in Letter to the Editor. Coastal Ocean Pollution Assessment News. 3, 15 (1983).

Gerard, V. A.: Growth and Utilization of Internal Nitrogen Reserves by Giant Kelp, Macrocystis pyrifera, in a Low Nitrogen Environment. Marine Biology. 66, 27-35 (1982).

Harding, L. W., Jr. and J. H. Phillips, Jr.: Polychlorinated Biphenyl (PCB) Uptake by Marine Phytoplankton. Marine Biology. 49, 103-111 (1978).

Kuwabara, J. S.: Micronutrient Requirements for Macrocystis pyrifera (L.) C.A. Agardh (Giant Kelp) Gametophytes Determined by Means of a Chemically Defined Medium, Aquil. Ph. D. Thesis, California Institute of Technology, Pasadena, CA. 170 pp. 1980.

Lüning, K.: Light (Chapter 9) in The Biology of Seaweeds, 786 pp. C. S. Lobban and M. J. Wynne, eds. Berkeley: University of California Press 1981.

Lüning, K. and M. Neushul: Light and Temperature Demands for Growth and Reproduction of Laminarian Gametophytes in Southern and Central California. Marine Biology. 45, 297-309 (1978).

Ricker, W. E.: Linear Regressions in Fishery Research. J. Fish.Res. Board Can. 30, 409-434 (1973).

Schafer, H.: Characteristics of Municipal Wastewaters in Biennial Report of SCCWRP 1981-1982. W. Bascom, ed. Long Beach, CA 1982.

Sverdrup, H. U., M. W. Johnson and R. H. Fleming: The Oceans, 1087 pp. New York: Prentice-Hall, Inc. 1946.

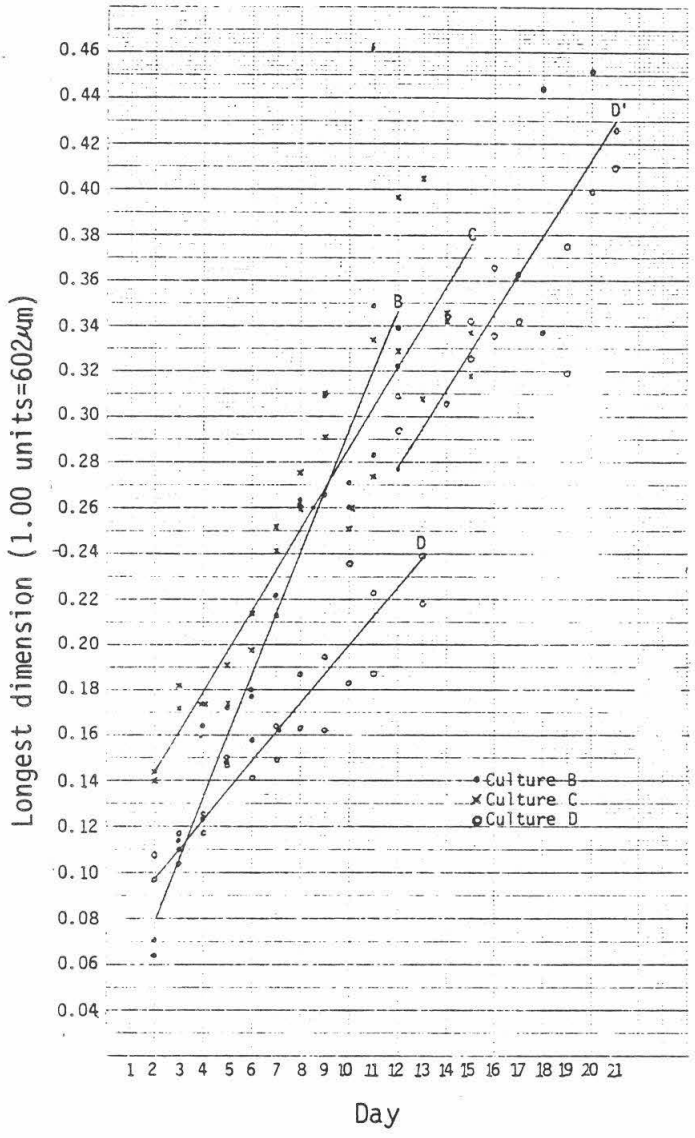

Figure 1. Control curves for Cultures B, C and D Longest dimension of gametophytes is plotted against day of growth using GM regression. Each point represents the mean of 20 gametophytes from the same slide. Regression equations are as follows with 95% confidence limits given in parentheses:

B: $y=0.027(\pm 0.003)x + 0.024(\pm 0.021)$
C: $y=0.018(\pm 0.003)x + 0.107(\pm 0.026)$
D: $y=0.013(\pm 0.002)x + 0.070(\pm 0.014)$
D': $y=0.017(\pm 0.006)x + 0.074(\pm 0.101)$

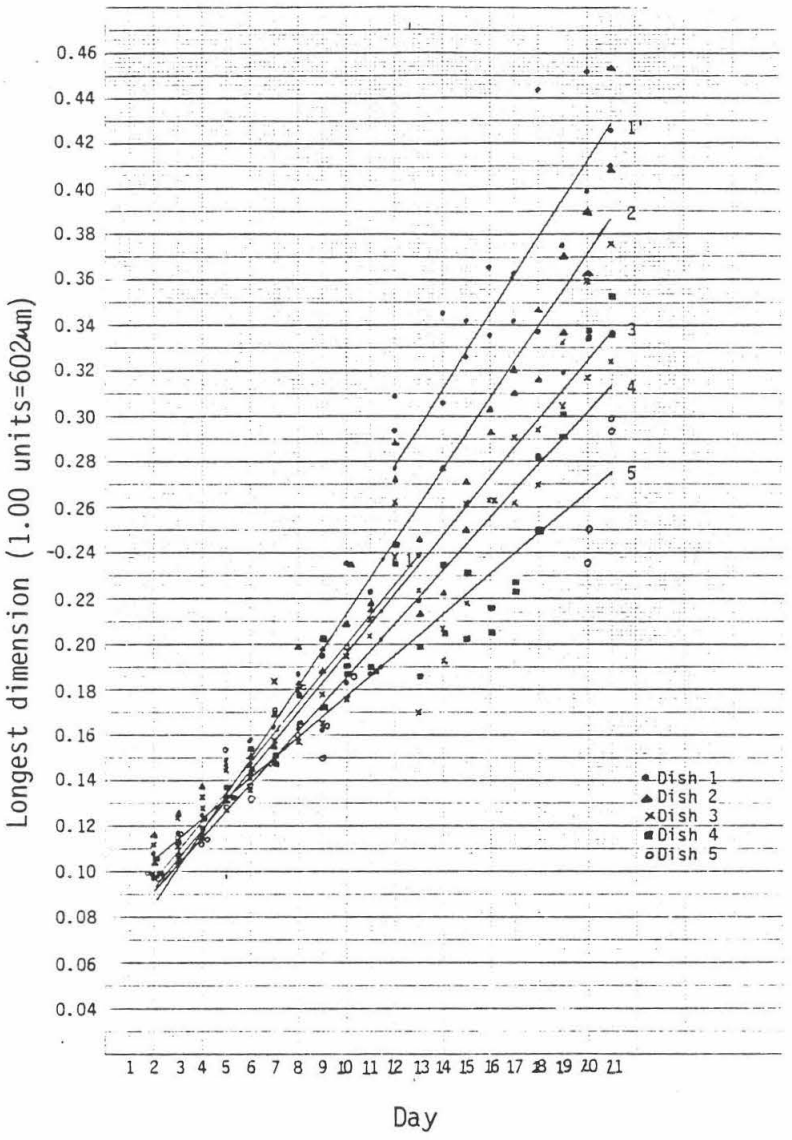

Figure 2. Growth curves for Culture D are plotted using same procedure as for Figure 1. Regression equations are:

Dish 1 (control) : $y=0.013(\pm 0.002)x + 0.070(\pm 0.014)$
1' : $y=0.017(\pm 0.006)x + 0.074(\pm 0.101)$
2 (2nd day renewal): $y=0.016(\pm 0.001)x + 0.053(\pm 0.012)$
3 (3rd day renewal): $y=0.013(\pm 0.001)x + 0.066(\pm 0.009)$
4 (4th day renewal): $y=0.012(\pm 0.001)x + 0.067(\pm 0.009)$
5 (5th day renewal): $y=0.009(\pm 0.001)x + 0.087(\pm 0.011)$

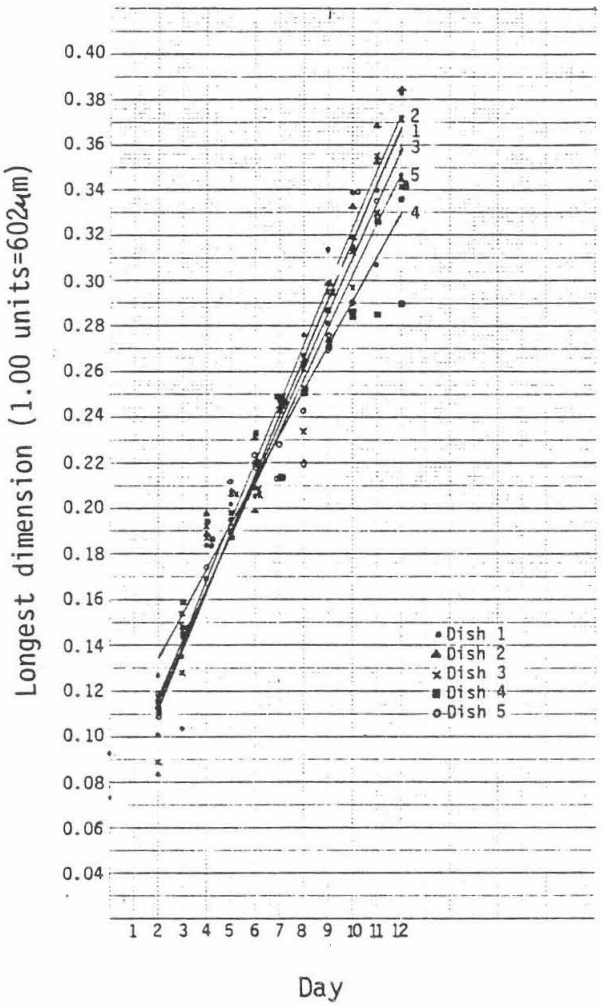

Figure 3. Growth curves for Culture E are plotted using same procedure as for Figure 1. Regression equations are:

Dish 1 (control) : $y=0.026(\pm 0.002)x + 0.060(\pm 0.014)$
2 (acetone control): $y=0.026(\pm 0.002)x + 0.064(\pm 0.014)$
3 (1μg/l PCB) : $y=0.025(\pm 0.002)x + 0.065(\pm 0.014)$
4 (5μg/l PCB) : $y=0.020(\pm 0.002)x + 0.093(\pm 0.014)$
5 (10μg/l PCB) : $y=0.023(\pm 0.002)x + 0.073(\pm 0.014)$

ELECTRICAL PROPERTIES OF $MOSI_2$

Wen Teh Chang
Sponsor: Dr. M-A. Nicolet and M. van Rossum

ABSTRACT

Electrical characteristics of thin film hexagonal $MoSi_2$ have been determined . The $MoSi_2$ films were obtained by ion mixing of as-deposited Si/Mo bilayer at 420°C with 300 keV Xe^+ ions at a dose of $5x10^{15}$ ions/cm^2 and by thermal annealing of as-deposited Si/Mo bilayer. $MoSi_2$ converts from the hexagonal to the tetragonal phase at ~700° C. Carrier concentration indicates that hexagonal $MoSi_2$ is not semiconducting.

INTRODUCTION

Metal silicides are studied for their possible use as gate interconnects and contacts in VLSI technology. Most silicides exhibit metallic conduction properties. $CrSi_2$ is an exception since it is semiconducting. Its crystal structure is hexagonal (C40). $MoSi_2$ has 2 phases, the hexagonal (C40) and the tetragonal phase. The hexagonal phase is the low temperature phase and has the same crystal structure as hexagonal $CrSi_2$. Therefore it is of interest to see whether $MoSi_2$ is semiconducting. Tetragonal $MoSi_2$ which is the high temperature phase has already been examined and found to be non-semiconducting [1] but the low temperature phase has still yet to be examined.

PRESENTATION AND DISCUSSION OF RESULTS

1. $MoSi_2$

The first step in making $MoSi_2$ was to prepare a Si/Mo bilayer. The substrate was a N-type (111) silicon wafer with a layer of SiO_2 grown on top. The substrate was cleaned by TCE, acetone, and methanol and dry-blown with N_2. A film of Si (2500 A°) and Mo (500 A°) were then deposited on the substrate by e- gun evaporation. Samples of the Si/Mo bilayer were then irradiated with 300keV Xe^+ ions at 420°C for 5 dose levels: 3x, 5x, 7x, 9x, and 10x 10^{15} ions/cm^2. The sheet resistance of each sample was determined from four point probe measurements and plotted against the corresponding dose. (See Fig. 1.). X-ray analysis after $5x10^{15}$ ions/cm^2 irradiation indicates formation of hexagonal $MoSi_2$ with no detectable Mo left unreacted. So a suitable dose to produce $MoSi_2$ at 420°C is $5x10^{15}$ ions/cm^2.

Two samples, one being an as deposited Si/Mo bilayer and the

other being a Si/Mo bilayer ion mixed at 420°C with $5x10^{15}$ ions/cm^2 , were thermally annealed in forming gas. All annealings were 30 minutes long. The unmixed bilayer was consecutively annealed between 200°C and 400°C in 100° steps. The ion mixed bilayer was annealed together with the now thermally mixed bilayer from 500°C to 900°C in 100° steps. At each temperature, Hall effect measurements and four point probe measurements were taken on the samples. (See Table 1.). From this information a plot of sheet resistance versus annealing temperature was made. (See Fig. 2.). The sheet resistance of the ion mixed bilayer is 20.9Ω/□ at first, rises to a peak value of 47.3Ω/□ after 700°C annealing and then drops to 14.3Ω/□ after annealing at 900° C. Other ion mixed bilayers begin with a sheet resistance of 40 to 50Ω/□ before annealing which suggests the presence of unreacted Mo in the sample of Fig 2a. However unreacted Mo is not conclusive from X-rays. After the drop in sheet resistance above 700° C X-rays show that tetragonal $MoSi_2$ forms. This agrees with the earlier results of Tsai et al. [2]. The sheet resistance of the thermally mixed bilayer is 10.1Ω/□ at first, rises to 26.4Ω/□ and drops to 12.6Ω/□ . Sheet resistance remains low due to unreacted Mo which is present up to the annealing at 600° C as deduced from X-ray analysis. Tetragonal $MoSi_2$ forms completely after annealing at 900°C from X-ray analysis.

Hall effect measurements on the ion mixed bilayer and the thermally mixed bilayer indicate that the carriers are holes (p-type). The hole concentration of the ion mixed bilayer is $9.14x10^{22}$ /cm^3 before annealing and $1.1x10^{22}$ /cm^3 after annealing at 900 C. No significant decrease in hole concentration appears at the transition temperature (700° C). However there is a drop of a factor of 10 at 600°C from $3x10^{22}$ /cm^3 to $.37x10^{22}$ /cm^3 in the ion mixed sample. The hole concentration of the thermally mixed sample does not change significantly from annealing at 500°C to 700°C. After 700° C Hall voltage becomes too small to measure for the calculations to be meaningful.

To summarize, hexagonal $MoSi_2$ is formed by ion mixing a Si/Mo bilayer as shown by X-rays; annealing at >700°C yields tetragonal $MoSi_2$. Carrier concentration of hexagonal $MoSi_2$ is on the order of 10^{23} which is too high for hexagonal $MoSi_2$ to be semiconducting. Resistivity of ion mixed hexagonal $MoSi_2$ is ~400uΩ cm if the thickness of the $MoSi_2$ film is calculated from the thickness of the original bilayer of Si/Mo before ion mixing.

2. $CrSi_2$

For comparison hexagonal $CrSi_2$ was produced by ion mixing at 500° C at a dose of $1x10^{16}$ ions/cm^2 of Xe^+ at 300keV. Structural information of hexagonal $CrSi_2$ was deduced from X-ray diffraction measurements. The resistivity is ~3800uΩcm as deduced from four point probe measurements. Hall effect measurements indicate that the carriers are holes. Hole

concentration is on the order of 10^{23} /cm^3 and mobility ~2.49 cm^2 /V-sec. The hole concentration agrees closely with values in literature [3] although the mobility is a little low in comparison.

CONCLUSIONS

1. Hexagonal $MoSi_2$ is produced by ion mixing at 420°C at $5x10^{15}$ ions/cm^2 dose of Xe^+ at 300keV.
2. Hexagonal $MoSi_2$ has been formed by thermal annealing (needs more study).
3. Transition of $MoSi_2$ from hexagonal to tetragonal phase occurs at ~700°C.
4. $MoSi_2$ is not semiconducting. Carrier concentration of $9x10^{22}$ is too high.

BIBLIOGRAPHY

1. M-A. Nicolet and S.S. Lau,in VLSI Electronics: Microstructure Science. 6 (N.Einspruch,G. Larrabee eds.) 330 (1983).

2. M.Y. Tsai, C.S. Petersson, F.M. d'Heurle, and V. Maniscalco, Appl. Phys. Lett. 37(3), 295 (1980).

3. I. Nishida and T. Sakata, J. Phys. Chem. Solids. 39, 499 (1978).

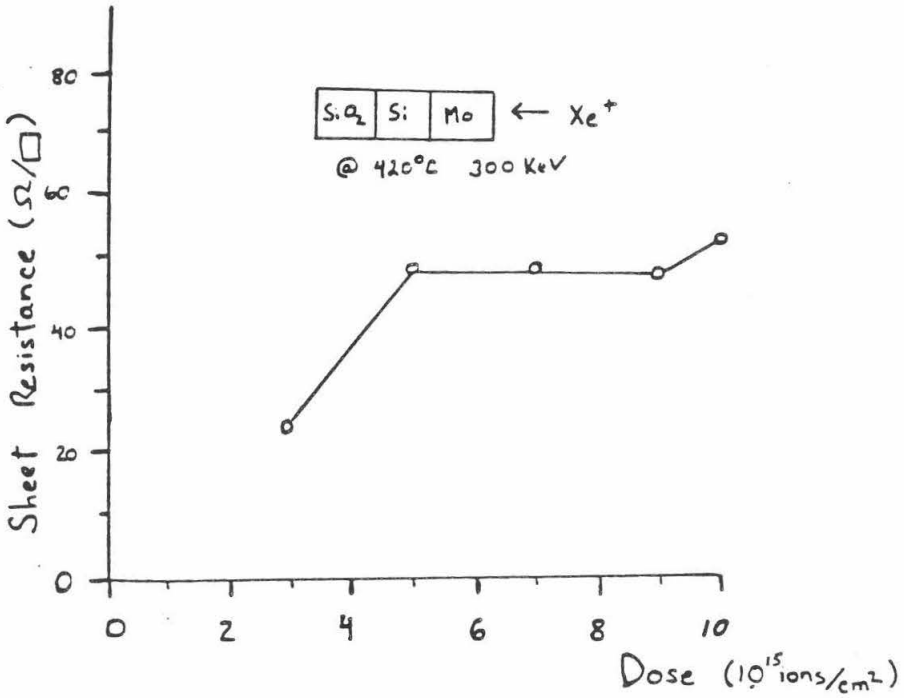

Fig. 1. Plot of Sheet resistance of Si/Mo bilayer ion mixed at various doses at 420°C

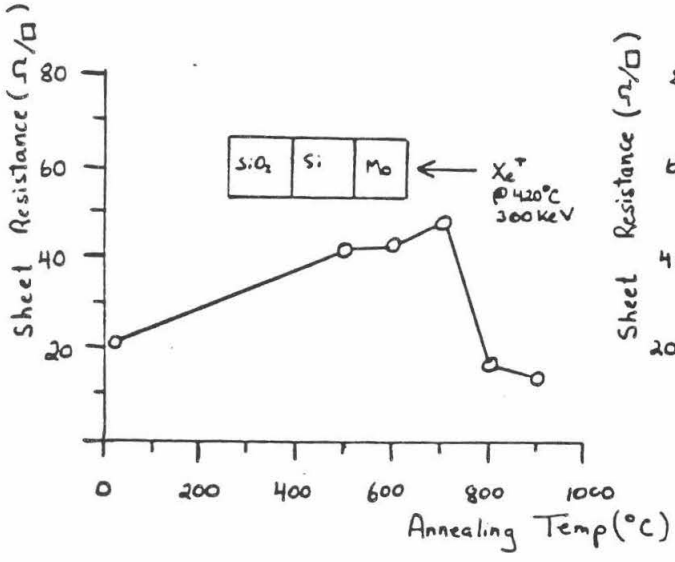

Fig. 2a. Sheet resistance of ion mixed $MoSi_2$ annealed between 500° to 900°C.

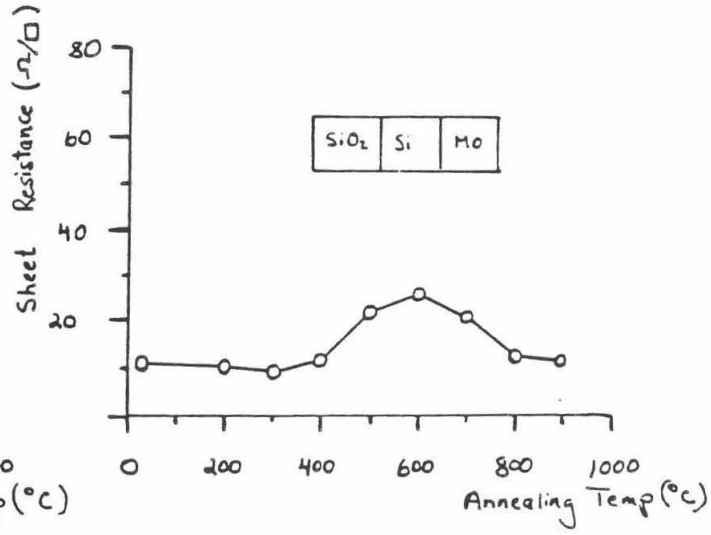

Fig. 2b. Sheet resistance of Si/Mo bilayer thermally mixed between 200° to 900°C.

All annealings were performed in forming gas for 30 minutes

Table 1. Electrical Characterization of Thermally Mixed and Ion Mixed Si/Mo bilayers at Varying Temp.

1: SiO_2 | Si | Mo — thermally mixed bilayer

2: SiO_2 | Si | Mo ← Xe^+ — ion mixed bilayer

	N		R_s		μ_p			N		R_s		μ_p	
	1	2	1	2	1	2		1	2	1	2	1	2
un-annealed	6.58	9.14	10.1	20.9	1.88	0.33	600°C	3.13	.37	26.4	42.9	—	3.94
200°C	6.58	—	10.0	—	—	—	700°C	5.81	.31	20.7	47.3	—	4.26
300°C	8.62	—	9.5	—	—	—	800°C	—	.83	13.7	16.9	—	4.4
400°C	16.5	—	10.9	—	—	—	900°C	—	1.10	12.6	14.3	—	3.97
500°C	6.7	3.0	22.7	42.3	—	0.49							

30 minute anneals

N - carrier concentration (10^{22} cm^{-3})
R_s - sheet resistance ($\Omega/\square$)
μ_p - hole mobility ($cm^2/V\text{-}sec$)

Table 2. Electrical Characterization of $CrSi_2$ and $MoSi_2$

	Preparation	Carrier Type	Carrier Concentration	Resistivity	Mobility
h - $MoSi_2$	ion mixed at 420°C.	p	$\sim 9 \times 10^{22}/cm^3$	$\sim 400\ \mu\Omega cm$	$\sim .3\ cm^2/V\text{-}sec$
t - $MoSi_2$	ion mixed at 420°C & annealed to 900°C	p	$\sim 1 \times 10^{22}/cm^3$	$\sim 140\ \mu\Omega cm$	$\sim 40\ cm^2/V\text{-}sec$
h - $CrSi_2$	ion mixed at 500°C	p	$\sim 6 \times 10^{20}/cm^3$	$\sim 3800\ \mu\Omega cm$	$\sim 2.5\ cm^2/V\text{-}sec$
*h - $CrSi_2$ [3] (from literature)	—	p	$7.8 \times 10^{20}/cm^3$	—	$\sim 13\ cm^2/V\text{-}sec$

h - hexagonal, t - tetragonal

THE CRITICAL BEHAVIOR OF THREE DIMENSIONAL ISING MODEL WITH INTERACTION DISORDER

ABSTRACT

A study is made of the three dimensional Ising model on a simple cubic lattice of size 10 x 10 x 10 with interaction disorder. The Monte Carlo importance-sampling method was employed, and the simulated results show a gradually smeared phase transition and deformed magnetization curves with shifted transition temperature as a result of the increasing magnitude of disorder.

Yi-Hong Chen

sponsored by

Dr. William L. Johnson

1. INTRODUCTION

In order to derive the thermodynamic properties of a system from the statistical theory, a certain physical model has to be used to describe the Hamiltonian of the system. Of the many physical models formulated for crystal and amorphous solids, the Ising model is a simple but yet widely applied model.

In the Ising model, each lattice site has a spin value of +1 or -1 and the Hamiltonion of the system with nearest-neighbour interaction is written as:

$$H = -\sum_{i>j} J_{ijk}\, s_i s_j - \sum_i h_i s_i$$

Where J_{ijk} is the interaction coefficient, and h_i the local external magnetic field.

Partly due to the lack of an analytic solution to the 3-d Ising problem and partly due to the requirement of the study of local disorder, computer simulation methods have been found to be extremely helpful for investigating the thermodynamic properties of crystalline and amorphous materials derived from the physical theory. Both the Monte Carlo renormalization group method and the ordinary Monte Carlo method have been used to study the Ising model in a random field $h_i = \pm H$ and a transition to a ferromagnetic state in a weak random field was found in three dimensions. In two dimensions it has been shown that there is a "smeared phase transition".

The objective of the project is to study the critical behaviour of the three dimensional Ising model with random interaction coefficients $J_{ijk} = (1 \pm b)J$ on a 10 x 10 x 10 lattice with periodical boundary conditions.

2. METHODS AND RESULTS

A. Monte Carlo (MC) Arbitrary Sampling Method

At the beginning of the project I used MC method with arbitrary sampling. The purpose of the method is to calculate the partition function of the system by randomly creating a large number of spin configurations to resemble the presence of all possible configurations of the system. From the energy density function thus produced, by integration:

$$Z = \int_0^\infty D(E) e^{-E/kT} dE$$

the partition function of the system could be found. From the partition function the entropy, free-energy and heat capacity could be calculated

readily:

$$S = k\ln Z$$

$$F = - kT\ln Z$$

$$C = \frac{\partial S}{\partial T}\ T \quad .$$

The result obtained from the method showed that it failed to generate a sharp phase transition at a critical temperature for the completely ordered lattice (crystal) even when the number of the randomly created configurations is as large as 10,000. Further analysis of the method revealed that the fallacy of the method is due to the fact that at temperatures around or below the critical temperature the most significant contribution to the partition function comes from those configurations with very large magnitudes of magnetization M, i.e. the configurations with large numbers of aligned spins. By letting each spin assume a value of +1 or -1 randomly, there is very little possibility that we can create a configuration with most of the spins having the same spin value; namely, the most important configurations were not among the samples randomly generated. So in the arbitrary sampling method, the accurate information at and below critical temperature is lost.

B. Series Expansion of Partition Function

Following the disappointment of the MC random sampling method, I tried to find an approximate analytic solution to the problem. To avoid the mistake in the previous method, the partition function is expanded as a sum over all different values of magnetization M. The main task of the method is to describe the energy level of a certain configuration in terms of M and other parameters. The energy is calculated in this way:

Suppose the total number of spins is N and the number of up spins is $N_\uparrow$, then $M = N_\uparrow - N_\downarrow$; $N = N_\uparrow + N_\downarrow$. Then the total number of all the configurations with $N_\uparrow$ up spins is $N!/N_\uparrow!\ (N - N_\uparrow)!$.

In the case where all of the $N_\uparrow$ spins are isolated from each other, the energy of the configuration due to the interaction is:

$$E = -J(N\ell/2 - 2N_\uparrow\ell)$$

where ℓ is the number of the nearest neighbours around a lattice site ($\ell = 6$ for simple cubic lattice), and $N\ell/2$ is the total number of pairs of spins. If we imagine whenever two originally separated up spins join together to be nearest neighbours a bond is then formed between them. When one such bond is formed, the energy level of the system will change by 3J. Since, the product of spin values between the original two spin neighbour pairs were -1, and these are replaced by the new product 1 between the same up spins:

$$J - (-2J) = 3J.$$

So the configuration with $N_\uparrow$ up spins and with n bonds between the up spins, have energy:

$$E = - J (N\ell/2 - 2N\ell + 3n).$$

From Bernoulli trials we can expect that the possibility function for a configuration to have n bonds in it will assume the form of Poisson distribution. Since the average number of bonds is:

$$A = (N\ell/2) (N_\uparrow/N) (N_\uparrow - 1/N-1).$$

Then the probability function is:

$$p(n) = \exp (-A) A^n/n!.$$

With this we can sum up the contribution from all configurations to the partition function:

$$Z = \sum_{\text{all states}} \exp(-E/kT) = \sum_{M=-N}^{N} \exp(-HM/kT)(N!/N_\uparrow!(N-N_\uparrow)! \sum_{n=o}^{n_{max}} p(n)\exp(-E(N_\uparrow,n))/kT)$$

$$= \sum_{N_\uparrow=o}^{N} \exp(-H(2N_\uparrow - N)/kT)(N!/N_\uparrow!(N-N_\uparrow)! \sum_{n=o}^{n_{max}} \exp(-A)A^n/n!\exp(-J(N\ell/2-2NL+3n)/kt)$$

Though this method provided an approximate analytic solution to the problem, it is impossible to use it to introduce randomness into the interaction coefficients. It seems that the computer simulation method has to be used to study systems with local disorder.

C. Monte Carlo Importance-sampling Method

The new approach I used was the MC importance-sampling method. In this method the configurations are sampled according to a probability exp(-E/kT). To do this I wrote a program in which the spins of the system all started with a certain configuration, say, all the spins are up, then I go through each lattice site to compare exp(ΔE/kT) with a number x randomly drafted between 0 and 1: if x is smaller than exp (ΔE/kT) then the spin on the site will be flipped, otherwise it remains the same. (ΔE is the energy change connected with the spin flip).

Usually after such a procedure has been applied to each lattice site several times, the system would reach its equilibrium configuration. For a higher temperature, the system starts with this configuration and then allowed to reach its new equilibrium through the above spin flip procedure.

The expectation values of M and E at a certain temperature can be obtained by simply calculating their arithmetic averages, since the weighting factor EXP(-E/kT) is already contained in the sampling.

The result shows that this method succeeded in generating a sharp phase transition at a critical temperature for crystalline material. (Fig. 3, curve for heat capacity with b = 0). This should not be surprising at all, since in the real physical situation a phase transition occurs as a consequence of the competition between the energy and the entropy of the system, and the spin-flipping procedure in this method just emulated this competition.

Being assured that this method could represent the real physical situation of a perfectly ordered crystal lattice, I substituted the J_o = const. in regular lattice by J_{ijk} that take on two different values $J_{ijk} = (1 \pm b)\, J_o$ randomly. The result thus obtained shows a gradually smeared peak of heat capacity with increasing values of b, and the temperature at which the peak of the heat capacity occurs (as well as the temperature region where the magnetization change most rapidly) shifted to smaller values. (Fig. 3 with b = 0.5 - 2.0).

These heat capacity curves are quite similar to those obtained from I. Morgenstern, K. Binder and R. M. Hornreich's study of the two dimensional Ising model in a random field $h_i = \pm h_i$.[1] And it seems that the peaks are smeared to the same degree with the same magnitude of disorder, except in random interaction situation when b becomes larger than 1 where some of the interaction coefficients become negative and a frustration of the spin in lattice structure causes a large fluctuation in the heat capacity.

The curves of the magnetization vs. temperature also show a gradual change in shape as the value of b is increased. (Fig. 1) The group of curves obtained from different values of b appear very much the same as the group of curves calculated from Handrich model[3] with different values of δ (δ is the standard deviation of the structure fluctuations in the disordered structure), though for a similar curve the structure fluctuation in the Ising model has to be twice as large, i.e. $b \sim 2\delta$.[4] Since many experimental results on crystalline and amorphous magnetic materials have already been fitted into Handrich model successfully, we can expect these results to fit into the Ising model with interaction disorder too, with a proper value of b.[2]

One small though noticeable feature of these magnetization curves is that there is a small dip in the curve at the temperature right above the transition temperature (except for the case when b is larger than 1), followed by a series of decreasing fluctuation around zero magnetization. This feature, being unable to be either explained by theory or verified by experiment, is probably caused by the finite size of the lattice under study. This can be understood intuitively as: when the lattice size is finite and a periodical boundary condition is imposed, certain spacial frequencies are either lost from or added to the system and this change in the Fourier components caused the "ringing effect" at the turning edge of the curve.

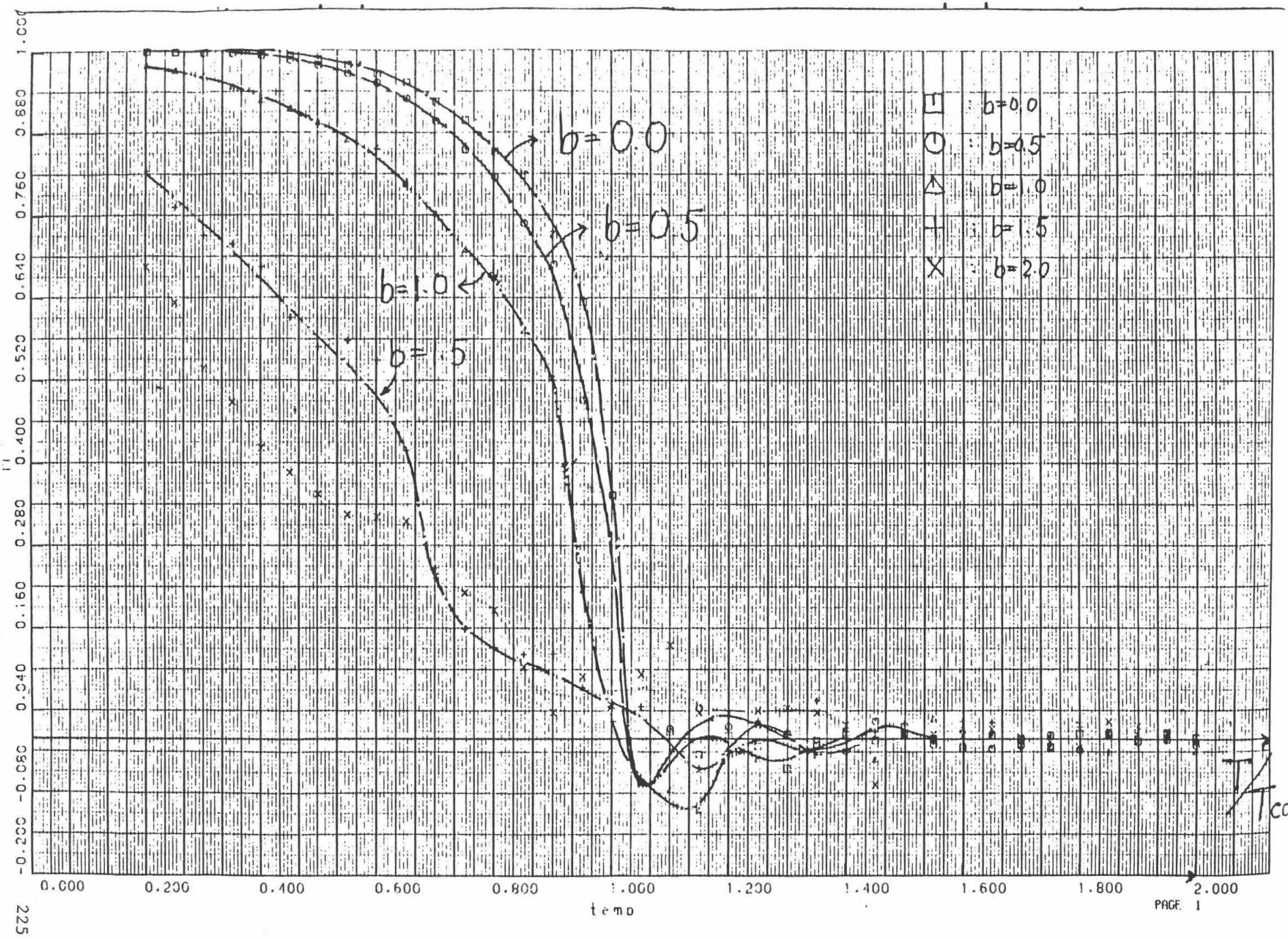

ig. 1. Magnetization vs. temperature curves. The x-coordinate is the ratio of the temperature of the system to the critical temperature of the three dimensional Ising Lattice with perfect order (J_o/kT_{co} = 0.221655) [1]

The same temperature scale is used for Fig. 2 and Fig. 3 as well.

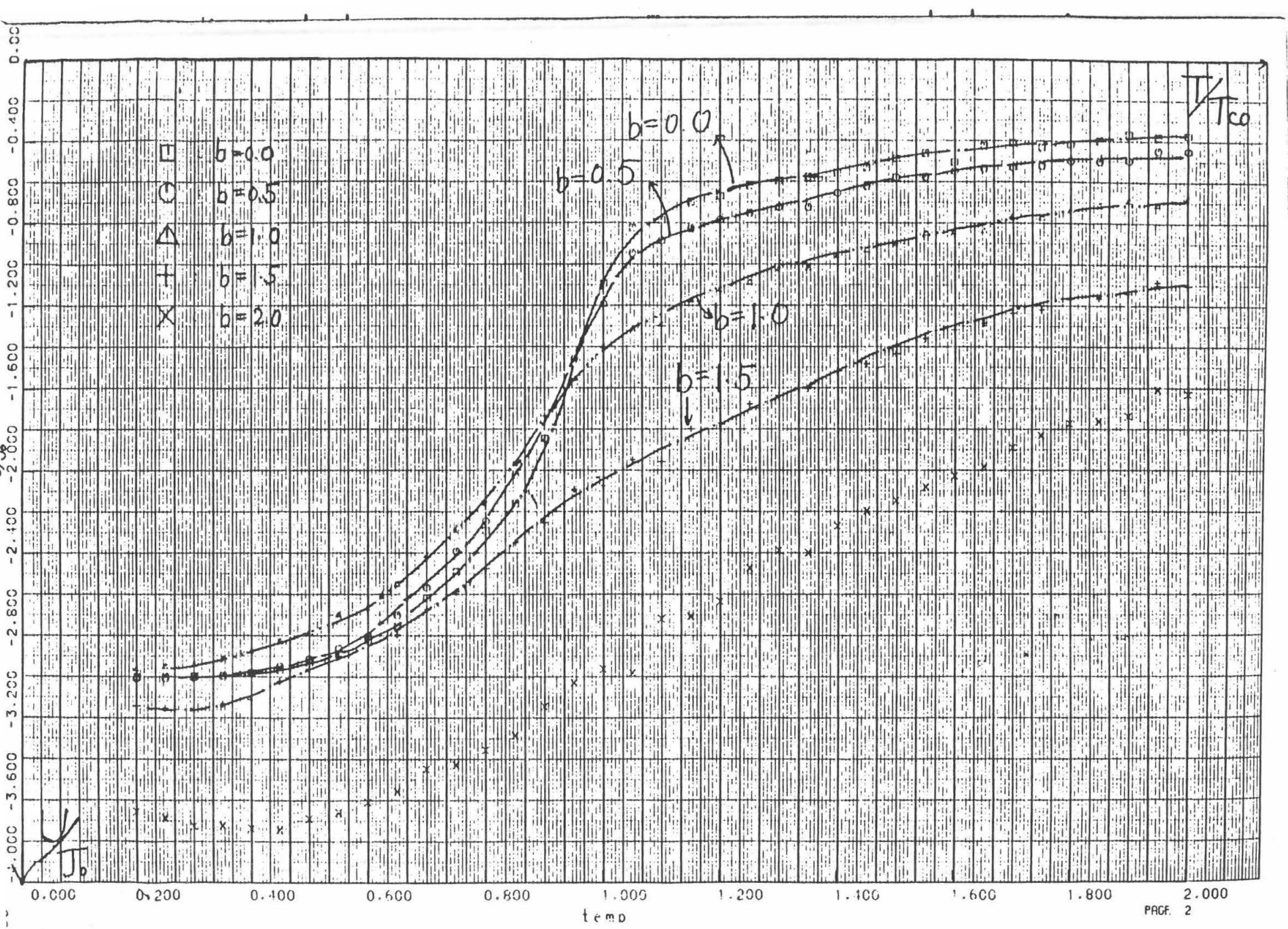

Fig. 2. Internal energy (scaled as $\frac{u}{J_o}$) vs. temperature (shown as a ratio to the critical temperature T_{co}).

Fig. 3. Heat capacity (scaled as $C \times \frac{T_{co}}{J_o}$) vs. temperature (the same temperature scale as in Fig. 1 and Fig. 2).

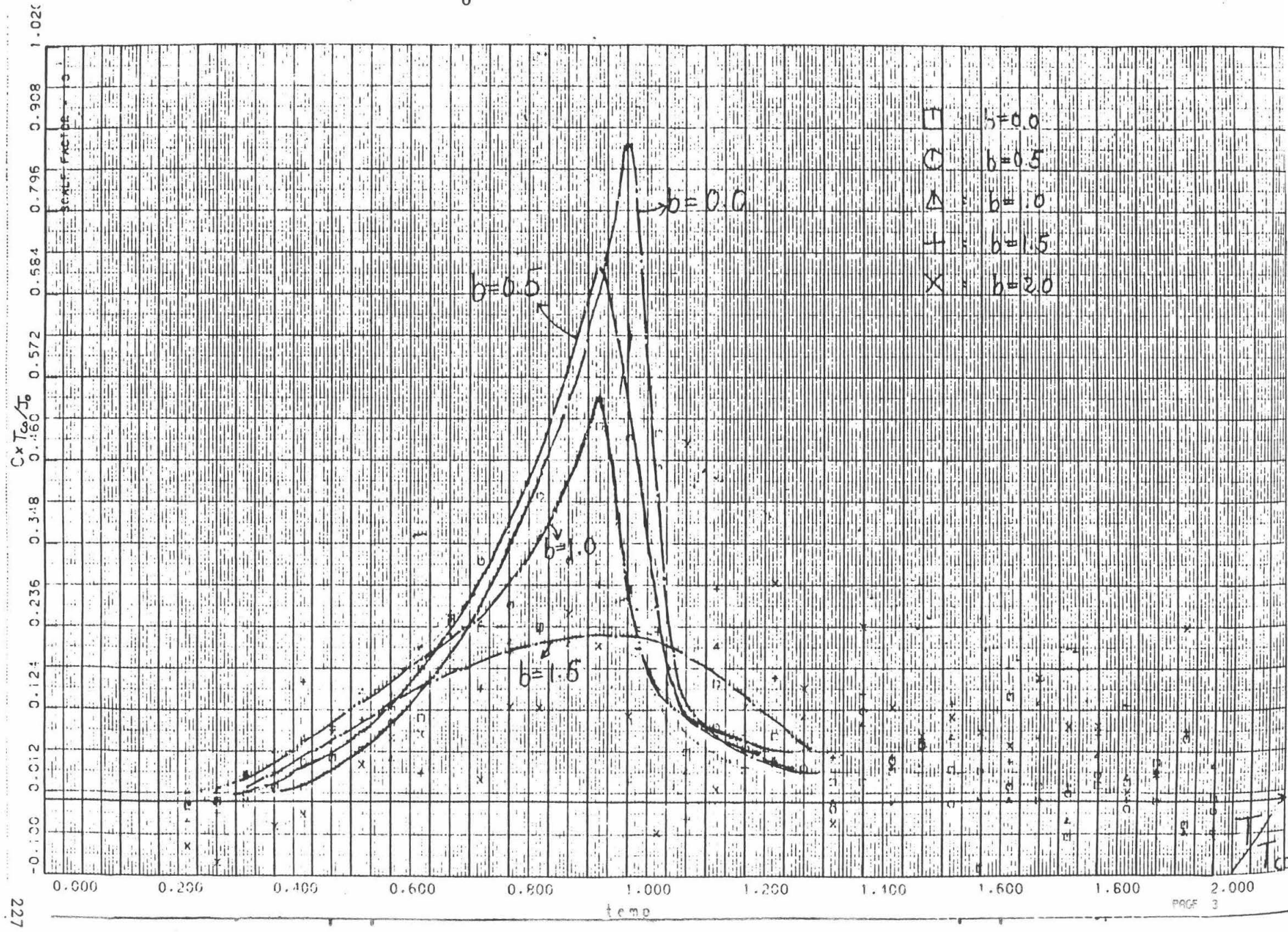

3. CONCLUSION

The study in this project validated the possibility of using the Ising model with random nearest neighbour interactions of the form

$$J = J_o(1 \pm b)$$

to describe the thermodynamic properties of amorphous magnetic materials, with the aid of Monte Carlo importance-sampling method. The computer simulated results from the model shows that when all the interaction coefficients are positive the phase transition is smeared and the transition temperature shifted as interaction disorder is introduced into the structure, in proportion to the magnitude of the interaction fluctuations: when the deviation of parameter fluctuation become so large that some of the interaction coefficients become negative (b larger than 1) frustration in the structure destroys the transition and large fluctuations in the thermal quantities occur.

The simulated results are also consistent with the results calculated from the Ising model in the random field for heat capacity and from the Handrich model, which is based on the Heisenberg model[3], for magnetization curves (Fig. 4), and the experimental results obtained from amorphous magnetic materials can be fitted to the simulated results as well. (Fig. 5)[2]

Further study of the subject is going to be done on the Ising lattice gas model. The isothermal curves of magnetization vs. external magnetic field will be simulated and the pressure vs. volume isothermal curves thus obtained through lattice gas model will be compared with that from the experimental results.

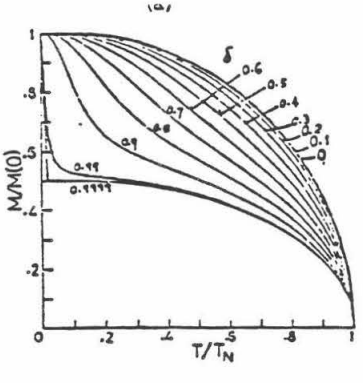

Fig. 4. The magnetization vs. temperature curves calculated from Handrich model.(4)

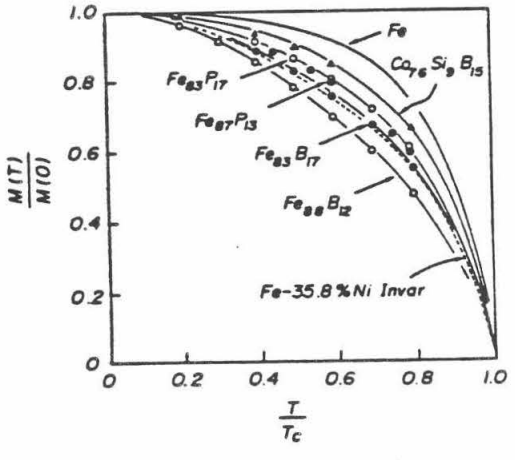

Fig. 5. Reduced magnetization curves of amorphous Fe-B and Fe-P alloys, together with those of amorphous $Co_{76}Si_9B_{15}$ alloy, crystalline Fe-35.8%Ni Invar alloy, and crystalline pure Fe.

REFERENCES

1. K. Binder, Application of the MONTE CARLO METHOD in Statistical Physics, Springer-Verlag Berlin, Heidelberg, 1984, Germany

2. K. Fukamichi, Rapidly Quenched Metals III, Vol. 2, 1978, p. 117, The Chameleon Press Limited, London

3. K. Handrich, Physica Status Solidi, Vol. 32, K55, 1969

4. Atsuko Ito, Amorphous Material--physics and technology-- p.83, Editorial Committee of the Special Project Research on Amorphous Material, 1983, Japan

Non-instrusive Measurement of Particle loading In Flow Through Pipes

Larry Chew

ABSTRACT

At present, there is no accurate, real time, non intrusive way of monitoring mass flow rate of pulverised coal through pipes in power plants. This causes incomplete combustion leading to pollution. A potential solution is Acoustic Resonance Measurement (ARM) which uses the fact that acoustic resonance will occur in fixed geometries at frequencies directly proportional to the sound speed. When small particles are suspended in the medium, the speed of sound is decreased. By measuring the reduction in the resonant frequencies, in principle one can infer the amount of solid material carried by the flow. In order to test this technique, an apparatus has been built consisting of a flow channel with a speaker and microphone attached to the test section. The driving frequency is slowly swept over a range and the amplitude signal picked up by the microphone. The peaks are recorded for different mass loading. However the predicted shift in peaks was not observed when powder was added. This is probably due to particles clumping together and thus increasing their effective diameter which reduces their effect on the sonic velocity. Since similar problems will exist in the coal dust, it is possible similar difficulties will be encountered in practical applications.

Non-instrusive Measurement of Particle loading In Flow Through Pipes

Larry Chew

1. Technical Problem

The ability to measure the flow through pipes of a two phase solid-gas mixture is an important industrial process. For example, in a power plant, pipes are used to feed coal-air suspension into various entrances of the furnace chamber. Since there is no accurate way of metering the flow rate and thus controllably and accurately manipulating it, an imbalance of coal flow into the furnace will occur, producing non-uniform combustion. One consequence of this is often unacceptably high levels of pollutants which is a problem to overcome. One solution suggested is the use of Acoustic Resonance Measurement (ARM). This method provides a measure of the ratio of mass of the particles to the mass of the mixture in the two phase medium by measuring changes in the resonant frequencies due to changes in the speed of sound caused by the presence of the particles.

The objective of this SURF project, then, is to use this ARM method to obtain an exact relationship between resonant frequencies and mass of particles in a pipe, providing a practical way of metering mass flow rate through pipes.

2. Theoretical Basis

Particles in a fluid both attenuate sound waves and reduce the speed of sound. Solid particles like coal dust suspended in a host gas affect the speed of sound primarily by changing the effective mass density of the fluid. This occurs if the particles are small enough to follow the fluid motion without lagging behind significantly (no slip condition). The decrease in the speed of sound is determined then by: $a^2 = a_0^2/(1+C_m)$ where a is the speed of sound in the mixture, a_0 is the speed of sound in pure air and C_m is the ratio of the mass of particles to the mass of gas in the mixture.

Theory, based on work by Temkin and Dobbins, shows that dispersion, the change in the speed of sound due to mass loading, depends on $\omega\tau$. ω is the frequency of the sound wave in radians per second and τ is the dynamic particle relaxation time which is a measure of how quickly a particle can respond to a change in the velocity of the surrounding fluid. Small particles respond quicker and thus their τ is small. According to Temkin and Dobbins, maximum dispersion occurs when $\omega\tau$ is

very small(no slip condition). For values of $\omega\tau$ greater than about 1, there is negligible effect on the speed of sound. For the frequencies of interest, this means that the particles must be less than 250 microns (~1/4 mm) to have an effect on the sound speed. Small particles move back and forth as the sound waves pass them and this increases the effective density of the fluid, whereas the larger particles cannot respond quickly enough and thus attenuate the waves without causing dispersion.

If air in a pipe is excited by an acoustic driver it will oscillate in two ways: longitudinally along the pipe and radially across the cross section of the pipe. A sketch of an oscillation in the transverse section of a pipe is shown in fig.1. These radial modes of oscillation will have their own natural resonant frequencies that depend on the diameter of the pipe, and on the speed of sound in the fluid in the pipe. Changing the density of the fluid will change the resonant frequency by changing the sonic velocity. Thus, by measuring the changes in the resonant frequencies, one can determine the particulate loading. This method is known as Acoustic Resonance Measurement (ARM).

3. Experimental Approach

The experimental set-up, illustrated in fig 2, consists of a 24" inside diameter cardboard tube with a microphone and speaker fixed diametrically opposite one another. The transmitted signal is obtained from a variable sine wave generator which is then amplified before being fed to the speaker. The signal is slowly swept over a range of frequencies. The microphone picks up the sinusoidal wave amplitude which has a peak at each resonant frequency. The signal is fed into a lock-in amplifier and finally recorded on a digital oscilloscope.

4. Results and Discussions

In the 24" diameter tube, the frequencies peaked at 338, 570, 703, and 777Hz which were identified as the (1,0); (2,0); (0,1); and (3,0) modes respectively. Note that the (m,n) mode means (number of nodal lines, number of nodal circle). This is shown in fig. 1.

To obtain different mass loading, talcum powder was weighed and added into the system. With a known powder weight and known volume of the system, the mass loading was calculated. 10 different amounts of powder ranging from 0oz to 40oz were added into the channel and the resonance frequencies recorded. For the maximum amount of powder, corresponding to a mass loading of 82%, a shift of 35% was expected. However

there was negligible frequency shift for all cases. The slight increase in temperature(2^{o} K) during the run was not enough to compensate for the expected decrease in the speed of sound. The talcum powder was observed to stick to the lucite walls of the test section due to static. It was suspected that the powder was accumulating elsewhere too. To reduce the problem, the flow channel was redesigned and rebuilt with a large cardboard tube and a stronger blower to help fluidize the flow. This did not solve the problem as there was still no shift in frequency.

If the powder was clumping together due to humidity, then the effect on the speed of sound would be reduced significantly as described earlier. To nullify this effect, a desiccant was suspended inside the channel to absorb any moisture present. This did not solve the problem either. It is felt that the powder must be clumping together for other reasons that remain unknown.

5. Conclusion

From the negative results obtained and the problems encountered in lab such as particle size distribution and effect of humidity, it seems that the ARM is too suceptible to external influences to be a good method to monitor mass flow rates. As it is, the problems faced in lab seem difficult enough and thus would be very difficult to overcome in a power plant environment where conditions are more difficult to control. On the other hand, certain difficulties with data aquisition suggest that this aspect of the technique should be examined more closely. Work on this project will continue during the coming academic year.

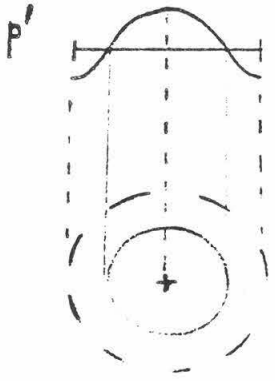

FIGURE 1. MODE (0,1) RESONANCE

Fig. 2 Schematic diagram of the apparatus for the acoustical resonance measurement.

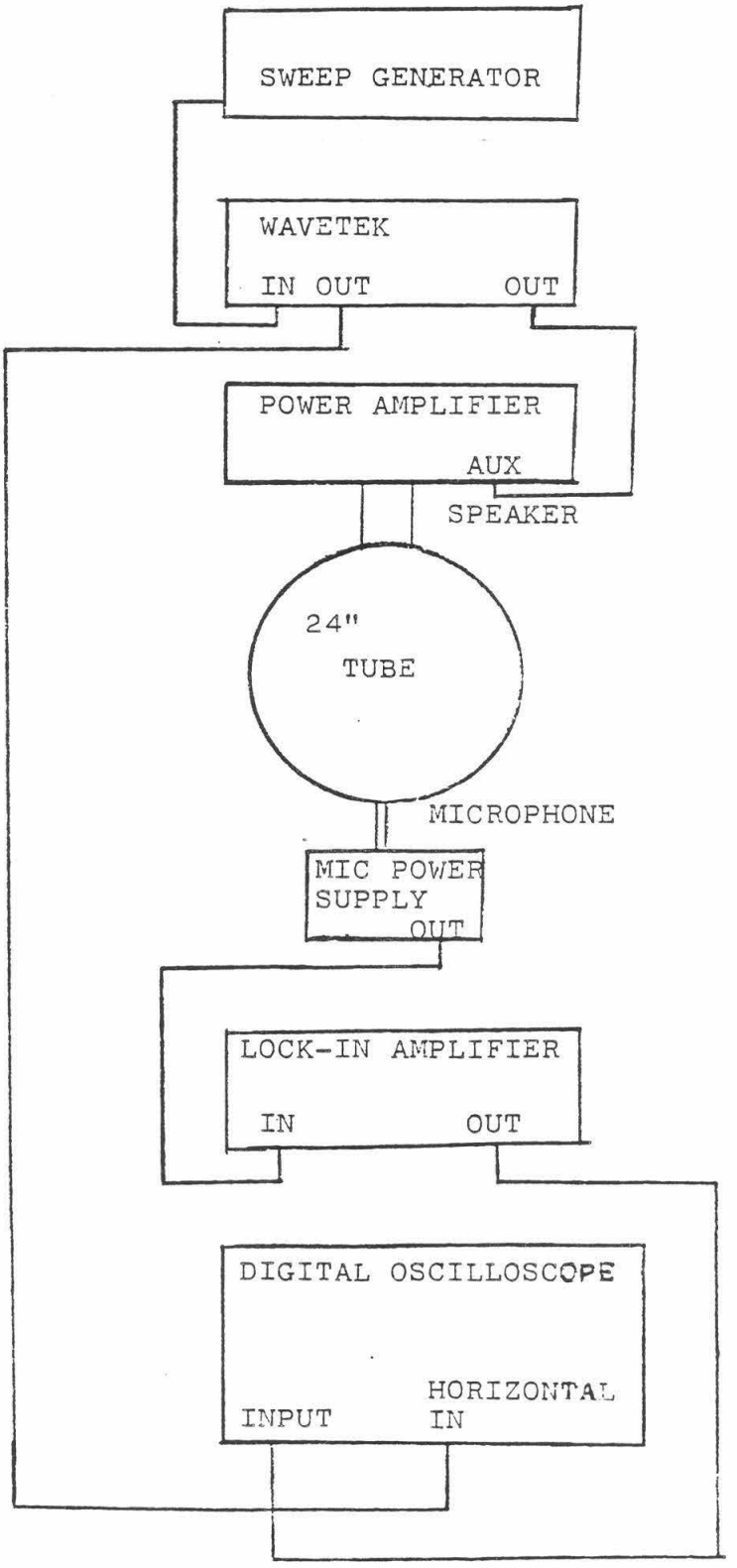

6. References

Morse P.M., Elements of Acoustics. Chap. 6, Wiley, 1948.

Temkin S. and Dobbins R.A., "Measurement of Attenuation and Dispersion of Sound by Aerosol", J. Acous. Soc. Am., Vol.40, #5, pp 1016-1024, 1966.

Vetter A.A., "Application of The Acoustical Resonance Reasurement To Determine Pulverized Coal Flowrate", Humbug Mountain Research Laboratories, Report HMRL-R-28B:3, 30th April 1982.

Spatial Characteristics and Sensitivity of the Photorefractive Incoherent-to-Coherent Optical Converter

Tammy L. Choy

Faculty Sponsor: Dr. Demetri Psaltis

Summer Undergraduate Research Fellowship
California Institute of Technology, Pasadena, California, 91125

ABSTRACT

Photorefractive bismuth silicon oxide incoherent-to-coherent optical converters have the potential to reproduce input images with high resolution.[1] In order to attain this potential, several properties must first be optimized. Two of these, the spatial frequency response and sensitivity, were investigated and the experimental technique and results are presented.

Spatial Characteristics and Sensitivity of the Photorefractive Incoherent-to-Coherent Optical Converter

Introduction

A problem in the area of optical processing occurs when an image needed by an optical system must be coherently illuminated but exists only in incoherent form. Thus, the recent demonstration of a simple incoherent-to-coherent optical converter utilizing a photorefractive $Bi_{12}SiO_{20}$ (BSO) crystal as the holographic recording media was an exciting developement.[2] It is believed that this converter will be able to function in real time producing coherent replicas with high resolution. However, before this can be accomplished, several important characteristics of the converter including spatial frequency response and sensitivity must be optimized.

Background

When two coherent beams of light are allowed to interfere within a photorefractive crystal, charge carriers are released from trap sites. The carriers, by means of diffusing and drifting in an externally applied electric field, are spatially redistributed and eventually become retrapped. This trapping induces a spatially varying electric field which modulates the index of refraction of the crystal through the electrooptic effect. The end result is a volume phase hologram recorded in the crystal. If the crystal is exposed to an incoherent beam containing the image to be converted, the grating is locally erased. Therefore, when the hologram is read out, areas illuminated by the incoherent beam diffract less light than those areas not illuminated. As a result, a negative reproduction of the input image is produced.[3]

Experimental Method and Results

The experimental set up is shown in Figure 1. The coherent writing and erasing beams are generated from an Argon laser of wavelength 488nm. The writing beams interfere within the BSO crystal to form a holographic grating with a spatial frequency of 450 lines/mm. The read out beam was produced by a helium–neon (He–Ne) laser of wavelength 632nm since the BSO crystal was not photosensitive at this wavelength. In our initial experiments, the incoherent image, another grating created by a Michelson interferometer, illuminated the crystal with a wavelength of 514nm and was incoherent with respect to the blue writing beam. It formed a grating whose spatial frequency could be varied from 0 to 50 lines/mm. The coherent read out was Fourier transformed so that the cross coupled orders could be separated from the DC order.

While the DC term is usually the order that passes directly through the crystal, I am using it to designate the main order that is diffracted due to the direct recording of the coherent grating. (Please see Figure 2.) The first orders are as indicated in the diagrams by +1 and –1.

Three experiments were carried out. The first was to determine if we could duplicate the previous study in creating an incoherent–to–coherent converter, the second to measure the spatial frequency response of the converter, and the final experiment to find the effect of changing the beam ratios on the diffraction efficiency.

We obtained good results from our incoherent–to coherent converter. After trying several gratings formed by the Michelson interferometer, it was replaced with a negative photographic slide. We continued using the green erasing beam to illuminate the image but also tried an incoherent white light source. A coherent image was produced as shown in Figure 3.

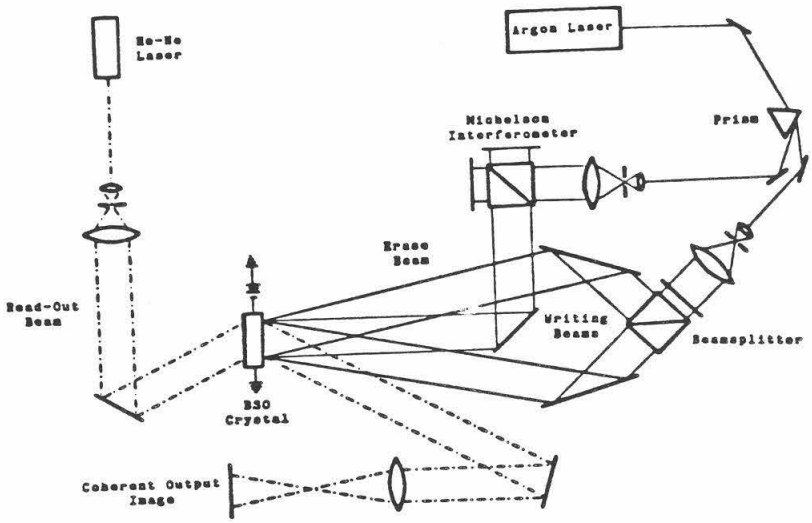

FIGURE 1

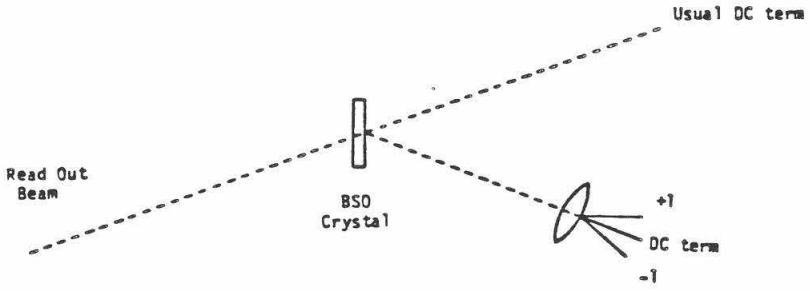

FIGURE 2

FIGURE 3

In the second phase, we tested the spatial response of the converter. Four separate measurements of the diffracted order were made as the spatial frequency of the Michelson interferometer was varied. Theory states that the spatial frequency response in lines per mm which is measured at one fourth of the peak diffraction efficiency should be $\frac{1.2\, n_o \Lambda}{\lambda_o T}$ for both incoherent and coherent fringes perpendicular to the face of the crystal where Λ is the fringe spacing, λ_o is the wavelength in air, T is the thickness of the crystal and n_o is the index of refraction.[4] It can then be shown that by allowing one of the beams to approach the crystal nonperpedicularly, a maximum spatial frequency response of $\sqrt{\frac{1.2\, n_o}{\lambda_o T}}$ can be obtained.[5]

The first experiment consisted of forming a grating in the direction of the electric field with the incoherent erasing beam intersecting the BSO crystal at a 90° angle. This resulted in a spatial frequency response of 6 lines/mm which is close to the theoretical value of 5 lines/mm.

The grating used in the second experiment was also formed in the direction of the electric field but this time the reading and erasing beams were collinear thus optimizing the Bragg matching condition. The spatial frequency response was 45 lines/mm as opposed to the theoretical value of 40 lines/mm.

These two experiments were repeated but the orientation of the grating was changed such that its wave vector was now perpendicular to the electric field. Theory predicted a value of 40 lines/mm since creating the grating perpendicular to the electric field automatically optimizes the Bragg condition. However, a spatial frequency response between 20 and 30 lines/mm was obtained for both experiments.

In the final set of experiments, an attempt was made to find the best beam ratio between erasing and writing beams. It consisted of two parts:

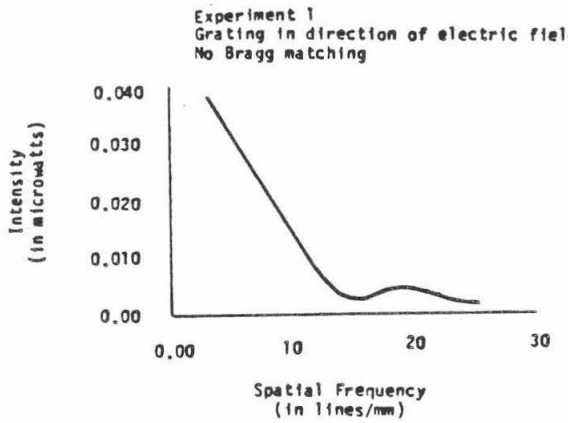
Experiment 1
Grating in direction of electric field
No Bragg matching
Intensity
(in microwatts)
0.040
0.030
0.020
0.010
0.00
0.00
10
20
30
Spatial Frequency
(in lines/mm)

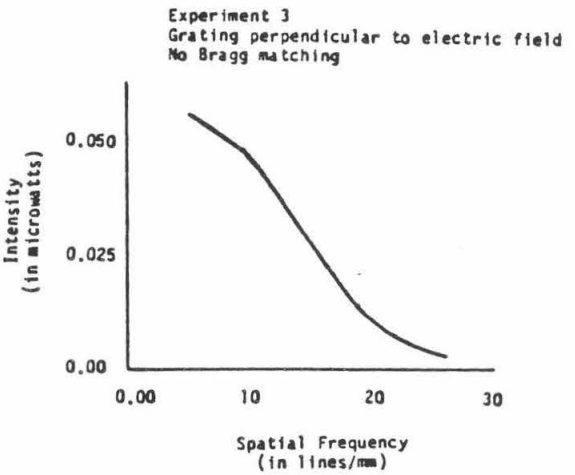
Experiment 3
Grating perpendicular to electric field
No Bragg matching
Intensity
(in microwatts)
0.050
0.025
0.00
0.00
10
20
30
Spatial Frequency
(in lines/mm)

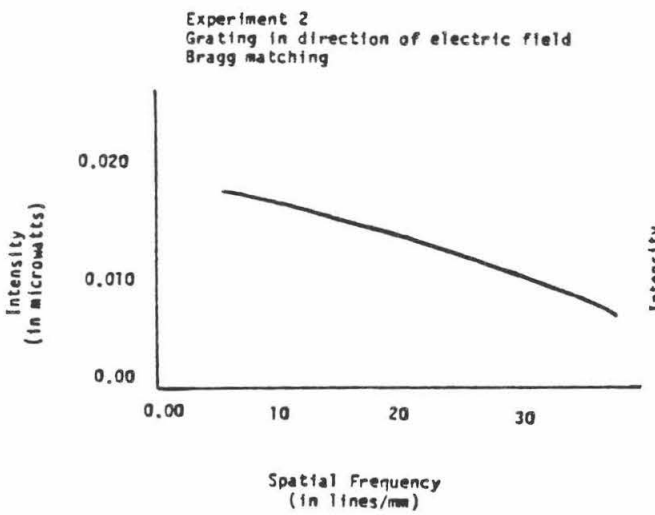
Experiment 2
Grating in direction of electric field
Bragg matching
Intensity
(in microwatts)
0.020
0.010
0.00
0.00
10
20
30
Spatial Frequency
(in lines/mm)

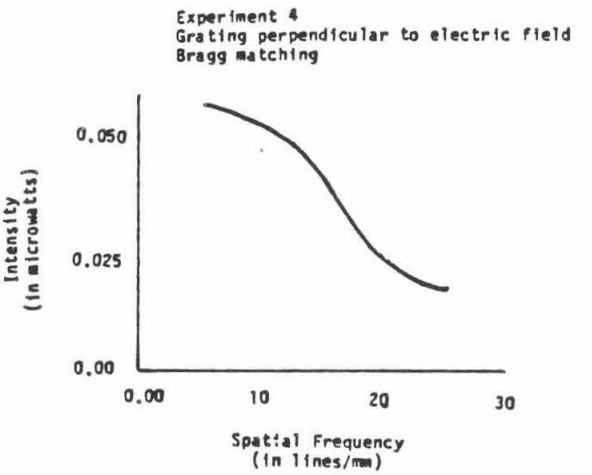
Experiment 4
Grating perpendicular to electric field
Bragg matching
Intensity
(in microwatts)
0.050
0.025
0.00
0.00
10
20
30
Spatial Frequency
(in lines/mm)

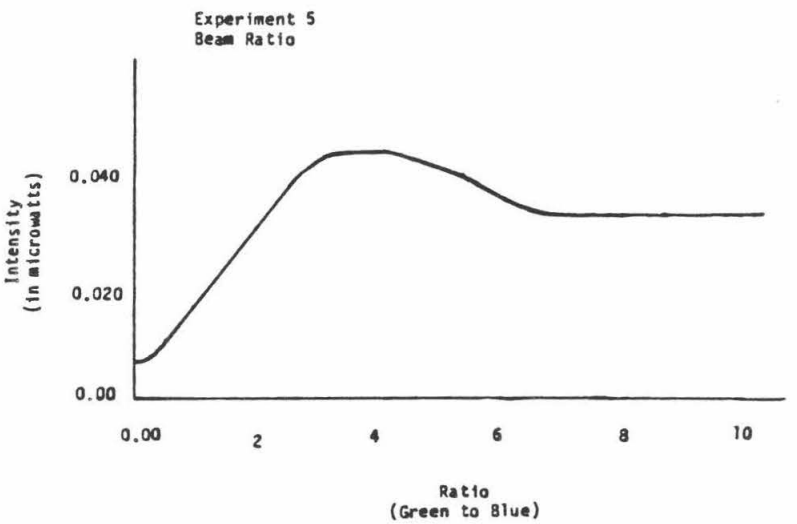
Experiment 5
Beam Ratio
Intensity
(in microwatts)
0.040
0.020
0.00
0.00
2
4
6
8
10
Ratio
(Green to Blue)

the first to check the DC term and the second to observe the first diffracted order. The experiment for the first order showed a peak at a ratio of 3.2 where theory states that there should be a peak at 2.0.[6] The difference in the peak ratios is probably due to the fact that theory is based on material constants which have not yet been accurately measured for BSO.

Conclusion

The research completed has indicated that the BSO optical converter can convert gratings of high spatial frequency quite efficiently. Still, there are several properties of the converter that can be investigated including the temporal response of the crystal and the effect of the applied electric field on the field diffraction efficiency. High resolution conversion appears to be very promising at this time.

References

1. Y. Shi, D. Psaltis, A. Marrakchi and A. R. Tanguay,Jr. "Photorefractive Incoherent-to-Coherent Optical Converter," *Applied Optics* 22,6665 (1983)

2. Ibid, 22,3665 (1983)

3. Ibid, 22,3665 (1983)

4. J. Yu, D. Psaltis, private communication

5. Ibid

6. Ibid

EXPERIMENTAL VERIFICATION OF NONLINEAR COUPLED WAVE THEORY FOR PHOTOREFRACTIVE MEDIUM

Young Hoon Chung

ABSTRACT: This report describes experimental measurement of phase conjugate reflectivity against various ratios of input beam intensities in photorefractive barium titanate. A comparison between the experimental result and the theoretical prediction is discussed. Three different methods to measure the nonlinear coupling constant of the crystal is also presented and compared.

Studies of nonlinear optical phase conjugation [1], photorefractive crystal such as barium titanate [2] and strontium barium niobate [3] have been assuming ever an increasing importance due to the large effective optical nonlinearities with milliwatt beams over the entire visible spectrum and novel nonlinear applications [4-10]. A conventional four-wave mixing (4WM) geometry is shown in Fig.1, where A_1 and A_2 are two counterpropagating pump beams, A_3 and A_4 are the phase conjugate and probe beam respectively. The probe ratio, pump ratio, and phase conjugate reflectivity are defined as follow,

$$\text{PROBE RATIO}=I_4(0)/[I_1(0)+I_2(1)]$$

$$\text{PUMP RATIO}=I_2(1)/I_1(0)$$

$$\text{PHASE CONJUGATE REFLECTIVITY}=I_3(0)/I_4(0)$$

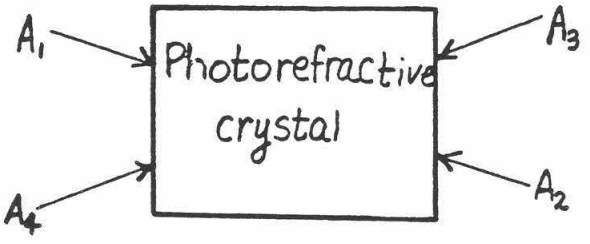

Fig.1 A schematic diagram of four-wave mixing in a nonlinear medium. A_1 and A_2 are the counterpropagating pump beams. $A_3$and A_4 are the phase conjugate and probe beam respectively.

A nonlinear coupled wave theory has been developed to describe the nonlinear interation between these four waves . Up to present, there has been no direct experimental evidence to verify this theory. The goal of this experiments described here was to check the theory.

The experimental arrangement is shown in Fig.2. The output of the Ar ion laser at 514nm was expanded by spatial filtering technique into the approximately 1-inch diameter beam. The total beam intensity $I_1+I_2+I_4$ was $0.3W/cm^2$. The nonlinear medium used was a $4.5x4.5x5mm^3$ barium titanate crystal. Since only a small part($4.5x4.5mm^2$)of the central portion of the expanded beam was used, we can approximate all the incoming beams to the crystal as plane waves. The half-wave plate and the polarizing beam splitter combination forms a lossless beamsplitter with a transmission and reflection ratio that can be varied simply by rotating the half-wave plate. In order to insure that only one grating (the transmission grating) dominated the system, the optical path lengths of beams 1 and 4 were adjusted to be the same, while the optical path difference between beams 2 and 4 was adjusted to be much longer than the coherence length of the light source (<1cm). The angle between beams 1 and 4 was made to be small (10^o) so as to increase the interaction length. The angle between the crystal axis and the angle bisector of beams 1 and 4 was 28^o. All the beams were polarized in the plane of the Fig.2 in order to utilize the large r_{42} electrooptical coefficient of the crystal. The phase conjugate beam was separated from beam 4 by a beam splitter and was detected by detector D_3. Part of the intensities of beam 1, 2 and 4 were reflected at the surface of the crystal and are detected by detector D_1, D_2 ,and D_4 respectively. All the data collected by detector D_1, D_2, D_3,and D_4 were sent to a HP9920 minicomputer for data analysis.

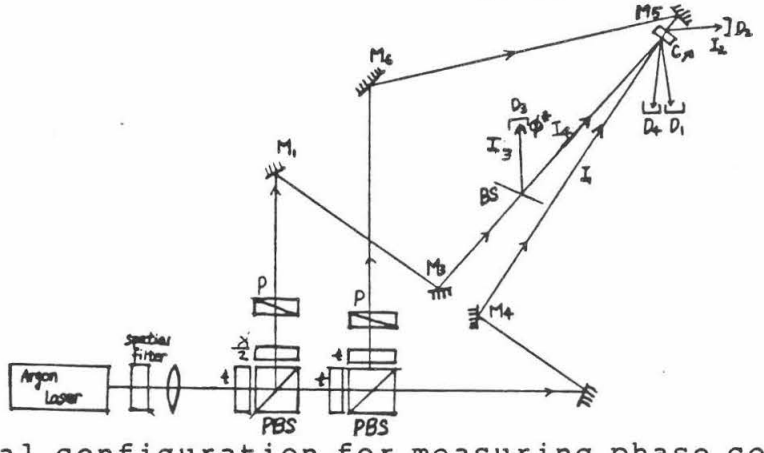

Fig.2 Experimental configuration for measuring phase conjugate reflectivity as a function of probe ratio. Using a cartesian coordinate system with the incident beam traveling along the abscissa, and the coordinate in inches the elements are 10 times amplification spatial filter (7,0);lens(12,0);half-wave plate,$\lambda/2$ and polarizing beamsplitters,PBS, (23,0)and(25,0); polarizers, P,(21,6)and(25,3);beamsplitter,BS,(30,8);barium titanate crystal, C(42,25); mirrors M_1(17,21), M_2(40,0), M_3(29,7), M_4(30,4), M_5(44,28), and M_6(25,23); detectors D_1(42,16), D_2(40,30), D_3(28,18), D_4(47,17); The crystal measured $4.5x4.5x5mm^3$ with crystal axis parallel to the 5 mm side.

EXPERIMENTAL RESULTS

The experimental results are shown in Fig.3(a),(b),(c). The phase conjugate reflectivity was plotted against the probe ratio at various pump ratios[11],a set of theoretical curves was also plotted. These theoretical curves give a best fit to the experimental curves if the nonlinear coupling constant $\gamma\ell$ is chosen to be -1.8. This provides the first method of determining the nonlinear coupling constant.

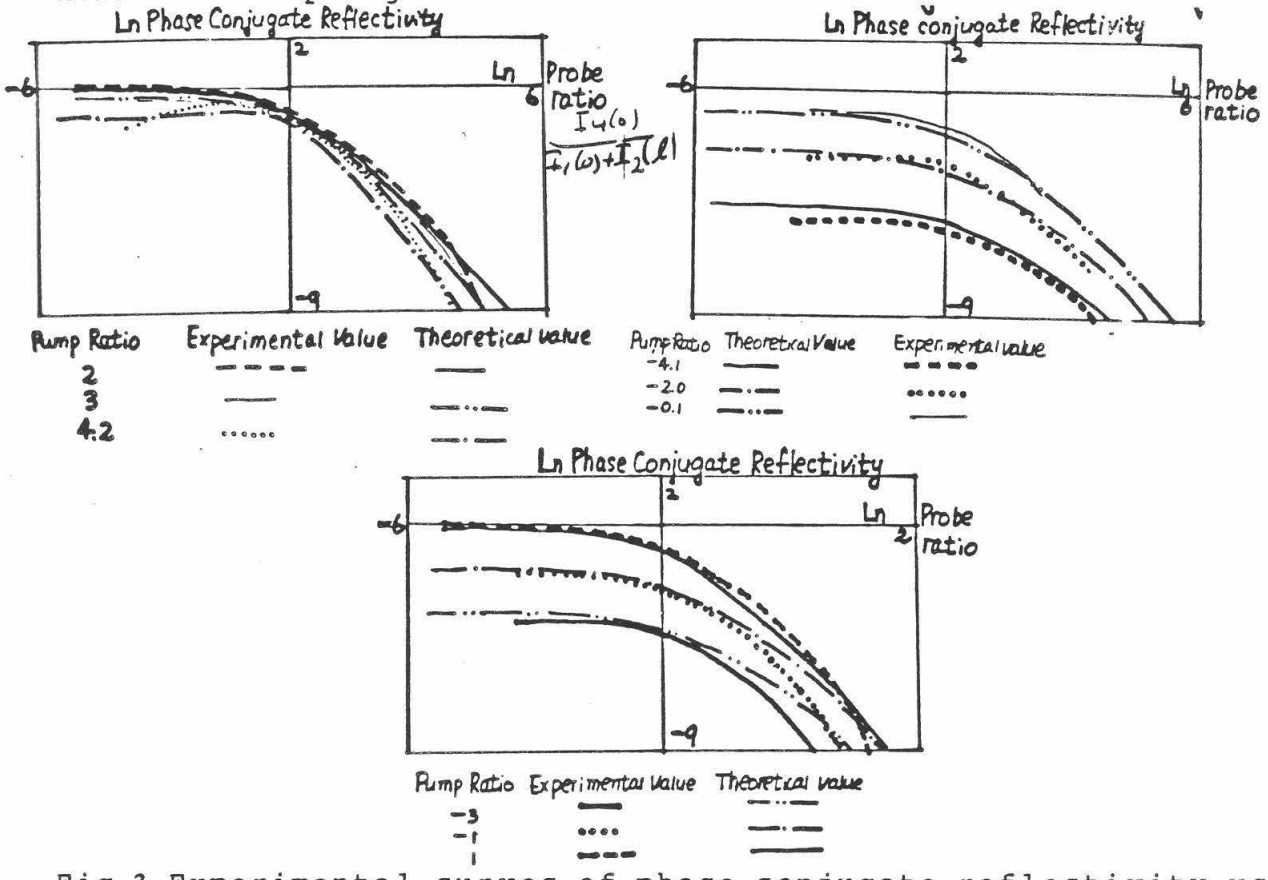

Fig.3 Experimental curves of phase conjugate reflectivity vs. probe at a given pump ratio for the coupling constant $\gamma\ell$=-1.8.

We also measured the phase conjugate reflectivity vs. the pump ratio at very small probe ratio(i.e undepleted pumps approximation which is $I_1, I_2 >> I_4$) in Fig.4. The experimental curve fits well with the theoretical curve except at very large and very small pump ratio. From the theory, the negative natural logarithm of pump ratio at the peak reflectivity for undepleted pumps approximation is equal to the nonlinear coupling constant [12]. From Fig. 4, the nonlinear coupling constant ranges from -1.5 to -2.0. This is consistent with the previous curve fitting coupling constant.

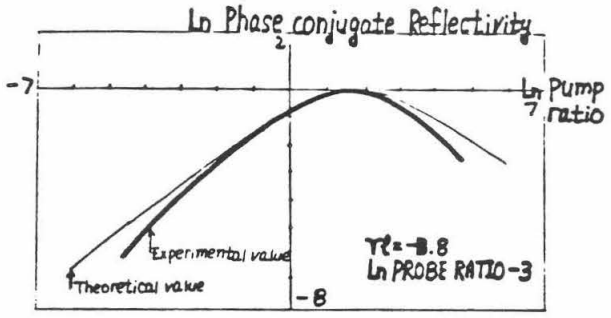

Fig.4 Phase conjugate intensity reflectivity of the transmission grating in the undepleted pumps approximation vs. the pump ratio $I_2(l)/I_1(0)$. THe coupling strength is $\gamma\ell=-1.8$.

Finally, we also performed a two-wave mixing experiment to measure the coupling constant directly. An The experimental arrangement was very similar to Fig.2 with beam 2 being blocked. A experimental plot of coupling constant $\gamma\ell$ against beam ratio is shown in Fig. 5. From the prediction of theory of photorefractive effect [13], the curve should be a constant straight line. The slight variation of coupling constant with various input beams ratio is quite surprising and is under current investigation. On the other hand ,this variation of coupling constant between (-1.5 to -2.0) agrees quite well with our previous experimental results.

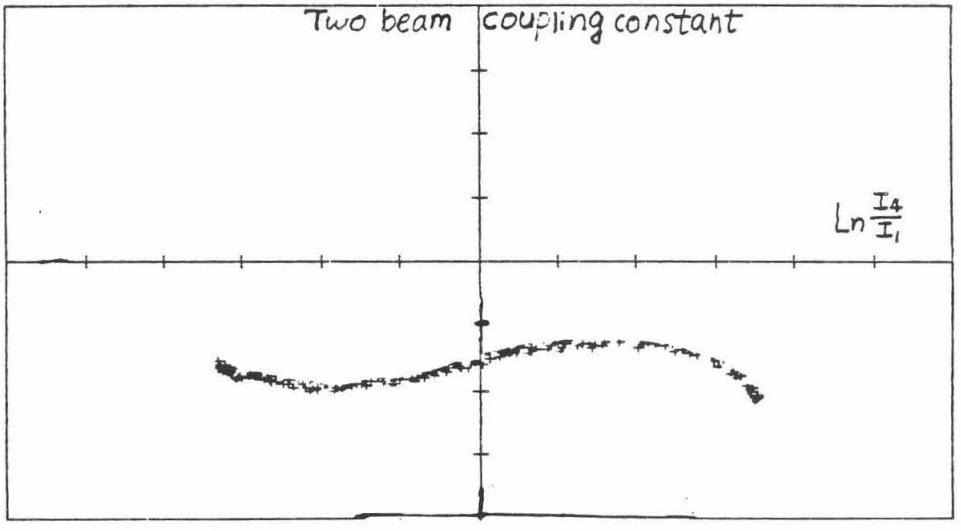

Fig 4. The two beam coupling constant vs. the ratio of the intensities of the two input beams.

DISCUSSION

The absorption of the crystal α, which is neglected in the coupled wave theory in reference [11], was determined experimentally to be approximately $\alpha=1.35$. Therefore a certain discrepancy between the theory and experiment is expected. Both the photodetector and signal amplifier did not response linearly at very low intensity. Therefore we omitted some data at high probe ratio in Fig.3. Further experiment on different kind of photorefractive crystals such as strontium barium niobate and bismith silicon oxide is planning to perform. Experimental searching for optical bistability in 4WM is also on the way, which is predicted by the coupled-wave theory.

CONCLUSION

The coupled wave theory for 4WM in photorefractive crystal is verified experimentally. The coupling constant of the crystal at the described orientation is experimentally measured by three methods which all give the consistent result -1.8.

Finally, I would like to thank to professor Amnon Yariv,my sponsor, for his generous support. I might not forget Sze-Keung Kwong in my life for his devoted and generous help in very way. Without him I could not finish my project as sucessfully as this. I am also thankful to Mark Cronin-Golomb who taught me how to use the computer.

REFERENCE

[1] Optical Phase Conjugation, R. A. Fischer Ed., Academic Press N.Y. 1982.
A.Yariv IEEE JQE. VOl QE-14, No.9,650(1978).

[2]J.Feinberg, D. Heiman,A.R. Tanguay, and R.W. Hellwarth J.Apply. Phys.Vol. 51, pp 1297-1305,1980.

[3]B. Fischer, M. Cronin-Golomb, J.O. White, A.Yariv and R.Neurgaonkar, Appl. Phys. Lett. 40, 863(1983).

[4]M.Cronin-Golomb,B.Fischer,J.O.White,J.Nilsen, and A. Yariv Appl. Phys. Lett. 41(3),219 (1982 AUG).

[5]B. Fischer, M. Cronin-Golomb, J.O.White,and A. Yariv Appl. Phys. Lett.41(2),141(1982July).

[6]M.Cronin-Golomb,S.K. Kwong,and A.Yariv Appl.Phys. Lett 44(8),727(1984 April).

[7]S.K.Kwong, M.Cronin-Golomb ,and A.Yariv To be publish Appl. Phys. Lett. Nov. 15.1984.

[8]J.Feinberg,Opt. Lett. Vol.8, No.11,569(1983).

[9]J.Feinberg,Opt. Lett. Vol.5, No.8,330(1980).

[10]J.O. White and A. Yariv Appl. Phys. Lett. 37,5(1980).

[11]M.Cronin-Golomb,B.Fischer, J.O.White ,and A. Yariv IEEE JQE Vol.QE-20, No.1,12,1984.

[12]B.Fischer,M. Cronin-Golomb,J.O.White,and A.Yariv. Opt.Lett. Vol.6, No.11, 519(1981).

[13]N.V. Kukhtarev, V.B. Markov, S.G.Odulov,M.S.Soskin and V.L. Vinetskii,Ferroelectrics 22,949(1979.

A Literature Review on the Effects of Air Pollutants on Works of Art

by Lisa Cummings
sponsored by Dr. Glen Cass

ABSTRACT

A comprehensive review of the effects of air pollution on works of art has been completed in order to identify those areas where research is still needed on the subject. This review incorporates research findings between the seventeenth century and the present. Measurements that have been made of levels of pollution, the chemical mechanisms involved in the deterioration of substances, and the sources of indoor pollutants are also included as background information. Then the specific deleterious effects of gases, acids, and particulate matter on both organic and inorganic materials in the museum environment are discussed. It is found that some of the most interesting opportunities for future research involve the potential for damage caused by unusual air pollutants generated inside of museums, including formaldehyde and acetic acid. In addition, very little information is available at present on the behavior of nitrogenous pollutants in the museum environment.

INTRODUCTION

At the present time, research into the chemistry of the interaction of artists' materials with atmospheric pollutants is being undertaken at Caltech. Recent work has shown that ozone at the levels found in Los Angeles photochemical smog will cause a variety of organic artists' pigments to fade prematurely. The hazard to artwork posed by other pollutants, such as SO_2, has been known for many years, but pollutants other than SO_2 have received much less attention. The purpose of this research project is to define the current state of the technical literature on the effects of air pollutants on works of art in order to identify presently unstudied pollutant problems that are likely candidates for future laboratory research.

The approach used in this work involves both computer literature search procedures and library research. A search was conducted for relevant research articles using the Dialog system available through the J. Paul Gerry Museum in Malibu. In addition, the library resources of the Los Angeles County Museum of Art and the Art and Archaeology Technical Abstracts were examined thoroughly. More than 500 research articles on the chosen subject were identified upon which this literature review was based. The actual literature review is available as a separate document. A summary of this work follows.

SUMMARY AND DISCUSSION OF RESULTS

Pollutants do not just harm the materials that are outside. Particles and smoke penetrate through openings in buildings, sulfur dioxide is absorbed by indoor surfaces, and defective appliances or draughts in flues allow pollutants to be dispersed inside. Many

experiments have been done relating indoor and outdoor concentrations of atmospheric contaminants. In 1959, smoke, SO_2, and H_2SO_4 were measured outside, in a naturally ventilated gallery, and in a fully air-conditioned gallery. It was found that the naturally ventilated room had 80% of the outside smoke conentration, whereas the air-conditioned one had only 11%. The SO_2 and H_2SO_4 levels were the lowest in the filtered room as well. In 1973, it was discovered that transitory concentrations of ozone indoors were not much less than those outdoors. Reaction with materials inside causes the ozone concentration to decline.

Emissions from building materials also cause indoor air pollution. Alkaline and acidic particles are released into the air by concrete. Rock, sand, and clay products contain Ra-226 which is the source of Rn-222 gas. Asbestos also can contaminate the indoor enviroment by the fallout of asbestos fiber-containing materials. The most common emission is that of formaldehyde from particle boards, urea-formaldehyde foam insulation, combustion appliances, paper products, floor coverings, carpet backing, and tobacco smoke. There have been few studies on formaldehyde measurements in the United States, but many experiments have been run in Northern Europe. Humans emit bioeffluents which consist of methanol, ethanol, acetone, and acetic acid.

In 1971, a study was made on reducing air pollutant levels indoors by using air-conditioning. Filters, such as activated charcoal, are excellent at lowering indoor ozone levels. A good ventilation system also proved effective in reducing formaldehyde concentrations.

Many papers have been submitted dealing with the indoor environment of museums. Galleries, archives, and libraries have particular problems with air pollution. The materials used in the construction of showcases and museum rooms emit harmful chemical compounds. Adhesive resins used in cabinets contain sulfuric or formic acid, injuring metals. Velvet, employed to line showcases, tarnishes silver. Treated wood products, especially oak, out of which shelves, cases, and frames are built, exude acetic acid, formaldehyde, hydrocarbons, and particles, corroding lead. Certain fabrics are sources of nitrogen and sulfur compounds.

The last half of this review discusses specific deterioration problems of particular materials. Sulfur dioxide in museums can form into sulphuric acid, which in turn combines with ammonia to form ammonium sulfate. These pollutants can cause the varnish on paintings to become opaque. Lead pigments react with sulfides to form lead sulfide which discolors light tints. Oxidation of paint leads to cracking, brittleness, and chalking. Hydrogen sulfide may react with the metal component of a paint, causing staining. Experiments have been run to determine the harm done to iron-, chromium-, and manganese-containing pigments by SO_2 and CO_2. An inclusive study on the effects of oxone on twenty-seven organic pigments was done where it was found that alizarin red pigments are vulnerable to ozone. Quinacridone reds and BON arylamide reds were discovered to be more resistant to ozone than the alizarin lakes. Yellow organic pigments fade severely when exposed to ozone, whereas chlorinated copper phthalocyanine green

pigments appeared to be resistant. A study on the photochemical deterioration of water colors in the presence of light, oxygen, and moisture was done in 1888 that is fairly comprehensive. The presence of light speeds up the generation of free radicals in organic substances that in turn increase the deteriorative process of oxidation.

Dyes also are victims of exposure to atmospheric pollutants. Fabrics dyed with blue and red anthraquinone dyes are sensitive to ozone. Fabrics that have been postcured or precured that are tinted with disperse dyes are faded by ozone and nitrogen oxides. Nitrogen oxides are responsible for the reddening of disperse blue dyes on cellulose acetate fibers. Dyeings on wool fade in the presence of sulfur dioxide.

Cellulosic materials are particularly susceptible to pollutants and light. Sulfur dioxide is an agent in the deterioration of paper. Particles in the atmosphere are also harmful to paper by providing acid radicals and metallic ions which provoke degradation. Ozone embrittles paper products. Cellulosic textiles are destroyed by atmospheric contaminants. Cotton and nylon experience reductions in their tensile strengths in the presence of nitrogen oxides. Dusts in the museum are major hazards to tapestries, clothing, and flags. Wood is disintegrated by SO_2 by absorbing the sulfur dioxide and converting it to sulphite, which is then oxidzed to acidic sulfates.

Oils, films, and resins are affected by pollution. Alkyd films, used as varnish, lose their gloss when exposed to ozone. Oxidation of oils is important in drying them, but often, because of the impure atmosphere, the oxidation continues, leading to the breakdown of the oils. Titanium dioxide films wrinkle after exposure to ozone. Other films that contain linseed oil are affected by sulfur dioxide, carbon dioxide, and ozone. The drying times of the oils are drastically altered in the presence of those pollutants.

Inorganic materials are hurt by atmospheric pollutants as well. SO_2, NH_3, dust, and aerosols deteriorate mural paintings and cause the growth of microorganisms that add to the erosion. Sulfur trioxide reacts with $CaCO_3$ (marbles and limestone) to form gypsum which washes away in the rain. Damage to metal sculptures is a problem in museums. Sulfur dioxide forms copper sulfates which corrode bronze artifacts. Metals corrode when hydrogen sulfide and humidity are present, although dry H_2S is hardly corrosive at all. Particulate matter causes pitting in almost all metals. Lead is tarnished in environments that are contaminated by drying paint vapors. Hydrogen chloride, sulfur dioxide, and ammonia corrode metals when the latter are covered by thin water films. Copper and zinc darkened when they were exposed to ammonia, but iron and steel did not seem to be affected. The SO_2 content of the atmosphere is responsible for rusting iron and steel artifacts. Sulfur dioxide pits the surface of stained glass. White crusts on glass are also formed by sulfur dioxide reaction products.

CONCLUSIONS

Topics that have not been covered well include the effects of air contaminants that originate within the museum environment on materials. Much research has been done on the sources of these contaminants, such as formaldehyde and ammonia, but the mechanisms of reaction between these pollutants and works of art have not been discussed. Studies done on the effects of pollutants on wood are also scarce. Experiments should be run on the simultaneous effects of light and pollutants on works of art. It seems that pollutants and light are dealt with separately in the current literature.

Subjects that have been researched extensively are the effects of pollution, especially sulfur dioxide, on inorganic substances. Little appears to be known of the effects of nitrogen oxides on artists' materials.

It seems that once a particular aspect of pollution and works of art is studied, many papers soon appear that are concerned with the same topic. The things that are known now about the corrosive effects of contaminants on materials have been reconfirmed many times, which leaves many other areas completely unresearched.

CREATION OF GRANULAR FLOW THROUGH AN ELECTRO-MECHANICAL SHAKER

by

Supriya Ghosh

Faculty Sponsor: Christopher E. Brennen

ABSTRACT

This paper reports on a study of the dynamic behavior (or "flow") of a granular material consisting of smooth, hard, inelastic particles. The particles in this case are A-285 glass beads. The beads are placed inside a lucite box attached to an electro-mechanical shaker oscillating sinusoidally in a vertical direction. The result is a "grain inertia" regime in which the beads collide instantaneously to create a random motion analogous to gas molecules in a dense gas. The motion, however, is not as random as one would like since the shaker creates a major vertical motion. A free-floating lid is being placed on top of the beads subjecting the granular force to an external pressure. The Impulse, I, generated from the cloud of particles keeps the lid at a fixed height, h. The measurement of this height gives us the density of the oscillatory function. In this paper, we have performed experiments which measure the height, when the amplitude and frequency of the shaker are being controlled. We noticed that the results for this oscillation were inherently unstable and a steady-state was difficult to obtain. The graphs of this function indicate that as the amplitude is increased, there is sudden increase in the density of the particles and this continues to occur until it reaches a higher set of values. This sudden expansion is probably because the particles are transformed from a compressed state to a region of rapid flow and greater turbulence.

INTRODUCTION

A lot of recent work has been devoted to understanding the mechanical properties of granular materials. Certain types of these flow regimes have been carefully observed. At extremely low strain rates the granular particle motion approaches the "quasistatic" regime. In this type of flow, the granular particles remain in contact for a long period of time and interaction between particles are characterized by long term frictional sliding at particle contact points. The most recent work on this type of flow regime has been reviewed by A. J. M. Spencer (1981) and A. Mroz (1980).

At the other end, when the shear rate is very high we approach the "rapid flow" regime. At this high shear regime, the primary interaction between particles is through instantaneous collisions between each other. The inertia of each particle becomes significant here. The global result is that the particles collide with each other randomly and create an environment which has its likenesses to gas molecules. The energy of this mechanically induced random motion is generally referred to as the "granular temperature". This temperature is directly proportional to the mean velocity of the particles. A thorough recent study on this rapid flow regime has been done by S. B. Savage (1983).

In this paper, our intent is to induce granular temperature in glass beads by shaking the particles with an electro-mechanical shaker instead of exposing them to a high-shear regime. The shaker maintains random granular motion by accelerating the walls that contain the particles. This motion will be created by the many particle-particle and particle-wall collisions. A freely-floating lid is being placed on top of the particles inside the shaker box. The vertical height of this lid rises and falls proportional to the granular force which the cloud of particles exerts on the lid. The other oscillatory motion that exists is caused by the particles colliding with the lid and the base plate once in each cycle of oscillation. Hence, the granular force created by the random motion is not equal in all directions, and has a dominant component in the vertical direction.

Rapid granular flows can be compared to the kinetic theory of dense gases. The properties of pressure, volume and temperature are being properly represented. In this particular case, the electro-mechanical shaker is providing granular "heat" to the assemblage of particles. The weight of the free-floating lid is measuring the variable of pressure, and the density is obtained from the mean height to which the lid rises above the base of the shaker box. Thus our oscillatory motion can be described as a density wave which travels up and down being reflected at both the base plate and the lid. Our goal in this experiment is to deduce an appropriate equation of state for this rapid granular flow regime by comparing the above mentioned variables to the granular temperature of the flow.

Setup

The objective of this experiment was fulfilled by a relatively simple experimental setup. The shaker is electro-mechanical and it oscillates

vertically through the use of two aluminum springs. There is a lucite box attached to it which contains the glass beads, and paper lids were made to fit freely into the box without permitting particles to enter the gap between the lid and the lucite side walls. The shaker is connected to a power amplifier and a function generator. The function generator insures the shaker's sinusoidal motion and it has frequency and amplitude output settings which control the shaker's oscillations. An accelerometer is attached to the plate of the shaker and it is used to accurately measure the amplitude of the oscillations.

The experiment itself involves the measurement of the height of the lid above the base of the box. On the front of the lucite box, two rulers were fixed for this. Then during the experiment, a stroboscope tuned to the right frequency was set beside the shaker so that the marks on the rulers could be seen properly. The experiment used A-284 glass beads. These beads can be termed as smooth, hard, inelastic, spherical particles. Different amounts of glass beads and different weighted lids were used for each experiment. Each experiment involved taking height measurements ar particular voltage and frequency settings. Usually 6 frequency settings were chosen and for each frequency there were 6 voltage or amplitude settings.

Observations

The cloud of beads bounce back and forth between the horizontal lid and the shaker base-plate maintaining a fixed height, h. We assume that the flight of the particles between bounces is not affected by anything except the acceleration due to gravity, g, and that the collisions with the lid and base-plate are governed by coefficients of restitution, ε_L (coefficient of the horizontal lid) and ε_p (coefficient of base-plate). The radian frequency and the amplitude of the acceleration of sinusoidal motion are denoted by Ω and a; the mass of the particles by m, and the weight of the lid by M. Thus the height of the lid which represents our density function depends upon these variables: the frequency of the oscillation, the amplitude of the vertical motion calculated by the RMS voltage, and the weights of the lid and of glass beads. We will then non-dimensionalize all these variables. When this is done, the oscillation is a function of the dimensionless amplitude of acceleration a/g, dimensionless spacing $(h-h_o)\Omega^2/g$, the coefficients of restitution, ε_L and ε_p, and a mass ratio M/m. During each oscillation cycle, the cloud of particles impart an upward impulse, I, to the free-floating lid. This is equivalent to a time-averaged upward force, F, on the lid given by $2\pi I/\Omega$; the corresponding dimensionless force is F/mg and can be tabulated as a function of a/g, $(h-h_o)\Omega^2/g$, ε_L and ε_p.

In Figure 1 we have plotted the dimensionless spacing $(h-h_o)\Omega^2/g$ against the dimensionless amplitude of acceleration, a/g, for a typical value of M/m of 0.078. In Figure 2 we show how increased amounts of beads and different weights of lid affect the critical amplitude of acceleration. We define the critical amplitude of acceleration as that value where the Impulse given by the particles make the lid accelerate to a much greater height.

From graphs like Figure 1 we have observed that at a certain critical amplitude of acceleration, a/g, the dimensionless spacing has a rapid

increase. This happens for each different frequency setting tested. We have found this near-exponential growth of the curve to be related to the variable, a/g. After the characteristic growth of the spacings, the change in each further spacing becomes steady. We have plotted these higher set of values during our analysis with another variable, namely the amplitude of velocity, a/Ω. The results obtained were quite interesting. For each different frequency setting it was evident that the spacings were being affected by the external pressure of the lid in a linear manner. In Figure 2 we note how the factor M/m affects the oscillatory solution. There was a linear relationship between the various mass effects and the mean amplitude of acceleration. To assure an unbiased measurement of the lid height spacing we measured two way: one was when the amplitude was steadily increased until the lid reached its peak, and second when the lid was already set at its peak and then allowed to come down. No appreciable difference was seen between these two curves. There was, however, a significant time-delay factor. When the amplitude of acceleration of the shaker was decreased, the frictionless lid took a considerable amount of time to settle into its new equilibrium position.

CONCLUSIONS

Our goal to create a "granular flow" regime be means of an electro-mechanical shaker was certainly fulfilled by this simple experiment. But a lot still needs to be done in this experiment alone. We used fixed coefficients of restitution throughout this experiment. Those values could be altered by changing the type of beads used or replacing the aluminum base-plate by a lucite one. As the amplitude was increased, the particles were moving from a state of very high density to a regime of "grain inertia". In kinetic theory, this property is similar to the change of phase from the state of a liquid to that of a gas. Hence, we notice the near-exponential growth of the spacing $(h-h_o)\Omega^2/g$, and this continued to occur until the spacing reached a stable region at a higher set of values. Our results show the critical amplitude of acceleration, where the spacing increases rapidly is independent of the frequency setting. If the coefficients of restitution were set differently and the results plotted on a single graph then the outcome might portray a band of curves all having the same general characteristics but each being set at a discrete level on the graph.

REFERENCES

Campbell, C. S. and Brennen, C. E. 1984. "Computer Simulations of Granular Shear Flows".

Savage, S. B. 1983. "The Mechanics of Rapid Granular Flows", Advances in Applied Mechanics Vol. 24, Academic Press.

Mroz, A. 1980. "On Hypoelasticity and Plasticity Approaches to Constitutive Modeling of the Inelastic Behavior of Soils", Int. J. Num. and Anal. Methods in Geomechanics.

FIGURE - 1

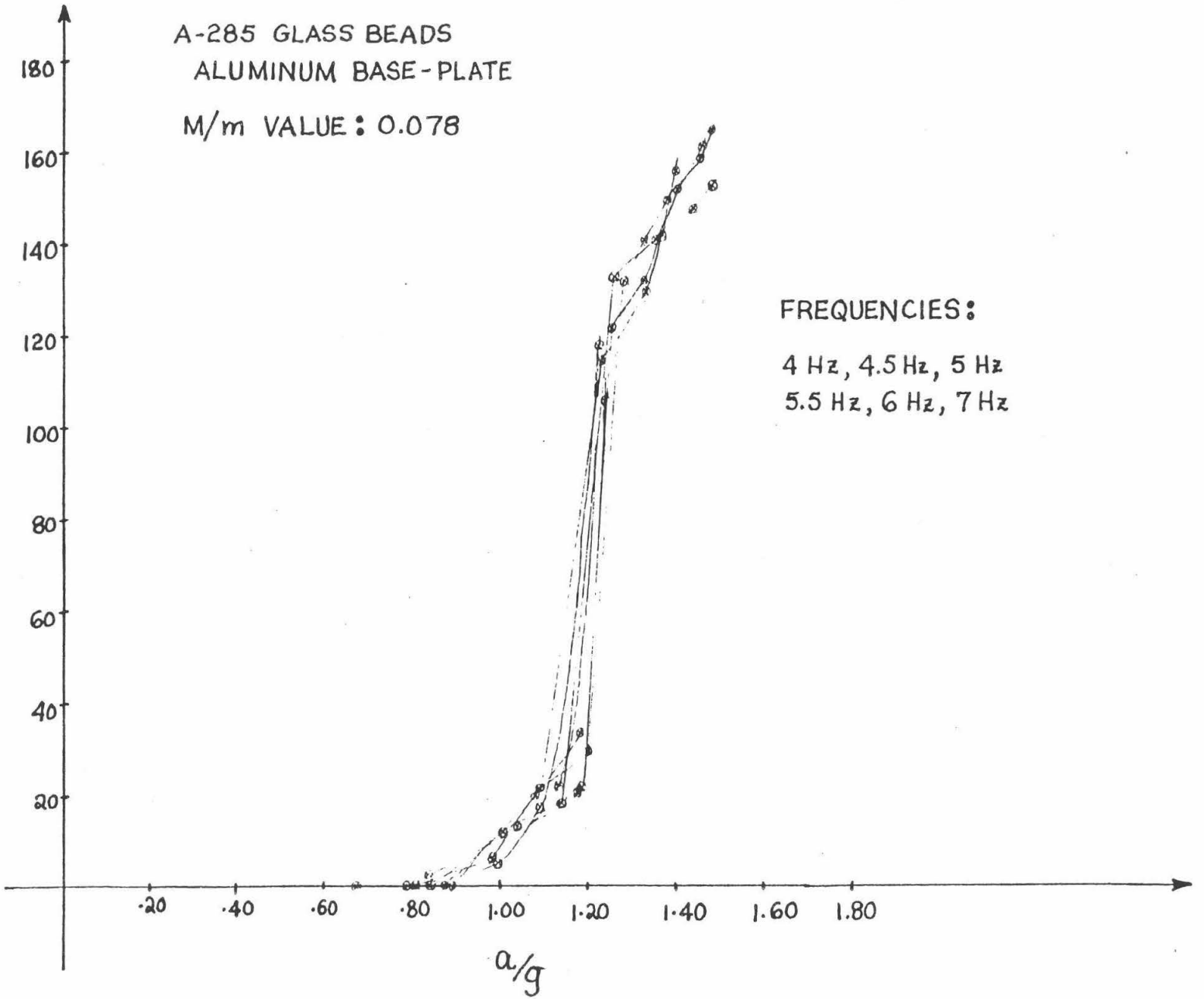
A-285 GLASS BEADS
ALUMINUM BASE-PLATE
M/m VALUE: 0.078
FREQUENCIES:
4 Hz, 4.5 Hz, 5 Hz
5.5 Hz, 6 Hz, 7 Hz
180
160
140
120
100
80
60
40
20
·20
·40
·60
·80
1·00
1·20
1·40
1·60
1.80
a/g
AMPLITUDE OF ACCELERATION
(h-h0)Ω²/g
DIMENSIONLESS SPACING

FIGURE-2 VARIATION OF THE CRITICAL AMPLITUDE OF ACCELERATION WITH THE MASS OF BEADS AND THE MASS OF LIDS.

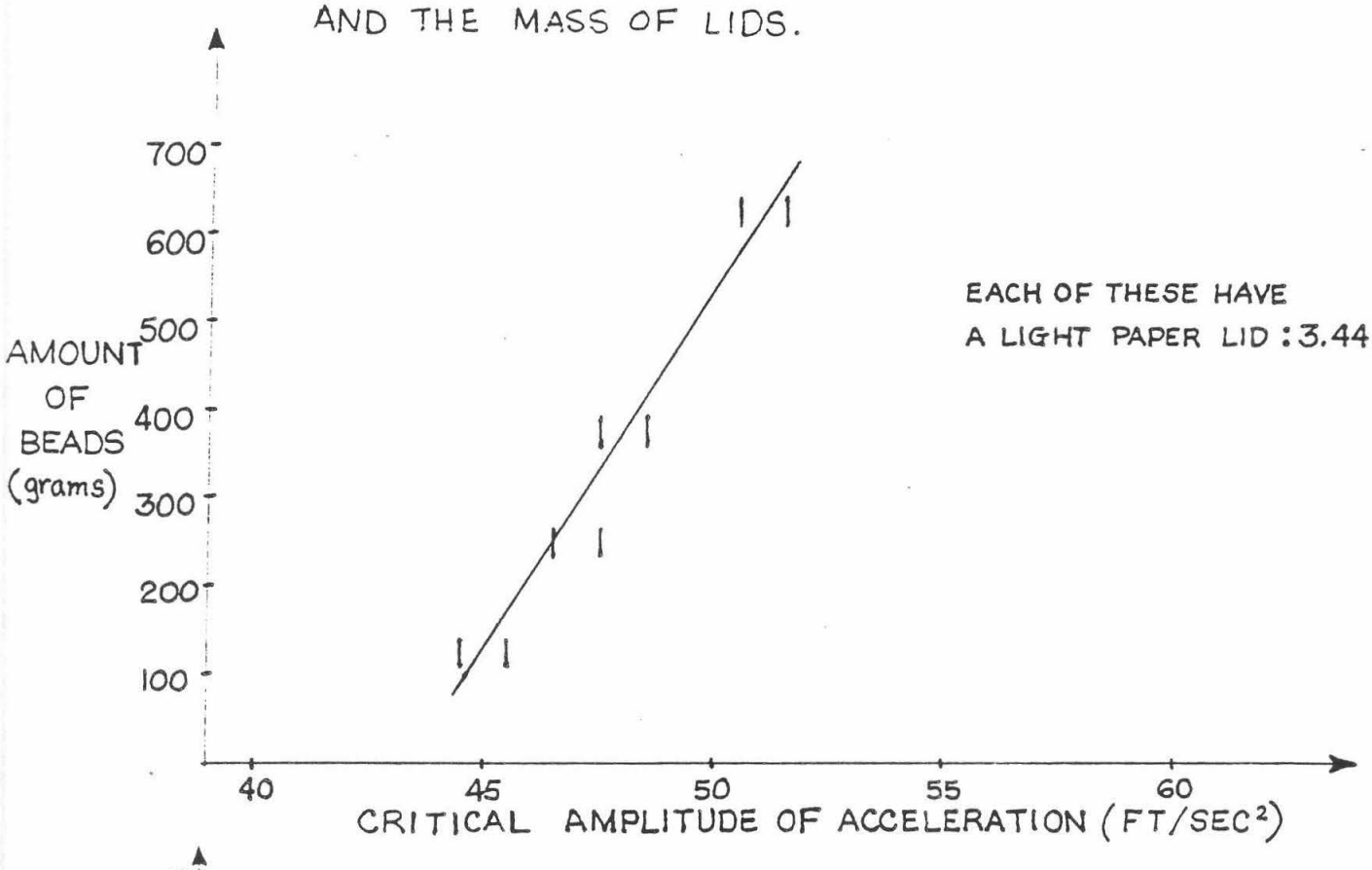

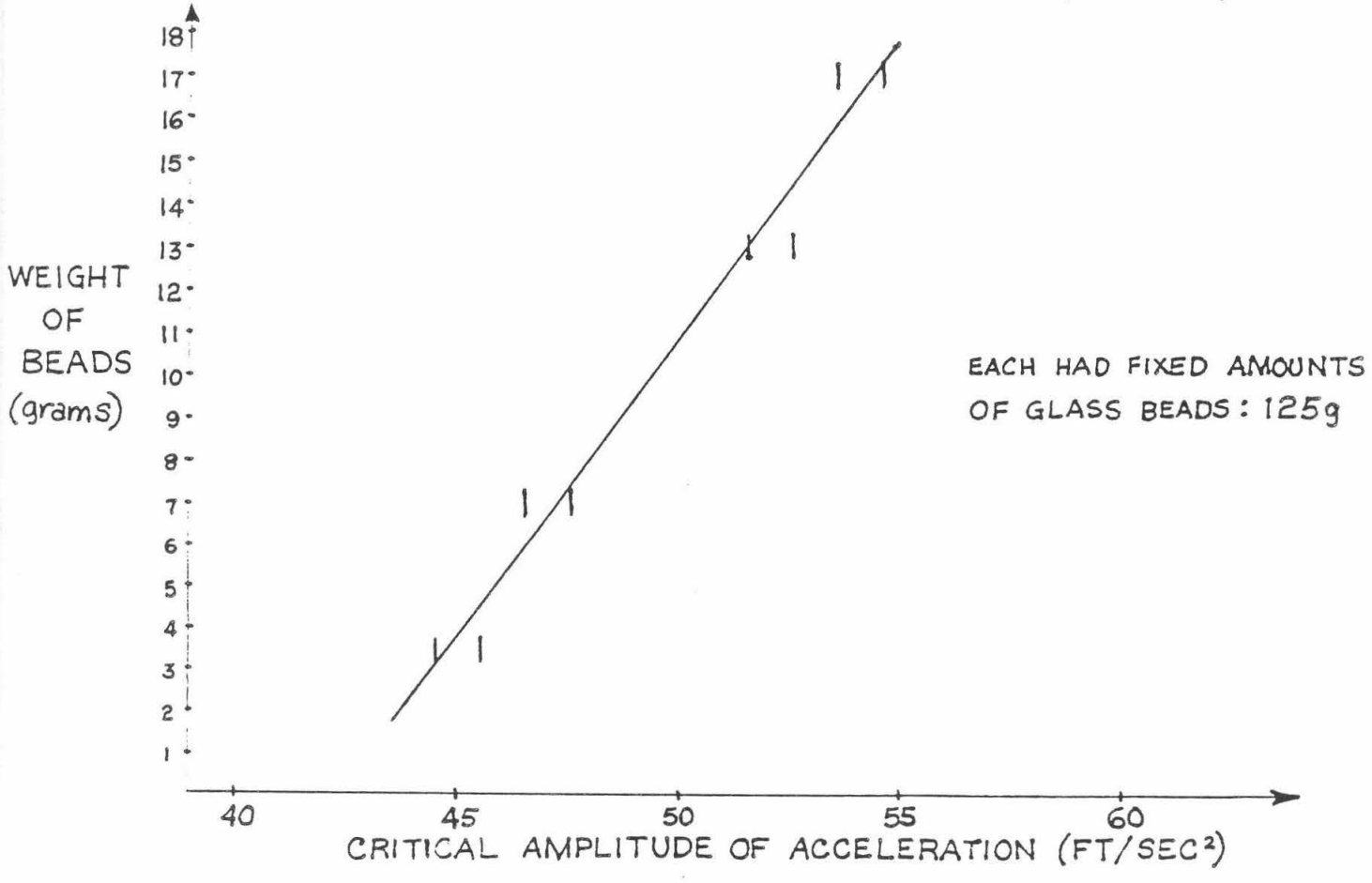

1984
Summer Undergraduate Research Fellowship
Final Report
August 31, 1984

Timing Comparisons Between a Pascal and a Prolog Parser

by

Keith Hughes
Sponsor: Fred Thompson

Abstract

Prolog, a logic-based programming language derived from a subset of the first-order predicate calculus known as Horn clauses, has received a large amount of attention lately, as the Japanese have decided to use it for their Fifth Generation Computer project. Many people have doubts as to whether or not Prolog can be used to make highly efficient production level systems. As part of a contract with IBM, Fred Thompson is rewriting his ASK system in Prolog to answer this question. This project is the first step towards answering this important question, by rewriting the ASK natural language parser in Prolog and see how the Prolog implementation compares with the Pascal implementation currently used. The timings have not been completed.

Introduction

Previous work for this project came from two different sources. Fred Thompson has worked on the ASK system as a growth out of his work with REL and POL. The Prolog system being used is one created by the author for IBM under the sponsorship of Jim Kajiya, a Caltech professor. Work here began with a Prolog interpreter to understand the issues involved in implementing Prolog. Then, how to compile Prolog into efficient machine code was examined and directly lead to the work this summer. Much will be left out of this introduction because of limited room.

1. ASK.

ASK (**A** **S**imple **K**nowledgeable System) was written by Fred and Bozena Thompson, of Caltech. The basic purpose of ASK is a highly extensible applications programming system for business, relying heavily on a natural language interface to the user. This makes communicating with the ASK system very easy and natural. The user is allowed to substantially increase the power of the system by modifying the grammer to the system and adding semantics which will build on what is already in the system, and extend it to a higher level of meaning. For instance, one could have image data in the database of ASK and add commands to the grammer with semantics to process this data. Finally, ASK handles it's own paging, since it knows best what information is needed, and when, and thus not seeking on the disk when it doesn't have to. For more information on ASK, see Thompson82. ASK was written in Pascal.

2. Prolog.

Prolog is a computer language that allows inferential, non-deterministic computing. A Prolog program is a set of logical assertions and implications, and the user query is shown to be logically consistent with this set. The proof procedure is resolution, and the major computation done is unification (finding the most general substitution of variables in a term). The proof procedure is done in a left to right manner in a depth-first search. The reader may ask (correctly), "What does all this mean???". Because of limited room, the reader is referred to Clocksin81. All that is needed

here is that Prolog allows complex programs to be written and debugged quickly.

3. The Project.

Prolog, when compiled, is as efficient as compiled LISP. With the implementation below, efficiency may be improved. But is it fast enough to do large production programming? Many people, IBM included, are interested in this question. Hence IBM is funding Fred Thompson to rewrite his ASK system in Prolog to see if a Prolog version will be close in efficiency as the existing Pascal version. This project, the first step in this endeavour, will compare the speed of the parser in ASK with a Prolog-based one. Much of the work to be done this summer was to figure out how to compile Prolog for an IBM/370, and how Prolog could bi-directionally talk to Pascal.

Discussion

4. Compiling Prolog.

The compiler for CRAPI (**C**altech **R**eally **A**wesome **P**rolog **I**mplementation) creates code which generalizes the tail recursion used in Warren80, and is described in detail in Warren83 (for more information on how CRAPI works than is given below, see Hughes84). Unlike former Prolog implementations which created an environment frame for every sub-goal attempt, which were then left around until backtracking removed them, CRAPI only creates environments when needed, and then removes them as soon as they are no longer needed. This may even be before the body of a clause is completely resolved. Because of this possibility, arguments are not pulled from their environment frame, as done previously, but are carried forward into argument registers (to be referred to as A1-An). The head of the clause which is trying to match the call then works with the A1-An registers. For example, the clause *a(X,Y) :- b(X),c(Y)* would be compiled into code similiar (minus optimizations) to

```
enter a/2
getvar X1,A1      % get first variable
getvar X2,A2      % get second variable
allocate          % create an environment frame
putvalue A1,X1    % get argument for b/1
call b/1          % try the b/1 clause
putvalue A1,X2    % get argument for c/1
deallocate        % frame goes away, no longer needed
execute c/1
```

As the reader can see, when the deallocate is done, the environment frame goes away, because it is no longer needed, since it has been copied into A1. Thus, memory is used in an efficient manner.

5. The Pascal ⇒ Prolog Interface.

To interface Pascal to Prolog, several routines must be written, either in machine language or Pascal, to handle the conversion from Pascal to Prolog.

5.1. Calling Prolog

The routines must do the following:

1 Convert Pascal structures into Prolog data structures. These must then be put into the Prolog heap (see Hughes84 for CRAPI data structures).

2 Pointers to the Prolog structures must then be put into the A1-An registers for the Prolog call.

3 The starting address of the Prolog predicate to start processing must be located, and then called.

For example, suppose there are routines *prolog_var*, *prolog_const*, *prolog_struct*, *put_prolog_arg*, and *call_prolog* accessable by Pascal. Then to start the Prolog goal

sentence(Semantic,[john,sees,mary],[])

from Pascal, the code would do something like this

```
semantic := prolog_var;                    % create a prolog variable
put_prolog_arg(A1,semantic);               % put var in register
list := prolog_struct((john sees mary))    % create list
put_prolog_arg(A2,list);                   % get list, put in A2
put_prolog_arg(A3,prolog_const(nil)); % put in A3
call_prolog('sentence/3');                 % and start goal
```

Prolog processing would then commence.

5.2. Getting the results

Once *call_prolog* returns, it will return TRUE or FALSE, depending on whether the goal succeeded or not. For all alternatives, a routine *backtrack_prolog* would have to be writen, to fail the current choice point on the Prolog-stack, and try to prove the goal again. *backtrack_prolog* would also produce TRUE or FALSE, depending on whether or not it found an alternative solution.

Continuing the above example, to get at the variable *Semantic* that was used in the Prolog call, a routine *get_prolog_var* must be written. This routine will go into the Prolog heap, dereference the variable, and then take the result and convert it into the wanted Pascal data structure. So, the call for above would be

```
result := get_prolog_var(semantic);
..... rest of processing
```

5.3. Prolog ⇒ Pascal

To go this direction, one must basically reverse the above steps. Other than that, not much else must be described.

6. The Prolog Parser.

ASK's parser is currently the Kay Powerful Parser. The grammer rules are stored in a database and are interpreted by this parser. These rules are rewritten into Prolog using a natural translation from BNF-like forms into Prolog. For more information on Prolog grammer rules, see Clocksin81.

Results

The timing comparisons have not been made. The IBM version of ASK will not be ready to use until early October. At that time, the ASK grammer rules in Prolog will be compiled and expanded into IBM/370 machine code, and hand spliced into the ASK code. The timing comparisons will be made then.

The major work done this summer has been writing the compiler and IBM/370 code that the Prolog instruction set would be expanded into, and designing the Prolog ⇔ Pascal interface. The machine code for the instruction expansions has been written, and debugged, and is working very well. The Prolog ⇔ Pascal interface has been planned out and should work by October. As one can see from what is above, writing the code for the interface will be very simple.

Conclusions

No conclusions can be made until the timing comparisons are made. But these cannot be done until ASK runs on an IBM. The author feels that the Prolog parser will compete favorably with the Pascal parser, but it remains to be seen.

Bibliography

Clocksin, W.F.; Mellish, C.S. "Programming in Prolog" Springer-Verlag: New York, 1981

Hughes, K. M.; Kajiya, J. "Prolog Implementation Notes" Unpublished as yet.

Thompson, B.H. & F.B. "Introducing ASK, A Simple Knowledgeable System" Caltech Technical Report 5054:TM:82, November 1982

Warren, D. H. D. "An Improved Prolog Implementation Which Optimises Tail Recursion" D.A.I. Reasearch Paper No. 141. University of Edinburg, 1980

Warren, D. H. D. "An Abstract Prolog Instruction Set" Technical Note 309, SRI, International, October 1983

SOME MODELS OF NEURAL MEMORY NETWORK

Pui-Tak Kan
Professor Robert McEliece, advisor

Abstract

The dynamics and memory capacity of some synchronous and asynchronous models of neural memory network are investigated.

Introduction

The neuron used in the model is the McCulloch-Pitts formal neuron(fig. 1). Such a neuron has many inputs and an output which take on the values 1 and -1. Let $x_1, x_2, ..., x_n$ be the inputs and x be the output of a neuron E. Let w_i(i= $1, 2, ..., n$) be the synaptic weights of the input x_i.

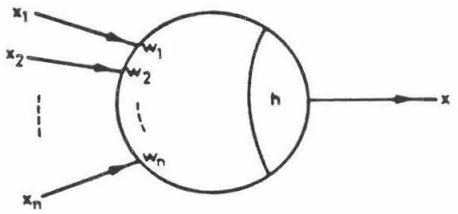

fig. 1 Neuron Model

Then the input-output relation of the neuron E is given by

$$x = \varphi(\sum w_i x_i - h)$$

where h is the threshold , and φ is the sign function defined by

$$\varphi = \begin{cases} 1, & \text{if } \sum w_i x_i \geq h; \\ -1, & \text{otherwise.} \end{cases}$$

The formal neuron fires(i.e. its output takes the value 1) only when the

weighted sum $\sum w_i x_i$ exceeds the threshold h.

Consider a neural network of n neurons $E_1, E_2, ..., E_n$. The output of each neuron is connected to the inputs of all the neurons. The synaptic weight of the output of E_i entering into E_j is denoted by w_{ji}. The $n \times n$ matrix $W = (w_{ij})$ is called the interconnection matrix of the network. The n-vector $\mathbf{h} = (h_1, ...h_n)$, where h_i is the threshold of the neuron E_i, is called the threshold vector. The matrix W and the vector $\mathbf{h}$ completely specify the network.

A Synchronous Nonsymmetric Network

A network is called nonsymmetric if the matrix W is nonsymmetric. A synchronous network is one in which the output of each neuron is transmitted to the inputs of all neurons with unit time delay. Let $x_i(t)$ be the output of E_i at time t, and call $x(t) = (x_1(t), ..., x_n(t))$ the corresponding state of the network at time t. Then the state of the network at time $t+1$ is given by

$$x(t+1) = \varphi(W \cdot x(t) - \mathbf{h})$$

where now φ is applied componentwise. We denote the overall transformation by T, so that $x(t+1) = Tx(t)$. A state x is a fixed point if $x = Tx$ holds. We wish to build the matrix W such that one can have any n vectors (the memories) to be fixed points of the network, with the additional property that if the initial state of the network, y, is close to a memory (in Hamming distance) then the state will converge to that memory. In other words, the network will have error-correcting capabilities with respect to the memories built in.

Suppose $\mathbf{h} = (0, ..., 0)$ and $x_1, x_2, ..., x_n$ are n vectors that we want W to memorize. We noticed that if we build W in such a way that x_i is an eigenvector of W with positive eigenvalue $\lambda_i (i = 1, ..., n)$ then x_i is a fixed point of W.

$$\varphi(W \cdot x_i - \mathbf{h}) = \varphi(\lambda_i x_i) = x_i \quad \text{because } \lambda_i > 0$$

Let $\lambda_1, ..., \lambda_n$ be n positive numbers and $\Lambda = \text{diag}[\lambda_1, ..., \lambda_n]$ be the corresponding diagonal matrix. Let $C = (x_1, x_2, ..., x_n)$(the matrix with x_i as the i^{th} column). Assuming that $x_1, ..., x_n$ are linearly independent, we can build W as

$$W = C\Lambda C^{-1}$$

It is easy to see that x_i is indeed an eigenvector of W with eigenvalue λ_i. If $x_1, ..., x_n$ are dependent, we can drop the dependent vectors, complete the system, and build W as above.

Computer simulations were done to investigate the dynamics behaviours of these networks. The memories $x_1, ..., x_n$ were randomly generated. The corresponding $\lambda_i's$ were chosen to be distinct to minimize the number of extra fixed points(if $\lambda_{i_1} = ... = \lambda_{i_k}$ then any linear combination of $x_{i_1}, ..., x_{i_k}$ will also be an eigenvector, and hence a fixed point).

For small values of n, a complete catalogue of the behaviour of all the 2^n states were made. For large n(up to 50), only states within a short Hamming distance from the memories were considered.

The results were not very encouraging. For small $n's$, simulations had shown that there are numerous extra fixed points—ranging from 10 to 18% of the 2^n states. The 'attractiveness' of individual fixed points is therefore weak and no radius of convergence can be observed.

Various modifications of the model(e.g. setting $w_{ii} = 0$ to avoid the trivial case that W is approximately a diagonal matrix) were tried to improve the attractiveness of the memory vectors. They were, however, unsuccessful.

Some Asynchronous Symmetric Networks

In the asynchronous mode, the outputs of the neurons are not updated simultaneously. Instead, one neuron is chosen randomly and its output updated according to the input-output relation every unit time (the remaining outputs are kept constant).

The W matrix of the standard Hopfield model [1] has the following form :

$$w_{ij} = \sum_s x_i^s x_j^s \quad \text{for } i \neq j$$
$$\text{and } w_{ii} = 0$$

where $x^s (s = 1, ..., m)$ are the memory vectors. Assuming that $\mathbf{h} = (0, ..., 0)$, computer simulations were done for $n \leq 50$ with randomly chosen memories.

It had been observed in [2] that if the number of memories stored, m, exceeds $0.15n$ then severe errors begin to occur upon recalling the memories.

That observation was reestablished in the simulations and it was found that none of the memories become fixed points if $m \gg 0.15n$. However, in some cases, it was observed that states close to the memories are fixed, indicating that some of the memory capacity are retained.

Professor McEliece has shown that, as n tends to infinity, if $m < \frac{n}{2logn}$ then the probability that the build in memories are fixed is 1. Moreover, the memories will have a radius of strong convergence $n\varrho$ (i.e. any state in the Hamming sphere of radius $n\varrho$ of a memory will converge to that memory in one synchronous step) if m satifies $m < (1-2\varrho)^2 \frac{n}{2logn}$. Simulation showed that the result is actually correct for $n\varrho \leq 2$ even for $n \leq 50$. It is noted that $0.15n > \frac{n}{2logn}$ in general. This may indicate that the memory capacity of the standard Hopfield model is substantially lower than that suggested in [2].

Some special examples of symmetric $W's$ were also considered. Their synchronous and asynchronous behaviours were compared by computing the probability and the mean time of convergence in the asynchronous mode. One of the examples is

$$W = \begin{pmatrix} 0 & 1 & 1 & 1 & 1 & 1 \\ 1 & 0 & 1 & 1 & 1 & 1 \\ 1 & 1 & 0 & 1 & 1 & 1 \\ 1 & 1 & 1 & 0 & -1 & -1 \\ 1 & 1 & 1 & -1 & 0 & -1 \\ 1 & 1 & 1 & -1 & -1 & 0 \end{pmatrix}$$

By considering the mean convergence time, it was found that although the asynchronous networks have better error-correcting capability than the synchronous ones in general, they take more computations to stablize(if one regards each update of the state in the synchronous network as n simultaneous computations).

Conclusion

A synchronous model was constructed by building the memory vectors into eigenvectors of the W matrix. Its memory capacity and dynamics were, however, shown to be unsatisfactory through computer simulations. Similar simulations were done for the standard Hopfield model; and some of the

observations in [2] were reestablished. Also, some results on the radius of strong convergence by Professor McEliece were verified.

Acknowledgement

I would like to thank the SURF program for giving me this opportunity to do research. I should also acknowledge Professor McEliece, my advisor, and Dr. Rodemich for their kind advices and patience in educating me.

References

1. Hopfield, J. J. *Human Memory, Error Correction Codes and Spin Glasses*

2. Hopfield, J. J. *Biophysics* 79 2554-2558, April 1982

OBTAINING PICTURES OF HIGH-SPEED TOKAMAK FLUCTUATIONS
(Original Title: Construction of a Streak Camera for Viewing Light Emissions from Tokamak)

written by Peter Konopka
faculty advisor: Stewart Zweben

The original purpose of this SURF was to construct a streak camera that would be able to take adequate pictures of certain high-speed light fluctuations in the Tokamak. Due to changes in my SURF advisor's future plans just prior to the commencement of this summer's SURF program, the purpose became to photograph these fluctuations in any way possible. This altered purpose was not acheived.

Little is known of the turbulence associated with plasma flow in the Tokamak. It is beleived that through the understanding and control of this turbulence, the Tokamak could be made more efficient and possibly a viable source of energy.

It has been determined that the concentration of ions on the edge of the plasma causes long spindles of light to form along the torroidal edge of the plasma. Since the varying concentration of ions is closely related to the turbulence, viewing the light is, in effect, viewing the turbulence. The light may be viewed without disturbing the flow with any kind of probe, so it is a preferable way to study the plasma's turbulence.

To learn the exact way these spindles of light relate to turbulence, the light must be studied. Hence, high quality pictures/film must be taken of the light fluctuations. If half of a million dollars was easy to come by, we could've bought a Hamamatsu streak camera, which would've done very nicely. Since this is not the case, it became necessary to borrow, construct or steal a camera with which to take pictures.

Dr. Zweben has been interested in this for some time. Using different arrays of photodiodes, he analysed the light fluctuations to determine that significant changes occur within the fluctuation's structure approximately every ten microseconds. A proper time resolution for a streak picture of these fluctuations would therefore be about ten microseconds per centimeter. Since a photograph is about ten centimeters long, the complete time width for a streak photograph is approximately one hundred microseconds.

Dr. Zweben had previously built a streak camera, but its lens system did not allow enough light in to develop a desired picture. The purpose of this SURF was to photograph these fluctuations in any way possible.

I tried for a while to make an improved version of Dr. Zweben's streak camera. However, it quickly became apparent that though I could improve the camera, I could not get an adequate picture either, due partially to my limited knowledge of optics, but mostly to my limited amount of spending money.

Early on in the SURF, I secured a grant from Grumman Aerospace in the form of a streak/framing camera. It has an image converter -- one of the devises I lacked for my home-made camera -- which electronicly intensifies the amount of light which enters the camera. This camera did not arrive until the last week of SURF. Unfortunately, its streaking and framing functions were all too fast. Someone in the Applied Physics department volunteered to attempt to alter the camera's electronics to slow it down enough to make it of use. He has not yet been successful in this attempt.

The middle of my SURF was taken up by working with a camera borrowed from Tom Bursch of the Jet Propulsion Laboratories. This camera did not streak or frame, but it did have an image converter, the ability to display pictures on a CRT, and the ability to store and recall pictures on magnetic tape.

The fastest shutter speed this camera could acheive was four milliseconds. Since this was too slow, a rotating mirror was set up to compensate -- in effect, creating a streak camera. The mirror was rotated to allow the reflected light to travel across the 1.25 centimeter camera lens in one hundred microseconds.

This set up did not yeild adequte pictures. We thought it might be that more light was needed. We tried puffing neutral ion density gas in front of the portal we were using at the time of the Tokamak's firing. This puffing of neutral density gas effects the light emitted in only one way -- it increases the intensity of the light approximately tenfold.

We still could not get any pictures with clear evidence of fluctuations. This was due to the inadequate resolution of the system inherent in the dispersion of light travelling from the Tokamak to the camera and inherent in the limited resolving capabilities of the image converter's light collecting device, the CCD (800x800 pixels in 1.6 square centimeters). Yet another reason for failure was that the depth of focus of the lens system was too large. The far edge of the plasma was also in focus, and therefore two sets of light flucuations were superimposed on top of each other, making neither of them clear.

A friend with a fancy Hamamatsu camera would have been ideal for this SURF.

RUNAWAY SOLITARY WAVES GENERATED BY A SUBMERGED MOVING DISTURBANCE IN HOMOGENEOUS AND STRATIFIED FLUIDS

Raymond Yu Shun Mak
Professor Theodore T. Wu, advisor

Abstract

Experiments were conducted to study the generation of solitary waves by a bottom bump moving steadily along the floor of a layer of shallow water. Over a transcritical speed range, new solitons were observed to appear and surge ahead of the bump, periodically and incessantly, on a homogeneous layer of water or at the interface of a two-layer-stratified fluid. Results show excellent agreement with existing theory.

Introduction

Solitary waves were historically first observed by John Scott Russell in 1834. This kind of wave distinguishes itself from ordinary oscillatory waves by having an elevation that, when spanning across a canal, propagate at constant velocity with a permanent form. The discovery of solitary waves, or solitons, led Boussinesq and Rayleigh to develop new theories which disproved Airy's shallow-water-theory that a wave of finite amplitude cannot propagate without change of form. Recently, interests were revived because of observations of solitary-like waves in various physical disciplines. Since then, it has been recognised as a challenging topic both for theorectical and experimental researches. However, all of these works were concentrated on propagation of free solitons after their generation. In 1981, Wu constructed equations of the Boussinesq class which theorized that runaway solitons could be generated by a steadily moving pressure disturbance on the free surface of shallow water.

This project was devoted to test Wu's theory by investigating the phenomenon of generating free surface runaway solitons in a homogeneous fluid and internal runaway solitons in a stratified fluid. For the convenience of experimental work, the disturbance was simulated by a submerged forcing agent.

A. Runaway Solitons in a Homogeneous Fluid

Experiments were carried out in a horizontal rectangular wave tank of 7.57m long and 0.74m wide. Bottom disturbance was provided by a two-dimensional bar spanning across the tank. The bar was in the shape of a bump with a circular arc top and a flat bottom. It has a chord length(L) of 4.9cm and a thickness(b_0) of 0.65cm . Clearance between the bump and the tank bottom was 0.15cm. Due to boundary layer effect around the bump, this clearance must be added to the bump thickness to give the effective bump thickness(b) of 0.80cm.

The bump was accelerated impulsively to constant velocities which were chosen to cover the range of depth Froude numbers $F_h = U/\sqrt{gh_0}$(where U is the constant velocity of the bump, g the gravitational acceleration and h_0 the undisturbed water depth) from 0.2 to 1.3.

Water depths(h_0) used were 4.0, 4.33, 4.83, and 5.33 cm, which give the ratios $b/h_0 = 0.20$, 0.185, 0.166 and 0.15 respectively.

As the bump was moved steadily along the tank bottom the surface wave elevation was measured using standard resistance-wire guages. Each of these wave guages consisted of two parallel resistance-wires submerged vertically. when the water level changed, the portion of wire submerged changed and its conductivity increased or decreased accordingly. Three such wave guages were fixed in position relative to the wave tank and one wave guage was carried along with the bump. Due to the symmetry in the wave tank arrangement, the three fixed wave guages were positioned so that they gave wave records of virtually 5 positions along the tank when the data of the forward and backward runs of the bump were combined. The moving wave guage was positioned one bump length in front of the bump in the forward run and four bump lengths behind the bump in the backward run of the experiment for the convenience of comparison with numerical results. Signals from the wave guages were amplified and fed into analog devices such as paper chart recorder and FM tape recorder in addition to being converted to digital signals and send to a computer.

B. Runaway Solitons in Stratified Fluid

The same wave tank and the same bump were used in the experiment with a two-layered stratified fluid. The fluid was made up of one layer of fresh water on top of another layer of strong brine. The brine was dyed with food color and was injected onto the bottom of the tank after the tank was filled with a layer of fresh water. This method of bottom injection was used to minimize the mixing layer in between. resulting density profile was measured with a conductivity probe before and after each series of experiments.

The interface position was defined as the point where $d\varrho/dy$ is the maximum. In this way, the resulting fluid can be considered as one layer of fresh water (of density = $\varrho_1 = 1.000$ grams per cc) of thickness h_1, laying over another layer of brine(of density = ϱ_2) of thickness h_2. The bump was driven along the bottom in the brine layer separately in the two transcritical ranges of the slow mode and the fast mode, respectively, based on the equation :

$$\text{critical speed} = c = [g(h_1 + h_2)]^{\frac{1}{2}} \left(\frac{1 \pm [1 - \frac{4rs}{(1+r)^2}]^{\frac{1}{2}}}{2} \right)^{\frac{1}{2}}$$

$$\text{where } s = 1 - \varrho_1/\varrho_2;\ r = h_1/h_2$$

Typical values of ϱ_2 was 1.055g/cc, and those of h_1 and h_2 were 2-10 cm.

Wave elevation at the interface was measured with special resistance-wire wave guages which had their exposed part of the wires always kept below the top surface and their lower ends extended below the interface. When the interface rose or dropped, resistance changed due to the different conductivities of fresh water and brine. At the same time the top surface was monitored for any wave propagation.

Results and Conclusion

In the homogeneous fluid, runaway solitons were recorded for all water depth used. As soon as the bump had acquired a steady speed, solitons began to form periodically in front of the bump and surged ahead one after another. Usually the tank was long enough to have one to three runaway solitons recorded. Immediately behind the bump was a depleted region, in which the water depth was considerably reduced from its undisturbed level , and followed by a train of oscillatory waves. For depth Froude number less than one, breaking would occur in the trialing waves when the disturbance was sufficiently strong. For depth Froude number larger than one, breaking sometimes occured in the runaway solitons. All of these characteristics and wave profile configurations agreed excellently with numerical results computed(by Lee) using Wu's equations both qualitatively and quantitatively.

In the stratified fluid employed in this study, interfacial runaway solitons were also observed visually at the transcritical range of the slow mode, while the top surface remained relatively calm, which was also in agreement with the theory.

With these new experimental data, Wu's theory was justified and new insights were gained into the generation of solitons in nature. Steady disturbance are now recognized to be capable of producing unsteady responses. The reward of studying solitons are beyond estimates because of its wide application in related fields of physics, applied mathematics, and various disciplines of engineering.

Acknowledgement

I am pleased to thank my advisor, Prof. T. Wu, for his valuable help and guidance. In addition, I also wish to thank Dr. George Yates, Seung Joon Lee, and Jinlin Zhu for their assistance, especially to S. J. Lee for letting me quote his numerical work not yet published. Finally, I would like to acknowledge my gratitude to the entire SURF committee and its staff members for making such unique experience possible for me.

References

1. Miles, John W. *"Solitary Waves" Ann. Rev. Fluid Mech.* 1980 12:11-43

2. Wu, De-Ming and Wu, Theodore Y. *"Three-dimensional Nonlinear Long Waves due to Moving Surface Pressure" Fourteenth Symposium, Naval Hydrodynamics. Ann Arbor* : August 23-27, 1982

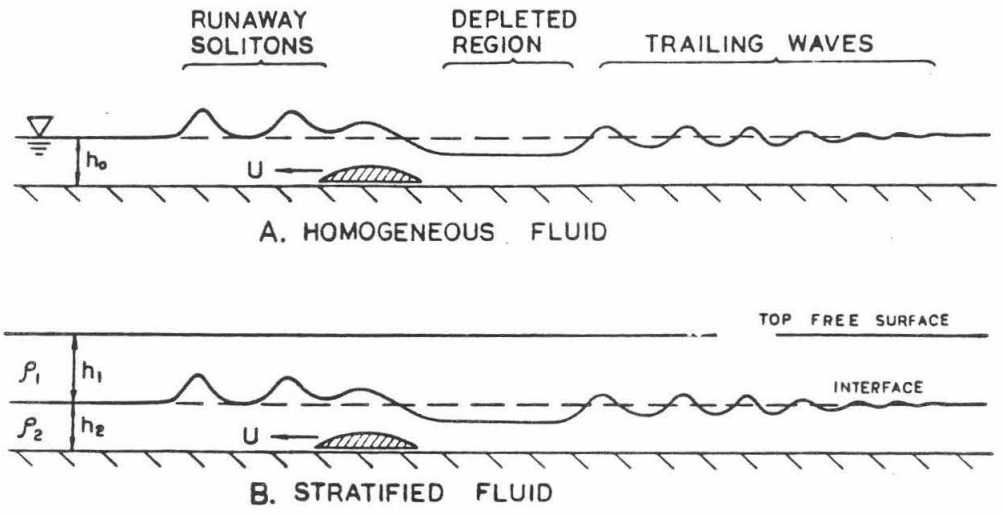

Fig.1 Sketch of wave profiles in (a) homogeneous, and (b) stratified fluids.

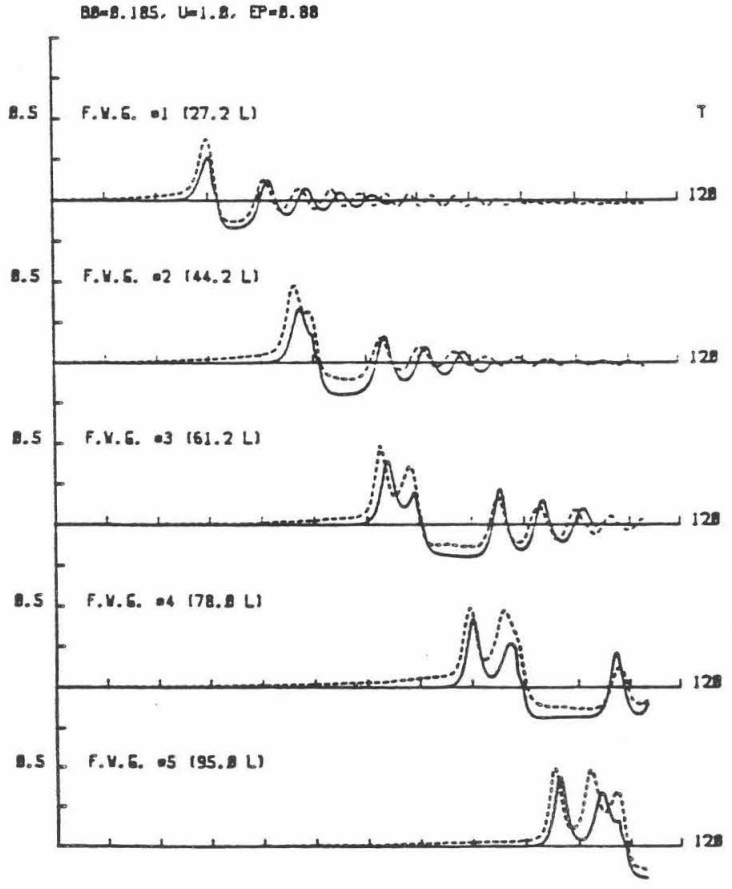

Fig.2 Comparison of wave records from 5 equally spaced fixed wave guages (dashed lines) and results from numerical computation (solid lines) , with water depth = 4.33cm and $F_h = 1.0$ in a homogeneous fluid.

IMPLIMENTATION TECHNIQUES OF FIR AND IIR FILTERS

TRUONG NGUYEN

Advisor: Prof. VAIDYANATHAN

Abtract

Computational time and Computer storage are important in the actual implementation of digital filters. The use of sign digit (SD) code in representation of filter coefficients reduces the computational time. This work studies a number of efficient techniques for the implementation of FIR and IIR filters. In particular, the concept of hierarchial design and a family of recursive filters with constant group-delay in the pass band are considered. The quantization effects on these filters are also studied.

SIGN DIGIT CODE

Sign digit code consists of three numbers 0, 1, and -1. It works similarly to binary number. For example,

$$1\ \text{-}1\ 0\ 1 = 5 = 1 * 2^3 - 1 * 2^2 + 0 * 2^1 + 1 * 2^0$$

Sign digit code is also called canonical form of represent binary number in the sense that the weight (number of nonzero bits) will be at least the same or less than the weight of the binary string. Rules for converting binary numbers to SD code are simple. Consider the pattern of converting any two bits binary number into SD code.

Binary		SD Code			
1 1	=	1 0 -1	1 + 2	=	4 - 1
1 -1	=	0 1	2 - 1	=	1
-1 1	=	0 -1	-2 + 1	=	-1
-1 -1	=	-1 0 1	-2 -1	=	-4 + 1

Similarly, the rule for three bits conversion can be derived. For instance,

1 1 1	=	1 0 0 -1	1 + 2 + 3	=	8 - 1
1 1 0	=	1 0 -1 0	2 + 4	=	8 - 2

Consider a typical binary number:

1 1 1 0 1 1 0 0 1 0 1 1 (weight = 8, length = 12)

Apply the converting rule to the first 3 bits, bits 5 and 6, bits 11 and 12,

1 0 0 -1 1 0 -1 0 0 1 1 0 -1

Follow the rule to bits 4,5 and bits 10,11

1 0 0 0 -1 0 -1 0 1 0 -1 0 -1 (weight = 6, length = 13)

Note that we continue to convert until all nonzero bits are seperated by a zero bit. We compromise a trade off between reducing the weight and increasing the length of the number.

QUANTIZATION

"*Brute force*" quantization truncates or rounds a binary string to a desired number of bits. It has been known for inaccuracy and significant errors for a small length. Since SD code representation insures a length of at least twice the complexities of the number, it, therefore gives more accurate result compared to *brute force* quantization. The following graph demonstrates the significant improvement of SD quantization on the response of a lowpass filter.

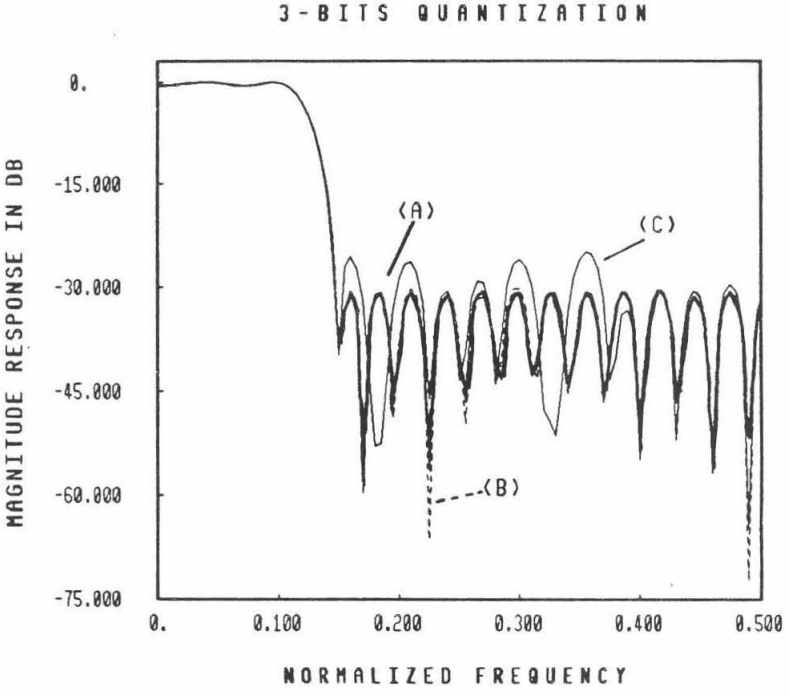

(A): Unquantized response (thick line)

(B): SD code quantized response (dashed line)

(C): *Brute force* quantized response (thin line)

RECURSIVE DIGITAL FILTER WITH MAXIMALLY FLAT GROUP DELAY

One of the difficulities in designing IIR filter is to obtain a linear phase or flat group delay in the pass band of the filter. Direct form representation of IIR filter is typically:

$$H(z) = \frac{\alpha}{\sum_{k=0}^{n} d_k z^{-k}}$$

where α is a constant, n is filter order and d_k is filter's coefficients. Substituting z=$e^{j\omega}$ into (1) to obtain frequency response of the filter:

$$\frac{H(e^{j\omega})}{\alpha} = \frac{1}{\sum_{k=0}^{n} d_k e^{-jk\omega}} = \frac{1}{R(\omega) + jI(\omega)}$$

where

$$R(\omega) = \sum_{k=0}^{n} d_k \cos k\omega$$

$$I(\omega) = -\sum_{k=0}^{n} d_k \sin k\omega$$

Phase angle:

$$\phi(\omega) = -\arctan \frac{I(\omega)}{R(\omega)}$$

Group delay:

$$-\frac{d\phi}{d\omega} = \frac{RI' - R'I}{I^2 + R^2}$$

where

$$I'(\omega) = \frac{dI}{d\omega} = -\sum_{k=1}^{n} k d_k \cos k\omega$$

$$R'(\omega) = \frac{dR}{d\omega} = -\sum_{k=1}^{n} k d_k \sin k\omega$$

To obtain a maximally flat group delay in the pass band, d_k [1] is:

$$d_k = (-1)^k \binom{n}{k} \prod_{i=0}^{n} \frac{2r + i}{2r + k + i}$$

where r is the group delay in second.

SD CODE QUANTIZATION OF GROUP DELAY FILTER

At low frequency, the group delay $\frac{-d\phi}{d\omega}$ of the filter is approximate:

$$\frac{-\sum_{k=1}^{n} k d_k \cos k\omega}{\sum_{k=0}^{n} d_k \cos k\omega}$$

Note that if both numerator and denominator are small, a small change in either one gives a large error. This is actually the case of this filter. Therefore, quantization of coefficients d_k is not the correct approach. Consider, however the cascade form of IIR filters:

$$\frac{H(z)}{\alpha} = \frac{1}{\sum_{k=0}^{n} d_k z^{-k}} = \frac{1}{\prod_{j=0}^{m}(1 - c_j z^{-1}) \prod_{i=0}^{\frac{n-m}{2}} (1 - 2r_i \cos\theta_i + r_i^2 z^{-2})}$$

where c_j are the real pole, r_i and θ_i are radius and angle of the complex poles. Since group delay and response of the filter depend on the products of these coefficients, SD quantization of these coefficients works well in this form. The following graph shows the significant improvement of group delay response due to quantization coefficients of cascade form.

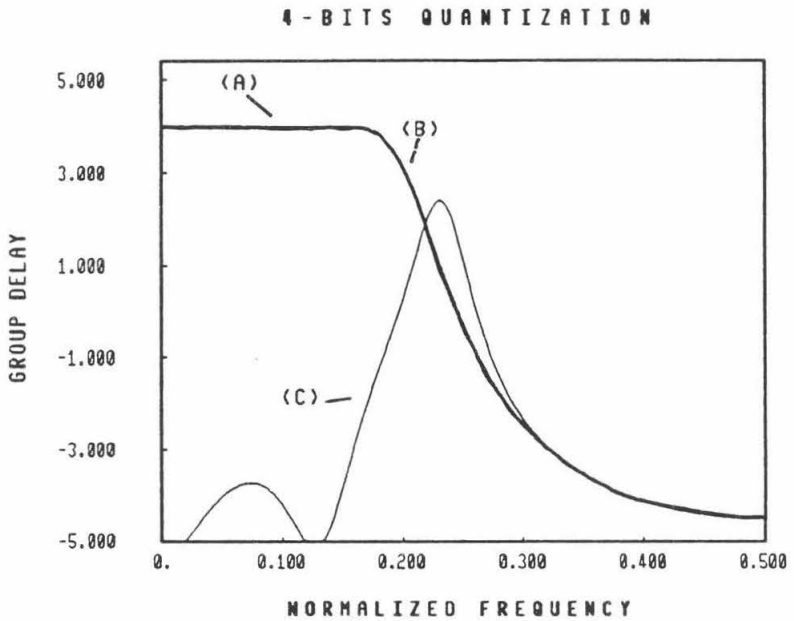

(A): Unquantized group delay (thick line)

(B): Cascade form quantization (dashed line)

(C): Direct form quantization. (thin line)

HIERARCHIAL DESIGN OF NONRECURSIVE FILTERS

Let's denote H_H , H_L , H_R to be the response of high, low and resulted overall filters respectively. High filter has errors δ_1 and δ_2 in the passband accordingly, while low filter has transition band frequencies ω_p and ω_s. The orders of these two filters (H_H , H_L) are generally low due to two free variables: transition band frequencies of high filter and errors of low filter. The frequency response of overall filter is obtained from substituting low filter's response into high filter. In another word:

$$H_R(z) = H_H(z)\Big|_{\frac{1+z^{-1}}{2}=H_L(z)}$$

The overall filter, as a result of nesting, has errors δ_1 and δ_2 in the pass band and stop band. The band edges are ω_p and ω_s .

QUANTIZATION OF HIERARCHIAL NONRECURSIVE FILTER

Quantization of overall filter give a response worse than quantization of both high and low filters. The following graph demonstrates this point.

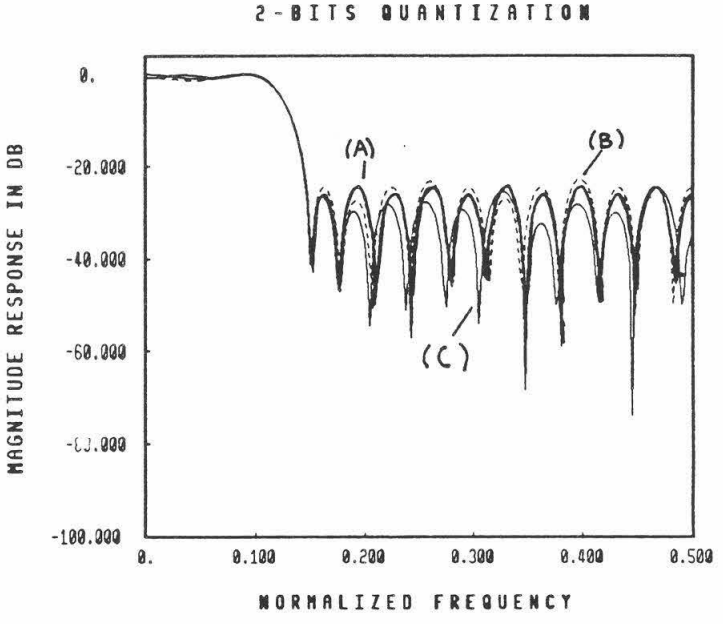

(A): Unquantized response (thick line)

(B): Direct design filter's coefficient quantization (dashed line)

(C): High and low filter's coefficient quantization. (thin line)

HILL'S FILTER [2]

Hill's analytical approach to design of FIR filters is programmed and tested.

"DRAWCURVE" PROGRAM

DRAWCURVE program converts a set of data points into a special formatted file for use of *DRAW* command (on **UNIX**). It can draw up to three curves each has an option of either solid or dashed. Title, labels on abscissa and ordinate, and labels of the curves are optional to the user. The size of the graph is normalized to unity for use in **TEX**. All graphs on this paper were plotted by *DRAWCURVE*.

CONCLUSION

Quantization yields better result compared to *brute force* quantization. By varying band edge frequencies of the high filter and errors of low filter, a wide range of low order filter can be nested to give a desired high order filter. Quantization of both high and low filters' coefficients in hierarachy filter gives better response than quantization the direct filter's coefficients. The effect of quantization depends on the presented form of the filter as in the case of recursive filter with maximally flat group delay.

REFERENCES

[1] Jean-Pierre Thiran, "Recursive Digital Filter with maximally flat group delay", IEEE Transactions on circuit theory, vol. CT-18, No. 6, November 1971.

[2] J. J. Hill, R. Linggard, and A. G. J. Holt, "An analytical approach to the design of nonrecursive digital filters", IEEE Transactions on Acoustics, speech, and Signal Processing, August 1975.

FILTER ANALYSYS SYSTEM

Kurt Schwartz

Sponsored by
Dr. P.P. Vaidyanathan

I have written a computer program whose purpose is to enable the user to study and manipulate the characteristics of a filter both numerically and graphically.

A filter is something that takes an input function made up of several component frequencies and only allows some of these frequencies to pass through. A stereo's graphic equalizer is a good example. A frequency response is a function that when graphically represented, shows the magnitude of the filter's output in a range of frequencies. Filters can be described by a ratio of complex polynomials.

This system allows the user to load the coefficients of the polynomials into the program from a data file (that has been previously generated), view the frequency response of the filter that is defined by the coefficients, and adjust the coefficients to obtain the desired frequency response. When you calculate the freqency response, the program asks for the number of iterations (the resolution), and the starting and ending frequencies for the calculation routine to use. When the calculation routine is finished, the program asks if you would like to display just the current results, or both the current and the previous results, and whether you want a normal or dB plot. The frequency response curve(s) are then displayed in the upper right hand quarter of the screen. The program then asks if you want to display the curve(s) on the full screen or not. If you do, then the curve(s) will be displayed using the full screen, complete with labeled axes. This was implemented in case you want to dump the contents of the screen to a printer.

The analysis system is written in Fortran. Dr. Vaidyanathan made available to me the frequency response calculation routines, in addition to the function generating routines. I wrote the controlling program that linked the calculation and display routines into an overall system. No graphics routines were previously available for Fortran, so I had to write special assembly language routines to accomplish the rudimentary graphics functions such as pixel addressing (turning on and off dots), line drawing, clearing the screen, and doing all these things in eight unique colors. See the appendix for more detailed information on the assembly language routines.

The system is designed to run on Zenith Z-100 microcomputers. The Zenith has some serious speed limitations, so I did almost all of the development work on a Texas Instruments Professional Computer. On the Zenith, it takes approximately two and one half minutes to compile this program, but on the TI, with its RAMdisk capability (a portion of memory is set aside and treated by the computer just as if it were a floppy disk, but it handles data transfers an order of magnitude faster), it takes about 25 seconds. I encountered many problems that had to be solved by trial and error, requiring many compilations. So, there was no choice but to utilize the TI's superior performance.

Since the TI handles graphics differently than the Zenith, I was forced to make another version of the assembly language grahics routines that I had written for the Zenith. This was not too much of a problem, because I had written the routines in a modular fashion, keeping almost all of the machine-dependent parts in one place, so I only had to modify the part that actually calculated the location of a dot in the computer's memory, and the part that turned on and off that dot.

The Z-100s that will be used for this system will initally have only two colors (black and white), and have a resolution of 640 dots horizontally by 225 dots vertically. (The Z-100 does support an interlace mode which doubles vertical resolution, however I chose not to implement it because it causes the display to flicker in a distracting manner.)

I started writing the controlling program in SSS Fortran. Halfway through the summer, I purchased an 8087 numeric coprocessor chip for the TI. Since SSS Fortran did not support the 8087, and was not very good at handling character output, I switched to Microsoft Fortran. Again, this required revising the assembly language routines.

I have made some observations as a result of my experience this summer. First, Fortran is NOT well suited for anything but pure number manipulation. Secondly, the only Fortran implementation which I have seen that is reasonably tolerable to work with is the VAX Fortran 77. The two Fortrans (SSS and Microsoft) that I worked with this summer fall far short of what should be expected of a programming language. I had problems with seemingly every new thing I tried to do, spending at least half my time trying to figure out why the language wasn't doing what it should have been doing, and I made many sacrifices of possible features simply because it was too difficult to do in Fortran. I will continue to upgrade this program during the school year, working in the C programming language, which will allow me to implement many of these features.

APPENDIX

Special routines were created for the system described in the body of this report. These routines, mostly in assembly language, can also be used by any Microsoft langauge such as Fortran, Pascal, Cobol, and C. This will enable the programs to do graphics, thereby greatly enhancing the capabilities of these languages. This appendix concerns itself with the mechanics of these routines with respect to the Zenith Z-100 microcomputer.

The Z-100 has a memory-mapped graphics display with three banks of 64K each of video RAM. These banks correspond to the three primary colors green, blue, and red. The pixel seen on the screen is essentially composed of three superimposed pixels, one in each color plane. Since each of the three color pixels may be on or off, eight different colors are possible. The colors and how they are generated is as follows:

0 - That color pixel is off
1 - That color pixel is on

Green	Red	Blue	
0	0	0	- Black, no pixels on
0	0	1	- Blue
0	1	0	- Red
0	1	1	- Magenta
1	0	0	- Green
1	0	1	- Cyan (light blue)
1	1	0	- Yellow
1	1	1	- White

If a monochrome display is used with the three memory planes, eight levels of intensity (brightness) can be produced, which correspond to the above colors. White is the most itense, and black is the least intense. Green is 59% of full luminescence, red is 30% of full luminescence, and blue is 11% of full luminescence. In the generation of intensity levels, the luminescence levels add algebraically so that magenta, being composed of red and blue, is 41% of full luminescence.

Within the 64K of any given color plane of memory, The most significant bit (MSB) of any given byte will be seen on the screen as the left-most pixel and the least significant bit (LSB) as the right-most pixel. In the following example, 1's indicate turned-on pixels.

```
Example:  1 1 1 0 0 0 0 0 <== SCREEN
          1 1 1 0 0 0 0 0 <== Video RAM (VRAM)
```

Since it is straightforward to define the location of a

pixel within a given byte, the problem that had to be solved was to locate the byte in the video memory.

The screen is organized as 640 (decimal) pixels [or 80 (decimal) bytes] horizontally across the screen. To the CPU, the top left-most byte is always at offset 0000. (These definitions apply to all planes.) The byte addresses increase from left to right on any given scan line. The line address increases from top to bottom of the screen. The least significant seven bits define the byte position in a given line, with 00 being the left-most. The most significant nine bits define the line address, with 000 being the top-most line.

Depending on whether the CRT controller (CRT-C) is programmed for nine scan lines or 16 scan lines (interlace mode) per character row, there will or will not be "holes" for entire lines in the CPU's address space. -- Holes refer to locations that do not appear. The actual screen is contiguous. For example, when the CRT-C is programmed for 9 scan lines, line 10 (hexidecimal) appears immediately below line 8 (hex).

Example 1:

The CRT-C is programmed for nine scan lines per character row, and the CPU writes F0 (hex) to segment 0C (hex), offest 693F (hex). 0C points to the blue plane.

Split 693F into 9 and 7 bits:

693F

```
==>  0110  1001     0011  1111
==>  0 1101 0010     011  1111
==>  0D2 (hex)      +3F (hex)
```

3F (hex) denotes the position of the byte across the screen from the left, which is the X coordinate. Therefore, the 693F location corresponds to the 64th (decimal) byte from the left. In Y coordinate 0D2 (hex), 0D refers to the character row number and the 2 refers to the scan line number within the character row. Since the CRT-C has been programmed for 9 scan lines per row of characters, the location corresponds to 13 times 9 plus 2 = 119 (decimal).

Data byte F0 (11110000, turning on the left four pixels) will appear on the 120th line from the top, and 64 bytes from the left.

Example 2:

You want to access the screen at a location 37 bytes from the left and on the 126th line from the top. 37 bytes from the left translates into byte address 24 (hex). The 126th line means that the intended byte appears on (126/9)

the fourteenth character row and the ninth line in that row. So, the the address of the line is 0D8 (The top row is row 0). Therefore, the VRAM location is

```
      0D8 (hex) + 24 (hex) ==> 6C24
        9 bits     7 bits
```

Using the assembly language routine that does the above calculation, I wrote an incremental line drawing routine based on the algorithm developed by J. Bresenham. Additionally, I wrote routines that drew a line from the last referenced point to a specified point, a box drawing routine (you give it the coordinates of two diagonal corners), a color setting routine, and a clear screen routine, all in assembly language. I also wrote an arc drawing routine which can be used to draw an arc sweeping any angle from 0 to 2*pi, with any aspect ratio (to generate elliptic arcs). Due to time constraints, this routine is written in Fortran. All of the assembly language routines are in one object module, which can be linked to any program written in a Microsoft compatible language.

AN UPPER BOUND TO THE NUMBER OF STABLE STATES OF THE HOPFIELD MODEL

FINAL SURF REPORT
SURF student: Jeannine-Marie St. Jacques
Supervisor: Y. S. Abu-Mostafa

ABSTRACT

The number of stable states of the Hopfield model of a biological neural network corresponds to the number of memories which can be stored in it. We have shown that there are at most N stable states in the model of a neural network of N neurons.

Introduction

Information in the Hopfield model is stored as stable states. A stable state $\mathbf{u}^s$ is a state which is a fixed point of the neural network. Each of the N neurons randomly and repeatedly looks at the weighted sum of all its inputs and then decides not to change from its previous state. To see how information is stored in the model, look at the example of pattern recognition and error-correction:

A person sees a face X and wants to decide if the face is that of person A or that of person B. The visual picture of the face is processed and the description is encoded into a binary vector $\mathbf{u}^X$ which contains the information describing the face. $\mathbf{u}^X$ is then fed into the particular neural network which remembers the faces of persons A and B. That is , $\mathbf{u}^A$ and $\mathbf{u}^B$, which contain the information describing faces A and B respectively, are stable states of this particular network. The vector $\mathbf{u}^X$ is

fed into the network by setting the i^{th} neuron in the network to the same value as the i^{th} component of the binary vector $\mathbf{u}^X$.

After a period of time, the state of the network is evaluated. If $\mathbf{u}^X$ is close to $\mathbf{u}^A$, $\mathbf{u}^A$ is the network's final state. The face is then recognized as belonging to person A and similarly if $\mathbf{u}^X$ is close to $\mathbf{u}^B$. If $\mathbf{u}^X$ is in between $\mathbf{u}^A$ and $\mathbf{u}^B$, the system will randomly converge to one or the other of the two states. Therefore, we have a model which makes decisions and has some error-correcting capability.

Number of Stable States

It is of interest to know the number of memories which can be stored in a network of N neurons in the Hopfield model. What is the maximum number K such that any K vectors of N binary entries can be made stable in a Hopfield network of N neurons by the proper choice of W and $\mathbf{t}$? We can restrict K to be at most 2^{N-1} because of the symmetry of the choice function. Since we have to have a network for every choice of the K vectors, and since there are $\binom{2^N}{K}$ such choices, but less than 2^{N^2} such networks [0], it follows that:

$$\binom{2^N}{K} \leq 2^{N^2}$$

which implies that $K = O(N^2)$. To be able to store and retrieve the order of N^2 arbitrary stable states in a Hopfield network with N neurons seems quite ambitious. Hopfield predicted experimentally that $K \approx 0.15N$ [2] and McEliece showed a statistical bound of $K \leq \frac{N}{2 \log N}$ [4]. However, these estimates restrict the construction of W to the sum-of-outer-products scheme [2]. We now improve on the $O(N^2)$ bound and show that the number of stable states K can be at most N, for every N, no matter how the matrix W is constructed.

Theorem

Let W denote a real-valued zero-digonal $N \times N$ matrix, and $\mathbf{t}$ denote a real-valued N-vector. Suppose that $K \leq 2^{N-1}$ is an integer satisfying:

> For any K-set of binary N-vectors $\mathbf{u}^1, \cdots, \mathbf{u}^K$, there is a matrix W and a vector $\mathbf{t}$ such that
>
> $$\text{sign}\left[\sum_{j=1}^{N} w_{ij} u_j^k - t_i\right] = u_i^k$$
>
> for $k = 1, \cdots, K$ and $i = 1, \cdots, N$.

then $K \leq N$.

Proof. Suppose that K satisfies this property. We construct K vectors $\mathbf{u}^1, \mathbf{u}^2, \cdots, \mathbf{u}^K$ as follows: The first entries in these vectors, namely $u_1^1, u_1^2, \cdots, u_1^K$, are binary variables $x^1, x^2, \cdots, x^K$ to be fixed later. The remaining $N-1$ entries in each vector are fixed ± 1's such that no two vectors have exactly the same entries (always possible since $K \leq 2^{N-1}$). We apply the condition of the theorem for $i=1$. For any choice of $x^1, \cdots, x^K$, there must be real numbers $w_{12}, w_{13}, \cdots, w_{1N}, t_1$ such that:

$$\text{sign}\left[\sum_{j=2}^{N} w_{1j} u_j^k - t_1\right] = x^k$$

for $k = 1, \cdots, K$, since $w_{11}=0$ (zero-diagonal). Therefore, for each of the 2^K choices for the values of $x^1, \cdots, x^K$, we must find a different threshold function of $N-1$ variables with K points in the domain. Let B_{N-1}^K be the number of threshold functions of $N-1$ variables with K points in the domain. We must have:

$$B_{N-1}^K \geq 2^K \qquad (1)$$

Cameron and Winder [1,9] (see the appendix), give the following upper bound to the number of threshold functions of $N-1$ variables with K points in the domain:

$$B_{N-1}^K \leq 2 \sum_{i=0}^{i=N-1} \binom{K-1}{i}$$

If $K > N$, then:

$$B_{N-1}^{K} \leq 2 \sum_{i=0}^{i=N-1} \binom{K-1}{i} < 2 \sum_{i=0}^{i=K-1} \binom{K-1}{i} = 2 \times 2^{K-1} = 2^{K}$$

So if $K > N$, $B_{N-1}^{K} < 2^{K}$ which contradicts condition (1). Therefore K must be at most N and the proof is complete. |

Conclusion

The theorem is a formalization of the fact that a Hopfield neural network cannot have more than N arbitrary stable states. Notice that the matrix W was not required to be symmetric, and this covers the generalization of the Hopfield model where the synaptic connections become directed ($w_{ij} \neq w_{ji}$). Also, there is no restriction on the method of constructing W and $\mathbf{t}$ in terms of $\mathbf{u}^1, \cdots, \mathbf{u}^K$. McEliece and Posner [5] predicted that a zero-diagonal symmetric matrix has an exponential number of stable states on the average. The above theorem predicts at most a linear number of *arbitrary* stable states for a zero-diagonal matrix.

References

[0] Y. S. Abu-Mostafa & J. St. Jacques, "Information capacity of the Hopfield model," to appear.

[1] S. H. Cameron, "An estimate of the complexity requisite in a universal decision network," *Bionics Symposium, WADD Report 60-600*, pp. 197-212, 1960.

[2] J. J. Hopfield, "Neural networks and physical systems with emergent collective computational abilities," *Proc. National Academy of Science, USA*, Vol. 79, pp. 2554-2558, 1982.

[3] P. M. Lewis & C. L. Coates, *Threshold Logic*, John Wiley, 1967.

[4] R. J. McEliece, private correspondence, 1984.

[5] R. J. McEliece & E. C. Posner, "The number of stable points of an infinite-range spin glass," to appear, 1984.

[6] S. Muroga, "Generation of self-dual threshold functions and lower bounds of the number of threshold functions and a maximum weight," *SCTLD (1962)*, pp. 169-184, 1962.

[7] C. E. Shannon, "A mathematical theory of communication," *Bell System Technical Journal*, Vol. 27, pp. 379-423, 1948.

[8] F. Tanaka & S. E. Edwards, "Analytic theory of the ground state properties of a spin glass: I. Ising spin glass," *Jour. Phys. F: Metal Physics*, Vol. 10, pp. 10, 1980.

[9] R. O. Winder, *Threshold Logic*, Ph.D. Thesis, Princeton University, 1962.

[10] R. O. Winder, "Bounds on Threshold Gate Realizability," *IRE Trans. Electron. Computers*, **EC-12, (5),** 561-4 (October 1963).

Characterization of Sulfur-Aldehyde Adducts in Hydrometeors

by Christine Tiller

Faculty Sponsor: Michael Hoffmann

Abstract:

It has been suggested that aldehydes and S(IV), released into the atmosphere from various pollution sources, may react to form stable addition products under certain conditions in fogs.(Munger et al., 1983,1984) None of these addition products have actually been identified in fogwater samples, however. Therefore, research was conducted in order to develop a procedure for the identification of aldehyde-S(IV) adducts in aqueous solution. Mobile Phase Ion Chromatography, using tetrabutylammonium chloride as pairing reagent and methanol as organic modifier, was found to succesfully achieve the separation of the formaldehyde and acetaldehyde adducts and S(IV).

Introduction:

Sulfuric acid is an important contributor to atmospheric pollution. It is a major constituent of acid rain, is a potential health hazard to humans and is harmful to vegetation. Sulfuric acid is produced in the atmosphere by the oxidation of SO2, which is emitted by fossil fuel combustion. Laboratory and field studies have indicated that droplet-phase chemistry is important in SO2 oxidation, which occurs, in part, by the following reactions:

$$SO_2(g) = SO_2(aq)$$

$$SO_2(aq) = H^+ + HSO_3^- \text{ (sulfurous acid)}$$

$$2HSO_3^- \text{ (S(IV))} + O_2 = 2HSO_4^- \text{ (S(VI))}$$

$$HSO_4^- = H^+ + SO_4^{--}$$

Aldehydes are released into the atmosphere directly from combustion sources and are also produced by photochemical oxidation of hydrocarbons. The secondary pathways are dominant, especially in urban areas. In the aqueous phase, aldehydes hydrolyze to form gem-diols which are resistant to photodecomposition. Hence, fog and clouds may provide ideal environments for the accumulation of aldehydes.

Sulfuric and sulfurous acids and aldehydes are ubiquitous in the atmosphere. Analyses of fogwater in the Los Angeles basin and the San Joaquin Valley have indicated unusually high concentrations of these components. The observed concentrations of S(IV) in fogwater droplets often exceed the level which would be predicted by a Henry's Law equilibrium model. In addition, concentrations of formaldehyde as high as 0.5 mM have been observed in Los Angeles fogwater. Other aldehydes, such as acetaldehyde and benzaldehyde, are also present. Equilibrium calculations indicate that high concentrations of S(IV) cannot be achieved without the formation of S(IV)-RCHO adducts.

Aldehydes react with HSO_3^- in aqueous solution to form hydroxyalkylsulfonic acids according to the following general stoichiometry:

$$HSO_3^- + RCHO = RHOCHSO_3^-$$

Specifically, the formation of the addition product of S(IV) with formaldehyde, hydroxymethanesulfonate (HMSA), follows two parallel pathways involving the nucleophilic addition of HSO_3^- and SO_3^{--} to the carbonyl C-atom of HCHO:

$$CH_2(OH)_2 = HCHO + H_2O$$
$$SO_2.H_2O = H^+ + HSO_3^-$$
$$HSO_3^- = H^+ + SO_3^{--}$$
$$HSO_3^- + HCHO = CH_2(OH)SO_3^-$$
$$SO_3^{--} + HCHO = CH_2(O^-)SO_3^-$$
$$CH_2(O^-)SO_3^- + H^+ = CH_2(OH)SO_3^-$$

The formation constant for HMSA has a maximum value of about 10^5 at low pH and decreases to 10^3 at pH 9. The adduct undergoes the following acid-base equilibria:

$$HO_3SCH_2OH = HO_3SCH_2O^- + H^+$$
$$HO_3SCH_2O^- = {}^-O_3SCH_2O^- + H^+$$

At pH levels found in fogs and clouds, HMSA will be in the monoprotic form. The reaction of HCHO and SO_2 may occur readily in the condensed phase due to the favorable thermodynamics for the dissolution of formaldehyde and sulfur dioxide in water.

Formation of aldehyde-S(IV) adducts has been suggested as a possible explanation for excess formaldehyde concentrations and the apparent stability of S(IV) observed in aerosols.(Munger et al., 1983,1984) However, these addition products have not as yet been directly identified in fogwater samples. All common methods for identification of fogwater components lead to the dissociation of any adducts which might be present, allowing only total S(IV) and total RCHO concentrations to be measured. The purpose of my project was to develop a quantitative method for identification of HMSA and other aldehyde-S(IV) adducts in aqueous solution.

Results:

Stock solutions of reagents were prepared in the concentration range of 10 μM to 200 μM. Na_2SO_3, HCHO, HMSA, and other reagents were used as purchased. Aldehyde-S(IV) adduct salts were prepared according to Blackadder and Hinshelwood (1958).

Major anions in fogwater samples are generally determined by High Performance Ion Chromatography (HPIC). Therefore, this instrumental approach was explored further. Experiments were carried out using the usual carbonate/ bicarbonate eluents. HMSA and S(IV) coelute under these conditions, suggesting that the HMSA dissociates to HCHO, which does not elute, and S(IV). Taking note of the fact that HMSA is most stable at pH 4, a 1 mM potassium hydrogen phthalate eluent was tried. However, HMSA and S(IV) still were not separated and the IC did not easily achieve equilibrium with this eluent. Further experiments indicated that HPIC was not likely to result in success.

Formaldehyde can be determined spectrophotometrically. It is known that S(IV) interferes with this procedure by forming HMSA. Based on this knowledge, experiments were

Mobile Phase Ion Chromatography

Eluent: 2 mM TBACl, 10% methanol
Flow Rate: 1 mL/min

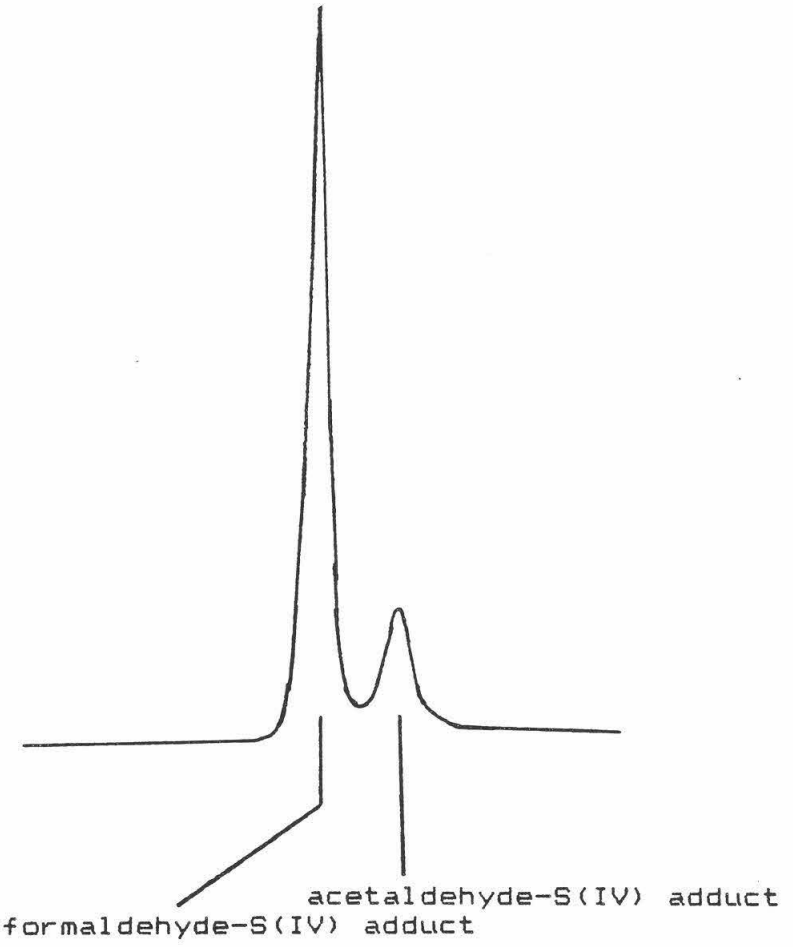

conducted to determine if the extent of S(IV) interference in a given sample could be quantitatively measured, thus providing an indirect determination of HMSA. This proved unfeasible, however, as the behavior of the S(IV) and HMSA in solution is unpredictable and some of the HMSA dissociates despite precautions taken to ensure its stability. Other attempts to determine HMSA by chemical means also proved fruitless.

Mobile Phase Ion Chromatography (MPIC) is an ion chromatographic method which has been succesfully applied to the separation of certain sulfonates, as well as other compounds. Attempts to create a column of this type according to Rotsch, Sydor, and Pietrzyk (1979) were unsuccesful and a commercial column was obtained. A silver resin suppressor column was used to suppress the background conductivity of the eluent. Tetrabutylammonium chloride (TBACl), tetrapropylammonium chloride (TPACl), and ammonium ion are the most common ion-pairing reagents used in MPIC. Methanol and acetonitrile are typical organic modifiers. Trial and error experimentation found that an eluent of 2 mM TBACl and 10% methanol at a flow rate of 1 mL/min is moderately succesful. HMSA elutes with a sharp peak and S(IV) does not elute. In addition, HMSA is well resolved from the acetaldehyde-S(IV) adduct. However, there is interference from some of the other anions commonly found in fogwater and cloudwater. This problem may be overcome by further adjustment of the MPIC operating conditions. Important parameters include type and concentration of pairing reagent, type and concentration of organic modifier, other modifiers, and pH.

Conclusion:

The primary conclusion of this project is that Mobile Phase Ion Chromatography can be used for the separation and identification of aldehyde-S(IV) adducts in aqueous solution. TBACl is an appropriate pairing reagent. Both HMSA and acetonitrile-S(IV) adduct elute with good peaks, using this type of eluent. 5 to 10 % methanol in the eluent is necessary in order to shorten the retention times to within a convenient limit of about 20 minutes. Further refinement is needed, however, if this procedure is to be applied to actual fogwater samples. For example, a suppressant is needed to counter the potential interference of many anions commonly present in fogwater. Also, further research is needed to determine if aldehyde-S(IV) adducts can be quantitatively measured using this procedure, or if merely qualitative identification can be achieved.

I would like to thank Bill Munger for all of the invaluable advice and assistance he gave me over the course of the summer.

Bibliography:

Blackadder, D.A. and Hinshelwood, C. (1958)
The Kinetics of the Decomposition of the Addition Compounds formed by Sodium Bisulfite and a Series of Aldehydes and Ketones. Part I.
J. Chem. Soc., 2720-2734.

Boyce, S.D. and Hoffmann, M.R. (1984)
Kinetics and Mechanism of Formation of Hydroxymethanesulfonic Acid at Low pH.
J. Phys. Chem., 88.

Munger, J.W., Jacob, D.J., and Hoffmann, M.R. (1984)
The Occurrence of Bisulfite-Aldehyde Addition Products in Fog and Cloudwater.
J. Atmos. Chem., 1.

Munger, J.W., Jacob, D.J., Waldman, J.M., and Hoffmann, M.R. (1983)
Fogwater Chemistry in an Urban Atmosphere.
J. Geophys. Res., 88, 5109-5121.

Rotsch, T.D., Sydor, R.J., and Pietrzyk, D.J. (1979)
High Performance Liquid Chromatographic Study of the Retention and Sorption of Sulfas of Porous Copolymers.
J. Chromat. Sci., 17, 339-344.

SECOND SOUND SHOCKS AT A GASEOUS AND SUPERFLUID HELIUM II INTERFACE

Student: Minami Yoda
Sponsor: Dr. Hans Liepmann

ABSTRACT:

I spent this summer looking at second sound shocks, both incident and reflected, and transmitted gasdynamic shocks at a gaseous-superfluid He II interface. Although we were able to obtain only a few Polaroid photographs of these interface shocks, we did eliminate many of the problems associated with the experimental setup for taking pictures of interface shocks.

INTRODUCTION:

"Superfluids display quantum effects on the macroscopic level and obey hydrodynamics on the microscopic level." (1) These quantum properties develop past a certain transition point (below 2.17°K for helium). The only materials that exhibit such macroscopic quantum phenomena are helium and the various metallic superconductors. These substances have many interesting properties--electric currents flow with virtually no resistance through superconductors, and superfluid helium can flow through small capillaries with no detectable viscosity (2).

Superfluid helium is explained by the two-fluid model of Landau (3). In this model, the superfluid is a mixture of two fluids--the normal component, which behaves classically, and the super component, which is the macroscopically occupied ground state of the superfluid. As the temperature of the superfluid decreases, the percentage of the super component increases until the fluid is all super component at absolute zero. Each component has its own density and velocity field--ρ_n and ρ_s, and $\vec{v}_n$ and $\vec{v}_s$, respectively. The density of the fluid is $\rho = \rho_n + \rho_s$ and the fluid velocity is $\vec{v}$, where $\rho\vec{v} = \rho_n\vec{v}_n + \rho_s\vec{v}_s$. Since there are two fluid fields, the two-fluid model predicts the existence of two modes of wave propagation in the fluid--first sound, involving perturbations in the pressure p and the velocity $\vec{v}$, where both the super and normal

components move as one, and second sound, involving perturbations in the temperature T and the relative (counterflow) velocity $w = \vec{v}_n - \vec{v}_s$, where the two components move oppositely.

Much of the fluid mechanics unique to superfluids can be observed best with second sound waves since the super and normal components move oppositvely; this makes second sound shocks an ideal tool for investigating the consequences of the two-fluid model. Researchers probing two-fluid mechanics with second sound shocks have usually taken large numbers of local (point) measurements of quantities such as temperature jumps and shock speeds. However, since we were interested in the geometry and appearance of second sound shocks, we needed a method of global observation, and so we took schlieren pictures (4).

Used extensively for studying flow phenomena, schlieren photography is a method for mapping the gradient of the refractive index. A parallel light beam is sent through the test section and then focused on a knife edge, which cuts out half the Fourier plane. The remaining light is then imaged onto a camera. The areas with gradients in the refractive index appear as dark and light areas; the areas without gradients appear ideally an intermediate gray. Since the gradient of the refractive index is proportional to the temperature gradient, second sound shocks can be seen very clearly using schlieren photography.

The problem that I worked on involved the interface between the superfluid helium and its vapor. Since there are two types of wave propagation in superfluid helium, a much wider than normal variety of wave reflection-refraction problems are possible.

Not all of the macroscopic boundary conditions holding across the interface are known when evaporation is taking place. Across a nonequilibrium interface, mass, momentum, and energy are constant in the superfluid and in the vapor. To determine the state of the gas we need to know three quantities: p, T, and $\vec{v}$ (the velocity); for the state of the superfluid we need to know four quantities: p, T, $\vec{w}$, and $\vec{v}$. If we give p, T, and $\vec{v}$ for the gas, thus completely specifying its state, then we

have three equations (mass, momentum, and energy) for the superfluid, but we need to know four variables to specify its state. If we give p, T, $\vec{v}$, and $\vec{w}$ for the liquid, then we have an overspecified system, since we only need three quantities to specify the gaseous state. We therefore need some other boundary condition in order to determine all our variables. Practically, this lack of a boundary condition means that we are unable to calculate the strengths of the shocks transmitted and reflected if we send in a second sound shock of a known strength. We believe that taking measurements of the transmitted and reflected shocks resulting from various strength initial second sound shocks would help clarify the boundary condition question.

PRESENTATION AND DISCUSSION OF RESULTS:

Our experimental setup consisted of a dewar and a shock tube with optical windows. The shock tube windows were sealed with compressed indium wire, and the windows had thin-film aluminum heaters on them to help prevent impurities from condensing onto the windows and therefore blocking the view. The dewar was surrounded by a vacuum jacket and cooled further with liquid nitrogen. Liquid (but not superfluid) helium was pumped into the dewar around the shock tube, and then helium gas under one to two atmospheres of pressure was pumped into the shock tube, where it condensed. The dewar and shock tube were then pumped down, thereby lowering the temperature (by evaporation of the liquid helium) below the transition point to about $1.7^{\circ}K$. Planar heat waves were produced by sending a top-hat voltage profile thourgh a planar Nichrome thin film heater located at the bottom of the rectangular test section in the shock tube. A strobe light of variable intensity, triggered after a specified delay time, provided the illumination.

About half the summer was spent trying to align the schlieren imaging system so that we would obtain uniformly gray backgrounds. Aligning the imaging system consisted of a tradeoff between a uniform background and less sensitivity: the more

light the knife edge cut off, the more sensitive the system became, but the more irregular the background became. Since our signals were so weak (a typical temperature jump was 10 mK), and our typical focal lengths were so small (approximately 30 cm)--the greater the focal length, the more sensitive the system--we had great problems achieving the necessary sensitivity with an acceptably uniform background. We tried various combinations of focusing mirrors and lenses, and even tried a spherical schlieren system, using a lens with extreme spherical aberration instead of a knife edge, before we obtained an acceptable sensitivity and uniformity of background.

After aligning the imaging system, we tried to run experiments. We ran into two major problems with our experiments: despite the window heater, we still would get a thin opaque film condensing onto our windows, making it impossible to see the test section. Also, the dewar was not well insulated, so that the heat influx evaporated the liquid helium often before we could take pictures. We tried to solve these problems by using a funnel to make sure none of the liquid helium would hit the windows directly while the dewar was filling up, and by simply filling the dewar with more helium. The funnel system lessened our problems with the windows icing up, and we ran out of helium less often in the last couple weeks, but then we ran into another problem--whatever was condensing onto the windows was also condensing in the tube that pumped gaseous helium into the shock tube, clogging up the tube and making it impossible for the helium to condense in the shock tube. We were unable to obtain any pictures with our 35 mm camera because of these difficulties, although we did obtain a number of test Polaroid pictures of interface shocks.

CONCLUSIONS:

Most of our major problems have either been worked out or will be in the near future--for example, the shock tube will be redesigned with a wider tube for pumping in helium gas--and so Dr. John Torczynski, who was my supervisor for this project, hopes to start running successful experiments early this school year. Although this summer was somewhat frustrating, I did obtain a very realistic view of research, and I learned many

valuable techniques for investigating fluid flow phenomena.

BIBLIOGRAPHY:

1. J. Scholtz, E. O. McLean and I. Rudnick, Phys. Rev. Letters 32 (1974) 147.

2. P. Kapitza, Nature 141 (1938) 74.

3. L. D. Landau, Zh. Eksp. Teor. Fiz. 11 (1941) 592; J. Phys. USSR 5 (1941) 71.

4. J. R. Torczynski, D. Gerthsen, and T. Roesgen, "Schlieren Photography of Second Sound Shock Waves in Superfluid Helium," Phys. Fluids 27 (1984).

The Spreading of Plane Salt Water Gravity Currents

Paul M. Young
1984 SURF
Sponsor: Edward E. Zukoski

Abstract

Measurements of various properties of a gravity driven salt water in water current are given. All data are from experiments in which the salt water inflow rate was kept constant during the run, while density difference and volumetric flow rate were varied from run to run. Plots of the results obtained are given and compared with various theoretical values.

Introduction

Gravity currents are a common and important phenomena, open the door of an air-conditioned room and a current of cold air flows out along the floor in much the same way as the hot gases generated by a building fire spread along the ceiling and down hallways. Many theories about such flow can be formed by considering energy conservation, inertial effects, and viscous effects. It is often not possible, however, to predict under what circumstances various factors will dominate. Thus to gain a better understanding of gravity currents one must have recourse to experimental methods. Much work has been done on this topic in recent years and much discussion and many theories are proffered in the references.

When modelling gravity currents with salt water flows, the method used by the author, theory indicates that the flow is originally dominated by a balance between inertial forces, and later dominated largely by a balance between inertial and viscous forces. An excellent discussion of this theory is given by Chen (1980). Another excellent discussion which demonstrates the relation of various types of gravity currents and the theories which pertain to them is given by Benjamin (1967). Other papers containing both experimental data and theories of interest are listed in the bibliography.

The primary aim of the author's research was to collect experimental data on such flows concentrating in particular on modeling the spread of building fires down hallways. The basic problem examined is: given a specific cavity expansion rate (or volumetric flow rate), how can the propagation rate of the front and the thickness of the spreading fluid be predicted? In order to answer this question data has been collected and comparison made to various theories.

Experimental Apparatus and Operation

These experiments were performed in a hollow lucite prism which

was filled with clear tap water and dyed salt water was injected into one end of the channel to produce the current. Fluorescent lighting fixtures illuminated the channel on one side, while a cart carry video recording equipment was wheeled along the other side to record the motion of the head of the current as it passed down the channel. Exact dimensions and operating features of the apparatus are shown on the enclosed diagram (A).

The fresh water was industrial water supplied from taps in the laboratory and the salt water was the same water with Morton Culinox Food Grade Salt added to obtain the desired density and Kriegrocine Blue Ex Conc. Powder added to dye the solution to visualize the flow. The specific gravity of the fresh water obtained from the taps was .9985 +/- .0003.

The channel was 6"x 6" and was filled with fresh water to the top before any salt water was injected, thus fixing the height of the surface. It should be noted that the outlet which permitted excess water to spill off was located above the salt water inlet. The location of this outlet is an important boundary condition since it fixes the flow in the ambient fluid.

Salt water was prepared in a bucket on the floor and pumped up to a bucket about 10' above the channel. This salt water was allowed to pass through a series of valves and pipes to a flow meter and into the channel. See for example the sketch of Diagram A. By reading the flow meter and closing down or opening up the appropriate valve volumetric flow rates between 30 and 300 cm^3/sec were obtainable. It should be noted that the salt water was allowed to fill an ante-chamber and pass through a stainless steel wool mesh before climbing to the level of the channel, into which it was then allowed to "spill". This was done as opposed to various other "lock release" experiments in which the salt water is collected at the level of the channel and a partition is withdrawn allowing the fluid to spread.

The channel was roughly 100" long and the salt water front was allowed to travel the entire length of the channel. On occasion the wave reflected off the back of the channel was followed upstream. Data taken include:

- o front propagation speed, from plot of front position vs time,
- o density difference between salt and fresh water,
- o volumetric flow rate (obtained from a calibrated rotameter)
- o head thickness,
- o tail thickness (most often just behind head, but occasionally at other locations).

Results and Observations

This research involved a very large amount of data taking and analysis, and for the sake of brevity only a small sample of this can be presented here. This review will concentrate only on those results which were most interesting and important.

Plot 1 is an example of a time vs. position plot of a typical run of the experiment. Features to notice are that the velocity remains fairly constant during the run, though it distinctly falls off just slightly towards the end, usually after a point suggested by Chen

(1980) and discussed below. Data points are taken from still frames of the video tape, graphed, and fit to appropriate lines whose slopes give the velocity. Often two distinct velocities can be determined. This is due to the fact that at the beginning of the run theory predicts a constant velocity, and later a velocity which falls off only as a -(1/5) power and is thus approximately constant by the end of the run.

About 40 runs of the experiment were recorded on video tape. Included were runs which viewed the spreading front from above as well as from the side, runs in which the camera remained at a fixed point during the run as well as runs in which the front was followed. A large variety of density differences and flow rates were used allowing for a maximum spread of data. All quantitative data has been stored in computer files while the source data is stored on video tape.

Theory predicts that in the inertial range of flows the velocity of the front propagation should be proportional to the cubed root of the product of the volumetric flow rate per unit width multiplied by an adjusted gravitational acceleration, that is, the density difference times the acceleration due to gravity. Thus we have

$$V = k^* (Q^*D^*g)^{(1/3)}$$

where Q is the volumetric flow per unit width, g is the acceleration due to gravity, D is the density difference divided by the density of the fresh water, which is slightly less than one in this case, and V is the velocity of the front. We wish to determine a value for the proportionality factor, k. This factor was calculated for many runs and the results were averaged to give a general value in the conclusion.

Theory in this same range also gives a prediction for the thickness of the flowing layer. According to Benjamin (1967)

$$Q/(g^*d^3)^{(1/2)}=((d-h)^2*h*(d^2-h^2))/(d^4*(2*d-h))$$

where d is the height of the channel in which the flow takes place and h is the height from the top of the flowing layer to the top of the channel. Plot 2 illustrates the theory vs. the experimental results.

Chen (1980) suggests a value for the point at which the flow changes from inertially dominated to viscously dominated. He found that at a position equal to:

$$(.1)*Q^2/((g*D*Q)^{(1/3)}*vs)$$

a transition occurs corresponding to a change from a steady to a slowly decreasing velocity. Qualitative examination of position vs. time plots indicate that this is a useful approximation.

Benjamin (1967) also gives a theoretical curve for a plot of

$$Q/(d^3*D*G)^{(1/2)} \quad \text{vs.} \quad V/(d*D*g)^{(1/2)}$$

the explicit formula for which is not given here but is shown on plot 3. Also on this plot are data points from other authors as well as our own. Inspection shows that while most sets of data follow the same functional curve, they are usually low by a scalar factor, which

is about .6 for our results. While further analysis will be required to fully understand the cause for this it is apparently a combination of factors arising from viscous effects, which are important at low Reyold's numbers, and mixing between the current and the ambient fluid which is not included in any of the theoretical treatments.

At one point during the course of the research it seemed that some of the injected fluid was not accounted for when a crude estimate of the total flow was made based on the thickness of the moving layer and its velocity. This prompted an investigation to discover whether or not the thickness of the layer grew with increasing distance from the front . As shown in plot 4, this was indeed the case.

A series of particularly interesting flow visualization runs were made. One of these experiments included an investigation of the flow when a 3/4" brass obstacle was placed on the floor of the channel to simulate a beam on the ceiling of a hallway. When compared with a control run, the velocity before the flow encountered the obstacle was changed by much less than one percent, while the velocity after the obstacle was 34% less. Since the relative dimensions of our model are roughly the same as those of a typical hallway, this is very likely a good indication of what goes on during a building fire in a real hallway.

Conclusions

Based on the results of this research it appears that beams on the ceilings of hallways are a very effective means of slowing the advance of hot gases down a hallway and thus impeding the spread of building fires.

When Reynold's number effects are considered the theories mentioned above appear to be very useful in predicting various qualities of gravity flows. Layer thicknesses are usually found accurately in regions of low Reynold's number, and thus minimal amounts of mixing at the current's head. Velocities are similarly predictable with a proportionality factor, k, of about 0.73 +/- .07. However, again the high Reynold's number flows behave differently from lower ones. The higher the Reynold's number, the faster the flow and the larger the constant, k.

Chen's suggestion of a transition point is supported by the results, though for particularly high flow rates the no slip condition along the channels floor begins to have an effect of slowing down the flow prematurely.

Gravity currents have a distinct tendency to increase in thickness with distance from the front, rising 20% in the first few flow widths, and gradually climbing another 20% at a considerable distance from the front.

As further investigations are made, particularly with the use of computer graphics, the dependence of various qualities of the flow on the Reynolds number and flow rate should become apparent.

It should be kept in mind that this report has been kept necessarily brief, but the author's notebook contains a much more complete record of the data obtained and analyses made.

REFERENCES

Benjamin, T. Brooke, "Gravity currents and related phenomena" J. Fluid Mechanics 1968, vol. 31, part 2, pp. 209-248.

Cetegen, B., Kubota, T. and Zukoski, E. E., "Entrainment in fire plumes." to be published in Combustion Science and Technology

Chen, J-C., "Studies on Gravitationally Spreading Currents." W. M. Keck Lab. of Hydraulics and Water Resources Report No. KH-R-40, C.I.T., March 1980.

Chen, J-C., and List, E. J., "Spreading of buoyant discharges." Proc. 1st CHMIT Seminar on Turbulent Buoyant Convection, Dubrovnik, 1976, pp. 171-182.

Didden, N., and Maxworthy, T., "The viscous spreading of plane and axisymmetric gravity currents" J. Fluid Mechanics 1982, vol. 121, pp. 27-42.

Lee, J. H., Jirka, G. H., and Harleman D. R. F., "Stability and mixing of a vertical round buoyant jet in shallow water" Energy Laboratory Report No. MIT-EL 74-014, Massachusetts Institute of Technology, Nov. 1974.

Simpson, J. E., "Gravity Currents in the Laboratory, Atmosphere, and Ocean", Annual Reviews of Fluid Mechanics, Volume 14, 1982.

Simpson, J. E., and Britter,R. E., "The dynamics of the head of a gravity current advancing over a horizontal surface.", J. Fluid Mechanics 1979, part 3, pp.477-495.

Wilkinson, D. L., and Wood,I. R.,"A rapidly varying flow phenomena in a two-layer flow."J. Fluid Mechanics 1971, vol 47, part2, pp. 241-256.

Wilkinson, D. L., "Motion of air cavities in long horizontal tubes." J. Fluid Mechanics 1982, vol 118, pp. 109-122.

Wood, I. R., and Simpson, J. E, "Jumps in layered miscible fluids." J. Fluid Mechanics 1984, vol 140, pp.329-342

Zukoski, E. E., "Influence of viscosity, surface tension, and inclination angle on motion of long bubbles in closed tubes." J. Fluid Mechanics 1966, vol 25, pp. 821.

Diagram A

Over flow
Fill Line
PUMP
Salt + H2O STORAGE BUCKET
MIXING BUCKET
~10 ft. high
Air Bleed
Flowmeter
To drain
To drain
Stainless Steel Wool Mesh
Salt Water Current
(Mirrors may be placed here)
Joint
Fresh water Ambient
Lucite Prism
100"
Air Bleed
6"

Run 37 [illegible] .11 6/15/54 P. Your

Plot 1

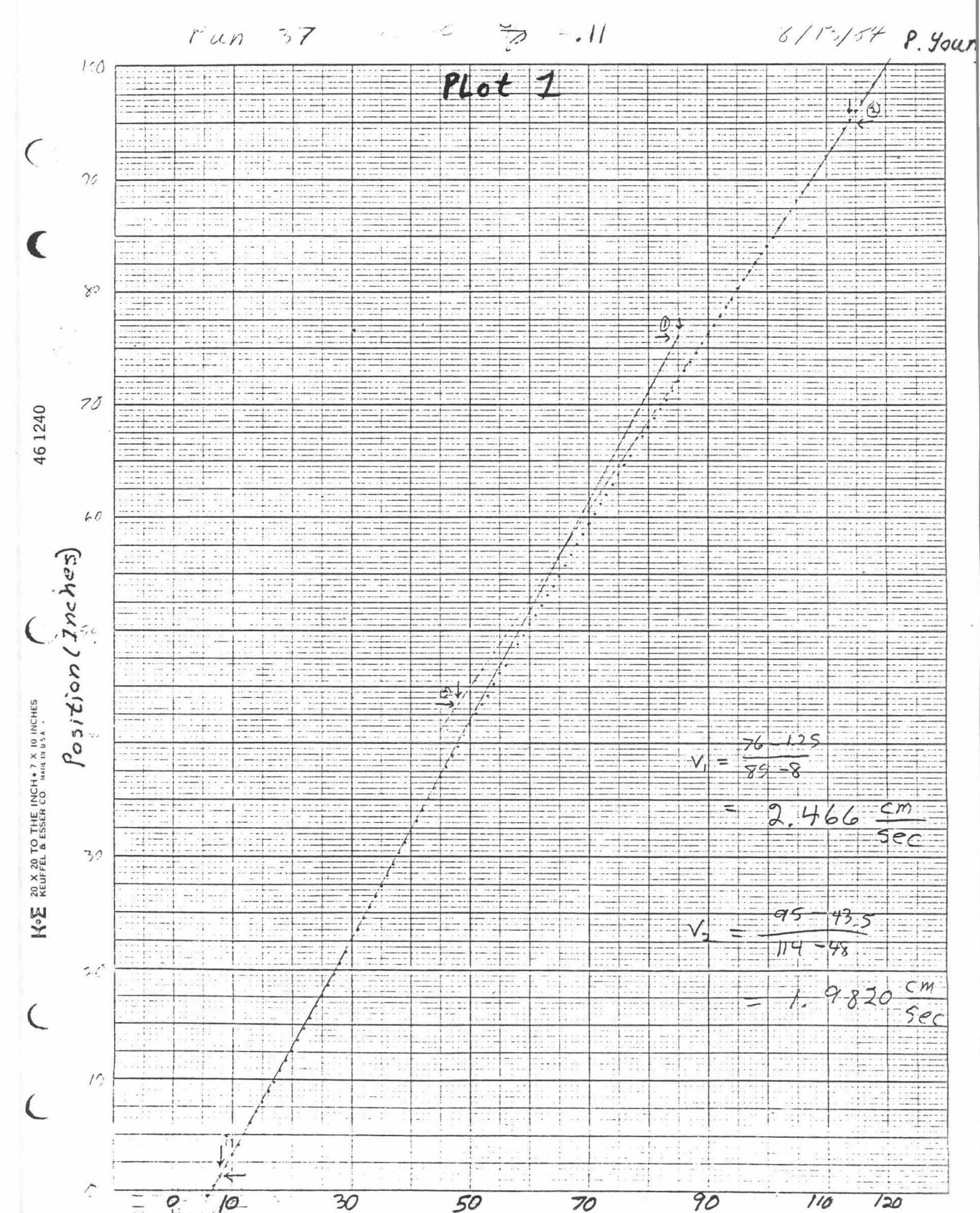

$$V_1 = \frac{76 - 1.25}{85 - 8}$$

$$= 2.466 \frac{cm}{sec}$$

$$V_2 = \frac{95 - 43.5}{114 - 48}$$

$$= 1.9820 \frac{cm}{sec}$$

P. Young

Plot 2

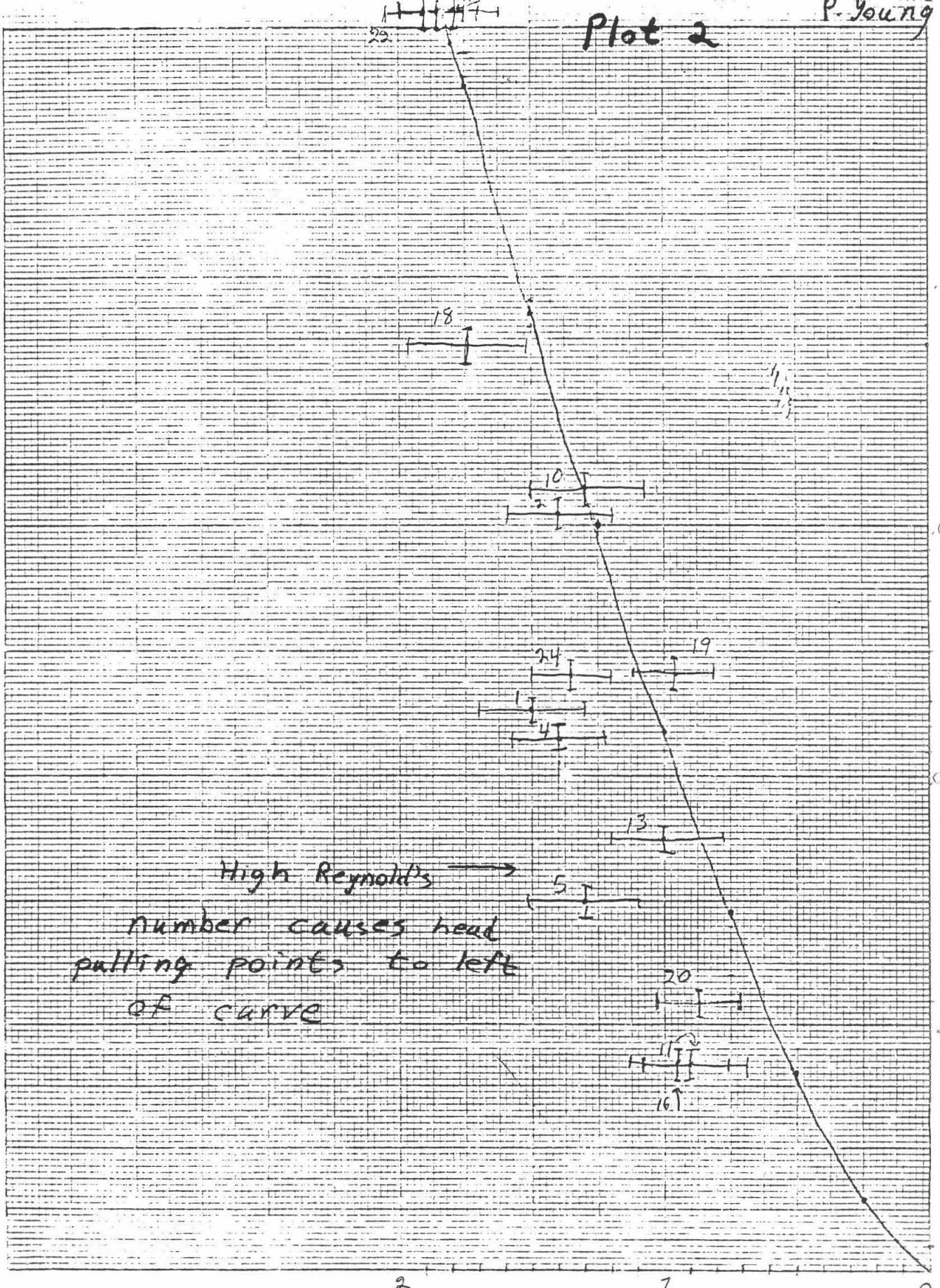

High Reynold's number causes head pulling points to left of curve

P. Young

Plot 3

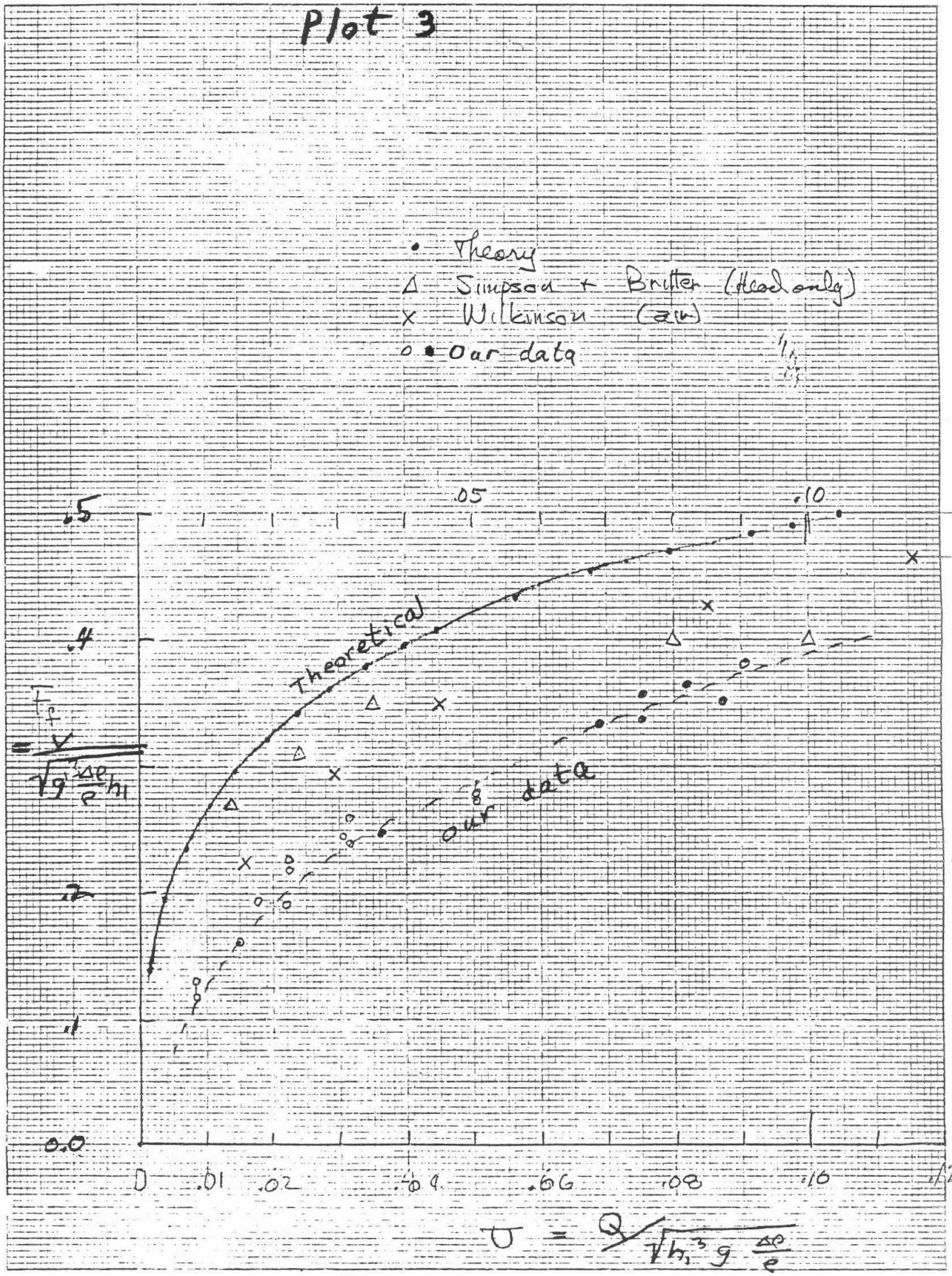

EFFICIENCY® 22-107
CROSS SECTION 20 X 20 TO INCH
AMPAD

Plots demonstrating increasing thickness of currents

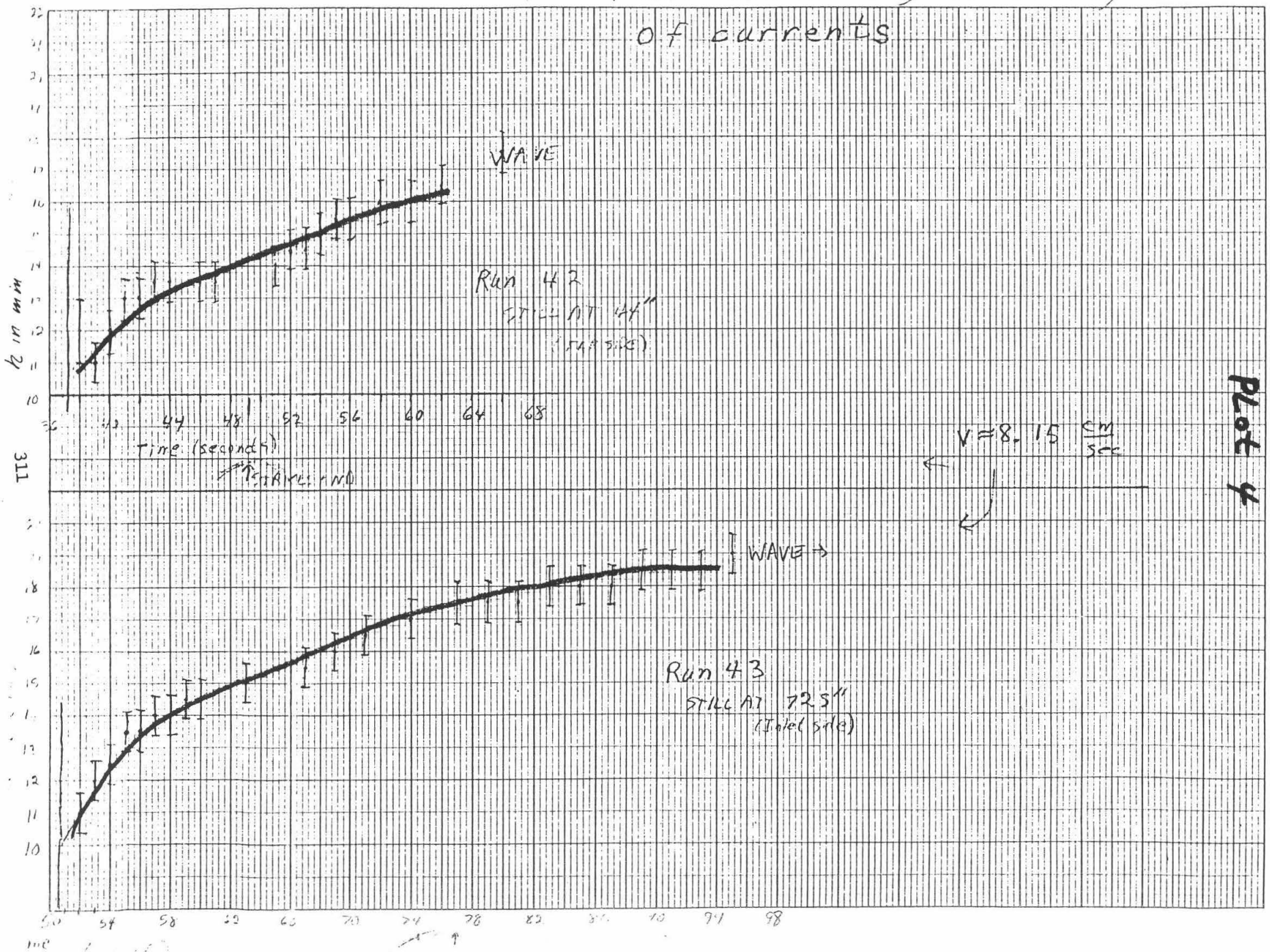

Plot 4

311

N. Young

the building that are 30 to 40% of that observed outside, with the peak concentration indoors lagging that outdoors by about one half hour.

The greatest variation in indoor ozone levels occurred among the final group of museums studied--those sites with no air conditioning. These buildings rely upon open doors and windows for ventilation and cooling. A description of the ventilation systems observed at these sites follows:

1) Pasadena Historical Museum--A few open windows, mostly on the second floor, provide poor ventilation. An exception occurs when the site is used for luncheons or meetings, when the large front door is left open for the duration of the meeting. On normal days, the building is reasonably well sealed, and outdoor air enters the building at a very slow rate.

2) Southwest Museum--A high-power fan in an open window forces about 5000 cubic feet of air per minute out of the building and initiates convection throughout the main portion of the building. Two exhibit rooms are largely unaffected by this continuous flow. Many open windows and doors allow large amounts of circulatory air to pass through the building.

3) Lang Gallery--One open window and one door open during public hours provide the ventilation at this site. The door is shut when the staff leaves for lunch or in the evening. Very little outside air is permitted to enter the facility. One or two fans circulate the air within the facility, but these fans do not force exchange with air outdoors.

4) Villa Montezuma--A dozen or so open windows and a door provide ventilation, while numerous fans circulate the air within the facility. A large up-draft can be felt on the stairwells of this largely vertical building as the warm interior air rises to be replaced at the ground level. Consequently, many of the first floor doors and windows serve as air inlets.

5) Serra Museum--Open doors and windows, generally large in size and few in number, provide for ventilation at this facility. No general circulation pattern can be noted, except for the one open door facing the ocean, which is subjected to a steadier breeze than the other open ports.

A summary of the ozone data collected at these sites is shown below. Again, all ozone levels are maximum hourly average values.

Geological and Planetary Sciences

A Search for Gravitational Lenses

Author: Gregory A. Burnett[1]
Sponsor: G. Edward Danielson[2]

Abstract: *A total of 152 high resolution images of quasars were investigated to see if any possessed distortions characteristic of gravitational lensing. Herein it is shown that ten quasars do have an elongated image: one is presented as a very good candidate; one is an extended object; and eight are presented as possible candidates. Further, six more quasars are listed which have close companions (separation ≤ 4.5 arc seconds.)*

Introduction

A gravitational lens is a system in which the path of light from one body is deflected by the gravitational field of another massive body. In our case this means that the light from a quasar is being deflected by a galaxy or a cluster of galaxies in such a way that the quasar appears to us a multiple object. It is predicted[3] that if the gravitational field of the galaxy is high enough, in the general case there will be an odd number of apparent images of quasars of different brightness and separations. In the best-established case, there are probably three images, but one of these is very faint and close to another, so that the image appears double. Further complicating the resultant picture will be the superposed image of the galaxy. If the lensing is caused by an extended cluster then there may be only one image in which case no lensing can be detected because of the lack of the other images.

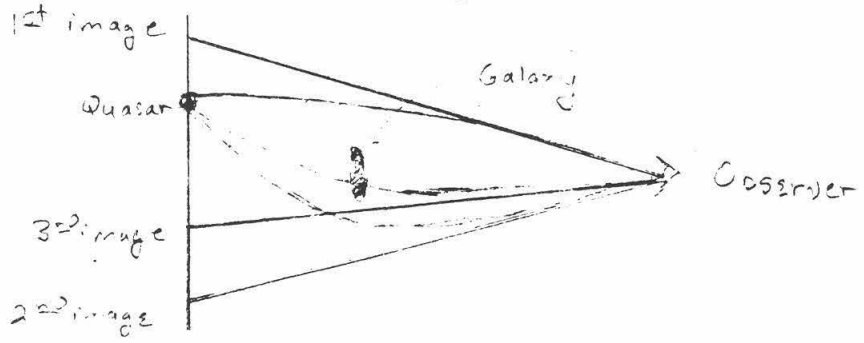

In the past, gravitational lenses have been discovered by chance, more or less, so that at present there are only five candidate systems known. With these known lenses the separations range from about 2 arc seconds to about 7 arc seconds. Yet, it is predicted that with the majority of the lens systems this

1. Summer Undergraduate Research Fellow, California Institute of Technology
2. Member of the Professional Staff, California Institute of Technology
3. Young, Peter, Gunn, James E., Kristian, Jerome, Oke, J. B., Westphal, James A., 1980, *ApJ*, **241**, 507.

separation will be on the order of about 0.5 to 1.0 arc seconds. Since ground-based observations allow for only about 1.0 arc second resolution, we shall get around this by composing a model star for each picture from the stars on that frame and compare it very carefully to the image of the quasar. By doing this it is hoped that more candidates for gravitational lenses can be found. Further, those quasars with resolvable companions shall be noted so as to not overlook the more obvious candidates.

Method

Herein, the term frame refers to a picture taken with the 200 inch telescope using the PFUEI[4] coupled with a Texas Instruments CCD.[5] From 1980 to 1981 Jerome Kristian, Don Schneider, and Peter Young took 100 second exposures of 187 different quasars. These were taken when the quasars were close to the meridian and under good seeing conditions. These digitial data were then put into a 500 by 500 picture format so the could be analyzed with a computer. Of these 187 frames, only 152 were suitable for final analysis.

The first step in analyzing a frame is to form a model star. Let $s_n(i,j)$ be the n^{th} star's image less d_n where d_n insures that $\sum_{ij} s_n(i,j) = 0$. In other words, the dc level of the image has been subtracted out. We similarly define $q(i,j)$ to be the image of the quasar less its dc component. We have subtracted out the dc levels because in the original data each image is standing on some sort of background. By subtracting out d_n, $s_n(i,j)$ will be independent of that background. We then define

$$S(i,j) \equiv \sum_{n=1}^{N} s_n(i,j).$$

This is to be known as the model star--also known as the point spread function. It is the sum of all the stars and represents the ideal star for the frame being considered. Note that since it is a sum of stars, its noise will be considerably reduced from that of any individual star. Since it is the direct sum of the images there is an implicit weighting in that brighter stars are better represented than fainter stars. This is reasonable for brighter stars are better defined as they have a better signal to noise ratio than do fainter stars.

Now that we have composed the model star for the frame, we must see how well each star and the quasar *fit* the model star. Define

$$\Delta^2_n \equiv \sum_{ij} [s_n(i,j) - a_n S(i,j)]^2,$$

where a_n minimizes Δ_n. We can interpret a_n as being the ratio of the intensity of the n^{th} star to the model star. Hence a_k/a_m is the ratio of the intensities of the k^{th} star to the m^{th} star. Δ_n gives us an idea of how well the n^{th} star *fits* to the model star. That is, if Δ_n were zero then the fit would be perfect.

We now assume that all the stars in the frame can be represented by a model star and that the only difference between the model star and the actual star will be the statistical fluctuations in the data. Further, as Δ_n scales like a_n we need to somehow *normalize* the Δ_n so that they can be compared. We do

4. Prime Focus Universal Extragalactic Instrument

5. Charged Coupled Device—used to record an image digitally with high effeciency

this as follows. After computing Δ_q, the difference for the quasar in the same way we find the Δ_n we then compute

$$\Delta'_q \equiv \frac{1}{a_q}\Delta_q \quad ; \quad \Delta'_n \equiv \frac{1}{a_n}\sqrt{\frac{a_n}{a_q}}\Delta_n = \frac{1}{\sqrt{a_n a_q}}\Delta_n$$

The factors of $1/a_n$ are easily seen to be account for the fact that Δ_n scales like a_n. Since statistical fluctuations in the data are of order $\sqrt{a_n}$, and, since the intensity scales as a_n, then, the greater a_n the better defined the star. Thus, we expect that after dividing by a_n, the Δ'_n will be less for brighter stars. We must account for this by multiplying by $\sqrt{a_n/a_q}$. The a_q comes in so that it does not appear in Δ'_q.

Next, we need to now how well the quasar fits in relation to the stars in the frame. Now, in order to determine if the quasar does deviate *significantly* from the model star we work as follows. The average, $\mu_{\Delta'}$, and deviance, $\sigma_{\Delta'}$ of the star's differences Δ'_n are

$$\mu_{\Delta'} \equiv \frac{1}{N}\sum_{n=1}^{N}\Delta'_n \quad ; \quad \sigma^2{}_{\Delta'} \equiv \frac{1}{N-1}\sum_{n=1}^{N}[\Delta'_n - \mu_{\Delta'}]^2.$$

Thus, the significant quantity to consider is how many sigma does the quasar fall from the mean or

$$\beta \equiv \frac{\Delta'_q - \mu_{\Delta'}}{\sigma_{\Delta'}}.$$

Thus, we take β as a measure of how *different* the quasar is from the stars in the frame. A large positive β indicates that the quasar is significantly different from the stars in the frame. A negative β means that the quasar matches the model star better than the average star on the frame does. Actually, better quantities to consider are the further normalized

$$\overline{\Delta}'_n \equiv \frac{\Delta'_n}{\sigma_{\Delta'}} \; ; \; \overline{\Delta}'_q \equiv \frac{\Delta'_q}{\sigma_{\Delta'}} \; ; \; \overline{\mu}_{\Delta'} \equiv \frac{\mu_{\Delta'}}{\sigma_{\Delta'}}.$$

Then, we have simply

$$\beta = \overline{\Delta}'_q - \overline{\mu}_{\Delta'}.$$

These allow one to quickly look at the figures and get a good idea of what they mean.

In actually constructing the $s_n(i,j)$ and $q(i,j)$ there is the problem of aligning the stars together to form the model star $S(i,j)$ and then aligning the quasar to the model star. The task is not trivial in that this must be done to accurate to at least a 1/10 of a pixel in order to get good results. This has been done to an accuracy of about 1/100 of a pixel just to be sure. The method used is to align the centroids of the stars as a first approximation and then to slightly shift the positions of the stars so as to minimize each Δ_n. Yet, this is slightly ambiguous as the $s_n(i,j)$ actually define $S(i,j)$. The ambiguity lies only in the actual position of where the stars should lie, their relative positions are fixed. The solution is approximated by using the centroided $s_n(i,j)$ to construct an $S(i,j)$ and then to shift the stars so as to find a local minimum in Δ_n. Here it is assumed that the first order solution is good enough to get to the global minimum. After doing this for all the stars a new $S(i,j)$ is constructed and the process is repeated for about five times. This method has been found to work quite well in practice. Once the final $S(i,j)$ has been constructed it is a simple task to find $q(i,j)$ as one just has to minimize Δ_q by shifting the quasar around.

Further, there is one more problem. When an image of a star falls upon

the CCD the center of the star may not be perfectly centered on a pixel. Thus, in constructing $s_n(i,j)$ each star must be *repixelated*. The method used is to conserve intensity over the image by a simple rebinning. This does somewhat degrade the resolution in the data, but, tests show that, in this case, it is not a significant problem.

Discussion

The above analysis has been successfully carried out on 152 quasars. Although this predicts which quasars are significantly different from stars via β, it does not say how they are different. For this, visual inspection of the residuals is employed. To be considered a good candidate the quasar less the model star $q(i,j)-a_q S(i,j)$ was displayed and the pattern of there being two regions of white (high data numbers) separated by a black rift (low data numbers). The reasoning behind this is that if one were to superpose two point sources separated by a fraction of their FWHM (full width at half maximum) and subtract out another that is centered directly between them, then one would expect that the maxima of the two superposed stars would result in two white regions and the maxima of the center star would result in a black region. This, has been found to be the best test of all in finding closely superposed objects.[6]

Results

When the 152 frames were analyzed, ten possible candidates were found. Jerome Kristian then took this list of quasars to take new frames of these objects. When these were analyzed it was found that only two retained their extended shape. It has not yet been decided to exclude the other eight as being candidates as the seeing on the new frames was not as good as on the original frames.

Quasars Believed to be Possible Candidates For Gravitational Lenses

Quasar	$\overline{\Delta}_q$	$\overline{\mu}_{\Delta}$	β	FWHM (")	N
Q0008+171	11.3	5.1	6.2	1.15	4
Q0030+034	9.0	3.6	5.4	1.12	4
Q0031+035	6.7	2.8	3.9	1.20	2
Q0051+291	12.1	1.6	10.5	1.07	2
Q0313+344	11.2	5.1	6.1	1.22	3
Q2128-123	92.5	22.4	70.1	1.28	3
Q2303+183	17.6	8.5	9.1	1.20	6
Q2305+187	30.5	21.9	8.6	1.29	5
Q2325+269	12.2	7.7	4.5	1.16	6
Q2334+019	35.9	11.2	24.7	1.26	2

Note that Q2325+269 means the quasar at 23 hours 25 minutes right ascension

6. See the examples at the end of this text.

and +26.9 degrees declination. In the above, FWHM is the full width at half maximum in arc seconds of the model star for the frame that contains the quasar. This gives us an idea of how well two objects can be resolved for that frame. That is, the lower the number, the better the resolution. The number N is the number of stars used to make the model star for the frame that contains the quasar. The quasars Q2128-123 and Q2305+187 (extended object) remained candidates under the new frames while the others did not. Besides closely lensed images which cannot be resolved, those which are separated up to about 4.5 arc seconds have been noted.

Quasars with companions ≤ 4.5 arc seconds away			
Q0031+035	Q0034+393[1]	Q1657+265	Q1756+237
Q1857+566[2]	Q2002-185	Q2003-025[1]	Q2005+403[1]
Q2115-174	Q2247+132[2]	Q2154-210	

Those marked with a [1] are members of fields with a high density stellar background and so are less likely to be lens systems. Those marked with a [2] have already been checked and have not been found to be lens systems.

Conclusions

It is believed that ten possible candidates for gravitational lenses with image separations ≤ 1 arc seconds have been found; another six quasars have close companions (separation ≤ 4.5 arc seconds) that may be secondary images. Further frames with very good seeing will be required in order that this list can be strengthened. As to whether these actually are lens systems will then require the measurement of the spectra of the objects. If the two spectra are identical then it can then be said that the quasar is indeed part of a lens systems. This type of analysis can be done most readily for those quasar in the second table, i.e. those with close resolvable neighbors. But, in the case of the first table, the objects will require extremely good imaging in order to be resolved. Spectral analysis of these objects will require non-groundbased measurements. That is, it will take the HRS[7] of the Space Telescope to obtain the spectra of the individual objects.

Acknowledgements

I would like to thank Don Schneider and Jerry Kristian for allowing me to work on this project and for all their help. Also, I thank Ed Danielson for sponsoring me on this SURF project and for providing me with all the materials necessary for its completion.

7. High Resolution Spectrometer

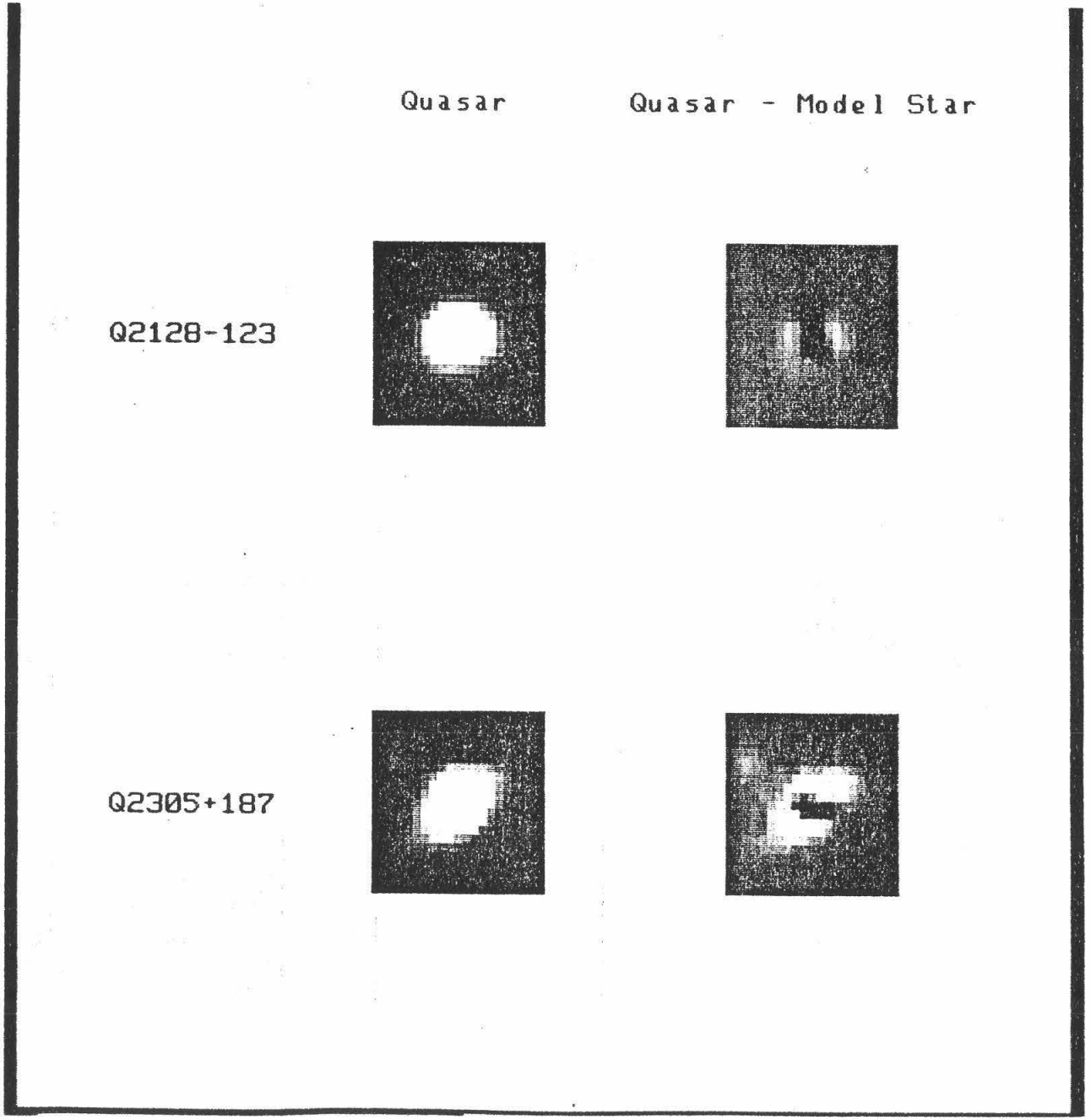
Quasar
Quasar - Model Star
Q2128-123
Q2305+187

The Shock Pyrometry Experiments of Iron

by Cathy Chang, Thomas J. Ahrens (Faculty Advisor),
Jay D. Bass, and Bob Svendsen

Abstract

By using an electron beam gun evaporation system, a sample consisting of 0.5 microns thick of iron layer was deposited on a sapphire (Al_2O_3) disk. The shock temperature of pure iron, measured in the shock wave experiment, is 5920°C at 300 GPa was obtained by driving a strong shock wave through the iron and measuring the color spectrum of the light emitted by the iron.

Introduction

The properties of iron and its melting temperature under the high pressure condition have long been of key geophysical and physical interest in models of the high pressure equation of state of iron, and may constrain the state of the earth's inner core. Geophysical data suggest that the liquid iron-bearing outer core may be in equilibrium with a solid pure iron core of radius 1,200 km (or depth of 5100 km at a pressure of about 330 GPa). Therefore, it appears that one of the very few constraints on the temperature in the core of the earth is related to the melting point of pure iron.

Many shock wave experiments have been performed on many different materials such as SiO_2 or NaCl. The results enable the scientists to have a better understanding of the equation of state as well as the structure and chemical properties of these materials at high pressure. Considerable interest has also centered on the problem of shock temperature measurements in opaque materials such as metals. A major part of those interests has been focused on the experiments that examine the thermal radiation from the interface between an opaque sample and a transparent anvil layer. Those works have been described by Grover and Urtiew[2] and form the basis of this research. Modern experiments for the dynamic compression of metals can provide measurement of the temperature of pure iron to compare with theoretical predictions in the 200-400 GPa pressure range, (a range over which present approximate theories predict iron, should meet). This range of temperature and pressure is achievable with the Caltech light gas gun. The concept of this experiment is to evaporate a pure iron layer of .5 μm thick onto a sapphire disk. The coating is then impacted by a high speed projectile and strong shock (up to 330 GPa) is driven into the coating and then the sapphire window. The radiation versus wavelength and time from the Al_2O_3-Fe interface is measured and interpreted in terms of the interface temperature, by the optical pyrometry method[3]. The feasibility of this type of experiment was demonstrated in 1979 by G. Lyzenga, then a Caltech graduate student in Applied Physics. He inferred a drop in the shock temperature of pure Ag which appeared to correspond to the melting at about 130 GPa and 4400 K with this kind of experiment. Thereby the shock temperature obtained from this experiment will certainly place a firm upper constraint on the temperature at the outer core-inner core boundary which is not now available.

Experimental

The sample used in this shock wave experiment is a sapphire disk (density 3.98 g/cm^3), 1.5 cm diameter, 3 mm thickness, with .5 μm of an even layer of

iron (density 7.88 g/cm^3) deposit on it. The purpose of the sapphire disk in this experiment is used as a transparent shock "anvil". It's known that the optical radiation from the shock-compressed material cannot escape from the opaque sample. Radiation from the free surface at the moment of shock arrival may be monitored, but such measurements pertain to the residual post-shock state of the sample. The sapphire disk is used to solve this problem, since it offers a close shock impedance match to iron and it also remains transparent at high shock pressure where many metals will become hot enough to radiate.

In order to prevent the gap and roughness between the interface of the sapphire disk and the iron, careful sample preparation is needed. There are several options for the preparation of sample such as vacuum deposition, sputtering, or electron beam deposition. The method of vacuum deposition was tried first in this experiment. However, it did not seem to be suitable for the purpose of iron. Mainly because for the deposition of iron, the condition of very low pressure such as 1×10^{-6} torr to 5×10^{-7} torr, is needed. It's impossible for the vacuum coating machine in the S. Mudd building to pump down to such low pressure. Also, the thermal expansion of iron is a main factor, too. It should be noted here that from many attempts of vacuum deposition of iron, it is observed that iron would not attach to the sapphire disk very well, partly because the required low pressure is not present. Also, a very thick layer of titanium (50 Å) was vacuum deposited on the sapphire disk. It was hoped that iron might stick on the titanium layer. However, the result did not show a promising outcome. The method of sputtering proved not to be successful. Since the sputtering machine in Steele is of the type employing a magnetron, on the other hand, the iron disk used for the purpose of sputtering played the role of a magnet which interferred with the process of sputtering. Nevertheless, the method of electron beam deposition is proven to be successful. The deposition of Fe was done in the e-gun (electron beam) evaporation system made by the Varian company. The basic principle behind this system consists of the electron beam which has been accelerated by the ion beam. The beam ejects iron atoms which in turn deposit on the sapphire disk. The energy source of this system is 3 k volts. The base pressure in the vacuum jar is 9×10^{-8} torr. The pressure goes up to 3×10^{-7} torr during the deposition. The rate of the deposition is 25 Å/sec. The final result is the deposition of 0.5 μm of iron film on the sapphire disk, due to the limitation of the machine. It should be pointed out here that a second layer of iron was unsuccessfully deposited on the first layer of iron, because of surface oxidation.

Besides the careful preparation of the sample, the thickness of the deposit of iron film has other constraints. The deposited iron layer has to be thick enough so that the temperature spike induced in the metal plate at the imperfect interface between the base plate and film does not have time to diffuse via Fourier conduction through the film and affect the measured temperature during the length of the experiment. The goal at the beginning of our research was to deposit 50 μm layer of iron. However, we could produce only a 0.5 μm thick layer of iron at best.

After sample preparation, it was driven to shock pressure of ~300 GPa via impact of 1.5 mm thick flyer plate accelerated to the speed of 5.771 ± 0.003 km/sec using the light gas gun. Thermal radiation emitted by the shock sample

during the period of shock wave transit was measured at 4 wavelengths simultaneously (450 nm, 600 nm, 750 nm, 900 nm) by the pyrometer and recorded by oscilloscopes. The oscilloscope with 750 nm failed to work in the experiment; however, the radiance was detected on a backup digital recording system. Comparing the three records at different wavelengths, the record at 900 nm shows the most "ideal" result. The emitted light radiation (as shown in Fig. 1) recorded at 900 nm, rises rapidly upon the shock passage through the interface. After that, a little spike of signal arises due to slight reverberation at the interface. The record signal then remains nearly constant, although a slight decay occurs. After a period (230 ns), rarefaction decompresses the interface and the recorded intensity decays to a value assumed to be the zero-pressure state of the sample. The data collected from the oscilloscope records (3 wavelengths) are summarized in Table 1.

In order to obtain the interpretation of the pyrometer signal in terms of the shock temperature, the measured value of spectral radiance is compared with the thermal radiation spectrum. According to the Planck blackbody radiation formula[4]: N_λ which is the spectral radiance of the sample equals $C_1\lambda^{-5}\ (e^{C_2/\lambda T}-1)^{-1}$ ($e_1^\lambda = 1.19 \times 10^{-16}$ wm^2/sr, $e_2 = 1.439 \times 10^{-2}$ mk, λ is the given wavelength and T, the temperature). In some cases, the radiation is not that of a blackbody, being reduced by a factor of e which is the emissivity[5]. The emissivity of the material mainly depends on its surface properties. Therefore, in this experiment, when the value of N_λ is measured, the emissivity and the shock temperature are used simultaneously to obtain the best fit of the Planck equation. From the equation: $N_\lambda = A_s T_L / A_L \cdot .25 \times 10^7/a$, N_λ is calculated. (A_s = Amplitude of the oscilloscope signal; A_L = amplitude of the calibration lamp; T_L irradiance of calibration lamp; a = area of window, $2.798 \cdot 10^{-5}$m^2). The best fit to the data, assuming $\varepsilon = 1$, is 5920° K. A fit to data from all 4 channels has not yet been conducted.

Conclusion

In summary, by using the light gas gun and the pyrometry technique in this shock compression experiment, spectral radiance of Fe has been measured at ~300 GPa. The shock temperature is calculated to be 5920°C. Since the temperature at the outer core-inner core boundary is thought to be controlled by the melting point of iron at the existing pressure at the boundary 330 GPa, the calculated melting point of iron at 5920°C will place a definite upper constraint on the temperature at the outer core-inner core boundary of the earth. The value achieved is ~1000° higher than previously estimated by Brown and McQueen (1980) Geophys. Res. Lett., 7, 533-536.

References

1. Stacey, F. C., Physics of the Earth, 2nd ed. John Wiley & Sons, 414 pp. (1977).

2. Urtiew, P. A., and R. Grover, Temperature deposition caused by shock interactions with material interfaces, J. Appl. Phys., 45 140-145 (1974).

3. Lyzenga, Gregory A., Shock temperature of materials: Experiments and applications to high pressure equation of state, Ph.D. Thesis (California Institute of Technology), 25-45 (1980).

4. Lyzenga, G. A and Ahrens, T. J., Multiwavelength optical pyrometer for shock compression experiments, Rev. Sci. Instrum. 50 1421-1424 (1979).

5. same as 4, p. 1424.

Figure Captions

Fig. 1. Radiance versus time for iron film shocked to 200 GPa. Duration of radiance signals is 230 ns; corresponds to shock transient time to Al_2O_3. Time divisions correspond to 100 ns.

Figure 1.

Oscilloscope records of thermal radiation intensity ~~in~~

(1) channel 1. wavelength 450 nm

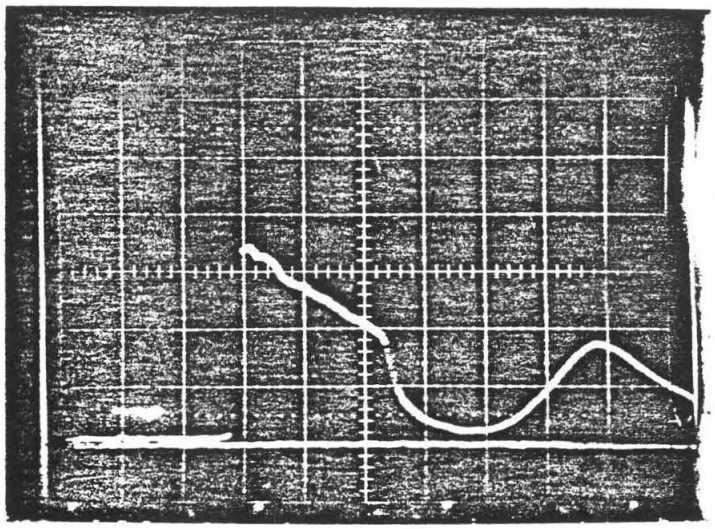

ch. 1
450

(2) channel 2

600 nm

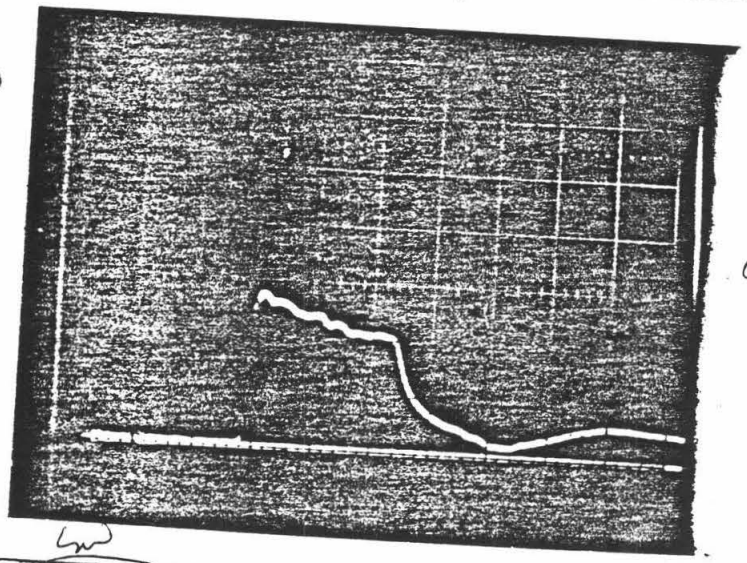

ch. 2
600 nm

time period?

(3). channel 3

900 nm

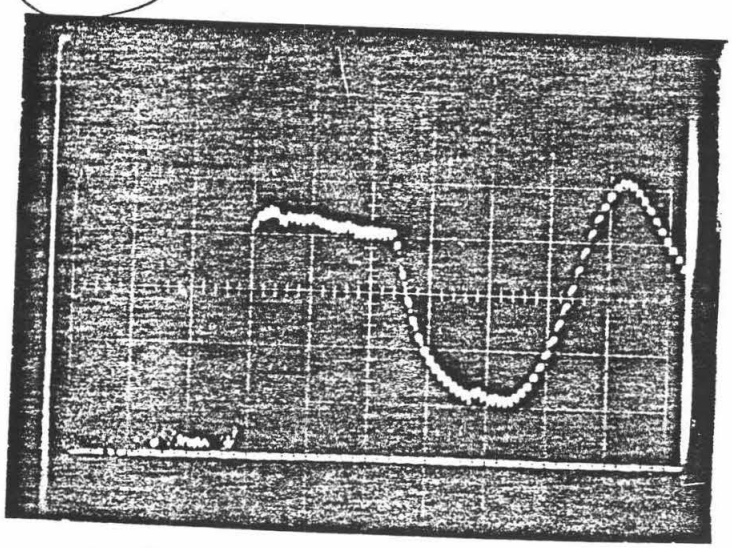

ch. 3
900

bar

Fig 1

Table 1

	calibration signal (mv)		start of shot signal (high) (mv)	end of shot signal (low)	
channel 1 ($450 \cdot 10^{-9}$m)	1.75	.35 div @5mv/div	660	360	(3.3 div @.2V/div)
channel 2 ($600 \cdot 10^{-9}$m)	12.5	2.5 div @/5mv/div	1300	1000	(2.6 div @.5V/div)
channel 3 ($900 \cdot 10^{-9}$m)	7.25	1.4 div @5mv/div	210	195	(4.2 div @50mv/div)

Table 2

λ(nm)		450	600	900
A_S	high (mv)	660	1300	210
	low	360	1000	195
A_L		1.8	12.5	7.4
I_L	($\mu w/cm^2 nm$ @ 50 cm)	908	2.90	5.01
N_λ	high	$2.975 \cdot 10^{13}$	$2.695 \cdot 10^{13}$	$1.270 \cdot 10^{13}$
	low	$1.623 \cdot 10^{13}$	$2.073 \cdot 10^{13}$	$1.180 \cdot 10^{13}$

(1)

A_S = amplitude of signal

A_L = amplitude of calibration lamp

I_L = irradiance of cal. lamp

N_λ = spectral radiance of sample

(2)

e \ T	T(°C)	$\sigma_{n\lambda}$
.95	5980	$.16 \cdot 10^{13}$
.94	5990	$.15 \cdot 10^{13}$
1 (blackbody)	5920	$.19 \cdot 10^{13}$

e = emissivity

T = shock temperature

Resurfacing Europa with Water

Glen Crawford
Advisor: David J. Stevenson

Summer Undergraduate Research Fellowship
California Institute of Technology

ABSTRACT

A thermal model of Europa is discussed, as are the implications of the presence of carbon compounds in Europa. It is determined that a mole fraction of $CO_2 \geq 0.005$ is necessary to cause resurfacing of Europa. Displacement profiles of liquid and gas filled cracks in the ice crust are shown and discussed.

Introduction

Voyager images of Europa, the second major satellite of Jupiter, show a bright smooth surface composed mainly of water ice and highlighted by many long bands of brown or dark grey which have been identified as fractures in the crust. Very few impact craters have been identified, and these are typically small in size (10-20 km) [1]. Many theoretical models have suggested that Europa consists of a silicate core, overlain with $\approx$ 100 km of H_2O, with the few tens of km closest to the surface being in the form of water ice [2]. Squyres et al. [3] have suggested that the surface features can be explained if the ice crust is regularly resurfaced by liquid water driven up from the ocean below by tidal stresses causing fractures in the crust.

The pupose of this work is to determine if such a tidal resurfacing mechanism can really work in present-day Europan conditions, and if so, what are the details of its operation and its consequences in terms of expected observations.

Results

The thickness of Europa's ice shell can be determined by solving the one-dimensional heat conduction equation, the thickness of the crust being the one dimension of freedom, with the boundary conditions being a temperature of 120 K at the surface and 260 K at the ice-water interface at the base of the crust. A total heat flux of the form $F=(\frac{F_t}{d})\ z+F_0$ was assumed, with F_0 representing radiogenic heat soiurces and F_t tidal heating, and d is the crust thickness to be determined. We used

$F_0 \approx 5\times10^{-3}$ watts/meter^2 and $F_t \approx 50\times10^{-3}$ watts/meter^2, which gave $d \approx 10$ km, fairly consistent with the results of Squyres et al. We expect interior heat flow will be anisoptropic so that the ice crust is of approximately constant thickness, even though thermal boundary conditions at the pole (T $\approx$ 40 to 50 K) would normally require a thicker crust near the pole.

Convection in the ocean or crustal layer of Europa will occur if the Rayleigh number is > 1000. In this case, the Rayleigh number is given by [4]:

$$Ra = \frac{g\alpha\Delta T z^3}{\nu\kappa} \qquad (1)$$

using parameters appropriate for Europa and water ice, g= 130 cm/sec^2; $\alpha=1\times10^{-4}$ deg K^{-1}; $\kappa=10^{-2}$ cm^2/sec ; and $\nu=10^{15}\ exp\,(25\times(\frac{T_m}{T}-1))$ cm^2/sec , where T_m = 273 K. We find Ra < 3 throughout the layer. Lowering the tidal heat flux to values comparable to the radiogenic heating still returns a non-convective solution. We conclude the ice crust dissipates heat entirely through conduction. We also note that for the liquid ocean, $\nu=10^{-2}$ cm^2/sec while other constants do not change, so Ra is quite large and convection occurs easily, so the ocean is essentially adaiabatic.

The chief difficulty in getting water to the surface of Europa is the problem of buoyancy: the water is more dense than the ice crust, and so will not want to rise any nearer the surface than

$$\Delta h = h(1-\frac{\rho_{ice}}{\rho_{water}}) \qquad (2)$$

where Δh = thickness of the crust, ρ_{ice} = 0.92 gm/cm^3, and ρ_{water} = 1.0 gm/cm^3. For h = 10 km, $\Delta h = 8\times10^4$cm ; the water will indeed boil if exposed to the surface, but the vapor pressure of water is small here (3×10^{-3} bars) and so the boiling is really insignificant. We also expect the water to freeze out on the walls of the conduit long before it reaches the surface. Further, the length of a crack, L, formed due a tidal stress T, is roughly:

$$L = \frac{T}{(\rho_{water}-\rho_{ice})g} \qquad (3)$$

For Europa, $T \approx 1\times10^6$ dynes/cm^2 = 1 bar, so $L \approx 1\times10^5$ cm, or only one tenth of the crust thickness. With these constraints it seems physically impossible to get water to the surface.

To try to overcome these problems we considered the presence of carbon compounds -- particularly CO_2, CH_4 and CO -- dissolved in the ocean and also contaminating the crust in the form of ices or clathrates. the gases are not highly soluble in water, so they will exsolve as the water rises up through the crust, forming buoyant gas bubbles* which may reach the surface, possibly entraining liquid water with them. If enough

* the term "bubbles" here may well be misleading. These "bubbles " are in no way small nor spherical, though they are buoyant. They typically have lengths of a few hundred meters and a width of only a few cm, since tidal stresses are significantly smaller than the shear modulus of ice; they also have a "tadpole" shape (see Fig 4f). The terms "cracks" or "tadpoles" will be used hereafter.

clathrate is present in the crust, the density of the crust may increase enough to permit 10 km cracks to form.

The total amount of carbon present on Europa is unknown; we tried to place appropriate limits on its abundance and work within these limits. We chose to examine carbon primarily in the form of CO_2, since we expect Europa was formed largely by carbonaceous chondrites, much like Earth, and in the presence of H_2O these chondrites may well have formed Earth-like abundances of CO_2 on a gram-per-gram basis. As a lower limit, we set the mass percentage of CO_2 in Europa equal to the mass percentage of CO_2 on Venus (approximately Earth-like, and easier to measure). As an upper limit, we assumed Europa was formed entirely by carbonaceous chondrites , which are typically $\approx$ 3 % carbon by mass, then assumed all this carbon went into forming CO_2. These limits gave a range of 10^{21}--10^{24} gm for the total CO_2 mass on Europa. Assuming all CO_2 is dissolved in the ocean, the mole fraction of CO_2 in solution, X_{CO_2}, was in the limits 2.6×10^{-4} to 0.21; the solubility of CO_2 at 265 K and at 100 bars pressure (the hydrostatic pressure at the base of the crust) is about 4×10^{-2} [5].

But at low temperatures and high pressures (easily obtainable in Europa's ocean), the CO_2–H_2O system forms a clathrate compound, $CO_2 \cdot 5\frac{3}{4}H_2O$ (see Figure 1) [6]. At the base of the ocean we expect T = 270 K and P = 1 kbar, well within the clathrate stability field. The formation of clathrate will dictate the equilibrium concentration of CO_2 in Europa's ocean, so we calculated phase diagrams for the CO_2–H_2O system undersaturated in CO_2(see Figure 2). The equilibrium concentration is fixed by the point that is on the liquid-ice phase boundary at 100 bars (the base of the crust) and on the clathrate-liquid phase boundary at 1000 bars (the base of the ocean) and at the constant temperature of about 272 K, since the ocean is approximately isothermal. Thus we obtain an equilibrium CO_2 concentration of $X_{CO_2}=3\times10^{-3}$.

Depending on the amount of CO_2 actually present, we can form different models of the interior of Europa. If we have a mole fraction $X_{CO_2}\geq0.14$ all the water and CO_2 present will tend to form clathrate since we are consistently in the clathrate stability field; thus the silicate core would be overlain with $\approx$ 100 km of clathrate, which would melt at its base, forming CO_2 liquid and water. The dense CO_2 liquid would sediment out, but the buoyant water would now rise towards the surface, causing periodic resurfacing. An all-clathrate layer is not inconsistent with any current observations of Europa; IR scanning of the crust, which would indicate the amount of CO_2 present, at least in the outermost layer, will not be achieved until the Galileo mission flyby.

We calculate that if $X_{CO_2}\geq0.005$, and if a mechanism can be found to contaminate the crust with clathrate, then the crust density would be sufficiently high to cause the cracks to extend to the point where the CO_2 gas in the liquid would exsolve; further, a clathrate contaminated crust will not conduct heat as well as a pure ice crust and tend to become thinner. The CO_2 gas will then form a gas crack at the top of the liquid crack , pinch off and rise because of its natural buoyancy, and will entrain a small volume of water with it. If $X_{CO_2}<0.005$ then cracks cannot propagate to the surface or even far enough to permit exsolution of CO_2. This mechanism may well work for other gases, primarily CH_4 or CO,

which are less soluble than CO_2 and so exsolve sooner, but are probably not nearly as abundant as CO_2.

A major portion of this project was concerned with calculating the displacement profiles of cracks propagating upward from the bottom of the ice crust, partially filled with water and partially filled with exsolved gas (see Figure 3). To do these calculations, a generalization of the results of Weertman [7] were applied to this specific case (and later, to an isolated, partially liquid-filled gas "bubble"). The final expressions are analytic but extremely messy and not very informative *per se*, and so are not presented here; instead, results in the form of crack displacement profiles are shown in Figure 4. The analytic expressions have been checked against numerical calculations and agree quite well; also, taking the appropriate limiting cases returns the results of Weertman. Figure 4 clearly shows the growth and pinch-off of the gas "bubbles" and the trapping of the liquid. The reader should note the wide variance in scales from horizontal to vertical; also in Figure 4e the blackened area indicates a negative displacement, allowed in the mathematical solution, but an unphysical result, so this solution exceeds the limiting crack length.

To calculate the behavior of the gas crack after it has pinched off, Weertman's theory was applied to the case of a gas-filled crack isolated in the crust with a small amount of liquid contained in the bottom. To a very good first approximation, the effect of the liquid on the crack shape and volume is small, so we can treat the crack as gas-filled and the resulting equations for crack propagation can be solved analytically. We find the solutions look graphically like Figure 5. Note all variables are defined in Table 1. We see that cracks do grow in length as they rise to the surface line L=h, but the effect is not a large on unless $h_0 \gg L_0$, in which case we may have an "explosive" crack as it nears the surface. For Europa, $h_0 \approx 67$ m, $L_0 \approx 500$ m, so we are clearly more in the region $L_0 > h_0$, and since the theory involved is really valid only far away from the surface, we consider the limiting case $h \gg h_0$, where we find $L \approx (\frac{L_0^4}{2h})^{\frac{1}{3}}$. Linearizing the equation for P' we find

$$P' = P'_i\left(1+\frac{1}{2h}(L-2h_0)\right) \qquad (4)$$

where P'_i is the initial pressure in the gas crack $\approx$ pressure in the solid $= \rho_s g h_i$.

Freezing-out of the gas or the liquid on the crust walls may be a problem if the crack is "slow" (v = 1 cm/sec), but we roughly calculate that rise time will be less than freezing time for the liquid if it has to rise no more than 2×10^4 cm and is "fast" (v = 10 cm/sec), which is likely to be true for CO_2. The gas will freeze out on the walls unless the ocean is well-mixed enough to provide enough gas so that the gas crack and the ice in the walls can reach pressure equilibrium. We calculate that the ocean would need to mix at a rate capable of transporting 2.7 liters of H_2O per second to the liquid surface to maintain this equilibrium. The ocean may not need to mix quite this well, however, if the crack encounters clathrate intrusions in the ice, which would release some of their CO_2 , supplying the crack with more of the gas it needs to keep from freezing.

Conclusions

We concur with the thermal model of Squyres et al. but contend that a mole fraction of $X_{CO_2} \geq 0.005$ must be present in Europa's ocean to cause resurfacing by water, via a clathrate contaminated crust and buoyant gas cracks forming in the crust. The gas cracks will rise through the crust and break through the surface if the ocean is well-mixed enough, and the crack fast enough, to prevent freezing of the gas or liquid.

References

[1] Lucchitta, B.K., and Soderblom, L.A., in *Satellites of Jupiter*, (ed. D. Morrison), University of Arizona Press, Tucson, 1982.

[2] Cassen, P.M., Reynolds, R.T., and Peale, S.J., *Geophys. Res. Lett.*, **6**, 121-124 (1979).

[3] Squyres, S.W., Reynolds, R.T., Cassen, P.M., and Peale, S.J., *Nature*, **301**, 225-6 (1983).

[4] Chandrasekhar, S., *Hydrodynamic and Hydromagnetic Stability*, Oxford University Press, London, 1961.

[5] Wiebe, R., *Chem. Revs.*, **29**, 475-81, (1941).

[6] Takenouchi, S., and Kennedy, G.C., *J. Geol.*, **73**, 383-390 (1965).

[7] Weertman, J., *J. Geophys. Res.*, **76**, 1171-1183, (1971).

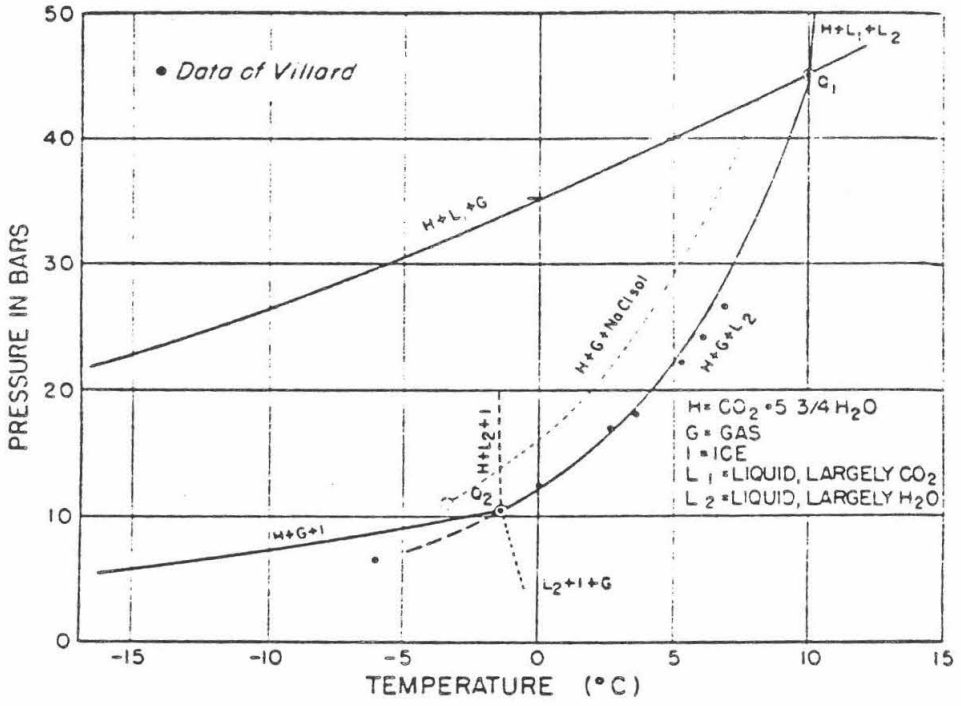

FIG. 1.—Dissociation pressure curve of the hydrate $CO_2 \cdot 5\frac{3}{4} H_2O$ at low pressures

FROM REFERENCE [6]

Phase Diagram for $H_2O - CO_2$ System

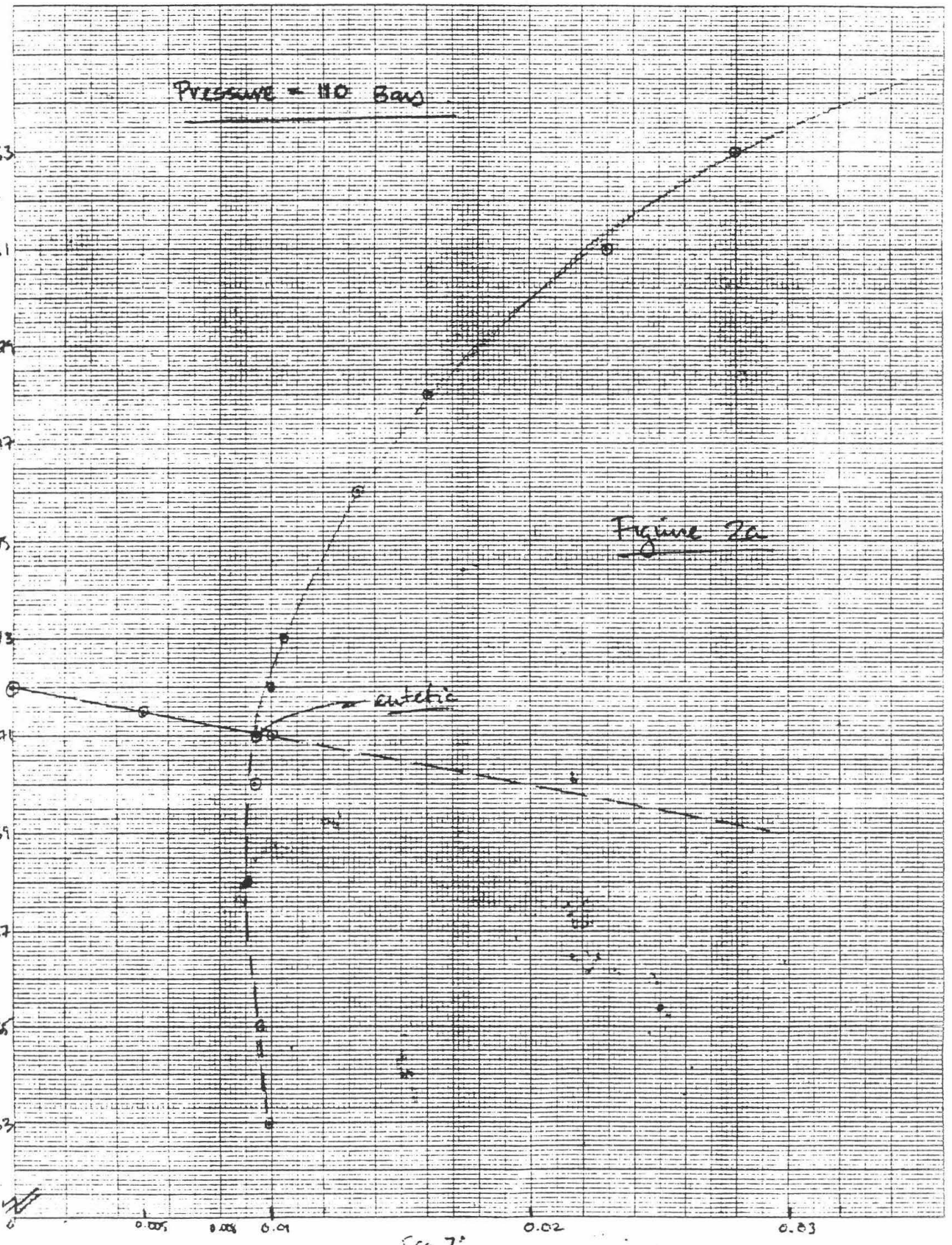

Figure 2a

46 1512

K·E 10 X 10 TO THE CENTIMETER KEUFFEL & ESSER CO. MADE IN U.S.A.

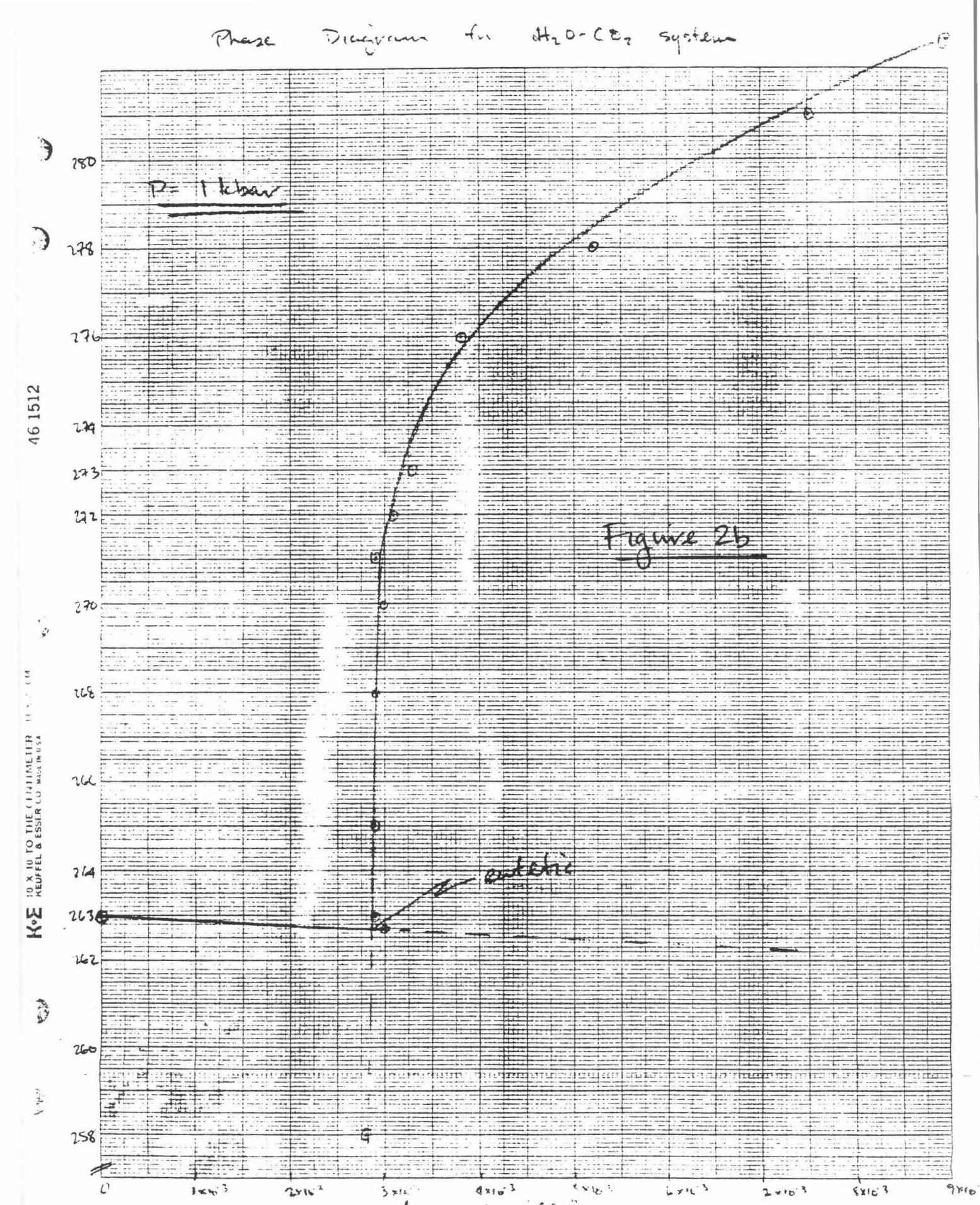
Phase Diagram for H_2O-CO_2 system
P= 1 kbar
280
278
276
274
273
272
270
268
266
264
263
262
260
258
endothic
0
1x10^-3
2x10^-3
3x10^-3
4x10^-3
5x10^-3
6x10^-3
7x10^-3
8x10^-3
9x10^-3
Figure 2b
46 1512
K&E 10 X 10 TO THE CENTIMETER
KEUFFEL & ESSER CO MADE IN U.S.A.

Figure 3.

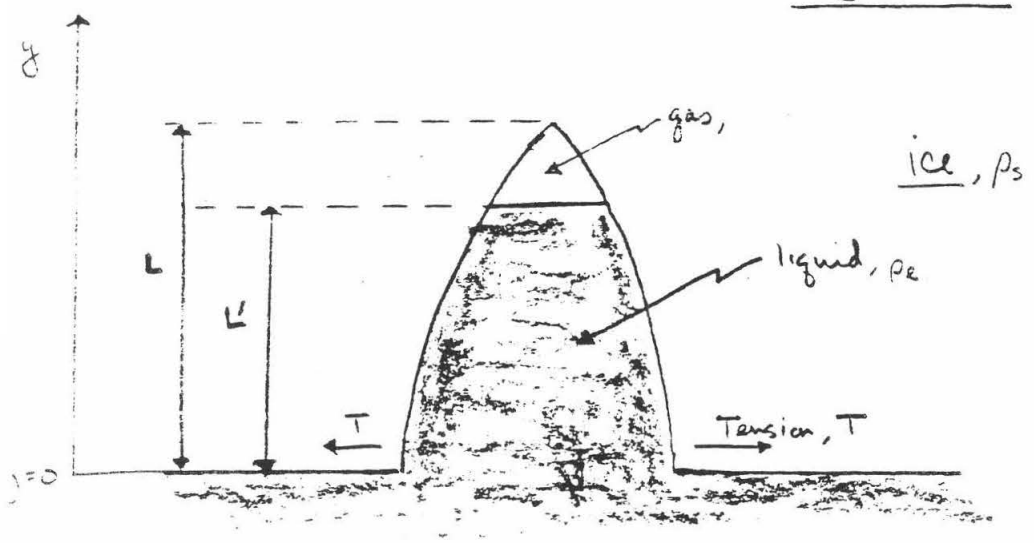

Stress field is. $\sigma = \begin{cases} -T - \rho_s g y + \rho_e g y & 0 < y < L' \\ -T + \rho_e g L' - \rho_s g y & L' < y < L \end{cases}$

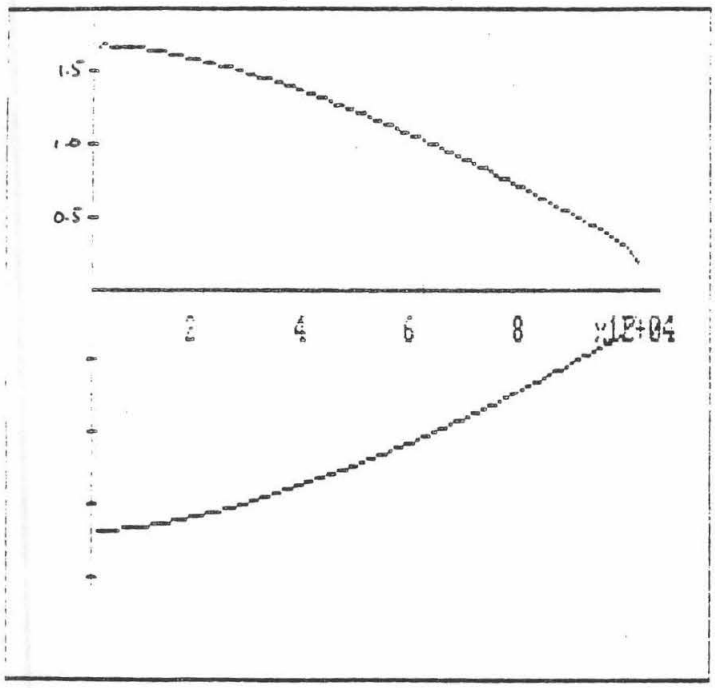

FIGURE 4A

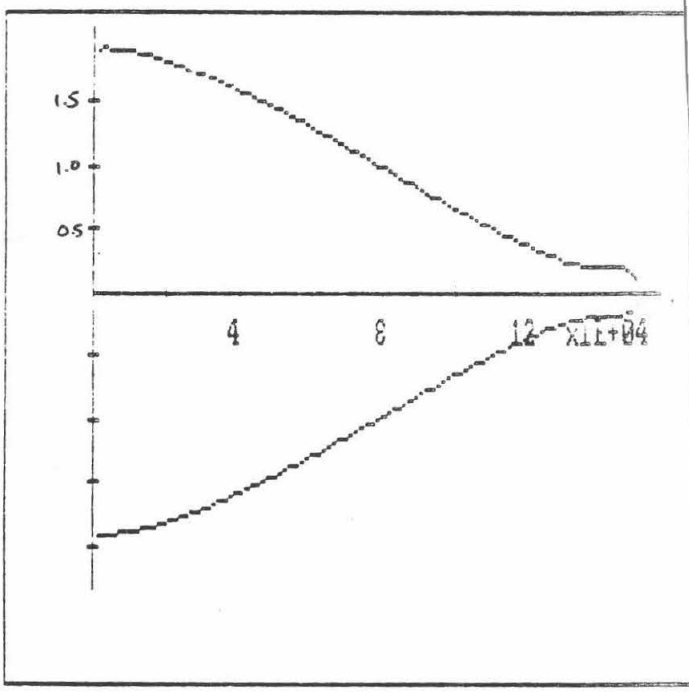

FIGURE 4b

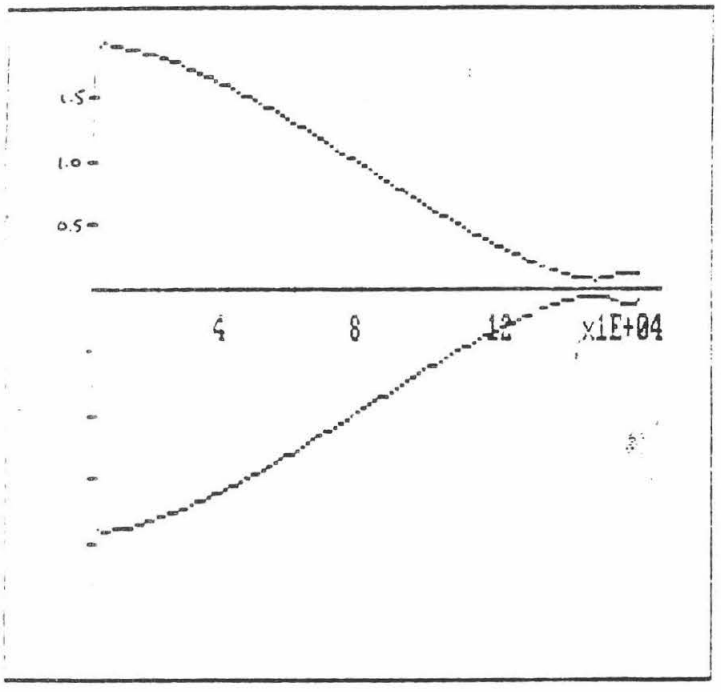

FIGURE 4c

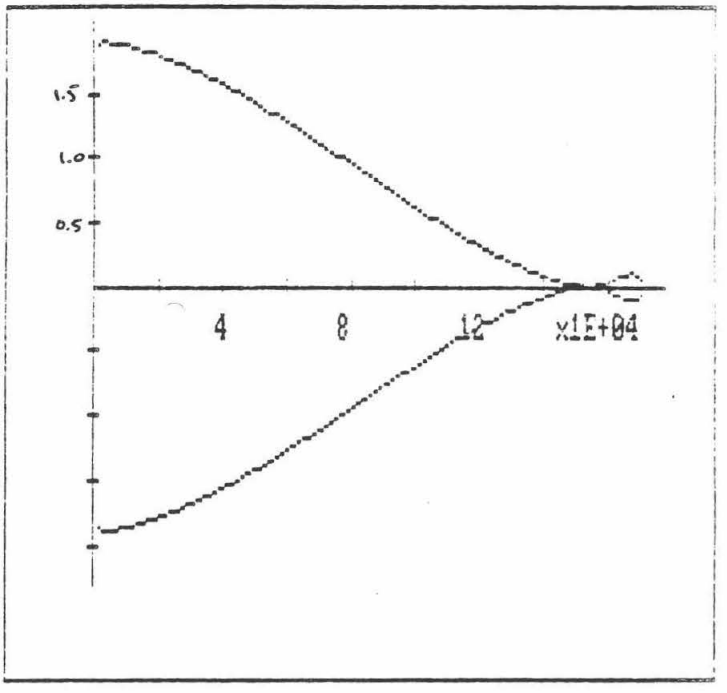

FIGURE 4d

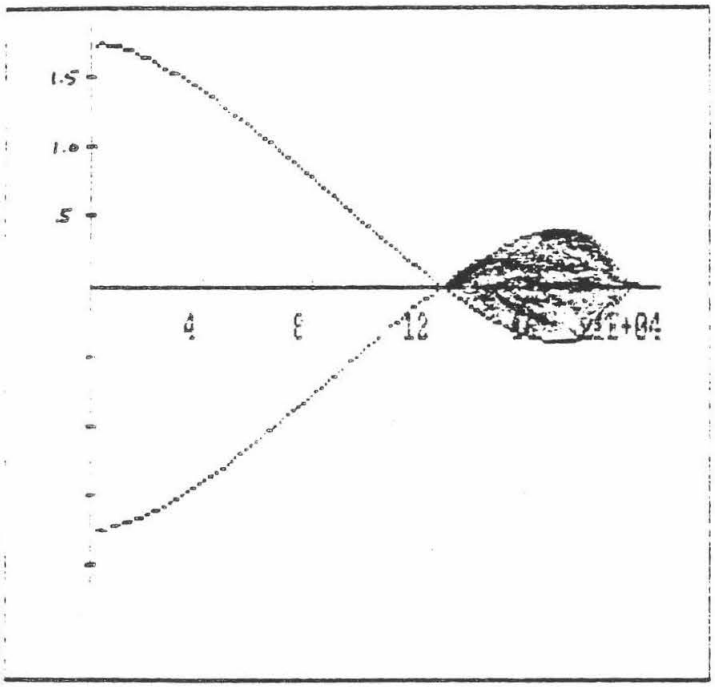

FIGURE 4e

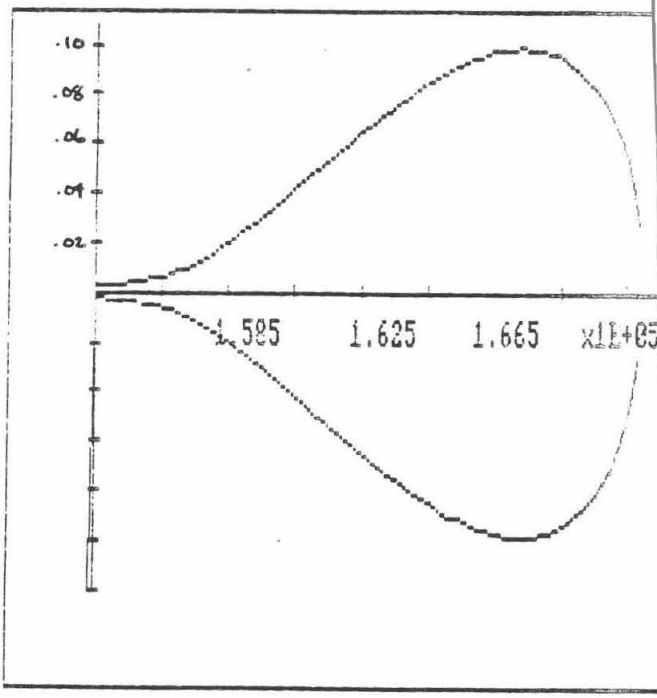

FIGURE 4f

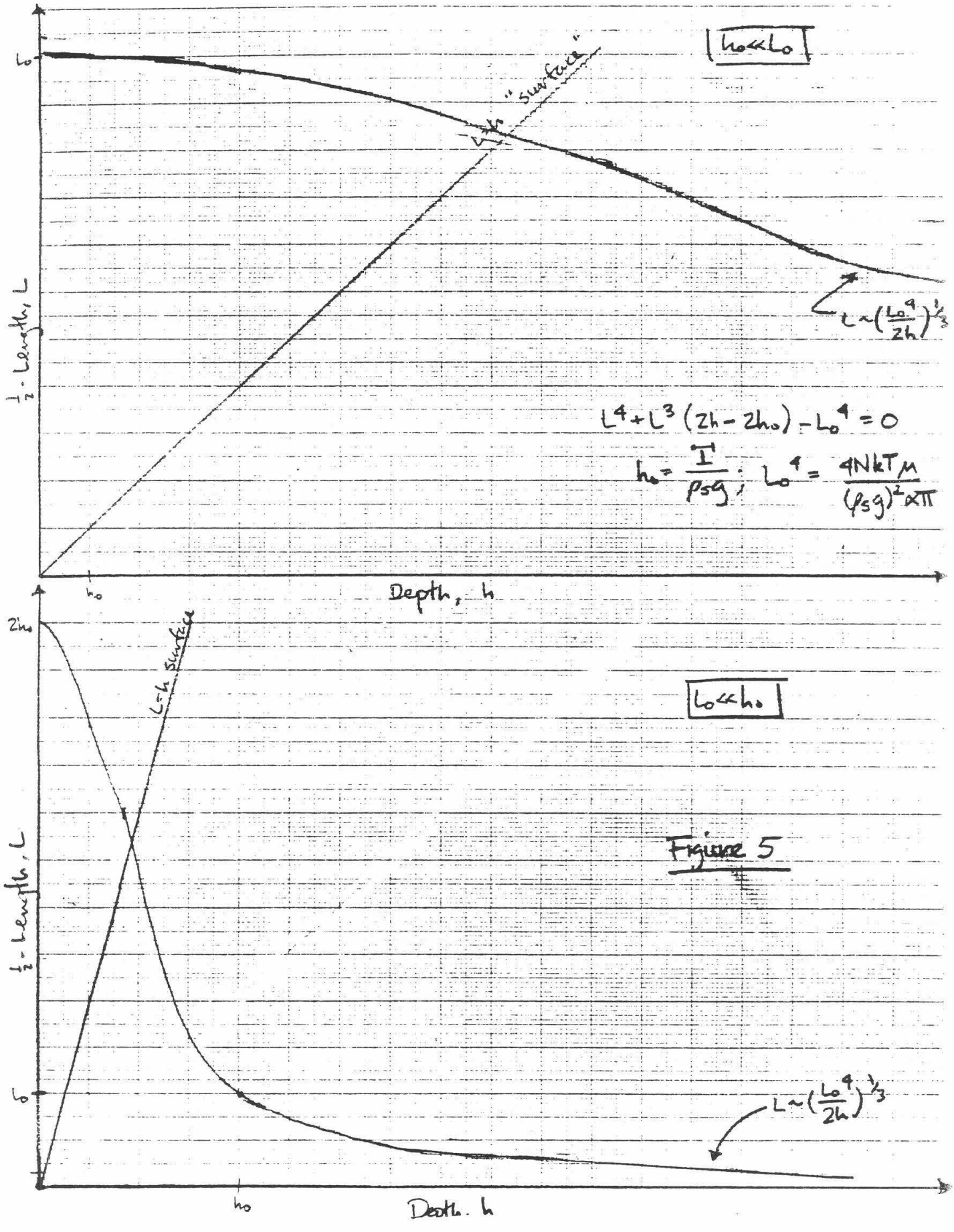
$h_o \ll L_o$
L_o
"surface"
$\frac{1}{2}$ · Length, L
$L \sim \left(\frac{L_o^4}{2h}\right)^{1/3}$
$L^4 + L^3(2h - 2h_o) - L_o^4 = 0$
$h_o = \frac{\Gamma}{\rho s g}$; $L_o^4 = \frac{4NkTM}{(\rho s g)^2 \alpha \pi}$
h_o
Depth, h
$2h_o$
$L = h$ surface
$L_o \ll h_o$
$L \sim \left(\frac{L_o^4}{2h}\right)^{1/3}$
L_o
h_o
Depth, h

Figure 5

Table 1

Figure 5 is a sketch of solns of the equation:

$$L^4 + 2L^3(1 - h_o) - L_o^4 = 0$$

where $h_o = \frac{T}{\rho_s g}$ and $L_o^4 = \frac{4NkT\mu}{(\rho_s g)^2 \alpha \pi}$

for the limiting cases $L_o \gg h_o$ and $h_o \gg L_o$

Here:

L = ½-length of crack
h = Depth of crack below surface
T = tidally-induced tension
ρ_s = ice density
g = Europan grav. acceleration
N = # of gas molecules trapped in crack
k = Boltzmann's const.
T = temperature
$\alpha = 1 - \nu$; ν = Poisson's Ratio
μ = rigidity of ice

Distribution of Late Holocene Tephra of Mono Craters

Paul C. Haase Faculty Sponsor: Dr. Kerry E. Sieh

An eruptive event near South Coulee of the Mono Craters, California, occured 1190±80 years ago and produced a sequence of predominantly orange-brown air-fall tephra which was distributed over the eastern Mono Valley and surrounding areas. Study was undertaken to predict hazards in this region of active vulcanism, especially that associated with recent seismicity near Mammoth Lakes, California. A small explosion pit, M 18, previously associated with the 1400 A.D. event, was examined. Excavation showed this crater to be roughly 5000 years old, making further work unprofitable due to extensive cover by ash. Correlation of the ash revealed it was the air-fall of the penultimate 800 A.D. eruption, with a distinctive orange-brown sequence of beds. Twenty sites exposing this ash were dug and recorded. An isopach map of the orange-brown unit was made. The coarser, near-source debris was blown north-east and the finer, more extensive tephra was carried north-north-east over 35 miles. At some altitude the direction of the prevailing winds must have changed. Further work can reveal the magnitude and significance of this event.

Introduction

The Long Valley-Mono Lake region east of the Sierra Nevada in Californis has long been known as a zone of recent volcanic activity. Both of Mono and Inyo Crater chains here have experienced at least two major events in the last 2000 years. In the past 5 years increased seismic activity indicating magma movement near the earth's surface near Mammoth Lakes, a town of over 300 in this active area, has caused concern about the dangers involved with a potential eruption. Study of recent eruptions nearby can provide information as to these hazards, and possible precautions. The last two eruptions of the Mono Craters are among those currently being studied.

Paul Haase SURF Report

Background and History

The Mono Craters are a 10-mile-long chain of late quaternary domes and flows of rhyolite, except one older dome of rhyodacite(Wood, 1977; Lajoie, 1968). Recent eruptive events have occured with approximate 600 year spacing, in about 100 A.D.(Sieh, unpublished data), 800 A.D. (Wood, 1977; Sieh, unpublished), and 1400 A.D.(Sieh, unpublished). The most recent major event involved magmatic eruptions at several, now covered vents in the north of the chain. The tephra produced, composed of about 80% white pumice, 15% grey micro-vesicular glass, and 5% black and colorless obsidian, has been found up to 80 miles away at Walker Lake, Nevada. Also associated with this episode are North Coulee, a large lava flow, and ash flows burying much of the plains northwest and northeast of the chain to the shores of Mono Lake.

The penultimate Mono Craters event, 1190±80 b.p.(Wood, 1977), is not as well constrained. The air-fall tephra produced, similar in average composition to that of the 600 b.p. eruption, has been covered by meters of the later tephras and ash-flows, making excavation difficult in many sites. The preservation environment at the time of its emplacement was apparently not as favorable as at 1400 A.D. as indicated by the low number of far-field outcrops(see Maps A and B) found. The sources for this eruption are probably buried beneath South Coulee, also a large lava flow, produced at this time. They may also include two explosion pits between South Coulee and Hill 9138.

Even less is known about the third eruptive episode back, about 1900 b.p. It is thought to include domes in the Punch Bowl area, at the extreme southern end of the Mono chain.

Procedure

To determine distribution of the tephra likely sites of preservation were located. Near-source these would usually be chosen on slopes to lessen the excavation required. Far-field sites would be chosen by an outcrop of white sand in road-cuts or stream gullies. A pit would be then dug by hand until the desired beds were clearly exposed, usually at an average depth of 1.5 to 2 meters. The beds would be photographed by both a polariod and 35 mm camera and then described in detail. Last, the pits would be filled back in so as not to disturb the environment or trap animals.

Discussion

The first pits were dug at M 18, a small explosion pit located between Crater Mt. and Hill 9138(see Maps A and B). M 18 was thought to have been associated with the 600 b.p. eruption. Pit "fa" showed that this was not so. This excavation revealed a base of coarse debris, almost certainly from M 18, covered by later tephras and ash flows. Some of the lower tephra showed the distinctive orange-brown of the penultimate event. This evidence combined with the geomorphology to give an age for this crater similar to that of Crater Mt. or 9138, about 5000 yrs (Sieh, unpublished communication). Further work at this site along the lines of the original proposal was deemed unprofitable at this time.

Next the penultimate tephras were examined at over 15 locations (pits "fc" to "fo" and "ig^2"). Sites "fc" through "fh" were dug on and around Hill 9138, near the South Coulee vent(s). "fl" to "fo" and "ig^2" were dug in the far-field, to the north and east of the chain. The tephra sequence was found to include a unit of distinctive orange-brown beds in

its lower middle. This unit was found at all sites and used as a marker for correlation. See Table 1 for a listing of thicknesses for each site. As this unit was relatively easily followed from site to site it was chosen for the preliminary isopach. Eventually, it should be broken up into parts and isopached, along with the white pumice-rich beds below and the finer-grained grey-to-white beds above.

At many locations west of the Mono Craters and northeast of Mono Lake no tephra deposits were found where they might be expected. Much time was spent searching these areas, with little luck. The lack of deposits is attributed to a poor environment for preservation at the time of the event and not that the ash never fell in these areas. The tephra is found in enough far-field locations to discount the latter possibility.

Results

The orange-brown unit was isopached as a whole and is shown in Maps A and B. Just north of the source(s), on 9138, this unit is thickest, reaching almost 200 cm in places. The 100 cm isopach is nearly circular, representing mostly material blown out of the vent on low angle trajectories and not affected by the wind. The 50 cm isopach makes a lobe elongated to the northeast. A low-level wind to the northeast is indicated. The 10 cm isopach is more an oval. The tephra making up these deposits was affected by transitory winds, northeast below and north-northeast above. The 1, 0.2, and 0.1 cm isopachs are all elongated lobes to the north-northeast, representing material blown by these higher-level winds. Such wind-shear is not uncommon and has been found in examinations of the 600 b.p. tephras as well. Likewise the wind direction found is similar to that found today and 600b.p.

Summary and Conclusions

The 1190±80 b.p. eruptive event of the Mono Craters was studied. An explosion pit thought to be part of the most recent activity was found to be about 5000 years old. The orange-brown unit of the penultimate episode was isopached. The map produced shows low-level winds which blew the tephra northeast and higher-level winds more to the north-northwest. This unit was found up to 35 miles from the vent(s).

This work is only intended to be preliminary. The isopachs are not fully constrained. They are useful, however, for predicting where tephra should or should not be found. When more fully constrained the volume, magnitude and significance of this eruption can be calculated by geophysical methods. This could have new implications for the dangers to Mammoth Lakes or the Mono Lake area should an eruption occur.

Acknowledgements

I would like to thank Kerry E. Sieh for his assistance on both the proposal and fieldwork, Marcus J. Bursik for providing slave labor in digging and logging the deep "fd" through "fh" pits, and all those associated with the SURF program for making this opportunity available.

Bibliography

Lajoie, K.R., 1968, Late Quaternary stratigraphy and geologic history of Mono Basin, eastern California(PhD. dissert.): Berkeley, Univ. California, 271p.

Sieh,, K.E., 1984, unpublished communications and field notes. Publication in progress, out in 1985-6(?).

Wood, S.H., 1977, Distribution, correlation, and radiocarbon dating of late Holocene tephra, Mono and Inyo craters, eastern California; Pasadena, California Inst. of Technology, pp. 89 - 95.

Table I

Descriptions of Sites*

Site	Orange-Brown Unit Lowest Bed(cm)	Top Bed(cm)	Thickness(cm)	Remarks
fa	3b @ 123	3e @ 170	47	
fc	3b @ 212.6	3e @ 271	58.4	
fd	3a @ 74.5	6j @ 253	178.5	
fe	1a @ 27	3b @ 201	174	
fh	1a @ 39	3b @ 233	194	
fj	2c @ 25	2c @ 32	7	deeper KES site "ga"
fl	2a @ 24.9	2a @ 25.0	0.1	
fm	2a @ 22.7	2a @ 22.9	0.2	
fn	2b @ 15.5	2b @ 16.2	0.7	same as KES site "ik".
fo	2b @ 9.0	2b @ 9.1	0.1	as KES "iq"
ig[2]	2b @ 23.6	2b @ 23.8	0.2	
	Revisited KES Sites			
bb	2e @ 42.2	2e @ 45	2.8	
gc	ø	ø	0.0	none found
ge	2 @ 33	2 @ 33.6	0.6	
	Additional KES Sites			
as	NA	NA	1.2	
at	NA	NA	6	approximate
du	2b @ 46	2k @ 67	21	
dv	2c @ 65	2f @ 74	9	Buried 3 m +
dx	2d @ 57.8	2j @ 103.5	45.7	
gd	NA	NA	0.4	unable to find again

* Listing only includes pits used to construct isopach maps A and B.

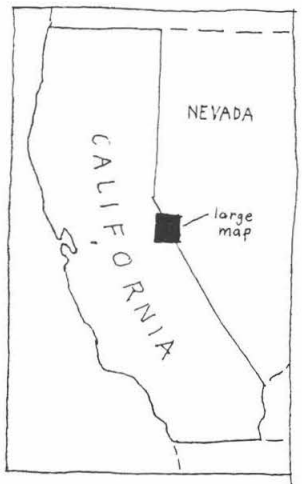

NORTH

KEY

- site location
- fz — site name
- 93 — orange-brown bed thickness (in cm)
- site new as of this report
- site known prior to this report
- estimated or infered isopach
- 2.0 — thickness @ isopach

ISOPACH

100 cm
50 cm
10 cm
1.0 cm
0.2 cm
0.1 cm

MAP A

(preliminary)

ISOPACH MAP of Orange-Brown Unit of ~700 A.D. Mono Craters Event

Geology by Paul Haase, Kerry Sieh. Interpretations by Paul Haase. Graphics by Paul Haase.

NEVADA
CALIFORNIA

Fletcher

Aurora

Bodie

Black Point

Negit Island

Paoha Island

MONO LAKE

Lee Vining

Panum Crater

North Coulee

MONO CRATERS

Crater Mtn

South Coulee

Punch Bowl

SCALE (in miles)

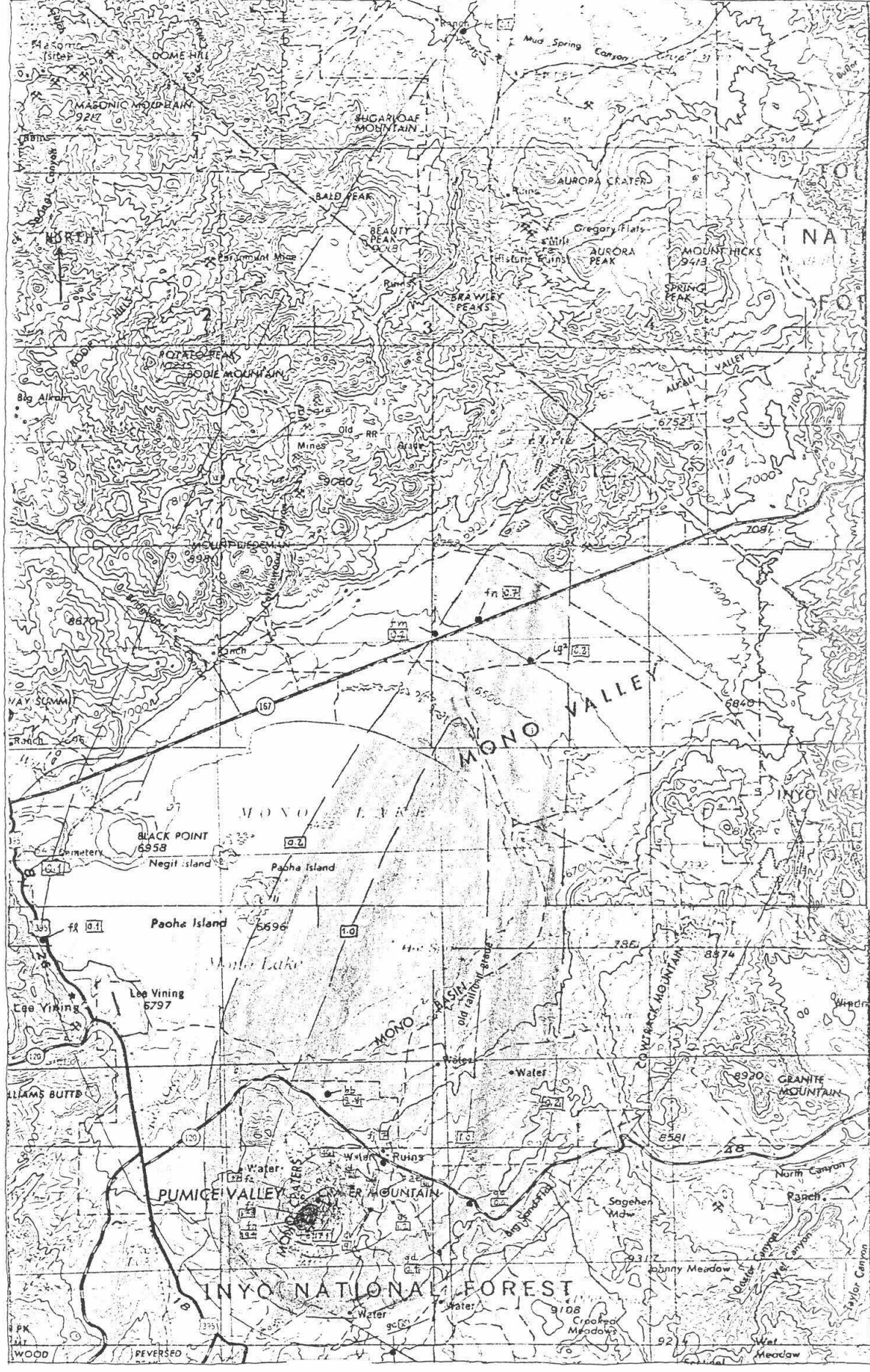

MAP B

(preliminary)

ISOPACH MAP of Orange-Brown Unit of ~700 A.D. Mono Craters Event, Showing Topography

SCALE (in miles)

0 5

For Key & Index Map, see Map A (above).

An Experimental Search for Bound GUT Monopoles Using a SQUID Magnetometer

Joseph Kovalik
Joseph Kirschvink

Current limits on the number of magnetic monopoles free in space or bound in matter do not give a very good indication of their overall numbers or effects. In this experiment, 643 kg of magnetic material and 180 kg of sea water were examined and no monopoles were found. This suggests that the flux of monopoles has remained constantly low and that further experiment is necessary.

The magnetic monopole first appeared in the early part of this century when Dirac (1931,1948) proposed the theoretical existence of a type of magnetic charge that would explain the quantization of electric charge and furthermore, would make Maxwell's equations fully symmetric. The initial problem in this proposition lay in its failure to introduce a mechanism for the production of such a particle and thus, its mass.

About ten years ago, with the advent of Grand Unified Theories, (G. t'Hooft, 1974 and Polyakov, 1974) a mechanism for the production of magnetic monopoles in the high energies of the Big Bang becomes available. The Grand Unification mass scale sets a value for the mass of the monopole between 10^{14}-10^{15} GeV or about 20 nanograms. This realization sets up some strong parameters that help to explain the failure of previous searches that did not take into account the slower, non-relativistic velocities, longer interaction path lengths with matter and apparent scarcity of the particle. The experiments performed as part of the SURF 1984 program realize the limitations produced and offer a new approach to the problem.

If magnetic monopoles exist, they can either be free particles travelling at appreciable, solar system velocities and evenly distributed about the Galaxy or as bound particles trapped inside matter where a locally strong magnetic field such as that near a magnetite grain could serve as a means to bind the monopoles.

The development of the SQUID or Superconducting Quantam Interference Device makes the detection of very small magnetic fields with a very high signal to noise ratio possible. By using such a device to search for magnetic monopoles in better defined regions, a somewhat clearer limit to the existence of monopoles is available.

The very small flux of magnetic monopoles through the galaxy places severe constraints on the number of monopoles that can be seen as either free particles or those trapped in matter. The Parker bound (Parker, 1970) that uses the background magnetic field of the galaxy to limit the possible contribution due to the presence of magnetic charges can change with the existence of monopolium or monopole-anti-monopole pairs (Dicus and Teplitz, 1983) that have a lifetime which is of the order of the age of the universe. The ultimate constraint is cosmological since the monopole density cannot exceed the limit imposed by the current expansion rate of the universe. Since a hidden or dark mass arises from studies of galactic and cluster dynamics, there is some

leeway in this number.

Many experiments have already attempted to detect the passage of free monopoles through space. Most have relied on conventional scintillation and ionization track detectors that do not specifically measure magnetic charge. The only result appeared from a baloon borne lexan polycarbonate plastic detector (Price et al, 1975), but the track later was attributed to the spontaneous fission of a heavy nucleus (Alvarez, 1975 and Price et al, 1978). Since the large mass of the monopole would produce a slow moving particle against a relativistic cosmic ray background, experiments using standard detectors are currently in progress including one at the Caltech Physics Department under B. Barish.

The real breakthrough in terms of direct magnetic charge measurement occurred with the advent of superconducting technology. Any net magnetic flux that passes through a closed conducting loop produces a potential related to the time rate of change of flux and subsequently, a current through the loop. The property of superconductivity allows the current to persist and the SQUIDs can then measure the current level. Since background noise due to thermal and mechanical oscillations should lie far below the current offset that a monopole would produce, a signal from a monopole would produce a unique and indistinguishable event.

On February 14, 1982, Blas Cabrera, performing an experiment using this type of apparatus reported a candidate event, but has been unable to find a repeated occurrence using an improved device.

The instrument used in this experiment is a two axis SQUID magnetometer in the Paleomagnetism and Biomagnetism Laboratory under J. Kirschvink. A 100 litre cryocooled dewar that allows a period of at least six months between refills houses the coils that are controlled by RF driven SQUIDs. A superinsulated room temperature access port extends all the way through the instrument so that samples can pass straight through the z-axiz coils (see fig. A).

Calibration of the instrument in terms of magnetic flux took place with an 140 cm. long solenoid that had a 6.1 cm. diameter and 39 turns/cm.. The solenoid was grounded using three 2 pF capacitors and further shielded from RF by Al foil. A battery and circuit with adjustable resistance produced the magnetic flux. A plot of the panel reading on the magnetometer versus voltage across the solenoid is on fig. B. Since a magnetic monopole has a charge of $n(hc/e)$ or $n(4X10^{-7})$Gauss-cm^2 where n is an integer, the minimum change in panel reading that would occur from a monopole passing through the z-axis would be 0.0090.

Since only a monopole field will produce a net flux through a loop, any magnetic fields produced by moving electric charges or dipoles would only cause momentary transient responses in the instrument when passing through the coils. A monopole, on the other hand, would produce a step like jump in the persistent current in the loop that lies far above the background noise. A sample passing through the coils should not significantly alter the current in the superconducting loops once it has passed through unless it has some sort of magnetic charge in it. The three inch diameter room temperature access allows samples of a few hundred grams to pass directly through the z-axis coils so that a significant amount of matter can be examined.

Theories regarding the ability of matter to stop and trap

monopoles through such causes as ionization, bremsstrahlung, Cerenkov radiation or eddy current losses to conductors (Cabrera et al, 1983), all seem to indicate that there is little possiblity for such occurrences with GUTs (Drell et al, 1983). Moreover, the binding of GUT monopoles to matter would be weak and small accelerations would tend to dislodge them. Since the number of monopoles is small by any calculation, the only hope of finding a trapped monopole would be in materials that lie beneath long interaction path lengths for long periods of time. The magnetic properties of this material should produce significantly large local fields that can trap monopoles.

All previous searches for monopoles bound in matter have neglected these facts. Various groups have searched moon rocks (Alvarez et al, 1971), ferromanganese pavement in the ocean floor (Fleischer et al, 1969) and even ocean water (Carrigan et al, 1975) in hope that these substances would come into contact with monopoles more often than others. Allthe experiments achieved negative results. Only the Alvarez experiment used superconducting loops that had limited resolution beacuse SQUIDs were not available. The others relied on pulsed magnetic fields to loosen the monopoles that would then pass through conventional particle detectors that do not measure magnetic charge.

In the experiments performed for SURF 1984, I examined three types of material that included blueschists, manganese nodules and ocean water. The blueschists represent a new attempt to define a possible material where a monopole can embed itself. Their retrograde histories indicate stable low temperature periods where they remained buried deep within the Earth's crust. This allows a long interaction path length before the monopoles reach the rock. Since the rocks have never reached temperatures higher than the Curie point of magnetite, they represent a fairly long time period of possible interactions. The IRM (Induced Remnant Magnetization) and AF (Alternating Field) Demagnetization curves in fig. C indicate that the blueschists show magnetic properties typical of magnetite. Thus, the rock contains many potential binding sites for monopoles.

The samples come from two regions that include the Pickett Peak Mountains and the Rand Mountains in the Mojave Desert. Approximately three quarters of a metric ton of material was collected and a significant portion of it crushed to a three inch size that can pass through the magnetometer. To reduce contamination in the lab, all samples were placed in plastic bags and then lowered through the instrument on a string. If the instrument registered a change greater than that of even half a monopole charge, the sample was remeasured. Since various factors such as mechanical or thermal stress in the loops or RF interference in the SQUIDs could cause a non zero change in the apparent persistent current, a repetition of the measurement allows certainty that a monopole exists in the sample unlike other searches where monopoles briefly pass through the detector without any subsequent measurements possible.

The manganese nodules and ferromanganese pavement prove suitable because they lie stable for long periods of time on the ocean floor where it is possible for them to come into contact with monopoles. They remain extremely magnetic and show characteristics that indicate large quantities of magnetite. These samples were

measured in the same manner as the blueschists and similar results appeared.

In total, 643 kg of material passed through the loops and this represents over an order of magnitude increase in the amount of material measured. A histogram of the number of occurrences against the magnetic charge appears in fig. D. The highest number of events is 125 at 0 charge. The maximum reading of charge on either side (-0.0050 to 0.0050) represents about half a monopole charge. Thus, no monopoles were found.

The sea water experiment took place because large amounts can easily pass through the magnetometer. About 180 kg of ocean water from La Jolla was pumped through the magnetometer and no monopoles were found. The strip chart reading in fig. E shows typical data from this experiment.

The number of monopoles trapped in bulk matter seems rather small with 0/643 kg of stable, highly magnetic material. GUT monopoles must then have either very long interaction path lengths (greater than a few kilometres) or a flux lower than the initial Cabrera experiment would suggest. A combination of these two factors together with the ability of monopoles to bind only weakly with matter would further reduce the likelihood of discovering a trapped monopole. Thus, it seems clear that the number of magnetic monopoles does nto exceed current theoretical expectations and that only further investigation will give a better indication of the true effect monopoles have on such things as the amount of dark matter present in the universe.

The only remaining and accessible place to search for GUT monopoles is in the primordial matter of the early solar system where monopoles would travel with the same speeds as the surrounding matter. Cometary rendez-vous missions would offer the best chance to examine this material.

Fig. A. A schematic representation of the SQUID magnetometer used in this experiment.

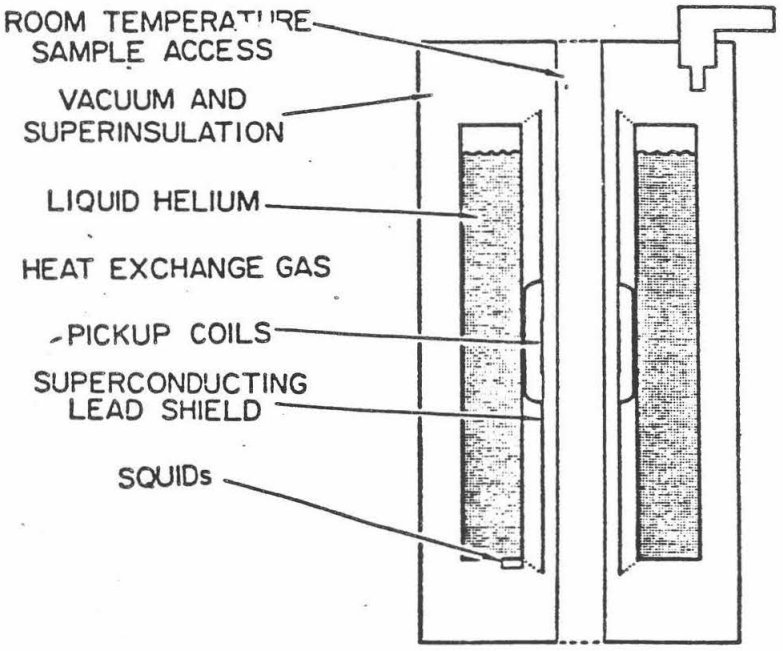

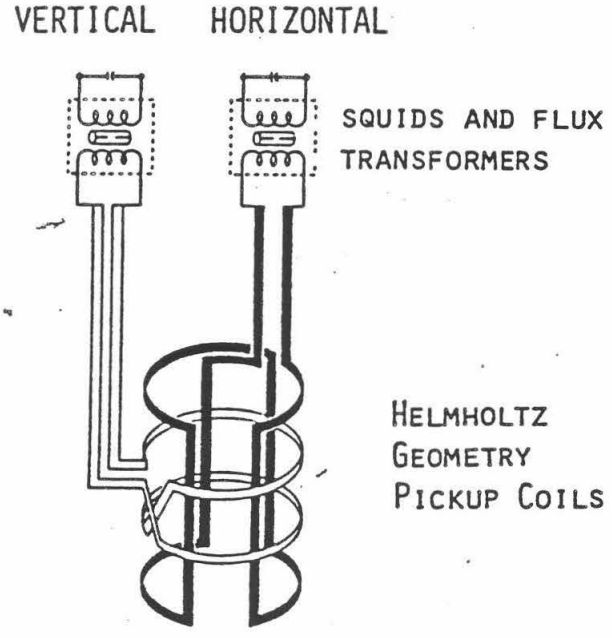

Fig. B A plot of panel reading on the magnetometer vs. magnetic flux expressed as voltage across the solenoid.

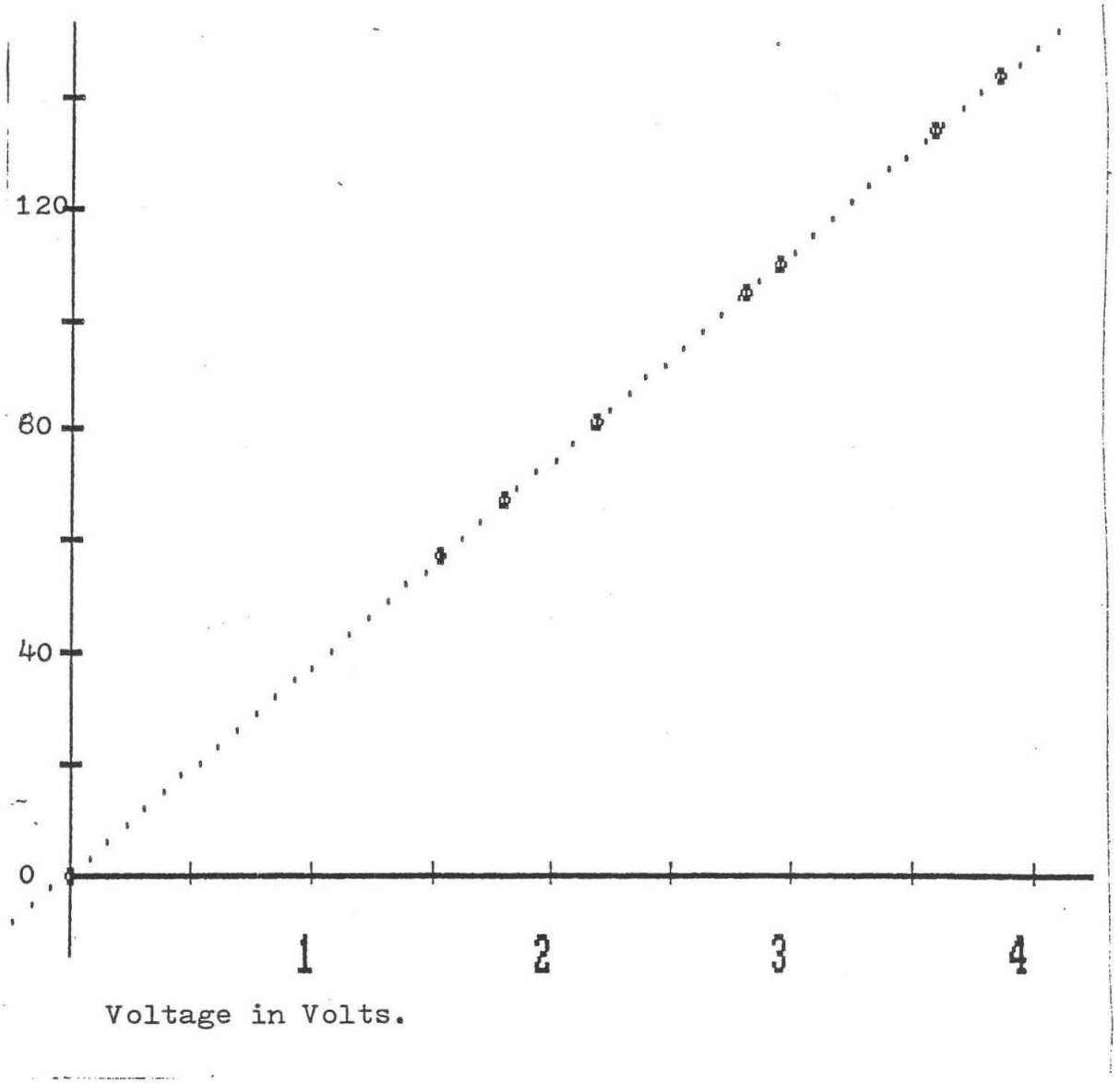

Fig. C. IRM and AF Demag. curves for Blueschists indicating the presence of magnetite.

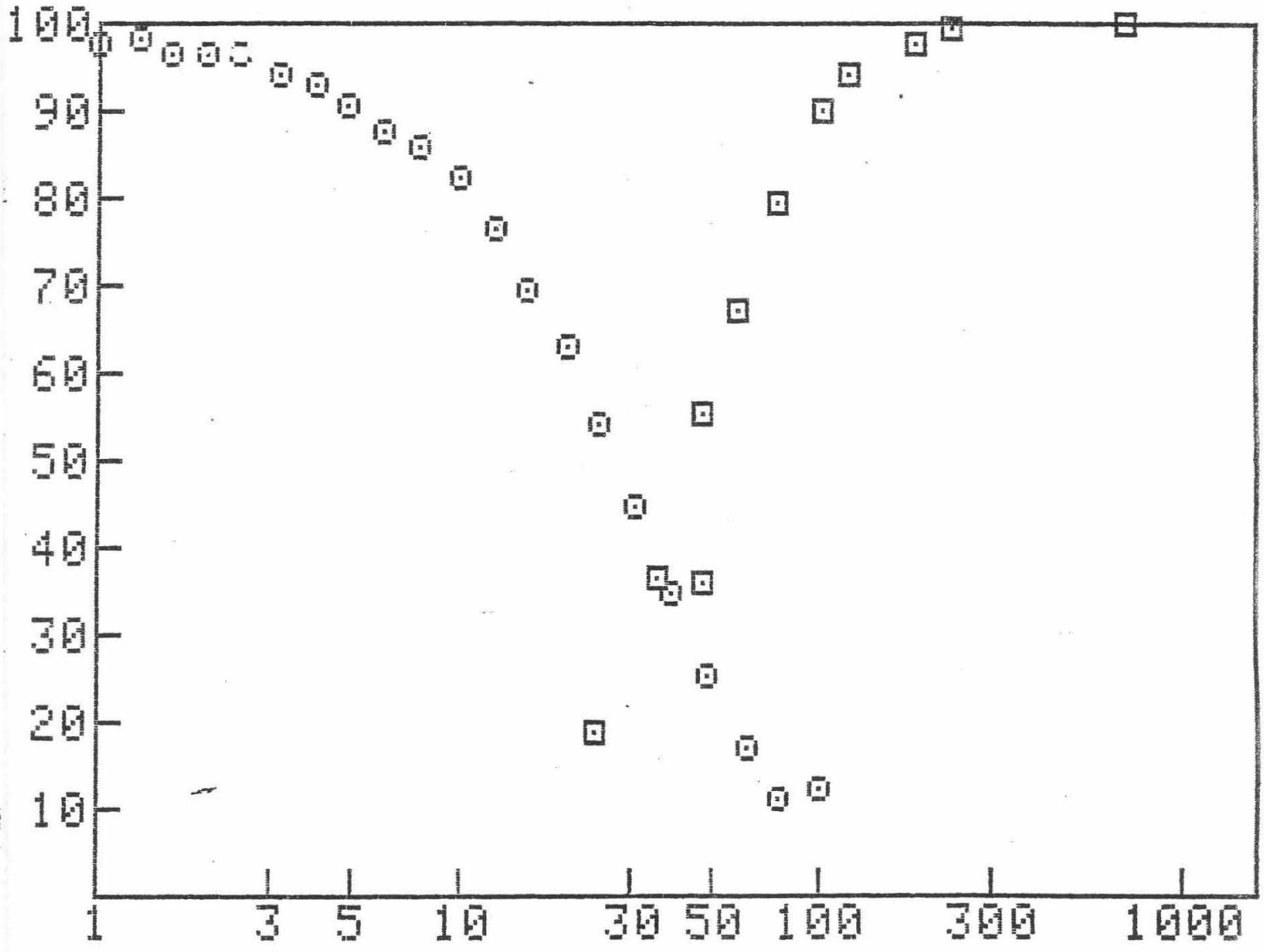

Fig. D A histogram of the number of samples at a specific charge. The highest peak at 0 corresponds to 125 events.

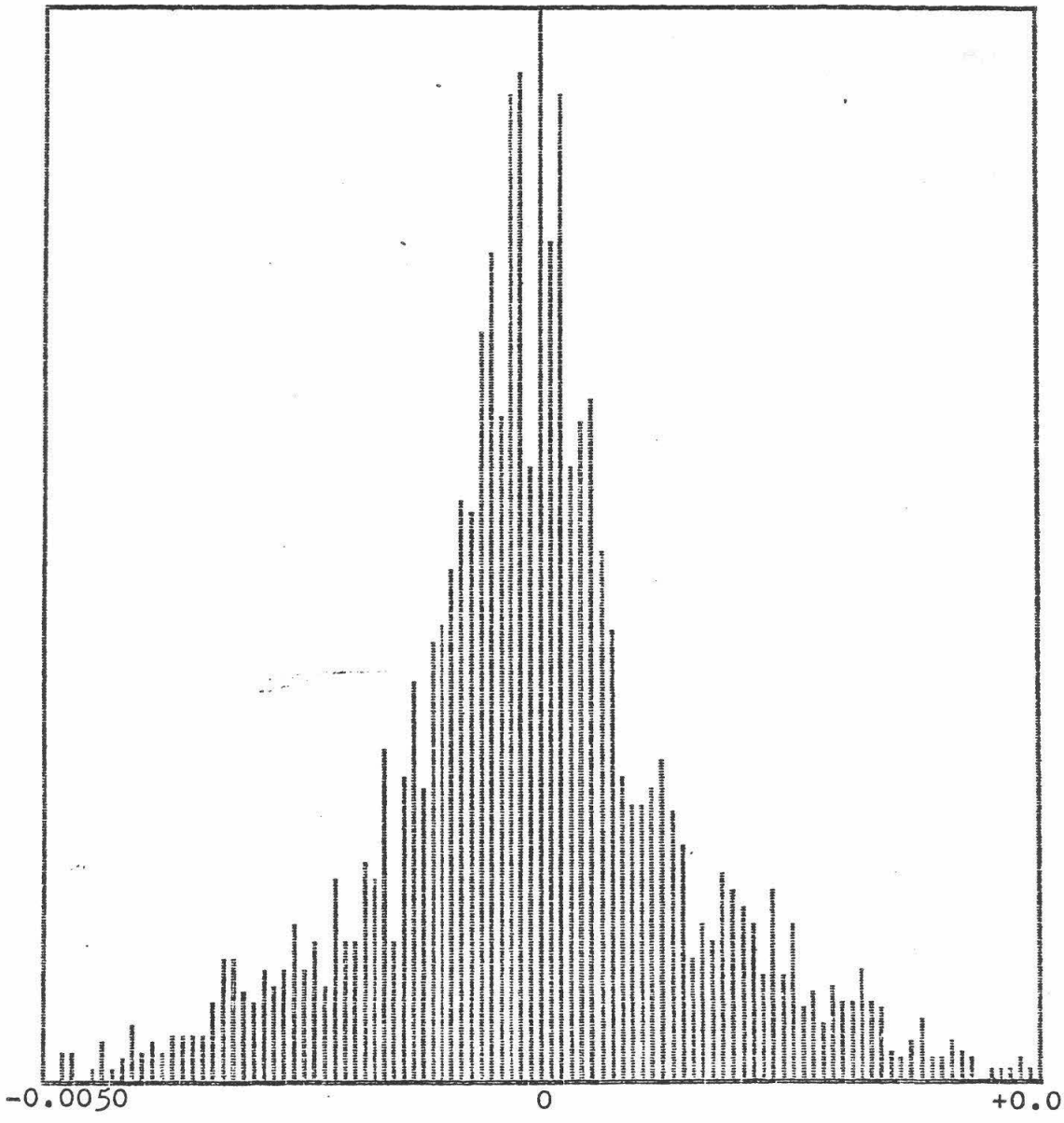

Difference in panel reading after sample passed through loops.

Fig. E A typical reading produced on a strip chart recorder from sea water passing through the magnetometer. Time is along the horizontal axis. A monopole would produce a step like jump in the reading that would be off-scale in this case.

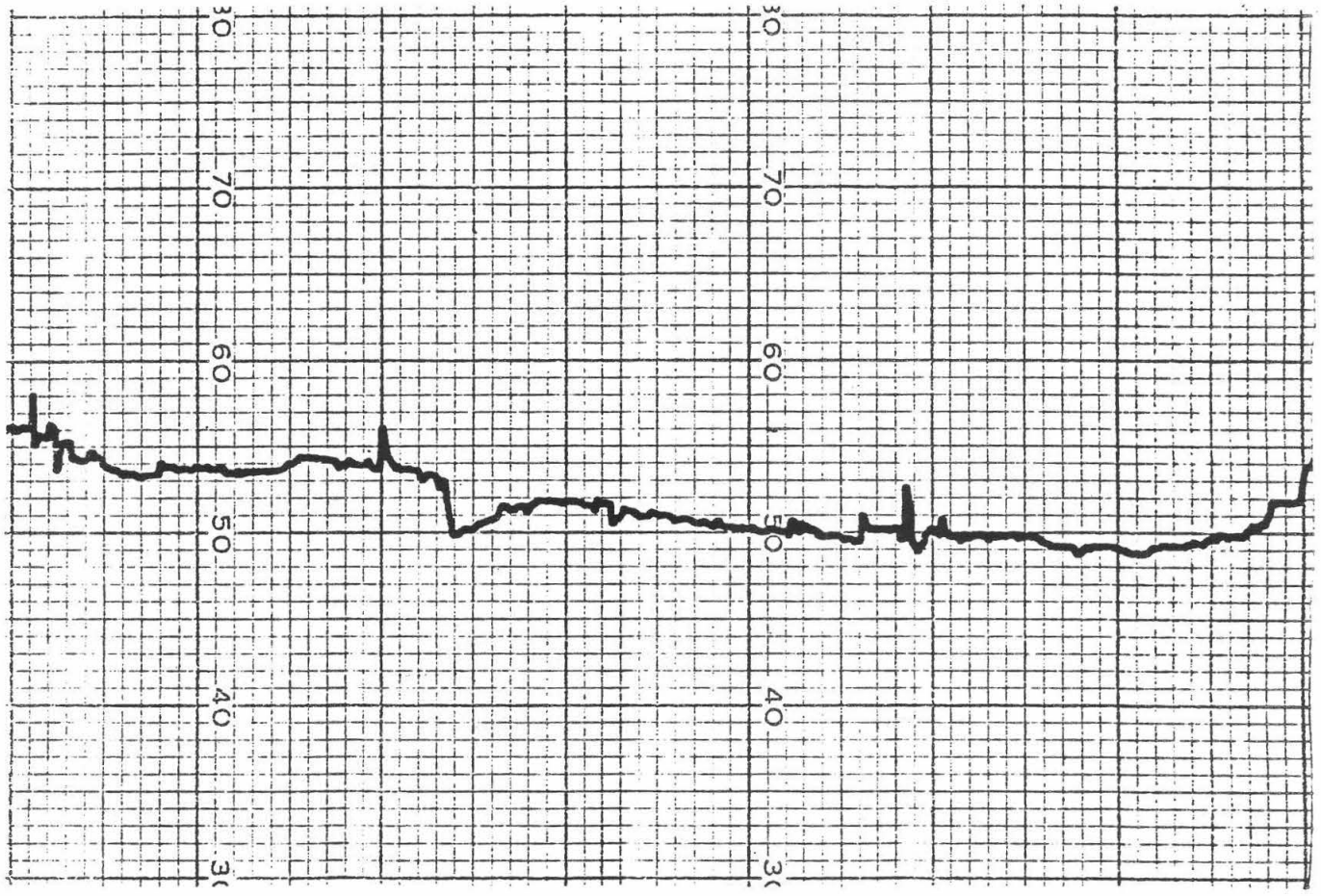

References

Alvarez, L. W. (1975). Analysis of a reported monopole event. in: W. T. Kirk (ed.), Proceedings of the International Symposium on Lepton and Photon Interactions at High Energies, (Stanford University), pp. 967-79.

Alvarez, L. W., Eberhard, P. H., Ross, R. R. (1970). Search for magnetic monopoles in the lunar sample. Science 167, 701-701.

Cabrera, B. (1982). First results from a superconducting detector for moving magnetic monopoles. Phys. Rev. Lett. 48, 1378-1381.

Cabrera, B., Trower, W. P. (1983). Magnetic Monopoles: Evidence since the Dirac conjecture. Foundations of Physics 13, 195-215.

Carrigan, R. A., Nezrick, F. A., Strauss, B. P. (1976). Search for misplaced magnetic monopoles. Physical Review D 13, 1823-25.

Dicus, D. A., Teplitz, V. L. (1983). Circumvention of Parker's bound on galactic magnetic monopoles. Nature 303, 408-9.

Dirac, P. A. M. (1931). Proc. Roy. Soc. Lond., Ser. A. 133, 60

Dirac, P. A. M. (1948). Phys Rev. 74, 817.

Drell, S. D., Kroll, N. M., Mueller, M. T., Parke, S. J., Ruderman, M. A. (1983). Phys. Rev. Lett. 50, 644-8.

Fleischer, R. L., Jacobs, I. S., Schwarz, W. M., Price, P. B. (1969). Search for multiply charged Dirac Magnetic poles. Physical Review 177, 2029-35.

Fleischer, R. L., Hart, H. R., Jacobs, I. S., Price, P. B. (1969). Search for magnetic monopoles in deep ocean deposits. Physical Review 184, 1393-7.

Fleischer, R. L., Price, P. B., Woods, R. T. (1969). Search for tracks of massive multiply charged magnetic poles. Physical Review 184, 1398-1401.

't Hooft, G. (1974). Nucl. Phys. B 79, 276-84.

Parker, E. (1970). Astrophys. J. 160, 383-404.

Price, P. B., Shirk, E. K., Osborne, W. Z., Pinsky, L. S. (1975). Evidence for detection of a moving magnetic monopole. Phys. Rev. Lett. 35, 487-90.

Price, P. B., Shirk, E. K., Osborne W. Z., Pinsky, L. S. (1978). Further measurements and reassessment of magnetic monopole candidate. Phys. Rev. D 18, 1382-1421.

Polyakov, A. (1974). Pis'ma Zh. eksp. teor. Fiz. 20, 430-433; JETP Lett. 20, 194-195 (1974).

BIOLOGICAL MAGNETOMETRY AND MAGNETITE IN POISONOUS NEWTS AND BLUE SHARKS: A Preliminary Report

By Karla Peterson

(Faculty Sponsor: Dr. Joseph Kirschvink)
(Funded By: Mr. Arthur Adam)

Abstract: *The goal of my project was to extract and characterize magnetic material in different organisms. A good portion of time was spent setting up the automatic biological magnetometer system. From the data I was able to collect I believe that both the poisonous newts and the blue shark embryos I studied have magnetite in their bodies.*

Introduction: The ferrimagnetic mineral magnetite (Fe_3O_4) was originally known to form only under conditions of high temperatures and pressures in igneous and metamorphic rocks. In recent years, though, magnetite has been found in a variety of animals serving different purposes. This matrix-mediated, organically synthesized mineral is the hardest and only ferromagnetic substance yet found in living organisms. Magnetite crystals which have been biochemically precipitated are easily distinguished from inorganic crystals be virtue of their unique shapes and trace element content. Originally found in the teeth of chitons[1] by Dr. Heinz Lowenstam (Caltech Professor Emeritus), magnetite has since been found in a plethora of animals including honey bees[2], magnetotactic bacteria[3], homing pigeons[4], dolphins[5], tuna[6], and salmon[7]. In addition, work had been done which suggests that monkey's[8], and humans[9] have an as-yet uncharacterized magnetic material (probably magnetite) in densities of 1-10 million crystals per cm^3 in some tissues.

Magnetite in chiton teeth is utilized purely because of its strength (the chitons eat algea which they scrape from rocks). The magnetotactic bacteria use it as a steering mechanism to get them down into the mud. There are several animals now (tuna, salmon, bees, pigeons...) for which a strong argument can be make that the magnetite is probably part of the sense organ that allows them to navigate[6]. But is this just a useful secondary function of an already present magnetite? The study of biomagnetism is still very new, and the purpose of my project was to study some more organisms because so little is known at this point.

Methods and Results: I wanted to start my extractions on small animals to perfect the technique. I first attempted to extract the magnetite from various tissues in blue shark embryos. (These were collected in 1978 off the coast of California.) After trying some new methods I returned to the method developed last year in conjuction with our study of the Chinook Salmon[7].

The method is as follows: The tissue is first dissected out with glass knives and ground up in a Kontes tissue grinder with distilled water. (This can take from three to five hours depending on how tough the tissue is.) The sample is then put in a buchiner funnel and ether is added. The ether dissolves the fats which surround the magnitite and make it float to the top. After the ether has dissolved some of the fat it is drawn off with a pipette and fresh ether is added. About five baths are required. In the next step filtered sodium hypercloride (clorox) is used to digest the rest of the tissue. The sample is centrifuged and the clorox exchanged until no digestion occurs. I used this method on several tissues from two embryos: brain, muscle, and gut, but not enough magnetic material could be seen to be extracted.

At this point I decided that I needed to do thorough magnetometry studies on these tissues before I continued. I wanted to concentrate on tissues with the most magnetism and the clean lab was also being used for an experiment that involved rocks and therefore was not very clean.

Our old rock magnetometer had been interfaced the the lab's Apple computers to do limited biomagnetic studies. Much of the software was transferable to our new biological magnetometer. I wanted to set up a good running system with as much automation as possible to decrease the number of times a sample had to be handled and therefore decrease possible contamination. I worked a long time integrating old and new ideas to get the system running. The components of the system are:

1) The magnetometer: The superconducting SQUID device that we are using for biology has a room-temperature top and bottem access to the sense region (see figure 1), which passes through a Helmholtz pair of superconducting coils. The current induced in the superconducting loops by the insertion of a sample is porportional to its magnetic moment,and the data is read by the Apple computer.

2) The Af demag unit: The alternating field demagnetization unit (which is a tool used in paleomagnetics) disorients lined up magnetic crystals and progressively demagnetizes them in steps by using higher and higher field strengths. In the new system the Af coil sits on top of the magnetometer so the sample can be zapped and lowered immediately into the sense region.

3) The impulse magnetizer: The impulse magnetizer is a coil of heavy gauge copper wire wrapped around a plastic tube. The coil is attached to a critically damped LRC circuit. Thus when the charged capacitors are discharged into the coil, a single magnetic field pulse in one direction is applied inside the tube. The peak field strength can be precisely controlled for conducting magnetization experiments (isothermal remanent magnetization, or IRM experiments). The impulse coil sits on top of the Af coil so the sample can also be remagnetized and measured immediately.

4) The stepping motor: Above all this there is a wheel attached to a stepping motor. This stepping motor is controlled by the Apple which raises and lowers the sample into the impulse coil, Af demag coil, and the sense region. The sample is suspended by a thin monofiliment fiber from this wheel.

5) The cooling system: The sample must remain frozen for the entire measurement process, so that thermal randomization of the magnetic paritcles will not occur. Before the automated system the sample would have to be frozen in liquid nitrogen between steps. The new cooling system works as follows: A dewer of liquid nitrogen is placed below the magnetometer with a copper coil in it. Gaseous nitrogen is then blown through the copper coil up into the lower port of the magnetometer which is stopped up with foam rubber to keep the heavier than air nitrogen in. This creates a stratified temperature column that keeps the inside below freezing. A thermo couple at the top of the column lets us know how cold it is inside and make adjustments by controlling the rate of the gas flow. Thus when a sample is loaded it can be taken threw the complete IRM and Af demag series without having to be removed.

The Af demag unit was not working by the time the system was all together so all I was able to do was IRM studies. The samples I started with were magnetically sensitive poisonous newts from New York, and one of the blue shark embryos. In a previous attempt at finding magnetite in the newts, none was found. But those newts have been dead and in alcohol for a while. I measured mine fresh dead and the quicker I measures them the stronger their overall moment.

Figure 2 is an example of the Af demagnetization and the IRM acquisition curve of a salmon that we studied two summers ago[7]. It is a good example of what magnetite "looks" like on one of these graphes. The graph is the peak field in millitesla versus the percent of saturation IRM (or SIRM).

The IRM curves for one newt and one shark are figures 3, 4, 5, and 6. As you can see the blue shark mouth best exhibits properties similiar to fine-grained magnetite. One of the reasons that the rest do not start at zero as they should is that they probably already had with a small moment and since.the Af was not working it was not possible to demagnetize them before I started. The SIRM is reletively strong (close to that of the salmon in figure 2), and is about two orders of magnitude greater than our background noise (which is approximately 2×10^{-8} emu) and one order of magnitude above our contamination level (which is approximately 3×10^{-7} emu).

Conclusions: From the data I have collected I conclude that:

1) The poisonous newts do have magnetite in them, contrary to previous studies.

2) The newt's poison may destroy the magnetite if they are not frozen and measured immediately.

3) The shark embryos contain magnetite.

4) The magnetite in these smaller animals might be scattered through the tissues enough to make it more difficult to extract than in larger animals.

References:

1) H. A. Lowenstam, Magnetite in denticle capping in recent chitons (Polyplacophora). (1962) *Geol. Soc. Amer. Bull. 73,* 435-438.

2) J. L. Gould, J. L. Kirschvink, and K. S. Deffeyes, Bees have magnetic remanence. (1978) *Science 201,* 1026-1028.

3) R. B. Frankel, R. P. Blakemore, and R. S. Wolfe, Magnetite in freshwater magnetotactic bacteria. (1979) *Science 203,* 1355.

4) C. Walcott, J. L. Gould, and J. L. Kirschvink, Pigeons have magnets. (1979) *Science 205,* 1027-1029.

5) J. Zoeger, J. Dunn, and M. Fuller, Magnetic material in the head of the common Pacific dolphin. (1980) *Science 213,* 892-894.

6) M. M. Walker, J. L. Kirschvink, S-B. R. Chang, A. E. Dizon, A candidate magnetic sense organ in the Yellowfin tuns, *Thunnus albacares. Science* (in press).

7) J. L. Kirschvink, M. M. Walker, A. E. Dizon, K. A. Peterson, Interacting single-domain magnets in the head of the Chinook salmon, *Oncorhynchus tshawytscha. J. of Comp. Physiology* (in review).

8) J. L. Kirschvink, Biogenic magnetite (Fe_3O_4): A ferromagnetic mineral in bacteria, animals, and man. (1980) *Proc. of the Inter. Conf. on Ferrites,* 135-138.

9) J.L. Kirschvink, Ferromagnetic crystals magnetite?) in human tissue. (1981) *J. Exper. Biol. 92,* 333-335.

Fig. 1

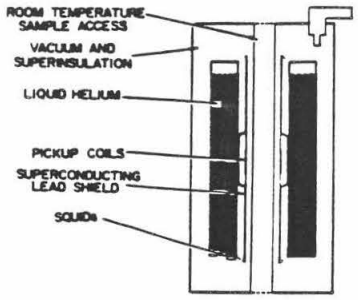

Fig. 2

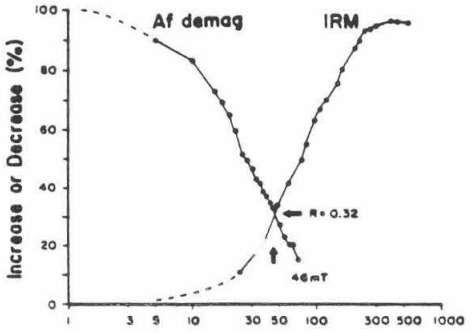

Progressive acquisition and Af demagnetization of IRM for salmon ethmoid tissue extracted from four fish.

Poison Newt
100% = 1.30 x 10^{-6} emu

Fig. 3

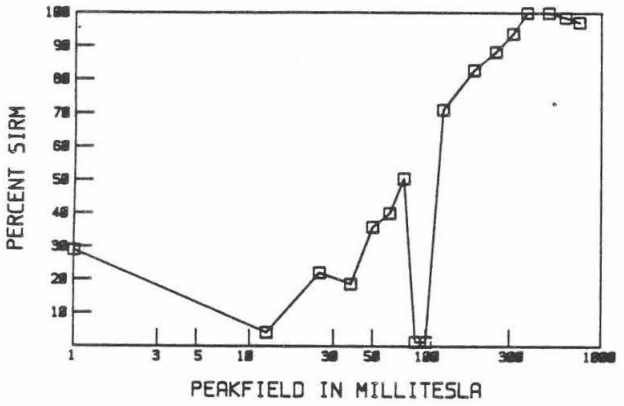

Decapitated Poison Newt
100% = 1.96 x 10^{-6} emu

Fig. 4

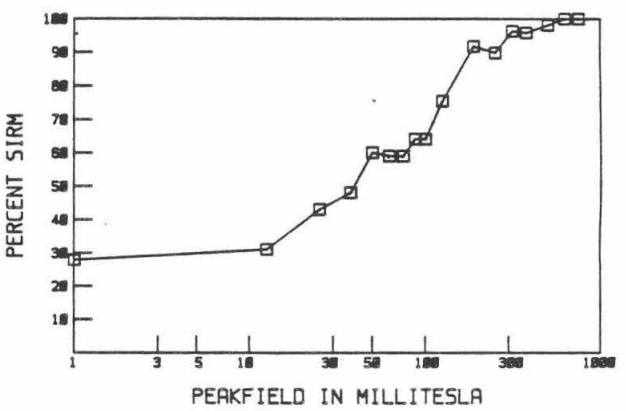

Blue Shark Head
100% = 5.96 x 10^{-6} emu

Fig. 5

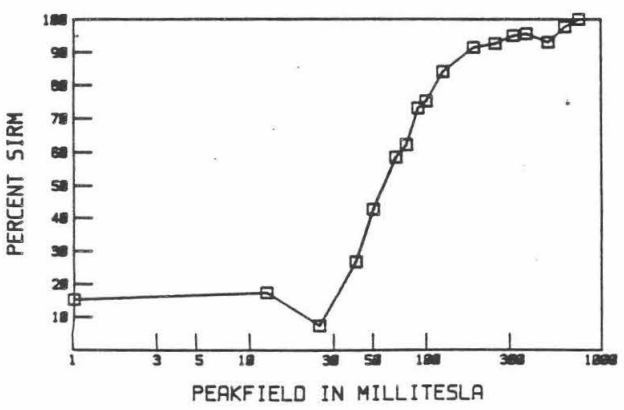

Blue Shark Mouth
100% = 4.08 x 10^{-6} emu

Fig. 6

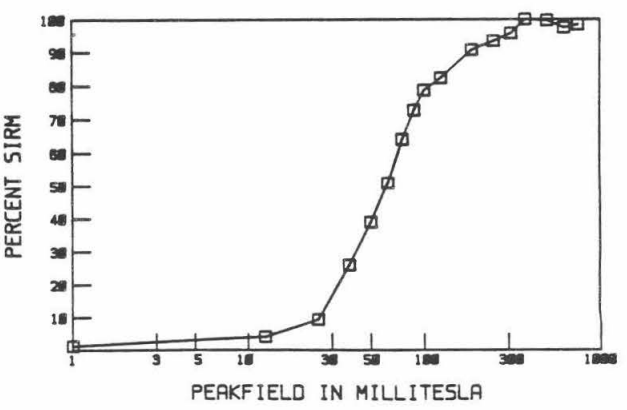

Formation of the Earth's Moon through Large Body Impact

Name: Yosufi Tyebkhan

Faculty Sponser: Dr. D.J.Stevenson

Summer Undergraduate Research Fellowship,

California Institute of Technology, Pasadena, California.

Abstract

I have set up a simple model to examine the characteristics of a disc, from which the moon could form, created by a large body impact with the Earth. The model assumes a cloud, consisting of the melt and vapour from the impact, in hydrostatic equilibrium. However the simple numerical intergrations were not completed and so it is not possble to draw conclusions about the validity of the proposed scenario.

Introduction

Current theories relating to the formation of the moon, namely fission, due to rotational instability, capture of a free body, and the accreation of the moon from the initial solar nebula, so called binary accreation, have serious pitfalls (see Wood 1977)[1]. It has been suggested by Cameron and Ward[2] that a large body impacting with the Earth could lead to the moon's formation through the process of accreation. It is this possibility that is investigated by analysing the physical characteristics of the resulting cloud by comparing calculated data with observable facts, namely the mass of the moon, the angular momentum of the Earth-moon system, and the energy availible from the impact.

Using a static approach, one where the cloud is assumed and physical quantities relating to it are calculated, two cases were studied:

i) An isothermal cloud with no spin.

ii) An adiabatic, spinning cloud.

The basic model is discussed first followed by the above in turn.

The basic model

The model is one in which there has been a large body (approximately 10^{26} grams), impacting with the Earth. The impacting body will have to fall through the Earth's gravitational potential well and therefore will have velocity equal to at least the Earth's escape velocity (v_e =11.2km/s). This gives rise to a specific energy (energy per gram) of about 6×10^{11} ergs. Assuming the impacting body to be made of SiO_2, one of the primary constituents of the Earth's crust and the moon,

this specific energy is sufficient to melt the entire body. If, therefore, the impacting body is massive enough, the existing atmosphere could be displaced and the desired cloud set up by both the vapourization of surface material and by material being thrown off the surface, similar to projectiles. A molten magma ocean is likely to be formed on the surface surrounded by the cloud consisting of an atmosphere section and, in the spinning system, a disc section, that is a distended part, along the equitorial plane, perpendicular to the axis of rotation.(see figure below).

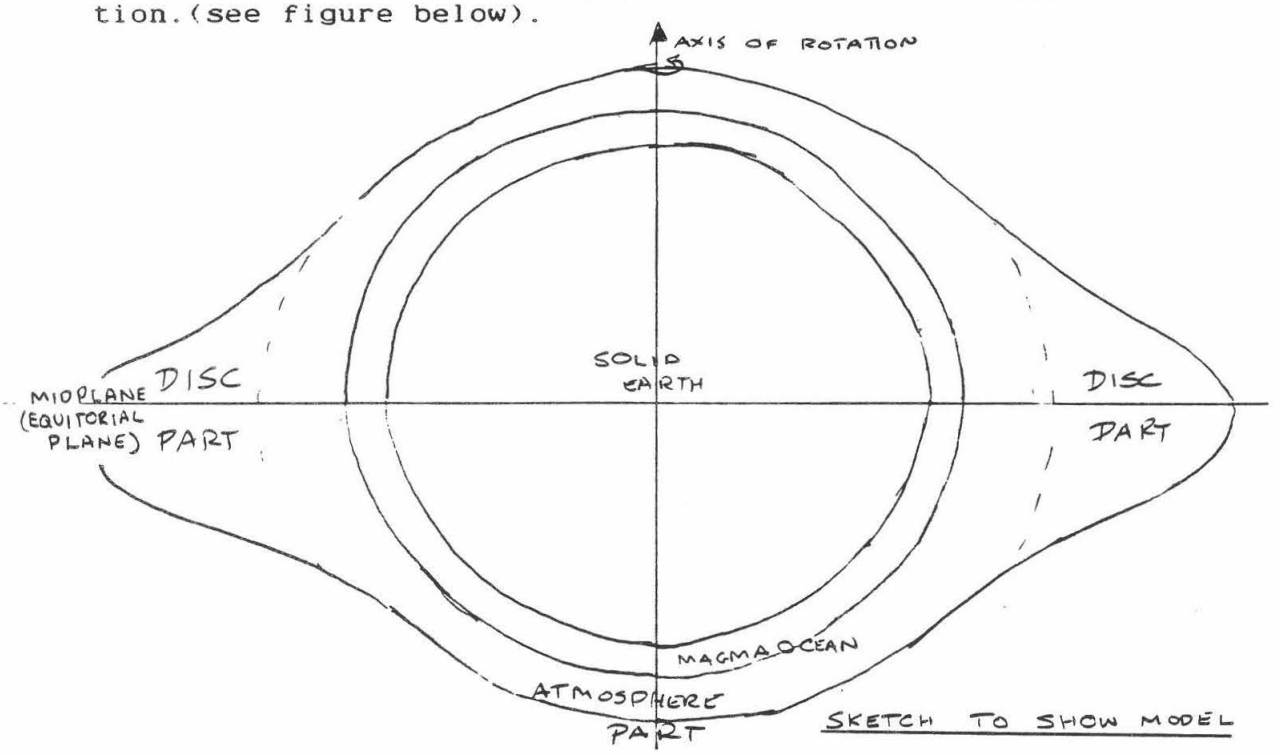

Isothermal cloud with no spin

With no spin, the system can be discribed by a single coordinate, the radial vector, r. Hence the equation of hydrostatic equilibrium is:

(1) $$dp/dr = -\rho g$$

where p is the pressure, ρ is the density, g is the acceleration due to gravity. For an isothermal enviroment we have

(2) $$p = C^2\rho$$

where C is the speed of sound. given by

(3) $$C^2 = kT/\mu$$

where k is Boltzmann's constant, T the absolute temperature, and μ is the molecular mass of the substance in question.

Considering a gravitational acceleration that varies with height, that is not restricting the discussion to scale heights (the characteristic length scale of the atmosphere) that are small with respect to the radius of the Earth, we obtain the following solution to (1):

(4) $$\rho = \rho_s \exp[GM_\oplus(1/r - 1/R_\oplus)/C^2]$$

where G is the Universal gravitational constant, and $R_\oplus$ is the radius of the Earth, and $M_\oplus$ is the Earth's mass. There are two contributions to the energy of the cloud:

i)The ejecta must overcome the Earth's gravitational field. The gravitational energy scales as the scale height as the more mass there is in the cloud, the greater the energy.

ii)The ejecta also gains thermal energy, both in the form of thermal agitation as well as that due to phase transitions. As the scale height is directly related to the temperature, it follows that as one increases so does the other.

Considering SiO_2 which is completely vapourized, and an impacting velocity equal to v_e ,(giving a specific energy equal to $1/2v_e^2$), scale heights of about 10^8 cm(about the radius of the Earth) are obtained with rough calculations indicating that enough mass is availible, for sufficiently large bodies, to form the moon. High temperatures are obtained, of the order of 10^4 K. The temperature and the scale height are greater than expected, but these calculations assume all the energy of the impacting body is transformed into either gravitational or thermal energy of the cloud. In a more accurate model, there will be rotational energy as well. The other assumption is that all incoming energy is thrown outwards. This is highly unlikely and calculations for smaller impacting bodies seem to imply that only about 1/100th of the energy will be thrown out.(see O'Keefe and Ahrens 1982.)

Adiabatic spinning cloud

In an atmosphere there is convective heat transfer and as a result, an adibatic lapse rate, the decrease of temperature with heigth, exists. It is therefore more accurate to represent

the atmophere by an adiabatic equation of state:

$$p/p_s = (\rho/\rho_s)^{1/1-\tau} \quad (5)$$

where the subscript, s, refers to the surface values of the variable and τ is a constant depending on the substance. (5) is obtained by considering a wet adiabat, one along which condensation occurs. It therefore follows that the pressure is the vapour pressure and that the vapour pressure relationship:

$$p = A\exp(-B/T) \quad (6)$$

can be used.(5) is an approximation to (6). is determined by use of vapour pressure tables[4], to be 1/20 for SiO_2.

With spin, the radial coordinate no longer suffices and the equation of hydrostatic equilibrium can be written thus:

$$\vec{\nabla} p = -\rho \vec{a}_e \quad (7)$$

where a_e is the effective acceleration, $g-w^2 r\sin\phi$, the balance between gravity and centrifugal forces.

It is useful to consider a potential fuction of the form:

$$\phi(s,z) = g_s R/(s^2 + z^2)^{1/2} + w^2 R_e^2 s^2/2 \quad (8)$$

where s and z are non-dimensionalized coordinates in the equitorial plane and along the axis of spin, respectively, g_s is the gravitational acceleration at the surface and w is the angular velocity of the cloud.

On combining (6) and (8) we obtain :

$$\rho(s,z) = \rho_s[(\phi - \phi_s)/20C_s^2 + 1]^{19} \quad (9)$$

where ϕ_s ,the potential at the surface, is an equi-potential surface passing through s=1,z=0 which is the surface of the Earth in the equitorial plane.

The potential function decreases outwards until $\vec{\nabla}\phi = 0$ at which point, it begins to increase. On the equitorial plane this point is given by:

$$s = (g/w^2 R_e)^{1/3} \quad (10)$$

From the boundry conditions it is apparent that the density should not increase. Asutible solution, therefore, is one where this hydrostatic solution, (9), is valid until the minimum value defined by (10). For densities further out than this we can have the material in Keplarian orbit such that $\vec{a}_e$ is zero, that is, $g \approx w^2 r \sin\phi$. This is where the disc begins.

For the disc, an isothermal approximation is valid and therefore we obtain a gaussian variation of density about *the mid-plane of the disc. The equitorial density is assumed* to vary as $1/s^3$ and the temperature as $1/s$, both consistant with previous disc models. We therefore have the following as the solution:

for the rigidly rotating atmosphere:

$$\rho = \rho_s[(\phi - \phi_s)/2OC_s^2 + 1) \quad \text{where } \phi = gR_\odot/(s^2 + z^2)^{1/2} + wR_\odot s^2/2 \tag{11}$$

in the disc: $\rho = (A\rho_s/s^3)\exp(-z^2/H^2)$

where $H^2 = 2kTs^2/\mu gR_\odot$ and $T = B/s$

A is a constant determined by imposing continuity on density from the atmosphere part to the disc. B is a similar constant for temperature.

We can therefore see that there several independent quantities that parameterize the problem;

i) w the angular velocity of the rigid section.

ii) ρ_s the surface density.

iii) T_s the surface temperature.

The density fuction can be integrated to determine mass, angular momentum, and the energy of the system. To obtain a disc which could give rise to the moon, all three of these quantities must lie within defined ranges.

Mass The mass of the disc must be at least twice that of the moon as the process of accreation will dump mass back into the central body. The mass of the moon is 7.4×10^{25}g.

Angular momentum By considering the present Earth-moon system, we see that we need a minimum angular momentum of 10^{40}g cm/s. A maximum can be determined by considering an oblique impact with all the momentum of the body being transfered to angular momentum. This gives a value of about 5×10^{41}g cm/s.

Energy This is constrained by the total energy of the impacting body. The distribution of energy is not obvious and is assumed

to all go into the cloud as previously mentioned.

The quantities relating to the disc proved easy to integrate. Integrating from the start of the disc, given by (10), to an outer disc radius, s_o, we obtain:

$$Md = C_1 \ln(s_o / s_i)$$

(12)

$$Ld = C_2(s_o^{1/2} - s_i^{1/2})$$

$$Ed = C_3(3Rg(1/s_i - 1/s_o) + 2\ln(s_o/s_i)[2.589\times10 + 2.0790\times10 (3T_f - T_i)]$$

s_i is defined by (10), T_f is the final temperature, and T_i the initial temperature which was taken as zero through out the calculations. C_1, C_2, C_3 are constants.

For the atmosphere, however, a more complex integral is to be evaluated. In polar coordinates it can be written:

(13)

$$Q\int_0^{\pi}\cos\theta\int_{r_o}^{r_{max}} f(r)\rho(r,\theta)\,dr\,d\theta$$

where $\rho(r,\theta) = [A(r^2 - r_o^2)\cos^2\theta + B(1/r - 1/r_o) + 1]^{19}$

$f(r)$ is a polynomial in r depending on which quantity is being evaluated

M is r^2, L is r^4

Q, A, B are constants

r_o is determined by solving for the surface where $\rho/\rho_s = 1$. Numerical methods were used as no satisfactory approximation, that was valid in all domains of interest, could be found. The r-integral can be approximated with an exponential whereby (13) becomes:

(14)

$$Q\int_0^{\pi}\cos\theta\int_0^{\infty} g(\beta)\exp(-D\beta)\,d\beta\,d\theta$$

$\beta = r - r$

$D = 19(B/r_o - 2A\cos\theta)$

The problem is therefore reduced to evaluating the θ-integral. An attempt has been made this integral numerically but results have not yet been obtained.

Conclusion

The initial simple model set up was instructive in giving some idea as to what values to expect for various quantities such as scale height and temperature.
The more interesting model has been reduced to numerically evaluating integrals which should give plots of the three quantities, mass, angular momentum, and energy versus the outer radius of the disc. Using the previously explained constraints, it should be possible to determine what values of the parameters, angular velocity, and surface density and temperature, will give rise to a situation from which the moon could be formed.

References

1) Wood, "Origin of the Earth's Moon", Planetary Satellites Editor Burns, J.A., University of Arizona Press, Tuscon. 1977

2) Cameron, A. and Ward, W., "The Origin of the Moon", Lunar Science Conference Abstracts Vol 7, pp. 120-122

3) O'Keefe, J. and Ahrens, T., "The interaction of the Cretaceous/Tertiary Extinction Bolide with the atmosphere, ocean and solid Earth", Geological Survey of America Special paper 190, 1982

4) Handbook of Chemistry and Physics, 62nd Edition, pp.D170 Chemical Rubber Company Press, Florida, 1981.

Humanities and Social Sciences

CHINESE AND OTHER ASIANS IN CALIFORNIA -- THE POLITICAL ROLES

Author: Jim Chen
Sponsor: Dr. Bruce Cain
Date: Sept. 14, 1984

Abstract:

This research is an attempt to understand the development of Asian Americans' political involvement in the California mainstream political system. First it is necessary to have an idea about the background and history of these special groups of people. Then attention is directed toward the many difficulties the modern Asian Americans faces. And finally, we take a look at several ways of their participation in politics including running for elections and contributions to interest groups and individuals.

- -

History

Historically, Chinese were the first Asians to arrive in America. There is even evidence of their presence in America before Columbus. At least we are sure they were already here in the state of California before the Gold Rush of 1849 (Chen, 1980). The Chinese remained the largest Asian immigrant group in California (and perhaps largest in U.S.) until just recently the Filipinos outnumbered them. Following the Chinese, Japanese started to immigrate to California in the late 1870's (10/17/77, LA Times); and then the Koreans and Filipinos came, too, in the early years of this century (9/10/78, LA Times). Finally, of course, there are Indochinese who escaped from the communists and came to the U.S. in the last decade.

An interesting question is: what made the Chinese to leave their country so much earlier than the other Asian ethnic groups? First of all, we have to keep in mind that practically all the early Chinese "immigrants" who came during and after the Gold Rush did not come as (or intended to be) true immigrants in the sense that they only planned to earn money and go back home -- typical sojourners. Because of their cultural and moral conception, they "left with the expressed intention of returning to the home and resuming their duties to the ancestors" (p.20, Chen, 1980). Another feature of these Chinese sojourners, which is unique among the Asian immigrants, is that they only came from a small region of southern China -- Guangdong Province. People of this region were suffering from poverty and the ruling of

the corrupted Ch'ing (or Manchu) government. So as soon as the news of the discovery of gold in California reached Canton (Capital of Grangdong), many poor people were willing to take a chance and left their homeland to seek fortunes abroad. Then the Taiping Rebellion, originating in China's southern provinces in 1850 and lasting until 1964, created even more civil disorder and caused more Guangdong people to move out. These events accounted for much of the early immigration by the Chinese into America.

At first the Chinese were welcome in California because they were hard-working, well-disciplined, skilled laborers who took not only jobs the white laborers would not take, but also jobs the white laborers could not take (Chen, 1980). The most famous example among many of their contributions to the then-wild-frontier California is the building of the western section of the first trans-continental railway whose difficulties were beyond the expections of the building company. After the railways were finished, these Chinese switched right away to farming which by that time had replaced mining as California's number one industry. Then came the economic crises of the 1870s when suddenly the stock market collapsed and brought many industries into bankruptcy, resulting in record-high unemployment. At that point, native Americans wanted the jobs they previously had rejected. Being a visibly distinct foreign group, the Chinese were blamed for taking away jobs (Chen, 1980). Soon they became the scapegoat of the public's fear and anger. With some politicians' amplification, the Chinese exclusion soon became a major issue and ,finally, a law in 1882. It lasted 61 years until 1943, during which period the Chinese in America had to endure all sorts of humiliation, injustice, and frequent violence. By the end of the exclusion, other Asians had startedto come to America. These later immigrants, including Chinese of the same period, came for the purpose of settling down permanently, because of either harsh economic condition, unstable political situation, family reunion, or simply enterprise ambition.

Today the Asians number more than 1.2 million in California alone, or about 5.3% of California's 23 million, distributed in various urban areas (from 1980 census data). There are four major ethnic groups of Asians in California: Filipinos (1.5%), Chinese (1.4%), Japanese (1.1%), and Koreans (.44%).

The Chinese concentrate in San Francisco (12% of city population), Hercules (10%), Oakland (4.4%), Sacramento (3.9%),Foster City (6.7%), and several cities in Los Angeles such as Monterey Park (15%), Cerritos (3.3%) and Montebello (5.5%). The Japanese are densely populated in Reedley (4%), La Palma (4.4%), and LA areas like Gardena (21%), Monterey Park (14%), Torrance (6.1%) and Montebello (5.1%). The Filipino population is more scattered; they are in Delano (14%), Union City (11%), and Monterey County. The Koreans are mostly in the LA areas.

In the comtemporary period, Asians have encountered many problems in the heavily concentrated urban "gettos." Common concerns are not different from the Blacks or the Hispanics: housing, health, elderly welfare, working conditions and low wages. A walk in the Chinatown in San Francisco or Los Angeles can reveal many of these problems (7/30/78 LA Times). In addition, special issues were raised. From Asian Week, these needs are summarized as the following.

Japanese are seeking to redress the survivors of the 110,000 Japanese American citizens interned during World War II. They feel that at least $20,000 should be paid to each victim in order to be fair. The Vietnamese particularly care for refugee admission and economic self-sufficiency (as oppose to the regulation on working while receiving grants). In response to the 26% increase of anti-Asian violence last year, the Asians demand affirmative action and unbiased law enforcement. Meanwhile they also fight for bilingual education, equal representation in the government, and the improvement of immigration laws and offices in favor of family unification (Therefore, unanimous opposition to the Simpson-Mazzoli bill which abandons the admission of siblings of U.S. citizens).

Political Involvement

To study the political behavior and influence of the Asian Americans, one would immediately think of looking at records of their activities in campaigns and elections. This direction is exactly where I have done. With the Guidance of my sponsor and the help of several co-workers, I found two available source of data. One is called The National Asian American Roster (NAAR) (one sample each for the two years, 1980 and 1982), obtained from the Asian American Studies Center in UCLA. It was compiled on the basis of family names by Don T. Nakanishi, who is a professor of Asian American study in UCLA. From these two rosters, I took out the Californian part and sorted the individuals by ethnicity and sex, on the basis of surnames. The biggest difficulty in doing so is the uncertainty involved: the Chinese and Koreans often have common names, whereas the Filipinos and Pacific Islanders have Spanish names. In order to decrease the degree of inaccuracy, phone calls were made to check with their secretaries or themselves. But only a small part out of one ('82) list (two lists have many similar ones) was checked in this manner. Other "obvious" names were just assigned to the "obvious" ethnicity. Therefore we have no way of detecting, say, a Filipino with a Chinese surname.

The other source is the publication by the California Fair Political Practices Commission (FPPC) which monitors the funding of each campaign in California since 1976. Seven possible samples were available: '76 general election (G) and primary election (P), '78 G & P, to go through each contributor and pick out the Asians (again, based on

surnames). The figures tend to be under-estimataed since companies owned by Asians might not have an Asian name and got out of the count. Nevertheless, every effort was made to minimize errors and I went on to analyze the data assuming the figures were not too far from reality.

The degree of difficulty for Asians to participate in American politics is imaginable: 1)they are merely five percent of the total population, with huge geographical and ethnical diversity among themselves; 2)they, especially the Chinese, were excluded the right to citizenships and volting until not long ago; 3)some of them have a language barrier; and 4)racism still pervades much of this society. In order to conquer these obstacles, the Asian Americans first have to mix in with the society. As my research has shown, the Asian office holders or candidates do not depend largely on the financial support of Asians. Furthermore, Asian contributors do not donate considerable amounts to Asian candidates (see Table 1)

Table 1: $ contributed by Asians to Asian and non-Asian candidates, figures x$1000 (from NAAR)

	76G	76P	78G	78P	80G	80P	81-2
Asian	5.7	0.0	0.4	0.1	0.1	20.4*	0.0
non-A	49.3	2.6	41.7	22.2	27.0	13.3	57.1

*note: including 20.0 loan

The only exception is the 80P, which includes a large loan presumably from a relative of the candidate (they have the same last name). An observation is clearly true: most Asian office-holders do not identify themselves with their particular ethnic groups as much as with the majority Americans. Afterall, they get most of their votes from the majority Americans, and without further emphasis, one would reason they attract Asian votes already.

Another step to join the political scene is to get together and produce a "louder voice." Ling in her paper supports this: "There are two general methods of wanting-in in Chinese American history: electoral politics and compliance with the mainstream society, and protest movements."(p.22) A recent example of the protest movements is the ouster of a volter registrar in San Francisco as a result of a petition signed by 5,000 Chinese. They were offended by his disparaging remark about Chinese (2/13/80, LA Times).

In the electoral politics scene, Japanese seem to be the most active. Of all Asian elected officials in California, those of Japanese ancestry add up to more than the rest combined. They occupy 58% of the seats taken by Asians. The Chinese follows at 25%, then the Filipinos at 9%, and the Koreans 5% (Table 2.1, 2.2).

Table 2.1: number and percentage (of total) of office holders in 1980 (from NAAR)

	Ch	Fil	Ja	Kor	other/?	total
#	24	6	66	4	6	106
%	23	5.7	62	3.8	5.7	100

Table 2.2: number and percentage (of total) of office holders in 1982 (from NAAR)

	Ch	Fil	Ja	Kor	other/?	total
#	29	11	68	6	3	117
%	25	9.0	58	5.1	2.6	100

Out of only two samples available, we already see a dramatic increase: from a total of 106 in 1980 to 117 in 1982 (10% up). And the trend is toward a catching up with the other three ethnic groups to Japanese (Table 3).

Table 3: the increase in number and percentage of office holders, ′80 to ′82 (from NAAR)

	Ch	Fil	Ja	Kor	other/?	total
#	5	5	2	2	-3	11
%	21	83	3	50	-50	10

If this tendency persists, then we can certainly predict in the coming years a near-saturation state for the Japanese (they have a small increase in number from ′80 to ′82), as well as a lot more new people coming from the other 3 groups, resulting in a net increase.

How about women office holders? Table 4 shows the comparison with men. Obviously they are still very inactive.

Table 4: number and ratio of male/female office holders in 1980 and 1982 (from NAAR)

	′80	′82	increase
M	83	91	9.6%
F	16	22	38%
M:F	5.2:1	4.1:1	1:4

Four or five men to one woman is a very big margin. But the good sign is that the number of elected women is increasing

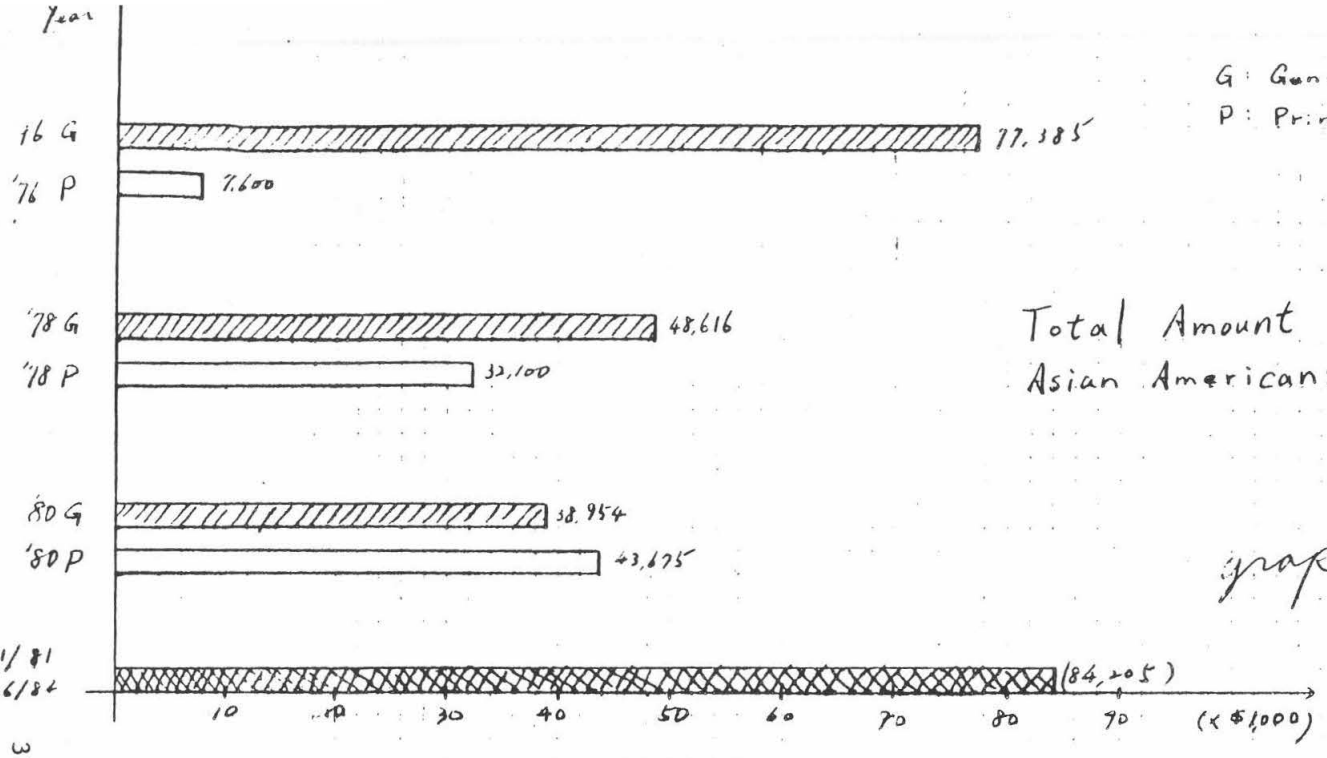

Total Amount Contributed by Asian Americans

graph 1

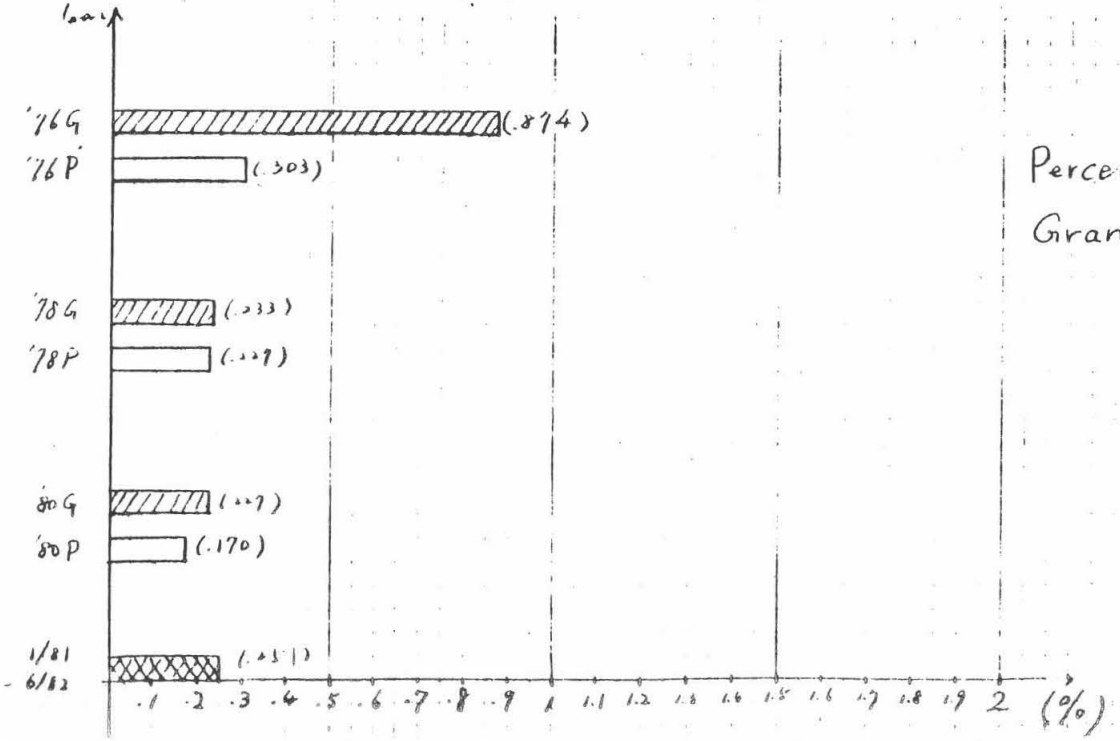

Percentage out of Grand Total

graph 2

at a rate 4 times faster than men. They have pulled the ratio from 5:1 to 4:1 within two years. Plus they also hold high-level offices -- e.g., Secretary of State of California, March Fong Eu. The Asian women are really not doing badly at all.

The contribution data, too, is limited by the available 7 samples spanning from '76 to '82. Therefore long-term trends can not be detected. About the contributions for primary elections, the amount increases over this period, but the percentage of the total Californian contribution decreases (see graph 1 & 2). The contribution for general elections actually decreases over this period. But we can not conclude a similar pattern for the future years, because, for example, a farm labor law issue came up during the '76 general election and drew a lot of attention. What we are sure about is that the Asian contributors respond very sensitively to issues particularly concerning their interest. Tanaka describes such phenomena as "issue oriented." In comparison with the population percentage (5%), the Asians seem to be "under- contributing" by a huge margin (the highest year is only less than one perdent of the total). In addition, analysis shows very irregular party preference (Table 5).

Table 5: $ contributed by Asians to the two major parties ,figures x$1000 (from NAAR)

	76G	76P	78G	78P	80G	80P	81-2
D	17.3	n/a	n/a	2.5	9.8	n/a	50.6
R	34.5	n/a	n/a	19.7	16.5	n/a	20.4

A postulate to explain this: an upper-middle class status is the reason for prefering the Republican whereas a status as social minority and the concern for the poor cause the inclination for the Democrat.

Conclusion

The Asians in America is gradually forming a force so powerful as not to be ignored. But because of the previous inhibition, the majority of them still need to be awakened for full participation of the mainstream politics. Also they need more strong leaders to unify them and act together as a group, and to improve the under-representation in the federal government (1.1% white-collar federal workers as compared to 1.6% national Asian population, and most of them do not have policy making power) (5/5/78, LA Times). They contribute financial support to campaigns, but not consistently enough. Added to these are many other hindrances for their political progress. In short, their political road ahead is still very rough, and their political rolls are yet to be fully developed.

BIBLIOGRAPHY

Asian Pacific Caucus of the Democratic National Committee (Convention Special), Asian Week, San Francisco, 1984

Chen, Jack. The Chinese of America, Harper & Row, publishers, San Francisco, 1980

L.A. Times: "Ethnic Group Dismayed by Resignation of 2 Asian-Americans Carter Named", p.20, part III, 5/5/78

L.A. Times: "The Chinatown Tourists Don't See", p.1 part IV, 7/30/78

L.A. Times: "After Years of Inaction, S.F. Chinese Flex Political Muscles", p.3, part I, 2/13/80

L.A. Times: "Half of Americans of Pacific Island or Asian Descent Live in California, Hawaii", p.19, part I, 5/27/81

Ling, Susie. "A History of Chinese American Political Activism," a paper for UCLA class AAS297, Professor D. Nakanishi, 12/14/1983

Tanaka, Ron. "Culture, Communication and the Asian Movement in Perspective", Journal of Ethnic Studies, 4/1/1976, pp37-52

Floating Exchange Rates and International Trade

by John McGowan

Sponsor: Robert Oliver

Abstract:

This paper examines two separate but related topics: how foreign exchange rates are determined and how exchange rates affect international trade. A review of economic literature and analysis of exchange rate data for the period 1966 to 1983 revealed no strong relationship between real interest differentials and real exchange rates, suggesting important additional factors in the determination of exchange rates. A simple, preliminary model of determination of trade proved ambiguous.

Introduction:

Exchange rates are important because they may play a significant role in influencing the structure of international trade and the distribution of productive endeavour among nations. In particular, in recent months, it has been argued that the dollar is "overvalued" against other currencies, leading to presumably deleterious effects on American industry. The primary motivation of the research that the author has been undertaking is to examine the validity of this concept.

A review of economics literature revealed that there has been very little work done on the effect of exchange rates on the structure of international production and trade. Since the breakdown of the Bretton Woods fixed rate system in 1973 most work related to foreign exchange has focused on how exchange rates are determined. As yet, no good model has been devised for explaining movements in the exchange rate.

In the empirical work that followed the review of the literature the author examined a couple of questions: first, is the real exchange value of the dollar high by historical standards in recent years, second, is there a statistically significant correlation between the difference between real interest rates in nations and the real exchange rate, and third, would a simple model work to describe changes in the volume of automobile imports as a function of exchange rates and other factors.

Presentation and Discussion of Results:

A proxy for the real exchange rate of the dollar against the Canadian dollar, Japanese yen, British pound, and the German mark was determined by taking the nominal exchange rate, expressed in units of foreign currency per dollar, and multiplying it by the United States consumer price index and dividing it by the foreing consumer price index. This was done for quarterly data from 1966 to 1983.

Presentation and Discussion of Results(cont'd):

This confirmed that the dollar has been high in real terms compared to its average during the 1970's in the last few years (1980-1983), although the dollar had been as high as it is now during the late 1960's.

A proxy for the real interest rate was determined by taking the nominal interest rate, either the T-Bill or call money rate depending upon what was available for the nation in question, and the annualized inflation rate calculated from quarterly consumer price index data.

Using quarterly data, there was no statistically significant correlation between real interest rates or real interest differentials and the real exchange rate in the cases of the United Kingdom, Japan, Germany, or Canada.

One would expect that if, ceteris paribus, the real interest rate in the United States rose, then investors would want to purchase dollars in order to invest in United States bonds. This would push up the real exchange rate. The lack of correlation between interest rates and the real exchange rate indicates the existence of other factors that are as or more significant than the real interest differential between nations. In particular, the author identifies political factors such as fear of socialist governments and so forth as the probable culprit.

Finally, the author tried to examine the effect that exchange rates have had on automobile imports over the last six years (1978-1983). The simple model that was used was:

```
x = a*y**alpha*(s/p)**eta
```

where

x is the volume of imports in units of traded good
a, alpha, and eta are constants to be determined by linear regression
s is the real exchange rate
p is the real (inflation adjusted) price of the good in exporting nation

Lacking data on prices, p was arbitrarily set to one, thus leaving an important factor out of the fit.

The fit produced a statistically meaningful result only in the case of auto imports from Canada in which case alpha was 8.42 and eta was 2.87 (a is simply a proportionality constant depending on units). What this means is that a doubling of the United States real gnp woul hypothetically produce an increase in auto imports by a factor of 2 to the 16th and a doubling of the exchange value of the dollar would produce a near octupling of U.S. automobile imports from Canada.

This result could be a fluke. There is a 66% chance that it is not a fluke, well below the 95% confidence level that is desired.

Conclusions:

1) It was determined that the real interest differential is not the strongly dominant factor in determining exchange rates. Other factors are quite important. In subsequent work, it will be necessary to control for other factors, as, for example, by choosing periods of relative political uniformity during which to examine the relationship of exchange rates and real interest differentials.

2) There is reason based on a preliminary analysis to believe that the crude model of import volume determination may be essentially correct. It would be best to try out the model on other components such as rice, wheat, ball bearings, and so forth in order to determine if more positive signals such as the Canada result occur. If possible, actual, inflation adjusted prices of the goods should be located and figured into the model.

Bibliography:

Note: In the course of reviewing the literature on exchange rates, the author examined a large number of articles. It would be impractical to list all of these here, particularly because they tend to overlap. The following is a list of articles that the author consulted extensively and that summarize most of what is known about exchange rate determination.

Dooley, Michael and Peter Isard. "The Protfolio-Balance Model of Exchange Rates and Some Structural Estimates of the Risk Premium" , International Monetary Fund Staff Papers, Dec '83

Dornbusch, Rudiger. "Expectations and Exchange Rate Dynamics" Journal of Political Economy, 1976, vol. 84, no. 61.

Hutchison, Michael, "Intervention, Deficit Finance and Real Exchange Rates: The Case of Japan", Federal Reserve Bank of San Francisco Economic Review, No. 1, Winter of 1984

Schadler, Susan, "Interest Rates and Exchange Rates", Finance and Development, Jun. 1984, Vol.21, No. 2.

Physics, Mathematics, and Astronomy

TITLE: DEVELOPMENT OF PHYSICS SOFTWARE USING THE PASCAL LANGUAGE

AUTHOR: GREGORY L. BAILEY

SPONSOR: GEOFFREY C. FOX
DEAN OF EDUCATIONAL COMPUTING

ABSTRACT: I HAVE DEVELOPED SEVERAL PASCAL PHYSICS PROGRAMS IN ORDER TO TEST THE USEFULNESS OF PASCAL IN THE CALTECH COMPUTATIONAL PHYSICS PROGRAM.

The purpose of this project was to take already extant software from the computational physics program and and translate it into the PASCAL language. With several different versions of the same program it was possible to compare the relative effectiveness of the various compilers and languages.

The methoid involved was to take the available computational physics software examples and select several programs that would make good demonstation programs. A good example program was one that involved a fairly interesting and nontrivial physics problem combined with fairly interesting graphics. After selecting the BASIC programs I wrote pascal programs to closely mimic them in structure and function. I also developed several programs of a purely mathmatical nature for the TURBO PASCAL compiler.

It was necessary to write seperate demonstration software for TURBO since the present release cannot handle external graphics libraries and the compiler does not support its own graphics. Therefore, a graphics oriented demonstration was impractical. This disadvantage was somewhat compensated for by TURBO's fast compilation, easy debugging, and general ease of use.

The I.B.M. compiler is considerably more powerful but it suffers from a rather lengthly compiling time. This is partly due to the need for two compiler passes and a seperate linker. This lengthly compilation makes " fiddling " with the code a time consuming and tiring process. On the bright side, the I.B.M. compiler does produca a listing that lists most of the errors in the program, allowing many errors to be fixed at once.

The H.P. compiler has many of the I.B.M.'s good points without the lengthly compilation time. The printer is also much faster. The H.P. also has a graphics library that, although it lacks many of the capabilities of the HALO package, is much easier to use than HALO. The equipment seemed somewhat better and the graphics were sharper.

TABLE COMPARING THE VARIOUS COMPILERS

	COMPILER SPEED	PROGRAM SPEED	GRAPHICS
I.B.M PASCAL	SLOW	FAST	HALO
H.P PASCAL	FAST	FAST	TURTLE
TURBO PASCAL	FASTEST	FAST	NONE
INTERPRETER BASIC	NONE	SLOW	TURTLE
COMPILED BASIC	VERY FAST	FAST	TURTLE

CONCLUSIONS:

1: PASCAL, with its highly structured format is ideal for writing simulations and physics problems in general.

2: The greater speed of a compiled language like PASCAL will greatly cut execution time for programs involving large arrays, nested loops, or much computation

3: A PASCAL section in the computational physics program will allow students to a wider variety of languages as well as using experience gained in other courses in this program.

SUMMARY OF PROGRAMS:

GRAVITY: SIMULATES THE PATH OF A PROJECTILE IN OUTER SPACE RESPONDING TO THE GRAVITATIONAL FIELD OF 1 TO 10 FIXED MASSES. THE USER SELECTS THE STARTING LOCATION AND MASS OF THE MASSES AS WELL AS THE STARTING POSTIION AND VELOCITY OF THE PROJECTILE. THIS PROGRAM IS AVAILABLE IN H.P. AND I.B.M. PASCAL.

CHARGES: DRAWS THE FIELD LINES AND EQUIPOTENTIAL SURFACES FOR A SYSTEM OF n FIXED POINT CHARGES. THE USER SELECTS THE NUMBER, LOCATION, AND VALUE OF THE CHARGES. THIS PROGRAM IS AVAILABLE IN BASIC, COMPILED BASIC, AND H.P AND I.B.M. PASCAL.

SPRINGS: USES ANIMATION TECHNIQUES TO SHOW THE MOTION OF A TWO MASS, THREE SPRING SYSTEM IN THREE DINENSIONS. THE USER SELECTS THE SPRING CONSTANTS AND THE MASS OF THE MASSES, AS WELL AS THEIR STARTING POSITION AND VELOCITY. AS AN OPTION GRAVITATIONAL FORCES AND DRAG CAN BE INTRODUCED. THERE IS A CHOICE BETWEEN TWO GRAPHICS MODES. THIS PROGRAM IS AVAILABLE IN BASIC, COMPILED BASIC, AND H.P. AND I.B.M. PASCAL.

DERIV: USES FORWARD, CENTRAL, AND EXACT APP-ROXIMATIONS TO COMPUTE THE DERIVITIVE OF A FUNCTION. THE PROGRAM DISPLAYS THE RESULTS AND ERRORS. THIS PROGRAM IS AVAILABLE IN TURBO PASCAL AND BASIC

RKN4: PREFORMS ANALYSIS USING FOURTH ORDER RUNGE-KUTTA TECHNIQUES AND DISPLAYS THE RESULTS TO THE USER. IS AVAILABLE IN TURBO PASCAL AND BASIC.

NOTE: THE H.P. AND I.B.M. PROGRAMS HAVE BEEN DEPOSITED WITH GEOFFRY C. FOX.

A Computer Graphics Representation of Stellar Nuclear Burning Processes

Peter Cho

Advisor: Dr. Juliana Sackmann

ABSTRACT

A three dimensional, color computer graphics movie has been created which visually dramatizes the violent astrophysical phenomenon of shell flashes in particular and stellar evolution in general.

Introduction

Stars undergo remarkable changes in their lifetimes. A star's surface radius can grow by more than a factor of one hundred, and its surface color can shift from bright blue to dim red. Moreover, the sites and rates of nuclear burning inside a star alter considerably as the body evolves. For the majority of its existence, a star burns hydrogen deep within its center. Later, helium ignites as core temperatures and densities rise above critical levels. After the core fuel has been exhausted, nuclear activity continues in thin burning shells which progress outward through the star's mass. One most interesting phenomenon occurs extremely late in a stellar body's lifetime - shell flashes. As its name implies, a flash represents an extraordinary thermal instability in which the energy released from a burning shell increases over ten thousand times above normal output. These run away nuclear processes reoccur periodically and grow in intensity until a peak is attained. Shell flashes, which have been found to significantly influence stellar development and structure, signal an aged star's approaching end.

The purpose of this project was to visually dramatize the phenomenon of shell flashes in particular and the changes associated with stellar evolution in general with the aid of computer graphics.

Discussion

The data which formed the basis for the computer graphics movie was taken from Sackmann's calculations for a three solar mass star. These computations follow the development of general stellar features such as surface radius, surface temperature and luminosity at several thousand key instances in the star's life. In addition, the calculations provide local values of temperature, density, and hydrogen and helium composition as functions of time and radial position within the star. With these parameters, nuclear burning rates for the proton-proton, carbon-nitrogen-oxygen, triple alpha, and carbon-helium reactions can be determined. The sum of these rates yields a total nuclear energy value. Thus a relationship linking stellar nuclear activity with radial location and time can be established.

Several preliminary plots of Sackmann's data which outlined the general history of the three solar mass body were prepared. Based upon these graphs, ninety critical time points were identified; the data associated with these points was manually entered into files on the computer science department's VAX 780.[1] This raw information was linearly interpolated in both space and time dimensions in order to regularize the intially uneven distribution of data. Nuclear energy values were subsequently computed and correlated with arbitrarily selected colors which were intended to visually convey degrees of nuclear activity. Dark red was associated with minimal energy output whereas orange, yellow and white were linked with successively greater burning rates. Thus a large array was established which related various colors with radial positions and times. Values for surface color, which were correlated with surface temperature, were also saved into this color array.

After the raw data had been transformed into color information, three dimensional images of the star with an octant cut away to reveal its interior were generated. Each of the 512 × 512 pixels in a full screen picture was mapped onto a three space point with the origin set at the screen's center. For any given frame, those pixels whose three space point's distance from the origin was less than the star's surface radius were colored as specified by the data in the color array. Similarly, those pixels which were mathematically located on the star's spherical surface were colored based upon the surface information.

1. Almost all of this project's computational work was performed on the CS VAX in PASCAL.

All visible surfaces in each of the images were ray-traced. In this technique the color intensity at any point is scaled to the dotproduct between the normal vector at that point and an arbitrarily positioned light source vector. The resultant shading of visible surfaces enhances the three dimensional appearance of a picture. The computer also antialiased each image. Antialiasing involves setting the color value at any pixel equal to the average of itself and its neighbors. This averaging method eases sharp transitions between contrasting color regions and helps to eliminate jagged edges.

A set of three dimensional coordinate axes and a clock were added into most of the frames to provide the viewer with spatial and temporal reference scales. Often these scales had to be adjusted so that certain critical events could be resolved. Other features such as a randomly generated background starfield and some introductory explanatory text were included in the movie for principally aesthetic purposes.

Approximately 3300 final images were generated and written into run-length-encoded PIX files that usually averaged one fifth of a megabyte in size.[2] In a run-length-encoded file, color information is not recorded for every individual pixel but rather for groups of pixels that all possess the same color; thus space is conserved. These files were saved on fifteen magnetic tapes for permanent storage. The movie was produced by first automatically transferring these files from the CS VAX to the Grinell frame buffer via the ETHERNET and then filming the pictures with a computer-controlled camera. The film was developed at FOTO-KEM laboratories and edited at JPL.

Conclusions

The beginnings of several new and potentially exciting finds have been uncovered as an unexpected and surprising side benefit from the work upon this computer graphics movie. Included among these are a new assessment of the geometry of flashing shells, evidence in support of a mirror principle at work among burning layers, indications of decoupling occurring between burning shells and core regions, and suggestions of post-flash surges in energy output from the hydrogen shell which may represent mini-flashes. Each of these

2. At a projection rate of 24 frames per second, this number of frames corresponds to over two minutes of movie.

phenomena warrants further study in the future.

Acknowledgements

The author would like to thank Dr. Juliana Sackmann for her support, guidance, and encouragement. The author also expresses his deepest appreciation to Brian Von Herzen, Bob Schaff and the computer graphics group for their generous, friendly and invaluable assistance. For the hospitality of the Kellogg Radiation Laboratory, the author wishes to thank Professors Charles Barnes and Steve Koonin. Finally, the author is grateful to Professors Roy Gould, Jim Kajiya, Ed Stone, and Fred Shair and the SURF program for financial support.

References

Allen, C.W., *Astrophysical Quantities* , London, Oxford University Press, c. 1963.

Foley, J.D. and Van Dam, A., *Fundamentals of Interactive Computer Graphics* , Reading, Addison-Wesley, c. 1982.

Sackmann, I.-J., 1977, Ap. J., **212** , 159.

———, 1980, Ap. J., **235** , 554.

———, 1980, *Highlights of Astronomy, Vol 5* , ed. P.A. Wayman.

The Luminosity Function of the Coma Cluster

and

The Color Gradient of the Draco Dwarf Spheroidal Galaxy

by Michael Crawford

Sponsored by Jeremy Mould

September 4, 1984

Abstract

Deep pictures of the Coma Cluster and Draco Dwarf have been obtained with the Palomar 60" and an RCA CCD in scanning mode. The Coma pictures are deep enough to allow the study of dim dwarfs which cannot be seen on the Palomar Sky Survey. Although the Draco Dwarf is quite nearby, it has such low surface brightness that only recently have sensitive enough detectors been available to do a color gradient, which yeilds chemical distribution information that is useful in studying the history of the galaxy. The initial data reduction has been done but the photometry still remains to be worked on. It will be completed during the school year.

Introduction

Boroson, Thompson, and Shectman (1983) have succesfully used the Palomar 60" with an RCA CCD in scanning mode to study the color gradient of several distant, large galaxies. In this project the same telescope and a similiar CCD is used to study the color gradient of a nearby but quite small galaxy, the Draco Dwarf Spheroidal Galaxy. The Draco Dwarf is quite significant in that it has a very low intrinsic surface luminosity, and so can be expected to be very sparsely populated. This suggests that Draco has not evolved much since its formation, and so still retains much information about its very early history. A color gradient essentially shows the abundance of heavier elements as a function of distance from the center, and so in Draco, can be expected to show the conditions of chemical distribution during its very early history. The Draco Dwarf is so dim that even though it is apparently large (~40 arc minutes across) it can barely be seen in the Palomar Sky Survey. This project has produced a series of scans which can be averaged to produce a quite deep and detailed picture of the galaxy in two colors, B and V. The color gradient is essentially the difference between the two pictures.

Luminosity functions of the Coma Cluster have been produced of the bright galaxies in the cluster, but it is known that most galaxies are dwarfs, which in the case of the Coma Cluster, have been indetectable until now. This part of the project aims to extend the luminosity function about two magnitudes fainter than can be done with the Palomar Sky Survey plates. Coma is particularly interesting because it is the densest cluster known, so the luminosity function can be expected to hold information on the effect of density on the distribution of galaxy luminosities, or effectively, the distribution of galaxy masses.

Presentation and Discussion of Results

The observations were taken on the nights of June 20 to 29, 1984, on the Palomar 60". Two full nights and parts of several others were interrupted by clouds, and the first night was plagued with instrumental problems, but about five full nights were spent getting good pictures. The night was started by taking dome flats, that is, out of focus pictures of the inside of the telescope dome which evenly illuminates the CCD and were later used to correct for sensitivity variations between each of the pixels in the CCD.

Snaps of standard stars were taken at the beginning, middle, and end of each night to provide an absolute calibration of the CCD, and more flats were taken at the end of each night. The standard used for Coma were taken from Landolt (1983), while the Draco field standard is from Stetson (1983)

The pictures of the program objects were taken by pointing the telescope at one end of a desired strip of sky and then slowly drifting the telescope in declination while the CCD chip was read out at the same rate in the opposite direction. The first five minutes of each exposure were thrown out because the objects on the chip were sampled by only part of the chip; the first object to be saved is the one that was just entering the chip when the exposure started. The chip, with the optical system that was used, covers 7 by 11 arc minutes; the scans were run long enough to get strips 7 minutes by about 1 degree long.

Coma was scanned through a 3 mm thick Schott BG38 (blue green) filter, which was selected to minimize the reddish sky glow found at Palomar. Draco was scanned through standard Johnson B and V filters. The telescope was configured with reimaging optics, which compressed the image, allowing broader coverage, at the expense of introducing some light scattering that proved to be a problem when bright stars passed across the chip.

Concurrently with some of the scans, Fernando Selman monitored the sky brightness separately with the Palomar 20", in a test of his proposal to make a very accurate sky subtraction of Coma to detect an intracluster glow which may be present due to the importance of tidal interactions between the galaxies. Instrumental problems with the 20" caused his results to be inconclusive, but he expects to be able to do his program succesfully in the spring. I wish to thank Selman for his invaluable advice and assistance with my own project.

The data was reduced by first subtracting a constant from each picture, which was produced by a DC bias in the electronics of the camera, and then dividing each picture by a normalized flat field frame to equalize the pixel responses. Innumerable problems with this resulted in delays which are the major reasons the project is not complete. One night's tape has errors, the tape drives were endlessly malfunctioning in Robinson, and the P60 CCD data collection system does not record the bias level for scans, just snaps. All of these have been worked out and the data nearly ready to have the photometry done.

An image processing program is being worked on which will average the scans while correcting for extinction so that the sheer volume of data to be handled can be reduced, as well as to increase the signal to noise ratio of the pictures. This is still in progress.

Photographs illustrating the difference between this work and the sky survey will be produced soon. The film is being developed now so the photos will be turned into the SURF office the week of September 10. Note that the faintest objects visible in the CCD pictures will be at least a magnitude fainter than can be seen in the sky survey print.

Conclusions

I do not yet have the work completed, so I have no quantitative conclusions. The data taken is of high quality, and it is clear what remains to be done, so I will continue with the work during the school year. The averaging program will be done soon and can be expected to be a useful addition to the Robinson package of image processing programs.

Bibliography

Boroson, Thompson, and Shectman, 1983, Ast. J., 88, 1707.

Landolt, 1983, Ast. J., 88, 439.

Stetson, 1979, Ast. J., 84, 1149.

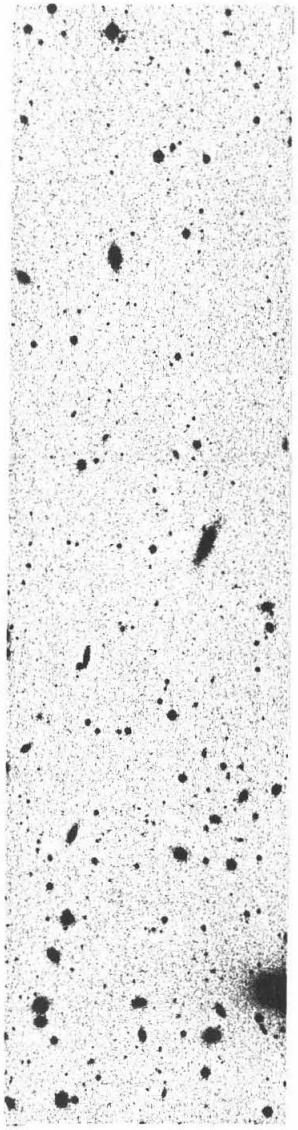

Sky survey

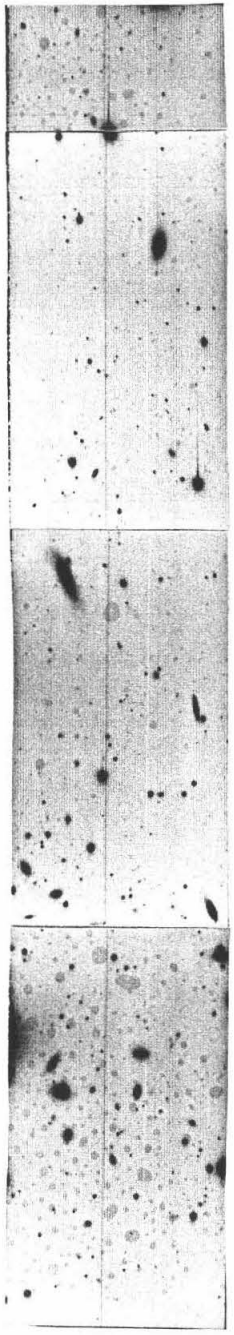

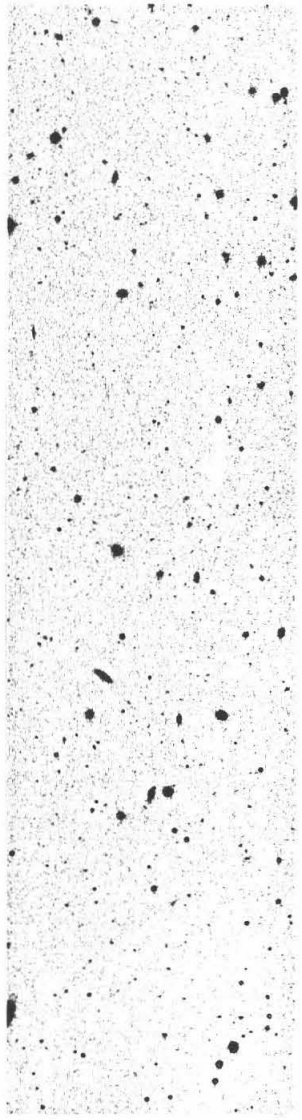

Sky survey

Coma Cluster

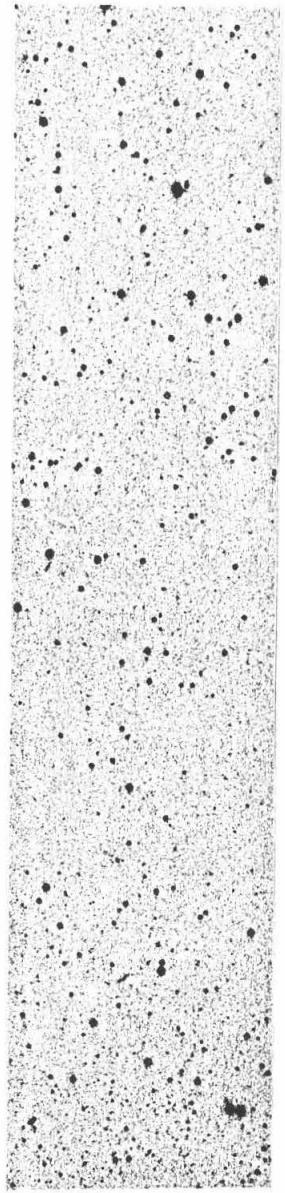

Sky Survey

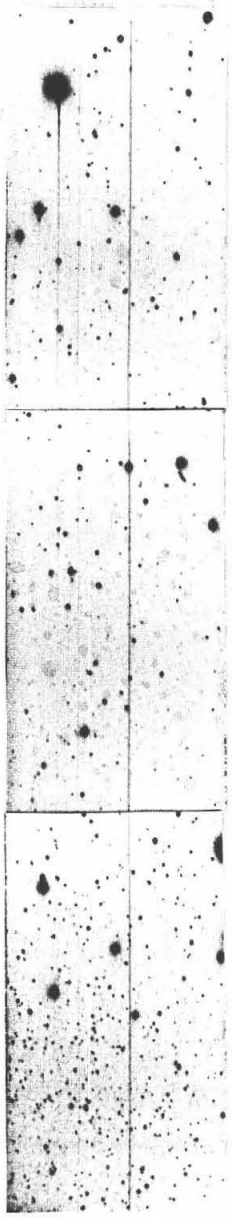

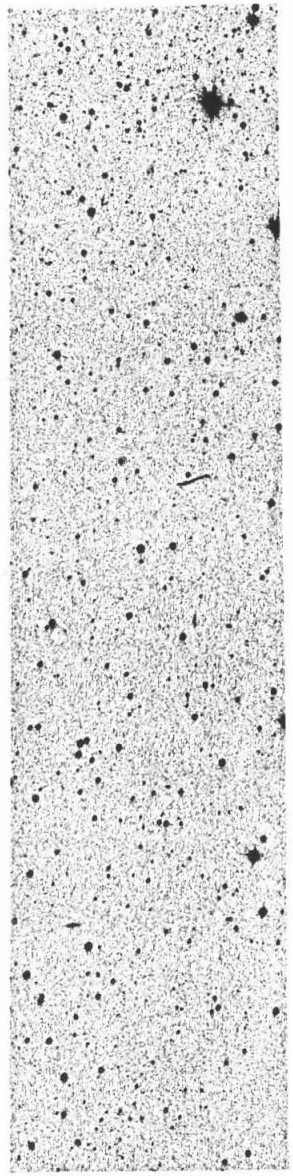

Sky Survey

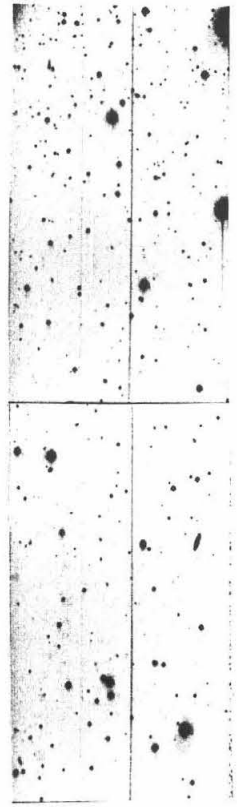

Model of a Mildly Relativistic Pair Plasma

Louis Cuellar

Dr. Roger Blandford (Sponsor)

submitted to

Summer Undergraduate Research Committee

Abstract

A simple model of a mildly relativistic e^+e^- pair plasma is presented along with basic numerical calculations of the photon flux being emitted from the plasma. There are four processes which are modeled: 1) pair production by interaction of gamma rays with lower energy X-rays. 2) Annihilation of these pairs to produce .5 mev photons. 3) Comptonization of the low energy photons by e^+e^- pairs. 4) Inverse Compton scattering of low energy photons to high energy gamma rays. A numerical solution to various initial photon and pair distributions is given. Both the e^+e^- and photon distributions are calculated self consistently by iteration until a stable solution is obtained. The resultant flat X-ray spectra differs from typical active galactic nuclei X-ray spectral index of about .7. (1)

Introduction

Relativistic plasmas in equilibrium with e^+e^- pairs have recently been becoming of increasing interest (Zdziarski, Ap.J. 1984 A.P. Lightman 1983)[2-3] because it is thought that pairs may play an important role in active galactic nuclei (AGN) such as quasars and Seyfert galaxies. Pairs may drastically change the basic properties and flux of photons being emitted from a plasma. Pairs can also maintain a high optical depth in the plasma and thus effect the photon distribution(Guilbert, Fabian, and Rees)[4]. It is also thought that pairs may have an important role in explaining the relatively flat spectral index of many AGN that have been observed (A.P. Lightman, Space Science Reviews). In this study I will examine the steady state solution attained in such a plasma under the assumptions of an optically thick and mildly relativistic pair density and temperature in the absence of magnetic fields.

Definitions

The pair plasma that is under consideration can be described by the following parameters:

a) dimensionless optical thickness t_T.

b) dimensionless temperature $\tilde{T}=kT/m_e c^2$. In this model the plasma is considered to be mildly relativistic $\tilde{T}\sim 1$.

c) radius R.

d) time is measured in units of R/c; dimensionless time $\tilde{t}=ct/R$.

The number of photons of occupation number n per unit volume is given by $\Phi(\nu)=8\pi\nu^3 n/c^3$. To make this into a dimensionless quantity multiply this expression by $\sigma_T R$, where σ_T is the Thompson cross section. Similarly,

one can define a dimensionless electron density of a given occupation number as $\tilde{N}(p)=4\pi p^3 f\sigma R$. In the rest of the paper I will rewrite the equations that govern the processes to be modeled in terms of the given parameters and dimesionless quantities. Let the variables $\tilde{p}$ and $\tilde{k}$ be the dimesionless momentum of the leptons and photons respctively; $\tilde{p}=p/m_e c$ and $\tilde{k}=k/m_e c$. Also define $e=\log(\tilde{k})$ and $q=\log(\tilde{p})$.

Processes

I) Pair Production

The only process that is considered for the creation of e^+e^- pairs is the two photon reaction $\gamma+\gamma \rightarrow e^+e^-$. The basic assumption is that the gamma ray of energy $\varepsilon_\gamma > m_e c^2$ will annihilate on any X-ray of energy $\varepsilon > m_e c^2/\varepsilon_\gamma$ with the Thompson cross section. The e^+e^- pair will be created with an energy of $\frac{1}{2}$ that of the γ-ray. Writing the equation in terms of the defined variables:

$$\frac{\partial \Phi}{\partial t} = -\Phi \int_{-\ell}^{\varepsilon} \Phi(\varepsilon')d\varepsilon'.$$

II) Annihilation of e^+e^- pairs

The assumption that is made for this process is that only the thermalized e^+e^- pairs will annihilate each other. The higher energy pairs are presumed to first lose energy via inverse compton scattering before annihilating. The temperature of the plasma is determined by the photon distribution. The compton temperature of the photons is given by $T=\frac{1}{4}h\langle\nu\rangle/k$. Thus thermalized leptons will take on a Maxwell-Boltzman distribution about the energy $p^2/2m_e \approx 3/2kT = 3/8h\langle\nu\rangle$. The model first calculates the plasma temperature, then all the pairs at or below

the thermal momentum bin are then assumed to be thermalized in a given time step. These electrons determine t_T for the next time step and will also annihilate each other with a cross section of $.1\sigma_T$. Thus the equation governing the thermalized electrons is $\partial\tilde{N}/\partial\tilde{t}=.1\tilde{N}^2$. The annihilated pairs are then a source of $\frac{1}{2}$ mev photons.

111) Inverse Compton Scattering

Relativistic e^+e^- will inverse compton scatter the low energy photons to higher energy. Let the e^+ or e^- have an energy of γ_{lep}. If the photon in the rest frame of the lepton has an energy less than $m_e c^2$ (Klien-Nishina limit), then scattering can occur of the photon with approximately the Thompson cross section. The energy of the photon before the scattering, in the rest frame of the electron and after scattering are in the ratios $1:\gamma:\gamma^2$. Thus conversion of low energy photons to high energy photons is by a factor of γ^2.[5]

The e^+ and e^- distribution will also change due to the scattering of these photons according to the differential equation for a given occupation number f(p):

$$\frac{df}{dt}=\frac{1}{p^2}\frac{d}{dp}(\dot{p}p^2f)$$

where $\dot{p}=(p^2-1)/m_e c^2\sigma_T cA(p)$ and A(p) is the energy density of photons that can be scattered by lepton of momentum p. Rewriting equation in dimensionless quantities, the relativistic pairs evolve via the equation

$$\frac{dN}{dt}=\frac{1}{2.3}\frac{d}{dq}\left(A(p)\left(pN-\frac{N}{p}\right)\right).$$

V) Comptonization

The low energy photon distribution ($k<m_e c$) will be altered by compton scattering off the thermal pair distribution of temperature T. The change in this distribution is governed by Kompaneets equation:[6]

$$\frac{\partial n}{\partial t}=\frac{kT}{m_e c^2}\frac{1}{x^2}\frac{\partial}{\partial x}\left(\left(\frac{\partial n}{\partial x}+n\right)x^4\right).$$

Rewriting equation:

$$\frac{\partial \tilde{\Phi}}{\partial \tilde{t}} = t_T \frac{\partial}{\partial e}\left(\tilde{T}\frac{\partial \tilde{\Phi}}{\partial e} - 3\tilde{T}\tilde{\Phi} + 10^e\tilde{\Phi}\right).$$

VI) Radiative Transfer

This part of the model is done very simply by assuming the photons will escape in a time $t_{esc}= R/c(1-t_T)$. There is also included a source term for photons so the transfer equation becomes:

$$\frac{\partial \tilde{\Phi}}{\partial \tilde{t}} = \tilde{S}_1 - \frac{\tilde{\Phi}}{1+t_T}.$$

There is also a source term for the pair distribution. In this model it is assumed that all the pairs cannot escape the plasma. Thus the transfer equation becomes:

$$\frac{\partial N}{\partial \tilde{t}} = \tilde{S}_2.$$

Numerical Calculations

The numerical modeling that is used seperated the pair and photon distributions into 50 bins. The bins are spaced logrithmically in photon and lepton momentum. The photon bins go from momentum 10^{-4} to 10^2 in steps of $10^{.12}$. The lepton bins are spaced from 10^{-1} to 10^2 in steps of $10^{.06}$. Each time step $\Delta\tilde{t}= .002$ the program will go

to each subroutine which models a process just described. The distributions are then updated in a temporary array until all the processes have been completed. Then the distributions are altered and the temporary array is set to zero.

For the numerical calculations the initial conditions are a low energy thermal lepton distribution, some source of low energy photons, and a source of relativistic electrons. After about 1000 time steps the program reaches an equilibrium. Figure 1 shows the photon distribution plotted as log(N(e)) as a function of e (e=log(k)). Notice that the X-ray region is very flat unlike the spectra from AGN which have a typical spectral index of .7 in this region. In the gamma ray energies the curve drops off sharply $\alpha = +2$ to $+3$ which is expected. In figure 2 the electron distribution is shown as log(N(q)) vs. q. Notice that the thermalized leptons dominate the low energy spectrum with a power law spectra for the relativistic leptons.

Approximations

Many assumptions are made in this model which need to be improved to obtain a more accurate photon distribution function arising from the plasma. These approximations and some improvements are listed by the process to which they pertain:

1) Pair Production

i) There are several reactions which could produce e^+e^- pairs in a mildly relativistic plasma.[7]

ii) The cross section for two photon scattering to produce pairs is very much energy dependent.[8]

iii) The e^+e^- pair will be created with a distribution of

energies dependent upon the photon energies.

2) Annihilation

i) If the energy density of the e^-e^- pair plasma becomes comparible to that of the photon gas, the approximation that the temperature is set by the photons is no longer valid.

ii) Include the energy dependent cross section for annihilation and place the created photons in a distribution of energies about $\frac{1}{2}$mev.[9]

3) Inverse Comptonization

i) Better the cross section for scattering to include dependent terms of the photon and lepton energy.

4) Comptonization

i) When the photon energy is about equal to $m_e c$ the cross section for scattering is decreased and the scattering is no longer elastic.

Summary

From the numerical calculations it is evident that the model needs to be improved before it can reasonably be compared to the spectra from AGN. The basic characteristics of the photon distribution in the present model is a very flat spectra in the X-ray band that drops off very sharply for $k > m_e c$. The pair distribution can also be seperated into two distinct regions. The first is the thermal distribution which has an equilibrium optical depth of $t_T \simeq 4$ or 5. The relativistic pairs have a power law spectra with the index $\alpha \simeq 1$.

Acknowledgments

I would like to thank Dr. Blandford for all the time and patience he gave me to allow me to complete this Surf project. I would also like to thank the Surf committee for sponsoring these summer projects.

References

1) A.P. Lightman, Space Science Reviews 33 (1982) 335.

2) A. Zdziarski, Preprint Series No. 1982 to appear in Aph. J. Aug. 15, 1984.

3) A.P. Lightman, Preprint Series No. 1781 to appear in Conference Proceeding (American Institute of Physics) Jan. 1983.

4) R.W. Guilbert, A.C. Fabian, M.J. Rees, Spectral and Variability Constraints on Compact Sources.

5) G. Rybicki and A.P. Lightman, Radiative Processes in Astrophysics (John Wiley & Sons) p. 198.

6) G. Rybicki and A.P. Lightman, Radiative Processes in Astrophysics (John Wiley & Sons) p. 215.

7) A.P. Lightman, Preprint Series No. 1781 to appear in Conference Proceeding (American Institute of Physics) Jan. 1983.

8) R. Svensson, Aph. J. 258 (1982) 335.

9) M. Kusunose and F. Takahara, Progress of Theoretical Physics May 1984.

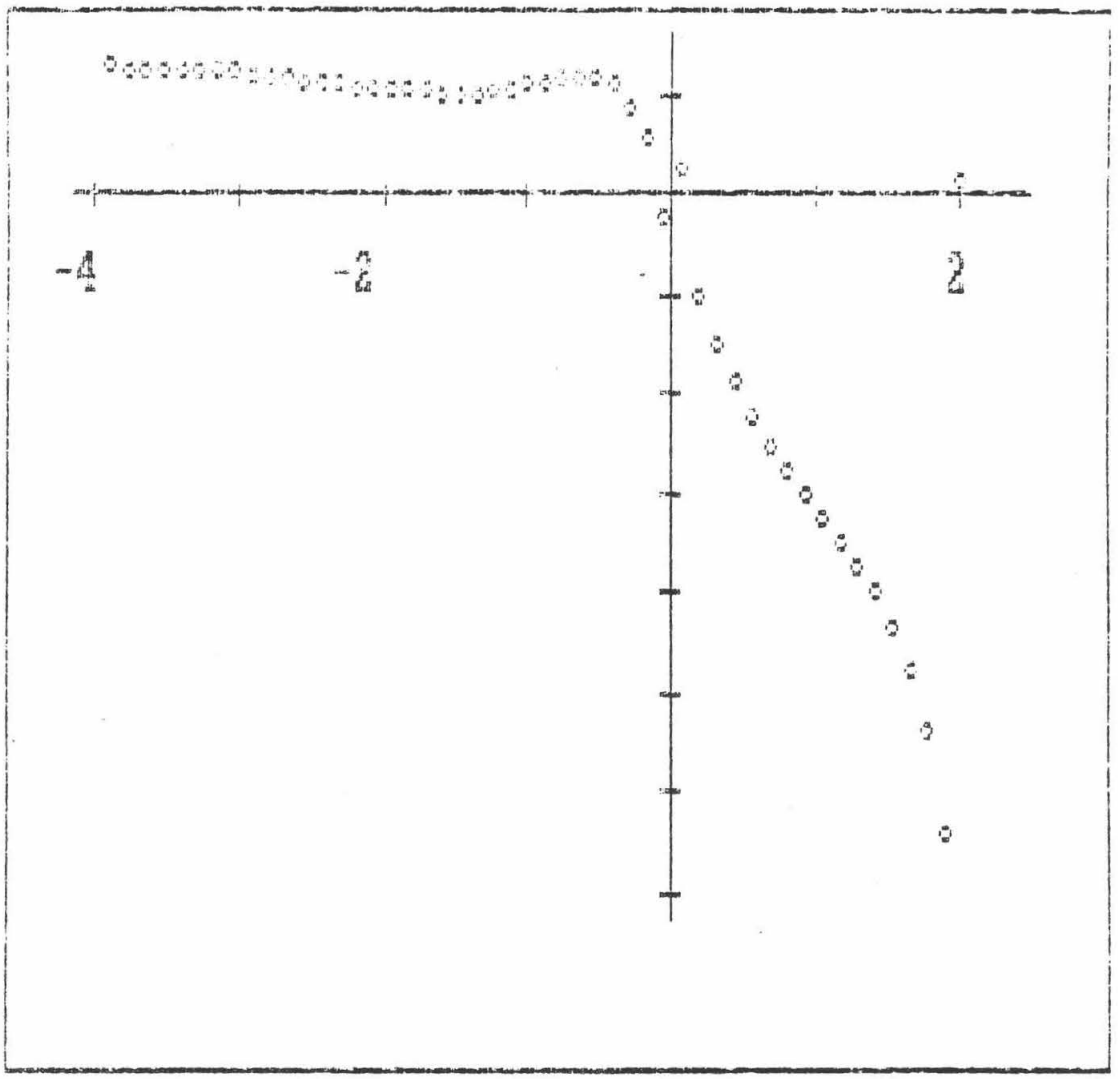

Figure 1

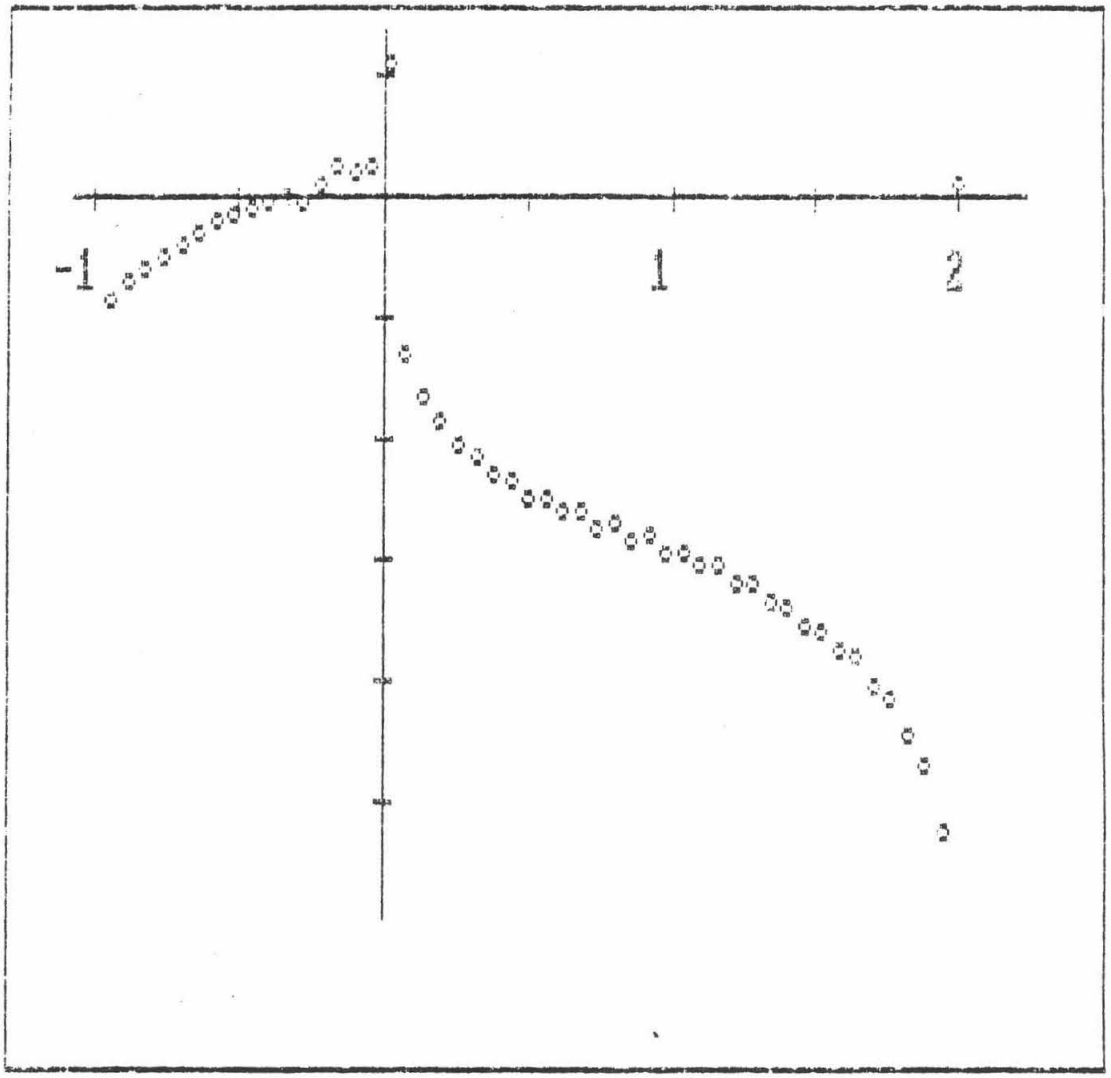

Figure 2

A Saltation Simulation

by Dennis R. Fatland

Dr. Peter Haff, Faculty Sponsor

Abstract

The phenomenon of a windswept granular surface such as desert sand is not well understood and is perhaps quite complicated. Granular surfaces often exhibit small ripples which move downwind due to energetic particle impacting called saltation. We used a computer to see if our saltation model would develope in a fashion similar to the real process.

Introduction

The first qualitative work on granular flow was done by R. A. Bagnold in the early 1900's, inspired by the many months Bagnold spent out in the Egyptian desert. Among his many contributions to the subject, encapsulated in his book The Physics of Blown Sand and Desert Dunes, is his demonstration using a long wind tunnel filled partially with sand that surface grains are excited in an interesting manner by a sufficiently strong wind. Initially these grains are pushed forward over the surface, dislodging others as the energy of the wind is transformed into the kinetic energy of the creeping surface sand. At some point the grains begin popping up off of the surface because of this energy transfer, which exposes them to direct acceleration by the driving wind. Thus when these grains are accelerated downwind as they fall and impact upon the surface, they have more kinetic energy than when they were dislodged up into the wind. Upon impact this increased momentum is transferred to the surface, often ejecting some other grain higher into the wind than the impacting grain had gone. Thus thousands of grains are popping into the air, accelerating downwind, and striking more grains. (Fig. 1)

Eventually the wind and sand reach an energetic equilibrium in which the impacting grains are so numerous that they eject on the average a single target grain, which reaches a maximum height equal to that of the preceding impacting grain. This maximum height is usually less than two feet. The flux, or number of grains passing some point per unit time, is constant under equilibrium conditions. As shown in photographs taken by Bagnold, the trajectory of a saltating grain resembles a triangle. The ascent is often near vertical, rounded over at the top, and the descent proceeds at a shallow angle of around thirteen degrees. The impact of each descending grain also pushes some grains across the surface, creating a second kind of sand flux

Figure 1

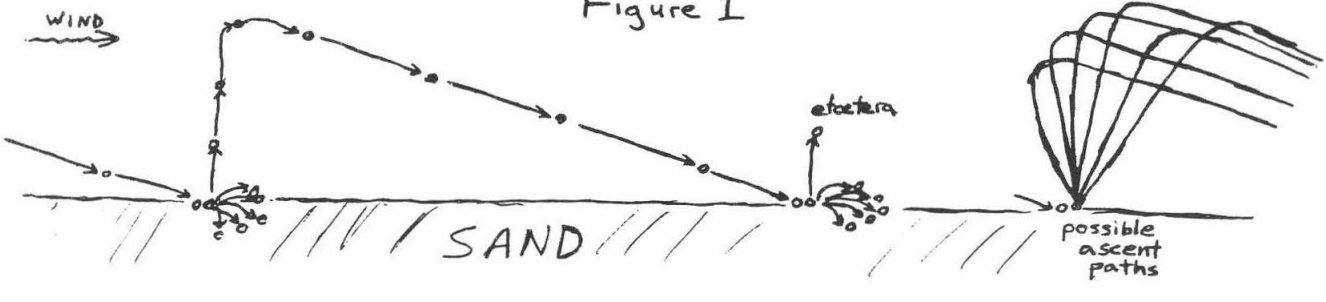

called surface creep.

Flat, level sand which is swept by strong wind for a sufficient amount of time, through some combination of the effects of saltation and creeping, forms regular surface ripples perpendicular to the direction of wind flow. These ripples are typically five centimeters long, which corresponds roughly to the distance along the ground between the point from which a grain is ejected and the point at which it impacts, which we call a single jumplength. (Fig. 2) A surface in the process of reaching this state appears first to form into smaller ridges which coalesce and merge into larger ripples. The first problem thus arises: How can a seemingly random series of thousands of impacts over a smooth surface give rise to a regular, periodic pattern?

Once a windswept surface has reached its characteristic rippled state, the ripples move slowly downwind while maintaining a constant shape. The purpose of this project was to make a model of this phenomenon using some simplifying assumptions which was readily adaptable to computer simulation. If the computer simulation produced a rippled surface from a flat one, then we could assume our model was in some sense accurate, and could then proceed to tinker with the simulation in an attempt to find out why it was accurate.

Figure 2

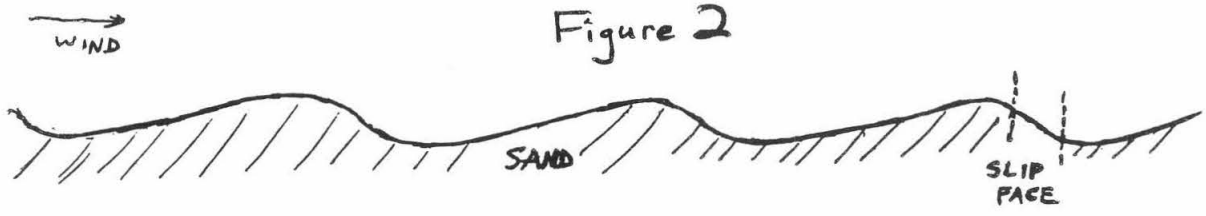

The principal assumptions made were as follows. A single grain will follow a trajectory which is precisely a triangle, with a descent angle of thirteen degrees. The stretch of sand we consider will be two rather than three dimensional, having height and length (in the direction of the blowing wind), but not transverse width. By taking this 'ant farm' approach we bring the problem to within computing limitations. This two dimensional stretch of sand is divided into a series of bins. The width of each bin is much less than the width of a typical ripple. The bins are numbered consecutively, and each has a corresponding value for the amount of sand in that bin. Sand can not support itself above a steepness, or slip angle, of around thirty degrees. Thus if at some time the slope of sand from one bin to an adjacent bin exceeds this angle, sand will spill from the higher into the lower bin until the slope between bins becomes permissable. So we have a peculiarly defined stretch of sand, say 1000 bins long. We now include saltation in the picture.

We assume that somewhere upwind of this stretch, grains are saltating. Eventually one appears at some height over bin zero and is descending at thirteen degrees. The initial height is determined at random. Since the descent is in a straight line and the surface is chosen to be initially flat, there is a range of bins from bin one to bin x which all have equal probability of being struck by the descending grain, where x is the maximum initial grain height divided by the product of the bin width and the tangent of the descent angle. (Fig. 3)

Once the descending grain is in position, it will move down and forward until it comes in contact with the surface. When this happens, one grain will be ejected vertically to a maximum height from which it will begin descending

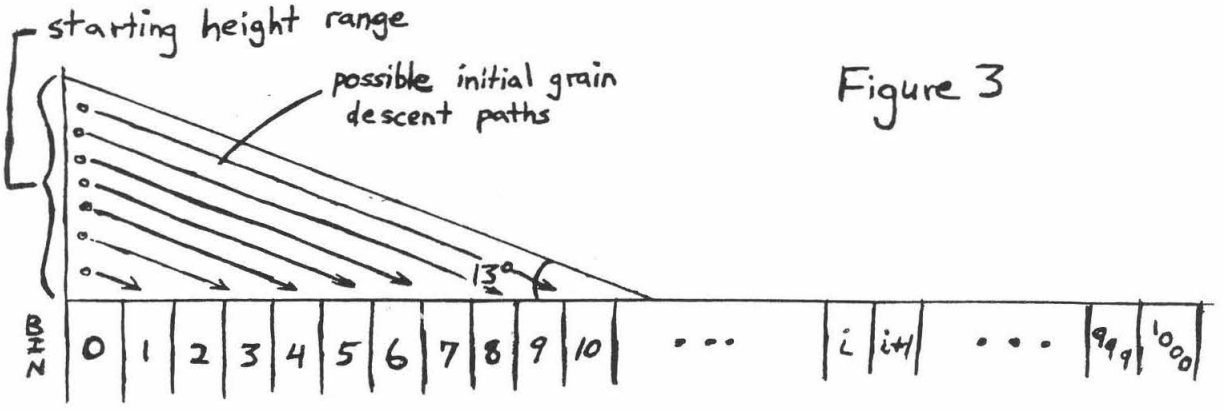

Figure 3

at thirteen degrees, simulating equilibrium saltation. In addition this impact will push some grains in the impact bin downwind, say one or two bins, simulating surface creep. The combination of particles pushed forward along the surface and ejected up into the wind by a single impacting grain is called the splash function of that grain. We do not know what this splash function is. We know that it depends on factors suchas wind velocity, particle size, particle shape, the amount of water in the granular material which can affect surface adhesion, and the density with which the particles are packed. None of this enters into the model. Instead we guess at a very simple splash function. A particle impacts on some bin, another is ejected up to its maximum height in order to descent and impact some number of bins downwind. Thus a grain starts at the beginning of the range of sand and propogates downwind to the end. This process of propogating a single saltating grain is repeated several thousand times to give us a final profile of the surface. In a real saltation environment, the interactions of thousands of saltating grains in the air at the same time and place is negligible compared with the interaction of sand and wind, so that the one grain at a time method is legitimate. Note that every time a grain propogates, or is fired down the range, all pairs of consecutive bins must be compared to ensure that the slip angle is not exceeded.

Results

The simulation produced some very positive results. Initial runs of the computer program involved the following parameters. A single bin is one unit wide and arbitrarily deep. In practice the program only used about eight units of depth. A box one unit square is defined to contain ten grains, so that the hieght of a bin is easily designated by one significant digit precision. That is, a bin with 507 grains in it has a bin height of 50.7 . This means that a single unit, or binwidth, is 10 = 3.126 grain diameters, which presents a problem when trying to draw a bin full of supposedly quantized grains. But since our splash function is rather empirical and does not involve the geometric properties of the sand, this is not a problem for the program. Also, a typical grain diameter is .2 mm, and the width of a typical ripple is 5 cm, or about 80 bins, so that we have no resolution difficulties.

Early runs of the program involved firing from two to six thousand grains in succession at the array of bins. Each grain would impact on one of the first thirty to forty bins, selected at random, and stay there. It would pop one grain forward one bin, and it would eject one grain upward a constant

height above the height of the impact bin, from whence it would descend. This was the splash function. The ejection height corresponded to a jumplength of twenty to thirty bins.

After several hundred grains were fired, the surface profile, which was initially flat, became rugged, a series of small bumps. After a thousand impacts these were clearly increasing in amplitude and width. After about ten thousand grains were fired, the one thousand bin range consisted of three clearly defined regions. The bins accessable by the first impact of each grain fired, bins zero through thirty or forty, remained consistently smooth, not deviating from their initial heights by more than a few grains. The second region began immediately with bins not accessable to the random initial grain flux and continued for two to four hundred bins. The surface here was irregularly rippled, but became more orderly toward the downwind end of this range. The amplitude of these ripples was about four units, or thirteen grain diameters from peak to trough. The third region was rippled with nearly perfect regularity, undoubtedly due to the simplicity of the model.

Regardless of the jumplength used in any given run, the sand would always reach a periodic, rippled profile, of wavelength precisely equal to the jumplength of that run. What did vary was the number of impacts required to arrive at this state. The smaller the jumplength, the sooner the ripples would appear, since each grain fired had a higher number of contacts with the surface. Once the ripples did arise, continued bombardment caused them to move slowly downwind, just as they ought.

The computer program was altered to periodically take 'snapshots' of the range of sand as it was bombarded, once every thousand grains. The jumplength was increased to around sixty bins in order to provide more detail. These runs, each involving around forty thousand impacts, showed how the sand evolved from flat to rippled. Initially, as before, the surface became discernibly bumpy. After a few thousand impacts there were an integral number of bumps in any given jumplength of bins. This integer was typically about ten. After more bombardment, some of the bumps merged and increased in amplitude, still maintaining an integral number per jumplength. This merging continued, taking progressively more bombardments between integers as the number of ridges per jumplength decreased. Finally the last two ripples coalesced into one ripple per jumplength, and thereafter further impacts only pushed this ripple forward. (Fig. 4)

Figure 4

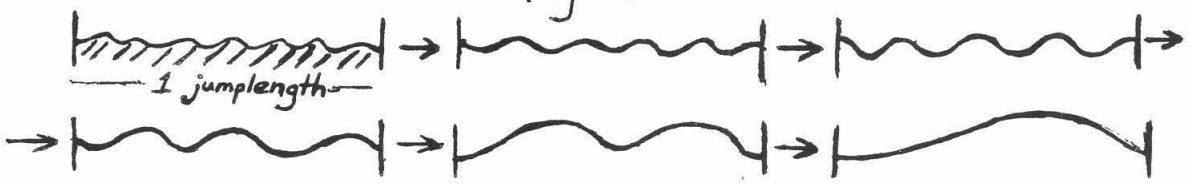

The shape of the ripples was not like those of real sand (Fig. 2), perhaps due to the splash function used. (Fig. 5) Saltation impacts tended to be on the upslope of each ripple, while most grain flux on the downslope of the ripple, shielded from impacts, was in the form of grains sliding down the incline. This is probably how the ripple moves. Impacts on the upslope push grains over the top, down to the bottom of the slip face, where they accumulate. Thus the sand is in a manner treadmilling.

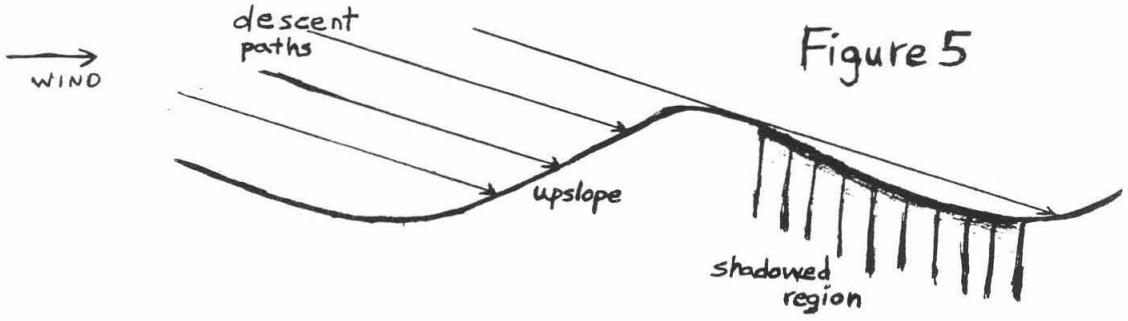

Figure 5

Two ripples merge, in the process of reaching the stable state of one ripple per jumplength, when a small ripple closely precedes a large ripple. The small one washes up against the larger, and assimilates much of its bulk. The second peak is subsequently washed down the shadowed side of the new larger ripple until it becomes indistinguishably flattened out in the trough. (Fig. 6)

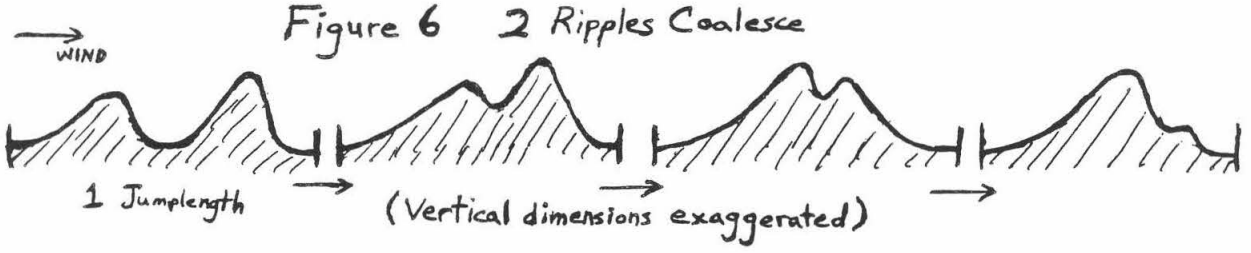

Figure 6 2 Ripples Coalesce

Conclusion

The model we used to simulate saltation was mostly successful, with the exception of the precise shape of the generated ripples. We still have not fully understood why the model works as well as it does. Ripples seem to arise from the coalescence of smaller ridges, which in turn seem to arise from a roughness in the surface caused by random bombardment. All of this is governed by grain flux over exposed and shadowed regions. Once we do understand this model more completely, it can be altered to include more complicated and accurate parameters, especially regarding the splash function, for further investigations.

My thanks to Dr. Peter Haff and Brad Warner.

POSITIVE ELEMENTARY INDUCTION ON FINITE FIELDS AND FINITE CYCLIC GROUPS

Tim Fernando
Professor Alexander Kechris, advisor

Abstract

Subclasses of finite cyclic groups and finite fields that contain all isomorphic copies of their elements, and in which membership can be decided in polynomial-time are shown to be precisely those subclasses definable in the language of positive elementary induction.

Introduction

This paper deals with *positive elementary induction* (first order logic plus least fixed point operators on formulas with positively occurring relation variables) as applied to finite fields and finite abelian groups. For background and notational conventions, see [2], [3], and [4].

Consider structures of the form $\mathcal{A} = \langle \{0, 1, ..., n\}, SUCC_A, \sigma_A \rangle$ where $SUCC_A$ is the usual successor relation and $\sigma_A \subset \{0, 1, ..., n\}$. σ_A is identified here with the string whose ith letter is 1 if $\sigma_A(i)$ and 0 otherwise. A set of strings Σ is said to be *inductive* if there is a positive elementary formula $\varphi(\overline{x}, S)$ such that $\sigma_A \in \Sigma$ iff $\mathcal{A} \models \varphi^\infty(\overline{0})$. As proved in [1], [4],

Theorem 0: *Σ is inductive iff Σ is polynomial-time computable.*

Now consider a class Ω of structures for a first order language L. Call $\mathbf{A} \subset \Omega$ a *polynomial-time subclass* of Ω if for all $\mathcal{A}$ in $\mathbf{A}$, if $\mathcal{B}$ is isomorphic to $\mathcal{A}$, then $\mathcal{B} \in \mathbf{A}$ (i.e., $\mathbf{A}$ does not discriminate between isomorphic copies), and if there is a turing machine $TM_{\mathbf{A}}$ that decides membership in $\mathbf{A}$ in polynomial-time. Using the same basic idea in Theorem 0, we show below that

Theorem 1: *For $L = \{+, 0\}$, $\Omega =$ finite cyclic groups, then for any polynomial-time subclass of Ω, there is a positive elementary formula $\varphi_{\mathbf{A}}(\overline{x}, S)$ such that for all $\mathcal{A}$ in Ω,*

$$\mathcal{A} \in \mathbf{A} \text{ iff } \mathcal{A} \models \varphi_{\mathbf{A}}^\infty(\overline{0}).$$

By defining analogues of $SUCC_A$ and σ_A, we can apply the proof of Theorem 0 to obtain Theorem 1. In fact, for any Ω, if a linear ordering on at least $\|\mathcal{A}\|$ tuples of $\mathcal{A}$ can be defined, then Theorem 0 can be proven for the structures $(\mathcal{A}, \sigma)$ where σ is a code in $\mathcal{A}$ of a string. We will later prove Theorem 1 for finite fields and finite abelian groups with successor relations on sets of

cyclic factor generators. (*N.B.* The converse is obvious regardless of L or Ω: if φ_A has arity m and $\mathcal{A}$ has order n, then $\mathcal{A} \models \varphi_A^\infty(\overline{0})$ iff $\mathcal{A} \models \varphi_A^{n^m}(\overline{0})$.)

Discussion

With regard to Theorem 1, the first issue to consider is the coding of $\langle Z_n, +_n, 0_n\rangle$. Let $C : \Omega \to \{1\}^*$, $\langle Z_n, +_n, 0_n\rangle \mapsto 1 \cdots 1$ (n copies). Given a coding C' for Ω used in input to TM_A, we assume that there is a turing machine $TM_{C'}$ that takes $C(\langle Z_n, +_n, 0_n\rangle)$ to $C'(\langle Z_n, +_n, 0_n\rangle)$ in polynomial-time. For instance, if in TM_A, $\langle Z_n, +_n, 0_n\rangle$ is coded as

$$1 \cdots (n \text{ copies}) \cdots 1001010100 \cdots$$

$$\cdots 001 \cdots (n \text{ copies}) \cdots 101 \cdots (n \text{ copies}) \cdots 101 \cdots (n-1 \text{ copies}) \cdots 1$$

where the first n 1's indicate the order of Z_n and the succeeding blocks of $00\bar{1}0\bar{1}0\bar{1}$ represent entries in the multiplication table (with i represented as i+1 1's), the following program takes $C(\langle Z_n, +_n, 0_n\rangle)$ to $C'(\langle Z_n, +_n, 0_n\rangle)$ in polynomial-time:

```
for k:=1 to n do print '1';
for i:=1 to n do
  for j:=1 to n do
    begin
      print '00';
      for k:=1 to i do print '1';
      print '0';
      for k:=1 to j do print '1';
      print '0';
      x:=(i-1+j-1)+1;
      if x ≥ n then for k:=1 to x-n do print '1'
      else for k:=1 to x do print '1';
    end.
```

Now the idea of the proof is to simulate with a system of positive elementary formulas whose induction variables represent space and time the action of $TM_{C'}$ followed by TM_A on the input indicated by a relation σ defined uniformly over Σ. Toward this end, for a structure with universe U, we define a relation R to be *nice* if for some k,

1) $R \subset U^{2k}$, and
2) if $F_R =_{def} \{\bar{x} \in U^{2k} : \exists \bar{y}(R(\bar{x}, \bar{y}) \vee R(\bar{y}, \bar{x}))\}$ and
$[\bar{x}] =_{def} \{\bar{x}' : \exists \bar{y}(R(\bar{x}, \bar{y}) \wedge R(\bar{x}', \bar{y}) \vee R(\bar{y}, \bar{x}) \wedge R(\bar{y}, \bar{x}'))\}$
then there is a bijection $\alpha_R : \{[\bar{x}] : \bar{x} \in F_R\} \to \{1, 2, ..., |U|\}$ such that $R(\bar{x}_1, \bar{x}_2)$ iff $\alpha_R([\bar{x}_1]) + 1 = \alpha_R([\bar{x}_2])$.

(It is useful here to think of R as a "successor" relation on $\{[\bar{x}] : \bar{x} \in F_R\}$.)

For cyclic groups, we then take $\sigma = F_R$ so that

$\langle Z_n, +_n, 0_n\rangle \models \sigma(\overline{x})$ iff the $\alpha_R([\overline{x}])$th letter in $C(\langle Z_n, +_n, 0_n\rangle)$ is 1.

(*N.B.* Had we taken $C : \Omega \to \{0, 1, ..., m\}^*$ with $|C(\mathcal{A})| = p(\|\mathcal{A}\|)$ for some polynomial p, then for R to be nice, we would have asked that $\alpha_R : \{[\overline{x}] : \overline{x} \in F_R\} \to \{1, 2, ..., p(\|\mathcal{A}\|)\}$ and then defined $\sigma_0, \sigma_1, ..., \sigma_m \subset F_R$ such that

$\mathcal{A} \models \sigma_i(\overline{x})$ iff the $\alpha_R([\overline{x}])$th letter in $C(\mathcal{A})$ is i.)

Next, define

$$\varphi(x, y, S) \Leftrightarrow x = 0 \vee \exists x'(S(x', y) \wedge x' + y = x).$$

Note that in every $\langle Z_n, +_n, 0_n\rangle$, exactly n iterations are required for φ to close. We can therefore use the Stage Comparison Therem to construct R:

$$R(x, y, x', y') \Leftrightarrow x, y <^*_\varphi x', y' \wedge \varphi(x', y', \{u, v : u, v \leq^*_\varphi x, y\}).$$

From here, we apply the proof of Theorem 0 in a straightforward manner to obtain Theorem 1.

Consider now the same question for finite fields and special structures of finite abelian groups. The following definitions of nice successor relations allow the formulation of analogues of Theorem 0. (Propositions similar to Theorem 1 would require that $\sigma_0, \sigma_1, \ldots, \sigma_m$ be uniformly defined in the language of positive elementary induction - for example, that $\sigma_0, \ldots, \sigma_m$ be added to the underlying first order language).

1. $L = \{+, *, 0, 1\}$, Ω = finite fields

$\varphi(x, y, S) \Leftrightarrow (x = 0 \wedge y = 0) \vee (S(0, 0) \wedge (x = 1 \vee \exists z(S(z, y) \vee z * y = x)))$

(multiplicative group is cyclic)

$SUCC(x_1, y_1, x_2, y_2) \Leftrightarrow x_1, y_1 <^*_\varphi x_2, y_2 \wedge \varphi(x_2, y_2, \{x, y : x, y \leq^*_\varphi x_1, y_1\})$.

2. Let $L = \{+, 0, SU\}$. Take the class of finite abelian groups G such that for some $Y = \{y_1, ..., y_k\} \subset G$ (with $k > 1$), $G = \sum[y_i]$ and the interpretation of SU is $\{(y_i, y_{i+1}) : i = 1, ..., k-1\}$. Observe that given SU,

$$Y(y) \Leftrightarrow \exists y'(SU(y, y') \vee SU(y', y)).$$

Let $<_Y$ be the linear ordering on Y induced by SU:

$$<_Y (y, y', S) \Leftrightarrow SU(y, y') \vee \exists z(S(y, z) \wedge S(z, y')).$$

For $x \in G$, define $n_1^x, ..., n_k^x$ such that $x = \sum n_i^x y$ where $0 \leq n_i^x <$ order of y_i. Define the system

$\eta_1(x, y, S_1, S_2, S_3) \Leftrightarrow \forall x' S_3(x') \wedge Y(y) \wedge (S_2(x, y) \vee \exists x'(S_1(x', y) \wedge x' + y = x))$

$\eta_2(x, y, S_1, S_2, S_3) \Leftrightarrow \exists y'(Y(y) \wedge y' \neq y \wedge (x = y' \vee \exists x'(S_2(x', y) \wedge x' + y' = x))$

$\eta_3(x, S_1, S_2, S_3) \Leftrightarrow \exists y(Y(y) \wedge (x = y \vee \exists x'(S_3(x') \wedge x' + y = x)))$.

Lemma: *In a first order language containing a constant symbol 0, let* φ_1,..., φ_k *be a system of positive elementary functionals. Then there is a positive elementary* φ *such that, uniformly over models of the language with*

cardinality ≥ 2,

$$\varphi^{\infty}(\bar{0},\bar{0},\bar{x}) \text{ iff } \varphi_1^{\infty}(\bar{x}), \text{ and } \varphi_1^{n}(\bar{x}) \text{ iff } \varphi^{n}(\bar{0},\bar{0},\bar{x}) .$$

Proof: Say $\varphi_1(\bar{x}_1, S_1, ..., S_k)$,..., $\varphi_k(\bar{x}_k, S_1, ..., S_k)$. The idea, as in [1], pp. 21,22, is to replace each $S_i(\bar{x}_i)$ by $S(\bar{c}_i, \bar{x})$ where $\bar{c}_i$ is as sequence (of fixed length) of 0's and w's with $w \neq 0$ (e.g., $\bar{c}_1 = \bar{0}$; $\bar{c}_2 = \bar{0}, w; ...; \bar{c}_k = \bar{w}$), and $\bar{x} = \bar{0}, \bar{x}_i$ with fixed length of $\bar{x}$ and the length of $\bar{0}$ depending on i. Let

$$\varphi(\bar{u},\bar{x},S) \Leftrightarrow \exists w(w \neq 0 \wedge$$
$$((\bar{u} = \bar{c}_1 \wedge \varphi_1(\bar{x}_1, \lambda\bar{x}_1' S(\bar{c}_1, \bar{0}, \bar{x}_1'), ..., \lambda\bar{x}_k' S(\bar{c}_k, \bar{0}, \bar{x}_k'))) \vee$$
$$\cdots \vee (\bar{u} = \bar{c}_k \wedge \varphi_k(\bar{x}_k, \lambda\bar{x}_1' S(\bar{c}_1, \bar{0}, \bar{x}_1'), ..., \lambda\bar{x}_k' S(\bar{c}_k, \bar{0}, \bar{x}_k')))))$$

By induction on n, show that for $i = 1, \ldots, k$, $\varphi^{n}(\bar{c}_i, \bar{x})$ iff $\varphi_i^{n}(\bar{x}_i)$. $\dashv$

From the lemma above, obtain $\eta(\bar{0}, x, y)$ and observe that

$$\bar{0}, x, y <^{*}_{\eta} \bar{0}, x', y \text{ iff } \exists j(y = y_j \wedge n_j^{x} < n_j^{x'}).$$

Define

$$=(x, x', y, S) \Leftrightarrow (Y(y) \wedge \forall y'(Y(y') \rightarrow \leq_Y^{\infty}(y, y'))) \vee$$
$$\exists y'(S(x, x', y') \wedge SU(y', y) \wedge \bar{0}, x, y' =^{*}_{\eta} \bar{0}, x', y')$$

Thus, for a linear ordering on G (or a successor relation with length $|G|$), let

$$x \prec x' \Leftrightarrow \exists y(=^{\infty}(x, x', y) \wedge \bar{0}, x, y <^{*}_{\eta} \bar{0}, x', y)$$
$$SUCC(x, x') \Leftrightarrow x \prec x' \wedge \forall z(x \prec z \rightarrow x' \preceq z).$$

We close this discussion with some notes on how to define σ_0,...,σ_m used for coding in #1 and #2, and thereby obtain analogues of Theorem 1. Observe that $Z_{m_1} \oplus \cdots \oplus Z_{m_k}$ can be represented by $1 \cdots (m_1 \text{ copies}) \cdots 101 \cdots (m_2 \text{ copies}) \cdots 10 \cdots 01 \cdots (m_k \text{ copies}) \cdots 1$. Moreover, there is a turing machine TM_{ab} which takes this representation to a coding (suitable for input to TM_{Λ}) of an addition table of the group in $p(\prod m_i)$ steps for some polynomial p. As before, we can then simulate the action of TM_{ab} followed by TM_{Λ} with a system of functionals. Therefore, for #2, we need only to define σ_0 and σ_1 such that

$$\sigma_i(\bar{x}) \text{ iff } \alpha_R([\bar{x}])\text{th letter of } \bar{1}0\bar{1}0\cdots0\bar{1} \text{ is i.}$$

Toward this end, it is convenient to modify the definition of our nice successor relation in terms $\lhd$ below:

$$\varphi(x, y, S) \Leftrightarrow x = y \vee \exists z(S(z, y) \wedge z + y = x)$$
$$\psi(x, y, S) \Leftrightarrow (\varphi(x, y, S) \wedge \forall y'(SU(y', y) \rightarrow S(y', y)))$$
$$\vee (SU(x, y) \wedge S(0, x))$$
$$x_1, x_2 \lhd x_1', x_2' \Leftrightarrow (x_1, x_2 <^{*}_{\psi} x_1', x_2') \vee (x_1 = x_2 \wedge x_1' = x_2' \wedge x_1 \prec x_1')$$

We could then take

$$\sigma_0(x_1, x_2) \Leftrightarrow SU(x_1, x_2)$$
$$\sigma_1(x_1, x_2) \Leftrightarrow \psi^{\infty}(x_1, x_2) \wedge \neg SU(x_1, x_2).$$

As for finite fields, we define $\sigma(x,y) \Leftrightarrow \varphi^{\infty}(x,y)$ (as given in #1) and insert the necessary turing machines to prepare the appropriate input to TM_{Λ}. Note that a finite field has cardinality p^m (for some prime p) and that its additive group is isomorphic to $Z_p \oplus \cdots \oplus Z_p$. So for a coding of the addition table of a field F with $|F| = q$, we can apply a polynomial-time turing machine TM_{ff} to take $1 \cdots (q \text{ copies}) \cdots 1$ to $1 \cdots (p \text{ copies}) \cdots 10 \cdots 01 \cdots (p$ copies$) \cdots 1$ (composed of m blocks of p 1's where $p =$ the least n such that n divides q, and $p^m = q$), followed by TM_{ab}.

Conclusions

Sentences in the language of positive elementary induction over finite cyclic groups and finite fields were characterized in terms of the complexity of algorithms that check these sentences. Attempts at more general results for abelian groups, however, fell short.

Acknowledgment

This project would not have been possible without my advisor, Prof. Kechris, and also Dr. P. Kolaitis. What ideas presented here that made some sense, I owe to them. I wish to thank them for their time and guidance, and apologize for any embarrassment this paper may have caused.

Thanks also to the SURF program and everyone connected with it.

References

[1] de Rougemont, M., Second Order and Inductive Definability on Finite Sructures, Ph.D. Thesis, UCLA 1983.

[2] Kechris, A.S., Lecture Notes on Positive Elementary Induction, University of Paris VII, 1978-79.

[3] Moschovakis, Y.N., *Elementary Induction on Abstract Structures*, Studies in Logic, No. Holland, Amsterdam, 1974.

[4] Moschovakis, Y.N., Lecture Notes, UCLA, Jan 13, 20, 1984.

[5] Moschovakis, Y.N., Abstract Recursion as a Foundation for the Theory of Algorithms, to apppear.

CALCULATION OF EIGENVALUES OF SYMMETRIC MATRICES USING THE CALTECH NEAREST NEIGHBOR CONCURRENT PROCESSOR

by Allen Gee
sponsored by Dr. Geoffrey Fox

The purpose of this project was to develop and implement an algorithm that could be used on the NNCP to calculate the eigenvalues of symmetric matrices. Although a fully working program has not been finished, the entire program for a four node processor has been written and partially debugged.

The concurrent processor is a parallel operating computer that is made up of several independent processors working at the same time. There are several programs available for calculating the eigenvalues of matrices using sequential machines. But these programs can be very slow when the matrix that it is working on is very large. A concurrent processor can do the job much faster because the matrix can be broken down into smaller sections which can then be worked on at the same time by the individual processors.

The program for the four node concurrent processor was divided up into three main parts or subroutines. First the matrix is divided into four sections, one for each of the processors, and downloaded to them. Since this program was designed to work on symmetric matrices only, only half of the elements in the matrices need to be operated on. This is why the elements are stored in a checkerboard pattern. In part A the cyclic Jacobi Method for finding eigenvalues of symmetric matrices is used to operate on the elements. An orthogonal transformation is used to reduce a chosen element to zero. Then the transformation is applied again to different elements. However, when an element is reduced to zero, the rows and columns of it and its symmetric partner are modified. So an element can be unzeroed by the zeroing of another one. But when each non-diagonal element is zeroed or updated in sucession cyclicly, the matrix will converge to diagonal form. The updating is is all done in the diagonal processors. However, not all the elements in the matrix are in the right position to be updated. Part B involves moving elements within the diagonal processors to the right positions to be updated, and in part C the elements are moved between certain off-diagonal processors and the diagonal processors. This is done by permuting the rows and columns of the matrix. This process is continued until the desired degree of diagonalization is attained. There is not enough space on this paper to explain the algorithm in much more detail. For a more complete description of the algorithm see "Cyclic Jacobi Method for the Eigenvalues of Symmetric Matrices" by G. Fox, July 1, 1984.

The point which I am currently at is in debugging part B. At one place in the program the computer just refuses to do what it is told. The problem was traced to two NNCP subroutines that are not executing. I suspect that the problem might lie in the concurrent processor simulator on the cithep VAX. The program can easily be modified to work on the sixty-four node concurrent processor, since parts A and B were written for a number of nodes. Part C will require a modification of its second half to make internode communication more efficient in the larger concurrent processors. Also, a part D will have to be written to move the elements in the off-diagonal processors not adjoining a diagonal processor into those that do, so that part C can be used to update them. Part D was not necessary in the four node case because there were no off-diagonal processors that were not adjoined to a diagonal processor. I estimate that this project will require three to four more weeks of work to finish.

I had two main problems with my surf project. First, the amount of supervision that I recieved was inadequate. The person that I could easily contact for help was only available three afternoons a week. My sponsor should appoint a co-sponsor for future surfers since he is generally too busy for daily help. Secondly, the NNCP programmer's manual was unclear at some points. Small individual examples should have been given, instead of the one large example program given at the end.

4 node

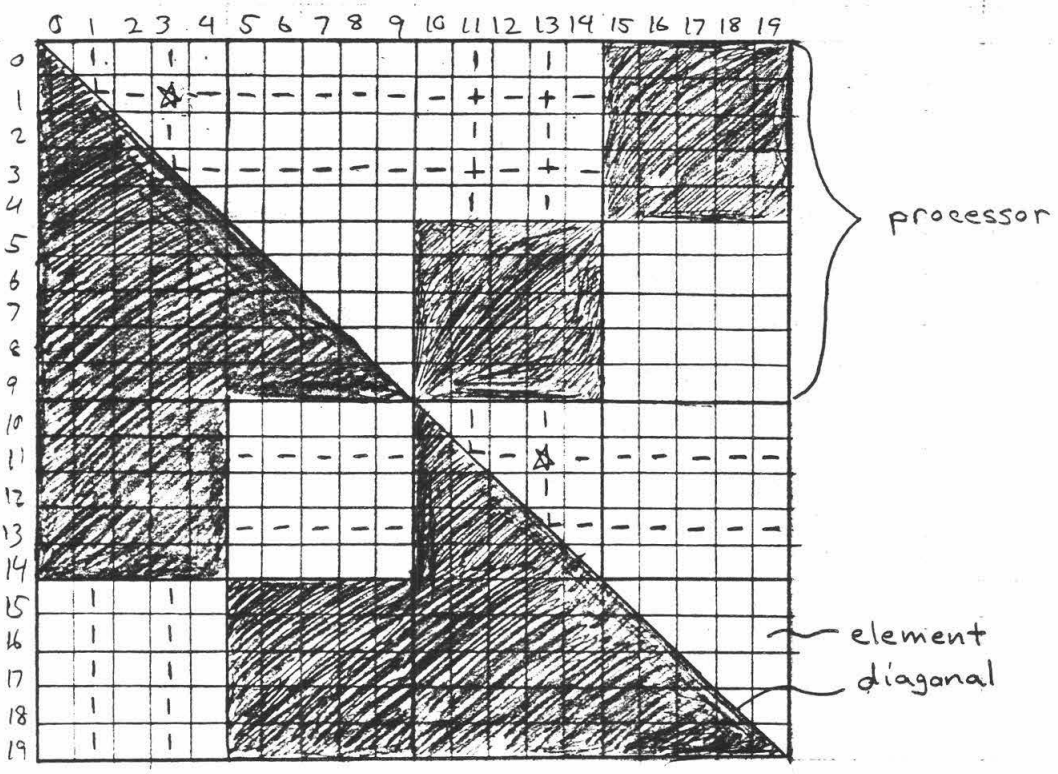

16 node ...

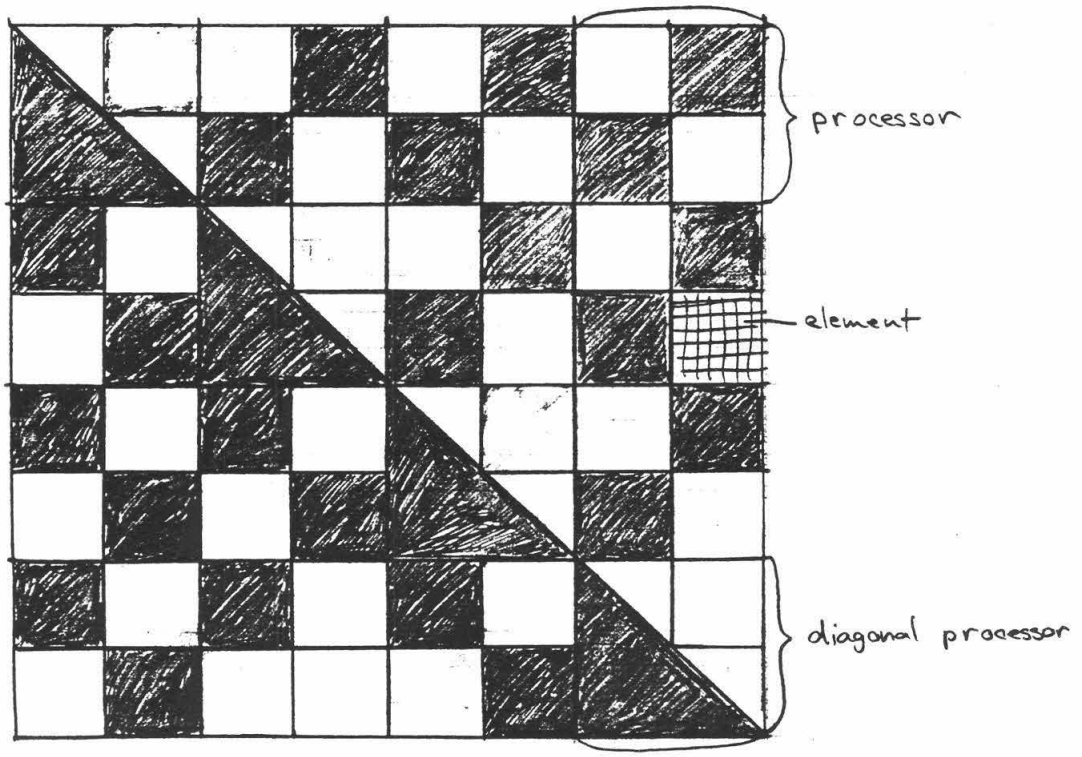

Sputtering Simulations with the Caltech Concurrent Processor

Burnham H. Greeley

Dr. Mark H. Shapiro

Abstract

Computer simulations employing the multiple interaction molecular dynamics technique provide a basic yet very powerful way of studying low to medium energy sputtering. The project described involves adapting and optimizing the problem to a new type of computer architecture, the parallel processor.

Introduction

Computer simulations provide a powerful tool in the study of sputtering and other surface sciences. In brief, early experimental work led theorists to approach the problem from a statistical viewpoint, employing ensemble averages over distribution functions[1]. While these theories adequately predicted sputtering yield as a function of energy along with ejected atom energy and angular distributions they suffer mainly from an inability to deal with features attributable to the regular structure of the crystal target. Binary collision (BC) simulation models, a different sort of computer simulation, followed next. At the outset, BC models provided little new information. However, theorists were able to include the target crystal structure, producing evidence of the channeling phenomenon.

The channeling effect led to the introduction the appropriately named channeling sputtering model. The channeling model succeeded in part because it explained satisfactorily the relative magnitude of the sputtering yields involved at low energies.

At higher energies approaches involving a spike concept become useful. These include the quasi-shockwave model, based on the idea that since energy and momentum must initially propagate outward from the ion impact point there must be a roughly cylindrical correlation for at least a portion of the cascade, the displacement spike model and thermal sputtering, based on the concept of a thermal spike as an enhancement to evaporation. Each model emphasizes different aspects of sputtering, and so all add in some sense to the overall understanding of the process.

Our main concern, however, lies with the multiple interaction molecular dynamics (MI) simulation model. The BC and MI approaches differ philosophically in a number of important ways. The BC model assumes a much larger degree of understanding of the physical system under consideration than the MI approach. This is necessary since the BC simulation relies on the physicists ability to determine which interactions may be safely neglected without noticeable error, among other things. While BC simulations have the advantage of requiring less computer time, they tend to be more complex and more assailible on the basis of the assumptions made.

MI simulations, on the other hand, tend toward a more basic, less aggressive approach. Take for example, the forefather of the code written for this project, a MI simulation program written in FORTRAN for a CYBER-760 by Dr. Mark Shapiro[2]. The code employs Newtons laws of motion alone as the physical principles in determining the trajectories of all particles involved. Other choices pertaining to the structure of the target lattice , the importance of thermal activity within the lattice and such are easily altered and left to the analysts taste. The target crystal is constructed in memory with a defined orientation.

Then, having integrated the choice of ion-atom and atom-atom potentials into the code, the ion is set in motion and the simulation is underway. Knowledge of the interaction potential allows easy calculation of the interparticle forces. The sum of the forces on each particle is then integrated using a simple numeric integration technique to obtain velocity corrections, then again to find each particles new position. After each iteration the time advances and the process repeats. Thus the program literally computes everything that occurs over a short time interval, hence the reason for refering to this type as a time-step program.

Time-step programs on normal sequential computers have a couple of major drawbacks. First of all, the program must store vast amounts of information for each particle, including current positions and velocities along with space to perform the necessary computations involving each. A minimal conservative estimate shows that each particle requires approximately 100 bytes or more (100 eight bit packets) of storage. If one requires better accuracy the space needed can easily double. Thus a model with 1,000 atoms would require over 100,000 bytes of storage. The ever decreasing cost of computer memory is rapidly making this an obsolete concern, but one cannot yet ignore it.

The second difficulty, and by far the most important, has to do with the run times for each simulation and how

these times grow as a function of the number of particles involved. Rough estimates for a typical sequential execution machine show an approximately quadratic dependence between the time necessary and the number of particles involved. Since the calculations required involve a large number of floating point operations for each particle a high speed machine is usually required to perform the calculations in any sort of reasonable time. This cost in computer resources of the standard type is prohibitive and rapidly becomes unmanageable as the target size increases.

This cost in resources is the major factor which prompted the initiation of this project. A new type of computer architecture under development at Caltech promises to provide a much more tractable time to target size correlation. Thus, the purpose of this project has been two-fold. One, to study the applicabilty of this new type of architecture to problems of this nature and two, to obtain essential information about the physics involved, particularly dealing with the question of event containment in the sputtering process.

Discussion

Physically the prime question of interest for the moment is one of event containment. In order to properly insure containment of the momentum and energy transfer the simulation must use large enough targets. If the sputtering cascade involves most of the target atoms the results may be inaccurate. For the purposes of simulation the containment target size may be defined as that size at which a further increase produces no noticeable change in the observables in question. It is currently felt that for 1 KeV Ar ions incident on a copper crystallite targets containing 400-500 atoms are sufficient for containment. However higher energies, in the range of 5 KeV, probably require targets in the range of 2000+ atoms. Once the containment question can be answered, research can move on to other questions such as yields, distributions and particle origins within the crystal.

As for the mechanical aspects of the project, the computer code used follows the approach taken by Shapiro* in his sputtering simulations. The equations of motion for each particle are integrated using a simple, standard predictor-corrector technique to determine the particles trajectory. The error induced through this method is kept within a chosen accuracy by setting a limit on the agreement between the predictor stage and the corrector stage. Should the error fall out of this limit the time-step is reduced by an arbitrary amount (1/2 in this case) and the results recomputed. This repeats until the error falls within the

proper limit. The simulation continues until either a specific cumulative time has elapsed (200 femtoseconds) or the remaining kinetic energies of all particles falls below a certain threshold (2 eV). This is usually sufficient to guarantee that all sputtering events have occurred.

The determination of the potential functions involved obviously plays a major role in the results of the simulation. Of interest is not only the use of the most accurate function, but also the sensitivity of various observables to the choice of potential. However, it was felt that this aspect had been sufficiently well dealt with to be neglected for the moment. As progress is made doubtless attention will return to this area.

The target machine for the final simulation code is the 64 node Caltech concurrent processor (hereafter refered to as the cube). Each node consists of an Intel 8086-8087 processor/math coprocessor pair, 128 kilobytes of memory and communication channels to six other nodes in the network. The communications usually consist of transfers of 64 bits between individual nodes. An intermediate host (IH) is used to control and communicate with the cube. Each node runs independently of the others, although at present each must be loaded with the same executable code. There is as yet no provision for loading different nodes with different programs. Given 64 nodes it is only necessary for each node to handle ~35 particles to get an overall total in excess of 2000 atoms. It is currently felt that targets of this size will provide a great deal of much sought information. Fortunately the potentials involved are short range (~1.5 lattice constants) so each node need only transfer information with its nearest neighbors. This transfer adds an additional overhead not found in the programs designed for sequential machines. However, consider momentarily the effect of adding particles to the simulation. For every 64 particles added only one additional particle must be added to each node, with only a fractional increase in communications cost. Thus rather than a quadratic increase in computation time we have much closer to a linear increase. This analysis breaks down of course in the case of very few or very large numbers of particles.

The whole concept of concurrent processing of course requires a somewhat new way of thinking for the programmer and adds to the complexity of the problem while removing some of the intuition. This tends to slow progress somewhat but is not a major concern.

At present the code is not complete for use on the cube. However, it has been possible to study the feasibility of the cube for this application. As noted before to obtain targets with 2000 or more atoms requires only that

each node handle the computations for about 35 atoms, whereas there should be sufficient memory for over 300 atoms per node at least. No data has been obtained for run-times on the cube, but again this will probably become the major restriction against increasing target size. The microprocessors involved don't have nearly the computing power of a large computer, however the fact that they are always dedicated to a single task should make up for this in part. Thus it appears that the only barrier to performing the simulations desired is a technical one.

Conclusion

The concurrent processors currently under development have initiated a new wave of projects similar to this one. Despite the somewhat longer development time required for computer codes designed to run on these new machines they are clearly a feasible, even desirable alternative to the standard sequential computer. While the concept of concurrent computation is certainly not globaly applicable, the advantages for a problem such as sputtering are obvious. As the level of technology progresses and these machines become more common place as well as more powerful we should see even greater returns.

[1] Don E. Harrison, Sputtering Models - A Synoptic View, Radiation Effects, Vol. 70, pp. 1-18, 1983

[2] Mark H. Shapiro et al., Computer-simulated Energy and Angular Distributions of Sputtered Cu Atoms, Brown Bag Preprint Series, code BB-12, November 1983

Design of a target chamber for use in isotope separation

Scott A. Grossman
Faculty sponsors: Dr. C. A. Barnes and Dr. R. W. Kavanagh

A study of the requirements of a target chamber used to make very pure ^{12}C targets, for use in the study of the reaction of $^{12}C(\alpha,\gamma)^{16}O$, has been made. The chamber has been designed and the necessary peripheral parts determined. An investigation of the cost of assembling this chamber has been made and has resulted in ordering a twelve port chamber to be made.

I. Introduction

The ratio of the amount of ^{12}C to ^{16}O at the end of the helium burning phase of a star's life is a quantity which must be known in order to make further quantitative predictions of the amount of heavy elements formed in later stages of stellar evolution. The three reactions which determine the amount of ^{12}C and ^{16}O are $3\alpha \rightarrow {}^{12}C$, $^{12}C(\alpha,\gamma)^{16}O$, and $^{16}O(\alpha,\gamma)^{20}Ne$. Since the reaction rate of $^{16}O(\alpha,\gamma)^{20}Ne$ is relatively small at helium burning temperatures, the ratio of ^{12}C to ^{16}O is mainly dependent on the first two reactions. The cross section of the reaction $3\alpha \rightarrow {}^{12}C$ is fairly well known, while it is not as well known for the reaction $^{12}C(\alpha,\gamma)^{16}O$.

One reason that the $^{12}C(\alpha,\gamma)^{16}O$ cross section is not well known is because at astrophysically relevant energies, around 0.3 MeV(c.m.),the cross section is so small that it is not technically feasible to study the reaction at such a low energy. Another difficulty is that the reaction $^{13}C(\alpha,n)^{16}O$ has a cross section many orders of magnitude larger than the $^{12}C(\alpha,\gamma)^{16}O$ cross section. Since the detectors count both γ's and n's, any ^{13}C could cause incorrect results.

One study of the $^{12}C(\alpha,\gamma)^{16}O$ reaction by Barnes and Dyer[1] used an enriched ^{12}C target and time-of-flight technique to reduce the neutron yield. The reaction was studied over the energy range of 1.41 to 2.94 MeV(c.m.), and an extrapolation of the data was made down to energies of astrophysical interest. The reaction was also studied in Germany by Kettner, Becker, Buchmann, Görres, Krawinkel, Rolfs, Schmalbrock, Frautvetter, and Vlieks[2] over the energy range 1.34 to 3.38 MeV(c.m.) by using a windowless helium target and a carbon beam. This data leads to a cross section in good agreement with the data of Barnes and Dyer, except in the energy range 1.41 to 1.87 MeV(c.m.), where the cross section value is about 1/3 of the Germans' value. The extrapolation of the German data yields a reaction rate three to five times greater than the rate determined by Barnes and Dyer.

Again the reaction $^{12}C(\alpha,\gamma)^{16}O$ is being studied at Caltech. A windowless helium target is being employed with a carbon beam. However, there are certain effects which are suspected of reducing the reliability of the cross section values as absolute quantities. There may be density gradients in the ^{4}He target; the detector efficiency may vary as a function of position; also, the number of incident particles is not easy to determine with a gas target.

II. The Experiment

In order to check the reliability of the $^{12}C(\alpha,\gamma)^{16}O$ cross section as an absolute value, an attempt is being made to study the reaction by using a ^{12}C target and an α beam at an energy near the resonance peak at about 2.4MeV(c.m.). The cross section values determined with the ^{4} He target could be scaled appropriately if necessary, since the reaction performed with a solid ^{12}C target does not have the uncertainties suspected with the ^{4}He target.

The ^{12}C target would have a tantalum backing with a layer of gold, which is thick enough to stop the incoming α's, evaporated onto it. About 1 cm^2 of ^{12}C would be deposited on this Ta/Au backing. If a current of 100μA of C^- ions was deposited on a 1cm^2 target for 2.2 hours, the target would have a thickness of 100μg/cm^2. An appropriate implantation energy would be around 60keV.

So that the target thickness can be known with greater precision, the reaction $^{12}C(p,\gamma)^{13}N$ could be studied. The cross section of this reaction is known, and the proton beam current and yield can be measured. Thus the target thickness can be calculated.

Finally the experiment can be performed, with an α beam at an energy of about 2.4MeV(c.m.). Since the 's can be counted and the current can be measured and the ^{12}C target thickness is known, the cross section of the reaction $^{12}C(\alpha,\gamma)^{16}O$ can be calculated.

III. Getting the Pure ^{12}C Target

Unfortunately, it is not possible to obtain a pure ^{12}C beam. The beam to be used in making the target has a natural isotope abundance of ^{13}C, which is undesirable to have in the target. The ^{13}C can be separated from the ^{12}C in a magnetic field.

I tested out a small magnet with a power source which would provide more than 600mA with the coils in series. This only provided a magnetic field of about 6200 gauss, and the desired 60° of deflection could not be achieved with 60keV C^- ions. I spent some time obtaining and hooking up a power supply and three phase variac which would supply about 1.35A of current through each coil with the coils in parallel. At this current the coils would require cooling, so several leaks in the magnet's cooling system had to be repaired. From the magnetic field vs. current data taken, it was apparent that the magnet would be saturated around 7500 gauss. However, using the maximum magnetic field available, modifying the pole faces, and making a small compromise in the implantation energy of the C^- ions, a 60° deflection would be possible.

There was a 60° magnet available which had significantly larger pole faces. Thus, it could deflect heavier ions and allow a wider range of options in future experiments. My data indicated that this magnet was becoming saturated at a low field of about 6000 gauss.

To use either of these magnets would require the addition of a straight through port on the vacuum chamber of the 30° magnet at the low energy end of the Pelletron accelerator. With this configuration, the large magnet could not be put in positon and allow enough room near the wall for safety purposes. Using the small magnet would still require modification of its pole faces, the construction of a vacuum chamber for it, the construction of a platform for it, as well as the design and construction of a target chamber, in addition to the modification of the vacuum chamber of the 30° magnet with the accompanying down time of the accelerator. This would be an expensive and

time consuming job.

An alternative method of isotope separation was found. If the target chamber were placed in the beam line, the 30° magnet which is already in use could be used. This avoids all the construction except that of the target chamber. The disadvantage to using this magnet is that it only gives a separation bvetween ^{12}C and ^{13}C of 2.0cm/m, whereas a 60° magnet gives a separation of 3.5cm/m. However, using a narrower slit width can compensate for this, so that the target should not have any more ^{13}C in it even if the 30° magnet is used.

IV. The Target Chamber

Since the target chamber will be on the main beam line, it is undesirable to break the vacuum in the target chamber every time a target is inserted into or removed from it. This can be avoided by putting the target on a linear feed through and separating this from the target chamber with a valve. With the valve closed, targets can be changed without disturbing the vacuum; with the valve open, one or more targets can be lowered into the tarbet chamber by means of the linear feed through. A feed through with 12 inches of linear travel allows placement of four targets, each about a centimeter long, in front of the beam.

In addition to a port on the target chamber for the target to enter, there sould be a port opposite to it into which the targets can extend if necessary. There will be two view ports so that the targets can be positioned or the appearance of the beam can be observed. There will be an electron suppressor to prevent any electrons knocked loose by the beam from hitting the target. This electron suppressor should be on a linear feed through so that it can be removed out of the path of the beam if necessary. There should be a port for a cold trap, which can capture any carbons which are not removed by the vacuum pumps. One port can have a rotary feed through which can position a piece of quartz in the beam line in front of the target so that the beam can be seen. An electrical feed through with at least six pins would be on another port. There must be four pins to read the current of each of the four slits, one to read the current off the target, and one to apply -300V to the electron suppressor. Finally, there must be four ports for the four slits, each on a linear feed through. The target chamber needs twelve ports. The ports will be positioned as three sets of four and they will be positions 90° around the pipe.

The target chamber will be 16.75 inches long with 6 inch o.d. flanges on the ends. The twelve ports will be 2.75 inch o.d. flanges. This piece will be made commercially at an estimated price of $975. The rest of the pieces, which are necessary for the target chamber and are commercially made, total $4016. Making the slits, electron suppressor, cold trap, quartz screen, and target holder and the assembly will have to be done in the shop here.

V. Conclusion

After making measurements on two magnets, it was determined that the easiest and cheapest method of isotope separation was to use the 30° magnet already in place. The vacuum chamber was designsed, taking into consideration that the vacuum of the system be broken as few times as possible and that all internal parts be removeable from the beam. The other parts which will be bought comnmercially have been found in catalogues and the price of each piece has been obtained.

After the study of the needs and requirements of target chamber, the chamber

with twelve ports has been ordered. Thus, the first step in setting up the experiment has been accomplished.

References

[1] P. Dyer and C. A. Barnes, Nucl. Phys. A233 (1974) 495

[2] K. U. Kettner, H. W. Becker, L. Buchmann, J. Görres, H. Krawinkel, C. Rolfs, Schmalbrock, H. P. Trautvetter, and A. Vlieks, Z. Phys. A--Atoms and Nuclei 308 (1982) 73

FE II LEVEL POPULATIONS IN THE HOLLOW CATHODE DISCHARGE

Scott Hudson : S.U.R.F. student

Ward Whaling : research advisor

ABSTRACT: Relative populations of 155 Fe^+ levels in an Fe+Ne+Ar hollow cathode discharge have been measured. Significant departures from a Boltzmann distribution exist. These can be explained in terms of charge transfer between Fe and Ne^+ and subsequent cascading.

INTRODUCTION

Previous Work

1. Duffendack and Gran

This work examined the effect of the charge transfer reaction:

$$Pb + Ne^+ \rightarrow (Pb^+)^* + Ne + \Delta E \quad (* \text{ denotes an excited state})$$

on Pb^+ energy level populations in an arc discharge. Emission spectra from both Pb+Ne and Pb+He discharges were recorded. Lines from Pb^+ states for which ΔE is small were enhanced in the Ne discharge (relative to the He discharge). Two features of the enhancement were interesting. First, the dependence of enhancement on ΔE showed no regularity for the levels as a whole. Within each spectral series (s,p,d and f), however, there existed a smooth dependence of enhancement on ΔE. Second, maximum enhancement occured not for $\Delta E=0$ but for some $\Delta E>0$ which was different for each series. These results indicate that, in addition to ΔE, the configuration of the excited state plays an important role in the reaction.

2. Johansson and Litzen

These workers studied the effect of charge transfer between Fe and Ne. Spectra from continuous discharges (in which charge transfer is thought to be dominant) were compared to spectra from pulsed discharges (in which electron impact should be dominant). Maximum enhancement was observed for $\Delta E=.1$ to .5 ev.

3. Danzmann and Kock

Their work showed the effect of charge transfer between Ti and Ar^+. Unlike the previous works, they were able to use transition probabilities to determine absolute population densities of eight Ti^+ levels. They observed population inversions in Ti^+ levels near the Ar^+ ground state. The populations were approximately a factor of five greater than a Boltzmann distribution would predict. When Ne was used in place of Ar no inversions were seen in these levels.

4. Humphrey, Adams, and Whaling

This research (a 1982 S.U.R.F. project) examined relative populations of 76 Fe^{o} levels using precise experimental transition probabilities. While the overall trend was a Boltzmann distribution, several levels were overpopulated by as much as a factor of ten. Large variations in population even occured between members of the same term. These effects could be explained in terms of a level's lifetime; levels of longer lifetime had higher populations.

Purpose of Present Work

The hollow cathode discharge has been used for decades as a spectral source with little understanding of the excitation mechanisms occuring within it. Recently interest in it has been renewed because of the possibility of its use as a laser source. It would be desirable for its optimum use to have a greater understanding of its excitation mechanisms.

The first three works cited above show that charge transfer reactions have an important effect on metal ion level populations. To understand their true significance, however, one needs to see their effect on the ion's population distribution. Because of the scarcity of transition probabilities this has been possible for only a few ions and then for only a small number of levels. Recently, however, an complete table of semi-empirical transition probabilities for Fe^{+} has been computed. Thus it is now possible to calculate relative populations for all Fe^{+} levels from which transitions can be seen.

DISCUSION

Experimental Method

1. Hardware

The spectrum was recorded on the 1 m Fourier transform spectrometer at Kitt Peak National Labratory. The cathode was an iron tube, 6 mm I. D. by 30 mm long through which flowed a 2.5 Torr Ne + .6 Torr Ar mixture. The discharge current was 850 mA.

2. Data reduction

The population of a level is determined from:

$$N_u = I_{ul} / (g_u A_{ul})$$

where I_{ul} is the intensity of the line emitted in the transition $|u\rangle \rightarrow |l\rangle$, A_{ul} is the transition probability, and g_u is the degeneracy of the upper level ($g_u = 2J_u + 1$). The measurement of I_{ul} usually involves negligible error for the lines used in this work. The principal source of uncertainty is A_{ul}. In general the A_{ul} values of Kurucz are of unkown accuracy. However comparison with those experimental values available suggest that, for the lines used here, the uncertainty is on the order of ±30%.

Results

Figures 1 and 2 show the final results. In figure 1 the populations of levels belonging to a given configuration have been circled and labeled in addition to being identified by parity. Figure 2 shows the same data in terms of the core formed by the six 3d electrons. Levels below 60,000 cm-1 are not included as their lines suffered noticeable self-absorbion. There are some interesting features:

1. The very large populations of the 4f and 5d levels: This is clearly the result of the charge transfer reaction:

$$Fe + Ne^{+} \rightarrow (Fe^{+})^{*} + Ne + \Delta E$$

The relatively low populations of the ^4D and e^2I terms suggest a maximum for this reaction for ΔE=3000 - 4000 cm-1 (.4 - .5 ev). This is in agreement with Johansson and Litzen.

2. The overpopulation of the 4d and lower 5s levels: These are far enough away in energy from Ne^+ that charge transfer should not be directly responsible. The most reasonable explaination would be cascading from upper levels. The highly populated 4f levels decay strongly (and almost exclusively) to the 4d levels thus selectively increasing the 4d populations.

The lower 5s group appears to be fed indirectly from the 5d levels. The 5d levels decay strongly to a group of 5p levels not shown. These 5p levels in turn decay strongly to the lower 5s group. Unfortunately these 5p→5s transitions are in a region (8000 A) where the spectrometer has a low response. Thus it was not possible to determine the 5p group's populations accurately enough to include them on the plot. However the measurments that were possible indicated that the 5p populations would appear in the area of the dotted circle.

3. The higher 5s levels: The distribution of these terms is peculiar. Their populations generally decrease as their energy approaches that of Ne^+. A probable explaination is as follows. The ground state of Fe^o has the configuration $3d^6(^5D)4s$. In the charge transfer reaction with Ne^+ one of 4s electrons is stripped away and the remaing ion is excited. The most likely excitation process should be one which leaves the $3d^6(^5D)$ core alone and merely promotes the remaining 4s electron. Thus one would expect final Fe^+ states with configuration $3d^6(^5D)nl$ to be most favored by the charge transfer process. Figure 2 shows that all the overpopulated levels have the $3d^6(^5D)$ core except for the higher 5s group.

4. Charge transfer with Ar^+: The levels just to the left of the Ar^+ energy are shifted up in population by a small factor. What is stiking is how small these effects of charge transfer with Ar^+ are as compared to those with Ne^+. The greater abundance of Ne in this source (about 4 times as much as Ar) might be a factor.

However a higher percentage of the Ar should be ionized due to its lower ionization potential so that Ar^+ could be more plentiful than Ne^+. A more likely reason is that none of the Fe^+ states near the Ar^+ energy have a $3d^6(^5D)$ core. By the argument given above they would therefore be less likely to be excited by a charge transfer reaction.

5. The general trend of the 4p levels: These give the gross appearance of a Boltzmann distribution although the uncertainty in the transition probabilities makes it difficult to analyze the details. They are probably primarily excited by electron impact which is a non-selective type phenomenon as opposed to the highly resonant charge transfer reaction.

6. Lifetime effects: No correlation between a level's lifetime and its population could be found.

7. Violation of the Wigner spin rule: According to this rule, the total spin in a charge transfer reaction should be conserved. The spin of Ne^+ is 1/2 and that of the Fe^o ground state is 2, thus the total spin is either 3/2 or 5/2. Since the spin of the ground state of Ne is 0, Fe^+ states with spin 3/2 or 5/2 should be favored. However the highly populated 4f group consists soley of doublet terms (spin 1/2).

CONCLUSION

The charge transfer reaction between Fe and Ne^+ appears to be the primary excitation mechansim in the Fe+Ne+Ar hollow cathode discharge. It directly excites Fe^+ states with small, positive ΔE. States with the same core as the Fe^o ground state are most favored. Lower levels connected to these by strong decay branches are subsequently overpopulated by cascading. The effects of charge transfer with Ar^+ are of much less significance.

REFERENCES

Duffendack O S and Gran W H 1937 Phys. Rev. 51 804
Johansson S and Litzen U 1978 J. Phys. B 11 L703
Danzmann K and Kock M 1981 J. Phys. B 14 2989
Humphrey J N et. al. 1984 J. Quant. Spect. Rad. Tran. 31 1
Kurucz R Smithsonian Astrophysical Obseratory Special Report 390

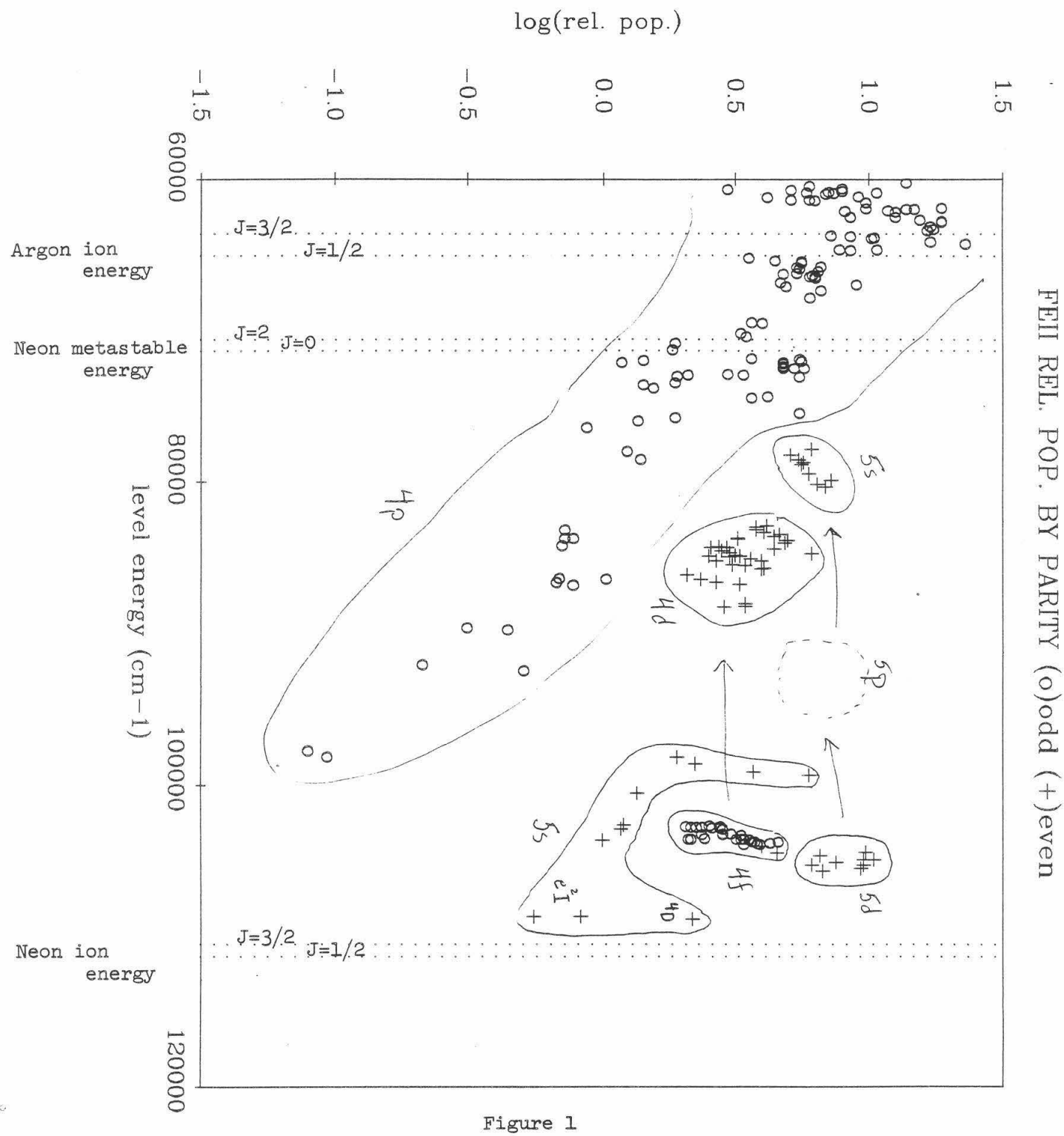
log(rel. pop.)
−1.5
−1.0
−0.5
0.0
0.5
1.0
1.5
60000
80000
100000
120000
level energy (cm−1)
J=3/2
J=1/2
Argon ion energy
J=2
J=0
Neon metastable energy
J=3/2
J=1/2
Neon ion energy
4p
5s
4d
5p
5s
4f
5d
4p
FEII REL. POP. BY PARITY (o)odd (+)even

Figure 1

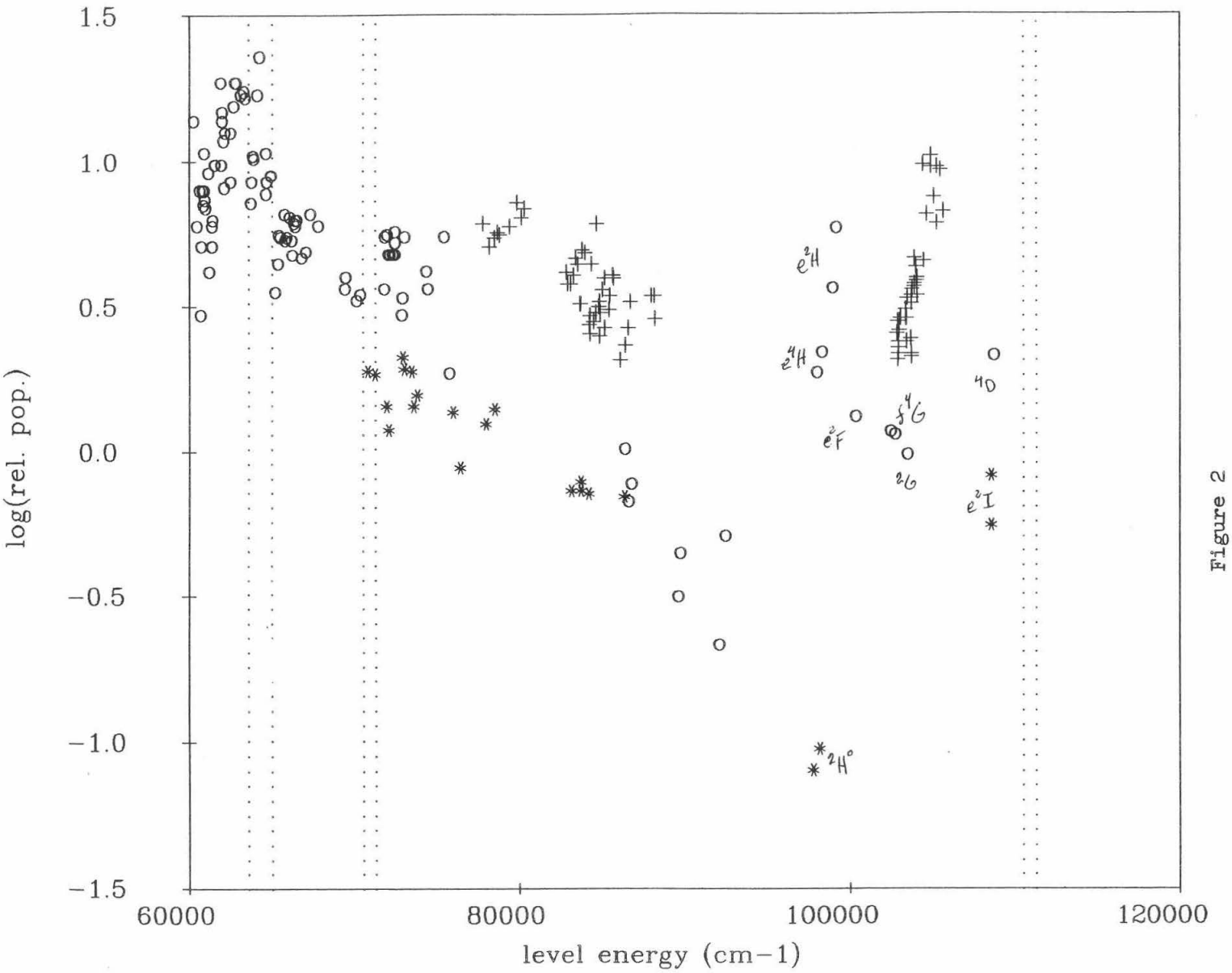
FEII REL. POP. BY CORE TYPE (+)3d^6(^{5}D)nl (o)3d^6(^{3}L)nl (*)3d^6(^{1}L)nl
1.5
1.0
0.5
0.0
−0.5
−1.0
−1.5
log(rel. pop.)
60000
80000
100000
120000
level energy (cm−1)

Figure 2

Small-angle X-ray scattering studies of the structure of latent nuclear damage tracks in dielectric solids

Eric H. Kawamoto

Professor Thomas A. Tombrello, Sponsor

Some preliminary qualitative studies of latent nuclear tracks in muscovite mica were attempted employing the technique of small-angle X-ray scattering (SAXS). Thin specimens of the dielectric mineral could be bombarded by energetic heavy ions in order to create latent damage tracks whose structure could be studied by SAXS. Patterned after similar studies carried out by Dartyge, SAXS experiments were designed to be performed on equipment which is still under development here at Caltech. Analysis of the information gathered from such experiments can shed light on the physical mechanisms responsible for latent track registration.

Introduction

Nuclear damage tracks are formed in dielectric solids as highly energetic ions (in these studies, on the order of 1 MeV/amu) pass through the substance and interact with those atoms of the solid in the immediate vicinity of the ion's trajectory. Point defects (vacancies and interstitials in the solid's lattice) and extended defects (deformations of lattice planes) are formed in the ion's wake, constituting latent track damage. Latent tracks are not visible through conventional optical microscopy, since the damage core (region of most severe damage surrounding the ion path) has a radius of 10-20 Å. To render tracks visible, the material is subjected to an etchant, which etches preferentially along the track (the defects in the damage core make the track more chemically reactive than the undamaged material). Observation of these tracks, which occur in minerals as a result of natural radioactive decay, has application to the dating of geological or lunar specimens. Technological applications of nuclear track technology include controlled irradiation and etching of materials to produce micropore filters (for extremely fine particulates of size 100-1000 Å or so), graded index-of-refraction anti-reflective surfaces, and surface texturing. Track registration also provides a means of recording or detecting the passage of fast atomic particles. [1] On the other hand, physicists are concerned with understanding the mechanisms responsible for the damage created by the passage of fast, heavy ions through matter.

Structural studies of latent (unetched) nuclear damage tracks have been carried out using techniques of transmission electron microscopy (TEM) and small-angle X-ray scattering (SAXS). Analysis of information about track radius vs. energy loss of the passing ion and point and extended defect regions which make up the track would be of considerable help in testing proposed models of track formation mechanisms. However, the TEM technique is unsuitable for these studies because structural details of the latent tracks have been found to fade under observation by the electron beam. [2] The SAXS technique is well-suited to these studies, for the tracks are not altered by the observation process; however, the main limitation of the method is that direct observation of the tracks is not possible. Instead, structural details are determined from the analysis of the intensity distribution of central diffuse scattering of X-rays from the tracks, a form of indirect observation somewhat reminiscent of that of X-ray crystallography.

Theory

When an energetic ion passes through matter, it loses its energy to the electrons in the immediate vicinity of the ion path. Figure 1 shows how $-dE/dx$ (stopping power) varies with the ion's specific energy as it passes through a solid. In this so-called electronic stopping regime, the ion (having energies around 1 MeV/amu, or speeds near 10^9 cm/sec) has a speed comparable to classical electron orbital velocities. Thus, the ion interacts mainly with the electrons rather than with the atomic nuclei, with which the ion will interact when it slows down to speeds near 10^7 cm/sec (energies around 1 keV/amu) in the so-called nuclear or atomic stopping regime. The form which these interactions take is generally believed to be ionization (energy is imparted to bound electrons, which then leave the scene to deposit their energy elsewhere) in the electronic stopping regime, and collision cascades in the atomic stopping regime (evidence of this is usually found near the very end of an ion's range). The main problem of nuclear track formation is one of energy transfer; namely, how the energy of electronic excitation near the ion path is transferred into atomic motion.

Figure 2 shows a cross-section through a latent track, showing schematically the point and extended defects created by the ion's passage. A "Coulomb explosion" model proposes that the energetic ion ionizes atoms along its path, creating an electron-deficient plasma cloud which cannot be "quenched" by electrons in the surrounding material (which occurs in good electrical conductors, thus accounting for the lack of track registration in conductors); this cloud then has time to "explode" by virtue of electrostatic repul-

sion, resulting in atomic motion away from the track core. A "thermal spike" model was later proposed that attempted a less microscopic explanation for track formation. The plasma cloud was thought of as a "hot", localized spike by virtue of the agitation of surrounding atoms caused by the deficiency of electrons. When the spike tries to relax to a state of thermal equilibrium, point defects aggregate to form extended defects. [3] A combination of these two models gave rise to the "thermalized ion explosion" model, which proposed that ion explosions cause heat transfer from the plasma cloud to the atomic lattice in order to establish local thermal equilibrium near the spike. [4]

Studies of the structure of these tracks performed by Dartyge, et al., led to a descriptive (phenomenological) model of track formation. SAXS and etching experiments on thin lamellae of mica which had been bombarded by heavy energetic ions revealed that the tracks were not continuous as once thought, but instead were made up of alternating or overlapping regions of point and extended defects (gap zones and core zones, respectively -- see Figure 3). The linear density of point defects along the tracks were found to vary approximately as the stopping power dE/dx, while that of extended defects had a more complicated dependence. It was proposed that the core zones were formed as point defects generated by ionization near the ion path aggregated near clusters of defects formed by multiple ionization spikes. What triggered these spikes was not known, however. [5]

A recent model proposed by Tombrello tries to explain how ionization spikes may have been triggered. By comparing the effective cross-section for triggering events (computed roughly from the available experimental data) with the effective K-shell ionization cross-sections of light elements in mica (namely carbon and oxygen), it seems plausible that a possible mechanism could be the following: a K-shell ionization event (ionization of an electron from one of the innermost atomic orbitals) could occur every so often as the ion passes through the material, in turn triggering an Auger decay of the K-shell vacancies thus produced (cascade of electrons of lower energy levels in the atom to fill the inner shell vacancy, resulting in the ejection of another electron), accompanied by the release of approximately 50 eV, which is sufficient to cause many atomic displacements (since the binding energy of a lattice atom is about 5 eV). [6]

In order to test the validity of these ideas, it is important to have more SAXS data on track-damaged specimens for a greater variety of materials. Although SAXS is used merely as a tool for structural determination, the technique merits a brief discussion of the physical foundations which particularly suit it to this type of work.

The basic theory of small-angle X-ray scattering was developed by A. Guinier around 1938. Since then, extensions and refinements of the theory as well as improvements in SAXS apparatus design have increased the versatility of this technique. It has been used for structural studies of polymeric materials, biological macromolecules, radiation damage in metals, inhomogeneities in metal alloys, and other fields of interest in physical metallurgy. Since the details being examined in all these cases is of the order of 10-1000 Å, X rays, whose wavelengths range from 1-10 Å, are well-suited for observation of these details. Traditionally, X-rays have been used in crystallography in order to study crystal structure, especially the spacing of crystal planes, which diffract X-rays particularly well. In small-angle scattering, the diffuse coherent scattering near the central maximum (undeflected beam) is of interest. To get a feeling for this, the Bragg relation

$$\lambda = 2d\sin\theta$$

indicates that the larger the crystal plane spacing d is for a given wavelength λ, the smaller the angle θ at which the waves will constructively interfere (see Figure 4). In a similar way, larger details give rise to scattering at smaller angles.

When an electromagnetic wave impinges on a free electron, the latter will oscillate in resonance with the wave, producing secondary waves as it is accelerated. The bound electrons of a particle will respond in like fashion, producing coherent waves which interfere. The intensity distribution of this "scattering", for the case of a free electron, is given by

$$I(\theta) = 7.90\times10^{-26} I_0 \cdot \frac{1+\cos^2 2\theta}{2} \qquad \left(\left(\frac{e^2}{mc^2}\right)^2 = 7.90\times10^{-26}\ cm^2\right)$$

Thus, this diffuse scattering increases at smaller angles and is very weak. For a particle of a given shape whose dimensions are comparable to the wavelength of the radiation used, the scattering intensity distribution can be calculated; the curve obtained will have a characteristic shape depending on the geometry of the scattering particle. (See Figure 5) When there is a sufficiently "dilute" suspension or solution of such particles (which may or may not be identical in size), the scattered intensities of the individual particles simply add. In a real substance, the "particles" are actually "islands" of electron density inhomogeneity (if the surrounding medium had the same electron density as the "islands", there would be no scattering), and the scattering intensity is proportional to $(\Delta\rho)^2$, the square of the electron density difference.

In practice, the scattering intensity pattern obtained from a sample is compared to curves calculated for scattering from dilute solutions of particles of simple geometry (e.g., rods or cylinders, hard spheres, ellipsoids, etc.),

which are well-known. The one whose shape matches most closely is then fit to the experimental curve to within experimental error by varying parameters of the modelling particles (i.e., varying the rod lengths or radii, sphere radii, or the lengths of the ellipsoid axes). Thus, the actual scatterers (in this case, the latent damage tracks) are modelled by a system of particles which produce an equivalent scattering. Thus, one arrives at an idea of how the electron density inhomogeneities are shaped and what size they may have. Although the exact shape of the scatterers cannot be deduced directly from the scattering curve, an estimate of the size of the scatterers (radius of gyration, analogous to that of classical mechanics), their volume, and surface area can be determined by preparing plots based on the fact that the scattering intensity curve has asymptotic forms

$$I(h) \sim e^{-\frac{h^2 R_g^2}{3}}$$

for small angles, (Guinier plot of log I vs. h^2) and

$$I(h) \sim \frac{S}{V}\frac{1}{h^4}$$

for large angles (Porod plot of I vs. h^{-4}), where h is the modulus of the scattering vector, R_g is the radius of gyration, and S/V is the specific surface area of the scatterers. [7]

The determination of track radius and the size of core zones is the main purpose of these SAXS studies. For points along the track, the relationship of track radius and the ion's energy loss (dE/dx) for different ions and different dielectrics will help to clarify models attempting to explain the track registration mechanism.

Procedure

The SAXS apparatus is shown schematically in Figure 6. Slits collimate the beam and help to reduce parasitic scattering, while Si and Ge crystals reflect and monochromatize the beam. The X-ray source is a high-voltage tube with a copper anode emitting CuKα radiation of wavelength 1.54 Å. A thinly-sliced specimen is placed in a sample holder, while film is loaded into a curved film holder equipped with a beam stop in order to prevent the intense undeflected beam from hitting the film and causing fogging. An aluminum canister houses the setup, enabling it to be evacuated in order to cut down on air scattering. The X-ray beam is then switched on to make a 24 hour exposure, for example, after which the film is developed in order to resolve the scattering intensity pattern.

The specimens were prepared from 1" square 5 μ and 10 μ slices of cleaved mica. They were bombarded in a tandem van de Graaff accelerator with Cl-35 ions having energies of 25 MeV for the 5 μ specimen (0.71 MeV/amu) and 43 MeV for the

10 μ specimen (1.21 MeV/amu), all at dosages (integrated flux) of 5×10^{11} ions/cm^2. The energies were chosen so that the ions would go completely through the thickness of the mica; the dosages were chosen so that there would be a sufficient number of tracks to give a significant scattering intensity but not so high as to amorphize the mica (characterized by blistering and deformation of the bombarded region).

Scattering patterns on film for the empty sample holder (background or parasitic scattering), an unirradiated mica specimen (control), and one of the irradiated samples (trial run) were obtained, but not under identical or optimal conditions. Problems with crystal alignment in the setup as well as X-ray tube malfunction and availability of accelerator time have greatly hindered experimentation.

Discussion

The main reason that no quantitative data could be obtained with the existing apparatus was that an electronic detector was not used. Film methods are obsolete and rarely used because of severe limitations on sensitivity and resolution. Film patterns are analyzed with the aid of a microdensitometer, which converts the darkness of the pattern into an intensity reading. However, such an instrument was not available here at Caltech. On the other hand, an electronic detector, a position-sensitive proportional counter (PSPC), was to be implemented for the acquisition of digitized intensity data. The PSPC is approximately a thousand times more sensitive than film, and data handling can be done much more easily by a computer. Delays in receiving the PSPC made the collection of numerical data impossible.

In a careful series of experiments to determine track characteristics vs. dE/dx, it is necessary to have very thin mica specimens for ions of lower energy, since dE/dx tends to decrease rapidly near the end of an ion's range in a material (and hence, at low energies -- see Figure 6). Thus, a thinner specimen means less variation in dE/dx over the length of the segment of track contained therein. However, excessively thin specimens of mica are difficult to handle because they are brittle, and they would tend to produce a very small scattered intensity (very thick specimens would prevent the X-ray beam from penetrating, while very thin specimens would not contain enough scatterers to produce much diffuse scattering; the optimal thickness to be used for SAXS experiments is one X-ray attenuation length, which, for mica, is on the order of 70 μ, while these experiments call for specimens thinner than 5 μ).

The final problem with the SAXS apparatus is the method

of collimation. The theory of small-angle scattering was developed for irradiation using a point-collimated beam; a slit-collimated beam would smear the scattering pattern. Fortunately, mathematical methods exist for correcting (desmearing) slit-collimated data so that the standard Guinier and Porod plots can be done and a full SAXS analysis can be carried out. [8]

Conclusions

At the time of this writing, the SAXS apparatus at Caltech is still in a stage of development. The PSPC and the associated hardware have not yet been implemented, which complicates the task of alignment of crystals and slits for optimal performance and makes the collection of any quantitative data almost impossible. However, the track sizes, which are known to be on the order of 10-30 Å, are well within the range of resolution on the SAXS apparatus. The sensitivity of the detector and electronics should accomodate the weak scattering intensity of the mica specimens, while the software which exists for desmearing and intensity corrections should be ready to analyze accessible digitized intensity data. In other words, experiments such as the ones done in France to study latent nuclear tracks by SAXS can be designed and performed on equipment at Caltech, but only after its development is completed.

Acknowledgements

I am indebted to Professor William L. Johnson in the Applied Physics Department for use of the SAXS apparatus, to Xian-Li Yeh for his guidance in its operation, and to Dr. Rogerio Livi for his help with the bombardment of the mica specimens. Special thanks must go to Professor Thomas A. Tombrello for his guidance and encouragement with this project.

References

[1] B. E. Fischer and R. Spohr, Production and Use of Nuclear Tracks/Imprinting Structure on Solids, Gesellschaft für Schwerionenforschung GmbH, 1982.

[2] P. B. Price and R. M. Walker, J. Appl. Phys., 33 (1962), 3400.

[3] see [1]

[4] L. E. Seiberling, J. E. Griffith, and T. A. Tombrello, Rad. Eff., 52 (1980), 201.

[5] E. Dartyge, J.-P. Duraud, Y. Langevin, and M. Maurette, Phys. Rev., 23B (1981), 5213.

[6] T. A. Tombrello, "Track damage and erosion of insulators by ion-induced electronic processes", in press.

[7] O. Glatter and O. Kratky, eds., Small Angle X-Ray Scattering, (Academic Press, London, 1982).

[8] C. G. Vonk, J. Appl. Cryst., 4 (1971), 340.

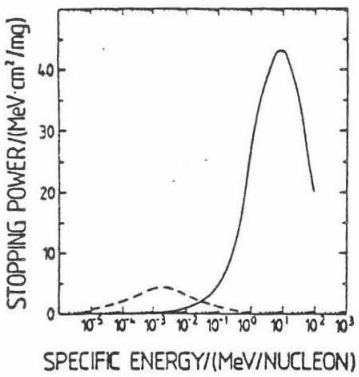

$-\frac{dE}{dx}$

Figure (1). *Atomic and Electronic Stopping Power of Heavy Ion in a Solid*[11]
(Here: Stopping power of ^{209}Pb ions penetrating through gold).
Atomic stopping (dashed curve) is dominant at very small specific energies, below about 0.01 MeV/nucleon. It corresponds to discrete encounters between the penetrating ion and the atoms of the solid, exchanging substantial fractions of the ion energy. Atomic stopping is responsible for most of the angular and range straggling of the penetrating ion.
Electronic stopping (solid curve) prevails at high specific energies, beyond about 0.1 MeV/nucleon. It corresponds to a quasi-continuous transfer of energy between the penetrating ion and the electrons of the solid, yielding a straight ion path.

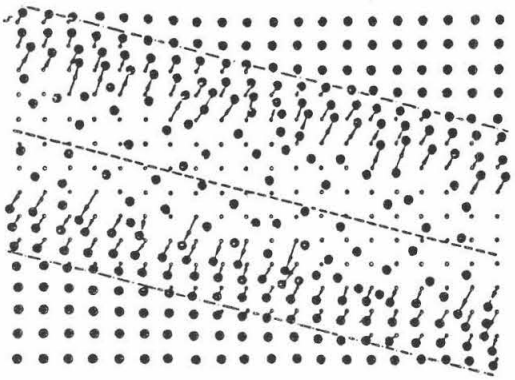

Figure (2). *Axial Section Through a Latent Nuclear Track in a Crystal*[10]
(Schematic Representation). The penetrating ion creates a positive ion cloud around its path, which "explodes" by electrostatic repulsion. This leads to atomic displacements (arrows), the magnitude of which decreases with the original distance of the atoms from the ion path. A disordered zone results, with a core of decreased density, surrounded by a sheath of increased density.

Figure (3)

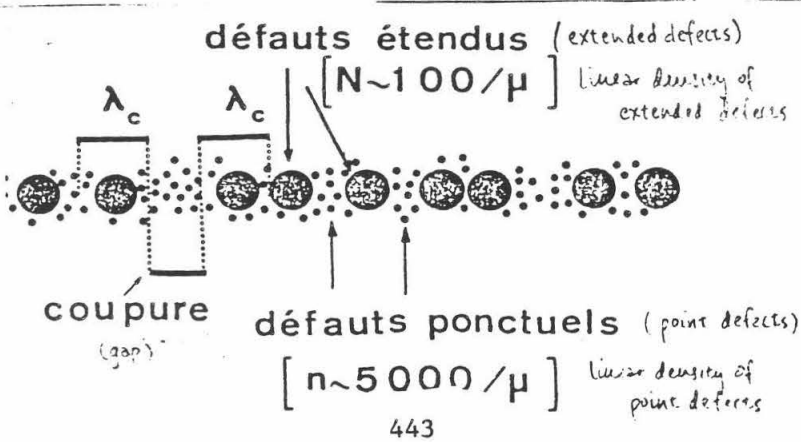

Figure (4)

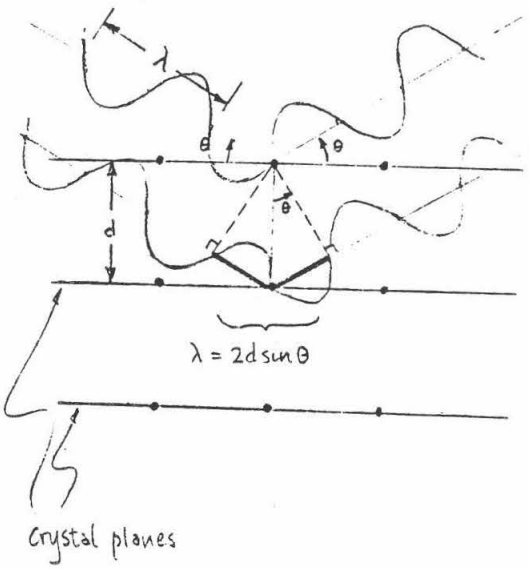

Figure (5)

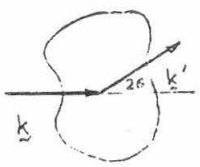

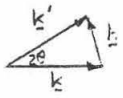

$\underline{h} = \underline{k}' - \underline{k}$
= scattering vector

$|\underline{k}| = \frac{4\pi \sin\theta}{\lambda}$

$\underline{k}$: incident wavevector

$\underline{k}'$: scattered wavevector

$|\underline{k}| = |\underline{k}'| = \frac{2\pi}{\lambda}$ where λ = wavelength

$\Rightarrow$

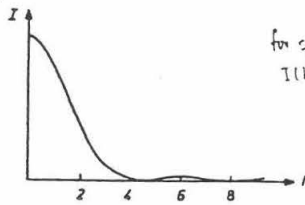

FIG. 2. Scattering intensity of a sphere.

for sphere

$$I(h) = (\Delta\rho)^2 V^2 \left[3\frac{\sin hR_0 - hR_0 \cos hR_0}{(hR_0)^3}\right]^2$$

where $\Delta\rho$ = electron density difference

$V = \frac{4}{3}\pi R_0^3$ for sphere of radius R_0

h = modulus of scattering vector

Figure (6)

$CuK\alpha_1 = 1.540562\,Å$

$CuK\alpha_2 = 1.54439\,Å$

Ge(220) : $2d = 4.00044\,Å$ resolution low intensity high

Si (220) : $2d = 3.84011\,Å$ resolution high " low

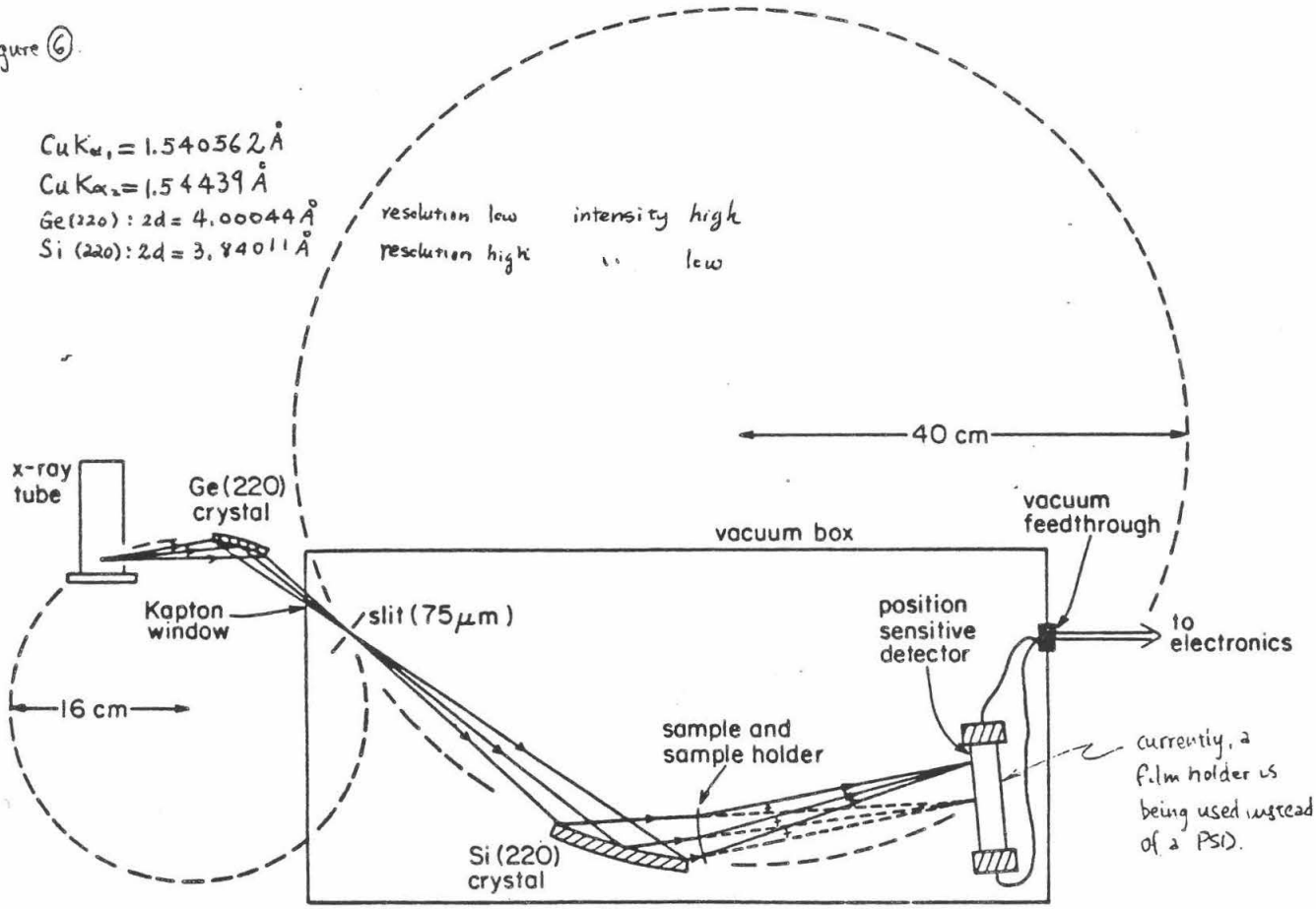

Figure (7).

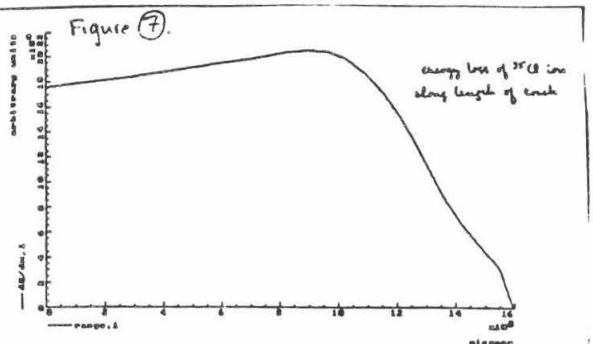

QCD, LATTICE, MONTE CARLO, INSTANTONS.

by
Rodney Kinney

sponsored by
Sorin Solomon

ABSTRACT

In order to better be able to study quantities which are related to the topological charge in lattice gauge theory of Quantum Chromodynamics, a method is introduced that will use global Monte Carlo steps to calculate the relative weights of the topological sectors while separate runs are performed in each sector. The Monte Carlo procedure is modified to prevent tunneling between sectors by restricting action density to be less than around 0.25 per plaquette. This value will, we hope, be both small enough to prevent tunneling and large enough not to affect the dynamics of the lattice.

Quantum Chromodynamics is a theory of around one decade old that has been introduced in the hope of providing a complete explanation of the observed behavior of the strong force. So far, QCD has provided impressive predictions that indicate that it could be the theory physicists are looking for, and has collected a large following of scientists. For a thorough review of QCD, see reference (1).

QCD is a quantum field theory in which quarks and gluons interact amongst themselves. The theory is a Lagrangian field theory. One defines a Lagrangian density, L, and the expectation of any physical observable is given by

$$\langle O \rangle = Z^{-1} \int O(L') \exp(-iS)\, dL' \; ; \; S = \int L\, d^3x\, dt \; ; \; Z = \int \exp(-iS)\, dL'$$

The integrations dL' are over all possible forms of the Lagrangian field, a difficult operation to carry out, or even to define. The imaginary exponent introduces oscillations that are difficult to manage, and matters are simplified by the variable change $t \rightarrow it$. This makes the time dimension equivalent to the three spatial dimensions. Physical results may be retrieved by analytically continuing back into real time. The rest of this paper will deal with Euclidean four dimensional space: three spatial dimensions and one imaginary temporal dimension.

The principally contributing terms to the integrand over configurations are those for which the action is minimal. Finding these configurations amounts to solving the set of field equations which are derived from the classical Euler-Lagrange equations used for solving Hamilton's principle of least action. The solutions which minimize the action are called topological solitons (also pseudo-particles), and have been the subject of much study, both as they relate to QCD (as well as solid state and plasma physics) and as purely mathematical objects.

In four-dimensional Euclidean space, there is a pseudoparticle called the instanton. One can define a quantity, called the topological charge q, which takes only integral values and depends on the configuration of the Lagrangian field. Configurations can be divided into groups with different q. Configurations with different q are said to belong to different topological sectors. One can prove that applying continuous infinitesimal changes to a configuration cannot bring it into a different topological sector. Thus, topological charge is conserved. The q=0 soliton is trivial: the vacuum. When the q=1 soliton was solved for (2), it was called the instanton. The physical interpretation of pseudoparticles is not certain, but their existence has been used to solve some symmetry-breaking problems that have plagued QCD in the past (3).

One parameter that emerges in QCD is the coupling constant, g. While the mathematics of QCD are too complicated to solve exactly, results can often be obtained through perturbation theory, usually by expanding around small g. Recently, a new approach to QCD has been taken in order to study the region out of the reign of perturbation theory, the realm of strong coupling. The method consists of defining the theory on a lattice, a four-dimensional, hypercubical lattice of points separated by links of finite length. With each link is associated a matrix of a particular group. For our studies, we have used the group SU(2). The field is defined on the links of the lattice such that when a particle moves from one site to another, its (vector) wave function becomes multiplied by the matrix of the link between the two sites. In a properly defined limit of lattice spacing going to zero, the continuum theory is retrieved, and physical results can be obtained. For a complete review of lattice gauge theories, see reference (4).

The action in a lattice gauge theory is defined as follows. Consider four sites at the corners of a square of the smallest size that the lattice spacing will allow. Such a square is called a plaquette. The transporter, U, around the plaquette is the matrix that is the product of the matrices associated with the links that are the sides of the plaquette. The action of the entire lattice is obtained by summing over all plaquettes i.

$$S_t = B \sum_i S_i \quad ; \quad S_i = 1 - \tfrac{1}{2} \mathrm{Re}(\mathrm{Tr}(U_i)) \quad ; \quad B = 4/g^2$$

S_i is what I will call the action of the i^{th} plaquette.

The expectation value of physical observables is defined in the same manner as in the continuum case, only that for lattice theories, the integral over all possible configurations becomes a sum that define-able, and even evaluate-able. To obtain all possible configurations of the field, one has merely to vary the matrices of the links throughout all combinations of values. Of course, this is still not a very practical thing to do. Instead, examine the expression for the averages of observables:

$$\langle O \rangle = Z^{-1} \sum O \exp(-BS) \quad ; \quad Z = \sum \exp(-BS) \quad ; \quad S = \sum_i S_i$$

One can see that with the correspondences B $(kT)^{-1}$ and S Energy, one has exactly the same expressions as appear for observables in a statistical system at temperature T. The problem of QCD with large

coupling constant becomes entirely analogous to a four-dimensional statistical system at high temperature, and weak coupling corresponds to low temperature. At this point, then, one can turn to methods used by statistical physicists to use computers to simulate systems in thermal equilibrium. The method most often used is that of Monte Carlo.

The idea of Monte Carlo simulations in lattice QCD is simply to start with the system in some initial configuration, and from there to offer small changes to the system, accepting new configurations with a Boltzmann probability

$$\text{probability} = \exp(-B(S_{new} - S_{old}))$$

Eventually the system reaches thermal equilibrium and the measurable quantities can be measured directly.

Monte Carlo simulations on the lattice run into problems when confronted with matters that have to do with topological charge. First of all, topological charge is difficult to define on the lattice. Some definitions have been presented (5), but they are complicated and take much time for a computer to work out. Also, they do not always give the correct value, and the effect can be quite noticeable. Another major problem is that any configuration on the lattice can be deformed into any other by continuous changes of the links. Topological charge is not conserved. In measuring values of quantitites such as $\langle q^2 \rangle$, the system is constantly tunneling between topological sectors, and one must continuously calculate q in order to be sure which sector one is presently in. The work we are carrying out is an attempt to resolve these problems and allow Monte Carlo studies of different topological sectors on the lattice.

The idea is to perform separate runs in each topological sector. We modify the Monte Carlo procedure so that the system cannot tunnel. We can then perform runs starting from a configuration of whose charge we are certain, and never have to compute the charge again. The value of any observable will be the average of its value in all of the sectors with appropriate weighting. The relative weights of the sectors can be found straight-forward-ly. The ratio of the weights of two sectors is the ratio of the probabilities for each to go into the other as given by the Boltzmann probability. My involvement has been in the prevention of topological tunneling.

The topological charge cannot change gradually; it must change from one integer to another and that change must take place at one particular step, at one particular link. If one can isolate the step which causes the tunneling, one can prevent the change. To this effect, it can be shown that there is a minimum emergy density in the vicinity of the link that changes the charge, such that at least one plaquette will have an action of greater than a certain value, which I will call epsilon. This epsilon is independent of both lattice size and B. If the monte Carlo updating procedure simply does not accept any configuration which has plaquettes of action greater than epsilon, then the system cannot tunnel. The work has been to find an epsilon which is large enough not too interfere too severely with the behavior of the lattice, but which will still prevent tunneling.

Monte Carlo runs were made on an SU(2) lattice of seven sites in each direction, a more or less typical size. Candidate configurations were generated by going link by link through the lattice, and at each link, multiplying that link by a random matrix close to the identity matrix. Once that change had been accepted or rejected, we moved on to the next link, and so on. One sweep is the process of going once through the lattice and updating each link in such a manner.

Normally, an instanton on the lattice left to itself at zero temperature (infinite B) will decay into the vacuum in about 200 sweeps. We tested our epsilon condition by performing runs at infinite B with different epsilons and watching for the instanton to decay into the vacuum. Those that did not decay froze into a state in which any change would either increase the action (and thus be rejected by the Boltzmann condition at zero temperature) or violate the epsilon condition. The system remained stationary in the q=1 sector. Unfortunately, the largest value of epsilon that prevented tunneling was around 0.25, and too small for most applications. For B in the region of interest, typical actions are large enough that the epsilon condition interferes too much with the system's natural behavior.

An alternative method of keeping down the energy density that we have since tried is to restrict the sum of plaquette actions of the six plaquettes surrounding any single link to be less than a certain value, which I will again call epsilon. This condition will also suppress tunneling, and is less restrictive than the first condition. The value that one can expect is six times the old epsilon, and indeed, our results so far have turned up an epsilon of near 1.5. A preliminary comparison of the results using this new epsilon condition looks quite encouraging, although more checks still need to be made.

Even if the new epsilon condition proves to be too restrictive, its effect can be lessened by going to larger lattice sizes. It is unlikely that the increased time needed for larger lattices will negate the advantages gained by our method. Also, epsilons of just under the critical value, while still allowing the tunneling, did restrict it so that the system did not tunnel until after 1500 steps or so, so there is hope that enforcing a relatively weak epsilon condition will be innocuous enough not to affect the behavior of the statistics of the lattice, but will still slow the tunneling so that one need check the topological charge much less often than is necessary now, and this will still greatly improve the prospects for the study of instantons on the lattice. These are matters for continued study in the future.

References

1. W. Marciano & H. Pagels, Physics Reports 36c, No. 3.

2. A. A. Belavin, A. Polyakov, A. Schwarts, & Y. Tyupkin, Physics Letters 59b, 85.

3. G. 't Hooft, Physical Review Letters 37, 8.

4. M. Creutz, L. Jacobs, & C. Rebbi, Physics Reports 95, No. 4.

5. T. Woit, Physical Review Letters 51, 638.

Galaxy Simulation with Concurrent Processors

S.A. Lewicki
sponsored by
Steve Otto and Nick Warner
California Institute of Technology

ABSTRACT

We discuss a present working disk galaxy simulation and its decomposition on the Caltech Nearest Neighbor Concurrent Processor architecture.

Introduction

Galaxy simulations have had almost a twenty year history. They have gone almost hand in hand with the development of computer science in those years, using all the latest advances in algorithms. The most successful of these simulations usually involved large gravitational n-body calculations in two dimensions. To allow computations to use 50,000 - 200,000 point particles moving under $\frac{1}{r^2}$ forces of self-gravitation, the codes make use of a cartesian grid of points over which potentials or forces are obtained. This can be done, because the mass distribution is relatively smooth, and the potential need only be taken at few places for a good approximation. Those $10^4 - 10^5$ can be used to represent a system of $10^9 - 10^{10}$, because the calculations use a "softened" potential; it is no longer $\frac{1}{r}$ but $\frac{1}{\sqrt{r^2+a^2}}$ with a equaling the softening value. The particle then no longer represent individual stars; instead they represent "clouds". This stunts the interaction between two stars so that they do not accelerate off each other causing unrealistic effects which could effect the simulation.

The simulation then appeared to be a "doable", interesting problem. Then everyone was doing it. It had become a "fad". If they got realistic looking spiral arms, they thought, "success", but few were making a serious attempt at carefully studying the dynamics or trying to compare with theory. Groups, right and left, then began to drop out of the scene. Two main groups, though, Miller and Hockney, stuck to it, creating better and better codes and actually studying and comparing to theory with some success.

Now you may ask, "If people have been doing galaxy simulations for twenty years, why do we need anymore? Hasn't everything already been done?" The answer is simply, "No." The dynamic properties of disk galaxies are still not fully understood. There are still many theories out there, all valid and reasonable, but have not been able to be proved. Only in the last few years have simulations been created which accurately reflect the dynamics and be can used to directly test those theories. These new simulations used many new techniques, one is a polar grid instead a cartesian. A polar grid offers many advantages. If one just looks at the problem, it appears a polar description is more naturally suited. A cartesian grid might introduce effects which can be measured as the system evolves and rotates. A polar description is a little tricky though. The best to use it is to have a polar grid mapped onto a cartesian grid using both description in the program.

Polar Grid and Equations of Motion

In the mapping from polar to cartesian, there is the following change of variable:

$$r = Le^{\alpha u}$$

$$\varphi = \alpha v$$

A polar grid described by r and φ then becomes a u by v cartesian grid for some convenient value, α, which determines the number of angular divisions along a ring at u = constant. For example, $\alpha = 2\pi/64$ corresponds to $N_\alpha = 64$ azimuthal values. L sets the scale length. With this mapping, the equations of motion become somewhat complicated. The Hamiltonian for the system is:

$$H = \frac{e^{-2\alpha U}}{2\mu\alpha^2 L^2}(P^2 + J^{2)} + V(u,v)$$

where P and J are the momenta conjugate to u and v, respectively, and μ is the mass of a particle. To use these equation numerically, they are translated to a time-centered "leapfrog" scheme where the position update uses the momentum value that corresponds to a time halfway between the old and new positions. The iterative equations for the momenta then become:

$$J^{(n+\frac{1}{2})} = J^{(n-\frac{1}{2})} + G^{(n)}$$

$$P^{(n+\frac{1}{2})} = P^{(n-\frac{1}{2})} + \frac{\exp(-2\alpha u^{(n)})}{\alpha}\left(P^{(n+\frac{1}{2})^2} + J^{(n+\frac{1}{2})^2}\right) + V(u,v)$$

where dimensioned units $(\mu L^2/\Delta t)$ have been divided out. The values, $P_a^{(n)} = \frac{1}{2}(P^{(n+\frac{1}{2})} + P^{(n-\frac{1}{2})})$ and $J_a^{(n)} = \frac{1}{2}(J^{(n+\frac{1}{2})} + J^{(n-\frac{1}{2})})$, in the equation for $P^{(n+\frac{1}{2})}$, are time-centered for the difference scheme, which makes the equation implicit, what I am solving for is also in the equation. When one makes it explicit, it becomes a large quadratic equation which unfortunately has to be solved for each particle. Similarly, the equations for the position update become:

$$u^{(n+1)} = u^{(n)} + \frac{\exp(-2\alpha u^{(n+\frac{1}{2})})}{\alpha^2} P^{(n+\frac{1}{2})}$$

$$v^{(n+1)} = v^{(n)} + \frac{\exp(-2\alpha u^{(n+\frac{1}{2})})}{\alpha^2} J^{(n+\frac{1}{2})}$$

The term $u^{(n+\frac{1}{2})}$ is time-centered like $P_a^{(n)}$ and $J_a^{(n)}$ which makes the equation for $u^{(n+1)}$ also implicit. But this one is trickier than the other implicit equation; this one cannot be solved directly, only numerically by Newton-Raphson's Method. Fortunately, this method converges quickly, but it still has to be solved for each particle. This Hamiltonian formulation, with the time-centered "leapfrog" scheme, is most commonly used, because it assures a Liouville theorem which means essentially it is reversible.

Potential Calculation

The potential calculation involves four steps:

First, the "D matrix" is constructed. It represents the potential energy interaction between two mass rings on the grid. It is essentially a table of 1/r values over the grid. This is then Fourier transformed creating the D matrix which is calculated and stored beforehand.

Second, the potential calculation proceeds through Fourier transformation of the density in the angular coordinate: $\sigma(u,v) \rightarrow \hat{\sigma}_n(u)$, where n is the index of the angular Fourier component. The potential energy of interaction between two such Fourier components is zero unless the indices match. This is the key to what is called the "finite convulsion theorem." It creates an incredible time saving. The naive way of formulating the algorithm would have been to look at the interaction between each star. Say I have n number of stars. For each star I would have to sum 1/r 's to all other stars. Then the number of calculations goes as n^n. For the number of stars I would like to simulate this would be impossible; so then a grid is an improvement. But again, say I have N grid points then I have N^2 calculations, and since I want as high a resolution as possible with many grid points, this too becomes an unfavorable algorithm. The "finite convulsion theorem" then saves the day. It eliminates one of the summations, because we

need only consider the Fourier components with matching indices. The calculation then goes as $\alpha N \log_2 N$ where N is the number of grid points, $\log_2 N$ is from the transform, and α is a constant depending on the transform.

For the third step, the D matrix multiplies the transformed density vectors in large iterative loop. And then a inverse Fourier transform completes the potential calculation. The forces are determined by interpolation with the nearest grid points, and the particle positions are then updated using the equations of motion above.

Concurrent Decomposition

When all of this is done concurrently, it runs even faster. This is my major contribution, because with a faster running code, one can study more. I use a finer grid, more radial and angular divisions, which is important, because it increases the resolution and lowers the effects the grid might have on the simulation. I can use more particles, which is important, because some dynamical effects can only be seen with higher densities.

The decomposition into a concurrent algorithm is straightforward. Each processor takes care of all the information for one ring of the polar grid. This is then called a one dimensional decomposition because each processor need only communicate with two neighbors, one in the forward direction and one in the preceding direction. Within each processor all of the particles and their attributes, their position coordinates and their momenta; the mass mesh they create; and the D matrix elements for that ring are stored and updated. The potential calculation requires the transformed density vector in the radial direction, so then its elements are passed along from processor to processor in a ring. The force calculation requires all the potential values in the neighboring ring so those are communicated.

Because a particle spends most of its time in one ring, this decomposition appears simple, but deceptively so. If a particle jumps a border during a position update, this and all of the attributes of the particle needs to be sent to the appropriate processor. This is not very difficult. While all of the stars are being updated, I would keep track of which and how many total crossed a border, then each processor communicates this information to either the forward processor or the preceding processor in one lump. The problem lies in how the stars are kept track of in each processor. There is one large list of stars and their attributes. If, say, star number one hundred jumps a border, then its attributes are communicated, but now there is a hole in the list of the original processor. It would be nice if we could fill this hole with stars coming in. This is done by a data structure method called "linked lists" which requires pointers a feature of C programming language, which I use, and other languages. Even with all of this communication, the code runs faster than on a sequential machine like a VAX.

To decide how much better it runs on a concurrent machine than a sequential, one considers two factors of the efficiency: load balancing and communication overhead. For my program both turn out rather well. Because of the exponential radial divisions, each ring has about the same number of stars. This is important, because the position update dominates the calculation, and the concurrent program only runs as slow as the slowest processor. In all parts of the program much communication is necessary, but still it is small compared to the number of calculations preformed.

Conclusions

So then overall, I took a current, well-performing algorithm and made it better by making it faster and able to handle more. With it this fall and beyond, I will first duplicate work that has already been done until I am satisfied my program works, and then study new topics in galactic dynamics not covered by the other groups.

Neutrino Background and Data Trackfit in Proton Decay

by John Morrison

Faculty Sponsor: Prof. John LoSecco

Submitted September 6, 1984

Abstract

An analysis of neutrino background in the proton decay experiment is done. Both neutrinos and antineutrinos were studied. The neutrino spectrum was fit to the atmospheric spectrum. The analysis is done both without and with the propagation of pions in water. The expected number of background events per year in 3.3 kilotons of water is 2.0 +/- 0.5.

A trackfit program written for montecarlo data is modified to run on actual data from the detector.

Introduction

Several of the various Grand Unified Field Theories predict that protons should decay. In an attempt to verify or disprove those theories, Caltech has been a part of a collaboration searching for proton decay.

The proton decay detector used by the collaboration, is a large chamber filled with pure water. 2048 photomultiplier tubes are placed along the walls and on the floor and ceiling to detect Cerenkov light from the products of the decay of a proton.

The photomultiplier tubes also detect light from any other event (with sufficient energy) occurring inside the detector. These extraneous events constitute the background. The detector is deep enough in the ground to be effectively shielded from some sources of background, such as muons.

Atmospheric neutrinos cannot be shielded at all. These neutrinos enter the detector from all directions. Practically all of them pass through the detector without interacting. However, some do interact every year. Out of those interactions, a few are expected to look like proton decay events. The problem is to determine the number of neutrino events per year which look like proton decay.

Some previous work had already been done. Bradley Brock did a senior thesis last year on montecarlo simulation of neutrino background, using the Argonne data. Alan Murray also did a senior thesis on neutrino background, using data from Brookhaven National Laboratory. Mann and Kafka recently asserted, working with neutrino-deuteron data from Argonne National Laboratory, that the background was negligible (less than .1 events per year per kiloton water.)

My work was in part an extension of Murray's. Runs were made on both neutrino and antineutrino data. The data was fit approximately to the atmospheric spectrum. Neutral current events were simulated from from the data. The analysis was done first without, and later with, the propagation of pions in water.

I also modified a program, previously written for montecarlo data, to do a pass on actual data obtained from the detector. This program fitted a track and a vertex to each event, and eliminated those events whose vertices were outside a fiducial volume.

Neutrino Background

For an event to be considered a potential proton decay candidate, it must satisfy certain requirements. Several different but related criteria have been used to determine if the requirements are met. The particular variables used here

were invariant mass and momentum, as determined from the Cerenkov energy.

The invariant mass is the magnitude of the momentum four-vector. In particular, it is defined as follows:

$$M^2 = E^2 - P^2$$

where P is the magnitude of the ordinary (three-vector) momentum, and E is the energy.

The invariant mass is both a Lorentz-invariant and conserved quantity in any reaction. In an ideal proton decay event, the invariant mass is equal to the rest mass of the proton, 938 MeV. The invariant mass as detected may be somewhat off; because of scattering of the products, detection efficiency, and errors in interpreting the data.

The other variable used in defining the region of proton decay was the magnitude of the momentum. In water, the protons are approximately stationary. However, because protons are Fermions and must obey the Pauli Exclusion principle, they are forced to have some momentum. This is called Fermi motion, and the momentum due to it is bounded by approximately 250 MeV. Again, the momentum actually detected may be somewhat off.

A neutrino background event was considered to be in the proton decay range if the following hold:

$$700 \text{ MeV} < M < 1100 \text{ MeV}$$

$$P < 400 \text{ MeV}.$$

These ranges were somewhat arbitrary, and are probably wide. However, one can easily narrow them, and it helps to see what happens around the proton decay region.

The neutrino data was in the form of two files from Brookhaven National Laboratory (BNL). One file consisted of muon neutrino events. The other contained muon antineutrinos. The events were generated in a seven-foot bubble chamber, filled with neon, and then processed in some manner. In the form available to me, each event was divided up into tracks. Each track was assigned an energy, a momentum, a particle mass number, a particle charge number, a track type (leaving, interacting, decaying, or stopping), and other labels. In addition, the entire event was assigned a vertex, a total energy, and other numbers.

The BNL neutrino energy spectrum was different from the spectrum of atmospheric neutrinos seen by the proton decay detector. To fit the data to atmospheric spectrum, the range of energy from 200 MeV to 7000 MeV was divided into "bins" 500 MeV wide. The number of events per bin was predetermined by the following power law:

$$N = 163 \times E^{-1.1} \quad \text{if } E < 1000 \text{ MeV},$$

$$N = 163 \times E^{-1.8} \quad \text{otherwise},$$

where E was the minimum energy of each bin. The total number of events was chosen to be 1525. An event with energy within a certain bin was included only if that bin was not already full. If the end of the file was reached before all bins were full, the data was reused. This resulted in some events in the lower end of the spectrum being used several times.

Before an event could be considered a "good event" -- one to be included in the spectrum -- it had to pass several cuts. The first was that it have no tracks with zero momentum. The second is that it must not have any missing tracks. This was verified by checking the difference between the total energy of the event and the sum of the energies of each track. The third is that the event contain at least one muon. The fourth is that the vertex must be within a fiducial volume, to avoid contamination from the walls of the bubble chamber.

If an event passes the cuts then each track is processed. Because of pion-proton ambiguity, an interacting positive pion was randomly turned into a proton 26 percent of the time, and a leaving positive pion was turned into a proton 18 percent of the time. The momentum is kept the same, but the rest mass and the energy are adjusted.

Next, the energy and the momentum of the Cerenkov light generated by the particle in water is determined. A subroutine named CEREN, written by Dr. Cortez, is called, with the energy and the rest mass of the particle as parameters. This subroutine, using tables for the given particle, integrates dE/dx over the distance required to put the energy below the Cerenkov level, and returns the energy lost. The momentum of the light is approximately obtained by multiplying the Cerenkov energy by the unit vector of the direction of the track. This is only approximate, because Cerenkov light is a cone rather than a beam of photons all moving in the same direction.

A muon has a certain probability of decaying before exiting the chamber. Likewise, a pion has a probability of decaying into a muon, which can again decay. To account for this, the Cerenkov energy is increased by 230 MeV 55 percent of the time if the particle is a muon, and 40 percent of the time if it is a pion. The momentum is also adjusted.

The energies and momenta obtained for the tracks are summed to obtain the energy and momentum visible in the proton decay detector. If the bin corresponding to the original (total) energy of the event is not already full then the event is included in the spectrum, and the invariant mass is calculated from the visible energy and momentum.

In studying electron neutrinos and antineutrinos, we had no actual electron neutrino data. It was therefore necessary to use the muon neutrino data. The process was identical except that, at the same point where pions were changed to

protons, muons were also changed to electrons, or positrons in the case of antineutrinos, keeping the momentum the same but changing the rest mass and the energy. Also, the electrons were not allowed to decay where the muons did before.

The events that were eliminated by the requirement that an event contain one muon were neutral current events -- events which produced a neutrino instead of a muon. However, a large fraction of them were not neutrino events at all, but instead were entering neutron events. It was not possible to separate the true neutral current events from the non-neutrino events. They they had to be simulated from the charged current data.

This was accomplished in a manner similar to the simulation of electron neutrinos. This time, the muon was changed to a neutrino, or to simply make the track vanish. This created a problem, in that charge was not conserved. In running the analysis without pion interactions, I chose to disregard this. When I reran the analysis to include pion scattering, I used an ad hoc method to conserve charge.

Thirty percent of the time for neutrinos and 25 percent of the time for antineutrinos, I changed the charge of the reactants. This meant doing nothing, because only data about the products was available. The rest of the time, I lowered the charge of a pion or proton in the case of neutrinos, and raised the charge of pions for antineutrinos.

When pion propagation was included, several changes were made. After correcting for pion-proton ambiguity, if a particle was a pion CEREN was not immediately called. Instead, the particle was allowed to propagate in water. A neutral pion always decayed, to be detected as two photons. A charged pion could scatter of a proton or oxygen nucleus, charge exchange with either to become neutral, be absorbed by either, spontaneously decay, or do nothing. Which it actually did was randomly determined, based on the various cross-sections involved. The actual routine to decide was written by Professor T. W. Jones, of University College, London.

CEREN was always called for the distance the particle traveled before interacting. If the pion charge exchanged, then it decayed into two photons. If it scattered, it was propagated again in a different direction. If this direction was greater than 20 degrees away from any other track, it was considered to be a new track.

The previous provision for the random decay of pions was eliminated. Instead, if a pion decayed after being propagated, the resulting muon was allowed to decay 55 percent of the time, as before.

The results for the analyses with and without the pion scattering are listed in table one. The results are somewhat biased because, in the antineutrino runs in particular, some low energy events were counted more than once, to fit the atmospheric spectrum. It was also just recently found that half the events in the antineutrino data were really neutrino events. I was advised not to rerun the antineutrinos. Instead, this was corrected by subtracting from each antineutrino result, half the corresponding neutrino result, and then doubling.

	No Scattering, Corrected;		Scattering, Corrected	
Muon nu.	6	6	7	7
Muon ant.	17	28	10	13
Electron nu.	10	10	5	5
Electron ant.	15	20	10	15
NC. nu.	0	0	1	1
NC. ant.	0	0	2	3

Table I
Number of events in the proton decay region for the various runs. Total number in all cases: 1525.

When scattering was included, the background went up slightly for muon neutrinos and for neutral current reactions. It went down considerably for muon antineutrinos and for electron neutrinos and antineutrinos.

After multiplying each by its appropriate scale factor (6 for muon neutrinos, 2 for muon antineutrinos, 3 for electron neutrinos, 1 for electron antineutrinos, 2.5 for neutrino NC, 1.2 for antineutrino NC), and summing, we get an overall rate of 2.0 +/- .5 background events per year in 3.3 kilotons of water (the amount contained in the fiducial volume of the proton decay detector).

Trackfit of Mine Data

I started out with the montecarlo trackfit program called PACMAN, and subroutines to unpack and calibrate the mine data.

PACMAN uses a complicated iterative proceedure to find a vertex and a single track direction for an event. It starts off at a first guess for a vertex and steps its way to an approximate vertex. The resulting track is valid only for single track events, but this does not matter, because what is important is the vertex. An event is saved if the final vertex is within a fiducial volume, at least 200 centimeters away from the walls.

After the data is unpacked and calibrated, it is in the form of a 6 by 2048 array labeled X and a number representing the number of tubes. X(1,N), X(2,N), and X(3,N) contain the X, Y, and Z coordinates of the tube. X(4,N) is the time the tube fires. X(5,N) contains the "Q", or the energy of the tube. X(6,N) contains the tube number, from one to 2048. N ranges from one to the number of tubes.

The problem was to translate the program, originally written for montecarlo data, to something that could read and use this data.

The final program is very slow, and as it stands, has to be run twice for each data file: once with a large stepsize, and again with a smaller stepsize on the smaller file output, from

the first run. So far, the final program has been run on two data files. One had 264 events, out of which only three remained in the fiducial volume. The other had 931 events, of which 17 were kept.

The program was also interfaced with another program, containing three other track-fitters. When it was run, the result was that, on most events, three vertices were consistent, while one was far off. The fitter producing the inconsistent point always varied. No one fitter was, as far as could be determined, always correct.

Conclusions

Out of 1525 events for each run, the numbers of events with momentum and invariant mass in the range required for proton decay is given in table one. With proper scaling, the rate of background expected is 2.0 +/- .5 events per year in 3.3 kilotons of water. The results are somewhat biased because some events were used more than once in the low energy spectrum, and because of contamination of the antineutrino data.

The trackfit program as modified for actual data appears to give a reasonably accurate vertex for events in the detector. The track returned is valid only for single-track events. Its vertices are usually consistent with the vertices given by three other fitters. However, the program is too slow to be of much use as it stands.

References

Brock, Bradley W., "Monte-Carlo Simulation of Background in an Underground Proton-Decay Detector with Argonne Neutrino Data", Senior Thesis, Caltech, 1984.

Kafka, T. and W. A. Mann et. al., "Two- and Three-Pion Production by nu-mu -- D Reactions Near Threshold: The Implications for Nucleon Decay Experiments", Argonne National Laboratory, 1984.

Murray, Alan G., "Invariant Mass and Particle Multiplicity in Charged and Neutral Current Neutrino Interactions", Senior Thesis, Caltech, 1984.

Ormazabal, Gaston Silva, "Single Pion Production in Charged and Neutral Current Neutrino Interactions", Ph. D. Thesis, Columbia University, 1984.

Segre, Emilio, "Nuclei and Particles", 2nd Ed., Benjamin/Cummings, Reading Mass., 1977.

2:

A Pair-Spectrometer Detector for $t(d,\gamma)^5He$

Mark Pitt
Sponsor: C.A. Barnes

This report describes a Monte Carlo program developed to calculate the optimum size of a pair-spectrometer detector for an experiment to measure the $t(d,\gamma)^5He$ cross-section. The optimum size has not yet been determined, but the results of the program are compared with experimental results for cylindrical NaI(Tl) detectors.

Introduction

The cross-section for the reaction $t(d,\gamma)^5He$ (ground state) in the low energy region (0-2 MeV) has been measured several times in the past[1-4] with results varying by a factor of 25 in some cases. It is important to have accurate knowledge of this cross-section because of its potential application as a diagnostic for deuterium-tritium fusion ($t(d,n)^4He$), which is the fusion reaction with the greatest possibility for early commercial use. The gamma rays produced in the $t(d,\gamma)^5He$ reaction would serve as a way to monitor the rate of the $t(d,n)^4He$ reaction, but in order to do this the cross-section must be known accurately.

The major experimental problem in measuring the cross-section of the $t(d,\gamma)^5He$ reaction is the $t(d,n)^4He$ reaction which competes with it. The $t(d,n)^4He$ reaction dominates the other reaction by a factor of about 100,000 in the energy region considered. Therefore a way must be found to separate the 16.7 MeV gamma rays of interest from the background of 14 MeV neutrons. Ther are two ways of doing this: time-of-flight separation and the use of a pair-spectrometer detector.

The time-of-flight separation technique takes advantage of the fact that gamma rays travel at the speed of light while 14 MeV neutrons travel at about two-tenths the speed of light. It has two disadvantages though. The first is that even under optimum conditions the accelerator beam strength is reduced by a factor of ten. The second disadvantage is due to the fact that the detector must be placed far (about 50 cm) from the detector. This reduces the solid angle covered by the detector.

The other method of discrimination between the neutrons and gamma rays is the use of a pair-

spectrometer detector. With a normal, cylindrical NaI(Tl) detector there is no way of distinguishing between whether a gamma ray or a neutron interacted in the crystal. However, by making use of an interaction which only occurs for gamma rays this problem can be overcome. The interaction is pair-production. It occurs when a gamma ray passes next to a nucleus in the crystal and transforms into an electron-positron pair. The electron and positron then slow down in the material by ionization energy loss and bremstrahlung emission. When the positron comes to rest it annihilates with a near-by electron to produce two 0.511 MeV photons going in opposite dierctions. To make use of this a detector made of six hexagonal pieces of NaI(Tl) placed around a central NaI(Tl) hexagon could be used (see Fig. 1).

Fig 1.
NaI(Tl)
Hexagonal
Array

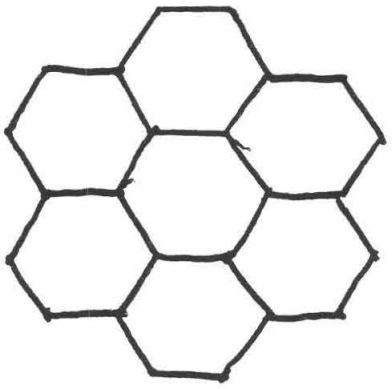

The gamma ray interacts in the central hexagon. If it pair produces then the two 0.511 MeV photons will be detected in oppositely placed hexagons. This coincidence of two 0.511 MeV gamma rays in opposite hexagons and an event in the central detector can only occur for gamma rays so the neutrons are discriminated against.

The hexagons in this detector have an optimum size for maximum gamma ray counting efficiency, and it is the goal of this project to find out what that size is. There are two competing effects which determine the optimum size. The two 0.511 MeV photons can only go so far before interacting so the central hexagon must be small enough to allow a majority of the 0.511 MeV

photons to deposit their energy in the outer detectors. On the other hand the central hexagon must be large enough that the electron and positron from the pair production event don't escape to the outer detectors and deposit energy there. This optimum size can be found using a Monte Carlo method as will be detailed below.

Theoretical Method

The Monte Carlo method used follows individual photons and all secondary particles that they produce. Photons were allowed to interact through pair production, the photoelectric effect, and Compton scattering. The probability of any of the events occcuring was sampled from the total cross sections, while the energies and directions of the secondary particles created were sampled from the differential cross-sections for each interaction. Photon histories were terminated when their energy fell below 0.100 MeV.

The electrons and positrons lost their energy through the method of logarithmic spacing. In this method the pathlength is chosen such that the energy of the particle is reduced by a constant k per step through ionization energy loss. At the end of each step the change in direction of the electron or positron from multiple scattering was calculated from a Gaussian distribution. The particles were also allowed to emit bremstrahlung photons. When the positron came to rest it annihilated and emitted two oppositely directed 0.511 MeV photons. These are the photons that make the pair spectrometer work. The electrons and positrons were followed until their total energy including rest mass fell below 0.700 MeV. At the conclusion of the calculation the following two parameters were calculated:

the full energy peak efficiency $\varepsilon_{PP}=A/N$
and the total intrinsic efficiency $\varepsilon_{TOT}=I/N$

where N=number of photon histories
I=number of histories in which the primary photon interacts at least once in the crystal
A=number of times that all primary and secondary radiation is absorbed. (In the case of the array of hexagons the triple coincidence condition must also be satisfied.)

ε_{PP} is a useful parameter because it is the one that needs to be optimized to find the best detector size. ε_{TOT} can be calculated analytically so it provides a check on the accuracy of the Monte Carlo method.

Results

The program was first run for single cylindrical NaI(Tl) detectors with isotropic point sources of gamma rays on the detector axis. This was done because there exists experimental[5] data for the photopeak in these situations and because the total intrinsic efficiency is easily calculated from the analytic expression:

$$\varepsilon_{TOT} = \frac{1}{(1-\cos\theta_{max})} \int_0^{\theta_{max}} \{1 - \exp(-\mu(E) L(\theta))\} \sin\theta \, d\theta$$

where θ_{max} = maximum polar angle subtended by the detector
$L(\theta)$ = distance traveled in the detector
$\mu(E)$ = total linear attenuation coefficient

These values are compiled in Table 1 along with the calculated one and two-escape peaks. In each case there were 5000 histories.

There were problems when I ran the program for the hexagonal array. No counts where recorded in the full energy peak for any of the sizes that I tested. I did not have time to resolve the difficulty, but I conclude that the difficulty is somewhere in the electron and positron transport. Either too much bremstrahlung is being emitted or the method of taking into account multiple scattering is not accurate. A more accurate method would be to sample the scattering angle from the Moliere[6] distribution. This will be adopted in a future version of the program.

Conclusions

The Monte Carlo program is fairly accurate in predicting the photopeaks of single, cylindrical NaI(Tl) detectors. It is less accurate in predicting the escape peaks as is evidenced by the fact that nothing is recorded when the program is run for a hexagonal array. One solution is to sample from a better multiple scattering distribution and to check and make sure that bremstrahlung radiation is being emitted in the correct quantities.

Table 1

Efficiencies for a Single Cylindrical Detector

ε_{pp} =intrinsic photopeak efficiency
ε_{tot} =total intrinsic efficiency
ε_1 =one-escape peak efficiency
ε_2 =two-escape peak efficiency

NaI(Tl) detector depth=7.62 cm= 3 inches
diameter=7.62 cm= 3 inches
distance to point source=10 cm
number of histories=5000

E(MEV)	ε_{pp} calc.	ε_{pp} exp.	ε_{tot} calc.	ε_{tot} theor.	ε_1 calc.	ε_2 calc.
0.511	0.40	0.41	0.676	0.668	------	------
0.835	0.24	0.27	0.584	0.585	------	------
1.276	0.14	0.185	0.520	0.513	------	------
2.00	0.089	0.12	0.455	0.447	0.0094	0.0054
2.75	0.071	0.093	0.436	0.423	0.032	0.016
4.00	0.064	0.065	0.412	0.406	0.045	0.017
6.00	0.059	0.042	0.410	0.405	0.060	0.017
8.00	0.039	0.029	0.392	0.395	0.041	0.014
12.00	0.021	0.020	0.437	0.429	0.026	0.007

Bibliography

[4] W. Buss, H. Waffler, and B. Ziegler, Phys. Lett. 4, 198 (1963).

[2] U.M. Bezotosnyi et.al., Soviet Journal of Physics 10, 127 (1970).

[3] A. Kosiara and H.B. Willard, Phys. Lett., 32B, 99 (1970).

[4] F.E. Cecil and F.J. Wilkinson, III, Phys. Rev. Lett., 53, 767 (1984).

[5] E. Waibel and B. Grosswendt, Nucl. Instr. and Methods 131 (1975) 143.

[6] H.A. Bethe, Phys. Rev. 89, 1256 (1953).

AN IONIZATION DETECTOR FOR THE CARBON TWELVE (ALPHA ,GAMMA) OXYGEN SIXTEEN RECOIL SPECTROMETER.

A. J. Roodman

Sponsored by Profs C.A. Barnes and B.W.Filippone

Abstract: The purpose, design, and operation of an ionization detector for the ^{12}C(alpha,gamma)^{16}O, or CTAG, experiment is described. Preliminary tests indicate that the CTAG detector has a resolution of 5% FWHM at a count rate of 1 KHz.

It is the objective of the CTAG experiment to measure the $^{12}C(\alpha,\gamma)^{16}O$ nuclear reaction to the lowest energy possible. This reaction is of astrophysical interest as its reaction rate determines the relative abundances of carbon and oxygen during the Helium burning stage of a star. It is, however, a very difficult cross-section to determine. At stellar energies the cross-section is at least 6 orders of magnitude smaller than the cross-section that can be measured in the lab. More importantly, the theoretical extrapolation is greatly complicated as a result of interference between two ^{16}O resonances with the same spin and parity. Measuring the cross-section to as low an energy as possible is a priority for just these reasons. Of course the cross-section drops off extremely quickly with energy, so to measure the cross-section at energies as low as 1 Mev (center of mass) it is vital to reduce the background as much as possible. The CTAG experiment incorporates a number of special features to do so.

These include: use of Kellogg's high current 3MV tandem pelletron accelerator, a helium gas target and carbon beam to avoid background associated with ^{13}C impurities in a carbon target, a windowless gas target to improve energy resolution, and finally a recoil spectrometer to further reduce background by requiring time-of-flight coincidence between the ^{16}O and gamma ray produced in the reaction. In other words, data is taken only when: 1) a gamma ray of the expected energy is detected in the array of NaI crystals surrounding the target, 2) a ^{16}O ion is detected in the ionization chamber, and 3) the time delay between the two signals is as expected. The recoil spectrometer consists of a magnetic quadrupole doublet to focus the beam, a Wien or velocity filter, a dipole magnet,

and the ionization detector, as shown in figure 1. The purpose of the spectrometer is to reduce the amount of carbon beam that reaches the detector to a level at which the detector can identify oxygen particles with high efficiency. This is accomplished by velocity analysis in the Wien filter and momentum/charge analysis in the magnet; the ionization detector will then reject any remaining carbon beam on the basis of its energy loss and differential energy loss measurements.

It was decided to use an ionization chamber, as opposed to say a silicon surface barrier detector, for a number of reasons. For the recoil system we require a detector that has: energy resolution under 10%, a maximum count rate of better then 10 KHz, timing resolution better than 5 nsec, an active area of at least 1.5 in diameter, all with nearly 100% efficiency. An ionization chamber meets all these criterion well[1], with the exception of timing resolution which is done with a separate multi-wire proportional counter. Although silicon detectors satisfy these requirements, they are very expensive and can easily be destroyed by high beam currents. Since ionization chambers are virtually indestructable, they are better suited for this application.

A schematic of the CTAG detector is shown in figure 2.; the components are a cathode plate, a Frisch grid, and two anode plates- a small plate to measure differential energy loss and a larger one to measure total energy. The theory behind this ionization chamber is really quite simple. The cathode is held at ground, while the grid is at +200 volts, and the anode is at +700 volts. The detector is filled with isobutane gas, which is ionized by particles entering the detector. Of course, the electrons are accelerated toward the anode which creates a small pulse in the voltage there. This pulse is proportional to the number of electrons

(which of course depends on the energy of the particle) and the voltage through which they fall. Without a grid the voltage drop will very widely with the distance between the particle's entrance position in the detector and the grid, destroying the detector's proportionality. With a Frisch grid, however, the anode plate is electrically shielded from the active region. Thus the pulse depends only on the distance between the grid and anode, which is the same for all particles, regardless of their position.[2]

Before designing the detector a number of important parameters had to be determined. First, based on a beam spot size of 1.5 inches in diameter and a maximum multiple scattering of 16 deg. for 3 Mev oxygen, the grid was placed a distance of 3.6 inches away from the cathode. Second, a polypropylene window 1.5 in. in diameter was satisfactorily stress tested at 20 torr (which incidentally was found to have a thickness of 60 microgms per sqcm, using a silicon detector). Third, at 20 torr the maximum possible range for any particle that might appear was calculated to be 10.4 in. for 16 Mev carbon, using the range tables in Ref. 3. For flexibility in future applications the detector was made 15 in. long. Fourth, a reasonable value for the electrical shielding inefficiency of the Frisch grid is 10%. Therefore 20-micron wire was spaced .5 cm apart on the grid and the anode was placed 1.2 in. from the grid,[4] to achieve 10% shielding inefficiency. Finally, the widths of the plates and grid were chosen so they would fit into a lucite frame which was designed to slide into an 8 in. diameter cylinder.

Unfortunately, the CTAG detector has not been tested with

a carbon or oxygen beam as of yet. A 90 degree Rutherford scattering experiment using a thin gold foil is planned, which will provide a test of energy resolution and count rate. The detector has, however, been tested with 5.8 Mev alpha particles from ^{244}Cm. The first test was to vary the voltages on the grid and the anode. This indicated that a grid voltage of 200 volts and an anode voltage of 700 volts will be satisfactory. Also, by varying the isobutane pressure the range of 5.8 Mev alpha particles was found to be 363.0 in*torr, which compares well with a value of 392.0 in*torr calculated from Ref. 3. The plot in Figure 3. illustrates this measurement. The two-dimensional spectrum shown in Figure 4. was taken at the voltages cited, with a gas pressure of 40 torr, no window, and the curium source mounted 1.0 inch in front of the detector. One axis is the signal from the small anode plate (delta E), and the other is from the large plate (E-delta E). The energy resolution here is only 10% FWHM, but this is in part due to energy straggling in the delta E plate, since spectrum taken with the two signals added show a resolution of 5% FWHM. A resolutionof 5% is obviously sufficient to distinguish between carbon and oxygen that vary in energy by more than 25%. Also a resolution of 10% for delta E is adequate to reject carbon background. Calculated delta E curves are shown in Figure 5.; note that for oxygen and carbon of the same momentum, dE/dx for the two ions differs from 15% to 80% for energies of 1-3 Mev (center of mass).[3] Finally, it is also possible to estimate count rate by assuming that the time it takes the electrons to drift past the grid determines the count rate. The drift velocity of electrons in isobutane is 2.5 cm/microsec,[5] so an optimistic estimate of the maximum rate is .28 MHz.

Hopefully the CTAG ionization detector will be sucessful in its role in the recoil spectrometer. As of now all evidence suggests that it will.

Acknowledgements: Let me express my sincere thanks to Profs. C. A. Barnes and B. W. Filippone, Research Fellow K. Chang, and R. Kremer for all their help in making this an interesting and rewarding summer.

REFERENCES:

1) D Shapira et. al., Nucl. Instr. and Meth. 129 (1975) 123-130.

2) P. W. Nicholson, NUCLEAR ELECTRONICS (1974) 13-20.

3) L. C. Northcliffe and R. F. Schilling, Nucl. Data Tables A7 (1970).

4) H. W. Fulbright, Nucl. Instr. and Meth. 162 (1979) 21-28.

5) K. Bethge ed., EXPERIMENTAL METHODS IN HEAVY ION PHYSICS 162.

Figure 1

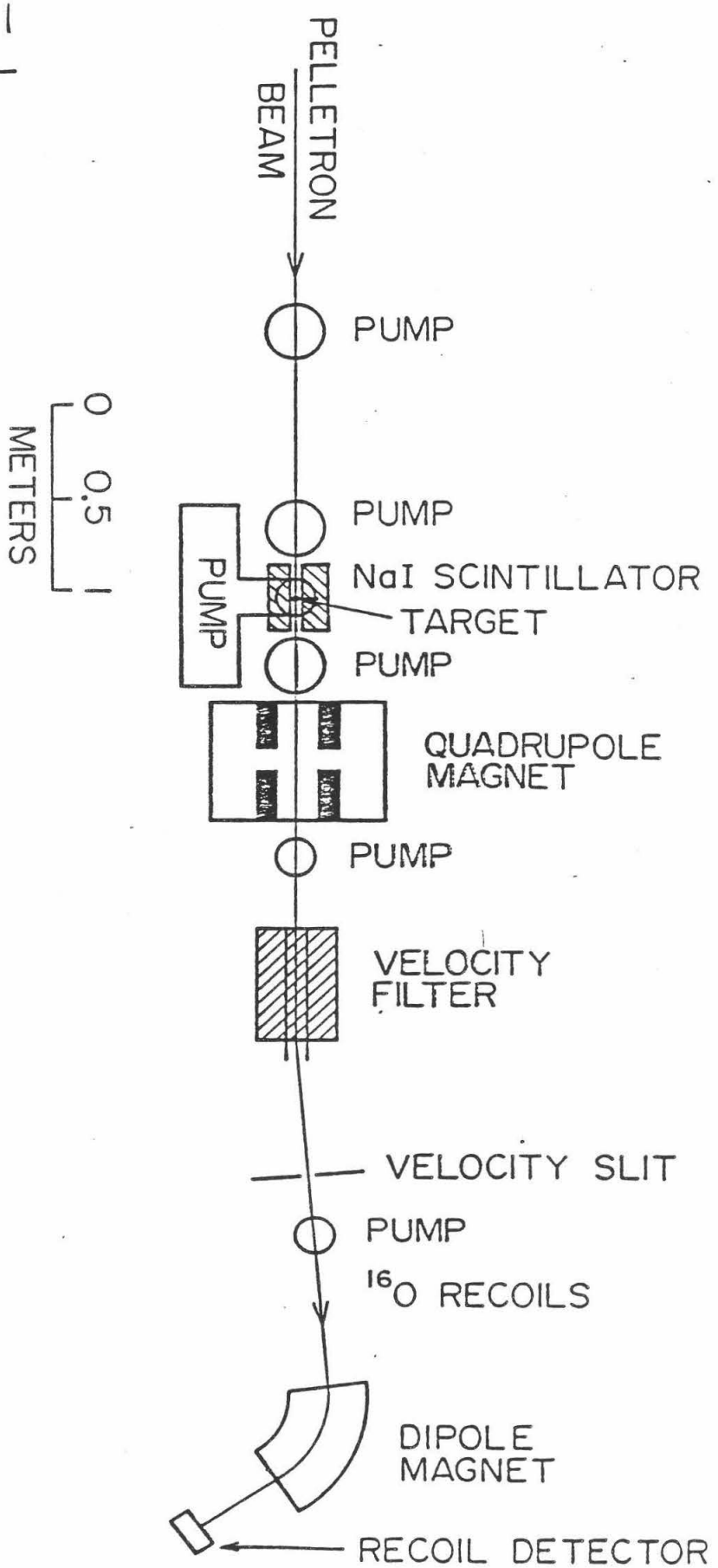

477 Fig. 1

Detector Schematic

Figure 2

Front :

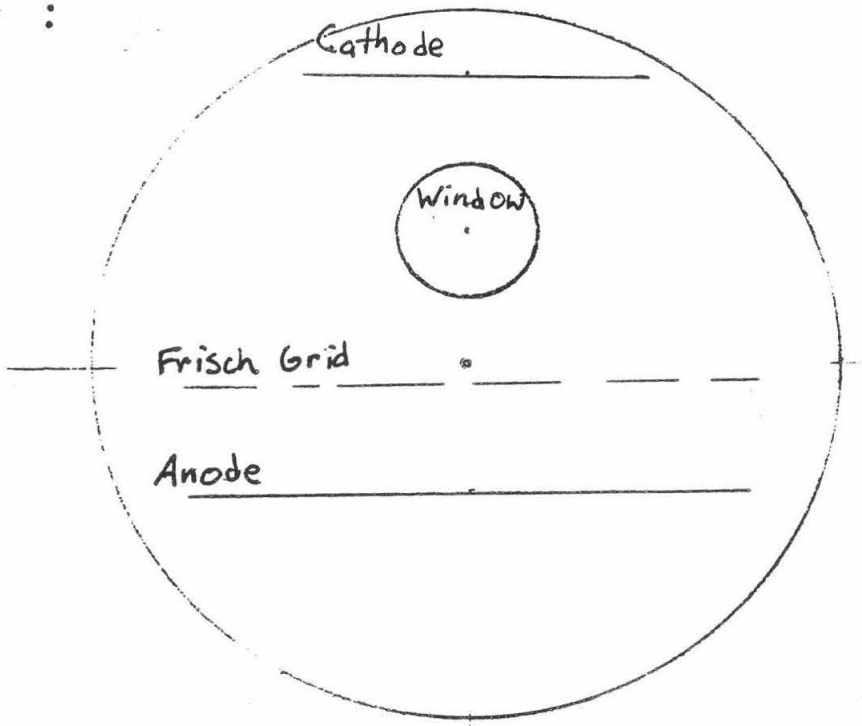

Side :

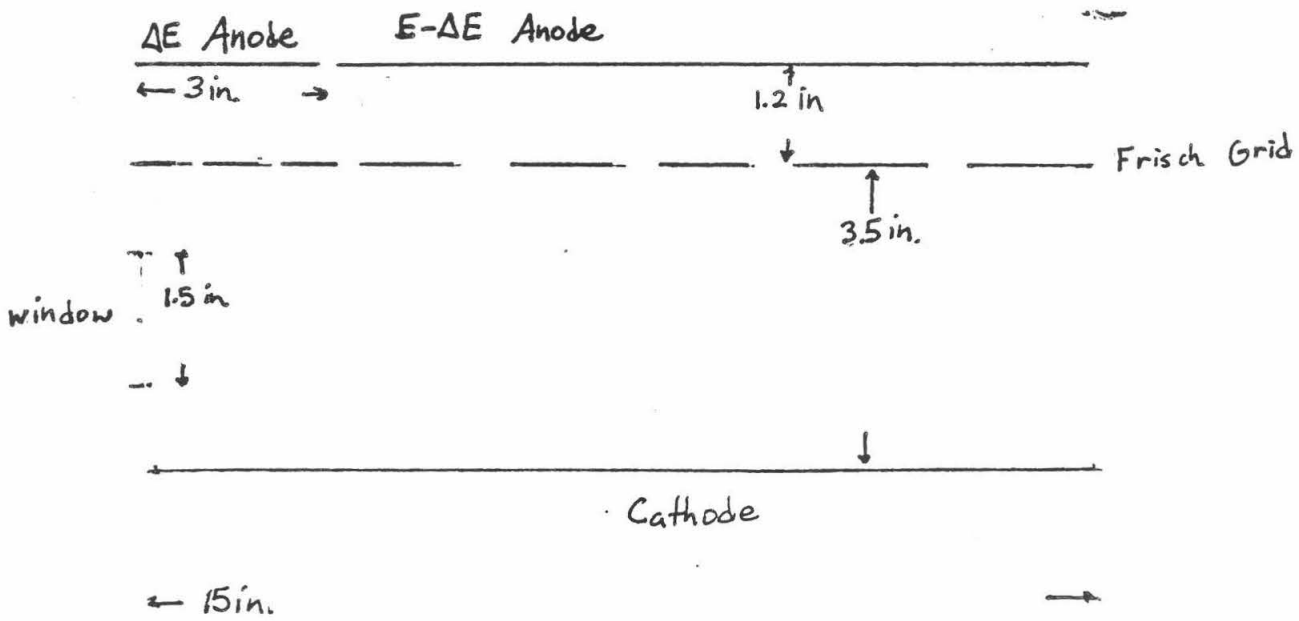

Range of 2.01 MeV. α particles Figure 5

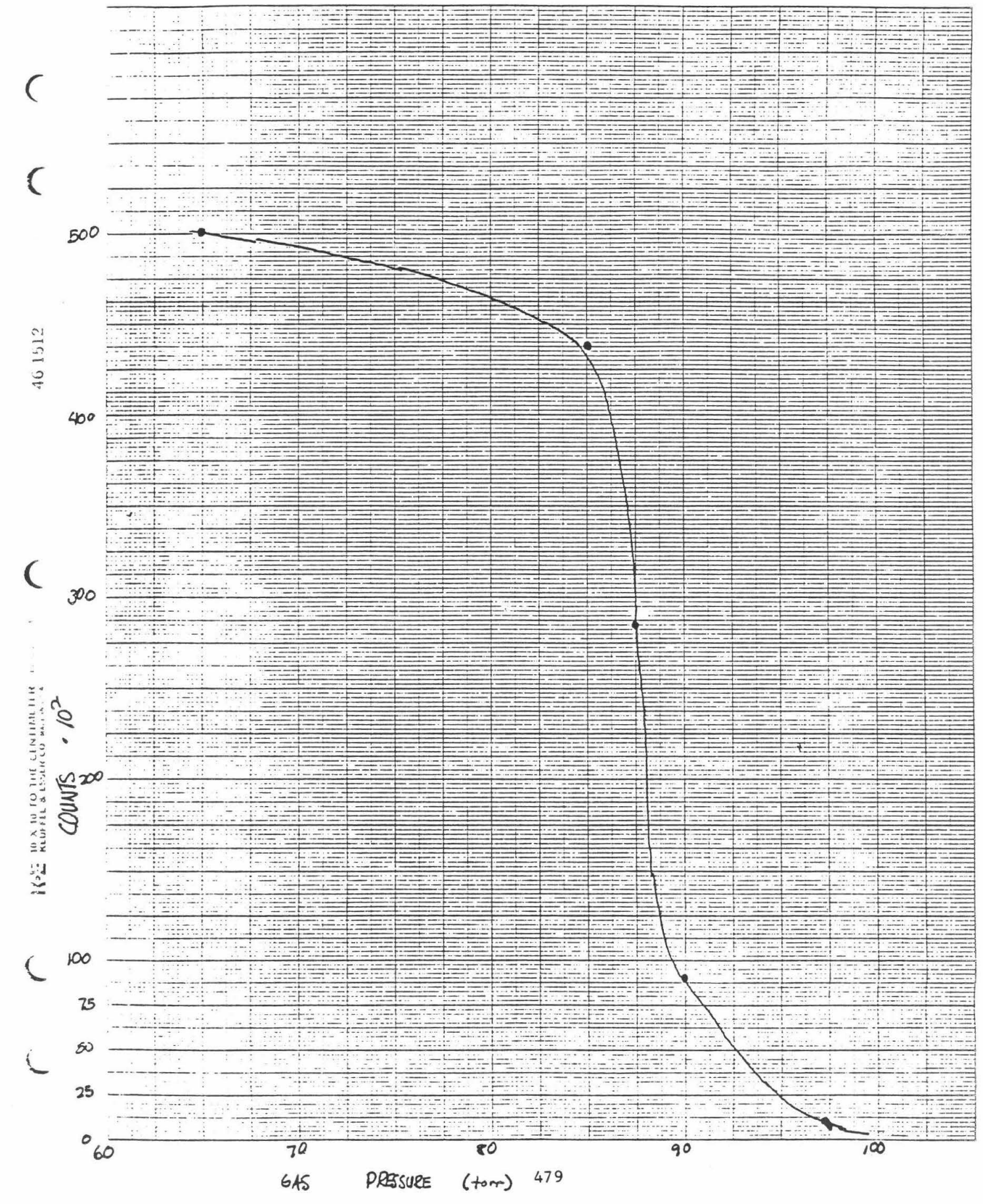

X: 1.32
CØUNTS: 183196
CENTRØID: 17.930
FWHM: 11.278

Y: 1.32
CØUNTS: 183196
CENTRØID: 8.257
FWHM: 2.710

Figure 4

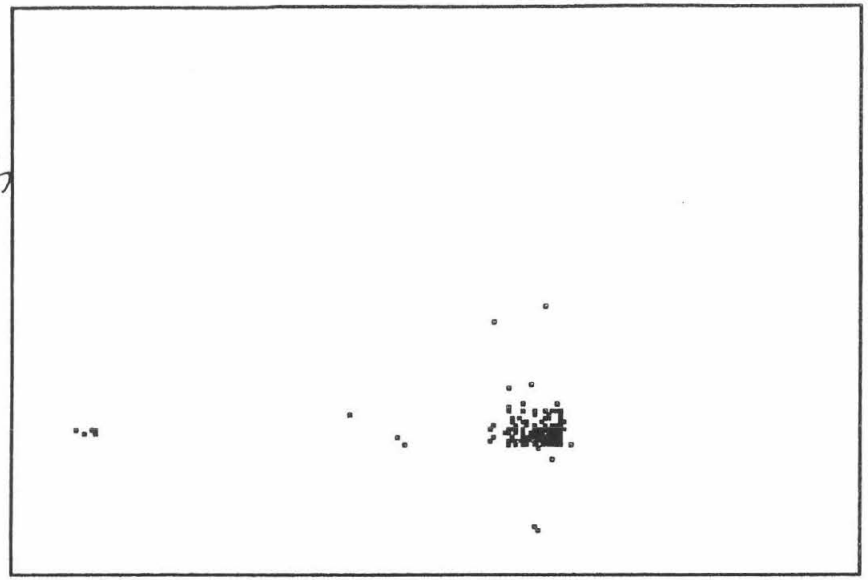

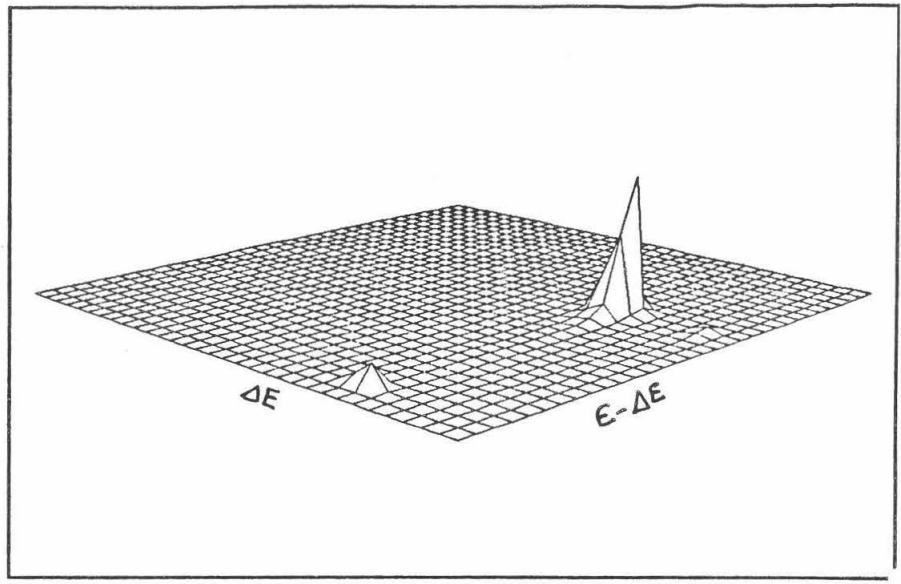

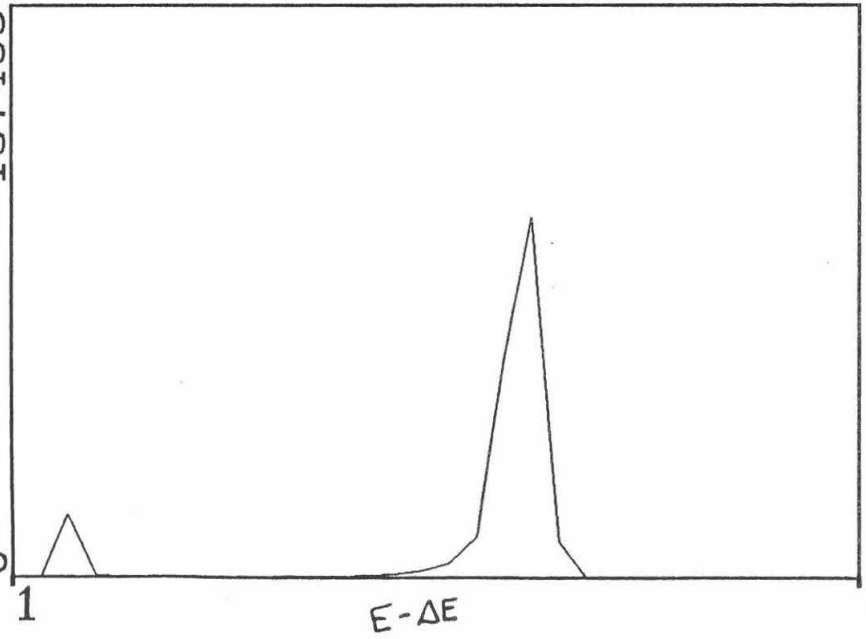

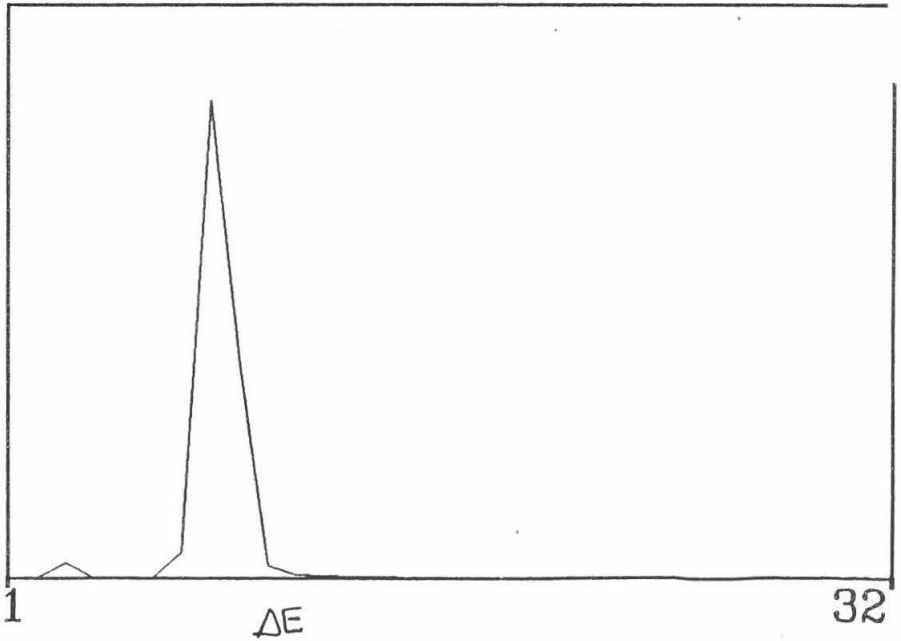

Figure 5

Isobutane

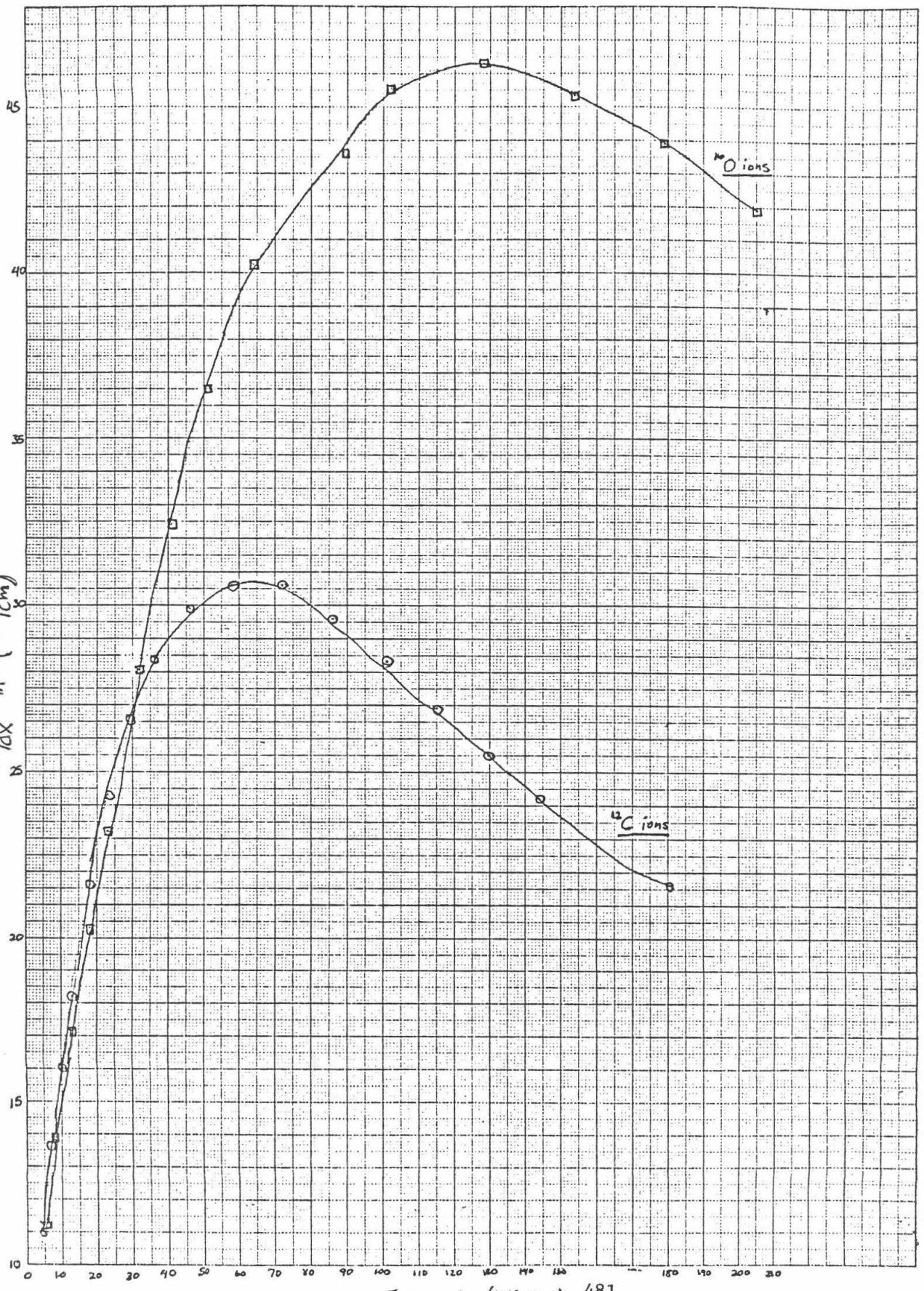

Visula-1: A Software Package for Interactive Three-Dimensional Graphics on the IBM Personal Computer

31 August 1984

Ryoji Watanabe

Faculty Sponsor: Geoffrey C. Fox

ABSTRACT

This project was an effort to produce an interactive three-dimensional graphics package for use in Caltech's computational physics lab. The design for this new package, called Visula-1, was completed. This design was only partially implemented. Continued work is planned.

Introduction

In the present project, we worked on the development of a software package for the graphical analysis and documentation of data and objects with three-dimensional extent. The package is primarily targeted for use by students in the computational physics courses, Physics 20-22, at Caltech; the basic workstation in the computational physics lab consists of an IBM Personal Computer XT equipped with an Amdek graphics adapter, an 8087 math co-processor, and 512k bytes of primary memory (RAM); an RGB color monitor; a monochrome monitor; and an IBM/Epson printer.

Functionally, this package follows in spirit the PLOT1 program* currently being used in Caltech's computational physics lab for the analysis and documentation of two-dimensional data.

---

*See G. Fox, N. Wilson, J. Pine, A. Skjellum, C. Stassen: "Computational Physics Laboratory Technical Notes-- 9 January 1984", a guidebook used in the courses Ph 20-22 at Caltech, for a description of the PLOT1 program.

Design of the Visula-1 System

Our new graphics package is called Visula-1. We describe now the overall design of Visula-1, which has been partially implemented as of this writing.

Three-dimensional data processed as input to the Visula-1 system exists initially in a text file describing a three-dimensional object. This object is composed of a series of line segments in a three-dimensional Cartesian space. To describe these line segments, we introduce an imaginary pointer, called the penpoint (because of the analogy to the act of drawing on a piece of paper with a pen), which "moves around" in the Cartesian 3-space. The movement of the penpoint is determined by the contents of the instruction file. As the penpoint moves, it is able to leave a "visible" trail just as a pen leaves a line of ink on paper; this trail makes up the line segments which compose the object.

More specifically, the instruction file consists primarily of a list of the Cartesian coordinates of points in the 3-space. This list describes the movement of the penpoint: the penpoint initially locates itself at the first point in the list; then, the penpoint moves from one point in the list to the next in a straight line, going through the entire list in this manner. Each point is prefixed by special command words that determine whether or not a trail is to be left while moving to the point.

An alternate way of specifying a single linear motion of the penpoint is as a displacement from its current location. Special command word prefixes signal such a movement; the prefix is followed by the destination point specified in a coordinate system translated so that the origin is located at the present location of the penpoint.

The primary role of the Visula-1 system is to process an instruction file and produce, on the monitor of the computer work station, a plot of the three-dimensional object described in the file. We expound here this process of mapping the three-dimensional object onto the two-dimensional computer screen.

Seven parameters, which we denote by x0, y0, z0, a, b, c, and m, determine the viewing conditions through which the plot is made.

(x0,y0,z0) specifies a point, in the same Cartesian 3-space within which the object is defined, called the viewpoint. When the plot is made, it will be as if we were viewing the object with our eye located at the viewpoint.

a, b, and c are called viewing angles. Let us imagine that we have placed a camera in the 3-space to take a photograph, to become the plot on the monitor screen, of the object. (x0,y0,z0) determines the location of the camera; a, b, and c determine how the camera is aimed (we go into more detail below).

m is called the magnification factor. It can be thought of as a parameter specifying the power of a telephoto lens attached to the camera introduced above (more detail below).

Let x, y, and z denote the axes of the Cartesian 3-space in which the object is defined. Let x', y', and z' denote axes parallel to x, y, and z, respectively, but translated so that the origin is located at (x,y,z) = (x0,y0,z0). We introduce the intersection plane and lines v and w; their orientations are shown in Figure 1.

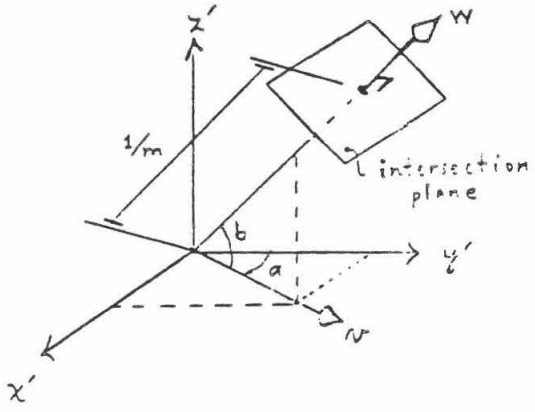

Figure 1

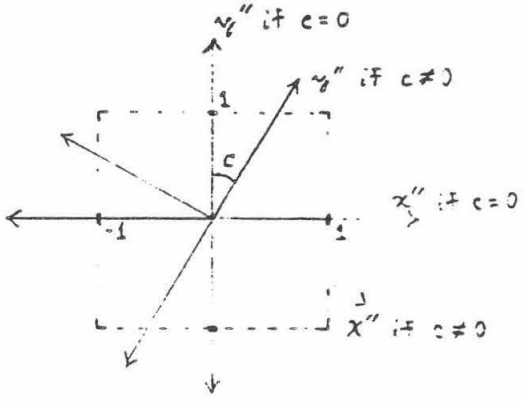

Figure 2

We now set up two-dimensional Cartesian axes on the intersection plane. Let x" and y" denote these axes. The origin of these axes is located at the point where line w intersects the plane. If viewing angle c is zero, then y" is along the intersection of the intersection plane and the plane determined by the x' axis and line v. If c is not zero, then axes x" and y" are rotated as shown in Figure 2.

A point on the three-dimensional object to be plotted and point (x0,y0,z0) are connected by a straight line; we find the point where this line intersects the intersection plane (see Figure 3). A point found in such a way is displayed on the monitor screen in a way such that (x",y") = (0,0) is mapped to the center of the screen and (1,1) and (-1,-1) are mapped to the upper right and lower left corners of the screen, respectively (actually, these bounderies are more like (1, 0.7) and (-1, -0.7) since the monitor screen is not perfectly square.

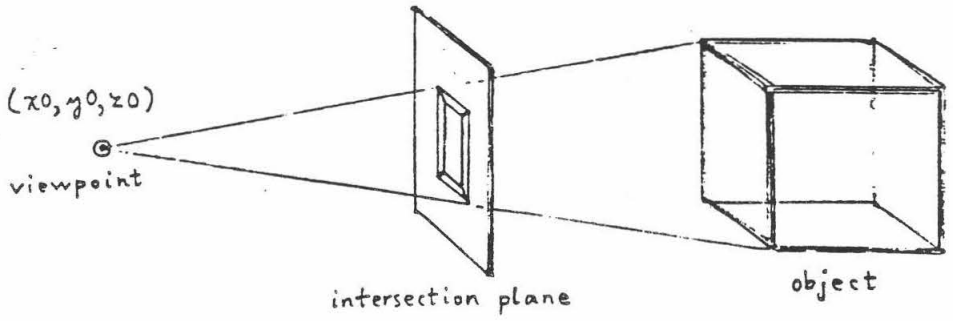

Figure 3

Visula-1 allows the viewing condition parameters to be modified interactively and rapidly to simulate being able to hold the three-dimensional object in one's hand to move and rotate it and to look at it from different angles. Plots that are produced on the monitor can be sent to the printer to yield hardcopies or can be stored in disk files for later review.

In the instruction file, besides the special command words used in describing the three-dimensional object, additional special command words facilitate the analysis and documentation of the plots of the object that are produced. These include special command words to specify the "pencolor" so that lines composing the object mapped onto the monitor are of a specified color, to add three-dimensional Cartesian axes to appear alongside the object, to define a three-dimensional boundary box which the extent of the object is not to exceed, to mark special locations on the object by small circles on the monitor where the special locations appear, and to place descriptive text on the monitor.

Current State of Implementation

As of this writing, the specifications for the Visula-1 system above have been only partially implemented. This partial implementation was written in the C programming language using the HALO graphics package for low-level graphics support and compiled with the Lattice 8086 C compiler. It runs under the PC Disk Operating System Version 2 on an IBM Personal Computer equipped with an 8087 math co-processor, an Amdek graphics adapter, and an RGB color monitor. We describe now this current implementation and its operation.

The interactive nature of the Visula-1 system establishes a requirement that the plotting process, the

mapping of the three-dimensional object onto the computer monitor screen, be fast. In trying to meet this requirement, we have introduced a process by which a description of an object, initially in the form of text in an instruction file, is encoded into a form better suited for rapid access by the plotting routine. This process is analogous to the compilation of a computer program text written in a high-level language. Because this encoding process can require a significant amount of processing, it was separated from the central plotting program to be accomplished by an independent encoding program.

The encoding program is called vs1comp. It is invoked by a command line to the operating system of the form

vs1comp file1 file2.

file1 is an instruction file, an ASCII text file. file2 is the name of the binary file to which the encoded version of the contents of the instruction file is output. A secondary task of vs1comp is to choose a set of viewing condition parameters appropriate for plotting the object; these parameters are also output to file2.

Currently, only two pairs of special command words in the instruction file are understood by the encoder. One of these appears in the line of the form

move absolute x y z.

This entry instructs the penpoint to be moved to point (x,y,z) in the Cartesian 3-space without leaving a trail.

A line of the form

draw absolute x y z

instructs the penpoint to be moved to (x,y,z) leaving a trail.

The central interactive plotting program is called vs1. It is invoked by a command line to the operating system of the form

vs1 file2.

file2 is the same file to which output was written by vs1comp above. vs1 reads the contents of file2 into memory. It then produces, on the monitor screen, a plot of the object initially described in file1 and encoded in file2; the viewing conditions chosen by vs1comp are used.

This early implementation employs a simple but primitive and inflexible scheme to interactively modify the viewing condition parameters; indeed, it was implemented mainly for testing the program. To describe this scheme, we imagine the viewpoint to be on the surface of an imaginary globe with the origin of the Cartesian 3-space at its center. Angles a and b are constantly modified, along with changes in the other parameters, so that the center of the globe is always mapped to the center of the monitor screen; angle c is always zero. The arrow kays located on the numeric section of the IBM PC keyboard move the viewpoint by modifying the "latitude" and "longitude" of the location of the viewpoint on the surface of the globe. The "+" and "-" keys decrease and increase, respectively, the radius of the globe by 1 thus moving the viewpoint toward and away from the center of the globe. the "Z" and "z" keys modify the magnification parameter, m, by a factor of 1.5 and 1/1.5, respectively.

Currently, there are no provisions for producing a hardcopy of a plot or for saving a plot in a disk file.

Outlook

We plan to continue work on the implementation of Visula-1 with the beginning of the 1984-85 school year.

PLOT1c: A Two-Dimensional Curve Plotting Program for the IBM Personal Computer

31 August 1984

Ryoji Watanabe

Faculty Sponsor: Geoffrey C. Fox

ABSTRACT

A two-dimensional curve plotting program called PLOT1 was written in 1983 for use in Caltech's computational physics lab. This program ran unreliably. In this project, we have successfully produced a reliable version of the program using the C language. The new program is called PLOT1c.

Introduction

In 1983, Professor Jerry Pine and Clare Stassen designed and implemented an easy-to-use two-dimensional curve plotting program for use in the courses Ph 20-22, Caltech's introductory computational physics labs. The program ran on the IBM Personal Computer equipped with an Amdek graphics adapter and an RGB color monitor, the basic work station in the computational physics lab. The program was called PLOT1* (without a 'c' suffixed).

The purpose of the PLOT1 program was to relieve the computational physics lab student of the tedious and mechanical task of producing, for analysis and documentation, two-dimensional plots of curves resulting from data output by computational experiments. Although PLOT1 performed many tasks that greatly expedited the work of the student, the program was too frequently seen to run unreliably and unpredictably; the use of the program significantly lost popularity.

---

*See G. Fox, N. Wilson, J. Pine, A. Skjellum, C. Stassen: "Computational Physics Laboratory Technical Notes-- 9 January 1984", a guidebook used in the courses Ph 20-22 at Caltech, for a detailed description of the PLOT1 program.

The technical nature of the majority of problems contributing to the unreliability of PLOT1 suggested that the problems were intimately tied to the programming environment in which PLOT1 was written. PLOT1 was written in a dialect of the BASIC programming language; the code was subsequently compiled to produce the final form of the program. The problems arose because of the following: PLOT1 is a large program whereas BASIC is a language best suited for use in writing very short programs; furthermore, programs written in BASIC are not ideally suited for compilation, as BASIC is, in the main, an interpreted rather than a compiled language.

In the present project, we undertook the task of completely rewriting the PLOT1 program in the C programming language. The C language was well suited for this undertaking: the development of large programs is easily managed with C; source code written in C is, from the start, intended for compilation to produce a fast and efficient program. Our main objective was to produce a program performing the functions of PLOT1 that ran much more reliably.

A Brief Description of PLOT1c*

The new program, our rewrite in C, is called PLOT1c. Equipment required to operate PLOT1c are the following: IBM Personal Computer with an Amdek graphics adapter and an RGB color monitor.

The primary output medium of PLOT1c is the RGB color monitor. The program maintains two separate pages of text and graphics that are displayed on the monitor. One of the pages, the menu page, displays information useful to the user concerning the current status of the program. The other page, the graph page, is used to display curve plots requested by the user and drawn by the program. Only one of the two pages is displayable at one time on the monitor; the user can move from one page to another quickly with keystrokes on the keyboard.

When the menu page is initially displayed, the program prompts the user for the striking of one of the designated keys (discussed below) to specify and initiate one of many actions the program can take. Some of the actions require further specification by the user; in such a case, the program will, by typing a line of instructions on

*A complete description of PLOT1c and an introduction to its use can be found in R. Watanabe: "PLOT1c User Manual--August, 1984", a document intended for distribution to students in Caltech's computational physics lab courses if PLOT1c is accepted for regular use.

the display, prompt the user for more input. When the action is completed, the menu page is again displayed and the cycle is repeated: the program prompts the user for the striking of one of the designated keys, as before, to specify and initiate the next action.

The following is a list of the designated keys, mentioned above, along with a description of the action each initiates.

'G' key (display [G]raph page) :
The graph page is displayed (replacing the menu page) on the monitor. The program then waits for the striking of nay key on the keyboard, which terminates the displaying of the graph page.

'L' key: ([L]oad data) :
PLOT1c maintains a large in-memory buffer of numbers, which is the source of data when curves are plotted by the program. The numbers in this buffer can be pictured to be arranged in columns, as in a table. Each column has associated with it a variable name and a unit name. This buffer is built up by reading disk files, prepared by the user, containing data that define one or several columns in memory when the files are read in by PLOT1c.
The 'L' key initiates the procedure to read in such disk files. The program asks the user to type in the name of the file, reads in the data from the named file, and adds the data to the buffer.

'P' key ([P]lot curve) :
The program asks the user to specify two columns in the in-memory buffer. The numbers in the two columns are paired up row-wise to produce a list of two-dimensional points. The program goes through this list of points, graphically connecting one point to the next in the list with a straight line segment, to produce an approximation of a curve. This curve is drawn on the graph page, scaled to automatically chosen variable ranges and against axes appropriately labeled and marked. If there were proviously drawn curves residing on the graph page, they are redrawn along with the new curve; thus, many curves can be placed on one graph.
The graph page is displayed to allow the user to see the newly drawn plot; the program waits for the striking of any key, which terminates the displaying of graph page.

'T' key: ([T]itle graph) :
The program prompts the user to type in a line

of text. This text is placed at the top of the graph page as a title for the graph at the next invocation of the 'P' key procedure.

'X' and 'Y' keys (set [X]- and [Y]-limits) :
The program prompts the user for information concerning how each limit in the variable ranges for the curve plots should be chosen. The user may either specify a limit to be automatically chosen by the program or manually set a fixed limit to be used unconditionally.
The 'X' key invokes the attribute setting procedure for the x- (horizontal) axis; the 'Y' key works for the y- (vertical) axis.

'C' key ([C]lear graph page) :
The graph page is cleared and the variable range limits are all set to be chosen automatically.

'H' key ([H]ardcopy) :
The program asks the user to specify the page of which a hardcopy is to be made; the specified page is sent to the IBM/Epson printer to be printed out.

'S' key ([S]ave plot) :
The program asks the user to specify a disk file name. A "snapshot" of the current graph page is saved into the named file.

'R' key ([R]eview saved plot) :
The program asks the user to specify the name of a file to which a "snapshot" of the graph page has been previously saved. The named file is read and the saved "snapshot" is reconstructed on the graph page.
The graph page is displayed to allow the user to review the "snapshot"; the program waits for the striking of any key, which terminates the displaying of the graph page.

'U' key ([U]nsave saved plot) :
The program asks the user to specify the name of a disk file to which a "snapshot" of the graph page has been previously saved. The specified file, along with the "snapshot", is deleted from the disk file system.

'F' key (change saved plot list [F]ile) :
The program maintains a list of existant files that have been written to by the 'S' key procedure and are thus holding "snapshots". A copy of this list is kept in a special disk file called the "saved plot list file". By default, the file "DEFAULT.SPL" is used as the saved plot list file. A different file can be

logged as the saved plot list file by using the 'F' key procedure.

With the initiation of the 'F' key procedure, the program asks the user to specify the name of a disk file; the named file is logged as the saved plot list file.

'V' key (display PLOT1c [V]ersion number) :

The version of the PLOT1c program being executed is disclosed on the menu page.

'?' key (on-line help) : :

The menu page is temporarily overwritten with a pageful of information that the user might find useful in operating PLOT1c. The program then waits for the striking of any key, which causes the menu page to be restored to the previous state.

An Assessment of PLOT1c

PLOT1c underwent thorough testing and debugging during its implementation. The source code defining the program grew incrementally around a small and simple kernal by adding one function at a time; each function was tested and debugged as it was added. The completed program performed without error when subjected to a variety of data and user input. We are thus confident that the primary objective of this project, that of producing a reliable program performing the functions of the program PLOT1, the predecessor, has been realized.

The programming environment within which PLOT1c was implemented afforded to us many capabilities without counterparts in the programming environment of PLOT1. Many of these capabilities were utilized to streamline the new program.

Further streamlining was achieved by seeking new and more logical means of accomplishing the functions of PLOT1.

Our experience demonstrates the inadequacy of a programming environment based on the BASIC language in supporting the implementation of a large program such as PLOT1; in contrast, the utility of the C programming language is demonstrated.

Experimental Search for Fractional Charges Produced by Relativistic Heavy-Ion Collisions

Author: Kevin Wilson

Faculty Sponser: Robert McKeown

Contributors: R. G. Milner, B. H. Cooper, K. H. Chang, J. Labrenz

W. K. Kellog Radiation Laboratory
California Institute of Technology, Pasadena, CA 91125

ABSTRACT

An experiment was performed to capture fractionally charged particles (FCP) produced in heavy-ion collisions and concentrate them on thin wires. The beam was ^{56}Fe at 1.9 GeV/nucleon, incident on a lead target. We have searched two of these wire for FCP with effective nuclear charge $Z = n + 1/3$ ($n = 1,2,3,...$) and large affinity ($\sim > 4$ eV) for negative ion (charge -2/3) formation. In addition, we have attempted to observe light (mass $\sim < 1$ GeV/c^2) FCP with $Z = 2/3$ or 5/3. No positive signal was observed, and concentration limits are reported.

In order to account for the reported observation of free fractional charge[1], a modification of QCD has been proposed by Slansky, Goldman and Shaw[2] which they call the glow model. The glow model allows that free fractionally charged particles (FCP) can be produced. Shaw et al. has speculated that the energies obtainable with the Bevelac may be sufficient for the production of FCP[2].

To test this hypothesis an experiment was done in May of 1983 at the Bevalac. There, a Pb and In target was bombarded with $3x10^{10}$ Fe- with 1.9GeV per nucleon[3]. The FCP produced by these collisions were collected and concentrated on thin wires.

We have received a few of the collection wires and have searched two of the wires for FCP. Our experimental technique is sensitive to FCP with $Z = n+1/3$ ($n = 1,2,3,4...$) which form negative ions of charge -2/3 with binding energy $\sim > 4$ eV. This covers about 20% of the periodic table of elements with fractional nuclear charge $Z = n + 1/3$[4]. Our experiment, when run at a rigidity of R = 1/3, is sensitive to FCP masses $\sim > 200$ MeV/c^2 and FCP masses $\sim <$ several hundred GeV/c^2. When run at a rigidity of R = 2/3, to search for FCP with a $Z = 4/3$ and $Z = n + 2/3$, we must insert an Aluminum window to filter out heavy ions, so we are limited to FCP mass $\sim < 1$ GeV/c^2 for these runs.

Experimental Technique

The Cu collection wires that we received from the Bevelac experiment needed to be made into suitable targets. This was done by using tweezers to wind a sample wire into a tight ball and then pressing the Cu ball into a piece of Niobium. This process minimized the handling of the wire and ~ 3/4 of the wire's surface did not touch anything except other wire surface and the Niobium. Sometime after the experiment was over, the remaining Cu fell out of the Niobium. This fortunate occurance allowed us to accurately ascertain how much Cu we had searched by weighing the sputtered samples.

The extraction of particles from the target was accomplished by sputtering the target with a 30 keV Ar+ beam in an ultra-high vacuum chamber. The sputter rate is ~ 10^{15} atoms/sec and the negative ion yield is typically 2-3 nanoamperes. We have verified that essentially 100% of the sputtered negative ions are collected and pre-accelerated by 70 keV of potential.

The negative ions then entered a tandem electrostatic accelerator which we typically operate at a terminal potential of 2 Mv. When searching for FCP with Z > 1, we use hydrogen as the stripper gas to minimize the stripping of more than one electron. For Z < 1 we use nitrogen as the stripper gas to maximize the stripping effiency for those ions. After obtaining a net positive charge, the ions are accelrated out of the tandem accelerator.

The FCP are then deflected in a transverse electrostatic field. Since FCP will have a different rigidity than normal ions, the tranverse electrostatic field is set so that only FCP enter the detector.

The detector measures the kinetic energy of each particle. Since the setting of the transverse field selects a certain charge to energy ratio, and the detector measures the energy of each particle, every particle that enters the detector can have its charge uniquely determined.

The FCP which strip from -1/3 to +2/3 in the gas stripper are degenerate in electric rigidity with the +2 charge state beam. Since the +2 beam is a heavy-ion beam, penetrating (low Z and low mass) FCP can be observed by using an absorber foil to eliminate the heavy ions. The remaining observed particles are in fact protons from hydrogen molecules breaking up in the stripper gas.

Background counts arise from rare scattering and charge exchange processes in the transport system. Lead bricks and active plastic scintillator veto counters were used to supress room background and/or cosmic-ray-associated events.

The fact that we were not always sputtering only Cu but partially hitting the niobium backing reduced the sensitivity also.

The wire samples we used were labeled Cu #5 which was kept at a +90 V during the Bevalac experiment, and Cu #12 which was kept at a -90 V during the experiment. The capturing efficiency for produced FCP of Cu #5 was estimated at .1% and Cu# 12, .25%[5].

Results

The region of expected pulse-height (the energy at which FCP are expected in the detector) was extended to account for any possible "pulse-height" defect (PHD). The PHD of the detector was calibrated by Rutherford scattering of monoenergetic ion beams and was verified to behave according to empirical

relations in the literature[5].

In table 1, we sumarize our results. Concentration limits are calculated according to two assumptions: a) total background rate in the pulse height window converted to a concentration, and b) level at which a statistically significant "peak" (2 sigma) would be evident in the pulse-height spectrum. Case (b) is valid under the assumption that the FCP are all of one species, i.e. same mass and nuclear charge. Case (a) applies if one assumes a variety of FCP species are present. The concentration limits are actually estimates since the transmission for FCP through the acceleration and transport system is inferred from the behaivior of integrally charged ions. This estimation of transmission for FCP is probably accurate to about a factor of two.

Conclusions

The results of this experiment set some constraints on the frequency of FCP production by heavy-ion collisions at the reported energies. The experiment does not eliminate the glow model as a possible modification to QCD, but requires that the theory have parameters that disallow production of FCP by heavy-ion collisions with the energy of 1.9 GeV/nucleon at a greater rate than our experimental limits. A more sensitive experiment is needed to determine whether it is even possible to produce FCP at the energies obtainable at the Bevelac.

We have plans to examine two more samples from the Bevelac experiment for FCP by searching for FCP that come off the targets as positive ions.

Glossary of Terms

Rigidity - The ratio of the net charge of the particle to its kinetic energy.

Sputter - The emmission of atoms (charged and nuetral) from a sample when bombarded by a suitable atomic beam.

Stripping of electrons - This refer to the process of taking electrons from an atom or molecule.

Tandem Electrostatic Accelerator - A tandem accelerator works by keeping its terminal at a fixed positive potential. Negative ions are accelerated up to the terminal potential, there they are stripped of electrons so that they have a net positive charge. They are now being repelled by the terminal potential, so they are accelerated back to ground potential.

QCD - Quantum Chromo Dynamics is a physics theory that explains the strong force.

References

1. LaRue et al., Phys. Rev. Lett. 46, 967 (1981).

2. Shaw and Slansky, Phys. Rev. Lett. 50, 25 (1983).

3. Shaw, Invited talk at the Sixth Heavy Ion Study and Workshop on Anomolies, Technical Report #83-60 (1983)

4. Lackner et al., Phys. Rev. D28, 28 (1983).

5. Shaw, Private correspondence.

Table 1

Results for Bevalac Cu

Polarity	R	Z	Stripper	Integral Counts: FCP/Wire · 1/f	Integral Counts: FCP/Wire	Integral Counts: FCP/Cu Atoms	Integral Counts: FCP/Fe-Pb collision	Peak Counts: FCP/Wire · 1/f	Peak Counts: FCP/Wire	Peak Counts: FCP/Cu Atoms	Peak Counts: FCP/Fe-Pb collision
+90V	1/3	n+1/3	H_2	$163 \cdot \frac{1}{f}$	2700	1.1×10^{-16}	1.4×10^{-4}	$26 \cdot \frac{1}{f}$	433	1.8×10^{-17}	2.2×10^{-5}
-90V	1/3	n+1/3	H_2	$1000 \cdot \frac{1}{f}$	16700	7×10^{-16}	3.5×10^{-4}	$251 \cdot \frac{1}{f}$	4200	1.8×10^{-16}	8.8×10^{-5}
+90V	1/3	1/3	N_2	$11.6 \frac{1}{f} \cdot \frac{1}{f_-}$	$77 \cdot \frac{1}{f_-}$	$3.3 \times 10^{-18} f_-^{-1}$	$4 \times 10^{-6} \frac{1}{f_-}$	$11.6 \frac{1}{f} \frac{1}{f_-}$	$77 \frac{1}{f_-}$	$3.3 \times 10^{-18} \frac{1}{f_-}$	$4 \times 10^{-6} \frac{1}{f_-}$
-90V	1/3	1/3	N_2	$50 \frac{1}{f} \cdot \frac{1}{f_-}$	$335 \frac{1}{f_-}$	$1.4 \times 10^{-17} \frac{1}{f_-}$	$7 \times 10^{-6} \frac{1}{f_-}$	$50 \frac{1}{f} \frac{1}{f_-}$	$335 \frac{1}{f_-}$	$1.4 \times 10^{-17} \frac{1}{f_-}$	$7 \times 10^{-6} \frac{1}{f_-}$
+90V	2/3	n+2/3	H_2	$5800 \frac{1}{f}$	97,000	4×10^{-15}	5×10^{-3}	$272 \frac{1}{f}$	4500	1.9×10^{-16}	2.4×10^{-4}
-90V	2/3	n+2/3	H_2	$36{,}000 \frac{1}{f}$	600,000	2.5×10^{-14}	1.2×10^{-2}	$1707 \frac{1}{f}$	28,000	1.2×10^{-15}	6.0×10^{-4}
+90V	2/3	4/3	N_2	$35{,}000 \frac{1}{f}$	2×10^5	1×10^{-14}	1.2×10^{-2}	$2500 \frac{1}{f}$	16,500	6.9×10^{-16}	8.7×10^{-4}
-90V	2/3	4/3	N_2	$110{,}000 \frac{1}{f}$	7.3×10^5	3×10^{-14}	1.6×10^{-2}	$17{,}000 \frac{1}{f}$	1×10^5	4.7×10^{-15}	2.4×10^{-3}

R = rigidity Z = nuclear charge f = transmission $10^{-3} < f_- < .1$

STUDY OF EXTRAGALACTIC HI AND CO IN IRAS GALAXIES

MIN SU YUN

FACULTY SPONSOR : NICK SCOVILLE

ABSTRACT : In order to explore their nature, the galaxies that were detected with excess infrared luminosity by the Infrared Astronomical Satellite (IRAS) have been studied at the wavelengths of 21cm (neutral hydrogen emission, HI) and 2.6mm (carbon monoxide emission, CO) using the 40m and 10m radio telescopes of the Owens Valley Radio Observatory (OVRO). At 21cm, 25 out of 53 observed IRAS galaxies -- 6 only marginally -- were detected while at 2.6 mm 16 out of 26 observed IRAS galaxies were detected. HI observations have hinted that many of these IRAS galaxies have had a history of galactic interaction. From CO observation, some correlation has been sighted between the CO emission and far-infrared emission among these galaxies.

I. INTRODUCTION

The Infrared Astronomical Satellite, which was developed and operated by the Netherlands Agency for Aerospace Programs, the U.S. National Aeronautics and Space Administration, and the U. K. Science and Engineering Research Council, surveyed various strong infrared sources in the sky at 12μm, 25μm, 60μm, and 100μm wavelength (Soifer et. al., 1984). From a series IRAS circulars published, galaxies with high 100μm flux were identified and were studied to determine their nature. It is believed that the infrared emission arises from dust heated by newly-formed young stars. Since correlation between the existence of HI and star formation has been suspected by many astronomers, HI study of IRAS galaxies was considered a good method to explore the nature of these galaxies. In addition, HI study also provides information about many physical properties of these galaxies such as radial velocity and even relative mass and size.

An even stronger relationship between the molecular gas and star formation has been suspected in recent years. Being the second most abundant molecular gas next to molecular hydrogen -- molecular hydrogen emission is practically not observable due to its symmetric molecular structure -- CO could provide much information on molecular gas in a galaxy.

II. HI OBSERVATIONS

The 40m telescope of the Owens Valley Radio Observatory was used for the observation of 21cm HI emission. With 20 arcminute beam and 50°K system temperature, 100KHz Acousto-optical Spectrometer (AOS) allowed me to detect objects up to 10,000 km/sec in radial velocity. However, strong baseline and interference noise limited the sensitivity of the telescope to about 0.02 Jy (1 Jy = 10^{-26} W m^{-2} Hz^{-1}) and made it very difficult to detect any source with radial velocity greater than 5,000 km/sec. All data were processed using VAX 11/40 computers at OVRO and Robinson.

A total of 53 IRAS galaxies and 14 non-IRAS, reference galaxies were observed in a period of three weeks with integration time between 1 and 3 hours. At 21cm, 19 IRAS galaxies -- 16 with previously known redshift -- were positively detected while additional 6 were detected only marginally. Observed for calibration purpose, 13 non-IRAS galaxies were also positively detected. Many of the undetected IRAS galaxies are suspected of having radial velocity larger than 5000 km/sec. Many of these IRAS galaxies are described as 'interacting', 'peculiar', or 'integral', and some of the HI profiles revealed some signs of disturbance.

Possible correlation between HI and far-infrared (100μm) emission has been sought by comparing various physical properties obtained from the HI observations. The most interesting finding concerns a relationship called the Fisher-Tully relation. The Fisher-Tully relation is a correlation between the absolute magnitude and the width of the HI profile of galaxies irrespective of their morphological type (Fisher and Tully, 1977). Although I only have limited number of data points, this correlation is observed with some scattering of points among the reference galaxies (See FIGURE 1). However, a much greater scattering is observed with no apparent correlation among the IRAS galaxies. Although it is not so apparent, it also appears that IRAS galaxies have relatively lower absolute magnitude compared with reference galaxies. Neither of these observations may turn out to be 'real' because of large uncertainties in measurements and small number of data points. Nevertheless, some conjectures have been made to explain these findings. The Fisher-Tully relation deals with the HI profile width at 20% peak while the width at 50% peak is used for this study. If galaxies have normal Gaussian-shape profile, it should not matter which width is used. If a galaxy is disturbed by the interaction with other companion(s) or by other means, however, the distortion of HI profile may result in the deviation away from normal distribution. The scattering and low luminosity can also be explained by the galactic dynamics of these galaxies. During a close encounter with another galaxy, a large portion of the total energy of the galaxy is shifted to the kinetic energy of the galaxy, leaving relatively less energy for internal dynamics. Considering that these galaxies have high infrared emission, it is also possible that the relatively low luminosity is due to a large amount of dust in these galaxies. A study with a larger sample and higher quality data is necessary to test these observations. A resonable correlation between the apparent HI mass and photographic magnitude was observed in both cases of IRAS and non-IRAS galaxies (See FIGURE 2). No correlation between HI and 100μm flux was observed.

III. CO OBSERVATIONS

The 10m telescope of the Owens Valley Radio Observatory was used for the observation of 2.6mm (J = 1 → 0) wavelength CO emission. The telescope has 65 arcseconds beam with effective system temperature on the sky of about 1000°K. 500MHz (about 1200 km/sec) bandwidth was used for the AOS observation. Bad weather reduced the sensitivity of the telescope and produced bad baselines. Due to high noise-level, only 2 sources were positively detected with signal to noise ratio greater than 2. Only marginal detection was made among 12 other galaxies. IC342, M51, and M82 were also observed for calibration. IRAS galaxies that have been already known to be detected were omitted from the observation due to limited observation time -- 2 weeks. An average of 2.5 to 3 hours of actual integration time was used on each source.

An interesting observation has been made by plotting the CO flux and 100μm flux of these galaxies (See FIGURE 3). There appears to be two different kinds of relationship between CO flux and 100μm flux. The galaxies along the steeper slope in general have a sharp peak with narrow profile width and are face-on while the galaxies along the moderate slope in general have wide profile width and are edge-on. It was suggested by Professor Scoville that this difference must be largely due to the inclination of the galaxies. But the lack of intermediate galaxies and the extent of the difference between two types seem to be more than inclination alone can explain. I speculate that this could be due to more fundamental differences in their galactic dynamics such as localized intense activity versus wide spread activity involving a large area.

A fairly good correlation has been found between the molecular hydrogen column density -- derived from CO observation (Young and Scoville, 1982) -- and 100μm flux (See FIGURE 4). The molecular hydrogen mass and 100μm luminosity seem to show some correlation with considerable scatter (See FIGURE 5). These correlations all support the idea that the high infrared emission from these IRAS galaxies are mainly due to the existence of large molecular clouds and vigorous star-forming activity.

IV. CONCLUSIONS

Some evidence of the history of galactic interaction has been found among many IRAS galaxies from HI observations although no direct relationship between HI and far-infrared emission was found. CO observations of IRAS galaxies seem to suggest that the existence of large amounts of molecular gas in these galaxies are directly related, if not responsible, for the large far-infrared flux. From both HI and CO observations, it is cautiously speculated that some galactic interaction has somehow resulted in a greater amount of molecular gas and a higher rate of star formation. The data obtained from the CO observations will be used in the near future to map the CO emission of some of these IRAS galaxies for better understanding of their nature. It would definitely be a good idea to test the findings of this study with more and higher quality data.

I would like to thank Professors Nick Scoville and K.Y. Lo for their valuable advice and assistance throughout the study. I also thank everyone at the Owens Valley Radio Observatory for their good cooperation and help.

V. BIBLIOGRAPHY

G. D. Bothun et. al., "The Distance and Properties of A Sample of ScI Galaxies", Astrophysical Journal, V. 278, 475-485 (1984)

J. D. Kraus, Radio Astronomy, Chapter 3, McGraw-Hill, New York (1966)

P. Nilson, Uppsala General Catalog of Galaxies, Uppsala Offset Center AB, Uppsala (1973)

M. S. Roberts, Galaxies and Universe, "Radio Observations of Neutral Hydrogen in Galaxies", p. 309-357, The University of Chicago Press, Chicago (1975)

A. Sandage and G. A. Tammann, A Revised Shapley-Ames Catalog of Bright Galaxies, Carnegie Institute of Washington (1981)

N. Scoville and J. S. Young, "The Molecular Gas Distribution in M51", Astrophysical Journal, V. 265, 148-165 (1983)

G. S. Shostak, "An HI Study of Scd Galaxies", Astrophysical Journal V. 198, 527-536 (1975)

J. Smith, "The Far-infrared Disk of M51", Astrophysical Journal V. 261, 463-472 (1982)

B. T. Soifer et. al., "Infrared Galaxies in the IRAS Minisurvey" Astrophysical Journal, V. 278, L71-L74 (1984)

R. B. Tully and J. R. Fisher, "A New Method of Determining Distances to Galaxies", Astronomy and Astrophysics, V. 54, 661-673 (1977)

J. S. Young and N. Scoville, "Extragalactic CO: Gas Distribution Which Follow the Light in IC342 and NGC 6946", Astrophysical Jounal, V. 258, 467-489 (1982)

Evidence for Non-Axisymmetric Nuclear Bulges in Spiral Galaxies

Dennis Zaritsky

Dr. K.Y. Lo - Sponsor

SURF 1984

ABSTRACT

Twelve spiral galaxies were studied and all have non-axisymmetric nuclear bulges. For those with the larger bar-like feature, NGC 6814, NGC 4254 and NGC 6951, the ratio of tangential force caused by the oval distortion to the radial force is greater than 10% at 5 kpc from the center, for NGC 488, NGC 7177, M 51 and NGC 7331 the ratio is between .1 and .01 at 1 kpc from the center and for NGC 628 and NGC 6946 the ratio is 0.0 at any distance greater than 1 kpc.

I. Introduction

Galactic structure is an active area of investigation. In terms of morphology the three main types of galaxies are ellipticals, irregulars and spirals. The spirals are classified as either normal or barred, and consist of a nuclear bulge, and a disk that contains spiral arms. The barred spirals have clearly visible stellar bars in the nuclear region.

Several studies have shown that in the barred systems the bar is able to generate density waves (Sanders and Huntley, 1976). Oval bulges and other deviations from axisymmetry are also thought to be able to generate the density waves (Kormendy , 1982).

The purpose of this research project was to identify non-axisymmetric mass distribution in normal spiral galaxies. This is interesting because it implies non-circular motion in the nuclear region, which may account for enhanced star formation activities in galactic nuclei. In addition, it may be the driving mechanism of spiral density waves, which are thought to explain the spiral arms (Lin and Shu, 1964).

II. Procedure

The galaxies were chosen to be close to face-on and bright, so that they are easier to analyze. All the pictures were taken on the Palomar 60 inch telescope with the charge-coupled device (CCD) camera. Gunn i and z, and Johnson V filters were used, their effective wavelengths are 8250,10000 and 5550 angstroms respectively. The i and z filters were used because at the longer wavelengths light is less affected by interstellar dust.

The images were then flat fielded to correct for the response of the individual detectors of the CCD. The Galaxy Aperture Surface Photometry computer package(GASP) was used to analyze the pictures. The process consists of subtracting the background, which is calculated by averaging the values of pixels on the edge of the frame. A check for background

gradients, to assure that the background is nearly constant across the image, revealed no systematic deviations above the standard deviation of the value. The program then finds equal brightness contours(isophotes) (Fig. 2) and fits ellipses to them. From the fitted ellipses position angle, axis ratio and mean brightness are calculated.

To tranform this data to the three dimensional brightness distribution and to calculate the quadrupole moments, the last tipped isophote with respect to the isophotes of the disk, and the bulge luminosity are needed. A tipped isophote can be a result of real twists, changing axis ratio or dust. The twists are discrete jumps in position angle which happen at the end of bars. The changing axis ratio results in a continuous change in position angle (Fig. 1). The dust causes back and forth changes in position angle. The effect of dust has been lessened in several ways. First, the images are in the i and z filters. Second, the images were visually examined to detect whether dust interefered. Third, the brightness profile is used as a guide because it deviates from the expected profile when dust interefers. Fourth, the bulge luminosity dominates the disk luminosity because the brightness of the bulge portion was always more than three times greater than that of the disk for the last tipped isophote. Fifth, when in doubt a smaller isophote was chosen.

To calculate the bulge luminosity, the i-band surface brightness profile of the galaxy was decomposed into the disk component and the bulge component. An exponential function was fit to a section of the image where the disk dominates. The function was then extrapolated and subtracted from the bulge (Boroson 1981).

A method to convert the surface brightness distribution into a volume brightness distribution was developed by Stark. Assuming that the bulge consists of similiar ellipsoids that have a different position angle than that of the disk, one axis is placed perpendicular to the plane of the disk, and the other according to the change in position angle between the bar and the disk, and the axis ratio of the last tipped isophote. The third degree of freedom is unknown and a family of one-parameter solutions is calculated.+ For this project the least elliptical(lowest axis ratio, a/b) solution was used.

The mass distribution is found by assuming that the bulge fits de Vaucouleur's surface brightness distribution,

$$B(r) = 10^{[-3.33(r^{1/4}-1)]},$$

and by assuming that the bulge consits of similar concentric ellipsoids with a constant mass to light ratio of 2.4. The mass to light ratio was derived by adopting a mass to light ratio of 20 in the B-band, which is converted to 2.4 for the i filter by assuming a (B-i) color index of 3. The de Vaucouleur's law did fit well to the disk subtracted bulges. The values of the diagonal terms of the inertia tensor were derived and from those the quadrupole moments were calculated (see Stark, 1977).

+ For a complete analysis of this technique see Stark, 1977.

III. Results

The measured and computed quantities are listed in Table 1. The position angle data shows three types of patterns. A continuous change, which is a result of the triaxial bulge, assuming concentric ellipsoids, a sharp sudden change, which is a result of a bar-like feature, and an up and down pattern, which is a result of dust. In NGC 6951, which is a barred spiral, the position angle shows a continuous change and then levels off into a plateau characteristic of a bar (Fig. 3). The same is seen in NGC 4254,and to a lesser extent in NGC 6814,M51 NGC 7331, NGC 7177, NGC 628, NGC 7217, and NGC 488. The up and down pattern occurs for example in NGC 6814 (Fig. 3). For this galaxy, the plateau level is most likely somewhere betweeen the maximum and minimum of these values. The error bars in figure 3 are only estimates of the error that result from the ellipse fitting. They do not include the effects of dust. The open squares represent the points were the fit to the isophote was not good. However, since most of these points follow the pattern fairly well it is reasonable to assume that they are on the whole not too far off.

All of the bulges of the galaxies analyzed display continuously twisting isophotes. This implies that they are triaxial and therefore, non-axisymmetric.

While Stark's approach is derived for a bar, we adopted it for all galaxies with a bar-like feature in this study as a first approximation to quantitatively estimate the deviation from axisymmetry. For those galaxies, the ratio of non-radial to radial acceleration, F_Q, is listed in Table 1. A ratio greater than 4% at 5 kpc from the center is thought to be sufficient to generate the arms(Sanders 1976). A ratio that is large enough is seen in NGC 6951, NGC 4254 and NGC 6814. A significant ratio is seen in M51 of 11% at 1 kpc. This agrees with the measurements made from tangetial streaming data, of 15 to 20 percent at 1.2 kpc (Tully, 1976). In NGC 6946 and NGC 628 an insignicant amount of tangential force is produced by the bar. All these calculations have been done for bars that are smaller than those in the galaxies since it was impossible to identify the last tipped isophote because of the dust, therefore, all the results are lower estimates.

The strength and size of the bar do not correlate directly with the Hubble classification. For example, NGC 4254 which is an Sc type galaxy has a tangential to radial force ratio of 11% at 5 kpc, on the other hand, NGC 488, which has a larger bulge and is an Sb type galaxy, has a tangential to radial force ratio of 4%. Other Sc galaxies, such as NGC 6946 and NGC 628, have a ratio of 0.00. While galaxies with very small bulges are not likely to have a strong bar, a large bulge does not imply a strong bar.

IV. Conclusion

In review, there are several items of importance. First, all the spiral galaxies that were observed show deviation from axisymmetry in the nuclear region. Second, galaxies that have not been classified as barred can have a 5% tangential to radial force ratio, which is large enough to force the gas into non-circular motion. Third, the size and strength of the bar does not correlate directly with Hubble type.

Future investigations should include a wider sample of galaxies and other types of measurements such as velocity and velocity dispersion

measurements. While some of the theoretical investigations show that a bar or oval distortion in the nucleus of spirals can be a generating mechanism for the arms, more investigation is needed.

ACKNOWLEDGEMENTS: First, I would like to thank the SURF program for making this project possible. I would also like to thank Dr. Lo for his time and effort, Dr. J. Cohen for giving me some of her pictures and using some of her observation time for my project, K. Shortridge for all his help with the computers and A. Stark for sending his notebook.

Figure Caption

Figure 1: A two dimensional example of how isophotes twist because of changing axis ratio. The top panel is face on and the bottom one is inclined. The isophotes with the larger ellipticites have their position angle rotated towards the dashed line less than the isophotes that are rounder. This effect will cause the twisting isophotes. This is analogous to the three dimensional triaxial case.

Figure 2: Isophotes for M 51.

Figure 3: Position angle, axis ratio and surface brightness data for four of the galaxies analysed. The open boxes represent points for which the ellipse fit was not good. The arrows on the right hand side of the position angle graphs represent the position angle of the disk of the galaxy.

Table 1 Data of the Twelve Studied Galaxies

Name	1	2	3	4++	5	6	7
	Type	D (Mpc)	r(max) (kpc)	i (deg.)	ϕ (deg.)	$\triangle$PA (deg.)	F_Q
NGC 6946	Sc(s)III	4.7	.3	30	32	32	0.0
NGC 6814	Sbc(rs)I-II	22.4	3.2	10	18	35	.16
M 100	Sc(s) I	21.2	---*	28	—	—	—
M 51	Sbc(s)I-II	6.0	.4	20	24	24	.11(@1kpc)**
NGC 4254	Sc(s)I/3	31.5	3.0	25	8	36	.11
NGC 6951	Sb/SBb(rs)I.3	22.4	4.2	30	33.5	56	1.82
NGC 3810	Sc(s)II	15.5	---*	50	—	—	—
NGC 7331	Sb(rs)I-II	4.2	1.6	74	38	4	.01
NGC 7177	Sab(r)II.2	15.0	.9	60	40	64	.09(@1kpc)**
NGC 628	Sc(s)I	10.6	.2	22	40	16	0.0
NGC 7217	Sb(r)I-III	16.3	---***	35	—	—	—
NGC 488	Sab(rs)I	47.6	1.9	24	71	18	.04
M 31+	SbI-II	.69	2.2	13	32	10	.04

column 1 - Classification according to Revised Shapley-Ames Catalogue

column 2 - Distance in Mpc assuming H = 75 Mpc/km/sec

column 3 - Semi-major axis of the bar-like feature in kpc.

column 4 - Inclination of the galaxy to the line of sight in degrees.

column 5 - The value of the third parameter for the solution used.

column 6 - The difference between the position angle of the isophotes of the bar and those of the disk.

column 7 - Ratio or tangential to radial force at 5 kpc unless where noted differently.

+ M31 from Stark, 1977
++ Inclination and distance from refences 5,12,13,14,15,16,17,18,24
* Dust interferes too much to make measurements.
** The value of the force ratio was calculated at 1 kpc for M 51 for comparison
with Tully's data and it was calculated at 1 kpc for NGC 7177 because the galaxy is not bright at 5 kpc.
*** No identifiable bar.

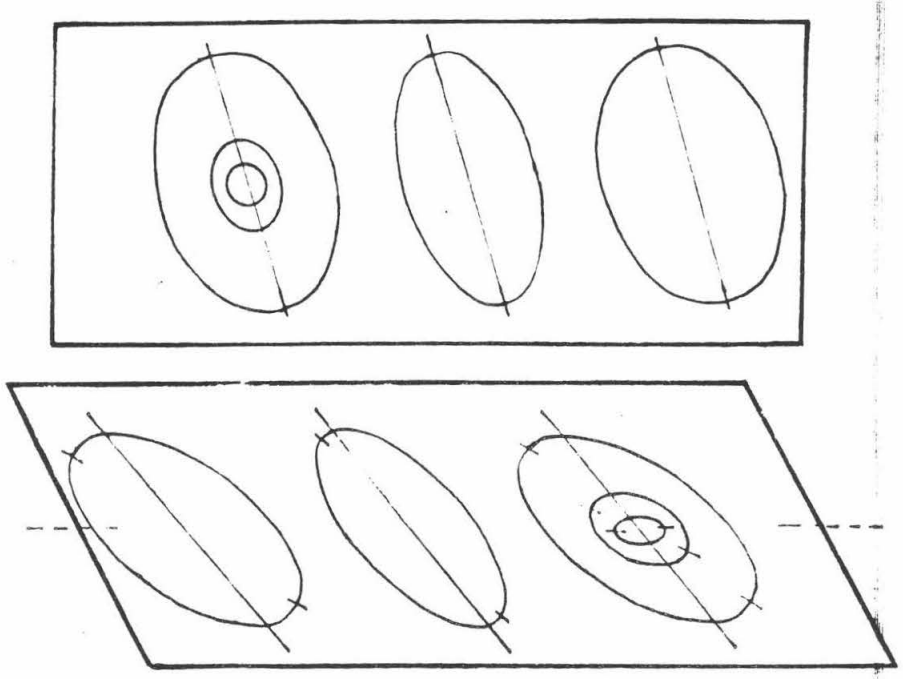

Fig. 1

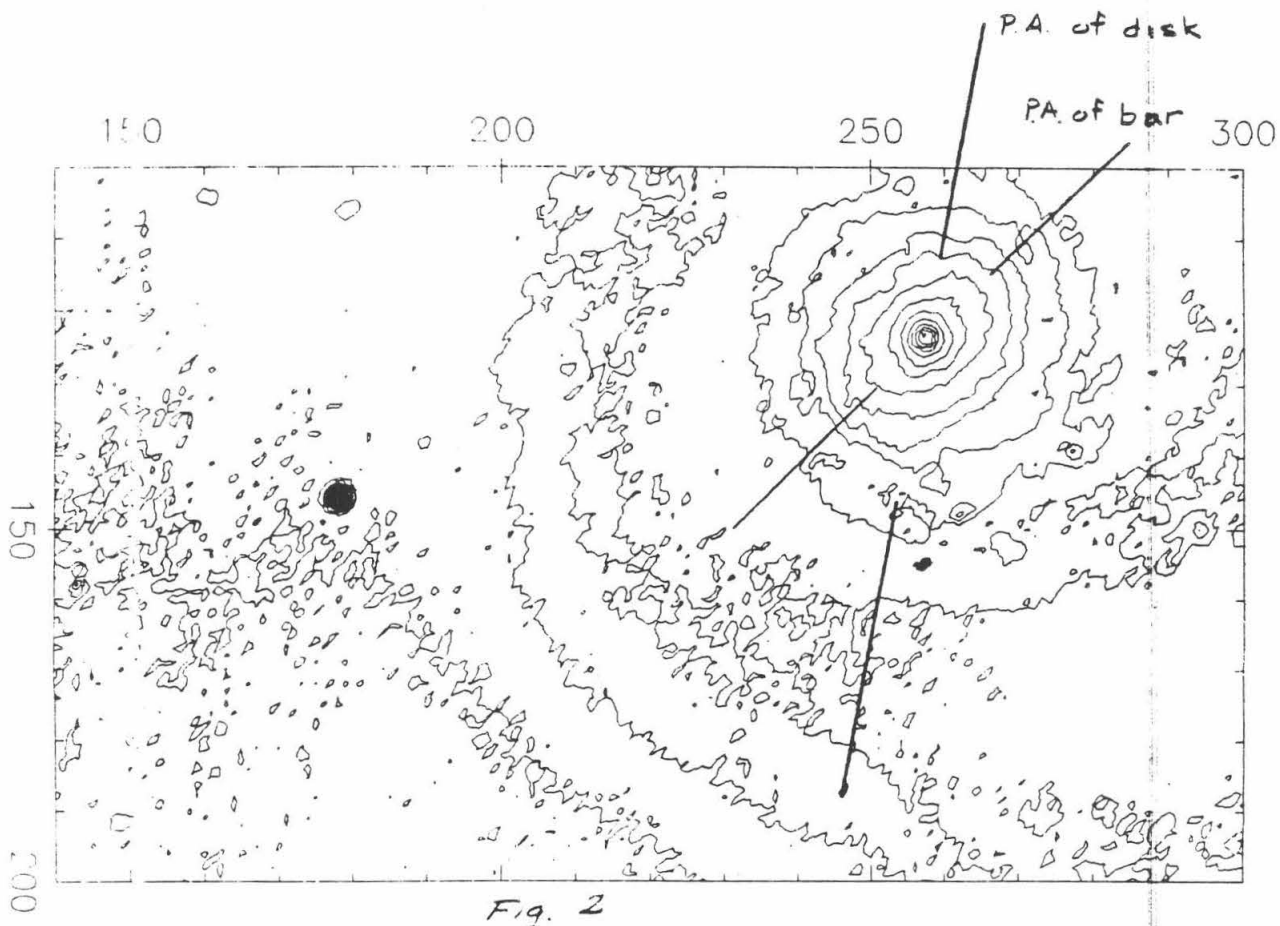

Fig. 2

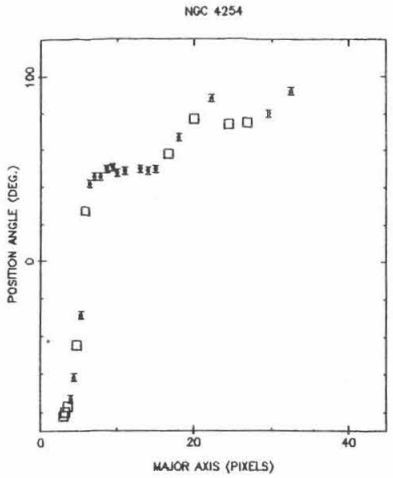
NGC 4254
POSITION ANGLE (DEG.)
MAJOR AXIS (PIXELS)

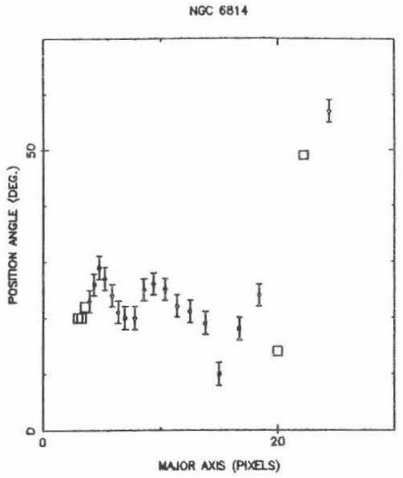
NGC 6814
POSITION ANGLE (DEG.)
MAJOR AXIS (PIXELS)

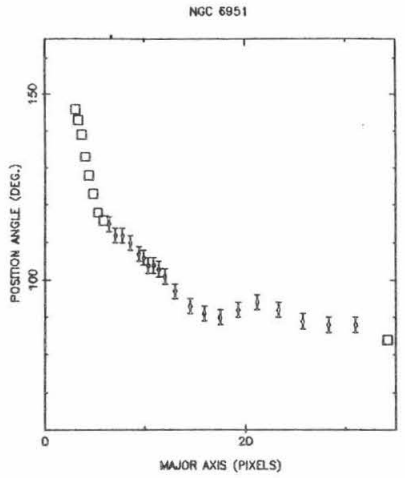
NGC 6951
POSITION ANGLE (DEG.)
MAJOR AXIS (PIXELS)

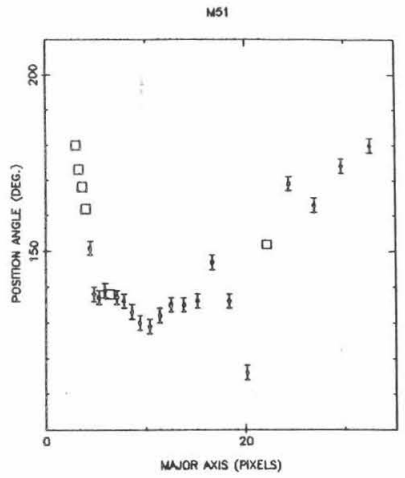
M51
POSITION ANGLE (DEG.)
MAJOR AXIS (PIXELS)

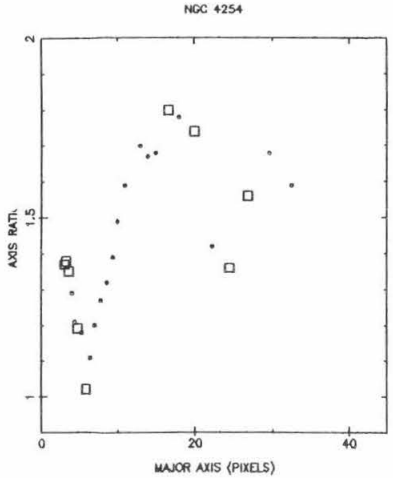
NGC 4254
AXIS RATIO
MAJOR AXIS (PIXELS)

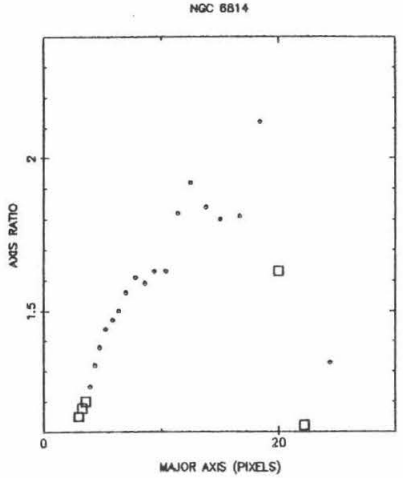
NGC 6814
AXIS RATIO
MAJOR AXIS (PIXELS)

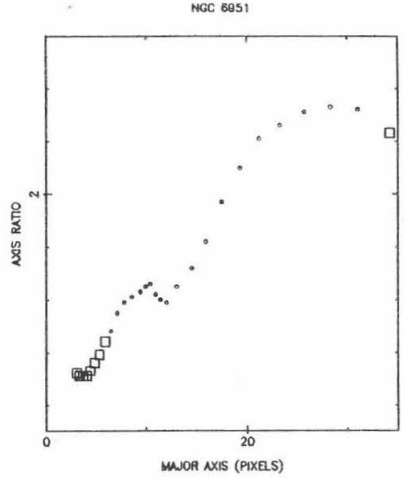
NGC 6951
AXIS RATIO
MAJOR AXIS (PIXELS)

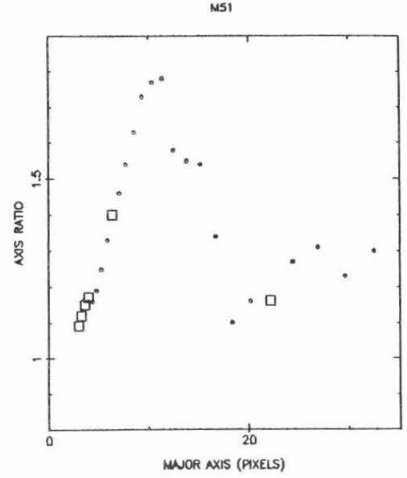
M51
AXIS RATIO
MAJOR AXIS (PIXELS)

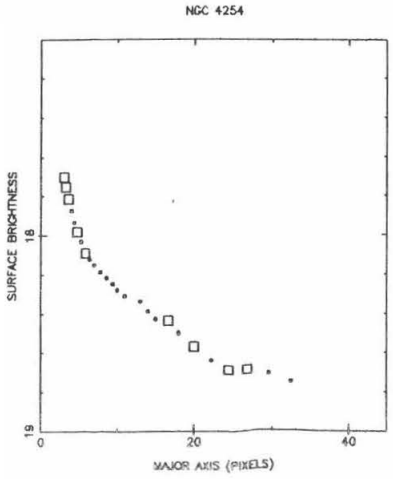
NGC 4254
SURFACE BRIGHTNESS
MAJOR AXIS (PIXELS)

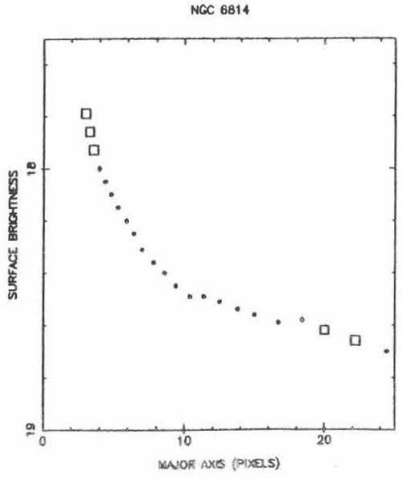
NGC 6814
SURFACE BRIGHTNESS
MAJOR AXIS (PIXELS)

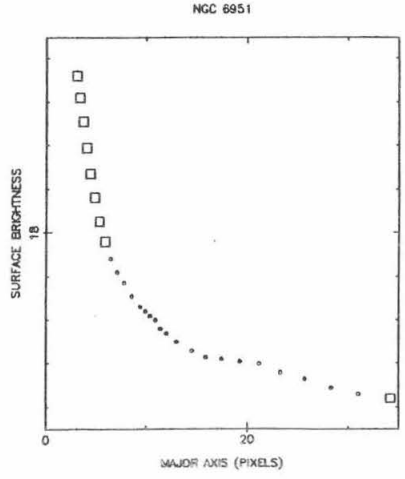
NGC 6951
SURFACE BRIGHTNESS
MAJOR AXIS (PIXELS)

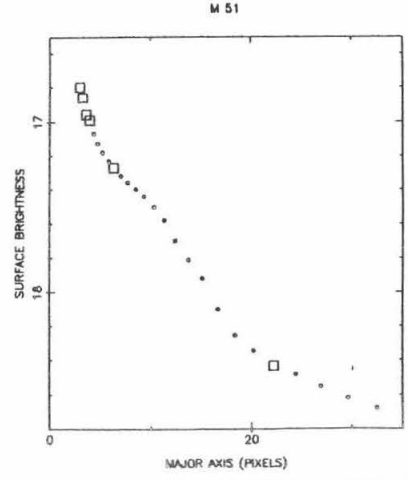
M 51
SURFACE BRIGHTNESS
MAJOR AXIS (PIXELS)

References

1. Botinnelli, L.,Chamaraux, P.,Couguenheim, L.,and Lauque, R.,1970, Astr. Ap, 6,453
2. Boroson, T., 1981,Ap. J.,46,177
3. deVaucouleurs, G., 1958,Ap. J., 128,465
4. deVaucouleurs, G., deVaucouleurs, A.,and Corwin, H.G.,Second Reference Catalogue of Bright Galaxies (Austin:University of Texas Press)
5. Dickel, J.R., Rood, H.J., 1978, Ap.J., 223,391
6. Hackwell,and Sheizer, 1983,Ap. J.,265,643
7. Hoessel, J.G.,and Mould, J.R.,1982, Ap. J.,254,38
8. Kormendy, J.,1983, Ap. J.,275,529
9. Kormendy, J.,1982, Observations of Galaxy Structure and Dynamics, 12th Advance Course Swiss Society of Astronomy and Astrophysics
10. Light, E.S.,Danielson, R.E., and Schwarschild, M.,1974, Ap. J.,194, 257
11. Lin, C.C., and Shu, F.S., 1964, Ap.J.,140,646
12. Matall, N.U., and Lindblad, P.O., 1970, Astr. Ap., 8,364
13. Nilson, Peter, 1973, UPPSALA General Catalogue of Galaxies
14. Palumbo, G.G.C.,Tanzella-Nitti, G.,and Vettolani, G., Radial Velocities from Catalogue of Radial Velocities of Galaxies (Gordon and Breach Science Publ.) 1983
15. Peterson, C.J., Rubin, V.C., Ford, W.K., and Roberts, M.S., 1978, Ap.J.,226,770
16. Rogstad, D.H., Rougoor, G.W., and Whiteoak, J.B.,1967, Ap.J., 150, 9
17. Rogstad, D.H., Shostak, G.S., and Rots, A.H., 1973,Astr. Ap.,22,111
18. Rood, H.J., and Dickel, J.R., 1976, Ap. J., 205,346
19. Sandage, A., 1961, The Hubble Atlas of Galaxies (Washington:Carnegie Institute of Washington)
20. Sandage, A. and Tammaan,G.A.,1974, Ap. J., 194,223
21. Sandage, A., and Tammaan, G.A., A Revised Shapley-Ames Catalogue of Bright Galaxies (Washington:Carnegie Institute of Washington) 1981
22. Sanders, R.H., and Huntley, J.M.,1976, Ap. J.,209,53
23. Send, 1982, Astr. Ap.,112,235
24. Shostak, G.S.,1978, Astr. Ap.,68,321
25. Stark, A.,1977, Ap. J.,213,368
26. Tully, B., PhD. Thesis, 1972, University of Maryland
27. Wade, R.A., Hoessel, J.G., Elias, J.H.,and Huchra, J.P., 1979, Pub. A.S.P., 91,35
28. Williams, T.B., and Schwarschild, M., 1979,Ap. J.,227,56

JPL

An Overview of the field of Optical Computing

SURF report of Peter Ashcroft
Submitted Sept. 11, 1984
Advisors: Dr. Alan R. Johnston and Dr. H. K. Liu

Abstract

Despite the great speeds now being realized with computers, it is apparent that in some applications, even the high rates presently being achieved are insufficient. Particularly problems requiring real time results such as speech, or visual recognition demonstrate the need for faster devices-perhaps faster than is possible, or practical electronically. One suggested means of attaining faster computation is through the use of light rather than electricity as the means by which data is thansmitted, and utilized. Offered here is a brief review of the present state-of-the-art of optical computing, as well as a review of the directions which this area may turn in the future.

Background

One of the basic phenomena of light is Fraunhofer diffraction. This effect is evident if light is made to pass through a narrow slit. Due to the wave nature of light, a collimated, monochromatic beam passing through such a slit will produce at a large distance a series of bright and dark spots. By large, I mean that

$$z \gg \frac{kx^2}{2}$$

where z is the distance from the diffracting screen to the pattern, k is the wave number of the illumination used$(\frac{2\pi}{\lambda})$, and x is the width of the slit.

Through the use of lenses, this Fraunhofer diffractiion can be observed on a much smaller scale. See figure 1. It can be shown mathematically that these diffraction patterns represent the Fourier transform of the spatial characteristics of the original pattern. In this case, the original pattern was a single slit, or in other words, a rectangular signal of light. Thus the series of bright and dark lines mentioned above, when scaled correctly, represent by their amplitudes the Fourier transform of a rectangaular signal. The scaling factor is reflected in the equation

$$\nu = \frac{x}{\lambda d}$$

where ν is the spatial frequency of the pattern, x is the displacement from center of a particular point in the Fourier plane, λ is the wavelength of the light used, and d is the focal length of the lens used.

Analog Optical Computing

Because the Fourier transform finds so many applications, and is so readily obtained, and an image

transformed this way can be simply filtered to remove undesired features, this technology has seen considerable development. This computation is fundamentally different from that of almost all modern computers because this computation is carried out by analog means rather than digitally. In the work I did, the pattern used was the 1951 Air Force resolution test pattern. See figure 2. Because this pattern is comprised of sets of horizontal and vertical transparent lines on an otherwise opaque background, the transform produced was basically cross shaped with one arm representing all the vertical components, and the other arm representing all the horizontal. I placed an adjustable iris on one of these arms, so that all the light in the Fourier plane but a section of one of the arms was blocked. By varying the size of the apperture, I was able to observe a "scanning" effect in the image reconstructed from the light which was able to pass the open iris. In other words, as the iris was adjusted to allow transmittence of different spatial frequencies, sets of lines which had not been illuminated became so, and because of the arrangement of the patterns on the plate, the effect was that of illumination sweeping over the image.

A similar application is the computation of the correlation of two functions. See figures 3a, 3b. Using a technique called matched filtering, the Fourier transform of a desired image is placed in the Fourier plane of an image being examined so that the amplitude of the light transmitted is directly related to the similarity of the two patterns. In this example, as with the example of the Fourier transform, a long and time consuming digital process is avoided through the use of an analog system which performs in the time required for light to travel the length of the device the entire calculation. Typically this would require a length of time on the order of nanoseconds. This has been applied towards the development of pattern recognition systems.

Another example of optical processing is the use of an acousto-optic device or surface accoustical wave (SAW). The theory behind such a device is as follows: a piezo-electric transducer is used to excite bulk or surface waves in a light transmitting material (either solid or liquid). These periodic areas of differing index of refraction function as a diffraction grating. Thus, by varying the frequency of the acoustic waves, the spacing of this this grating can be adjusted, and the angle at which the incident light is diffracted also can be adjusted. One simple application for such a device is for use as spectrum analyzer. See figure 4.

The applications of analog optical processing extend to numerical problems such as matrix multiplication also. As shown in figure 5, multiplication of a vector by a matrix is performed virtually instantaneously by this method. The LEDs represent by their intensities the elements of the vector. The matrix information is encoded on a mask such

that the transmittance at at a given point corresponds to one element of the matrix. Due to the fact that the transmission of the mask can only take on values between 0, and 1, this method may appear to be somewhat limited, but if all the values of interest in the matrix are scaled to fall into this range, the problem is avoided. The lens arrangement is such that light from each LED falls on one and only one row of the mask, and the light from each column of elements which passes the mask is directed onto one of several detectors. Each detector corresponds to a specific column of the mask. The light transmitted by a given element of the mask represents the product of the value of an element of the vector (the amplitude of the light from the LED), multiplied by an element of the matrix (the transmission of that part of the mask). Because the light from each element in a given column falls on the same detector, this operation is the summation of products, and the detectors represent the elements of the vector which is the product of multiplication of a vector and a matrix.

This method is not without drawbacks though. One of the most serious is the fact that the system is committed to that particular operation. In addition, although the matrix can be altered, it can not do so quickly. If the mask is a transparency that must be physically removed, and replaced, it is cumbersome. There has been some work with liquid crystal light valves (LCLV) for the mask, but as yet, they do not react quickly enough.

Digital Optical Computing

These analog systems are capable of great speed as a result of their parallel nature, and the fact that they function at the speed of light. They are limited though by their dedication to a specific operation. This is to be contrasted with the great versatility presently being enjoyed by digital machines. Although analog devices as I have described them will find ready application in a few specialized situations, the greatest advances through optical technology will be digital. It would be a mistake to assume that optical digital computers must be exactly analogous to existing electronic systems simply because that's the way it had been done before. The simple analog devices decsribed illustrate the potential that optical computers have to perform parallel operations on an array of data in a way not done previously with electronic computers. It would be just as foolish though to ignore the advances and techniques that have come about in the development of electronic computers. The ideal then would be a hybridization of the two.

In order to do digital computation optically, a way must be found for signals to combine non-linearly. That is to say, a way must be found that logical symbols can be combined in a way similar to the way electrical voltages are processed in logic gates. One way that this could be done would be to let 0's and 1's be represented in the form of a polarization. Another idea is to represent them as various

phase delays so that they would combine differently with a third reference signal.

Conclusion

Optical processing holds promise as a means of supplanting or in some cases replacing electronic computers. One advantage is that light can be modulated faster than electrical signals. In the case of integrated circuitry, the resistance and capacitance of interconnecting electrical lines limit the speed at which data can be transmitted. Light signals do not encounter these effects, and thus are faster. Another problem frequently encountered with electronic circuitry is cross-talk. This is particularly the case when several lines run parallel to each other, and are being modulated at high speeds. Optical systems avoid this problem, and in fact can even be allowed to cross each other without interference if the angle between the guides is not too small, and the light is from a broadband source such as an LED.

Given that optical devices have such tremendous potential, and that they will see development in the near future, we ask ourselves what form this development will take. The future will see development along the lines of both digital and analog devices. Those devices that most change the nature of computation will be those which incorperate both approaches; recognizing that any digital process is in its most minute analysis the result of analog phenomena, but exploiting the versatility of modern digital precedents. The ideal implementation of optics in the field of processing will be a hybridization. Already, diffraction gratings, beam splitters, holographic lenses, and acousto-optic deflectors have been fabricated on two dimensional substrates of Lithium Niobate just as electronic circuits have been placed on Silicon. If these and other devices can be used to produce digital components that exploit the parallel processing capabilities of light, optical computing will be the next major development in the field of computing.

Bibliography

1. C.M. Verber, "Integrated-Optical Approaches to Numerical Optical Processing," Proc. IEEE, vol. 72, pp.942-953, 1984
2. D. Psaltis, "Two-Dimensional Optical Processing Using One-Dimensional Input Devices," Proc. IEEE, vol. 72, pp.962-974, 1984
3. A. Sawchuk, "Digital Optical Computing," Proc. IEEE, vol.72, pp. 758-779, 1984
4. J.W. Goodman, F.J. Leonberger, S.Y. Kung, R.A. Athale, "Optical Interconnections for VLSI Systems," Proc. IEEE, vol.72, 1984
5. D. Psaltis, D. Casasent, "Time-and Space-Integrating Spectrum Analyzer," Applied Optics, vol.18, pp.3203, 1979
6. Y.Z. Liang, D. Zhao, H.K. Liu, "Multifocus Dichromated Gelatin Hololens," Applied Optics, vol.22, pp.3451-3456, 1983
7. H.S. Stone, "Parallel Processing with the Perfect Shuffle," IEEE Trans. on Comp., vol.c-20, pp.153-161, 1971
8. J.W. Goodman, Introduction to Fourier Optics, McGraw-Hill, N.Y., 1968
9. H. Stark, Applications of Optical Fourier Transforms, Academic Press, N.Y., 1982
10. R.J. Collier, C.B. Burckhardt, L.H. Lin, Optical Holography, Academic Press, N.Y., 1971
11. W.T. Cathey, Optical Information Processing and Holography, John Wiley and Sons Inc. 1974

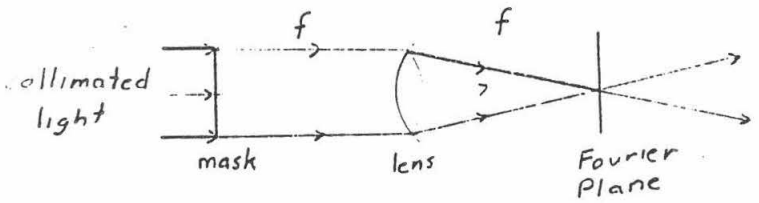

fig. 1

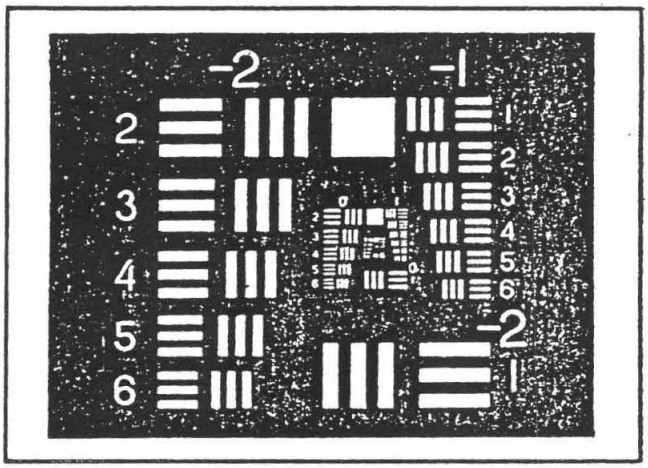

USAF 1951 TARGET

fig. 2

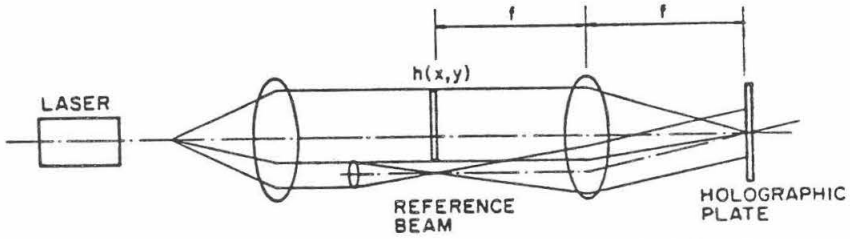

Recording setup using a minimum number of optical elements.

fig. 3a

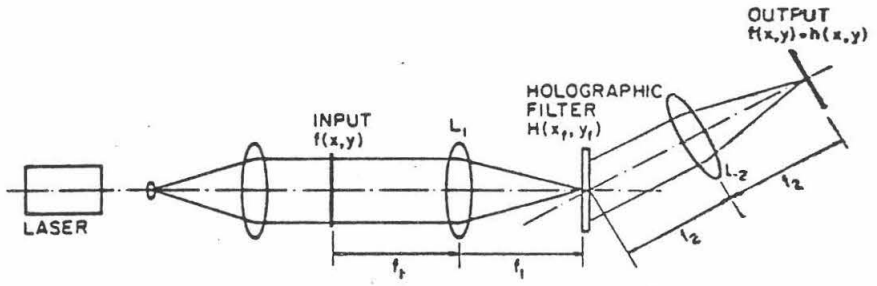

Optical correlator using a holographic filter.

fig. 3b

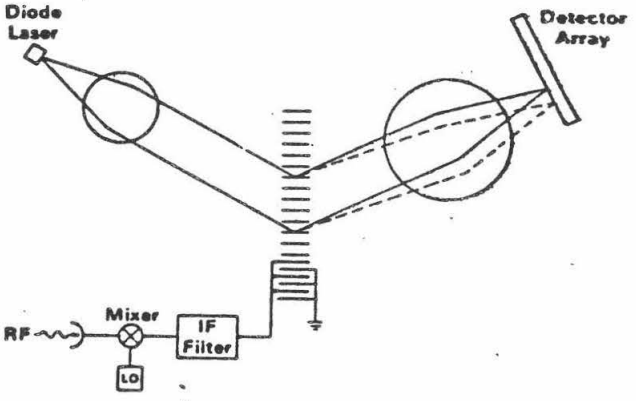

Schematic of an integrated-optical spectrum analyzer.

fig. 4

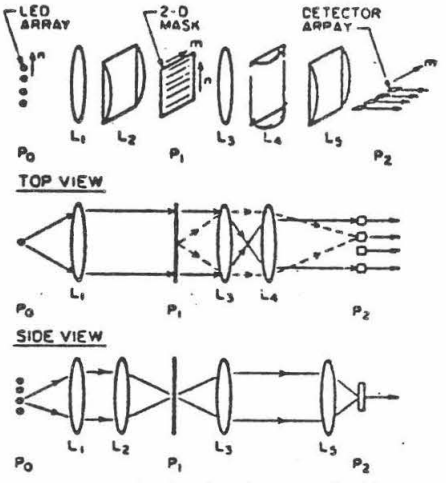

Vector–matrix multiplier, implemented with an array of LEDs.

fig. 5

ASTEROID PHOTOMETRY AT TABLE MOUNTAIN OBSERVATORY

Clea Bures

Sponsored by Dr. Alan Harris (J.P.L.)

ABSTRACT: The asteroid photometry program at Table Mountain Observatory involves taking photometric data on a number of asteroids - including newly discovered earth-approaching asteroids. From this data rotation periods and phase relations (brightness of the asteroid as a function of the angle of illumination) are determined.

INTRODUCTION: A century after the first asteroid was discovered, Oppolzer noticed that the brightness of asteroid 433 Eros varied periodically. This periodic variability - now associated with all asteroids - is generally considered to derive from the irregularity of the asteroid's shape, although other factors such as the color and the composition of the asteroid must also be considered. As the asteroid rotates it will reflect unequal amounts of light towards the Earth due to the differing surface areas the light is being reflected off. These periodic variations in brightness can be plotted to create what is called a "light curve". This is then used to predict the rotation rate of the asteroid. When enough data has been obtained on an asteroid, a phase relation plot can be constructed. This plot illustrates the brightness of the asteroid as a function of the illumination. The data for these plots can be obtained by making photoelectric observations of the asteroids involved.

PURPOSE: My project has two distinct purposes:

1. To find or confirm the rotation rates of as many asteroids as possible. At the present time there is insufficient data available to : infer collisional processes in the asteroid belt, to formulate and test theories regarding the origin of the asteroid belt, and to test theoretical models of light scattering from asteroids.

2. To construct a phase relation plot for asteroid 433 Eros using data from past observing runs. This plot can be used to predict physical properties of the asteroid.

PRESENTATION AND DISCUSSION OF RESULTS: As I mentioned previously, my project consisted of two distinct parts. The first part - determining rotation rates and constructing light curves - involved four observation runs at Table Mountain Observatory. Also related to this part of my project was an observation run at Mt. Palomar with E. H. Helin and her asteroid search and survey group. During this observation run we used the 18" Schmidt telescope to search for previously undetected near-earth asteroids. The technique we used involved taking four or five minute exposures of each of the four chosen fields. We would then repeat this procedure using the same sequence. Thus we obtained four pairs of field plates, each pair being separated by an interval of about 35 minutes. These photographic plates were then scanned for asteroids using a stereoscopic viewer. I had hoped that an interesting earth-approaching asteroid would be discovered during the run, so that I could follow it up at Table Mountain Observatory. However, although this group has discovered numerous asteroids, none of note were found on that run.

Despite this, I still had an opportunity to observe a newly discovered earth-approaching asteroid at Table Mountain. This asteroid was assigned the temporary name of 84KD and along with asteroids 704, 269, 521, 10, 188, 101, 8 and 686 comprised my asteroid observation program for the summer. For the asteroid program at Table Mountain the 23" (61 cm) Cassegrain reflector combined with a pulse counting photometer (Johnson/Morgan V band) with a S-20 photocathode was used. Palomar Sky Charts and an ephemeris were used to locate the asteroids to be observed. For each asteroid an appropriate (close in color, size, brightness, and location) comparison star was found so that the relative brightness of the asteroid could be determined. On a good observing run quite a few asteroids would be observed for several nights in a row. For each asteroid the following photmetric readings, using an integration time of eight seconds, were taken throughout the night:

1. Four readings of the asteroid, recording the starting time.
2. Two readings of the sky surrounding the asteroid.
3. Four readings of the comparison, recording the starting time.
4. Two readings of the sky surrounding the comparison.

Blue readings were taken reasonably often so that color and extinction coefficients could be determined.

The reduction of the data was fairly simple. first we found the average value for each of the sets of measurements listed above. Then we examined the data and every time data was taken on the asteroid we were concerned with, we recorded the time of the asteroid observation and the average value for each set of readings. Then we subtracted the average sky readings from the appropriate asteroid or comparison reading. We then used a computer to generate an air-mass plot to determine the extinction coefficient so that we could correct for the air mass difference between the asteroid and the comparison. After applying this correction to our asteroid and sky readings we calculated the relative magnitude of the asteroid as follows:

$\Delta M = 2.5 \text{ Log } (C/A)$ where ΔM is the relative magnitude of the asteroid.
A is the corrected average asteroid reading for a given time.
and C is the corrected comparison average reading.

When ΔM is plotted against time we have our light curve. To determine the rotation rate of an asteroid we note the periodicity of the maxima and the minima on the light curve. Most asteroids will display light curves with two maxima and two minima, as they have roughly four 'sides'. We can also superimpose light curves from several days to find the best match.

As an example of how to determine rotation rates from light curves I shall use the light curves from 84 KD. As you can see below it would be impossible to determine the rotation rate from only one light curve, since there is not enough time covered by either light curve. However, you can tell from the light curve taken on the 17th that the period is between two and three hours. If you then superimpose the two you can see that the period must be close to 2 hours and 29 minutes. This is determined by the fact that the superposition is made such that the hour 5 from the 16th lies on the hour 5.83 (5 hours and fifty minutes) of the 17th graph. This gives an elapsed time of 24.83 hours. The number of rotations is an integer and the period is between 2 and 3 hours. Hence the period of 84KD must be 2 hours and 29 minutes.

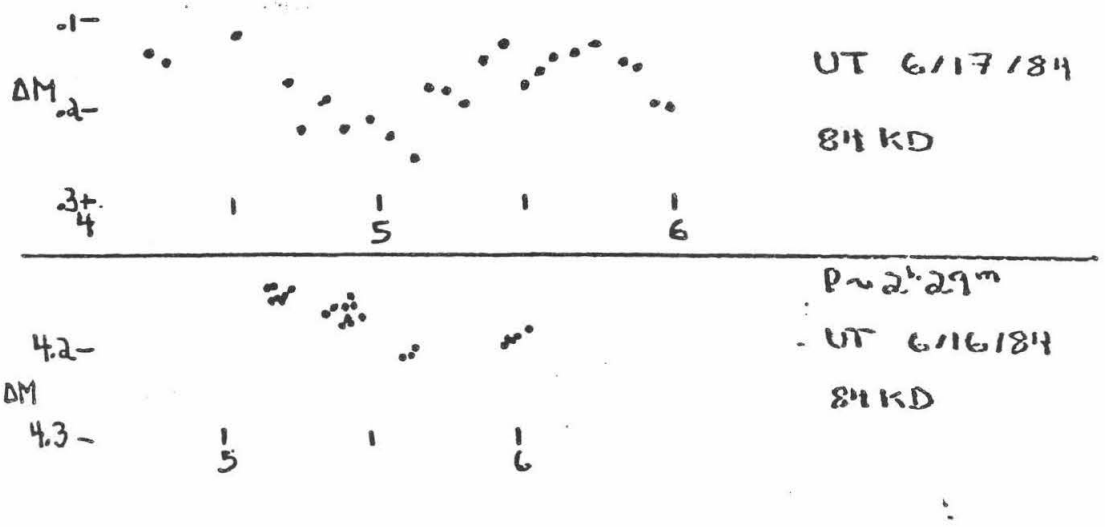

The second part of my project involved constructing phase relation plots for 433 Eros. This consisted mainly of reducing data that had already been taken, but I did have to standardize some stars. When phase relation plots are formed you need the absolute magnitude of the asteroid, not just the relative magnitude, so in order to insure correct results one must standardize all the comparison stars used with the asteroid to a set scale. The way this is done is to compare the brightness of each comparison star to a standard star (a bright star whose magnitude is definitely established). The observation program for this is very similar to the one for normal observations, only it is two stars being compared -- not an asteroid and a star.

The data reduction necessary to produce a phase relation graph is time consuming, but relatively easy. There are three steps:

1. Light curves must be plotted for each day observations were made. First one must correct the data so that it is reduced to 0 UT phase angle for the central night in each set of successive nights. Then the points must be replotted back into a single cycle using the known rotation rate, which is 5.2699 hours for 433 Eros. Using data from successive days, a composite light curve can be plotted.

2. Standardization of all the comparison stars used for 433 Eros is the next step. Each night that standard stars were observed will need data reduction. What you must do for each night is to compare all of the stars' readings for the entire night. To compare two stars legitimately they must have at least one set of readings within an hour of each other, and the air mass must not differ by more than 0.25 AM. Then you tabulate a list of magnitude differences with error estimates. Finally you solve the equations using a least squares fit.

3. Now you can derive the phase plot. First, tabulate the maximum and minimum magnitude for each light curve. These points comprise the data set. Then you use this equation to calculate the absolute magnitudes.

$V(\alpha)=\Delta V + V_{comp} - 5\log(r\delta)$ Where $V(\alpha)$ is the absolute magnitude of the asteroid.

V_{comp} is the standardized magnitude of the appropriate comparison star.

ΔV is the difference between the magnitude of the asteroid and its comparison.

'δ' is the distance from the earth to the asteroid in AU.

'r' is the distance from the sun to the asteroid in AU.

These values for the absolute magnitude are then plotted against their phase angles to form the actual plot.

The phase relation plot for Eros 433 (on the next page) shows some rough results. The phase relation can be estimated at 0.1 and the phase coefficient can be roughly determined to be 0.03 mag/ deg Also we can compare the ratios of the polar view magnitude, the maximum equatorial view magnitude, and the minimum equatorial view magnitude to give us an idea as to the shape of the asteroid. The pole-on view has the highest magnitude as it is the cross-sectional view of the two larges axes, the maximum equatorial view shows the cross-sectional view of the larges axis and the smallest axis, and the minimum magnitude equatorial view shows the cross-sectional view of the two smallest axes. Normally we could use the ratios between these differing views to determine the actual ratio of the axes of the asteroid. However, at the large phase angles we are observing we would not see shadows, etc. and can only qualitatively state that the approximate ratios of the axes support the theory that Eros is shaped like a cigar. This particular study is not complete - Eros needs to be observed at a wider range of phase angles to produce really useful results.

CONCLUSIONS: There were very few actual conclusions to my project. However, there were some. The rotation rate of 84KD was calculated to be about two hours and twenty-five minutes. Data was collected on several other asteroids, which should hopefully prove useful in the future. A phase relation plot was constructed for 433 Eros, and although its usefulness is limited due to the small range of phase angles it includes, it did provide some useful information to be added to the information already collected on Eros. Finally, several light curves were obtained, increasing the amount of data available on asteroids.

433 Eros Phase-relation plot

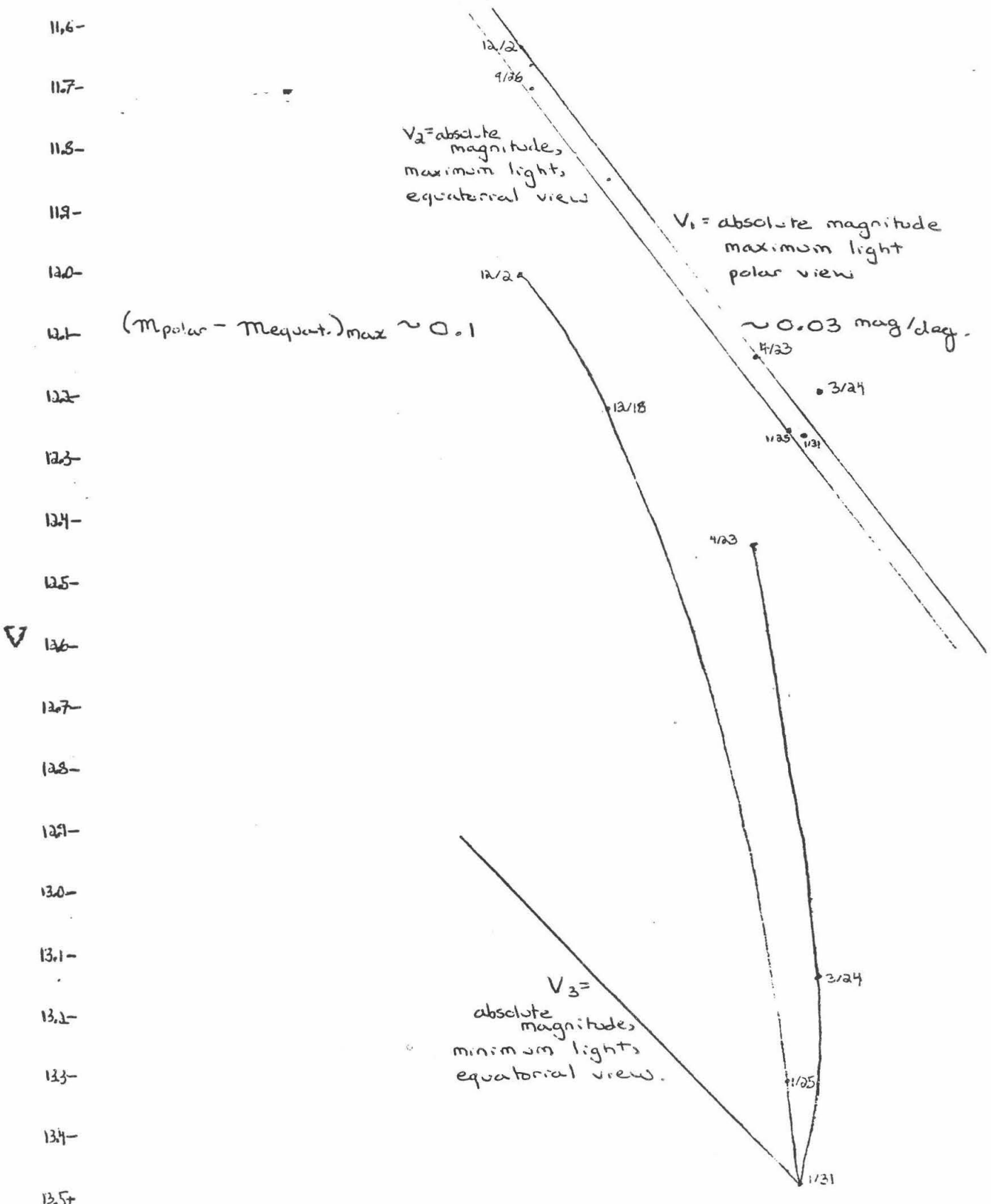

BIBLIOGRAPHY:

Binzel, "Photometry of Asteroids", Solar System Photometry Handbook, Genet, Russell T. (Ed.),1983.

Burns,J.A. and Tedesco,E.F. , "Asteroid Lightcurves : Results For Rotations and Shapes", ASTEROIDS, Gehrels, T. (Ed.), 1979.

Harris,A.W. and Young,J.W., "Asteroid Rotation IV. 1979 Observations", ICARUS 54, 1983.

Survey of MHD Waves in Earth's Distant Magnetotail

by William H. Butler, sponsored by Bruce T. Tsurutani

Abstract

A survey of magnetohydrodynamic waves in earth's distant magnetotail is presented. The wave properties both in the spacecraft frame and in the plasma frame are discussed. Correlation with substorms and streaming energetic ions will give more support to the plasmoid picture of the magnetotail.

Introduction

The interaction of the radially outflowing solar wind with the earth's magnetic field forms a magnetic tail pointing downstream (radially outward) from the earth. This tail consists of two regions of high intensity (~8 nT) magnetic field and low density plasma, called *lobes* between which is sandwiched a sheet of plasma where the field drops off sharply due to diamagnetic effects (see Figure 1). Sometimes there also exists an intermediate region, called the plasma sheet boundary layer (PSBL), between the plasmasheet and either lobe. This PSBL is characterized by a slight (~10%) decrease in the field magnitude.

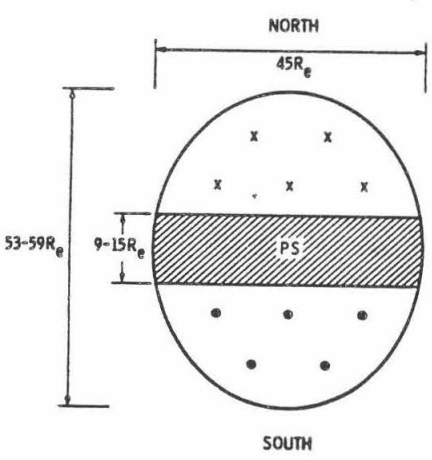

Fig. 1. Structure of the magnetotail near ISEE-3 apogees on passes 2 and 4. Note the two lobe structure. X's and dots represent magnetic field lines.

The data studied was gathered by the spacecraft ISEE-3, which made six passes through the magnetotail, including two passes (numbers 2 and 4) extending out beyond 200 earth radii (R_E). Data analyzed in this paper were obtained during a 20 day period near apogee on pass 2 (221 R_E), and a 25 day period near apogee on pass 4 (238 R_E). This data, while clearly showing the presence of the two lobes and the plasmasheet, also showed the intermittent presence of magnetic field waves in the PSBL. Many of these wave events and their properties in both passes have been catalogued.

Although the list of waves is not comprehensive, it does contain enough wave events so that statistical comparisons with other geomagnetic indicators can be meaningful.

Discussion

Wave Identification

The spacecraft ISEE-3 measures and transmits the direction and magnitude of the magnetic field six times a second. This high resolution data is recorded on tape, and is also averaged over 3 second intervals, so that 18 data points are reduced to one. Since the resolution of the computer's line printer is approximately 1500 horizontal points per page, this allows one to graph four minutes of high resolution data, or one hour of 3 second averaged data on each page. The 3 second plots have been produced for the entire time period between day of year (DOY) 24 and DOY 43 (1983), when ISEE-3 was near apogee of pass 2, and between DOY 169 and DOY 193, near the apogee of pass 4. An example of a three second plot is given in Figure 2. One can see high frequency field variations in the PSBL, an indication of waves. Since the waves typically have period ~10 sec, a 3 second plot will show each wave event, but some periods of random fluctuation may also look like waves. However, once a likely time period has been selected, one may go back to the high-resolution tapes to do a principal axis analysis (PAA) on a short (≤3 min) time period.

A PAA calculates the covariance matrix and diagonalizes it to determine the direction of maximum, intermediate, and minimum field variance. The PAA will first graph the field in a |B|, φ, ϑ coordinate system, then in a B_x, B_y, B_z system (see Figure 3), then in a B_1, B_2, B_3 system. This latter system is chosen as follows: The magnetic field varies most strongly in B_1, and varies least strongly in B_3. B_2 is formed such that $B_1 \times B_2 = B_3$. The PAA program next produces 3 hodograms, in which one axis is plotted against another, as in Figure 4, where B_2 is plotted against B_1. The average propagation direction of the wave experiences the least fluctuation, which is B_3. Therefore the B_1 vs. B_2 hodogram shows the wave cycles very clearly. When B_{1-3} are computed, their eigenvalues λ_{1-3} represent how strongly that component fluctuates. For this wave event $\lambda_1/\lambda_2 = 1.1$, indicating nearly circular polarization. A large number of the properties of the waves can be determined from this PAA. These properties are listed for each wave event in Table 1. The ϑ_{kB} values will vary from 0 to 90, because the information available wtill only determines the wave propagation direction to within a sign. Thus, for small ϑ_{kB}, the wave may be propagating nearly parallel or nearly anti-parallel to **B**.

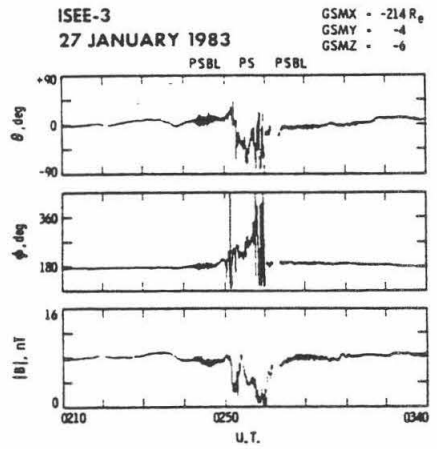

Fig. 2. An example of a 3 second averaged plot. Note the high frequency variations of the field within the PSBL, and the sharp decrease in field strength as the plasmasheet is entered. The high field, quiet periods to the sides indicate that ISEE-3 was in the lobe regions.

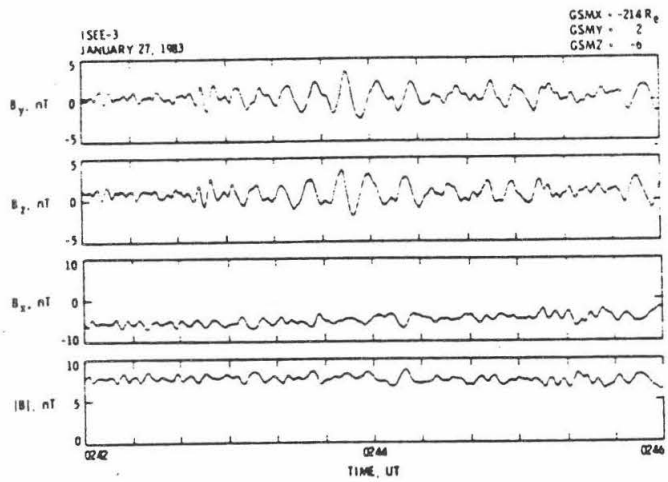

Fig. 3. A high resolution graph of a time interval within the PSBL from Figure 2 clearly shows the presence of waves.

Rest Frame Analysis

Obviously, all these measurements take place in the spacecraft frame of reference. Since the spacecraft is near apogee, it is moving slowly (~200 km/hour) relative to the earth. However, the waves are propagating in plasma which typically convects downstream at about 250 km/sec. Therefore the true frequency has been Doppler shifted when recorded by ISEE-3. Two equations are necessary to correct for this shift:
The Doppler equation

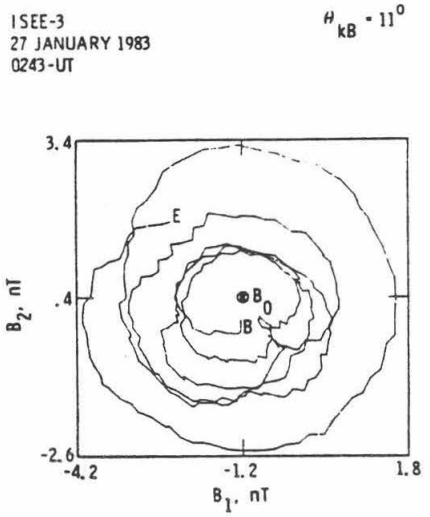

Fig. 4. This hodogram of B_2 vs B_1 shows that the wave is nearly circularly polarized, and is right handed (B and E indicate beginning and end of the interval, and B_0, the ambient field, is shown pointing into the page).

$$f_{sc} = f_p\left(1 + \frac{V_p \cos\vartheta_{kV}}{V_{ph}}\right) \qquad (1)$$

and the dispersion relation

$$V_{ph}^2 = V_A^2\left(1 \pm \frac{|f_p|}{\Omega^+}\right) \qquad (2)$$

where

f_{sc} is the observed, shifted frequency
f_p is the rest frame frequency
V_p is the plasma velocity relative to ISEE-3
ϑ_{kV} is the angle between k and V_p
V_{ph} is the rest frame wave phase velocity
V_A is the Alvén speed ($\frac{|B|}{\sqrt{4\pi\rho_e}}$, ρ_e is the plasma density)
Ω^+ is the proton cyclotron frequency ($\frac{eB}{m_p c}$).

The approximations used in this dispersion relation are $f_p \approx \Omega^+ \ll \Omega^- \ll f_{pe}$, where f_{pe} is the plasma frequency $(\frac{4\pi n e^2}{m_e})^{1/2}$. Since the plasma is moving parallel to the field lines, $\vartheta_{kV} = \vartheta_{kB}$, where ϑ_{kB} is calculated by the PAA. Values of V_p and ρ_e were compiled by Los Alamos National Laboratory from other data sent from ISEE-3. Thus, the only unknowns are f_p and V_{ph}. The ± in Eq. (2) is refers to right (+) or left (-) hand polarized waves (in the rest frame). By combining (1) and (2) to eliminate V_{ph}, we obtain (3):

$$\frac{1}{\Omega^+ f_p^2}(f_{sc} - f_p)^2(\Omega^+ \pm |f_p|) = \frac{V_p^2}{V_A^2}\cos^2\vartheta_{kV}$$

Note that if a wave propagates anti-parallel to V_p, and has $V_{ph} < V_p$, the observed polarization will be

the opposite of the rest frame polarization. Thus, for a given wave event, one must test both rest frame polarizations to find all possible rest frame solutions. For the wave and plasma parameters observed, Eq. (3) always yields three solutions for observed right hand waves (two right hand and one left hand), and one solution for observed left hand waves (left hand). These solutions were found by a computer root finding algorithm, and are listed in Table I.

Wave Generation

By far the most likely mechanism for wave generation is cyclotron resonance with streaming protons in the PSBL. The first order resonance condition for this instability is

$$\omega - |\mathbf{k}|\,|\mathbf{V}| \cos\vartheta_{kV} = n\,\Omega^{+}$$

where ω is the rest frame frequency, k is the rest frame wave number, V is the proton velocity, n=1 for first order, and Ω^{+} is the ion cyclotron frequency. For the observed waves, $\omega - \Omega^{+} \approx .5\ \mathrm{sec}^{-1}$, $|k| \approx 10^{-3}\ \mathrm{km}^{-1}$, and $\vartheta_{kV} \approx 15°$. These values give V≈500 km/sec, which results in a proton energy of 2.5 keV. Although the instrument designed to detect ions with these energies failed in 1980, there does exist a one-to-one correspondence between the presence of waves and the presence of streaming higher energy (35-250 keV) ions (Tsurutani et al., 1984). It seems likely that when >35 keV ion streaming is detected, ions of lower energies, including ~2.5 keV, are also streaming.

Wave Correlations with other Geomagnetic Indicators

The Auroral Electrojet (AE) index is an indicator of how much current is flowing through the high latitude ionosphere, which in turn indicates how much solar wind energy is being input into the magnetotail. A tape of the AE indices, containing one data point per minute during DOY 1-55, was used in making the histograms in Figures 5-7. By comparing the background AE (Figure 5) with the PSBL AE, one can see that the PSBL is usually detected during periods of high AE. The wave events show an even slightly stronger correlation with AE (note the averages listed in each figure).

The significance of this correlation is as follows. Substorms are thought to cause reconnection of magnetic field lines in the near magnetotail (Vasyliunas, 1975). This reconnection process can form *plasmoids*, or bubbles of closed magnetic field lines which will propagate down the tail at velocities of approximately 700 km/sec. At the point of reconnection, field lines are annihilated, and the energy thus released is thought to accelerate ions from the plasma sheet into the edge the a lobe, creating a PSBL. Those protons which are accelerated to ~2.5 keV would produce the observed PSBL waves. Fifteen plasmoid events have been tentatively identified (Hones et al., 1984), of which 13 occur within a few minutes of a wave event. These plasmoids also have a positive correlation with AE, the average being 355 nT.

A more straightforward mechanism for generating the ion streams is that the substorm simply injects energetic ions into the near earth PSBL. These ions will then move down the tail, producing waves all along the way. This mechanism, however, is unlikely. The waves of the amplitude observed on ISEE-3 would cause isotropization of the streaming protons in resonance in about five minutes, whereas a 2.5 keV proton would require about 45 minutes to reach ISEE-3 from earth. This mechanism would be possible if the protons could stream through part of the tail while producing lower amplitude waves. This scenario is less likely than the plasmoid scenario since there is no reason to suppose that waves will be produced at some times and not at others.

Conclusion

The high correlation between wave events, plasmoids, and substorms lends more support to the plasmoid picture of the magnetotail. The catalog of wave events and properties will be helpful to those who will continue to study the magnetotail.

References

Hones, E. W. Jr., D. N. Baker, S.J. Bame, W. C. Feldman, J. T. Gosling, D.J. McComas, R. D. Zwickl, J. Slavin, E. J. Smith, and B. T. Tsurutani, Structure of the magnetotail at 220 R_E and its response to geomagnetic activity, *Geophys. Res. Lett.*, *11*, 5-7, 1984

Tsurutani, B. T., W. H. Butler, E. J. Smith, I. G. Richardson, S. W. H. Crowly, Abstract, Magnetosonic waves in the geotail, To be published in *EOS* in 1984.

Vasyliunas, V. M., Theoretical models of magnetic field line merging, I, *Rev. Geophys. and Space Phys.*, *13*, 303-336, Feb. 1975.

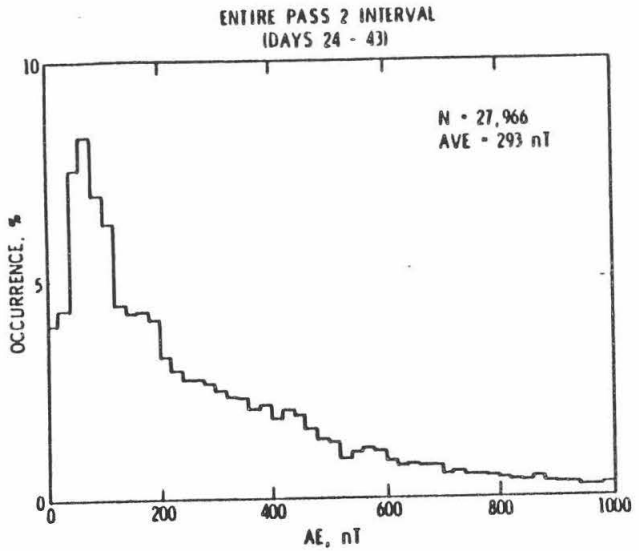

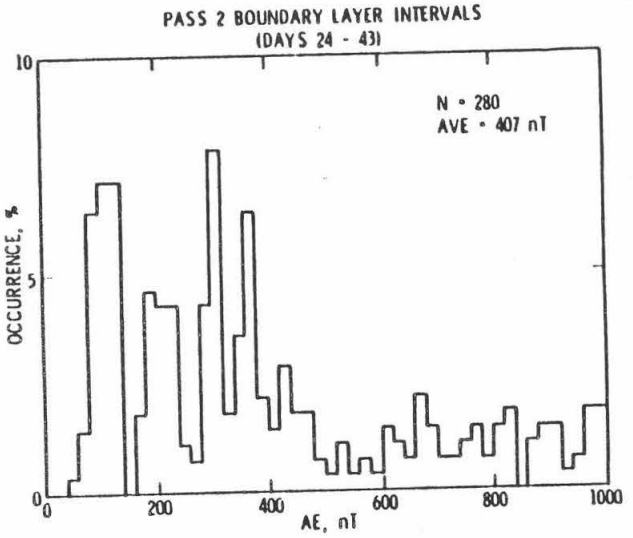

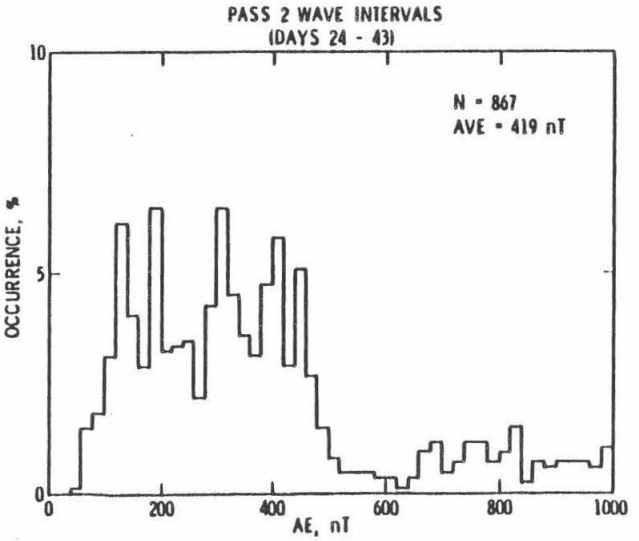

Figs. 5-7. These histograms bin AE data during the indicated intervals into bins 20 nT wide. By comparing the shape and average of Figures 6 and 7 with that of Figure 5, one can see that PSBLs and waves are usually detected during periods of high AE.

Table I. Wave Properties

	Measured Properties											Rest Frame Properties							
					$\frac{\lambda_1}{\lambda_2}$	ϑ_{kB}	$\lvert B\rvert$	T_p	ρ_e	V_p	V_A	R-AP		R-P		L-AP		L-P	
DOY	Time	T sec	amp nT	Pol			nT	sec	cm^{-3}	km/sec	km/sec	T sec	V_{ph} km/sec	T sec	V_{ph} km/sec	T sec	V_{ph} km/sec	T sec	V_{ph} km/sec
24	0254-0257	3.6	3.6	R	1.93	34.2	12.9	4.9	0.7	200	340	2.4	590	4.9	480	5.3	70		
	0257-0258	1.6	1.8	R	1.72	28.0	12.8	5.1	0.7	200	330	1.2	770	2.1	620	5.2	50		
	0308-0311	11.0	5.0	R	1.04	1.9	10.9	6.0	0.6	200	310	5.9	440	17.2	360	7.1	120		
	0410-0411	6.8	5.0	R	1.19	20.7	12.7	5.2	0.7	200	330	4.1	500	9.9	410	5.7	100		
	0416-0417	7.5	6.6	R	1.24	8.6	11.7	5.6	0.7	200	310	4.3	460	11.5	370	6.4	110		
25	1146-1148	15.7	2.6	R	1.75	16.8	8.3	7.9	0.1	250	570	10.7	760	21.3	670	8.5	160		
26	1009-1012	3.8	2.3	R	1.38	11.0	8.1	8.1	0.2	150	400	3.0	760	4.7	650	8.2	50		
27	0242-0243	5.5	1.7	R	1.07	4.1	7.8	8.4	0.06	100	690	5.0	1100	6.0	1100	8.4	40		
	0248-0251	15.0	1.5	R	1.43	30.5	7.5	8.8	0.06	350	670	10.0	910	21.6	790	9.7	210		
	0309-0312	9.5	1.2	R	1.14	40.3	8.1	8.2	0.1	200	560	7.7	800	11.5	730	8.3	80		
	0415-0417	11.0	2.6	R	1.10	17.5	7.3	9.0	0.08	150	560	9.0	790	13.2	730	9.2	80		
	0750-0751	16.0	1.7	R	2.64	5.3	7.1	9.2	0.1	400	490	7.3	740	27.3	570	11.8	230		
	1347-1348	4.0	1.0	R	1.85	10.2	7.1	9.2	0.1	100	490	3.6	930	4.5	860	9.3	30		
	2043-2044	5.3	2.8	R	1.15	10.1	7.5	8.8	0.2	250	360	3.4	690	7.8	530	9.4	90		
28	0818-0821	11.7	5.2	R	1.19	17.9	6.5	0.1	0.2	100	320	9.3	460	14.4	410	10.4	50		
29	0012-0014	2.5	1.6	R	1.85	15.3	10.9	6.0	0.4	250	380	1.7	790	3.5	620	6.2	70		
	0013-0016	15.5	6.0	L	1.45	18.2	10.7	6.1	0.4	250	370							26.9	320
	0239-0241	7.5	3.6	R	1.60	24.1	9.8	6.7	0.5	350	300	3.1	540	13.4	370	8.8	150		
33	1138-1141	9.1	1.9	L	2.36	5.6	7.5	8.8	0.09	150	540							13.7	330
	1717-1720	7.8	2.1	L	2.47	15.3	9.1	7.2	0.1	150	630							10.9	370
	1932-1934	11.6	5.4	R	2.10	25.5	9.6	6.9	0.3	250	380	6.8	540	17.4	450	7.4	100		
35	0512-0515	9.4	1.0	R	1.28	20.4	10.3	6.4	0.3	150	410	6.9	570	12.1	510	6.6	80		
	0532-0534	13.8	1.7	R	1.73	13.4	9.8	6.7	0.3	150	390	9.7	510	18.4	460	7.0	80		
37	0736-0739	5.0	1.8	R	1.57	8.8	7.4	8.8	0.05	250	730	4.1	1300	6.1	1100	8.9	60		
	1345-1348	5.5	1.9	R	2.00	27.4	7.6	8.7	0.04	300	830	4.5	1400	6.7	1300	8.8	100		
	1508-1509	11.3	0.9	R	1.55	33.4	7.1	9.2	0.05	200	690	9.0	990	13.4	900	9.5	110		
	1653-1655	18.3	1.1	R	2.13	3.0	5.4	2.2	0.03	350	680	11.7	970	26.1	820	13.3	200		
38	1544-1545	3.1	2.4	R	1.15	40.0	12.6	5.2	0.09	260	920	2.7	1600	3.7	1400	5.2	70		
39	0448-0451	4.0	2.7	R	1.29	26.0	9.8	6.7	0.2	250	480	3.0	870	5.2	720	6.9	90		

Table 1. Catalog of selected wave events. Amp is wave amplitude, T_p is the proton cyclotron period, other T's are wave periods, R and L indicate handedness, P and AP indicate assumption of parallel or anti-parallel wave propagation.

Guide Star Availability for the ASTROS Star Tracker

by Dara J. Chang
under faculty sponsor Richard Stanton, Ph.D.

Abstract. The ASTROS star tracker requires guide stars to provide accurate star image coordinates. Provided a list of astronomical targets, the availability of guide stars for each of these targets had to be determined along with any possibly complicating multiple star systems. After checking over three hundred targets, less than one percent had either no guide stars or some other complication.

In order to readily understand the work that was undertaken for the ASTROS project, the ASTROS star tracker must be introduced. ASTROS, an acronym for Advanced Star and Target Reference Optical Sensor, is part of a Shuttle payload that will be launched in early March 1986. This payload, consisting of three large ultraviolet telescopes and a smaller wide field camera, will observe Halley's Comet and various other astronomical objects. The star tracker provides extremely precise measurements of star image coordinates as inputs to the Image Motion Compensation system used to stabilize the science instruments' focal planes, thus keep the telescopes pointing at their desired target.

Obviously, the ASTROS star tracker needs stars to provide star image measurements. The stars the tracker will use are called guide stars and must meet certain requirements. The purpose of my project was to check if guide stars were available for all the targets planned and if there were any multiple star systems that might interfere with the accuracy of the star tracker.

The first task was to locate each target on a star atlas and determine the stars within the star tracker's field of view which was generalized from a rectangle to a circle 2.5 degrees in diameter. Since the orientaion of the rectangle can vary, a circle was the best alternative. Star availability information was derived from direct observation of the circled target area on the Sky Atlas 2000.0 by Wil Tirion. Star availability was decided on the basis of whether there were one or more stars brighter than 7.5 magnitude within the 2.5 degree diameter circle drawn around the target. If there were no stars brighter than 7.5, the magnitudes of the stars that are there were noted. If the precise magnitude of a star could not be found in any of the books listed under Sources, the magnitude was simply noted as greater than 7.5 - the smaller the star's magnitude, the brighter the star.

Binary or multiple star syystems inside the drawn circle on the atlas were only considered problems if their components' magnitudes were within 2.5, the separation between components was between 5 and 180 arcseconds, and if there were less than three stars 0.5 magnitudes bighter than the system within the circle.

To determine all the information needed, intense perusal of the books listed under Sources was the only approach possible and necessary. A simple and slow method, it was extrememly effective. All the targets on the list from the Wisconsin Ultraviolet Photo-Polarimeter Experiment, one of the three telescopes, were checked for guide star availability and multiple star complications. Of the over three hundred targets, less than one percent had problems. These were noted and given to my project sponsor for final decisions.

Sources

Aitken, Robert, New General Catalogue of Double Stars Within 120° of the North Pole, Vol. I and II, Washington, D.C., Carnegie Institute of Washington, 1932.

Becvar, Antonin, Atlas of the Heavens-II Catalogue 1950.0, Cambridge, Sky Publishing Corporation, 1964.

Hirshfeld, Alan and Sinnot, Roger W., editors, Sky Catalogue 2000.0: Volume I, Stars to Magnitude 8.0, Cambridge, Sky Publishing Corporation, 1982.

Tirion, Wil, Sky Atlas 2000.0, Cambridge, Sky Publishing Corporation, 1981.

A HANDHELD EMERGENCY LOCATOR TRANSMITTER

Larry Doan
Sponsor: William S. Read

The purpose of this project is to design and construct a handheld emergency locator transmitter (ELT) operating at 406.025 Mhz. Survivors of wrecked planes and ships will use this handheld device as a signal beacon so that search and rescue satellites currently in orbit can pinpoint their locations and implement rescue procedures. Experimenting with the design and construction technique, it is found that with more work a device can be built that meets the specified size and power output and reliability constraints.

I. Introduction

Presently, emergency locator transmitters transmit over the 121.5 Mhz and the 243 Mhz bands. These two bands are becoming increasingly "noisy" with radio amateur transmissions. Therefore, many experts are advocating a change to the 406.025 Mhz frequency. In fact, there is already at least one ground listening post designed to receive only this frequency as part of the international search and rescue satellite-aided tracking (SARSAT) system.[1] At this time there are no commercial ELT's on the market operating at 406.025 Mhz, and this project is an effort, when successful, to encourage commercial manufacturers to make the new ELT. Another major goal of the project is to keep the physical size of the device as small as possible, perhaps as small as a cigarette package. If the complete transmitter can be handheld, it will benefit survivors of wrecked planes and ships greatly since they can take it with them and transmit a signal up to the satellites. With bolted-down and cumbersome existing ELT's on the market, there is no way for the survivors to take the transmitter with them; instead, they must hope that the built-in "crash sensors" of the transmitter have triggered by the force of the crash. These sensors are very unreliable: a study has shown that they trigger only about 35% of the time.[2] As such, there is even more motivation to build a handheld transmitter. The size of the complete device has been set as 2.2 in. by 5 in. This is not a rigid constraint although it is realized that the more compact the device is, the more justified is its value. Furthermore, the transmitter must be able to put out between 1 and 5 watts of power continously for 50 hours, the time being an FCC requirement.

---

[1] Space World, November 1983, p.22.

[2] Aviation Consumer, October 1, 1979, p.17.

II. Experiments and Results

The first design consideration in designing the transmitter is to design the oscillator to generate a signal. To keep the frequency of the signal stable a crystal must be used in the oscillator circuit. In the first 2 weeks of the project, an oscillator circuit was designed, built, and tested. The crystal used was a 121.5 Mhz crystal since there were many of these conveniently available. When tested, the output showed a stable signal within 3 kHz of 121.5 Mhz. This slight deviation is due to the fact that high frequency crystals tend to oscillate a few kHz below their designated frequencies. However, this small amount of error is very tolerable in ELTs since the signals they transmit are not precisely at some frequency but tend to wide-band, passing into neighboring frequencies.

The next phase of the project involves multiplying the 121.5 Mhz signal by 3 to bring it up to 364.5 Mhz. Since this is still in a prototypical stage, 364.5 Mhz was felt to be close enough to the desired frequency of 406.025 Mhz so that the results at 364.5 can be applied for use later at 406.025. In theory, frequency multiplying is loosely based on the theory of the Fourier series: a nonsinusoidal wave can be constructed from an infinite number of sine waves of different frequencies. Applying this, we feed the 121.5 Mhz signal from the oscillator, assumed to be sinusoidal, into a very nonlinear transistor stage (class C) to break it up into a very nonsinusoidal waveform at the output. Now since the output is, in theory, composed of an infinite number of sine waves all multiples of 121.5 Mhz, we need appropriate circuitry at the output to tune in the desired frequency, in this case 364.5 Mhz, the third harmonic. Experimentally, it was expected that complications would develop at 364.5 Mhz not apparent at 121.5 Mhz. At about 250 Mhz and going on up, discrete electronic components become very unreliable: capacitors act as inductors while inductors act as capacitors, and wires act as inductors. Also, at these high frequencies, there are all kinds of stray capacitances and inductances all over the circuit board, and unwanted interactions and couplings between components, cables, etc. that one must be very careful in laying out his circuit board so that these effects do not become dominant and kill the desired results. A multiplier circuit was built on regular printed circuit board with reliable components and good grounding for the signals. When the circuit was finally tested, it was a complete failure as it could not tune in to the desired 364.5 Mhz signal at all. Instead, the output was filled with unwanted signals, the lowest being 50 Mhz and the highest being about 2 Ghz. Then different parts of higher qualities were substituted, circuit layout was changed many times to minimize stray reactances, and a solid grounding plane was used in the backside of the circuit board for better grounding. However, the situation did not improve . Finally, it was decided that "chip" componenets should be used. These are tiny resistors and capacitors specially developed for high-frequency work. Also, it was decided that the design should be modified somewhat to acco-

modate a 100.000 Mhz crystal so that a 400.000 Mhz signal can be produced. 400.000 Mhz is a lot closer to 406.025 Mhz but it's still close enough to 364.5 Mhz so that no major modifications need to be made. A new circuit board was built and tested and the results were much better. The output showed a signal within 5 kHz of 400.000 Mhz and it was a stable signal. The error of 5 kHz is still acceptble. All other harmonics such as 100, 200, 300, and 500 Mhz were at least 20 dB down, or 100 times weaker than the main 400 Mhz signal. However, the power output of 0.1 mW was about 10 times lower than expected. This poses great potential problems since it would then take about 5 subsequent stages of amplification to bring the signal up to the 1-5 watt range, and that number of stages would exceed the size limit of the device.

At the end of the 10 week period, a circuit board measuring 1.7 in. by 5.5 in. was built and partially tested. There are four amplifier stages on the board and the first two of those have been tested. The resulting output so far is a signal within 5 kHz of 400.000 Mhz at 10 mW of power. The stability of this signal after a time of countinuous operation and with respect to extremes of temperature remain to be seen as time ran out.

III. Conclusions

More time is needed to complete the development of the transmitter. So far the results are encouraging. It is now known that generating the correct frequency is straightforward. So to obtain 406.025 Mhz we will use a 135.342 Mhz or a 101.506 Mhz crystal and multiply the signal from the oscillator using a very similar circuit as the circuit developed with 400.000 Mhz. More work need to be done to investigate the weak power output coming out of the multiplier stage. Although we can use the weak signal from there and amplify it to the desired power level, a 10 time loss of power may indicate that there is a fundamental problem with the circuit and so needs to be corrected. Once this problem is solved, all the subsequent amplifying stages are relatively straightforward. Then it will be time to construct a good antenna for the transmitter and test the reliability of the whole device. It is believed that the transmitter can be easily be handheld since a circuit board with all the components for the transmitter, plus or minus one stage, has been constructed and met the size limitations with no major difficulties.

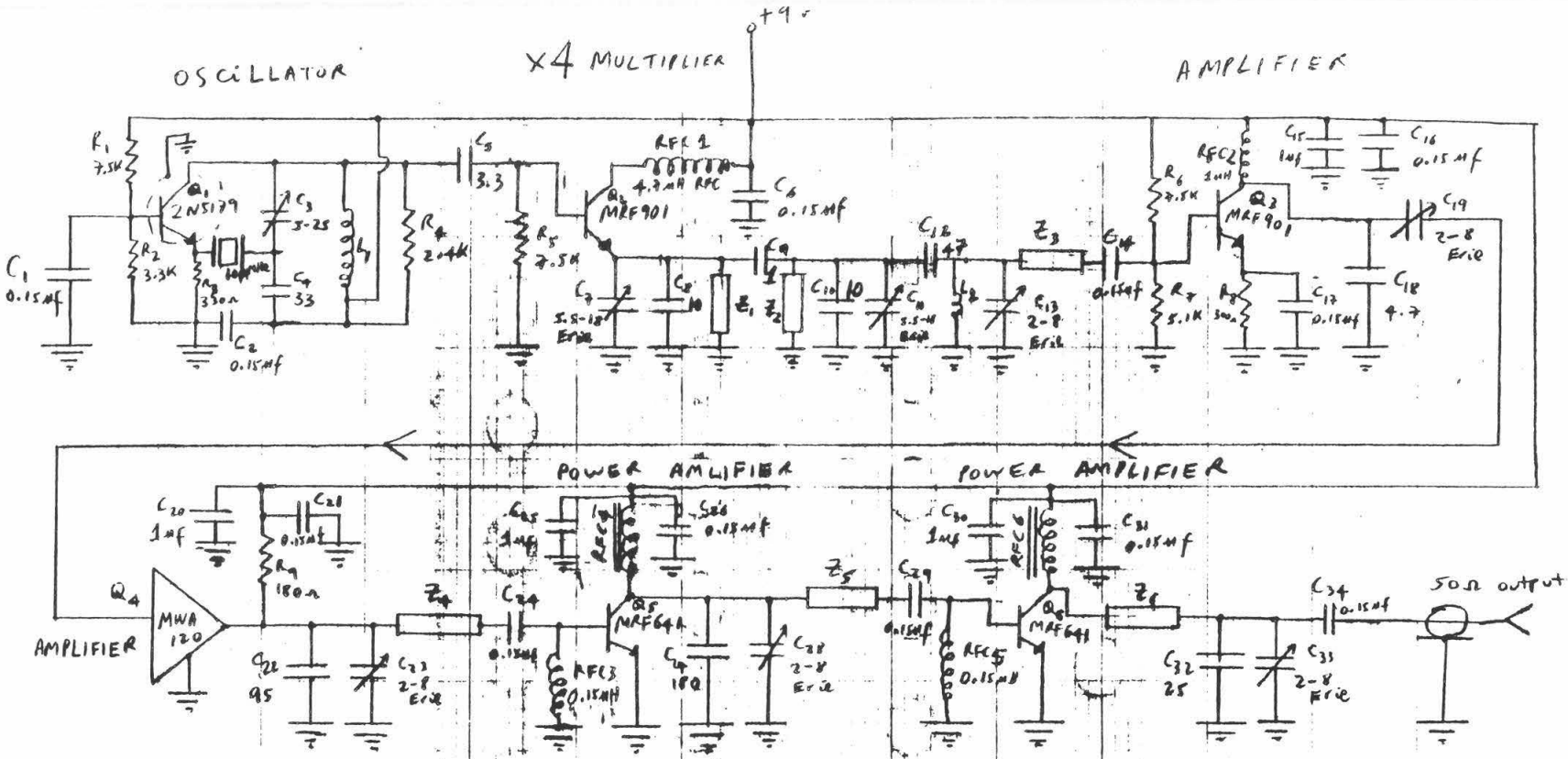

Notes

1. All capacitors in Pf unless otherwise noted.
2. RFC 4 and RFC 6 are Ferroxcube type chokes.
3. Z_1 and Z_2 are microstriplines used as inductances for the two tank circuits.

5w 400MHz Hybrid Transmitter

The Data Analysis of the IO Radical Self-reaction

by Stefan Feuerabendt

Dr. Stan Sander, Faculty Sponsor

Abstract

Flash Photolysis has been used to obtain the relationship between pressure and the branching ratio for the reaction of the IO radical with itself. Data analysis ambiguities resulting from a linear least-squares fit compelled the writing of a program to incorporate a non-linear least-squares fit to the data. This should reduce uncertainties in the rate constant determination.

Introduction

The self-reaction of halogen oxide radicals (XO) has been investigated by Stan Sander and Robert Watson using the BrO radical.

$$XO + XO \xrightarrow{k_a} X_2 + O_2$$
$$\xrightarrow{k_b} 2X + O_2$$
$$\xrightarrow{k_c} X_2O_2$$

The Branching ratios are defined as follows:

$k_{a/k}$, $k_{b/k}$, $k_{c/k}$ where $k = k_a + k_b + k_c$.

Sander and Watson determined accurately the values of these ratios for BrO.

Sander has measured the sum of the rate constants for the IO radical. This value is 5×10^{-11} cm³/molecule/s. A finite amount of I radical exists in the troposphere. This can react with O_3 to form an IO radical.

$$I + O_3 \longrightarrow IO + O_2$$

The determination of the branching ratios is necessary to accurately model ozone chemistry in the troposphere. The purpose of this research was to determine the branching ratio, $k_{b/k}$, using the I radical and ozone as reactants. This is possible since k_b is essentially cancelled out; the newly created I radical reacts with O_3.

Discussion

The measurement of $k_a + k_c$, call this k_1, was to be accomplished using Flash Photolysis. This technique uses an intense flash of light created by exciting a Xe flash lamp. The light reacts with I_2 to create I radicals.

$$I_2 + h \longrightarrow 2I$$

The concentration of I_2 is held at a small enough amount to ensure extremely quick and complete conversion to I. Reaction is complete in a few hundred microseconds. The I radical then reacts with the ozone. IO radical concentration was measured using ultraviolet spectroscopic measurements at 427nm,

the wavelength at which IO absorbs. Several flashes were needed each experiment; consequently, a signal averager was incorporated to reduce noise.

Several experiments were conducted at both 50 torr and 350 torr. The data analysis consisted of a least-squares fit to a linear relationship. Two problems were seen to exist. The first consisted of a distinct curvature in the linear relationship thought to exist. This dilemma was explained later by Dr. Sander, who determined a relationship between the amount of I radical and the pressure. The curvature existed only in the 50 torr experiments, thereby resolving the problem. That is, the I radical existed longer at a lower pressure, which resulted in a destruction of the linearity in the first few hundred microseconds.

The second problem was more serious. It consisted of the error introduced by converting the data to a linear relationship. The data consisted of a measurement of the ratio of light intensity before and after the flash took place. The data wsa then transformed into a linear relationship as follows:

$$\ln(I_o/I) = sl[IO] \quad \text{Beer's Law}$$

$$sl[IO] = \text{optical density}$$

$$\frac{d[IO]}{dt} = -2k_1[IO]^2$$

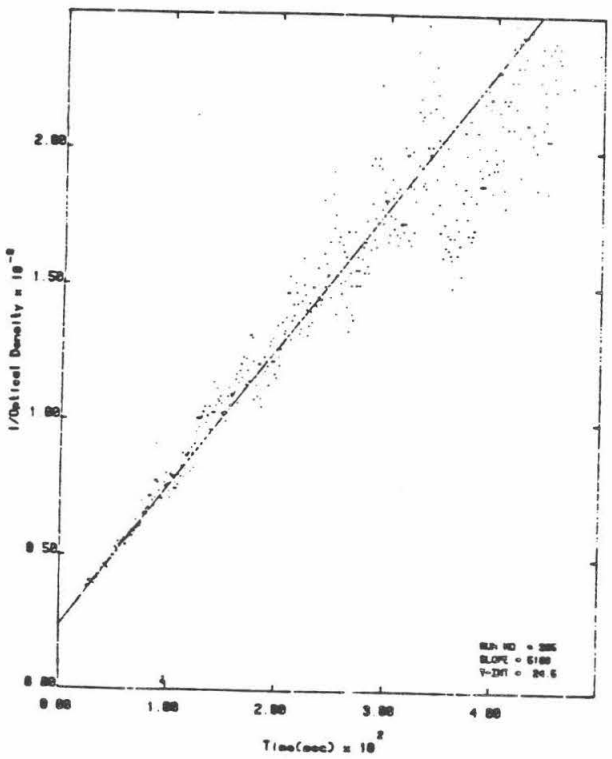

Linear data analysis plot

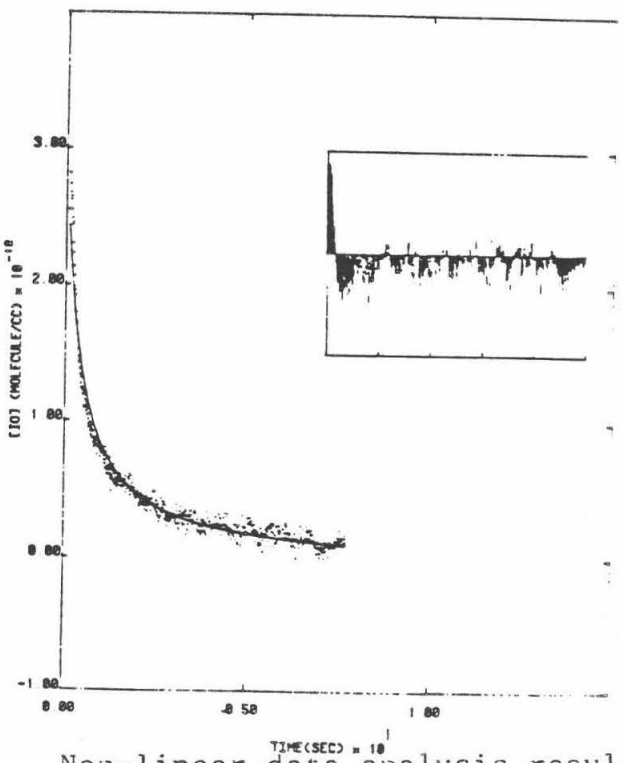

Non-linear data analysis results in less variation at low [IO].

$$\Longrightarrow 1/[IO] = 1/[IO]_o + 2k_1 t$$

$$\Longrightarrow 1/(sl[IO]) = 1/(sl[IO]_o) + (2k_1/sl)t$$

This is a linear relationship between the inverse of the optical density and time. The problem is that as [IO] approaches 0, I approaches I_o so the 1/[IO] has large variations. This gives a large distribution around the resulting line at low values of [IO]. A more uncertain fetermination of k_1 results. The results from the experiments using this method of analysis are as follows:

Pressure (torr)	Slope
349.2	3948
350.0	4455
349.5	4126
350.4	5500
350	3670
61.0	5041
60.9	4058
61.7	7509
61.5	6456
60.9	5016

Large variations are clearly prone to occur using this method.

A possible solution lies in the fitting of the non-linear function using a least-squares algorithm. The algorithm chosen is one created by Marquardt. The algorithm requires giving initial guesses of the two parameters in the fitting function, computing how well the fitting function fits the data, adjusting the parameters by minimizing the partial derivatives of the fitting function with respect to the parameters. This is continued until the fit is suitably close to the data.

The result is a program written in BASIC for the Tektronix 4052 computer. The program takes in data from a magnetic tape and produces a non-linear fitting function of the form

$$y = a_1/(1 + a_1 a_2 t).$$

It also plots the fitting function with the data. In addition, the program plots the residuals, which are defined as the difference between the fitting function and the data at 100 microsecond intervals.

Tests were attempted for the program. False data was generated, and the program iterated close to the data after only two or three iterations. The program has not been successfully tested however.

Conclusion

The non-linear fit reduces the dependence of the error on the value of the data considerably. This is evident from the residuals plot produced by the new data analysis program. A much more confident determination of the branching ratio should result when the program is fully tested. The program fits well to test data generated by Dr. Sander, but has not been fully tested on real data.

Bibliography

Phillip R. Bevington
Data Analysis and Error Reduction for the Physical Sciences
McGraw-Hill, New York, 1969.

Thomas 1. Isenhour, and Peter C. Jurs
Introduction to Computer Programming for Chemists
Allyn and Bacon, Boston, Mass., 1979.

Stanley P. Sander, and Robert T. Watson
"Kinetics and Mechanism of the Disproportionation of BrO Radicals"
Journal of Physical Chemistry, 1981,85,4000.

THE RELATIONSHIP BETWEEN FULL DISK SOLAR MAGNETIC FLUX AND IMF STRENGTH AT 1 A.U.: AN OVERVIEW

by

Gerard Jungman

Faculty Sponsor: Dr. James Slavin (JPL)

ABSTRACT

ISEE-3 and IMP interplanetary magnetic field measurements and Mt. Wilson magnetograph full disk flux measurements were collected for the period March 1, 1967 to May 4, 1984. Over this interval, covering most of Solar Cycles 20 and 21, correlations were sought between the interplanetary magnetic field and the sun's magnetic field. Both the IMF and solar fields were observed to be weakest near solar minimum and strongest near maximum. However, the trend was weaker in the interplanetary field and the overall linear correlation coeffiicient between IMF magnitude and Mt. Wilson solar flux was only 0.38. The IMF parameter most sensitive to solar flux was the absolute magnitude of the field component normal to the plane of the ecliptic, B_Z, with a correlaation coefficient of 0.62. This result was interpreted as being due to enhanced hydromagnetic wave and transient activity near solar maximum when the solar flux levels are greatest. However, analysis of the IMF magnitude log distributions showed that they remained Gaussian in character throughout the 17 year interval.

Introduction

The basic model for coronal expansion due to Parker[1] predicts the distortion of the solar dipole field into a characteristic Archimedean spiral pattern. The hydrodynamic process of expansion dominates the magnetic pressure in the case of the Sun as the hydrodynamic energy density exceeds the magnetic energy density by a factor of approximately 100. "Frozen" field lines are then carried outward by the supersonic solar wind plasma. This "freezing" of field lines is a consequence of the high conductivity of the plasma. Consider the situation in a reference frame moving with the plasma. Due to the high conductivity the spatial derivatives of the electric field go to zero. Manipulation of the induction equation yields

$$\frac{d}{dt} = \iint \nabla \times (\vec{J}/\sigma) \cdot \vec{dA}$$

One sees that the time rate of change of the magnetic field through a given surface goes to zero as conductivity, σ , tends toward infinity; there is no diffusion across field lines. This gives rise to an interplanetary magnetic field, or IMF, which is coupled in a complicated, poorly understood way (due to instabilities and transient activity) to the solar magnetic field. Variations in the IMF parameters and the solar magnetic fields with the solar cycle have been previously studied[2,3,4], but generally in separate investigations. The following is a study of the relationship between the solar and interplanetary magnetic fields over a large portion of the last two solar cycles.

The Data Set

The IMF data set employed in this analysis is composed of hourly averages reduced from the ISEE-3 and IMP spacecraft observations for the period January 1, 1964 to May 4, 1984. The cartesian components of the field in the following discussions refer to the geocentric solar ecliptic coordinate system. The solar flux data, kindly provided by Dr. Robert Howard and the Mt. Wilson Observatory, are full disk magnetograph flux values averaged over 4 Carrington rotations for the period March 1, 1967 to May 4, 1984. They provide a measure of the total rectified magnetic flux passing through the solar reference surface[4].

Figure 1 displays a time history of the solar flux measurements over Carrington rotations 1415-1749 (i.e., years 1967-1984). The enhancements in the middle 1500s and the late 1600s correspond to the cycle 20 and 21 maxima. Figure 2 is a time history of IMF magnitude at 1 A.U. averaged over 4 Carrington rotations (1 CR = 27.275 days) for a visual comparison with the solar flux. Another IMF parameter of interest is the logarithm of the field strength. It has been shown by Burlaga and King[5] that the IMF magnitude is generally log normal normal distributed. Hence, the use of statistical averages and moments

have rigorous interpretations when the logarithms are used. Figure 3 presents a time history of $10^{\langle \log B \rangle}$*. For both representations it is clear that IMF strength is highest near solar maximum and weakest near minimum with the signature strongest during the recent 1978-1980 peak in solar activity. Overall, the amplitude of the variation in the IMF is weaker than in the Mt. Wilson solar flux values. In particular, little enhancement of the IMF was observed during the cycle 20 maximum, while the solar flux parameter showed a clear peak.

Linear Correlations

Figure 4 presents a linear correlation plot of solar flux versus <B>. Least square best fits obtained by regressing both axes on the other are displayed. Points representing averages with less than 50% temporal coverage for the IMF have been deleted. The correlation is not striking, but it is clearly present. Hence, while long term increases in the solar field tend to produce increases in interplanetary field magnitude, there is a large unpredicted variance. The causes are probably related to long term variations in the nature of the solar wind source regions and their magnetic fields.

The most interesting result of the IMF component correlations concerns $\langle |B_z| \rangle$, the component normal to the plane of the ecliptic. As shown in Figure 5, the magnitude of B_Z is highly correlated with solar flux. This is also the field component most sensitive to Alfven wave activity because its average value is near zero[1,3]. An Alfven wave may be detected as an oscillation of the B_Z vector without a change in total field strength.** Also, this component may play a role in the theory of galactic cosmic ray modulation as suggested by Thomas and Goldstein[6]. Their theory suggests that at times of solar reversal the Sun "sheds" closed flux structures. It is predicted that the net B_Z magnitude associated with these structures is approximately 0.1 nT as they convect past 1 A.U. Figure 6 indicates that the net averaged B_z, with sign, is distributed about zero. However, 0.1 nT is quite small and transient deviations of this magnitude are often observed. As shown in Figure 7, the correlation between field component parallel to the plane of the ecliptic and the solar flux was weaker than with B_Z or the total field.

B Distribution

As noted earlier, previous studies have found the IMF magnitude to be log normal distributed. Typical histograms of B and the corresponding log B distribution are shown in Figure 8. Given the correlation of B with solar flux, one may ask whether the high <B> values are caused by an overall increase in IMF strength or by an increase in the frequency

*"<>" indicates time averaging

**Alfven waves are transverse oscillations of the magnetic force lines in a magnetohydrodynamic fluid.

of high magnitude transients. The latter situation would be detectable as a decrease in the Gaussian character of the log B distribution. This condition may be quantified by a χ^2 normality test.

Figure 9 displays a summary plot of the distribution parameters together with the solar flux and IMF magnitude. To a high degree of accuracy the distributions appear to retain their Gaussian character with the only significant changes being the translation of the mean. Though there is some correlation of χ^2 with the solar flux level, the χ^2 parameters always stay within the limits of a Gaussian distribution. This result supports the idea that the level of Alfven wave activity may increase (i.e., enhanced $\langle|B_Z|\rangle$) without producing secondary peaks in the field distribution.

Summary

The three main results of this study are: 1) a linear correlation between IMF intensity and the Mt. Wilson solar flux measurements is present, but it probably only indicative of a more complicated underlying relationship, 2) there is a strong correlation between $|B_Z|$ and solar flux most probably due to an increase in the magnitude of hydromagnetic waves and transient activity near solar maximum, and 3) the distribution of IMF magnitudes does not change in character significantly over the course of the solar cycle.

REFERENCES

1. Parker, E.N., Interplanetary Dynamical Processes, Interscience, New York, 1963.

2. King, J.H., Solar cycle variations in IMF intensity, J. Geophys. Res., 84, 5983, 1979.

3. Slavin, J.A., E.J. Smith, and B.T. Thomas, Large scale temporal and radial gradients in the IMF: Helios 1,2 ISEE-3, and Pioneer 10, 11, Geophys. Res. Lett., 11, 279, 1984.

4. Howard, R., and B.J. LaBonte, Surface magnetic fields during the solar cycle, Solar Physics, 74, 131, 1981.

5. Burlaga, L.F., and J.H. King, Intense interplanetary magnetic fields observed by geocentric spacecraft during 1963-1975, J. Geophys. Res., 84, 6633, 1979.

6. Thomas, B.T., and B.E. Goldstein, The effect of solar field reversal in the modulation of galastic cosmic rays, Solar Wind 5, ed. M. Neugebauer, pp. 441-448, NASA CP-2280, Washington, D.C., 1983.

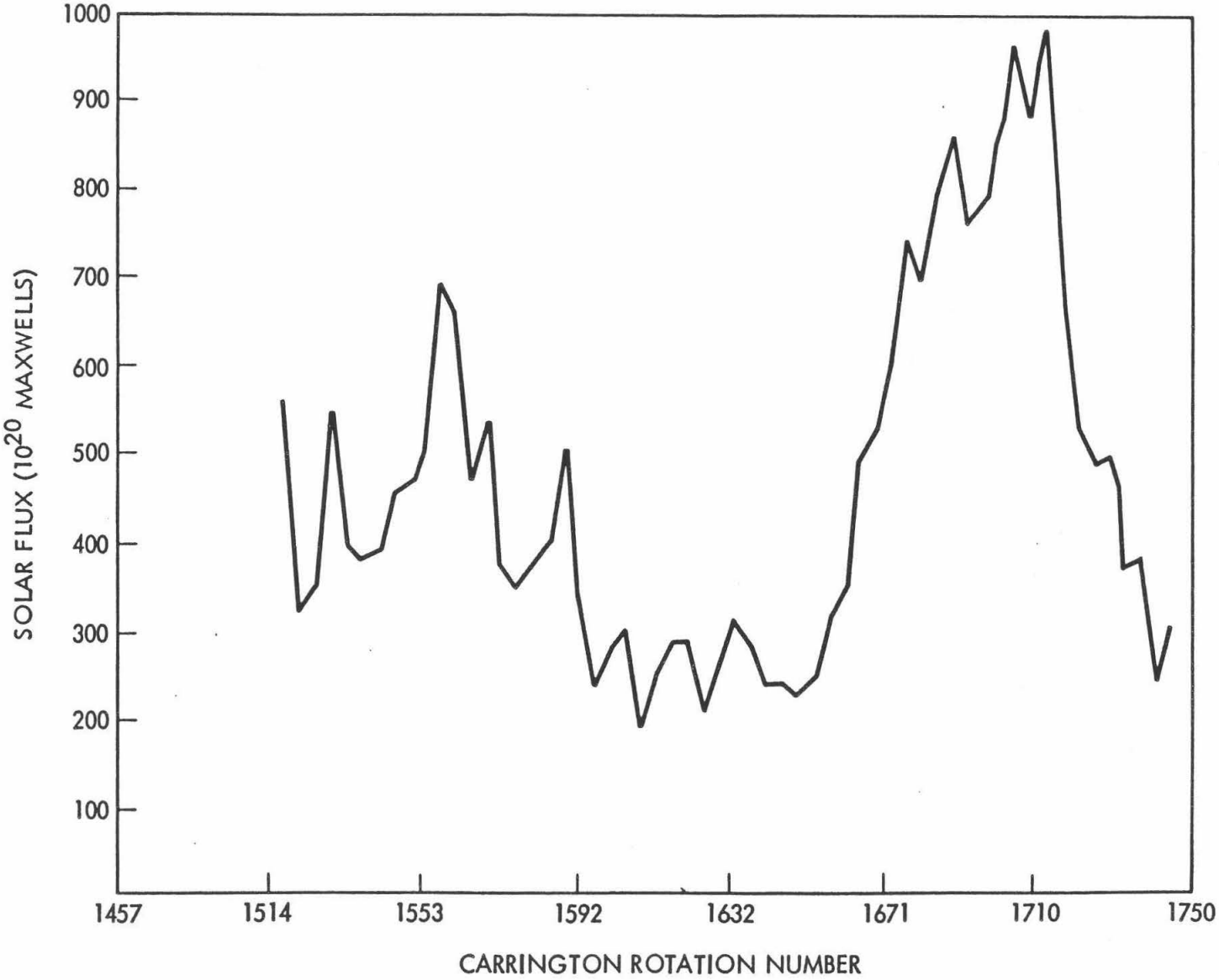

Figure 1. A time history of the Mt. Wilson solar flux parameter.

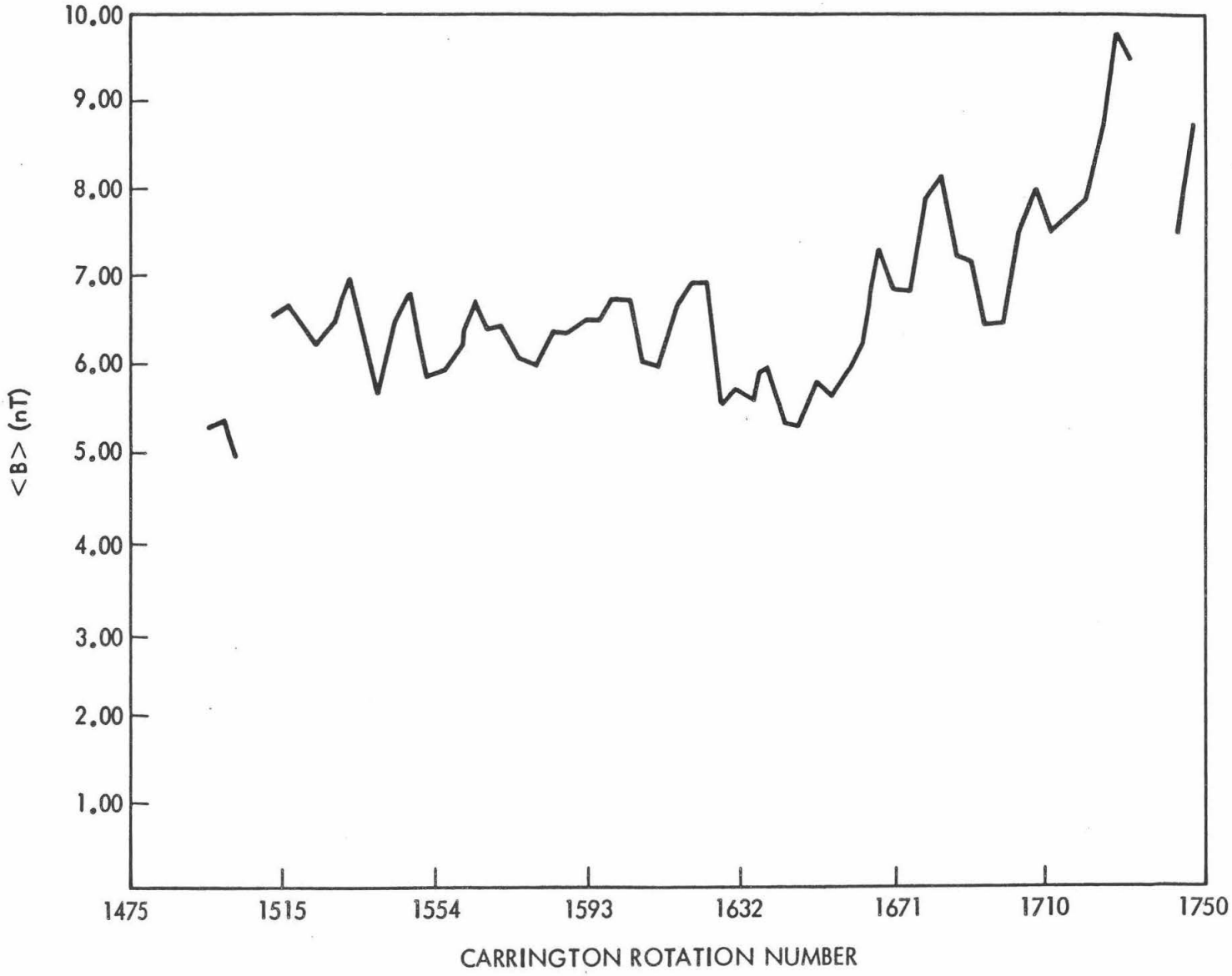

Figure 2. A time history of <B> averaged over 4 Carrington rotation intervals.

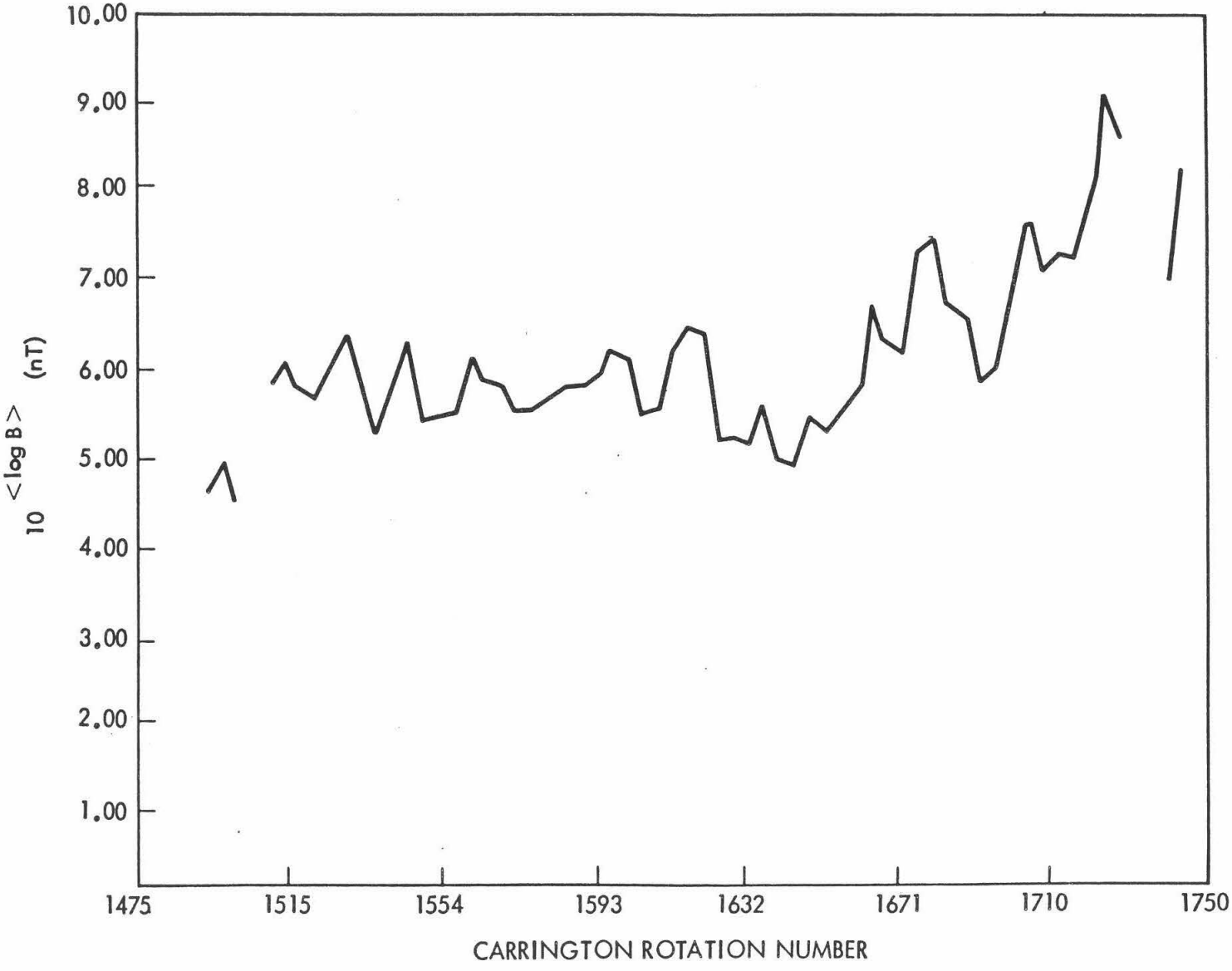

Figure 3. A time history of $10^{\langle \log B \rangle}$ averaged over 4 Carrington rotation intervals.

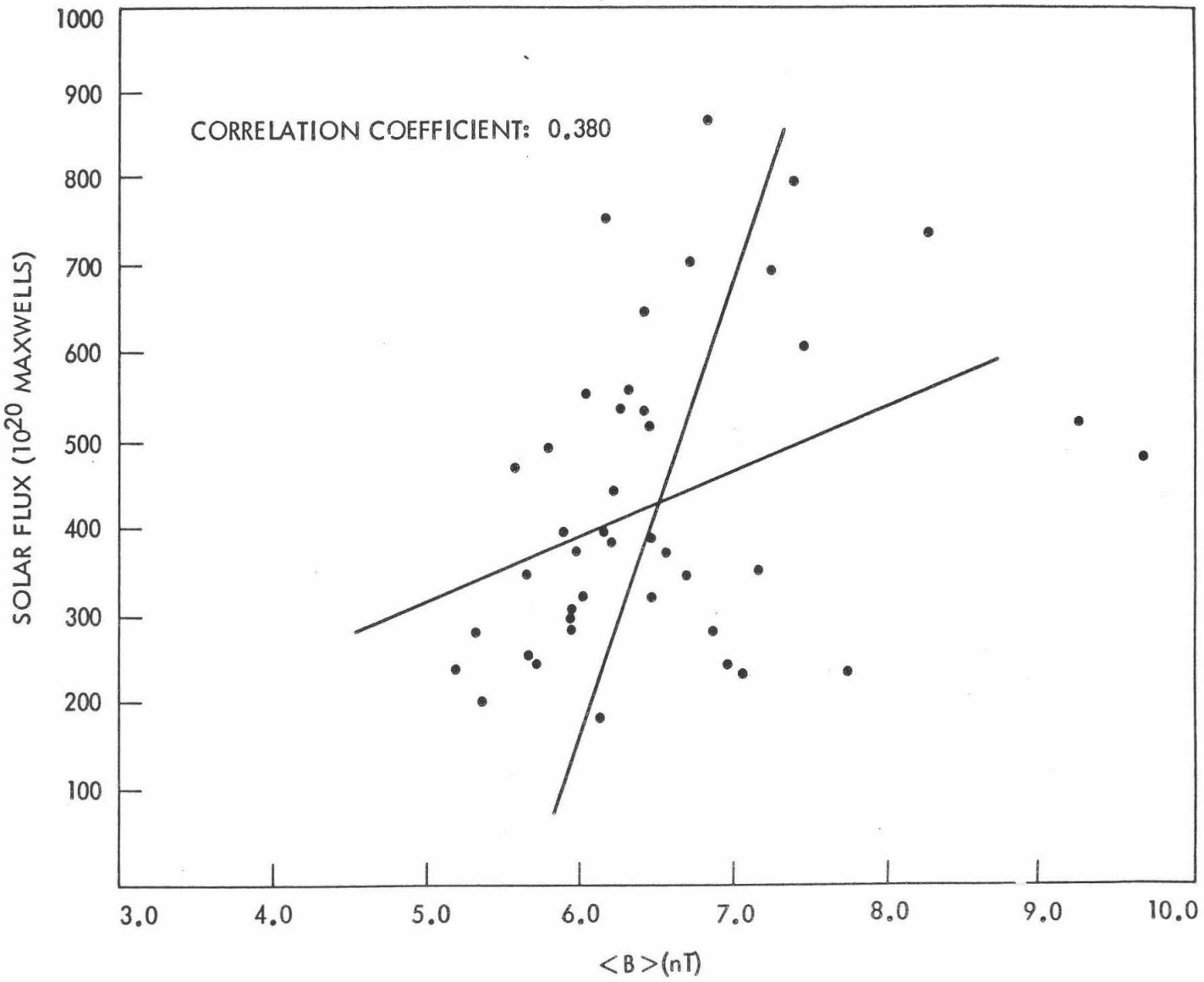

Figure 4. Linear correlation between IMF magnitude and full disk solar flux.

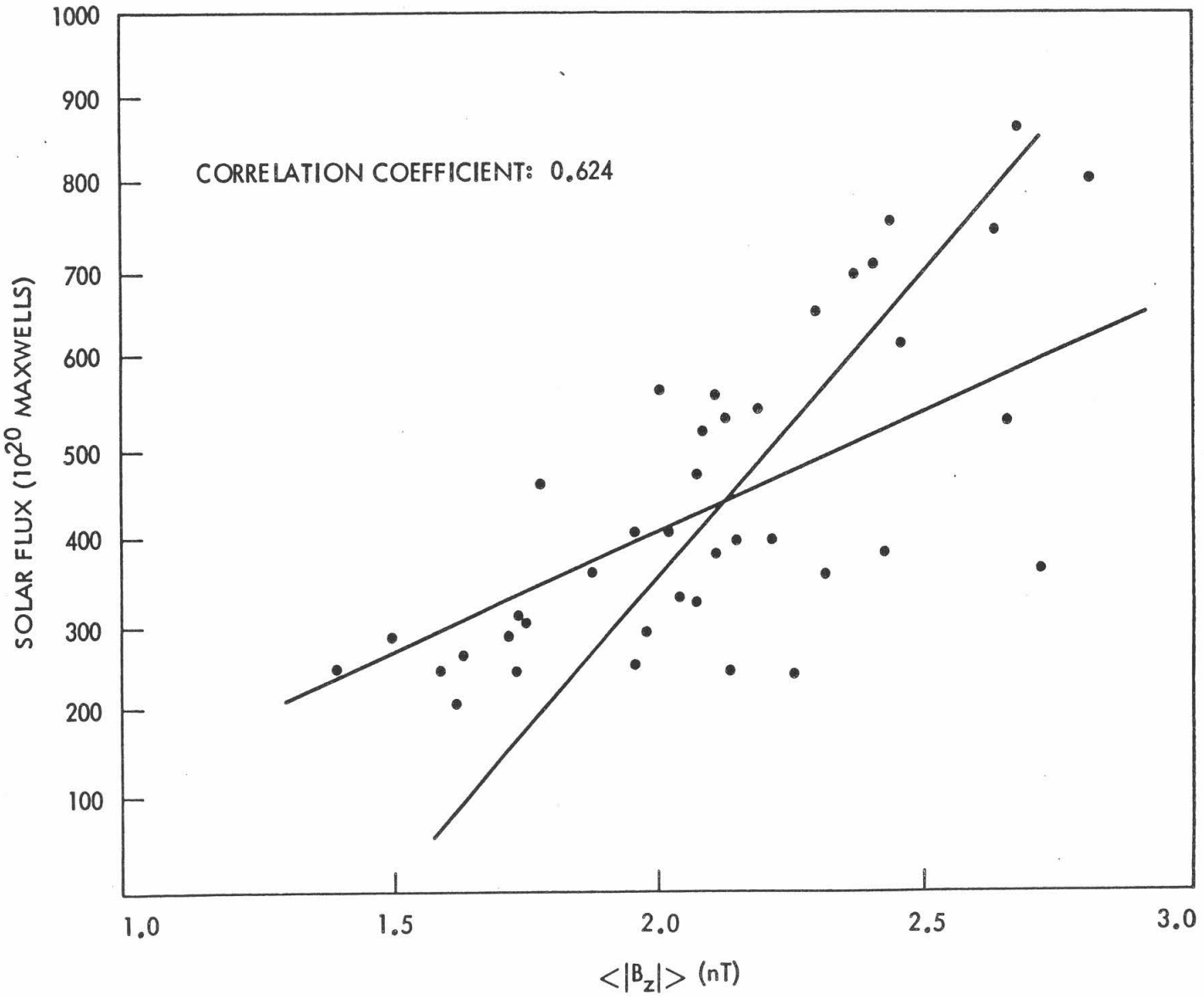

Figure 5. Linear correlation between the absolute value of B_z and full disk solar flux.

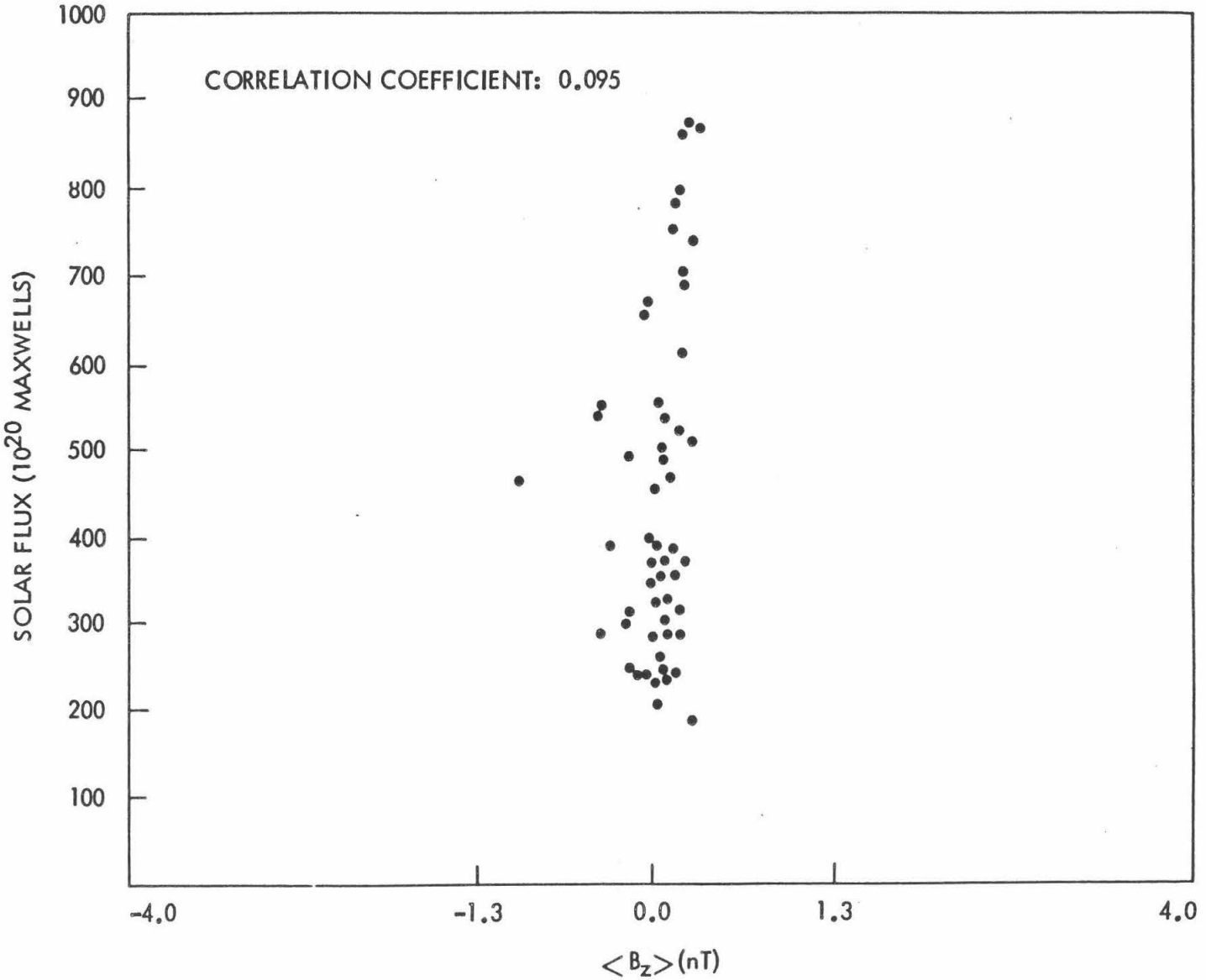

Figure 6. A plot of full disk solar flux versus B_z.

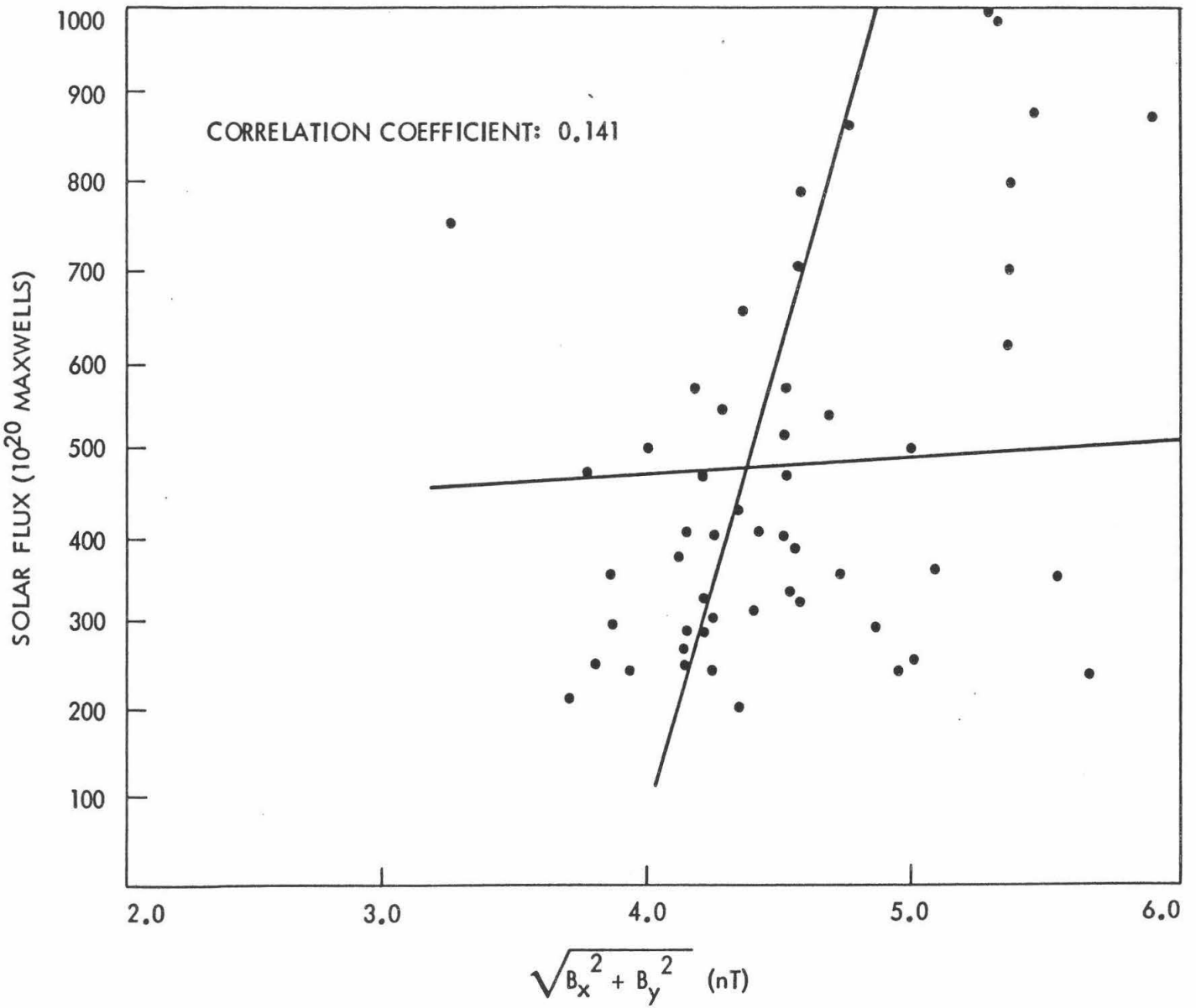

Figure 7. Linear correlation between the IMF component parallel to the ecliptic and full disk solar flux.

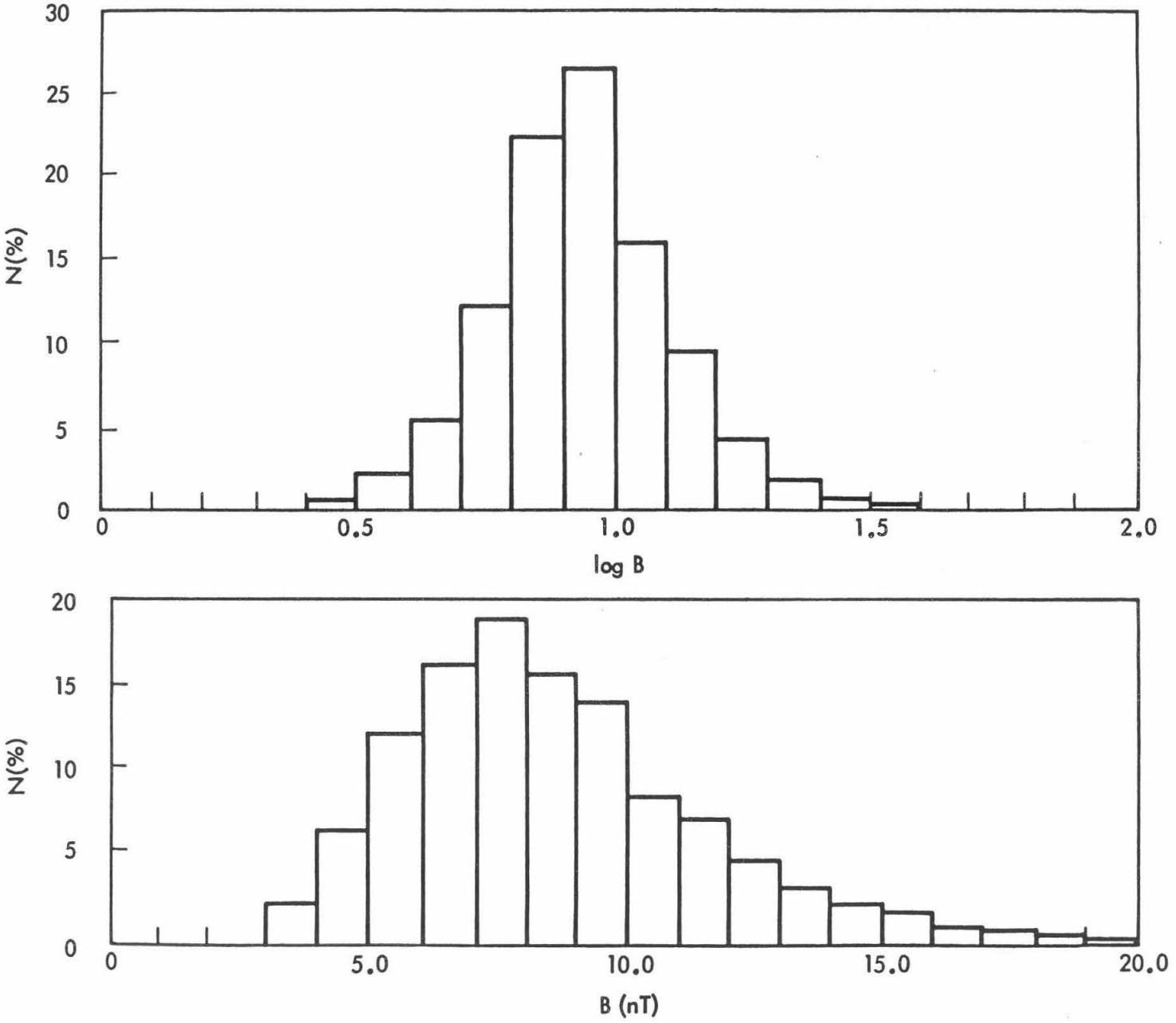

Figure 8. Typical B and log B distributions in the interplanetary medium.

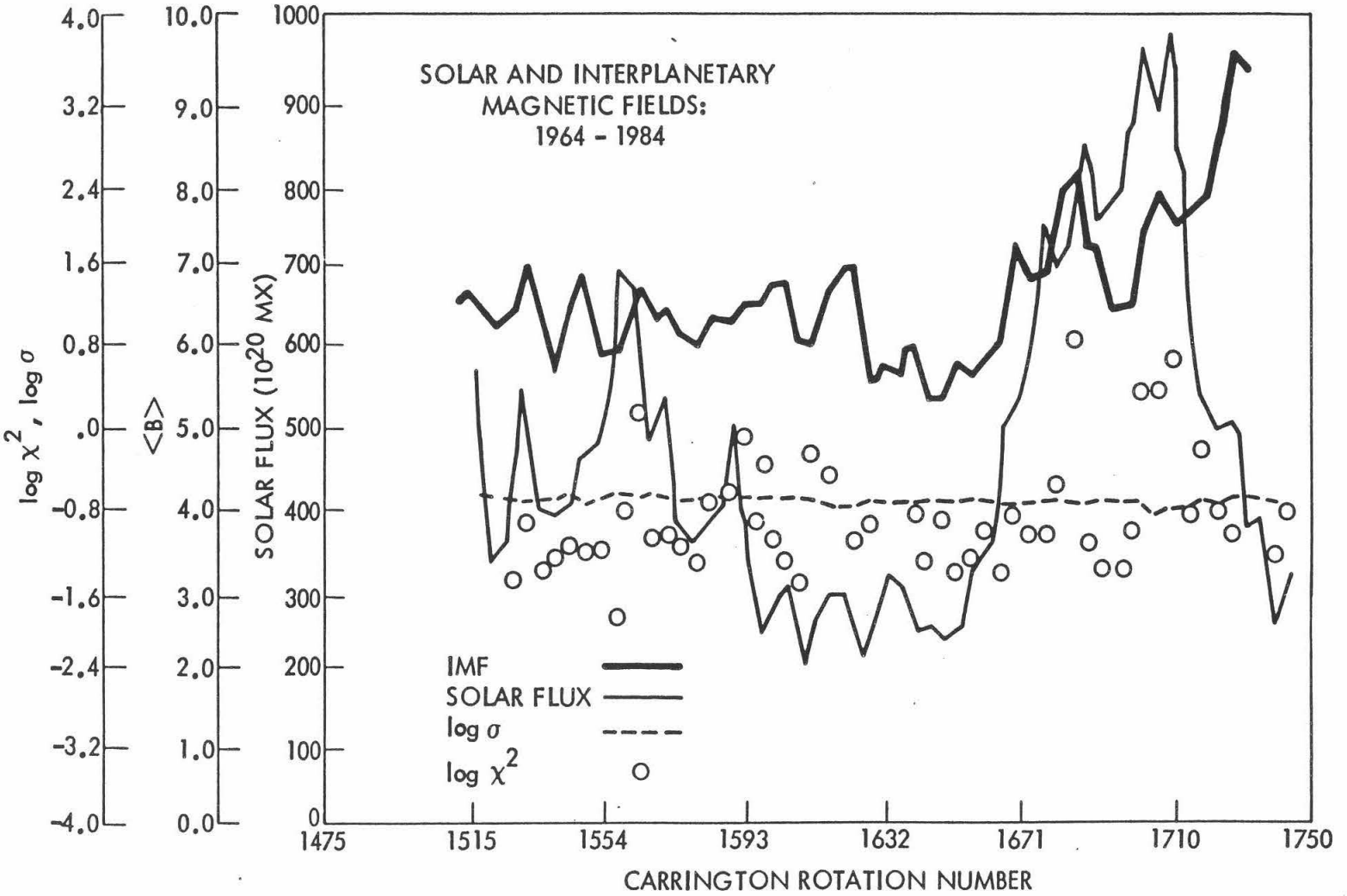

Figure 9. Summary plot of IMF distribution parameters and the full disk solar flux.

MODELING JUPITER'S MAGNETOSPHERE USING PIONEER DATA: POLYNOMIAL APPROXIMATION OF DUSK DAWN CURRENT SYSTEMS

by

MIKE A. RIGLER [1]

under the direction of

BARRY T. THOMAS [2]

SEPTEMBER, 1984

1. Undergraduate, California Institute of Technology, Pasadena, California 91126

2. Jet Propulsion Laboratory, California Institute of Technology, Pasadena, California 91109

ABSTRACT

The Jovian magnetospheric field, measured by Pioneers 10 and 11, can be well modeled by a combination of current systems comprising the planetary dipole, an azimuthally symmetric current disc, an image dipole representing the effects of magnetopause currents, and a dusk-dawn tail sheet which extends along the disc into the dayside magnetosphere. The model suggests that the Jovian cusp is at a much lower latitude than the earth's cusp. Until now, however, the dusk-dawn currents have been approximated by an infinite current sheet with no return current system. A second order polynomial approximation to the magnetic field of a more plausible dusk-dawn current system also gives a low-latitude cusp.

INTRODUCTION

The Jovian magnetosphere is very complex and similar in many ways to the earth's magnetosphere, which has been studied extensively. The magnetic field of Jupiter's powerful dipole is complicated by electric current systems in trapped plasma, and also by the rapid rotation of the planet because Jupiter's rotational and dipole axis are not aligned. This entire interrelating system is compressed and shaped by the solar wind, and effectively contained within a sharp boundary, the magnetopause. The Voyager and Pioneer space probes were equipped with magnetometers. During the Jupiter flybys they measured the magnitude and direction of the magnetic fields in the regions along the flyby trajectories, providing the data used to help develop Jovian magnetospheric models (See Figure 1).

One aspect of the models under contention, is the nature of the currents in the trapped plasmas near Jupiter. These plasma particles enter the magnetosphere via the cusp region. Previous models of the Jovian magnetospheric field have used an equatorial disc current (magnetodisc) which is dependent on local time, and a radial current flow which is latitude dependent, or is local time dependent, or which has low-latitude return currents. Low-latitude return currents, however, might require a low-latitude cusp, and a low-latitude cusp is not a feature of this model. The local-time dependent and latitude dependent systems seem physically implausible and there is evidence to contradict radial currents. Radial equatorial currents produce magnetic field lines which spiral out toward the dawnward direction in both of the dayside quadrants (See Figure 2), whereas the Pioneer data suggests the field lines curve away from the noon meridian, bending tailwards in both dayside quadrants (See Figure 3). As mentioned, the low-latitude cusp idea is inconsistent with this model. Evidence exists, however, for a low cusp latitude. Pioneer 11 encountered high particle fluxes during low-latitude excursions and periodicity in expected cusp regions. Pioneer 10 data suggests a low-latitude separatrix between open and closed lines in the near tail, indicative of a low cusp. Also, Jupiter's auroral zone has been observed at low latitudes ($\sim 75^{\circ}$). Aurora are caused by particles entering the upper atmosphere along the cusp lines.

These doubts prompted the development of a new model (Jones et al., 1981) which extends the dusk-dawn tail current sheet into the dayside magnetosphere, coplaner with an azimuthally symmetric magnetodisc (See Figure 4). This current sheet might result from centrifugal forces and angular momentum conservation. Jupiter, with its rapid rotation, might fling plasma farther out against the solar wind than the earth can, allowing a tail-like current on the dayside. Such a current sheet produces field lines which curve away from the noon meridian in both quadrants.

These currents were included in a magnetospheric model which was optimized by fitting to the Pioneer 10 and 11 magnetic field data (Thomas and Jones, 1984), and the results are promising. The optimized model describes the data well and its field line profile indicates a low-latitude cusp. In this preliminary fitting, the dusk-dawn currents were represented by a sheet of finite thickness and width, and infinite length. An additional fitting had the length limited to the magnetopause boundary. While the length limitation or lack thereof did not significantly affect the results, it was the concern of the authors that the absence of return currents in the representation might be responsible

for an artificially low cusp location, or for otherwise affecting the field line profiles.

The next step, then, was to correct these deficiencies in the dusk-dawn current sheet and see if the field changes or if the quality of the fit diminishes. This report presents the results of fitting the model, with an improved current system, to Pioneer 11 data. This time the magnetic field of a dusk-dawn current with a north and south return current system was approximated by a second order polynomial. The objective was to observe changes in the resulting field line profiles -- particularly a change in cusp location.

METHODS AND RESULTS

The Model

The Jovian magnetospheric field can be thought of as the superposition of the planetary dipole field and the perterbation field. The perterbation field represents the effects of solar wind, rotation, currents . . . etc., and in the model it falls naturally into four sources: the image-dipole field, the tail-sheet current field, the magnetodisc field and the dusk-dawn current-sheet field. The superposition of these four fields is the perterbation field.

The image dipole field is used to represent the contribution of magnetopause currents. There is, of course, no actual dipole sitting upstream of Jupiter but the approximation is valid if the magnetopause boundary cross-sections are nearly conic sections. Since the solar wind is fairly uniform and constant and the dipole potential varies inversely as distance squared, the conic section approximation is not unreasonable and indeed the earth's magnetosphere resembles a paraboloid. Nevertheless, this might still be a weak link in the model and might require closer inspection. The image dipole was parameterized by an upstream distance along the Jupiter-Sun line (X_I) and a ratio of image to planetary dipole moments (M_I).

The Biot-Savart law was used to compute the magnetic fields of the source currents, so they were arranged in the form of current carrying loops and strips. The azimuthally symmetric magnetodisc was represented by an equatorial disc of finite thickness, with an inner and outer radius, and separated into a concentric series of paired circular current loops, the pair separation representing the disc thickness. The concentric loops were separated by one Jovian radius (1Rj). The general disc axis was aligned with the dipole axis and inclined to the rotational axis. A real magnetodisc would not be able to rigidly corotate with the planet; the outer regions would fall behind, giving the disc a spiral warp. To represent this in the model, the longitude of the axis of each ring pair was allowed to vary with radius. The parameters required to describe the magnetodisc were: the inner radius (R^I_D) and outer radius (R^O_D), the tilt angel (TILT), the twist rate ($d\Theta$), and the longitude of the axis of the innermost ring pair (Θ_D), the ring thickness (dZ_D), the disc current scaling factor (I_o), and the radial dependence of the current of each ring pair. The current diminishes radially according to the Power Law $I = IoR^{-P}$.

The tail currents are the result of plasma trapped or delayed in the elongated field lines extending from the nightside magnetosphere. For the purposes of the model, the tail was divided into a finite number

of infinite dusk-dawn ribbons, each of finite thickness and width, and all carrying the same current. The tail current sheet was hinged to the magnetodisc on the nightside and allowed to rock and move up and down in synchronism with the tilted, rotating magnetodisc. As with the magnetodisc, the tail could not be expected to be perfectly rigid for its entire length, so the representation was not entirely realistic except for the near tail. The field contributions of the far tail currents are so neglegible, however, that is was not important to know their exact location. Thus, the parameters needed to describe the tail currents were its thickness (dZ_S), its cutoff distance (X_T), and the current per unit width (J_{oT}).

The model requires the tail sheet to somehow extend along the magnetodisc out into the dayside. The earlier version of this model simply used the infinite dusk-dawn strips of the tail. The dusk dawn sheet could not be everywhere coplaner with the warped magnetodisc so it was made coplaner with the ring pair nearest the spacecraft radius. The dayside sheet current was given an independent current which diminished with sunward distance, according to the Power Law, $J = JoX^{-a}$. Parameters of the current sheet, then, were the inner current (Jos), the Power Law index (a) and the dayside extent of the current sheet (X_S).

A different approach was taken with the new version of the model. To counter the deficiencies of the infinite sheet, a dusk-dawn sheet roughly confined to within the magnetopause was hypothesized. At the dawn end, the current splits to go north and south and each half returns via the magnetopause boundaries to rejoin at the dusk end (See Figure 5). Rather than attempting to place restrictions on these currents, we examined the magnetic field resulting from such a configuration. The field is divergence free. Symmetry arguments reduce it to the form (to second order):

$$Bx = A_1z + A_2xz$$

$$By = A_3yz$$

$$Bz = A_4 + A_5x + A_6x^2 + A_7y^2 - \frac{(A_2+A_3)z^2}{2}$$

where the x-axis is approximately the Jupiter Sun line, the y-axis is the dawn-dusk line and the z-axis is the dipole axis. Field component directions limit the signs and relative sizes of a few of the coefficients. This new version of the magnetic field of the dusk-dawn currents has the seven parameters A_1 through A_7.

The Fitting Procedure

The model parameters (of both versions) were optimized using a multivariable computer minimization routine designed to minimize the residual(s):

$$s^2 = \sum_{k=1}^{3}\sum_{i=1}^{N}\frac{(B_k^o(r_i)-B_k^c(r_i))^2}{3N}$$

where B^o = observed (pioneer 11) field
B^c = computed (model) field
k = indicates field dimensional component
r_i = location in Jovian spacetime coordinates of the ith data point

The data points used in this fit were 10 minute vector magnetic field averages from the Pioneer 11 inbound and outbound trajectories, when the spacecraft was between 20 Rj and 46 Rj from Jupiter. This is within the minimum observed magnetopause boundary during the Pioneer flybys. The data from more distant regions is highly variable and could include events not having a lasting effect on the magnetosphere. At any rate, the second-order polynomial would be unreliable in these regions. A bolder data set awaits a less fragile approximation.

Before the fitting algorithm was used to fit the model it was tested extensively. In addition to learning how to set convergence criterion and other options, I uncovered a few useful characteristics of the algorithm. The computer time required for convergence increases drastically with increasing numbers of variables. As it turns out, the routine takes too long if it is asked to process more than twelve or so variables. An intelligent choice of starting values can also reduce computer time. The order in which the variables are arranged is important (the order in which the algorithm perceives them). They should be arranged in order of sensitivity (i.e. their impact upon the residual). A local minimum can give a false convergence. Restarting the algorithm after resetting the variables to the latest values can shock the routine out of local minima so multiple runs are often necessary for convergence. Second order polynomials, however, are no challenge to the algorithm.

With this knowledge to aid the fitting process, the infinite sheet model was fit with the data. The preliminary runs used only 20% of the data (every 5th data point) to reduce computer time while the sensitivities of all of the sixteen parameters was gauged. Average values of the four most insensitive variables became constant values. The remaining variables were arranged in estimated order of importance and the runs were continued until the residual reached 2.4 gamma (the perterbation fields in question are of the order of 10 to 50 gamma).

Good starting values were selected for the seven polynomial coefficients and the polynomial field model was fitted to the Pioneer 11 data. Preliminary runs were made with all of the non-polynomial parameters held constant while the seven polynomial coefficients stabilized at a fairly low residual. The relative sensitivities of the twelve non-polynomial parameters were tested and four of them were found to be at least 10 to 100 times more sensitive than the others. These four parameters: the disc current scaling factor (I_o), the inclination of the ring pair axes (TILT), the disc power law index (p), and the rate of twist in the disc ($d\Theta$), were from then on allowed to vary with the seven polynomial coefficients. The rest of the parameters were usually held constant but a few were judged sensitive enough to merit occasional addition to the variable list to test their stability.

The residual of the polynomial field model reached 3.1 gamma (and was still slowly continuing to drop). The best fitting values of the parameters for both the infinite sheet model and the polynomial field

model are shown in the table. Also shown are the cusp latitudes and the physical cusp angles, and the field-line profiles are displayed in Figures 6 through 9. The cusp latitudes for the two models are about the same but the physical cusp angle of the polynomial version is higher. The high-latitude field lines of the polynomial version curve tailward sooner than those of the infinite sheet model. The best fitting polynomial can be plotted by itself. It resembles the field of a sheet like current.

CONCLUSIONS

The cusp is at a low-latitude despite the current sheet improvement. The lack of return currents was probably giving an artificially low cusp angle, but now the high-latitude lines are more tightly confined within the current loops. The second-order polynomial seems capable of adequately approximating a dayside sheet-like current system. It is significant that the polynomial field retained a dusk-dawn current-sheet configuration during the fitting process. If some other process, like a radial current system, was dominant, the non-polynomial variables would have been able to partially absorb the shock to the residual caused by the intrusion of an incorrect field into the model. It is very unlikely that the optimized polynomial would still be a recognizable dusk-dawn sheet field. This is further evidence for a low-cusp latitude and it is further evidence for the azimuthally symmetric magnetodisc and a dusk-dawn sheet-like current system in the dayside magnetosphere. If, however, the old radial current model is eventually found to be a more accurate description, then the low-cusp latitude will allow a more plausible radial return current system, thus eliminating the need for local-time or latitude dependence. The dusk-dawn sheet model is simpler though, and fits the data well.

TABLE OF OPTIMIZED PARAMETERS

Parameters	Infinite Sheet Model	Polynomial Field Model	Units
I_o	.821	.688	amp x 10^8
p	1.57	2.11	
TILT	11.2	11.0	deg
Θ_D	33.9	33.9	deg
$d\Theta$	1.16	1.21	deg/R_J
R^i_D	12.6	12.6	R_J
R^o_D	106.	108.	R_J
dZ_D	.608	.608	R_J
J_oT	.536	.460	amp x $10^5/R_J$
X_T	503.	503.	R_J
M_I	15.4	8.79	
X_I	190.	190.	R_J
J_oS	.930	---	amp x $10^6/R_J$
X_S	284.	---	R_J
dZ_S	2.02	---	R_J
a	.628	---	
A_1	---	-.460	
A_2	---	.00844	
A_3	---	.00313	
A_4	---	7.59	
A_5	---	.0583	
A_6	---	-.00409	
A_7	---	-.000909	
Residual:	2.4	3.1	nT
Cusp Lat:	66.25	70.25	deg
Cusp Ang:	18.7	44.12	deg

FIGURE CAPTIONS

Figure 1. Unit vector magnetic field projections on the local meridian plane along the Pioneer 11 inbound and outbound trajectory.

Figure 2. The field lines of a radial current system: a spiral of the the same sense in both dayside quadrants.

Figure 3. The field lines of a dusk-dawn current system: The lines turn tailward in both dayside quadrants.

Figure 4. A noon-midnight meridian schematic of the model field sources, including the planetary dipole, an upstream image dipole, a magnetodisc and dusk-dawn currents in both the dayside and nightside magnetosphere.

Figure 5. A dusk-dawn sheet current with north and south return currents.

Figure 6. A noon-meridian field line projection of the magnetosphere of the infinite-sheet model.

Figure 7. As Figure 6, with a more detailed view of the cusp region.

Figure 8. A noon-meridian field line projection of the polynomial-field model magnetosphere.

Figure 9. As Figure 8, with a more detailed view of the cusp region.

REFERENCES

Jones, D. E., J. G. Melville, II, and B. T. Thomas, Equatorial disc and dawn dusk currents in the frontside magnetosphere of Jupiter: Pioneer 10 and 11, J. Geophys. Res., 86, 1601, 1981.

Thomas, B. T., and Jones, D. E., Modelling Jupiter's magnetospheric currents using Pioneer data: Evidence for a low-latitude cusp, J. Geophys. Res., April, 1984.

ACKNOWLEDGEMENTS

I would like to thank Barry Thomas and Doug Jones for letting me take part in their project, and for spending their valuable time with me, and I would like to thank Ed Smith for his invitation to the SURF applicants. I would also like to thank the entire JPL Space Physics Group and everyone responsible for the SURF program at Caltech for sharing their resources with me.

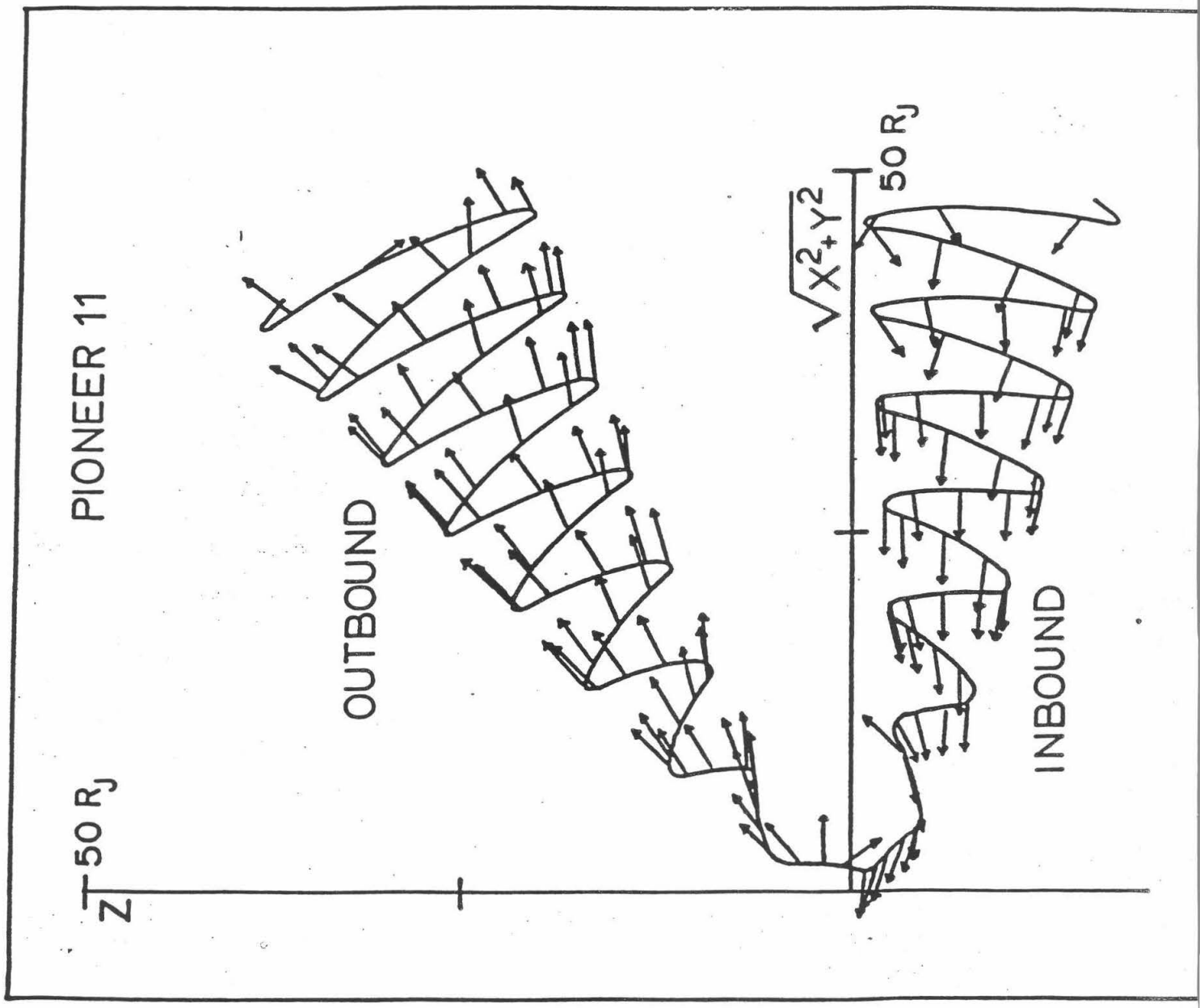

FIGURE 1

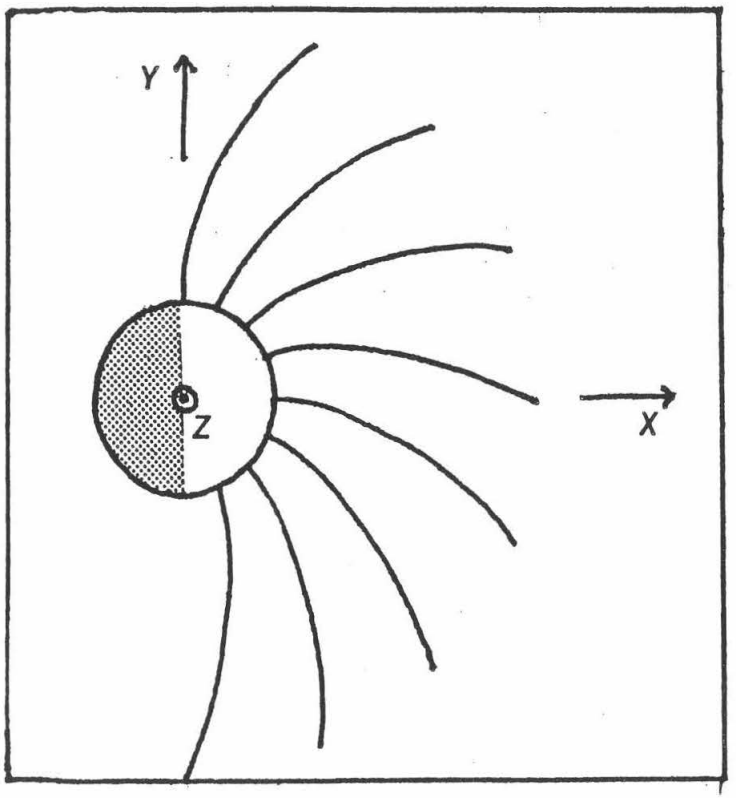

Figure 2

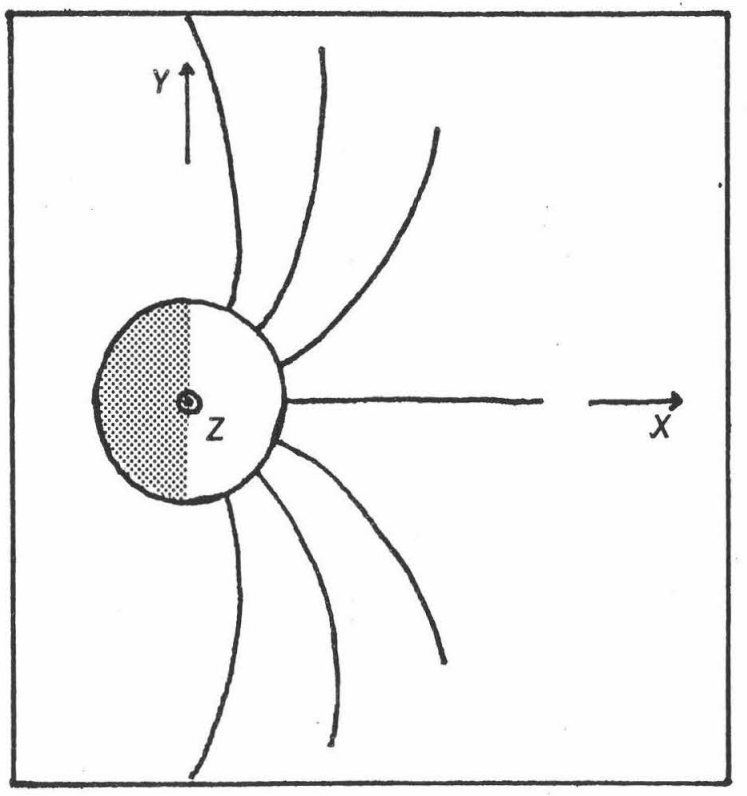

Figure 3

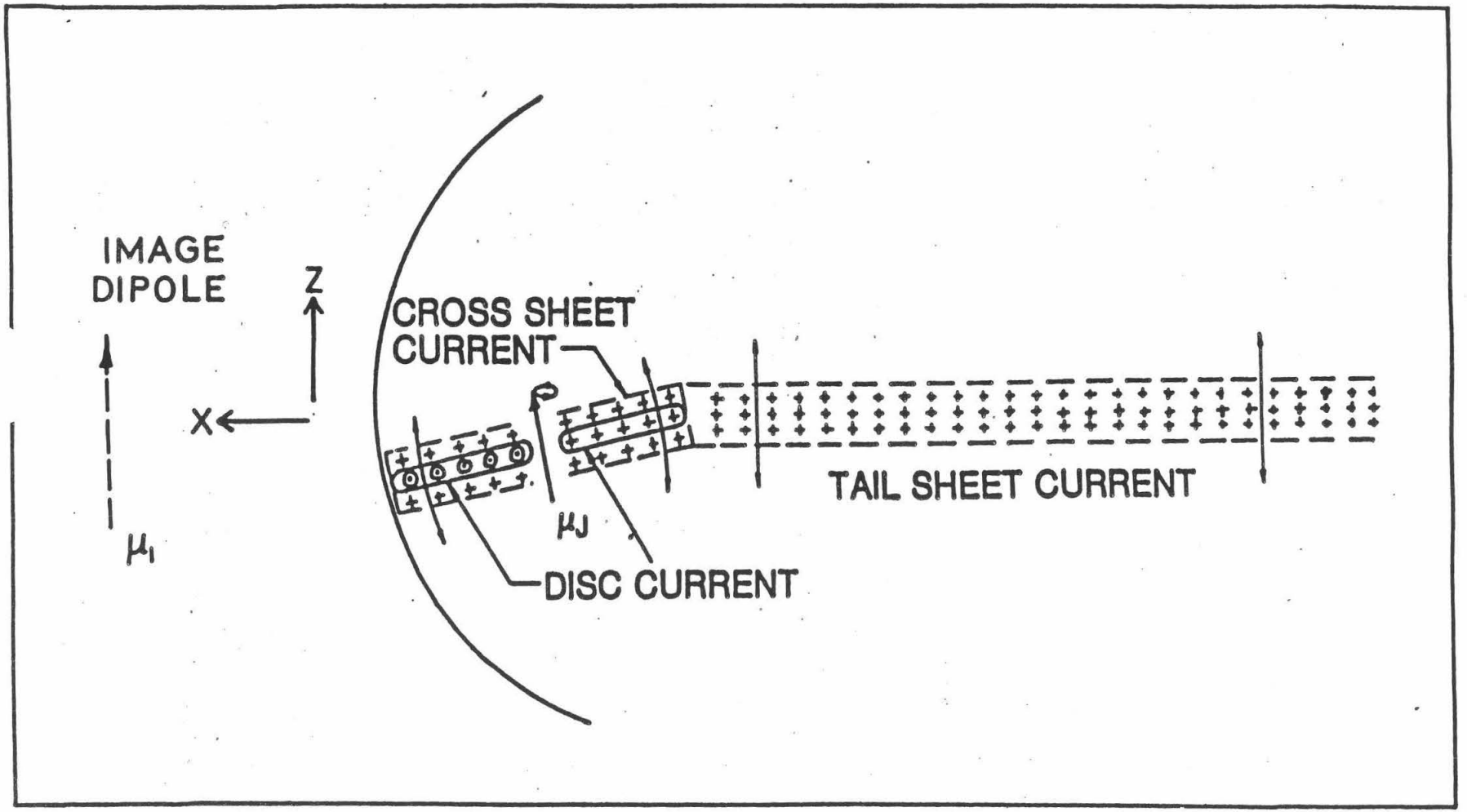
IMAGE
DIPOLE
Z
X
μ_I
CROSS SHEET
CURRENT
μ_J
DISC CURRENT
TAIL SHEET CURRENT

FIGURE 4

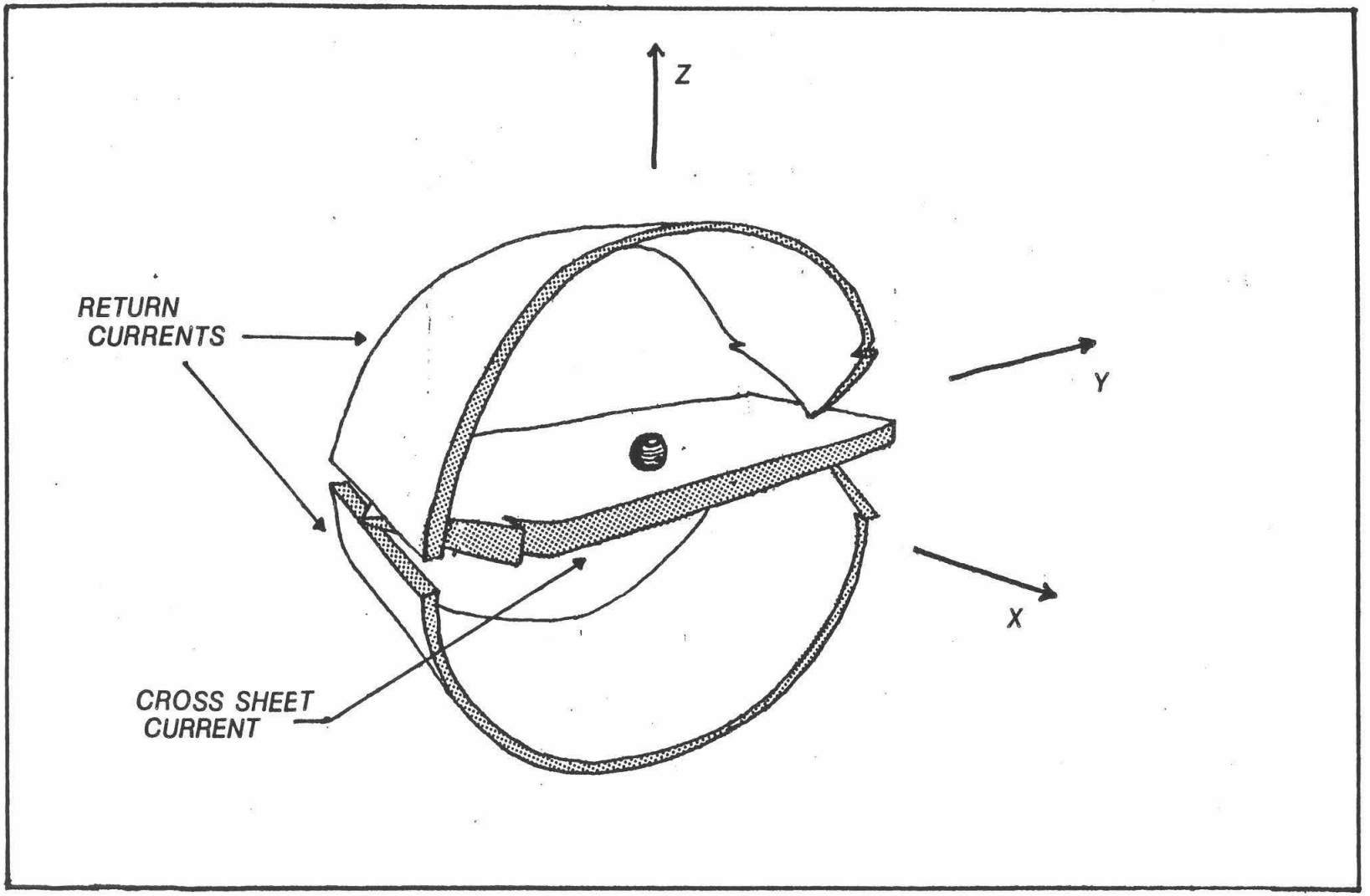

Figure 5

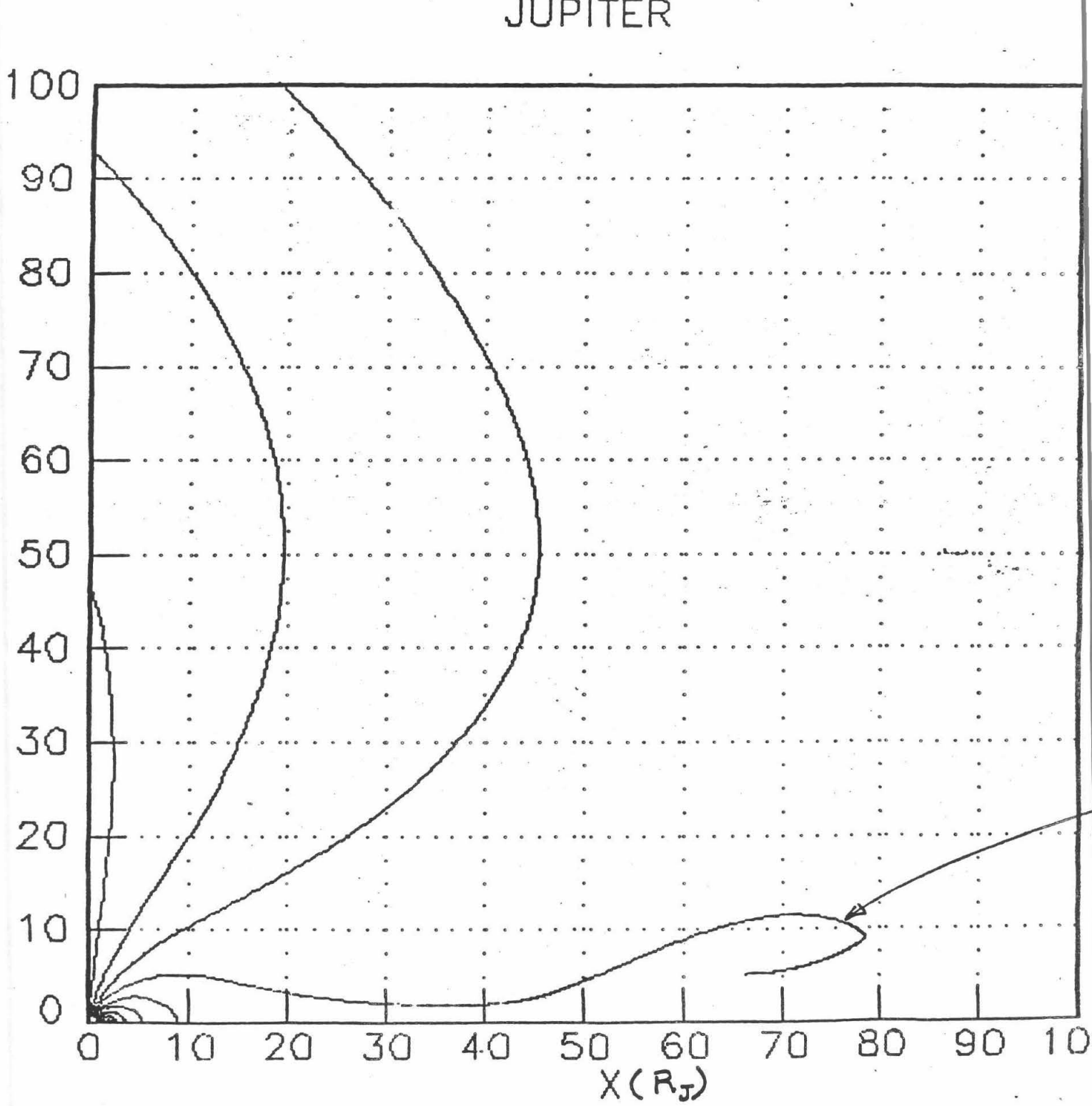
JUPITER
100
90
80
70
60
50
40
30
20
10
0
0
10
20
30
40
50
60
70
80
90
10
X(R_J)

FIGURE 6

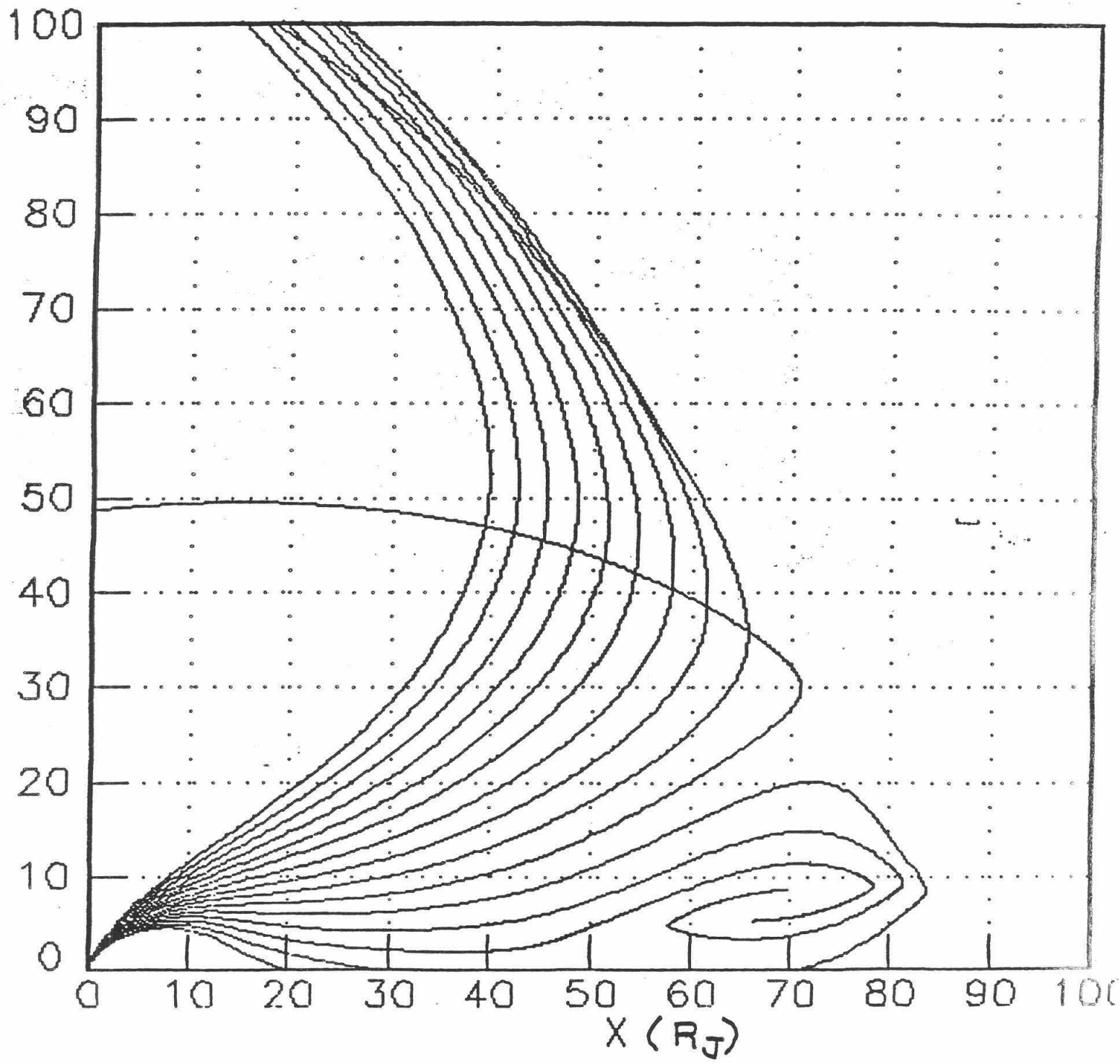
JUPITER
100
90
80
70
60
50
40
30
20
10
0
0
10
20
30
40
50
60
70
80
90
100
X (R_J)

FIGURE 7

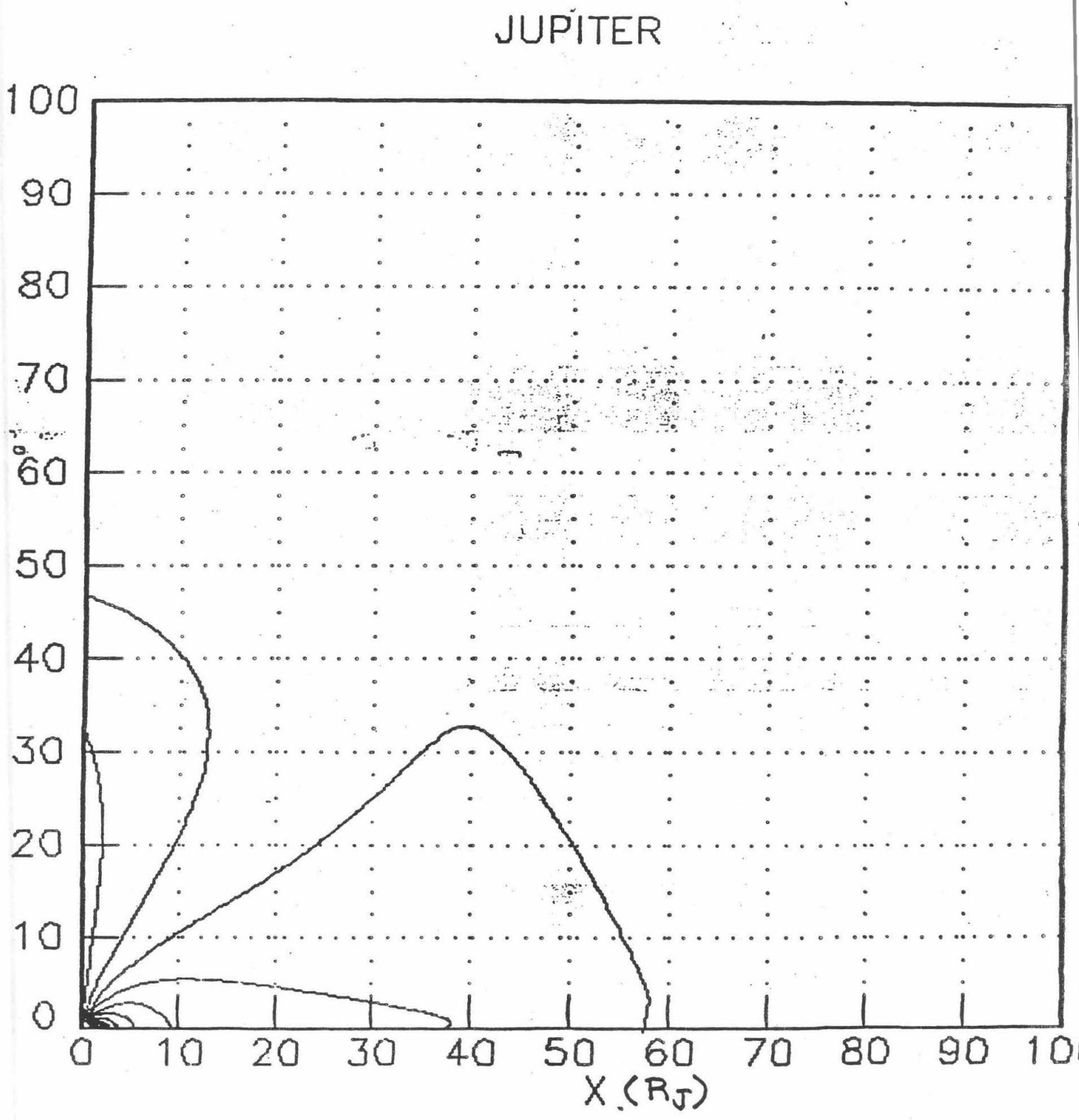
JUPITER
100
90
80
70
60
50
40
30
20
10
0
0
10
20
30
40
50
60
70
80
90
100
X (R_J)

FIGURE 8

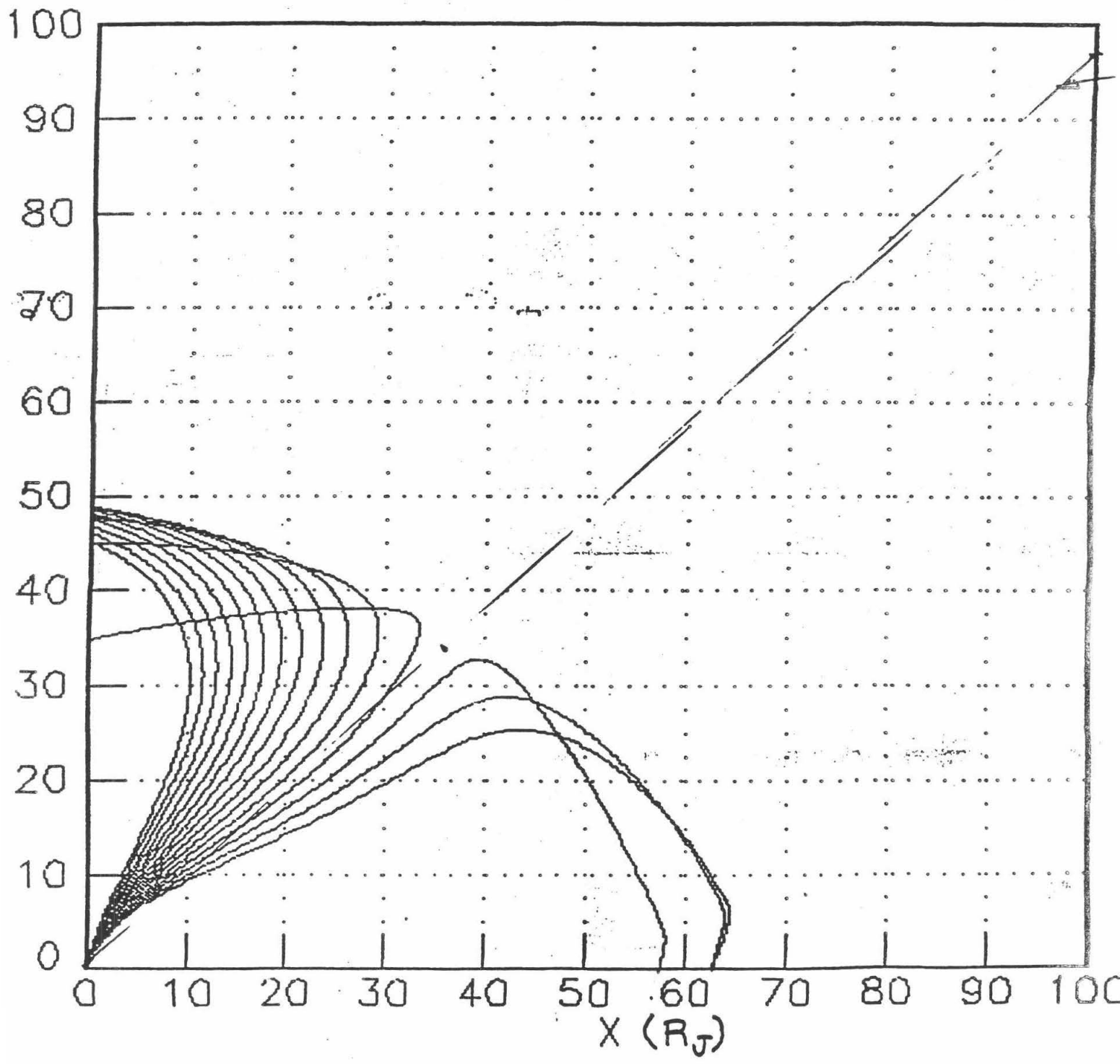
JUPITER
100
90
80
70
60
50
40
30
20
10
0
0
10
20
30
40
50
60
70
80
90
100
X (R_J)

FIGURE 9

ADIABATICITY IN THE EXPANDING SOLAR WIND

Jeffrey A. Valenti, Dr. Edward J. Smith

ABSTRACT: Pioneer 10 and 11 data is used to determine whether rarifaction regions in the solar wind are expanding adiabatically. Temporal variations in the wind characteristics make the determination of a radial gradient difficult, so a study of temperature versus density is used instead. The result indicates that regions that are free from interactions may indeed expand adiabatically.

INTRODUCTION: Fast moving solar wind streams overtake slower moving streams, forming what are known as corotating interaction regions (CIR's), or compression regions. Between these compression regions are areas that are relatively free of such interactions and are referred to as rarifaction regions. Many studies have been conducted, testing whether the solar wind expands adiabatically. Typically, radial gradients are calculated and then compared to theoretical values that are consistent with adiabatic expansion. These studies have shown that, on the whole, the solar wind does not expand adiabatically [Smith and Barnes, 1982]. Much of this departure from adiabatic behavior is attributed to heating within compression regions, which is caused by interactions between two colliding wind streams.

In this study, only rarifaction regions are examined. Methods of identifying rarifaction regions are discussed, with an emphasis on algorithms applicable to a computer. Radial gradients for these rarifaction regions are calculated and compared to theoretical values predicted for adiabatic expansion. Difficulties in this method of analysis are discussed, and an alternate technique is developed in which rarifaction regions at Pioneer 10 are matched up with their counterparts at Pioneer 11. By removing the heating effects due to corotating interactions, this study searches for other sources of heating in the solar wind. If this study shows that the wind expands adiabatically, this would indicate that there is no other major source of heating in the solar wind; whereas, a deviation from adiabaticity would indicate that there exists some other source of heating, such as that due to mass loading by non-neutral interstellar ions.

IDENTIFICATION OF RARIFACTION REGIONS: Corotating interaction regions are often characterized by a sudden increase in the magnetic field strength, followed by a period of sustained high magnetic field, and then either a gradual decline or a sudden drop in the magnetic field. Magnetic fields can also be used to identify rarifaction regions, except the emphasis is on fields that are relatively low.

The identification algorithm used in this study requires the determination of the mean field for a 27-day period (approximately one solar rotation). Any region in which the hourly averages remain below this mean field for at least 24 consecutive hours is identified as a rarifaction region. A new mean field is determined for each 27-day period until the entire data set has been analyzed. While the average is easier to determine than the mean, it tends to be higher, and using it as the threshold occasionally includes a few additional hours in a rarifaction region. For the purposes of this study, it was decided that missing the extreme of a rarifaction region was preferable to including part of a compression region. Thus, the more conservative criterion was chosen.

The results of this computer analysis were quite satisfactory. By using this algorithm, 144 rarifaction regions were observed by Pioneer 10 between Day 64, 1972, and Day 282, 1975; and 250 rarifaction regions were observed by Pioneer 11 between Day 96, 1973, and Day 341, 1981. Magnetic field data was not available for dates other than these, so no identification was possible outside these parameters. The computer-determined boundaries agreed well with samples estimated by hand. The frequency of observed rarifaction regions decreases with increasing radial distance, as would be expected if these regions were slowly merging together. As described later in this report, the rarifaction regions observed at Pioneer 10 match up with those observed at Pioneer 11, further vindicating this method of rarifaction identification. It is important to remember that this algorithm does not guarantee the identification of every rarifaction region, but it will consistently identify only rarifaction regions.

DETERMINATION OF RADIAL GRADIENTS: Once the rarifaction regions were identified, it became possible to study radial gradients without the complicating influence of corotating interactions. Averages for the various solar wind parameters were computed for each rarifaction region. The logarithms of these averages were plotted versus the logarithms of the radii; and by means of linear regression, the radial dependences were ascertained. These dependences, along with the theoretical values one would expect from an adiabatically expanding plasma, are summarized in the table below:

Table of Radial Dependences in the Solar Wind

	Temp.	B-mag	B-y	Density	Vel.
Pioneer 10	-0.76	-1.59	-1.50	-2.53	0.0
Pioneer 11	-0.71	-1.18	-0.94	-1.48	0.0
Adiabatic	-1.33				0.0

Although there is no quantitative determination of the uncertainties associated with these dependences, subsequent analysis indicates that these uncertainties are quite large. Both spacecraft should experience the same radial dependences; however, the values at Pioneer 10 are consistently higher than those at Pioneer 11, varying by as much as 60 percent. Examination of the graphs shows a large amount of scatter characteristics of low precision. Additionally, the points seem to cluster in groups that lie predominantly above the line during one interval and predominantly below the line during another. Further analysis shows that the points are above the line during solar maximum and below it during solar minimum.

The low precision in the radial dependences is caused by temporal variations in the solar wind characteristics. During the ten years covered by this study, the sun went from solar maximum through solar minimum and back to solar maximum again. Pioneer 10, whose magnetometer ceased after only five years, operated exclusively during a period of declining interplanetary magnetic field, which accounts for the larger than expected radial dependences. The dependences observed by Pioneer 11 are closer to prediction, since it functioned for an entire solar cycle.

REMOVAL OF THE TIME VARIATION: When researchers were trying to determine radial gradients for the solar wind as a whole, they too were faced with the problem of removing temporal gradients. Their solution was to scale the Pioneer data according to measurements made by ISEE-3 orbiting the sun at 1 AU. While this method is effective when one is dealing with an overall average of wind parameters, it is impractical when dealing with only rarifaction regions. Each region observed at a Pioneer spacecraft must be matched up with its equivalent at ISEE-3; however, rarifaction regions are still poorly defined at 1 AU. Consequently, another means of removing time variations is required.

While it is not possible to match up a rarifaction region to its counterpart at 1 AU, it is possible to match up the regions observed by the two Pioneers. There is a delay time between the two spacecraft due to the difference in heliocentric radius and the difference in heliocentric longitude. When this delay time is calculated, using observations by the Pioneers to determine wind speed, the rarifaction regions can be matched up with 80 percent efficiency.

In this study, 69 regions were observed by both Pioneer 10 and 11 between Day 96, 1973, and Day 266, 1975. Since two such regions leave the same spot on the sun within days of each other, any changes observed in the properties of the plasma are due solely to its radial expansion and are independent of temporal variations.

With the time variations removed, the solar wind may be tested for adiabaticity. To do this, the logarithm of the ratio of the temperature is plotted versus the logarithm of the ratio of the density. Temperature and density measurements are available at both Pioneer 10 and Pioneer 11 for only 33 of the 69 matched-up rarifaction regions. If the solar wind is expanding adiabatically, and if two degrees of freedom are assumed, then a slope of 2/3 would be expected. In fact, a slope of 0.47 was found.

However, one of the rarifaction regions used in this analysis was slowed considerably and heated when it overtook a more distant rarifaction region. When this point was removed, a slope of 0.57 was obtained. As in the study of radial gradients, no quantitative error analysis is available; however, this result could indeed be consistent with adiabatic expansion.

CONCLUSION: In this study, it was determined that regions that are free from corotating interactions may indeed expand adiabatically. This would imply that the heating due to mass loading by non-neutral interstellar ions is negligible. Radial gradients were found to be ineffective as tests for adiabaticity, due to temporal variations in the interplanetary magnetic field. Rarifaction regions were characterized as regions in which the magnetic field strength remains below the mean for at least 24 hours. Finally, it was found that rarifaction regions that were observed at Pioneer 10 could be quite successfully matched up with similar regions at Pioneer 11.

BIBLIOGRAPHY:

Goldstein, B.E., and J.R. Jokipii, Effects of Stream-Associated Fluctuations upon the Radial Variation of Average Solar Wind Parameters, J. Geophys. Res. , 83,1095, 1977

Slavin, J.A., E.J. Smith, and B.T. Thomas, Large Scale Temporal and Radial Gradients in the IMF: Helios 1,2, ISEE-3, and Pioneer 10,11. J. Geophys. Res., 11, 279, 1984

Smith, E.J., Solar Wind Magnetic Field Observations, Solar Wind Five, 1981

Smith, E.J., and A. Barnes, Spatial Dependences in the Distant Solar Wind: Pioneer 10 & 11, Solar Wind Five, 1982

Thomas, B.T., and E.J. Smith, The Parker Spiral Configuration of the IMF between 1 and 8.5 AU, J. Geophys. Res., 85, 6861, 1980

Tsurutani, B.T., and E.J. Smith, Interplanetary Discontinuities: Temporal Variations and the Radial Gradient from 1 to 8.5 AU, J. Geophys. Res., 84, 2773, 1979

THE USE OF PIEZOELECTRICS FOR STIFFNESS MODULATION

S. A. Wolf*, California Institute of Technology;
J. L. Fanson**, California Institute of Technology;
J. C. Chen***, Jet Propulsion Laboratory

ABSTRACT

The problem of damping vibration in Large Space Structures (LSS) is analyzed. Damping of a one-dimensional system by 'Stiffness Modulation'-type control has been shown feasible. Use of internal force producing actuators for vibration suppression of low-order systems has also previously been shown successful. Recently developed piezoelectric benders can theoretically be applied for this purpose and their use is proposed and analyzed.

I. Introduction

Traditionally, spacecraft have been analyzed as stiff bodies with relatively high frequency normal modes. However, recent improvements in outer space construction techniques, largely aided by the development of the Space Shuttle, have demonstrated the possibility of assembling large objects in space, such as antennæ ,solar sails, space platforms, etc. Such structures are relatively flexible and any disturbance to them, say, a collision with a meteor or even the act of positioning, is more likely to produce a wave-like motion rather than a simple vibration.

This type of motion is more difficult to control. This is in part because the *theory* of control is not as well developed but, more importantly, the *methods* of control are not there yet. Standard techniques such as use of rockets or momentum wheels are more geared towards pointing of smaller structures. Furthermore, such methods may well damage the LSS.

Also, rockets change their mass dramatically as the fuel is consumed, adding to the control problem, and they require refueling which is always expensive and often *impossible*. Electricity is, however, plentiful when photovoltaic cells are utilized so an electrically based technology is much preferable.

II. Theoretical Considerations

The suppression of vibration in a one-dimensional system has been analyzed by Chen[1] and will be briefly summarized here. The transverse vibrations of a vibrating string obey the following partial differential equation:

$$\rho \frac{\partial^2 y}{\partial t^2} = \frac{\partial}{\partial x}\left(T \frac{\partial y}{\partial x}\right). \tag{1}$$

---

* Undergraduate Student, Applied Mathematics Division

** Graduate Student, Applied Mechanics Department

*** Member Technical Staff, Applied Mechanics Technology Section; Member AIAA

The initial condition used was: $y=0, \partial y/\partial t = \sin(\pi x/L)$ at $t=0$, and the boundary condition was $y=0$ at $x=0, L$,

where y = transverse displacement
x = axial coördinate
t = time coördinate
ρ = mass density per unit length of the string
T = tension in the string
L = length of the string

The system stiffness is, in this simple case, represented by the linear tension, T, in Eqn. (1). By modulating the tension, which is always tangent to (in the 'plane' of) the string in various ways, Chen was able to introduce successful damping with a monotonic decrease in total energy.

This approach was then generalized to a more complicated system where the tension was no longer a scalar quantity (which it is for the string). Fanson[2] used a three-degree-of-freedom spring-mass system and demonstrated positive energy dissipation. The method used was a modal damping approach rather than a direct closed-loop feedback in order to utilize the more complete theoretical machinery available. The important result as regards the current project is that this type of control can be implemented in the direction of the spring force, and hence does not rely on anything *outside* the system.

Independently of the above, a very relevant experiment was done at Hughes Aircraft. Robert Forward[3] took a 66 centimeter long, 4 cm diameter fiberglass tube with a rigid weight at the top (the assembly had a mass of over 1800 grams) and damped out transverse modes of approximately 33 Hz in frequency using piezoelectric transducers weighing a total of less than six grams! His control scheme was a closed-loop feedback approach but the result is still *very* encouraging.

III. The Piezoelectric Bender

A piezoelectric (pē ā′ zō i lek′ trik) substance produces a voltage when physical strain is present and, vice versa, deforms when a voltage is applied. The word itself means "pressure-electricity", the prefix coming from the Greek word *piezin*, meaning "to press". Coulomb seems to be the first person to postulate the existence of the phenomenon and Hankel coined the name in 1881.[4] The first conclusive experiments verifying the existence of the piezoelectric effect were conducted by Jacques and Pierre Curie in 1880.[5]

The phenomenon occurs because some crystals have a non-symmetric arrangment which creates a net electric moment. A deformation then changes this moment so a potential is created. Likewise, an applied potential will result in deformation. Recent developments in ceramic technology have enabled the construction of "solid solutions" of Lead -zirconates and -titantes which have very controlled piezoelectric properties.

This type of material expands and contracts with an applied voltage. When made into thin sheets and sandwiched together a 'bender' is made which then bends when connected to an electric potential. Thus we see the existence of an entirely electric transducer whose feasibility for use will be studied.

IV. The Development of an Experiment

The important consideration here is the development of a method to test how much force the ceramic benders can produce. A 'piezoelectric bender test kit', consisting of eight pairs of variously sized benders, was purchased. The largest pair measured 2 inches by .375 inches by .020 inches and this size seemed most convenient (it is also the size used by Forward in his work).

These benders act very much like a capacitive element in a circuit and a preliminary test was carried out. This consisted of connecting the bender to a frequency generator in a very simple circuit. The frequency was turned up to the easily audible range and the voltage increased. An easily heard sound was created and scanning throughout the frequency range of the generator revealed that the resonances of the bender itself were not very sharp and were of high enough frequency that any test of force or moment generated would not be interfered with by any instabilities due to a time-increasing amplitude.

At one point, the circuit was disconnected and the sound continued! The reason for this was that the oscilloscope was still hooked up. The resistance through the probe and scope is over one *million* ohms so apparently very little power is required to cause the bender to oscillate at audible frequency.

In order to test the static force produced it was decided to attach the ceramic to a thin metal beam. The partial differential equation describing a beam with an applied force is:

$$\rho\frac{\partial^2 y}{\partial t^2} + \mu\frac{\partial^4 y}{\partial x^4} = f(x,t). \tag{2}$$

where y = transverse displacement
x = axial coördinate
t = time coördinate
ρ = mass density per unit length of the beam
μ = flexibility of the beam
f = forcing function

We can simplify this greatly by "removing" the time dependence. This is done to the equation by ignoring the time dependence (the $\partial/\partial t^2$ term) and is done in the laboratory by operating at low enough (one tenth of the lowest beam resonance) frequency that only the simplest solutions of the equation are needed. This *quasi-static* approach means that any force near the clamped end of a one-end-clamped one-end-free beam will result in a linear beam at points past the driving force. Thus

Off-Campus Projects

SIZE DISTRIBUTIONS OF IMMUNE COMPLEXES

AUTHOR: JAMES DUNN

FACULTY SPONSOR: PROFESSOR CLARK COLTON

ABSTRACT

Size distributions of immune complexes formed from BSA and two of its monoclonal antibodies were studied using ultracentrifugation and gel permeation chromatography. A theoretical model based on thermodynamics was used to simulate this system. It was found that this model did not predict the experimental results well.

INTRODUCTION

The immune system produces antibodies in response to the presence of foreign particles, or antigens. There is evidence which suggests that neoplastic disease is immunologically-mediated (Hellstrom, 1971, Badger, 1976, Giuliano, 1979). It has been shown that there are circulating factors that can block a number of immunological functions, thus providing an atmosphere which facilitates tumor cell growth. Immune complexes, or large aggregates of antigens and antibodies, are among the possible circulating factors.

Studies to date have mainly focused on the effect of treatments that remove these circulating factors. Few studies have been performed to analyse these treatments (Arend, 1974, Kijlstra, 1977). It is essential that if this methodology is to be understood and to be generalized to include other antibody-related diseases, a full understanding of the phenomena must be attained.

This study is to measure the size distributions of immune complexes. Other such studies are performed with only one type of antibody (Steensgaard, 1982, Husby, 1983). Since the body actually produces different antibodies that bind to many sites on the antigen, a more desirable model system is to include many different antibodies. As a first step toward this, the present study uses one antigen and two monoclonal antibodies. Theoretically, it is possible to form large complexes from these three components. A mathematical model based on basic thermodynamic principles is used to simulate the experimental results. The goal is to formulate a model that gives accurate predictions so that it would aid in the full understanding of the system.

RESULTS AND DISCUSSION

Linear sucrose gradients (10-35 w/w percent) were used in these experiments. Ultracentrifugation was carried out in an SW50.1 rotor at 4°C. Mixtures of the antigen (bovine serum albumin, denoted BSA or B) and the monoclonal antibodies (denoted Ab1 or A1 and Ab2 or A2) in phosphate buffer were allowed to equilibrate at 37°C for one hour and were subsequently stored at 4°C for 3-5 hours. The 200 μl of sample was then layered on 4.6 ml of sucrose. The gradients were spun for 14 hours at 50,000 RPM and were then fractionated into 4-drop fractions, approximately 170 μl each. The densities of the fractions were determined by measuring their refractive indices. The sedimentation coefficients were calculated manually following McEwen's method (McEwen, 1967). In the calculations, the particle density was taken to be 1.35 g/cm^3.

Purities of the antibodies and BSA were checked by gel permeation chromatography and ultracentrifugation. BSA was raiolabelled with I-125, and the radioactivity was followed by a gamma counter. UV absorbance at 280 nm was also used to follow the amount of immune complexes (IC). The counts in each

fraction was normalized by dividing by the total counts in the particular sucrose gradient. Each antibody was first mixed with BSA at antibody excess to ensure complex formation (Fig. 1). The sedimentation coefficient of BSA was found to be 5S and that of the simple complex (presumably B-Ab) to be 8S.

Two sets of experiments with all three components were carried out at various BSA to Ab1 to Ab2 ratios. The second set of experiments used six-fold higher concentrations than the first set. In each set of experiments, the concentration of the antigen was kept constant. The ratios used were 1:1/10:1/10, 1:1/4:1/4, 1:1/2:1/2, 1:1:1, 1:5/2:5/2, which covers concentrations ranging from antigen excess to antibody excess. Repeated experiments showed reproducible patterns (Fig. 2).

Sephadex G-200 columns (43x1.5 cm) were also used to study the size distributions of IC. The sample was prepared by the same method described earlier. Fractions of 1.7 ml were collected at a flow rate of 0.12 ml/min. Void volume occurred at fraction 15; Ab occurred at fraction 24; BSA occurred at fraction 29 (Fig. 3).

For the theoretical model, it was assumed that the antigen has two distinct epitopes for the two monoclonal antibodies. Each antibody is assumed to be bivalent and that each binding site of each Ab is independent. Under these assumptions, the reaction

$$\text{X-Ab} + \text{B-Y} \rightleftarrows \text{X-Ab-B-Y}$$

obeys the equilibrium expression

$$K = \frac{(\text{X-Ab-B-Y})}{(\text{X-Ab})(\text{B-Y})}$$

where X and Y are any molecules. The system is thus characterized by two association constants of the antibodies, K1 and K2. These constants are obtained by independent experiments using radioimmunoassays.

There are ten types of complexes that can be formed, excluding cyclic complexes. They can be grouped into two general types, depending on whether the number of antigens is odd or even. The concentrations of all complexes can be expressed in terms of the equilibrium concentrations of BSA, Ab1, and Ab2 (Table 1). To obtain these values, one applies the mass balance:

$$x_0 = x + \sum_{j \geq 0} K_1^{2j} K_2^{2j} x^j y^j z^{2j+1} (j + K_1(j+1)x + K_2 jy + K_1 K_2 xy(j+1))$$

$$+ K_1^{2j} K_2^{2j} x^j y^j z^{2j+2} (jK_2^2 y + (j+1)K_1^2 x + (j+1)K_1 K_2^2 xy + (j+1)K_1^2 K_2 xy$$

$$+ (j+2)K_1^2 K_2^2 x^2 y + (j+1)K_1^2 K_2^2 xy^2)$$

$$y_0 = y + \sum_{j \geq 0} K_1^{2j} K_2^{2j} x^j y^j z^{2j+1} (j + jK_1 x + (j+1)K_2 y + (j+1)K_1 K_2 xy)$$

$$+ K_1^{2j} K_2^{2j} x^j y^j z^{2j+2} (K_2^2(j+1)y + K_1^2 jx + K_1 K_2^2 xy(j+1) + K_1^2 K_2 xy(j+1)$$

$$+ K_1^2 K_2^2 (j+1)x^2 y + K_1^2 K_2^2 (j+2)xy^2)$$

$$z_0 = \sum_{\underline{j} \geq \underline{0}}^{---} (2j+1)K_1^{2j}K_2^{2j}x^j y^j z^{2j+1}(1 + K_1 x + K_2 y + K_1 K_2 xy) +$$

$$(2j+2)K_1^{2j}K_2^{2j}x^j y^j z^{2j+2}(K_2^2 y + K_1^2 x + K_1 K_2^2 xy + K_1^2 K_2 xy + K_1^2 K_2^2 x^2 y + K_1^2 K_2^2 xy^2)$$

where x=(Ab1), y=(Ab2), and z=(BSA). The system is fully specified by imposing x_0, y_0, and z_0, the initial concentrations of the three components. Using the Newton-Raphson method, an iterative procedure is employed to solve these simultaneous equations.

The fractions of IC thus genarated are weighted according to the number of antigens in the IC. This is to simulate experimental behavior. The known composition of the complexes are converted to molecular weights by assuming the molecular weight of BSA to be 66,000 and that of the antibodies to be 150,000 (Fig. 4).

These bar graphs are further transformed to simulate experimental results by assuming Gaussian distributions for the IC (Steensgaard, 1982). The molecular weights are converted to sedimentation coefficients by the Svedberg equation:

$$S = M^{\frac{2}{3}} \frac{1-\bar{\upsilon}\rho}{\bar{\upsilon}^3} / \left[N6\pi\eta\left(\frac{0.75}{N\pi}\right)^{\frac{1}{3}} \frac{f}{f_0}\right]$$

where M is the molecular weight, $\bar{\upsilon}$ is the partial specific volume of the particle, ρ is the density of the medium, η is the viscosity of the medium, N is Avogadro's number, and f/f_0 is the friction factor. $\bar{\upsilon}$ is taken to be 0.74 cm/g in all calculations. f/f_0 is taken to be 1.3 for BSA (Tanford, 1961) and to be 1.5 for complexes so it best fits experimental data (Fig. 5). The Gaussian distribution is given by the following:

$$f(S) = \frac{I}{\sigma\sqrt{2\pi}} \exp\left[-\tfrac{1}{2}\left(\frac{S-S_m}{\sigma}\right)^2\right]$$

where σ is the standard deviation given by experimental band widths. Here it is taken to be 0.75. S_m is the sedimentation coefficient computed by the Svedberg equation, and I is the weighted fraction (Fig. 6).

In both sets of ultracentrifugation data, one sees a general trend of growth in the amount of complexes as one goes from antigen excess to antibody excess. There appears to be a limiting size of IC in each set of experiments, since increasing antibodies from 1:1:1 to 1:5/2:5/2 does not change the profiles significantly. Comparing the two sets of graphs, even though the general outlines are similar, there are major differences. At antigen excess, the two are quite similar. However, as the ratio increases to 1:1/2:1/2, one notices that the peak of IC occurs at 9S for the less concentrated set (the first set), but the corresponding peak of the other set (the second set) occurs at 11S. The 9S value of the first set is not too different from that of the simple complex (B-Ab), which is 8S. Thus, no big complexes are formed in the first set of experiments. On the other hand, for the second set of experiments, the 11S corresponds to Ab-B-Ab so that larger complexes are formed. For both graphs at antibody excess, the outlines are broad so that they represent the envelope of many peaks. The outlines of the second set at antibody excess is particularly broad, ranging from 8S to 14S. In an

experiment with eight-fold higher concentrations, IC peak at 14S is observed.

When the IC are being separated, there is the corresponding change in their environment. Thus, if the reverse reaction is sufficiently rapid, re-equilibration may occur during the centrifugation. To investigate this problem, GPC experiments were performed. Due to the nature of GPC, the mixtures in the column became diluted 10 to 20-fold during the process of separation. This would encourage dissociation of the IC. However, since the patterns produced by GPC are consistent with those produced by centrifugation, one infers that the dissociation occurs very slowly so that re-equilibration is negligible in these experiments.

Since both GPC and ultracentrifugations involve changes in concentration, it would be ideal to study a system without perturbing its concentration. Quasielastic light scattering is one such method. By passing a laser beam through the sample, it is possible to quickly obtain information with regard to the size distributions of the particles. However, only preliminary experiments were carried out using this technique.

Comparing the computer simulations to the experimental results, one sees that they give approximate behaviors at antigen excess. However, beyond that, the model gives much broader distributions that are composed of multi-peaks which are not observed experimentally. In particular, the model predicts large complexes, such as peaks bigger than 16S, which are never seen in the experiments. Also, at antibody excess, increasing the ratio from 1:1:1 to 1:5/2:5/2 gives significant changes in the simulations.

Perhaps the simplest explanation to account for the difference is that the multi-peaks are inadequately resolved so that only one peak is observed experimentally. This is not likely, since good separation is seen for low molecular weight markers. Also, in the GPC experiments, where good separation is seen for high molecular weight markers, the similar one peak is observed as well.

The analogous explanation is that perhaps the band widths of IC are much bigger so that only an envelope is observable. This is possible though unlikely because experimentally higher molecular weight markers do not have much bigger band widths.

One may also postulate that the larger IC formed are too big to remain soluble and is therefore precipitated. This is not the case here, as no precipitation is seen and the total radioactivity is recovered at the end of the experiments.

Another possibility is that the mixtures are not at true equilibrium after incubation at 37°C for one hour. Rather, a steady-state is reached and is observed. Thus, at a particular concentration, certain IC are kinetically favored, and the barrier to reach equilibrium is high. This would explain the difference between simulations and experiments.

Turning to the problems associated with the model, the most obvious assumption that could be wrong is that the binding sites on the two arms of the antibodies are independent. It is quite likely that once one arm is bound, the binding of the other arm becomes sterically hindered. Alternatively, the configurations of the IC are such that further additions of antigens or antibodies are unfavorable. Thermodynamically, the binding constant of the other arm is therefore changed; kinetically, this may slow down the process of equilibration so that equilibrium is difficult to reach.

Similarly, the assumption that the association constants are the same for the binding of BSA to antibodies and for the binding of IC to antibodies may be unreasonable. These constants may actually decrease as the molecules

become bigger so that the formation of larger complexes is limited.

Other questions to be investigated include cooperativity and cyclic complex formation. Positive cooperativity does not appear to be present in this case, for it would encourage the formation of even larger complexes. The assumption that cyclic complexes do not form in apprciable amount is probably valid, since the smallest cyclic complex, B-Ab-B-Ab, would have sedimentation coefficient of 13S, which is larger than most of the sedimentation coefficients of the observed complexes.

CONCLUSIONS

The experimental results indicate that large complexes are formed as a result of high concentrations and excess antibodies. The model which assumes mass-action laws and independent bindings predicts formations of large complexes that are not observed experimentally. Further investigations on these assumptions and on other systems of antigen-antibodies are necessary to obtain better understandings of this phenomenon.

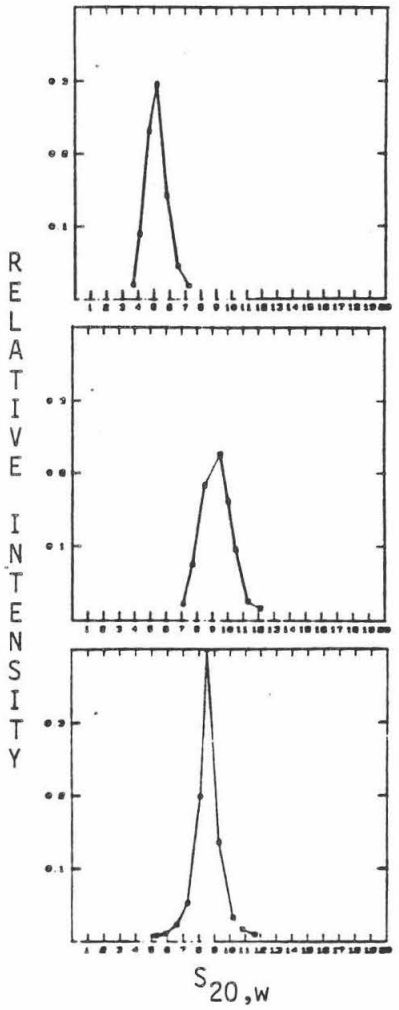

Figure 1 The top graph is pure antigen; the middle graph is antigens mixed with excess Ab1. The bottom graph is antigens mixed with excess Ab2. $S_{20,w}$ is the equivalent sedimentation coefficient in water at 20°C.

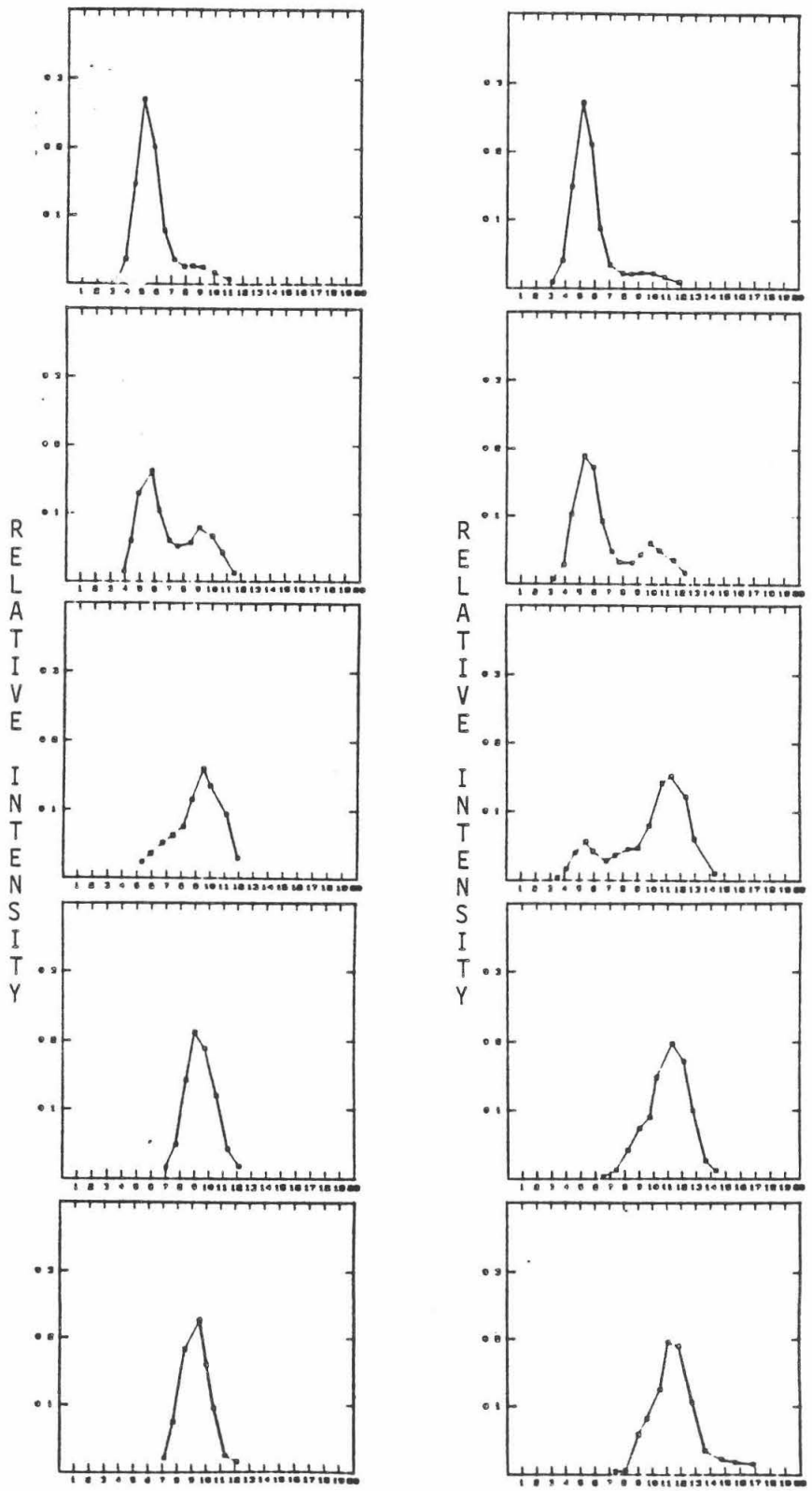
BSA:Ab1:Ab2
1:1/10:1/10
1:1/4:1/4
1:1/2:1/2
1:1:1
1:2:5/2
RELATIVE INTENSITY
RELATIVE INTENSITY
$S_{20,w}$
$S_{20,w}$
(BSA)=3.0x10^{-7}M
(BSA)=1.8x10^{-6}M

Figure 2

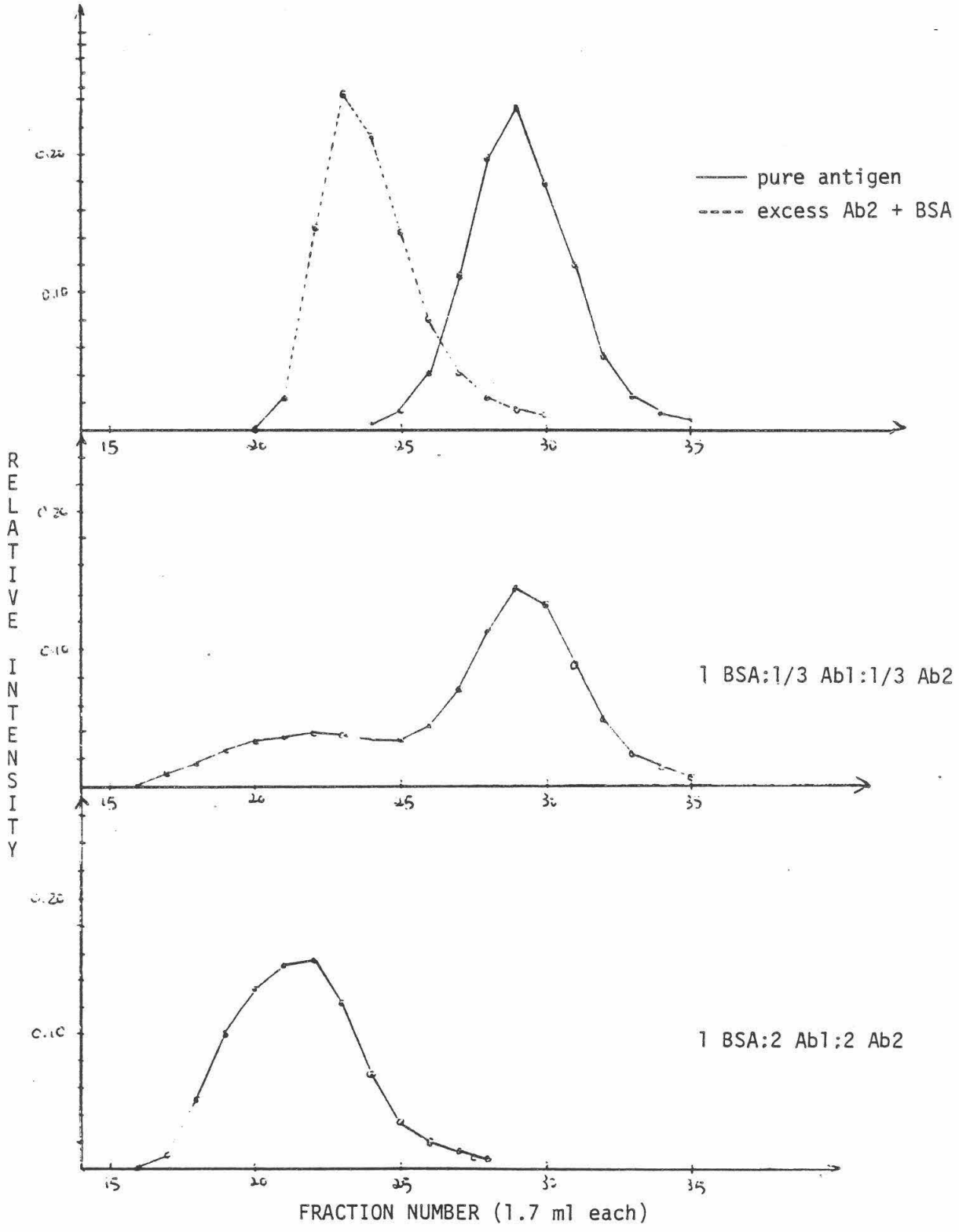

Figure 3 GPC fractions. (BSA)=3.0×10^{-7}M in all experiments.

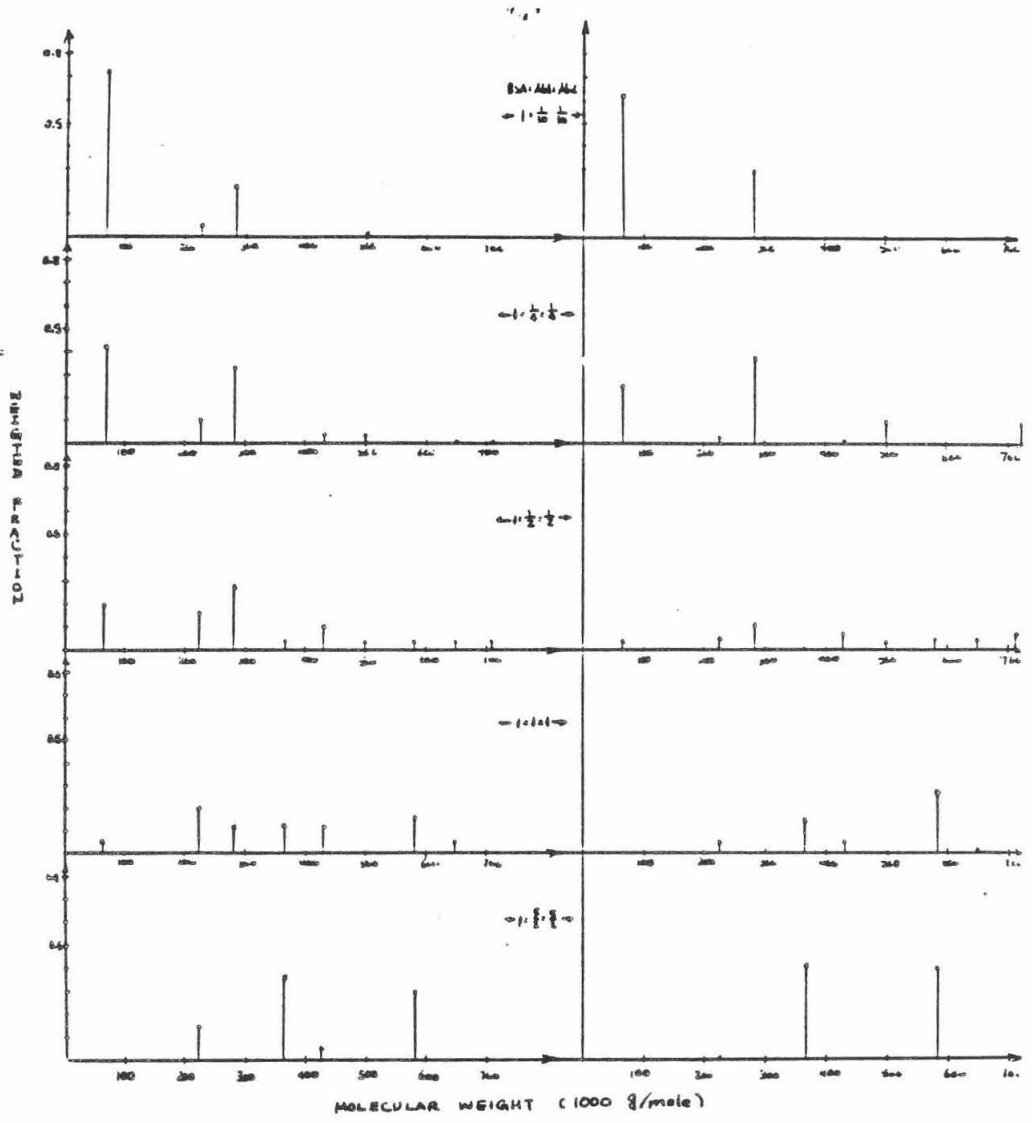

[BSA]: 9.0×10^{-7} M
First Set

[BSA]: 1.8×10^{-6} M
Second Set

Figure 4 Histograms generated by computer simulations. The species is plotted if the weighted fraction is greater than 0.01.

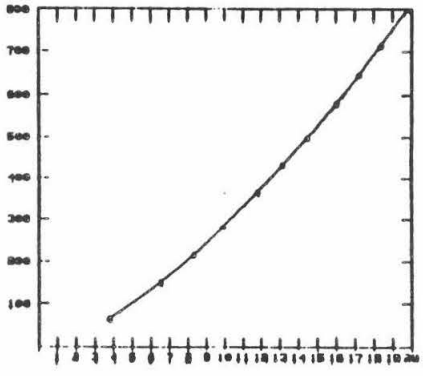

Figure 5 Molecular weight (in 1000 g/mole) vs. sedimentation coefficient (in Svedberg).

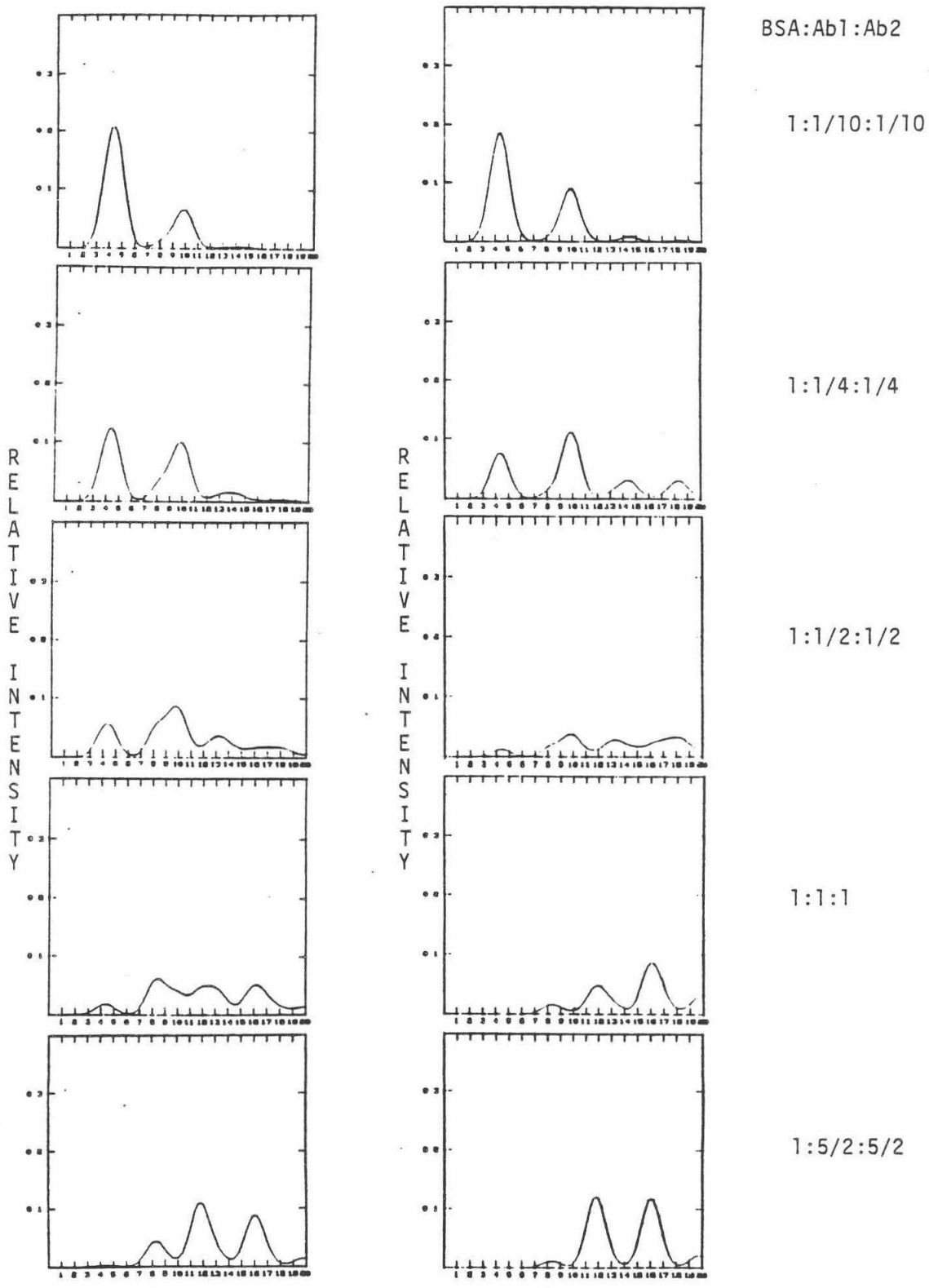
BSA:Ab1:Ab2
1:1/10:1/10
1:1/4:1/4
1:1/2:1/2
1:1:1
1:5/2:5/2
RELATIVE INTENSITY
RELATIVE INTENSITY
$S_{20,w}$
$S_{20,w}$
(BSA)=3.0x10^{-7}M
(BSA)=1.8x10^{-6}M

Figure 6

2j+1 molecules of B

Complex	Molecules of A1/ Molecules of A2	Concentration
B-A1-...-A2-B	j/j	$K_1^{2j} K_2^{2j} x^j y^j z^{2j+1}$
B-A1-...-A2-B-A1	j+1/j	$K_1^{2j+1} K_2^{2j} x^{j+1} y^j z^{2j+1}$
A2-B-A1-...-A2-B	j/j+1	$K_1^{2j} K_2^{2j+1} x^j y^{j+1} z^{2j+1}$
A2-B-A1-B-...-A2-B-A1	j+1/j+1	$K_1^{2j+1} K_2^{2j+1} x^{j+1} y^{j+1} z^{2j+1}$

2j+2 molecules of B

Complex	Molecules of A1/ Molecules of A2	Concentration
B-A2-...-A2-B	j/j+1	$K_1^{2j} K_2^{2j+2} x^j y^{j+1} z^{2j+2}$
B-A1-...-A1-B	j+1/j	$K_1^{2j+2} K_2^{2j} x^{j+1} y^j z^{2j+2}$
B-A2-...-A2-B-A1	j+1/j+1	$K_1^{2j+1} K_2^{2j+2} x^{j+1} y^{j+1} z^{2j+2}$
B-A1-...-A1-B-A2	j+1/j+1	$K_1^{2j+2} K_2^{2j+1} x^{j+1} y^{j+1} z^{2j+2}$
A1-B-A2-...-A2-B-A1	j+2/j+1	$K_1^{2j+2} K_2^{2j+2} x^{j+2} y^{j+1} z^{2j+2}$
A2-B-A1-...-A1-B-A2	j+1/j+2	$K_1^{2j+2} K_2^{2j+2} x^{j+1} y^{j+2} z^{2j+2}$

Table 1 Ten types of IC are grouped according to the number of antigens. For each group, the "basic" unit is shown in the first row. All the others are built by adding Ab1/Ab2 to the basic unit.

Bibliography

Arend W.P. & Mannik M. (1974) Determination of soluble immune complex molar composition and antibody association constants by ammonium sulphate precipitation. *J. Immunol.* 112, 451.

Badger A.M., Merluzzi V.J., and Cooperband S.R. (1976) Immunostimulatory and immunosuppressive factors in human cancer ascites fluids: effect on the primary plaque-forming response *in vitro*. *Cell Immunol.* 27, 126.

Giuliano A.E., Ranger D., Golub S.H., Holmes E.C., and Morton D.I. (1979) Serum-mediated immunosuppression in lung cancer. *Cancer* 43, 917.

Hellstrom Il, Sjogren H.O., Warner G., Hellstrom K.E. (1971) Blocking of cell-mediated tumor immunity by sera from patients with growing neoplasmas. *Int. J. Cancer* 7, 226.

Husby S., Steensgaard J., Feldt-Rasmussen U. & Date J. (1983) Molecular distribution of preformed thyroglobulin immune complexes. *Immunol.* 48, 401.

Kijlstra A., Knutson D.W., V.D. Lelij A. & Van Es L.A. (1977) Characteristics of soluble immune complexes prepared from oligovalent DNP conjugates and anti-DNP antibodies. *J. Immunol. Meths.* 17, 263.

McEwen C.R. (1967) Tables for estimating sedimentation through linear concentration gradients of sucrose solution. *Anal. Biochem.* 20, 114.

Steensgaard J., Jacobsen C., Lowe J., Ling N.R. & Jefferis R. (1982) Theoretical and ultracentrifugal analysis of immune complex formation between monoclonal antibodies and human IgG. *Immunol.* 46, 751.

Tanford C., Physical Chemistry of Macromolecules, John Wiley & Sons, New York, 1961.

EFFECT OF TRANSMITTER RELEASE ON MEMBRANE MORPHOLOGY OF SQUID SYNAPTOSOMES

Anirvan Ghosh

Abstract

The effects of neurotransmitter release on membrane morphology were studied in synaptosomes prepared from squid optic lobe. Freeze-fracture studies identified two distinct populations of intramembrane particles, but the heterogeneity of the synaptosome preparation and difficulties in assessing the level of synaptic activity produced large standard deviations in the measurements and prevented a clear determination of the correlation between these particles and transmitter release.

Introduction

In freeze-fracture studies of fast-frozen frog neuromuscular synapses Heuser and Reese (1,2,3) found that stimulating the motoraxon produced exocytotic pits at discrete sites known as active zones, and showed that these pits correspond to sites where a single synaptic vesicle fuses with the presynaptic plasmalemma to release a quantum of neurotransmitter. Following synaptic activity, additional large intramembrane particles became evident in the protoplasmic leaflet of the axon terminal. These authors hypothesize that the additional particles originate in the synaptic vesicles and appear in the P-face when the vesicles fuse with the plasmalemma during transmitter release.

The effect of transmitter release on intramembrane morphology has also been studied in torpedo synaptosomes (Israel et.al. (4,5)). Although these authors did not report observing any active zones, they observed an increase in the ratio of larger E-face to smaller P-face particles after chemical stimulation and aldehyde fixation. To assess the effects of aldehyde fixation and see if these morphological observations were specific to torpedo synaptosomes, we conducted experiments on fast-frozen and freeze-fractured squid synaptosomes to study the intramembrane particle distributions on E- and P-faces of stimulated and unstimulated preparations.

Methods

Our studies were done on synaptosomes from the squid optic lobe. Prior to rapid freezing, the synaptosomes were incubated at room temperature in artificial sea water for 30 minutes. Part of the preparation was then treated with veratridine to depolarize the synaptosomes and enhance neurotransmitter release before fast-freezing.

Specimens were mounted on aluminum disks and rapid-frozen by dropping them onto a copper block cooled with liquid Helium. Frozen specimens were stored in liquid nitrogen and fractured at -114°C in a Balzers 360 freeze-fracture machine. Immediately after fracturing the synaptosomes were unidirectionally shadowed with platinum from an electron beam gun placed at a 45° angle from the specimen.

The replicas were floated off on household bleach to digest underlying tissue, rinsed in water, and mounted on EM grids.

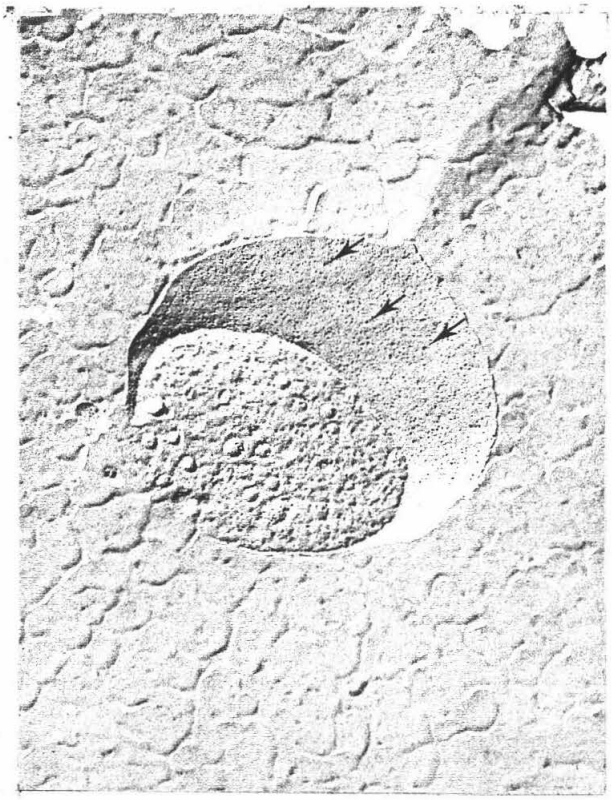

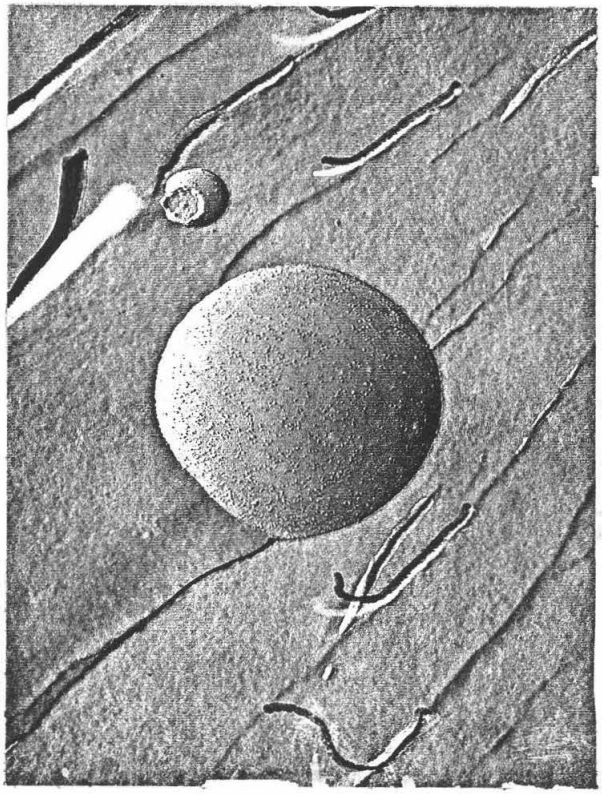

(top left) P-face of synaptosome treated with veratridine and partially cross-fractured. Note the synaptic vesicles in cross-fractured region.
(top right) E-face of synaptosome treated with veratridine and partially cross-fractured.
(bottom right) P-face of unstimulated synaptosome.

Some of the large particles on the P-face of the stimulated synaptosome are indicated by arrows.

Results

In both stimulated and unstimulated preparations we observed two populations of P-face particles (7-8 nm, and 11-13 nm) and a single population of E-face particles (11-13 nm).

The average density of both the larger P-face particles and the E-face particles is greater (approximately 3:2) in the stimulated specimens than in the controls. However, the standard deviation is close to 30% and suggests a heterogeneity in the preparation. No obvious increase in the ratio of E-face to P-face particles was observed indicating a concomitant increase in both E- and P-face particles during stimulation.

Discussion

We believe there are two major reasons for the large standard deviation in our data. Although thin sections showed that only about half the membrane bound structures in these preparations are synaptosomes, they cannot be recognized by their membrane structure in freeze-fracture views. Consequently, non-synaptosomal structures may have been counted as synaptosomes in the stimulated and unstimulated preparations. Also, it is likely that during the preparation of synaptosomes some are mechanically stimulated. Therefore our 'unstimulated' controls probably contained some stimulated synaptosomes.

Two distinct populations of particles are observed on the membrane faces, but whether or not transmitter release changes their distribution cannot be determined without a more homogeneous preparation and better unstimulated controls.

Acknowledgements

This research was carried out in Dr. Thomas S. Reese's Laboratory of Neurobiology, NIH, NINCDS, at The Marine Biological Laboratory, Woods Hole, Massachusetts. The work was supported by Caltech's Summer Undergraduate Research Fellowship and sponsored by Dr. Reese.

References

(1) Heuser J.E., Reese T.S., et al. J. Cell Biol, 81, 275-300, 1979.

(2) Heuser J.E. and Reese T.S. "Changes in the structure of presynaptic membranes during transmitter secretion", Neurobiology of chemical transmission, Otsuka M. and Hall Z.W. ed. John Wiley & Sons, 1979.

(3) Heuser J.E. and Reese T.S. J. Cell Biol. 88, 564-580, 1981.

(4) Israel M., et at. Advances in Biosciences, 35, 173 - 182, 1982.

(5) Israel M., et al. J. Ultrast. Res., 75, 162-178, 1981.

Real Time Thin Film Thickness Analysis

Praveen Asthana

Dr. Tim Strand

Abstract

Interferometry is a powerful method for inspection, profiling or thickness measurement, but it can produce ambiguous results. This ambiguity can be removed by using white light interferometry; however, spectroradiometric analysis of white light interferograms is slow and expensive. This project investigates the possibility of speeding this process by applying matched filtering techniques to the spectral signatures of the white light fringes.

Theory

The theory has its roots in white light interferometry. For two beams of intensity I_1 and I_2, the resulting irradiance is:

$$\bar{I} = \bar{I}_1 + \bar{I}_2 + 2\sqrt{\bar{I}_1 \bar{I}_2}\cos\delta$$

where δ is the phase difference between the two waves. For two beams with uniform spectral distribution, the putput signal will have the form:

$$S(k,h) = a + b\cos(kh + \phi)$$

where a and b are related to the intensities, k is $\frac{2\pi}{\lambda}$, h is path length difference and ϕ is a constant.

Since a matched filter function is being constructed, it will have the form: $M(k,h_i) = F_i(k) = N\,S^*(k,h_i)$ N is Normalisation (3)

The matched filter function would be real and identical to the signal function for some specified h_i (path length difference)

The detection process involves a correlation between the output from the filter and the output from the sample. This requires an integration over the spectrum with a detector to produce an output G : $G = \int_{k_1}^{k_2} \bar{I}(k,h)\,F_i(k,h_i)$

Using this method it should be possible to perform the spectral domain matched filtering optically by constructing a matched filter. It was decided to perform the experiment using thin films. For a thin film, this matched filter would also be a thin film (note eqn 3).

Mathematically, the basic idea is presented below. Assume a reasonably collimated ray of white light bouncing off a thin film:

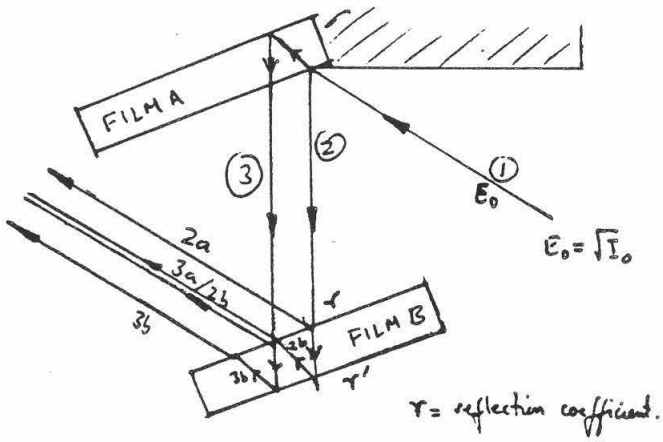

There will be two rays coming off film A (front and back). When these two rays hit film B, the result will be four reflections. But if the two films are of equal thickness, rays 3A and 2B will interfere constructively and produce a peak in intensity. Thus there will be a correlation when filter thickness equals sample film thickness; or more correctly, when the path length differences are equal.

Method

Before setting up the actual experiment, a computer simulation was carried put. By changing certain variables in the computer model, the best operating conditions could be determined. The program was written in fortran and basically it carried out the following operation: $G = \int_{\frac{2\pi}{\lambda_1}}^{\frac{2\pi}{\lambda_2}} (E_a + E_b \cos kh)(E_a + E_b \cos kh_i)\, dk$ | $k = 2\pi/\lambda$, $E_a = E_0(r^2 + r'^2)$, $E_b = E_0 r r'$

Since we are dealing with a correlation process, there should be some form of normalisation. The normalisation process was determined to be:

$$G = \int_{k_1}^{k_2} I(k,h)\, F_i(k,h_i) \Big/ \sqrt{\int_{k_1}^{k_2} I^2(k,h)\, dk \int_{k_1}^{k_2} F_i(k,h_i)\, dk}$$

Basically the computer would simulate a thin film system. The idea of the experiment was to see if it was possible to pick out a certain thickness of thin film (say h=2μ) when a matched filter (a thin film of thickness 2μ) was used. The computer program would change the sample thickness from say 0 to 5μ while keeping the filter thickness constant. The peak will be when the filter thickness equals sample thickness.

The resulting unnormalised graph is shown overleaf. When the normalisation was used, contrast improved markedly. In the graph, the filter thickness used was 3.4μ. This sinc function is a result of the perfect square bandwith of the spectrum used. (The F.T. of a square bandwith is a sinc function).

An interesting feature is that the side lobes around the main [illegible] are not symmetrical. This is because of superimposing terms.

The Experiment

The simplest way to do this experiment would be to use a wedge shaped thin film as a sample. This wedge would be movable across an aperture thus giving a range of sample thicknesses. Considerable difficulty was encountered in making a suitable wedge shaped thin film, especially one with a good contrast in refractive indices between film and substrate.

Using a wedge shaped pellicle beamsplitter, a set of readings was taken. Intensity peaks at the detector appeared at the expected film thicknesses; however, there was not enough of a variation in the sample film thickness to provide a complete curve.

Ultra-thin (150μ)glass plates were tried. It was easy to find wedge shapes in the glass plates and the experiment was set up as below. The results were encouraging: the peak in intensity occurred when the two (filter and sample) glass thicknesses matched. Thus there was some indication that the theory worked, even for samples that were so much thicker than the coherence length of white light.

When working with the glass plates, care had to be taken to make sure that the two pieces of glass had the same dispersion.

The graph is shown overleaf.

SKETCH

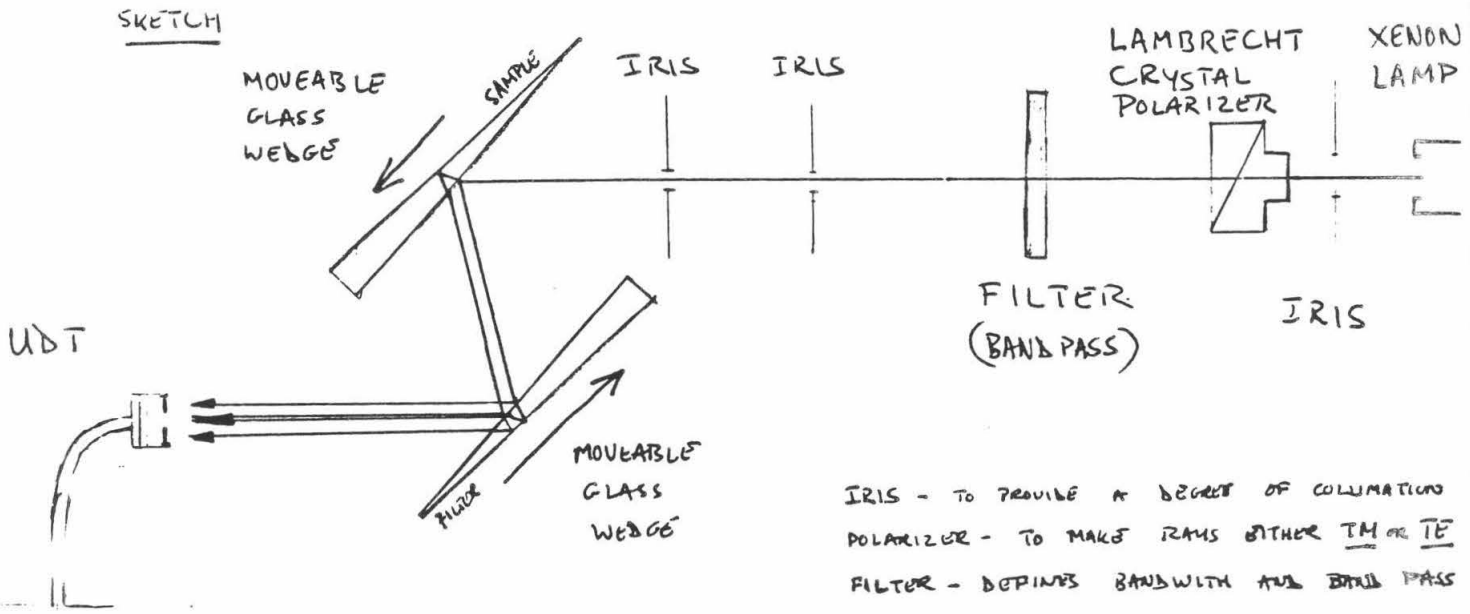

IRIS - TO PROVIDE A DEGREE OF COLLIMATION

POLARIZER - TO MAKE RAYS EITHER TM OR TE

FILTER - DEFINES BANDWITH AND BAND PASS

IT IS ALSO POSSIBLE TO ILLUMINATE WHOLE PLATE AND JUST MOVE DETECTOR.

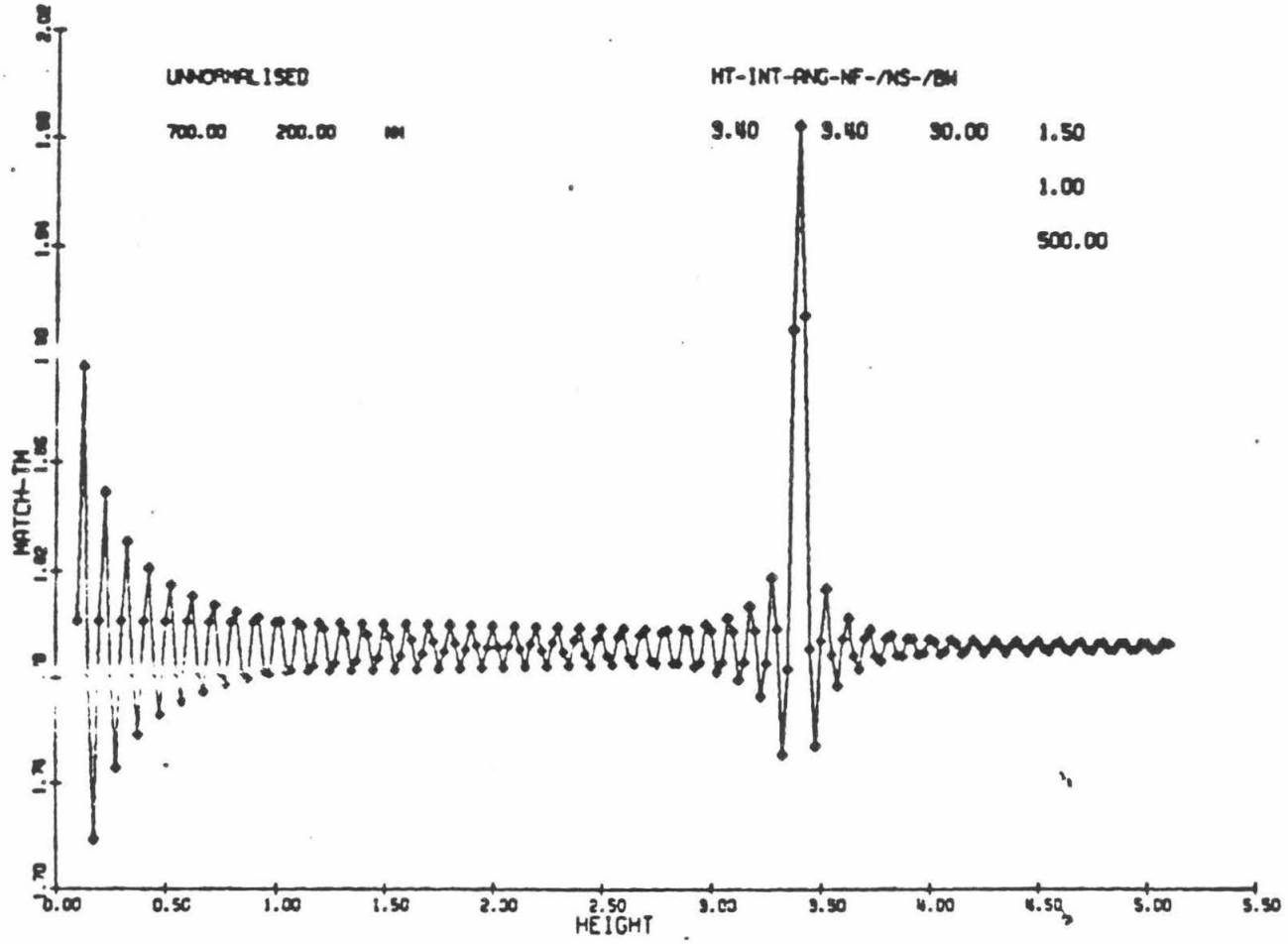
UNNORMALISED
700.00 200.00 MM
HT-INT-RNG-NF-/NS-/BM
9.40 9.40 90.00 1.50
1.00
500.00
MATCH-TM
HEIGHT
0.00
0.50
1.00
1.50
2.00
2.50
3.00
3.50
4.00
4.50
5.00
5.50

Thin film simulation

The results from the glass plates were insufficient to determine whether the theory was completely working. According to the theory, in the domain from minus infinity to infinity, there ought to be three peak systems : one at P=S, one at P=-S, and one at P=0. P is the phase difference acquired in the sample by the light and S is the phase difference acquired in the filter(the 'phase difference' is between the front and back reflections in the film). See theoretical graph overleaf.

But it was difficult to use a thin film system that would give results in the range minus infinity to zero. It was decided to physically simulate a thin film wedge using a white light interferometer. The experiment was set up as below:
The experiment was set up such that it was run by an IBM PC-XT. The interferometer arm was movable by a piezo electric crystal such that a change in voltage of one volt moved the arm by .02u. By moving the arm of the Michelson interferometer, it was possible to simulate the phase difference arising from a series of thin films. The results are shown in the page ~~after~~ next.

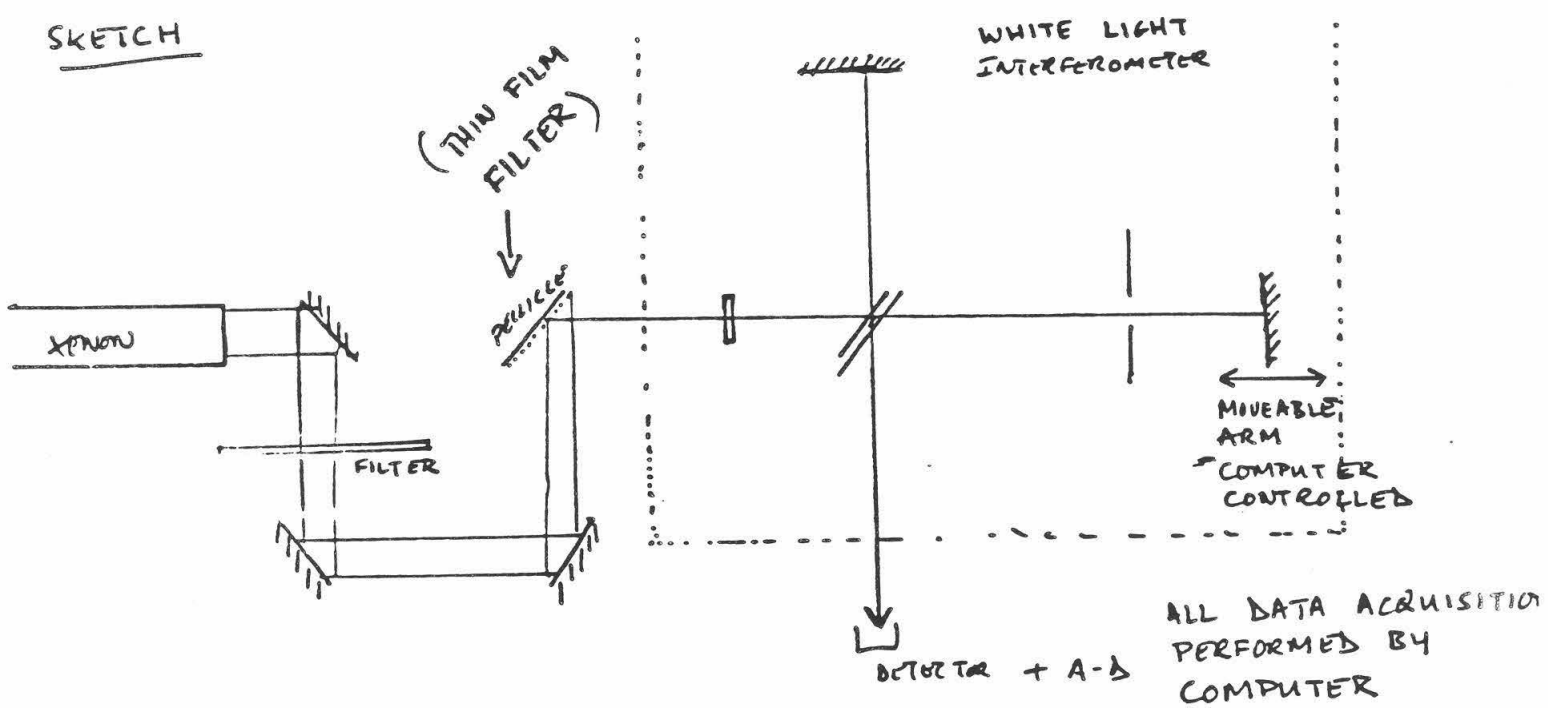

FIRST A RUN WAS CONDUCTED WITH JUST PLAIN WHITE LIGHT
THEN A RUN CONDUCTED WITH 1μ PELLICLE
THEN A RUN CONDUCTED WITH 3μ PELLICLE (3.4μ)

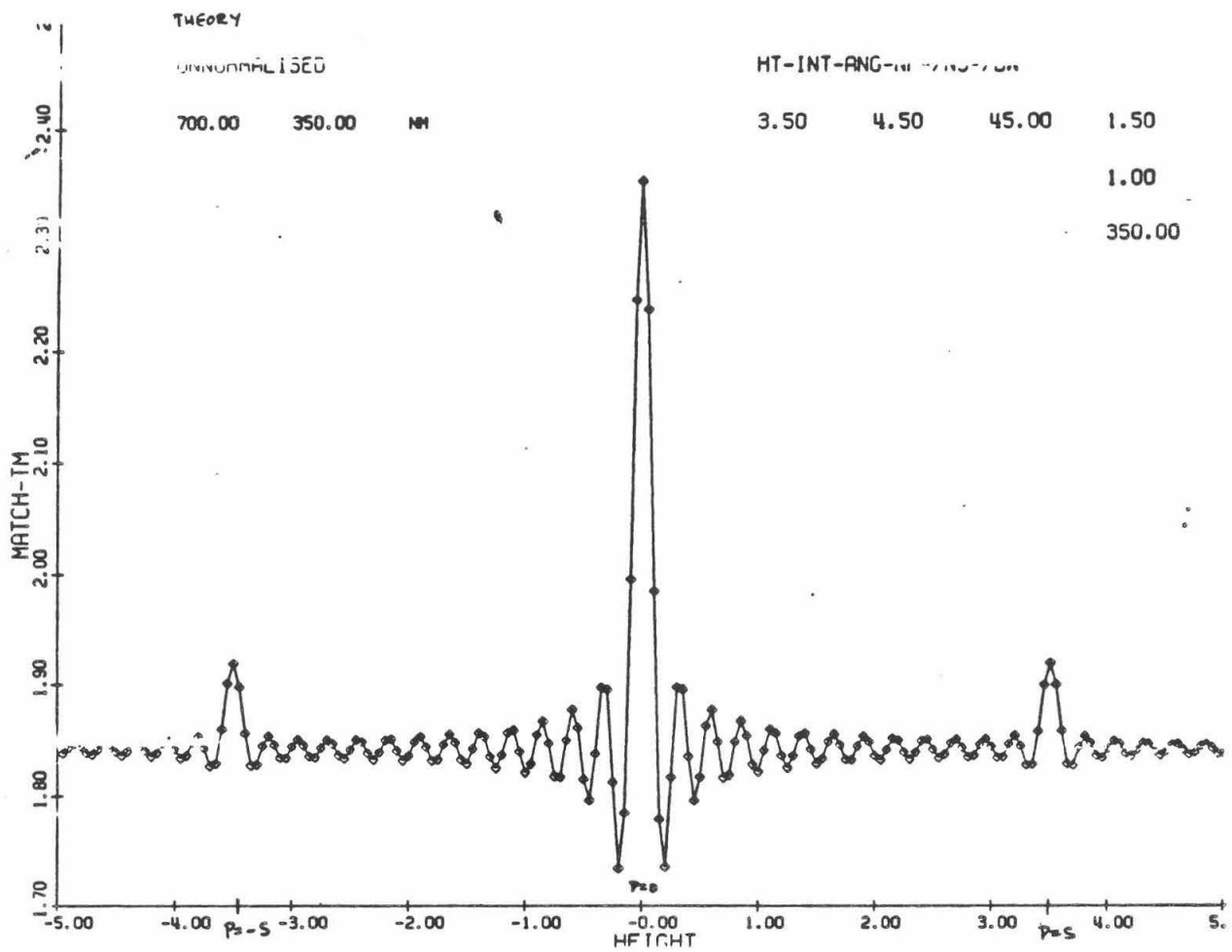

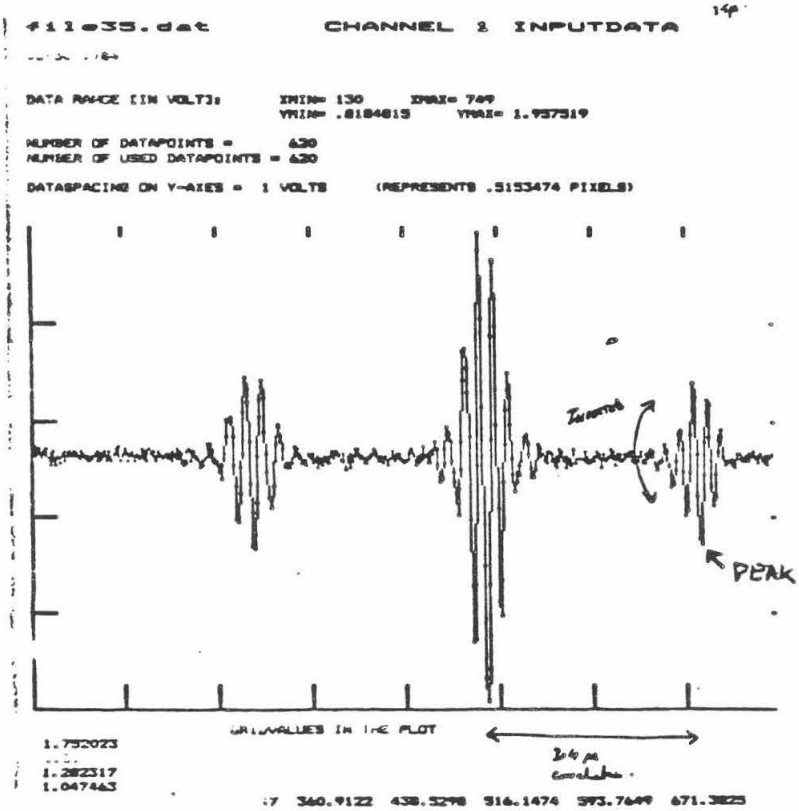

AN INTERESTING FEATURE IN THIS EXPERIMENTAL GRAPH IS THE INVERSION OF THE PEAK.
THE PEAK ESSENTIALLY APPEARS TO BE 180° OUT OF PHASE.
THIS IS BECAUSE THE RAYS, AS THEY BOUNCE OFF THE PELLICL ACQUIRE A TOTAL PHASE LAG OF 180° AS A RESULT OF THE REFLECTION AT 45 DEGREES.

Conclusion

From the results of the interferometer set up, it appears that the theory works and can be applied. An experiment was carried out using films of Varcum 6000-6 resin on silicon wafers to determine if this method could be used for an inspection process. The results were quite successful.

This method of using white light matched filtering can have many applications in areas where spectroscopic techniques are being used. For example it can be used to measure the contents of a mixture of gases fairly rapidly. The advantage of this method would be speed and simplicity.

SURF Leadership Roundtables

The SURF Leadership Roundtables, sponsored by AMETEK, Inc. were very successful and enthusiastically attended by 45 SURFers.

The first Roundtable was held June 13, and the discussion leader was Robert L. Shafer, a certified management consultant and retired Senior Associate, Institute of Management Consultants, New York. Mr. Shafer talked about qualities of leadership which are necessary in the executive levels of a company. (See Appendix A) SURFers who attended were Donald Buchholz, Yi-Hong Chen, Larry Chew, Mike Crawford, Peter Konopka, Yousfi Tyebkhan, Tad White, and Paul Young.

Dr. Robert Durbeck led the second SURF Roundtable on June 18. Dr. Durbeck is the Research Technical Staff Manager of the IBM Research Division in San Jose. He discussed his own career, current opportunities for scientists and engineers, and personal and technical qualities that he feels are important to be successful at IBM. SURF students in attendance were: Mark Adams, Yi-Hong Chen, Greg Bailey, Supriya Ghosh, Burnham Greeley, Ting-Ling Kao, Karla Peterson, and Ryoji Watanabe. The discussions were enthusiastic and very informative.

On July 11, Mr. Victor Veysey led the third SURF Roundtable. Mr. Veysey has been Director of the Caltech Industrial Relations Center; Assistant Secretary of the Army; Congressman from the 38th and 43rd Districts of California in the U.S. House of Representatives; and Assemblyman, California Legislature. The Roundtable was titled "Leadership in the Public Sector" and discussion centered on opportunities, problems and the importance of technical people serving in government. The SURF students attending Mr. Veysey's Roundtable were Lisa Cummings, James Douma, Tim Gould, Joseph Kovalik, John Morrison, Robin Wilson, Minami Yoda, and Dennis Zaritsky.

The fourth Roundtable was held August 1 under the leadership of Mr. Richard Hayman, founder, Chairman and Chief Executive Officer of Haskel, Inc. a firm manufacturing compresed air driven pumps, high pressure valves and accessories. Mr. Hayman talked about how he began his business, the various stages of growth, the problems and the rewards. Students attending Mr. Hayman's Leadership Roundtable were Peter Cho, Young Hoon Chung, Glen Crawford, Ted George, Simon Goldstein, Santosh Krishnan, Bill Sharpe, and Aaron Roodman.

Mr. Robert Zurbach was the discussion leader for the SURF Roundtable held August 9. Mr. Zurbach, former president of the Associates of the California Institute of Technology, is a retired Vice President of Reliance Steel. His primary topic concerned volunteerism. He described his philosophy of returning a portion of his resources to society through volunteer effort, and the activities which he has chosen to support in this way. The students participating were Clea Bures, Dara Chang, Larry Doan, Stefan Feuerabendt, and Andy Wolf.

The final 1984 SURF Roundtable was presented on August 15 by Mr. Al Schaff, Vice President, Electronics Development of AMETEK, Inc. AMETEK is a highly decentralized and diversified manufacturing and high technology company. Mr. Schaff's discussion covered leadership in a company such as AMETEK, the qualities employers seek in hiring and promoting employees, and what opportunities a new employee might expect to find. SURFers who attended the AMETEK Roundtable were Marc Buffet, Diane Chen, Scott Hudson, Jerry Jungman, Alan Marumoto, Charles Reel, Mike Rigler, and Janice Sakai.

The response to the SURF Roundtables was most enthusiastic, and we plan to continue the program in 1985.

CALIFORNIA INSTITUTE OF TECHNOLOGY

1984 SURF Noon Seminar Series
12:00-1:00 PM, 153 Noyes

Monday, June 11: 1984 SURF Program Orientation Meeting

Friday, June 15: Roger D. Blandford, Professor of Theoretical Astrophysics

Neutron Stars

Neutron stars are observed in radio pulsars and x-ray sources. The observations will be reviewed and some derived properties of neutron stars will be discussed.

Monday, June 18: Dr. Robert Durbeck, Research Technical Staff Manager, IBM Research Division, San Jose, CA

IBM Research Activities

An overview of research activities within IBM with emphasis on several projects under way at the San Jose Laboratories.

Friday, June 22: Bruce E. Cain, Associate Professor of Political Science

Hispanics in California

Hispanics have become a pivital force in California politics. The changing demographics of the hispanic population will be examined, and their political behavior will be discussed.

Monday, June 25: Shirley Thomas, Technical Writer and Consultant

The Written Report

Professional scientific and engineering reports possess certain features and characteristics. This presentation summarizes some of them so that students may prepare their reports in a more professional manner.

The format specified for SURF reports is that designated by the American Institute of Physics. Beyond the format, students need to understand the principles underlying good report writing.

Material must be organized so that a logical outline may be prepared. Relative importance of specific points must be designated through use of

headings, subheadings, second level subheadings, third level subheadings, and listings. A report must be written in proper order; for example, the Introduction is not written first, though it appears at the first of the report.

The writing style must be simple, unambiguous, clear and devoid of deadwood. Reports must accommodate a diverse readership; all readers will not be specialists in the report discipline. The language must be specific and accurate. Necessary data must support the conclusion.

Tables and figures must be properly prepared. Graphics should be used extensively, whether they be photographs, hand drawings, photo- copied drawings, or photocopies of parts. Correct use of abbreviations characterize a professional report. Use of checklists is valuable. Correct grammer is imperative.

Friday, June 29: George R. Rossman, Associate Professor of Mineralogy

The internal chemistry of gemstones is subject to modification by a variety of technologies ranging from rudimentary heating to bombardment with high energy radiation. A number of these processes will be surveyed and the atomic level transformations will be examined.

Friday, July 6: Arden L. Albee, Professor of Geology;
Chief Scientist, JPL

Space Science at JPL

Dr. Albee will summarize the science objectives of the deep space missions currently under development at JPL. He will also discuss a number of remote sensing instruments that will be developed for shuttle flights to study the earth.

Monday, July 9: Gerald D. Skellenger, Assistant Department Head,
Power Systems Research, General Motors Research
Laboratories

Power Systems Research at General Motors

The power trains of contemporary and future vehicles are complex combinations of dynamic components. Integration of these components, using fundamental physical technologies, into an effective and efficient system is the subject of power systems research at GM.

Friday, July 13: John D. Roberts, Institute Professor of Chemistry

Use of Nuclear Magnetic Resonance in Imaging

Nuclear magnetic resonance (NMR) spectroscopy has been widely used in chemical structural and quantitative analysis for more than thirty years. In the last two or three years, there has been an almost explosive growth of NMR for medical diagnosis, especially for brain and whole-body imaging, as well as for detection of metabolic diseases. Some of these developments will be illustrated and explained.

Monday, July 16: William Whitney, Manager, Information Systems Research Section

Research After Graduaton: Can It Be Done?

The answer is yes, although the overhead seems high and growing. This talk will be an informal discussion of things that new graduates ought to know when taking jobs in research organizations, things that probably no one will tell them. Topics will include money, power, politics, and factors in personal success and failure.

Friday, July 20: Norman H. Horowitz, Professor of Biology, Emeritus

The Rise and Fall of Lowellian Mars

For most of this century, discussions of the question of life on Mars and the nature of the Martian environment were dominated by the views of Percival Lowell, the man who popularized the ideas of a Martian civilization and Martian canals. Although Lowell died in 1916, his influence was so strong that it was not until 1963 - six years after the space age opened - that scientists began to realize that the real Mars was far different from the one he had painted. This talk will describe the astonishing revolution that occurred in the '60s in our comprehension of both Mars and Mars observers.

Monday, July 23: Thomas R. McDonough, Lecturer in Engineering

How to Give a Seminar

We will discuss how to give an effective presentation using slides, Vugraphs, and blackboard. (See Appendix B)

Friday, July 27: Barbara J. Wold, Assistant Professor of Biology

What Cancer Can Tell Us About How Cells Work

The study of cancer has a very long history but the field has changed dramatically in the past few years due to the productive wedding of cell biology and molecular biology. This talk will focus on these recent developments.

In particular, a definitive feature of cancer cells is that they proliferate uncontrollably. We will ask why they do this and what these perturbations in growth control can tell us about how normal cells work.

Monday, July 30: Sally J. Asmundson, Director, Career Development Center

Developing Your Career Options

A thoughtful assessment of your personal goals and values combined with information on career and educational fields will enable you to recognize the most satisfying career choices for you. Strategies for gaining experience and gathering career information will be presented, and those services offered by the Career Development Center will be outlined.

Friday, August 3: Peter B. Dervan, Professor of Chemistry

Design of Molecules that Bind to DNA

The work of Professor Peter Dervan and his group is aimed at understanding those factors critical for the sequence specific recognition of DNA and RNA by small molecules. The group has developed two methods for determining where small molecules bind on native DNA. MPE·Fe(II) footprinting utilizes a synthetic DNA cleaving molecule, methidiumpropyl-EDTA·Fe(II) and high resolution denaturing gel electrophoresis. The DNA cleavage patterns generated by MPE·Fe(II) in the presence of bound drugs reveal the location and size of the binding sites of small molecules on native DNA. The other method, affinity cleaving, is based on the attachment of DNA cleaving moieties such as EDTA·Fe(II) to sequence specific DNA binding molecules which creates sequence specific DNA cleaving molecules. Analyses of DNA cleavage patterns using high resolution denaturing gel electrophoresis reveal the binding site and preferred orientation of small molecules on native DNA. The attachment of EDTA·Fe(II) to other sequence specific DNA binding molecules such as antibiotics, polypeptides, or oligonucleotides may form a basis for the design of synthetic double strand DNA cleaving molecules of defined target sequences and binding site sizes.

Monday, August 6: Norman A. Gjostein, Long Range and Systems Research Laboratory, Ford Motor Company

The Role of Advanced Technology in the Automotive Industry

The whole range of new technologies in the rapidly changing and dynamic automotive industry, including: newly emerging technological applications relative to engines, transmissions, structural materials, on-board electronics and the use of computers in the engineering, design and manufacturing processes.

Friday, August 10: Hans W. Liepmann, Theodore von Karman Professor of Aeronautics

The Nature of Turbulence

The history of turbulence research, the impact of turbulence upon technical problems, and the state of the art, will be discussed.

Monday, August 13: Dr. Paul Carroad, Carnation Research Laboratory

High Temperature–Short Time Processing of Food

This seminar will cover the motivation for HTST food processing with respect to product quality and commerical sterilization. First order kinetics will illustrate destruction of quality parameters and microorganisms. Aseptic processing and high vacuum flame sterilization will be discussed as recent applications of HTST processing.

Friday, August 17: Fred E.C. Culick, Professor of Applied Physics and Jet Propulsion

Subsonic Aircraft Aerodynamics 1902-1984:
The Impact of Electronic Computers

The fundamental physical principles of aircraft aerodynamics have been known since 1902. Theory based on those principles has been strongly conditioned by the computational tools available. With recent developments of large high speed computers, it is becoming possible to calculate quantitative details of flows about complete aircraft. This talk will summarize the evolution of theory and results from the beginning to the present.

SURF Bibliography

(This is a listing of papers prepared by SURF students and which have been published in scientific journals.)

1. "Crustal Structure Near the Eastern Transverse Ranges", *Am. Geophys. Union Trans. Eos, 60* p. 876 (Abstract), N.W. Clayton*, J.B. Minster**.
2. "Coulomb Distortion of Pion Spectra from Heavy-Ion Collisions", *Phys. Rev. Letters,* Vol. 43, p. 1581 (1979), K.G.Libbrecht*, S.E. Koonin**.
3. "Flux Pinning by Magnetic Impurities in an Amorphous Superconducting Alloy", Report to the Department of Energy, (1980) D.L. Whiting*, (worked with W. Johnson**).
4. "IUE and Visual Spectrophotometry of Markarian 9, Markarian 10, and 3C 390.3", *Astrophysical Journal,* Vol. 243, p. 445 (1981), R.W. Goodrich*, J.B. Oke**.
5. "Structure and Transcription of Normal and Abnormal Globin Genes", *J. Supermolecular Structure of Cellular Biochem.*, supp. *5*, 381 (1981). N. Proudfoot, M. Shander, S. VandeWoude*, T. Maniatis**.
6. "Repetitive Sequences of the Sea Urchin Genome II. Subfamily Structure and Evolutionary Conservation", *Journal of Molecular Biology* (1981) 149, 15-39. R.H. Scheller, D.M. Anderson, J.W. Posakony, L.B. McAllister*, R.J. Britten, E.H. Davidson**.
7. "Repetitive Sequences of the Sea Urchin Genome, Distribution of Members of Specific Repetitive Families", *Journal of Molecular Biology* (1981) 145, 5-28. D.M. Anderson, R.H. Scheller, J.W. Posakony, L.B. McAllister*, S.G. Trabert, C. Beall, R.J. Britten, E.H. Davidson**.
8. "Molecular Basis of Genetic Defects in Human Globin Genes", *J. Supermolecular Structure of Cellular Biochem.*, Supp. *5*, 229 (1981). M. Shander, S. VandeWoude*, N. Proudfoot, T. Maniatis**.
9. "Organization and Expression of Multiple Actin Genes in the Sea Urchin", *Molecular and Cellular Biology*, July 1981, p. 609-628. R.H. Scheller, L.B. McAllister*, W.R. Crain, Jr., D.S. Durica, J.W. Posakony, T.L. Thomas, R.J. Britten, E.H. Davidson**.
10. "Infrared Photometric Observation of BL Lac Object BL Lacertae (2200-42)" *Annual Report of the Mount Wilson and Las Companas Observatories*, 1981-1982, R. Pogge*, (Worked with G. Neugebauer**).
11. "Absolute Spectrophotometry of Very Large Redshift Quasars", *Astrophysical Journal,* Vol. 255, p. 11 (1982), D. Korycansky*, J.B. Oke**.
12. "Experimental Study of Autorotation with Flow Visualization", Received Third Place Certificate of Merit at American Institute of Aeronautics and Astronautics Minta Martin Student Competition for presentation of a technical paper, University of California, Irvine, April, 1982. I. Sugioka* (worked with F.E.C. Culick**).
13. "Electrical Characteristics of Thin Ni_2Si, NiSi, and $NiSi_2$ Layers Grown on Silicon", Paper presented at the Electronic Materials Conference 1982, June 23-25, Colorado State University, Ft. Collins, CO, and a manuscript to be published in the *Journal of Electronic Materials.* E. Colgan* (worked with M-A. Nicolet**).
14. "Erosion of Frozen Sulfur Dioxide by Ion Bombardment: Applications to IO", *Geophysical Research Letters*, Vol. 9, No. 10, Oct. 1982, pp 1151-54, C.L. Melcher, D.J. LePoire*, B.H. Cooper, T.A. Tombrello**.

15. "Shock Compaction of Ferrous Alloy Powders", to appear in Third Conference on Rapid Solidification Processing at the National Bureau of Standards, Gaithersburg, MD, December 6-8, 1982, T.J. Ahrens, D. Kostka*, P. Kasiraj, T. Vreeland**.

16. "Interspersed Sequence Organization and Developmental Representation of Cloned Poly(A) RNAs from Sea Urchin Eggs" *Journal of Molecular Biology,* In Press. J.W. Posakony, C.N. Flytzanis, R.J. Britten, E.J. Davidson** (Gary Mockli* helped with this work though not an author on the paper).

17. "Sputtering of SO_2 by High Energy Ions", *Radiation Effects,* To be Published in 1983. D.J. LePoire*, B.H. Cooper, C.L. Melcher, T.A. Tombrello**.

18. "Two-Phase Gravitational Instabilities in Thin Disks with Application to the Origin of the Moon", To be published in *Lunar & Planetary Science Abstracts,* XIV (1983). A.C. Thompson*, D.J. Stevenson**.

19. "Study of Ni-Nb System by Ion Mixing," Submitted to *physica status solidi (a).* K.T. Kung*, B.X. Liu, M-A. Nicolet**.

20. "Electrical Characteristics of Amorphous Iron-Tungsten Contacts on Silicon" *Applied Physics Letters 42* (11). M. Finetti, E. T-S. Pan*, I. Suni, M-A. Nicolet**.

21. "Rapid Grain Flow in a Vertical Chamber", in preparation, K. Hui*, P. Haff**.

22. "A Possible Phase Transition in $(Zr_2Ni)_{1-x}B_x$ Metallic Glasses" To be submitted to *J Non-Cryst Solids,* A.Y.L. Mak*, W.L. Johnson**.

23. "Atomic Level Populations in the Hollow Cathode Discharge", To be submitted to *Journal of Quantitative Spectroscopy,* J.N. Humphrey*, D.L. Adams, W. Whaling**.

24. "Shock Wave Consolidation of an Amorphous Alloy", Proc. of Liquid Amorphous Metals V, August 15-19, 1983, UCLA, P. Kasiraj, D. Kostka*, T. Vreeland, Jr.**, and T.J. Ahrens.

25. "Isolation of New Yeast DNA Replicaton Mutants Using Permeabilized Cells", Proc. Natl. Acad. Sci., *80,* in press, C-L Kuo, N-H Huang*, J.L. Campbell**.

26. "Suppressors of a Temperature-Sensitive Copy-Number Mutation in Plasmid NTP1", Molec. Gen. Genet., in press, D.R. Moser, C.D. Moser, E. Sinn*, J.L. Campbell**.

27. "Beta Decay Phenomenology of Nuclear Fission Products", submitted to *Nuclear Physics A,* J.A. Behr* and P. Vogel**.

28. "X-Ray, Radio, and Infrared Observations of the 'Rapid Burster' (MSB 1730-335) During 1979 and 1980", *The Astrophysical Journal, 267*:301-309, April 1, 1983, R. Pogge*, (worked with G. Neugebauer**).

29. "Formation of the Galilean Satellites in a Gaseous Nebula", *ICARUS, 52,* 14-39 (1982), J. Lunine*

30. "The Relative Timing of Microwaves and Hard X-Rays in Solar Flares", *The Astrophysical Journal,* 279, 875-81, April 15, 1984, M.E. Cornell* (worked with H. Zirin**), G.J. Hurford, A.L. Kiplinger, B.R. Dennis

31. "Assesing Constituency Involvement: The Hemel Hempstead Experience", *Parliamentary Affairs,* Vol 35, No. 1, Winter, 1982, D.B. Ritchie*, B.E. Cain**.

i "Atomic Level Populations in the Hollow Cathode Discharge", *J. Quant. Spectrosc. Radiat. Transfer,* Vol. 31, No. 1, pp. 1-5, 1984, J.N. Humphrey*, D.L. Adams, W. Whaling**.

33. "Hemispheric Differences in Split-Brain Monkeys Viewing and Responding to Videotape Recordings", submitted to *Behavioral and Neural Biology,* C.K. Ifune*, B.A. Vermeire, C.R.Hamilton**.

34. "Beta-Decay Phenomenology of Nuclear Fission Products", *Nuclear Physics,* A411 (1983) 199-208, J.A. Behr* and P. Vogel**.

35. "Study of Charge Asymmetry in the Reaction $e^+ + e^- \rightarrow \mu^+ + \mu^-$ with the Forward Counters of the Mark J. Detector at Petra", *The Journal of Undergraduate Reseach in Physics*, Vol. III, No. 1, T.L. Kwok* (H. Newman**).

* - SURF student
** - Faculty Sponsor

APPENDIX A

June 1984

Dear Surfer:

In a letter received from Dr. Fred Shair, Chairman, SURF Committee, Caltech, he suggest the topic "Personal Leadership in an organization" for our discussion on June 13, 1984.

It could be mentioned that leadership is little more than the use of organized common sense in the solution of problems that are as a rule simple and ordinary, but important! Unfortunately, the subject is more complex and many significant questions which inevitably are raised cannot be answered in one, short meeting.

We can start the meeting with the subject of leadership and state that its role in an organization is also dependent upon the discipline of scientific thoroughness and precision, of meticulous regard for facts. "If you do not get the facts, the facts will get you!"

Successful leadership usually indicates the development of a performing team over a long period of time. The fundamental principle is to develop the capacity to take awkward, cumbersome, organizations and transform them into highly, co-ordinated, dynamic, mechanisms that prove productive to society and to all individuals concerned with the operation.

It is suggested that to take a highly, complicated organization and control the human variables within or skilfully guide the operation itself through a maze of outside forces, requires effective participation by the leader. The title for today's discussion could be: "Don't hold the lantern while you mother chops the wood." One might add that no Olymic Medals are awarded to those on the sidelines! It is respectfully submitted for your consideration that success is directly proportional to the degree of effective participation by all interested and concerned parties. Your participation at this meeting is most cordially invited and your imput is important to to all members present.

In order to start our discussions on a realistic basis, let's agree that leadership is earned by hard work, under stress conditions and that one should not expect outside "gifts" while practicing their art.

A very logical question is whether one who seeks leadership in a certain discipline can reasonably anticipate a sense of achievement, a contribution to society, obtain financial security, maintain health and have fun in a rapid growing and changing society.

Some of us who are old in the service and have struggled through problems faced in leadership, would acknowledge the above question with an affirmative position in all respects.

Since we have discussed participation as one of the prime factors in leadership development, one major consideration that requires consideration is the quality of the organization that may attract the attention of a potential and developing leader. It is well to remember that in making a selection of an organization, it is similar to getting on an elevator, it is as easy to press the "Up" button as the "Down" button.!

It would appear prudent for a potential leader of an organization of his or her choice, to study the particular operation with the certain relevant factors in mind. Your studies will hold you in a very enviable position as the ability to do scientific work is largely the ability to formulate a problem in specific terms. A faulty definition of any problem can result in wasted effort, the collection of irrelevant facts, the failure even to see vital facts and often the wrong methods of analysis and measurement.

It is respectfully suggested that once you have established your career goals, it may prove prudent, to study the organization with the following factors in mind:

a. The efficiency of the organization as it is presently operated.

b. Its adequacy in the light of organizational needs met and unmet.

c. The changes, if any, which should be made in it.

d. Its ability to compete over a long period of time.

e. The quality of leadership.

In the form of a question, the statement would read: How effective is the operation functioning? In light of existing operational needs, what is it doing it should continue to do, modify, or abandon and what is it not doing that it should undertake. Has the organization failed to keep pace with changing conditions and opportunities. Can you accept a position in good faith and perform as a leader under the conditions in which the above questions have defined a corporate profile?

It should be recognized that every leader of an organization is faced with the necessity of making major efforts towards measuring the accomplishments of their operation and plan the means whereby they may better clarify corporate goals, resulting in an improvement in the adequacy and efficiency of the

operation. Your association with professional leaders of stature, is most significant in your career as a person and a leader. Remember that "Birds of a feather tend to develop the same type of plumage."

One can conclude that any organization that you select to serve as a leader, should demonstrate the highests ethics, integrity, performance, an ability to compete, with a high morale in which their is a strong loyalty toward shared objectives, and a sense of mutual pride in accomplishments. There is nothing wrong in being a "tough" buyer!

As you complete your analysis of an organization in which you are considering becoming a leader in it's operation, it is critcal that all major factors have been thoroughly understood and that no unknown factors exists that would substantially change your career decisions.

A summary of a few "bench marks" may prove helpful and are listed as follows:

a. Formulate your "Career Questions" in specific terms.

b. Certain that your facts are valid and relevant.

c. Place emphasis on the quality of the staff as it is the most delicate part of any operating mechanism.

d. Where certain factors are largely matters of opinion, be careful to recognize that condition; and, formulate your conclusions based on facts only if there is sufficient factual data to justify it.

e. Avoid hasty judgement and wait until all the facts are available.

f. In making your interpretations, give most weight to data having the highest reliability.

g. Be on guard against rationalization as a means of forcing recalcitrant facts into conformity to some apparent trend. (The president of an organization can be a very strong salesmen!)

h. Submit your interpretations and tentative career decision to others, qualified to counsel and in a position to be acquainted with the opportunities that are being evaluated.

i. Make it a point of honor to give careful thought to

contrary opinion.

j. In your final analysis, formulate your interpretations as simply and clearly as possible with frequent and precise reference to supporting or contradictory data.

The above points have been submitted for your consideration in attempting to bring forth that facts or opinions you have obtained, may become a matter of conviction and form the basis of action, resulting in a career of your choice.

Now for a brief focus of our attention on certain fundamentals of leadership. Cicero said: "The eloquence of speech is brevity." Perhaps, he was not asked to comment on the salient factors, essential to sound corporate leadership!

For purposes of clarification, the subject of leadership will be limited to the area of those significant fundamentals that are essential for long term leadership performance. The factors listed will be the basis for our discussion.

The first step in leadership is a venture of faith, with inspired enthusiam against a known goal and a capacity to over-come major obstacles. Embarking on a new experience in leadership must take into account two well-recognized factors. They are: (1) Strengths and (2) Responsibility. Strength would be defined as the ability to chose the right aim and pursue that aim responsibly over a long period of time. Responsibility would be defined in such terms in which individuals speaks and acts as if they were accountable to all who may be affected by their thoughts, words or deeds.

Once you have ventured on the pathway of leadership, you must determine your goals and where you want to go. Keep your vision ever before you because dreams are important. Where there is no vision, individuals parish. Work your insights and hunches and make yourself a "Discoverer."

One of the requirements of outstanding leaders is their recognition that it is more important to have a "higher standard of thinking" than to enjoy a "higher standard of living." The accumulation of wealth, while it has it's merits, is no substitute for the true attainment of life's goals.

With a clear perspective regarding the demands of leadership, it becomes obvious that achievement in any profession is an " inch by inch' struggle and requires total commitment and an uncommon persistence.

A good leader in his game plan, has learned to have a "ready reserve" when the going gets tough. If leaders play their game to the edge of their mental and physical strengths, they will find a condition that will limit life's many offerings.

While the leadership standards that have been suggested may appear discouragingly high, any quality of leadership must be evaluated on three major premises. They are: (11) Integrity; (2) Knowledge of subject; and, (3) Performance. It is unmistakably clear that integrity is not a value that can be compromised in management. The leader is honest or dishonest and there is no "grey" area. In other words, " never deal with a man you cannot trust!" The knowledge required to successfully lead an organization is essential for long term success. This factor can be enhanced by additional training as may be required in certain disciplines. Performance is the value required of every leader. It is doubtful if any organization can be effectively established or capable of avoiding the weakness of prior years or conserve the wisdom of advancing years without total recognition of the significant role as relates to the values of Integrity, Knowledge of the subject, and Performance of its leaders.

It is proposed that a strong leader has developed certain insights into the art of human relations. The corporate leader has learned early in his profession to select capable members of his staff and assists them in their performance under well defined functions and organizational structure.

A "Laundry List" of leadership values is respectfully submitted for your consideration. This by no means exhausts the list!

a. Goals. Select goals wisely with a sense of realism.

b. Plans. Set up a definite plan of action - be specific. Leadership is similar to taking a sail boat safely out of the harbor. i.e. It is a matter of "tacking" from point to point, avoiding the "rocks and shoals" and then enjoying the "Blue" water.

c. Quality. Performance is the name of the game and this value can only be achieved by a commitment to providing the highest quality of product or service.

d. Control. Whether it be an art or scientific approach to the matter of organizational controls, this area of leadership is essential for success.

e. Participation. A requirement for all members of the team but the leader must be "out in front."

f. Evaluation. Perhaps the weakest factor in leadership! Constantly monitoring performance and taking corrective action is written on the "Scoreboard" as to whether you have won or lost the game.

g. Appreciation. Recognition and appreciation expressed for a "Job Well Done" is a critical factor in the development of a strong, sound team. "You cannot grow oranges in a cold climate!"

h. Communication. Learn to communicate at all levels of the organization. Be an exceptional listener!

i. Patience. Worthy projects take time. Things which go up fast also contain the elements to rapidly drop!

j. Problem Solving. A leader must develop the skills related to problem solving.

k. Decisions. Learn to make good decisions in a reasonable time. There are seldom all the facts necessary to provide complete assurance that the correct decision has been realized. It is the professional leader that has developed skills in which good decisions are constantly made with only limited data available.

m. Doctrines. Be wary of false doctrines as they can drain your strength and health. i.e. "Keeping up with the Jones."

n. Health. If your mind is to maintain a sharp edge, it requires a life long program of proper diet, rest, exercise, training in one's discipline, recreation, mental and spiritual development.

o. Creative. Be an innovator as a basic qualification for leadership. " Do not plan to trod thru life in the footsteps of others!"

p. Emotional stability. Limit you destructive analysis to metal components and systems; never allow destructive analysis to apply to yourself.

q. Moderation. Be cautious when it involves playing the the extreme positions in a game. Performance required that is based on "beyond the state of the art" can make life miserable for the leader and organization.

r. Association. Participate in professional societies and maintain a life long association with Caltech.

s. Time. Time is of essence and cannot be expended on insignificant matters.

t. Attitude. The attitude of a leader is a most contagious factor in an organization. Keep it positive and along constructive lines.

u. Forgivness. If an associate makes a mistake, the leader must move forward without hostility.

v. Meditation. Learn how to control the "signal to noise ratio" in the maze of organizational demands surrounding the leader. This is a solo operation in a quiet spot, allowing the mind to relax and study the problem. If you sit on a rock, people may think you are around the bend! However, if you sit on a rock with a fishing pole, you are then considered a sportsman! (Of course, in the latter case, it is preferable to be near water!)

w. Counsel. Share your thoughts with some person you trust, who is experienced and has your interest at heart.

x. Courage. It takes courage to make a significant contribution by any organization in a competitive world. Study your risks and take resolute action!

y. Appearance. Be yourself at all times. "Phony" leadership seldom lasts over an extended period. The professional scouts in the bleachers, are the ones who count and recognize the real ball player!

z. Assignments. If you are going to be a leader, don't start by" carrying soneone's hat."

The above thoughts on "Personal Leadership in an Organization" are submitted as points of philosophy on leadership training. It is hoped that upon your review of the material, helpful hints have been listed that will contribute to a sense of leadership accomplishment in the years ahead.

The future for each of you is so vast in challenges and achievement that each will be recognized for their respective contributions to mankind. In terms of professional leadership, each will experience a sense of personal satisfaction and achievement when viewed from a command postion in the future.

We would like to acknowledge with gratitude the assistance of Dr. Fredrick H. Shair, Mr. Edward Baum and Mr. Samuel P Krown,

SURF Committee and the Administration and Faculty who have contributed towards the establishment and development of the Surf program.

Cordially,

Robert L. Shafer

Certified Management Consultant
Senior Associate, Institute of
Management Consultants.

7/84 SURF LECTURE: MAIN TECHNIQUES OF SEMINAR PRESENTATION
by Thomas R. McDonough

1. Eye contact. Always look at the audience when possible.
2. Voice: SPEAK UP! (Unless there is a microphone.) Avoid a monotone.
3. Language:
(a) Body. Use occasional, smooth gestures; avoid stiffness and nervous, meaningless motions. Don't play with chalk, pen, pointer, etc. Don't lean on the table or blackboard. Wear a suit.
(b) Verbal.
(i) Use good grammar and enunciation, avoid excessive slang, avoid "uh," "gonna," "you know," "kind of," "sort of," "OK."
(ii) Always consider your audience: A general audience can't understand jargon. Put things as simple as reasonably possible.
(iii) Don't advertise your failings, e.g., by saying, "I'm sorry," or "I don't know."
(iv) People with strong accents: Put. A. Little. Pause. Between. Each. Word. And. Speak. Loud.
4. Organization: Be sure to prepare an introduction and a conclusion. The conclusion should remind the audience of the most important points. Rehearse the introduction and conclusion thoroughly.
5. Visual aids: Use them if possible, plan their use carefully, and use them instead of notes. Face the audience whenever you can. Check out the room, light switch, blackboard, projector, microphone, pointer, etc. ahead of time. Run all your slides through the projector if possible, to verify that they are in correct order and not backwards or upside down. Make sure the projectionist knows the proper sequence and orientation of the slides. Use a pointer. Use color to simplify complex diagrams. Don't block the board or screen with your body. Remember Murphy's Law: Anything that can go wrong, will.
6. ENTHUSIASM! Create the impression that you are really interested in the subject. Remember "Dr. George" (meteorologist) and Richard Feynman. Also, humor is good, in moderation.

REFERENCES (with Caltech library number, when I have it)

Connolly: "Effective Technical Presentations" (PN 4121 C6, 1968)
Dietrich & Brooks: "Practical Speaking for the Technical Man" (PN 4121 D533, 1958)
Loney: "Briefing and Conference Techniques" (PN 4121 L645, 1959)
Mambert: "Presenting Technical Ideas, A Guide to Audience Communication"
Wilcox: "Oral Reporting in Business and Industry" (PN 4121 W385, 1967)
Springer, S.P., and Deutsch, G.: "Left Brain, Right Brain," W.H. Freeman, San Francisco, 1981 (quality paperback; no practical advice, but it helps you understand the mechanisms of the brain that you are trying to stimulate).
Walters, Barbara: "How to Talk With Practically Anybody About Practically Anything" (inexpensive paperback; possibly out of print; very good tips on the art of conversation).
Kodak: They publish several good paperback books on making slides and on running sophisticated slide shows (e.g., with multiple projectors and synchronized tape recordings). See any photo store. A good one is "Planning and Producing Slide Programs" (#S-30, $6.95).
Molloy, J.T.: "Dress for Success"; "The Woman's Dress for Success." (Well-researched studies of the best clothes to wear to impress others. Main conclusion: Wear dark gray or dark blue conservative suits. Both books are in quality paperback; the first is also in inexpensive paperback.)

TO LEARN MORE: Take Ch 90, Ge 102 or my E10; or join the JPL/Caltech Toastmasters Club. To visit the club, which meets at JPL, call Mark Bassett (797-0794, days). If you move out of this area, you can find the location of the nearest such club by writing to Toastmasters International, 2200 N. Grand Ave., P.O. Box 10400, Santa Ana, CA 92711.